Damage-Free Seismic-Resistant Self-Centering Concentrically-Braced Frames

by

David Alan Roke

Presented to the Graduate and Research Committee
of Lehigh University
in Candidacy for the Degree of
Doctor of Philosophy

in

Structural Engineering

Lehigh University

September 2010

ProQuest LLC
789 East Eisenhower Parkway
P.O. Box 1346
Ann Arbor, MI 48106-1346

Approved and recommended for acceptance as a dissertation in partial fulfillment of the requirements for the degree of Doctor of Philosophy.

_____
Date

_____
Dr. James Ricles
Dissertation Co-advisor

_____
Dr. Richard Sause
Dissertation Co-advisor

_____
Accepted Date

Committee Members:

_____
Dr. John L. Wilson
Committee Chair

_____
Dr. Le-Wu Lu
Member

_____
Dr. Constantin Christopolous
External Member

_____
Dr. Robert Tremblay
External Member

ACKNOWLEDGEMENTS

The research presented in this dissertation was conducted at the Engineering Research Center for Advanced Technology for Large Structural Systems (ATLSS), Department of Civil and Environmental Engineering, Lehigh University, Bethlehem, Pennsylvania. During the study, the chairmanship of the department was held by Dr. Stephen P. Pessiki.

The author would like to thank his research advisors, Dr. James M. Ricles and Dr. Richard Sause, for their guidance, direction, patience, and advice. The author would also like to thank Dr. John L. Wilson, the chair of his research committee, for his advice and input. The author appreciates the time and contributions of his other committee members, Dr. Le-Wu Lu, Dr. Constantin Christopoulos, and Dr. Robert Tremblay.

The author would like to thank the following people for their contributions to his research: the laboratory staff, particularly John Hoffner, Dave Altemus, Todd Anthony, Joe Cheszar, Joe Griffiths, Russ Longenbach, and Roger Moyer; the ATLSS staff, particularly Peter Bryan, Betty MacAdam, Tommy Marullo, and Gary Novak; and fellow researchers, particularly Dr. Choung-Yeol Seo, Brent Chancellor, and Nate Gonner. The author would also like to thank his fellow students at Lehigh who helped him get through rough patches in his work; particularly Nicole Leo Braxtan and Cheng Chen.

This research was supported by the National Science Foundation, AISC, and PITA. Funding was also provided through the Gibson Fellowship and the G.W. Harris Fellowship.

The author would like to extend his deepest thanks to his family and friends who have offered support. The author extends special thanks to his parents, who have been his most steady supporters since he first left for college more than a decade ago. Most of all, the author is extremely thankful for the help, support, patience, and love of his wonderful wife Meg and his beautiful daughter Emma. This dissertation is for them.

TABLE OF CONTENTS

LIST OF TABLES

LIST OF FIGURES

ABSTRACT

A self-centering concentrically-braced frame (SC-CBF) system was developed to resist earthquake loading without structural damage or residual drift. An SC-CBF is a concentrically-braced frame with column base details that permit column uplift at a specified level of lateral force. This column uplift and the subsequent rocking of the SC-CBF soften the lateral force-lateral drift behavior of the system. Vertically-oriented post-tensioning bars provide restoring force and self-centering behavior that reduces the potential for residual drift. The SC-CBF members are designed to remain elastic under the design basis earthquake. Energy dissipation elements can be used to reduce the response of the SC-CBF system.

The scope of this study includes the development of a design procedure for SC-CBF systems, a parametric study of different SC-CBF configurations, analytical and experimental studies of a large-scale SC-CBF test structure, and evaluation of the performance of the SC-CBF test structure.

A performance-based design procedure and the associated design criteria were developed for SC-CBF systems. Nonlinear dynamic analyses of several 6-story prototype buildings with different SC-CBF configurations were performed to establish the lateral force behavior of the system and to study the influence of several design parameters on this behavior. An analytical model was developed to predict the earthquake response of SC-CBF systems. Hybrid simulations of the earthquake response of a large-scale SC-CBF

test structure were performed to validate the analytical model. The seismic performance of the SC-CBF test structure was evaluated with respect to the performance-based design approach and criteria.

The results of this study indicate that the SC-CBF system performs very well under earthquake loading, and that the SC-CBF is a viable alternative to conventional CBF systems. The softening of the lateral force-lateral drift response of the system was due exclusively to the column uplift behavior; the beams, columns, and braces of the SC-CBF remained elastic. The performance of the SC-CBF test structure satisfied the performance-based design objectives and criteria.

The analytical and experimental results presented in this dissertation show that the performance of the SC-CBF systems can be designed to achieve reliable damage-free performance under the design basis earthquake. The probability of structural damage and residual drift under the design basis earthquake is low. The proposed performance-based design procedure and associated design criteria provide conservative estimates of design demands and provide excellent overall performance. The analytical model developed by this research provides accurate estimates of the earthquake response of SC-CBF systems.

CHAPTER 1

INTRODUCTION

1.1 Overview

Buildings with conventional lateral force resisting systems are designed to protect their occupants during earthquakes. The building is expected to be damaged by the earthquake but should not collapse. The damage is expected to be repairable, but these repairs may not be economically feasible. In current practice, it is considered impractical to design a building with a conventional lateral force resisting system to sustain no damage under the design basis earthquake. This research is developing an alternative lateral force resisting system that is intended to be damage free under the design basis earthquake.

Conventional concentrically-braced frame (CBF) systems are a commonly used lateral force resisting system. These systems are economical and have excellent stiffness; however, CBFs have a low lateral drift capacity before serious damage of the main structural members initiates. Under the design level earthquake, CBFs are expected to undergo drift demands that will yield or buckle the braces. This damage leads to residual lateral drift after the earthquake.

Avoiding residual lateral drift is a critical aspect of reducing post-earthquake social and economic disruption. Miranda (2009) has found that many building losses during

earthquakes are associated with residual lateral drift from structural damage, rather than collapse. The damage that causes the residual drift may be repairable, but since the damage and residual drift render the building temporarily unfit for use, it is often more economical to demolish rather than repair the building.

Buckling-restrained braced frames (BRBFs) have been developed to increase the lateral drift at which CBFs sustain serious damage to the main structural members (e.g., Fahnestock et al. 2007a, 2007b). However, BRBFs also exhibit residual lateral drift, as illustrated in Figure 1.1, which shows the floor displacement histories for a four-story BRBF system under a maximum considered earthquake (MCE) level ground motion.

Self-centering concentrically-braced frame (SC-CBF) systems are being developed to maintain the advantages of conventional CBFs, economy and stiffness, while increasing the lateral drift capacity before structural damage initiates and reducing the residual lateral drift (Roke et al. 2006). These systems have vertically-oriented post-tensioning (PT) bars that provide restoring forces and self-centering behavior, which reduces the potential for residual drift. The SC-CBF members are designed to remain elastic under the design basis earthquake.

This research on SC-CBFs is part of a project on self-centering earthquake-resistant steel frame systems funded by the National Science Foundation (NSF) George E. Brown, Jr. Network for Earthquake Engineering Simulation Research (NEESR) program. The project includes experiments on a large-scale SC-CBF test structure at the Real-Time

Multi-Directional (RTMD) Earthquake Simulation Facility located at the Advanced Technology for Large Structural Systems (ATLSS) Center at Lehigh University.

Previous research on self-centering structural systems, also performed at the ATLSS Center, includes work on precast concrete systems and steel moment-resisting frame systems. This previous research has indicated that self-centering systems can be designed to perform as intended with reduced damage and residual drift relative to conventional structural systems.

Self-centering systems are a relatively new structural engineering concept. As such, additional research, both analytical and experimental, is necessary. The purpose of the research discussed in this dissertation is to establish the SC-CBF as a viable lateral force resisting system for earthquake-resistant buildings. Analytical and experimental studies are included to establish the SC-CBF system performance and to develop SC-CBF design criteria.

1.2 Research Objectives

The overall objectives of this research program are to develop the SC-CBF system and to provide a probabilistic performance-based design procedure for the SC-CBF system that achieves reliable damage-free performance under the design basis earthquake. The specific objectives necessary to achieve the overall objectives are the following:

1. To establish the desired lateral force behavior of the SC-CBF system, including specific limit states that may occur under earthquake loading;

2. To develop performance-based design (PBD) objectives, criteria, and procedures for the SC-CBF system to control the occurrence of these limit states;

3. To study the advantages and disadvantages of different SC-CBF configurations;

4. To develop a nonlinear analytical model to simulate the earthquake response of SC-CBF systems;

5. To validate this analytical model through comparisons with experimental results from earthquake simulations on a large-scale SC-CBF test structure;

6. To validate the PBD procedure for SC-CBF systems and demonstrate that a properly-designed SC-CBF system can be a superior earthquake-resistant structural system.

1.3 Research Scope

To achieve the research objectives, ten research tasks were undertaken. These tasks are:

1. Determine desired lateral force behavior for the SC-CBF system and identify structural limit states. The SC-CBF system is intended to achieve reliable damage-free response to the design basis earthquake; therefore, a softening of the lateral force-lateral drift behavior of the SC-CBF system must occur from nonlinearity without member yielding. Structural limit states in the lateral force behavior of an SC-CBF system are identified.

2. Develop PBD criteria for the SC-CBF system. PBD objectives are developed by determining the earthquake input levels at which each limit state is permitted to occur. PBD criteria are developed for selected limit states based on estimated probabilities of dynamic responses exceeding the design demands.

3. Develop PBD procedure for the SC-CBF system. A probabilistic design procedure is proposed that considers the PBD criteria for the SC-CBF system.

4. Investigate seismic response of different SC-CBF frame configurations. Six-story SC-CBFs with a variety of configurations are designed for a prototype building. Nonlinear static and dynamic analyses are performed to validate the behavior of the SC-CBF system and to study the effect of the different frame configurations. The response of the SC-CBF system is evaluated with respect to the PBD criteria established for the system.

5. Develop an analytical model for SC-CBF systems. A detailed nonlinear analytical model is created in OpenSEES (Mazzoni et al. 2009) to represent the SC-CBF system. The main components of the model are the SC-CBF, the adjacent gravity columns, the basement substructure, and the lean-on column, which is used to account for P-Δ effects on the SC-CBF system.

6. Perform laboratory experiments on an SC-CBF test structure. A large-scale SC-CBF test structure was designed by Gonner (2009), following a PBD procedure similar to the one outlined in this research. Hybrid simulations are

performed to investigate the seismic response of the SC-CBF test structure in the laboratory. These hybrid simulations are performed using ground motion input at three seismic input levels: the design basis earthquake (DBE) level, the maximum considered earthquake (MCE) level, and the extreme MCE level.

7. Perform nonlinear dynamic analysis using an analytical model of the SC-CBF test structure. The nonlinear analytical model developed for the SC-CBF system is applied to the SC-CBF test structure. The boundary conditions of the analytical model are calibrated based on the boundary conditions in the laboratory. Nonlinear dynamic analyses are performed to determine the response of the SC-CBF test structure under DBE-level, MCE-level, and extreme MCE-level ground motions.

8. Compare analytical and experimental results. To validate the analytical model of the SC-CBF test structure, a comparison of the analytical results and the experimental results from the hybrid simulations is performed. Two analytical models are considered in this research: a predictive (general) model, and a calibrated model for which the initial conditions of the model (e.g., initial force in the PT bars) are calibrated to the conditions in the laboratory.

9. Assess the seismic performance of the SC-CBF test structure. The SC-CBF test structure response from the nonlinear dynamic analyses is compared to the design performance objectives for the SC-CBF system. The probability of the

dynamic response exceeding the factored design demands is assessed for selected structural limit states. Response quantities that affect nonstructural systems are also considered.

10. Validate the SC-CBF design procedure and develop recommendations for improvement. The PBD procedure and criteria for the SC-CBF system developed by this research are a first attempt at a probabilistic design approach to control the seismic performance of the SC-CBF system. The assessment of the performance of the SC-CBF test structure provides a basis for suggesting improvements to the PBD procedure.

1.4 Organization of Dissertation

The remaining chapters of this dissertation are organized as follows:

- Chapter 2 discusses previous research related to the SC-CBF system.
- Chapter 3 introduces the intended behavior of an SC-CBF under lateral loading, including limit states that are expected to occur.
- Chapter 4 describes the PBD objectives for the SC-CBF system. The structural limit states are associated with performance levels. Relationships between these performance levels and two levels of earthquake input (DBE and MCE) are presented in this chapter.
- Chapter 5 discusses a configuration study on the SC-CBF system. The configuration study is used to demonstrate the lateral force behavior of the SC-

CBF system and to determine the effect of changing several overall system layout parameters on the earthquake response of the system.

- Chapter 6 discusses the estimation of design demands for the SC-CBF system. These design demands are determined probabilistically; a certain probability of the response exceeding the design demands is established. The consequences of the response exceeding the design demand for each limit state are considered in establishing an acceptable probability of the response exceeding the design demands.
- Chapter 7 presents a probabilistic PBD procedure for the SC-CBF system based on the PBD objectives discussed in Chapter 4 and the estimated design demands discussed in Chapter 6.
- Chapter 8 discusses the SC-CBF test structure that was designed according to the PBD procedure (Gonner 2009), and compares the design calculations for two different SC-CBF configurations. The geometry and components of the SC-CBF test structure are discussed. Details of the analytical model and how the elements and boundary conditions are calibrated to laboratory conditions are also discussed.
- Chapter 9 presents predictions of the dynamic response of the SC-CBF test structure to DBE-level, MCE-level, and xMCE-level ground motions. From these results, a set of ground motions were selected for conducting laboratory hybrid earthquake simulations.

- Chapter 10 discusses results of laboratory hybrid earthquake simulations on the SC-CBF test structure and the correlation of the results with the predictions presented in Chapter 9, which are based on nominal values for selected structural parameters (e.g., initial force in the PT bars).
- Chapter 11 presents the correlation of the results of laboratory hybrid earthquake simulations on the SC-CBF test structure with results from a calibrated nonlinear analytical model. Selected structural parameters (e.g., initial force in the PT bars) are calibrated in the model to more accurately reflect test-specific laboratory conditions.
- Chapter 12 evaluates the performance of the SC-CBF system with respect to the PBD objectives discussed in Chapter 4 and the PBD criteria discussed in Chapters 6 and 7.
- Chapter 13 summarizes the research program and offers conclusions and recommendations for future research.

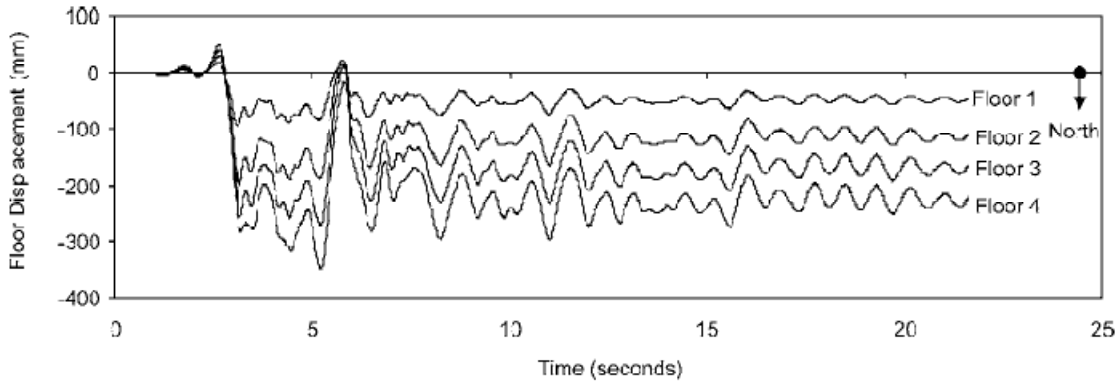

Figure 1.1 – Floor displacement response for MCE simulation of a four-story BRBF test structure (Fahnestock et al. 2007b)

CHAPTER 2

RELEVANT PRIOR RESEARCH

Self-centering (SC) lateral force resisting systems are a recent development in earthquake-resistant structural systems. SC systems are intended to sustain less structural damage and residual drift than conventional structural systems under severe earthquakes, while maintaining the strength and stiffness of conventional structural systems.

SC systems differ from conventional structural systems in that critical connections in SC systems are prestressed (post-tensioned) and are designed to decompress at a specific level of earthquake loading. After decompression, a gap opens between the elements at those connections. The post-tensioning provides a restoring force to return the connection to its closed state after an earthquake (i.e., providing self-centering). Decompression and gap opening causes softening of the lateral force-lateral drift response of the SC system without damaging the structural members. Energy dissipation elements that are deformed by the gap opening behavior are often included in the system to reduce the seismic response of the system.

In this chapter, results of recent research related to the development of self-centering concentrically-braced frames (SC-CBFs) are considered. These research results are organized into six topics: (1) unbonded post-tensioned precast concrete shear wall systems, (2) the peak base shear demand in concrete shear walls, (3) unbonded post-

tensioned precast concrete moment-resisting frames (MRFs), (4) steel SC post-tensioned MRFs (SC-MRFs), (5) steel SC-CBFs, and (6) peak ductility demands for SC systems.

Research on SC systems began with studies of unbonded post-tensioned precast concrete shear walls and unbonded post-tensioned precast concrete MRFs for buildings. Unbonded post-tensioned precast concrete walls have joints at the base that permit uplift and rocking at the base, which soften the base shear-roof drift response. Vertically-oriented post-tensioning returns the system to its initial position. The behavior of the unbonded post-tensioned precast concrete wall systems is very similar to that of the SC-CBF system.

Unbonded post-tensioned precast concrete MRFs have post-tensioned connections between the beams and columns that decompress and open at the beam-to-column interface under earthquake loading. Unbonded post-tensioned concrete MRFs are not discussed in this chapter, as they are not relevant to the development of steel SC-CBFs.

Steel SC-MRFs have post-tensioned connections between the beams and columns. These connections decompress and open under earthquake loading, similar to precast concrete MRFs. Several types of SC-MRFs are discussed here. These systems have different elements near the connections between the beams and the columns, in parallel with the post-tensioned connections, to dissipate energy when the connections open.

SC-CBF systems have been developed by combining the concepts of post-tensioned concrete shear walls (i.e., gap opening at the base of the structure) with those of the steel

SC-MRFs (i.e., post-tensioned steel connections). Results of several investigations related to SC-CBFs are presented in this chapter.

The response of SC systems to seismic input is different from that of conventional structural system. Previous research on the ductility demands for SC systems is also summarized in this chapter.

2.1 Review of Research Related to the SC-CBF System

2.1.1 Unbonded Post-Tensioned Precast Concrete Shear Walls

An unbonded post-tensioned precast concrete shear wall is a lateral force resisting system that exhibits similar behavior to the SC-CBF system proposed in this dissertation. Kurama et al. (1999a, 1999b) introduced the behavior and design concepts for unbonded post-tensioned precast concrete walls. Unbonded post-tensioned precast concrete walls were developed with the goal of reducing the earthquake-induced damage that occurs in conventional cast-in-place concrete walls and in precast walls designed to emulate cast-in-place walls.

Unbonded post-tensioned precast concrete walls are constructed by post-tensioning precast wall panels across horizontal joints (Kurama et al. 1999a). Figure 2.1 shows a schematic of an unbonded post-tensioned precast concrete wall. The horizontal joints and unbonded post-tensioning in the system permit opening of gaps between panels and subsequent rocking of the wall panels. Figure 2.2 shows a schematic of the two modes of behavior of the system: gap opening (with panel rocking) and shear slip. Gap opening is the desired mode of response, and is resisted by the gravity loads in the wall panels and

the vertical post-tensioning force, which tend to close the gaps at the joints upon unloading. Shear slip is an undesirable mode of response because it leads to permanent drift.

The base shear-roof drift behavior of an unbonded post-tensioned precast wall, based on gap opening behavior, is shown schematically in Figure 2.3(a). Four limit states are identified in this figure: decompression, softening, yielding, and failure. The decompression limit state is the condition at which the gap opening initiates along the horizontal joint between the wall and the foundation. Softening is the beginning of a significant reduction in the lateral stiffness of the wall due to the gap opening response and nonlinear behavior in the wall panels. Yielding is the point at which the post-tensioning steel reaches its yield strain. The failure limit state is reached when crushing of the concrete at the base of the wall causes axial-flexural failure of the wall.

Figure 2.3(b) shows the hysteretic behavior of an unbonded post-tensioned precast concrete wall under cyclic lateral load. These results are from a nonlinear analytical model described by Kurama et al. (1999b). The limit states of softening, yielding, and failure are indicated in the figure. The hysteresis loops for this system dissipate less energy than those for an equivalent elastic-plastic system; however, there is no residual drift after unloading prior to failure.

Kurama et al. (1999a) established performance-based design (PBD) criteria for the unbonded post-tensioned precast concrete wall system. These objectives are shown in a

schematic of base shear-roof drift response in Figure 2.4. Kurama et al. (1999a) related these performance objectives to the previously-defined limit states.

The behavior of unbonded post-tensioned precast concrete walls was validated analytically using nonlinear static pushover analyses and nonlinear dynamic analyses (Kurama et al. 1999b). From these results, which include a parametric study of nine properties that affect the response of the system, a seismic design procedure was proposed (Kurama et al. 2002). Nonlinear dynamic analyses showed that the unbonded post-tensioned precast concrete wall system is a viable alternative to conventional cast-in-place concrete wall systems in seismic regions. The gap opening response in this system is an effective way to control damage and the post-tensioning across the gap helps to self-center the system (i.e., to eliminate residual drift). The nonlinear analysis model used by Kurama et al. (1999b) was later validated with experimental results by Perez et al. (2007).

To ensure that gap opening response occurs rather than shear slip, it is necessary to ensure that the base shear capacity of the wall is greater than the demands under earthquake loading. Kurama et al. (1999a) found that the first mode response alone was insufficient to predict the peak base shear demands from dynamic analyses because the softening of the lateral force-lateral drift response of the system resulted in period elongation that increased the contribution of the higher modes to the inertia forces. Kurama et al. (1999a) cited research by Aoyama (1987) and Kabeyasawa (1987) as the basis for a base shear design demand estimate that accounts for higher mode inertia force contributions.

2.1.2 Base Shear Design Demand for Concrete Flexural Walls

Kurama (1999a) cited the report by Aoyama (1987) of studies by Kabeyasawa (1987) on pseudo-dynamic simulations of a full-scale 7-story reinforced concrete building, performed as part of a U.S.-Japan cooperative research program. This research program was intended to study the behavior of a frame building with a concrete shear wall. The behavior of the shear wall was dominated by flexure (forming a flexural hinge at the base). The simulation results indicated that nonlinear response in the structure increased the story shear and base shear demands on the test structure. Aoyama (1987) reports that Kabeyasawa used modal decomposition to develop an estimate of the base shear demands. Only mass orthogonality of the mode shapes is required for this analysis. The total restoring force vector $\{f_r(t)\}$ can be written as the sum of the first mode restoring force vector, $\{f_1(t)\}$, and the higher mode restoring force vector, $\{f_h(t)\}$:

$$\{f_r(t)\} = \{f_1(t)\} + \{f_h(t)\} \tag{2.1}$$

where, for a linear elastic response (Chopra 2007):

$$\{f_r(t)\} = \sum_{n=1}^{N} (A_n(t)) \cdot \Gamma_n \cdot [m]\{\phi_n\} \tag{2.2}$$

where,

$A_n(t)$ = the modal pseudo-acceleration of the n^{th} mode

Γ_n = the participation factor for mode n

$[m]$ = the structural mass matrix

$\{\phi_n\}$ = the mode shape for mode n

Using mass orthogonality of the modes, $\{f_n(t)\}$ can be written as:

$$\{f_n(t)\} = (A_n(t)) \cdot \Gamma_n \cdot [m]\{\phi_n\} = \frac{\{\phi_n\}^T \{f_r(t)\}}{\{\phi_n\}^T [m]\{\phi_n\}} [m]\{\phi_n\} \tag{2.3}$$

For nonlinear response, the peak response in mode n is unknown; for design, it is necessary to approximate the peak response of the higher modes (i.e., $A_{n,max} \approx \max(|A_n(t)|)$). To approximate the peak value of $\{f_h(t)\}$ for nonlinear response, $\{f_{h,max}\}$, the amplification of the higher mode response is considered by approximating the peak modal acceleration of mode n using a constant amplification factor for the higher mode response as follows:

$$A_{n,max} \approx (1 + \Delta\omega_n) \cdot \ddot{u}_{g,max} \tag{2.4}$$

where $\ddot{u}_{g,max}$ is the peak value of the ground acceleration $\ddot{u}_g(t)$.

Substituting Equation 2.4 into Equation 2.2, $\{f_{h,max}\}$ is then approximated as:

$$\{f_{h,max}\} = -[m] \sum_{n=2}^{N} \Gamma_n \cdot \{\phi_n\} \cdot (1 + \Delta\omega_n) \cdot \ddot{u}_{g,max} \tag{2.5}$$

For modes 3 through N, however, $\Delta\omega_n$ is found to be negligible (Aoyama 1987). Therefore, $\{f_{h,max}\}$ can be written as follows:

$$\{f_{h,max}\} = -[m](\{i\} - \Gamma_1 \cdot \{\phi_1\} + \Gamma_2 \cdot \{\phi_2\} \cdot \Delta\omega_2) \cdot \ddot{u}_{g,max} \tag{2.6}$$

where,

$\{i\}$ = influence vector = $\{1\ 1\ 1\ \ldots\ 1\ 1\ 1\}^{T}$ for an N-degree-of-freedom system

$[m]\cdot\{i\}\cdot \ddot{u}_g(t)$ = the total force vector, assuming no dynamic amplification

$\Gamma_1\cdot[m]\{\phi_1\}\cdot \ddot{u}_{g,max}$ = the first mode force vector, assuming no dynamic amplification

$\Gamma_2\cdot[m]\{\phi_2\}\cdot \Delta\omega_2\cdot \ddot{u}_{g,max}$ = the amplification of the second mode force vector

The first mode design base shear is determined as the static ultimate load carrying capacity under the inverted triangular loading (Aoyama 1987). The peak higher mode base shear is estimated as:

$$\begin{aligned} V_{b,h,max} &= \{i\}^T\{f_{h,max}\} = -\{i\}^T[m](\{i\}-\Gamma_1\cdot\{\phi_1\}+\Gamma_2\cdot\{\phi_2\}\cdot\Delta\omega_2)\cdot\ddot{u}_{g,max} \\ &= -D_m\cdot M_{total}\cdot\ddot{u}_{g,max} \end{aligned} \tag{2.7}$$

where the higher mode design coefficient, D_m, is (Aoyama 1987):

$$D_m = \{i\}^T[m](\{i\}-\Gamma_1\cdot\{\phi_1\}+\Gamma_2\cdot\{\phi_2\}\cdot\Delta\omega_2) \tag{2.8}$$

and,

M_{total} = total mass = $\{i\}^{T}[m]\{i\}$

A value of 0.7 is recommended for $\Delta\omega_2$, so the value of D_m ranges from 0.27 for a five-story structure to 0.30 for a nine-story structure (Aoyama 1987). The results from this method are shown to be an upper bound to the base shear demand for concrete shear wall systems.

Eberhard and Sozen (1993) used Kabeyasawa's method to estimate the peak base shear for reinforced concrete shear walls tested on a shaking table. The estimated base shear values were found to be reasonable, conservative predictions of the peak response. The recommended design base shear demand was:

$$V_k = V_n + D_m \cdot W \cdot A_e \tag{2.9}$$

where,

V_k = estimated base shear for the entire structure

V_n = base shear capacity calculated by limit analysis with a triangular force distribution (simulating first mode response)

D_m = 0.30 for medium-rise buildings

W = total weight of the structure

A_e = effective peak acceleration coefficient

2.1.3 Self-Centering Steel Moment-Resisting Frames

Early research on SC systems (e.g., Kurama et al. 1999a, 1999b, 2000) focused on concrete structural systems; however, SC systems have been adapted for use in steel structural systems. Ricles et al. (2001) introduced self-centering connections for steel moment resisting frame (MRF) systems. These connections permit gaps to open at the beam-to-column interface. Figure 2.5 shows a conventional MRF connection (Figure 2.5(a)) and a post-tensioned MRF (PT-MRF) connection (Figure 2.5(b)), as proposed by

Ricles et al. (2001). The PT-MRF connection includes top and bottom seat angles to dissipate energy. These connections provide self-centering behavior.

A schematic of the moment-rotation behavior of the PT-MRF connection is shown in Figure 2.6. The limit states indicated in the figure are: (1) decompression, (2) initiation of angle yielding, (3) full plastic yielding of the seat angles, (4) unloading, (5) yielding of post-tensioning (PT) strands, (6) reversal of seat angle yielding, (7) full plastic yielding of the seat angles, and (8) gap closure. Nonlinear analyses of a prototype structure using PT-MRF connections showed that the PT-MRF performs as intended and exceeds the performance of a typical welded MRF.

Ricles et al. (2002) performed large-scale subassembly tests of a series of PT-MRF connections with W24x62 beams. The subassembly test setup is shown in Figure 2.7. Typical PT-MRF connection response is shown in Figure 2.8. The hysteresis loops are similar to those from Kurama et al. (1999a) for unbonded post-tensioned precast concrete walls. The subassembly self-centers after unloading (i.e., there is no residual drift) even after loading to 3% drift (Ricles et al. 2002). These results indicate that gap-opening behavior at the beam-to-column interface can be used in steel connections to reduce damage and the associated residual drift of steel MRFs. PT-MRF connections require proper detailing; in particular, reinforcing plates are needed on the beam flanges, and shim plates are needed at the interface between the column flange and the beam flanges to maintain good contact between the column and the beam flanges.

Garlock et al. (2005) presented subassembly tests similar to those presented by Ricles et al. (2002). The test specimens presented by Garlock et al. (2005) had full-scale PT-MRF connections with W36x150 beam sections. Reinforcing plates and shim plates were included in the test specimens. The tests presented by Garlock et al. (2005) show that PT-MRF connections perform as intended when the beam members do not buckle and the PT steel does not yield.

Garlock et al. (2007) presented a discussion of steel PT-MRFs and the associated collector elements that connect the PT-MRF to the floor diaphragm. The gap opening response of the PT connections effectively expands the length of the MRF (along the beams), requiring flexibility in the collector elements. Additionally, Garlock et al. (2007) outlined a PBD approach for steel PT-MRF systems. The design objectives presented for the PT-MRF system are to achieve immediate occupancy (IO) performance under the design basis earthquake (DBE) and collapse prevention (CP) performance under the maximum considered earthquake (MCE), as shown in Figure 2.9. Two PT-MRF systems were designed using this PBD approach. Nonlinear dynamic analysis results suggest that further research is required on the details of the PBD approach; however, the PT-MRF connections had sufficient strength, and the design criteria for the limit states of angle fracture and strand yielding were satisfied.

Ricles et al. (2001, 2002) and Garlock et al. (2005, 2007) studied PT-MRF systems that dissipated energy through yielding of the top and bottom angles at the PT-MRF connections, as shown in Figures 2.5(b) and 2.6. The angles become damaged and may require repair. To dissipate energy in the PT-MRF connections without damaging

structural elements, friction elements were developed by Petty (1999), who investigated a friction-based lap connection to provide energy dissipation in PT-MRF connections. This lap connection used a brass shim plate bolted between two steel plates to generate a friction force. The cyclic behavior of the lap connection is shown in Figure 2.10. The coefficient of friction for the steel on brass friction surface was found to be approximately 0.45.

Rojas et al. (2005) studied a PT-MRF system with friction-based lap connections near the beam-to-column interface, similar to those studied by Petty (1999). Figure 2.11 shows a typical post-tensioned friction damped connection (PFDC). This connection uses a PFDC to dissipate energy rather than the angles used in previous studies (Ricles et al. 2001, 2002; Garlock et al. 2005, 2007). The cyclic behavior of the PT-MRF with PFDCs is shown in Figure 2.12. Comparing these hysteresis loops with those of the PT-MRF with angles for energy dissipation (Figure 2.6), the PFDC hysteresis loops are rectangular rather than rounded due to the rigid-plastic behavior of the PFDC elements. Nonlinear analysis of the PT-MRF with PFDCs (Rojas et al. 2005) showed that the system performs as intended, with minimal residual drift after an earthquake ground motion and no damage to the structural members.

One disadvantage of the PFDC is the friction element at the top flange of the beam, which conflicts with the floor slab. To eliminate this issue, Wolski (2006) developed a bottom-flange friction device (BFFD) to dissipate energy through friction in an element connected from the column to only the bottom flange of the beam. A typical PT-MRF connection with a BFFD is shown in Figure 2.13. The BFFD is oriented in the same plane

as the web of the beam in the MRF, unlike the PFDC, in which the friction element is oriented in the plane of the flanges of the beam. The orientation of the BFFD creates a larger distance between the center of rotation and the friction force, increasing the moment contribution from the BFFD and, therefore, increasing the energy dissipation. However, due to the asymmetry of this connection detail, the moment-rotation behavior of the BFFD is asymmetric, as shown in Figure 2.14. Experimental and analytical studies (Wolski 2006) show that the BFFD is a viable energy-dissipating system for a PT-MRF. However, further study of PT-MRFs with BFFDs showed that the strains in the top flange of the beams are significantly larger than those of a PT-MRF with PFDCs due to the asymmetry of the system (Iyama et al. 2009). These increased strains lead to larger beam sections or significantly longer reinforcing plates on the beam flanges, increasing the fabrication costs of a PT-MRF with BFFDs.

To eliminate the asymmetric behavior of the PT-MRF connections with BFFDs, Lin et al. (2008) developed a web friction device (WFD) for SC-MRFs, to be used with post-tensioned beam-to-column connections. Each WFD consists of a brass shim bolted through channels on each side of the web of the beam. The web of the beam has slotted holes to permit motion of the beam with respect to the channels that are fixed to the column flange. Figure 2.15 shows an SC-MRF that has post-tensioned connections with WFDs. The expected moment-rotation behavior of this system is shown in Figure 2.16. This behavior is similar to that of the PT-MRF with PFDCs (see Figure 2.12); however, the WFD does not interfere with the floor slab. Lin et al. (2008) presented experimental

data on an SC-MRF with WFDs, which show it can achieve performance objectives of no structural damage and no residual drift under the DBE.

2.1.4 Self-Centering Steel Concentrically-Braced Frames

The SC-CBF system is being developed to achieve economical damage-free performance under the design basis earthquake, thereby significantly reducing the repair costs in a structure without significantly increasing fabrication and erection costs. This section summarizes research performed at Lehigh University to develop the SC-CBF system, as well as other recent research on similar systems.

2.1.4.1 SC-CBF Research at Lehigh University

Ongoing research at Lehigh University has extended the concepts of unbonded post-tensioned precast concrete walls to steel concentrically-braced frames (CBFs). The critical prestressed connection in a steel self-centering CBF (SC-CBF) is at the base of the SC-CBF column. Post-tensioning forces and gravity forces prestress the column base connection (i.e., prestress the column to the foundation). The specified level of prestress and the details of the column base permit the column to decompress and uplift at a specified level of applied overturning moment. Roke et al. (2006) introduced the behavior of the SC-CBF system and presented preliminary performance-based design (PBD) objectives for the SC-CBF system. The expected behavior of the SC-CBF system is similar to that of the unbonded post-tensioned concrete wall system. A set of SC-CBFs, including an SC-CBF with additional energy dissipation (ED) elements, were designed and subjected to nonlinear static and dynamic analyses. These nonlinear analyses showed

that the SC-CBF system exhibits the intended behavior under earthquake loading, and that ED elements can significantly reduce the peak drift response of the system.

Roke et al. (2009) introduced a method for estimating the member force design demands for the SC-CBF system. Gonner (2009) applied the concepts introduced by Roke et al. (2009) to design a large-scale SC-CBF test structure for experiments including hybrid earthquake simulations at the Real-Time Multi-Dimensional (RTMD) Earthquake Simulation Facility at the Advanced Technology for Large Structural Systems (ATLSS) Center at Lehigh University. A performance-based design procedure was used to design the SC-CBF test structure. Gonner et al. (2010) presents details of the test fixture and instrumentation for the SC-CBF test structure. This dissertation presents some results from hybrid simulations performed on the SC-CBF test structure (Chancellor et al. 2010).

2.1.4.2 Other Research Related to the SC-CBF System

Other current research is developing systems that are similar to the SC-CBF system being developed at Lehigh University. Some of this research is summarized below.

2.1.4.2.1 Concentrically-Braced Frames with Energy-Dissipating Braces

Christopoulos et al. (2008) developed a self-centering energy dissipative (SCED) steel brace member that was intended to sustain large axial deformations without damaging the brace member and to provide stable energy dissipation without residual drift. The SCED member shown in Figure 2.17 consists of two concentric bracing members, PT steel tendons, and friction-based energy dissipation elements. The total area, modulus of elasticity, initial pretensioning force, elongation capacity, and length of the tendons are

selected to determine the strength, postelastic stiffness, deformation capacity, and tendency to self-center of the SCED system. The SCED member is detailed such that relative movement of the two bracing members activates the friction elements and elongates the PT tendons. Christopoulos et al. (2008) performed full-scale quasi-static tests on a prototype SCED member that uses Aramid based tendons and friction-based energy dissipation. Figure 2.18 shows the response of the prototype SCED member to axial loading. Figure 2.18(a) shows the force-deformation response of the member without the friction elements; only the PT force prevents the relative motion of the bracing members, and no energy is dissipated during the response. Figure 2.18(b) shows the force-deformation response after tightening two of the six total bolts in the friction element. Figure 2.18(c) shows the force-deformation response after tightening four of the six total bolts in the friction element. Figure 2.18(d) shows the force-deformation response after tightening all six bolts in the friction element. Increasing the friction force by tightening more bolts increases the energy dissipation capacity and strength of the SCED system. Self-centering of the member is maintained through the application of the initial PT force. Figure 2.18(e) shows the force-deformation response of the PT tendons to cyclic loading. The PT tendons elongate symmetrically when the member is in tension or compression. The PT tendons were then released at the end of testing and the SCED member was subjected to a cycle of response with only the ED elements resisting the relative motion of the bracing elements; the force-deformation response of the member in this condition is shown in Figure 2.18(f). Tests performed by Christopoulos et al (2008)

validated the expected behavior of the SCED member, which achieved stable and repeatable self-centering hysteretic response under cyclic loading.

Tremblay et al. (2008a) extended the study of the SCED member. Figure 2.19 shows the hysteretic response of three types of braces: Figure 2.19(a) shows the response of a conventional brace, Figure 2.19(b) shows the response of a buckling-restrained brace (BRB), and Figure 2.19(c) shows the response of an SCED brace. As mentioned in Chapter 1, BRBs often exhibit large residual deformations after an earthquake; SCED braces are intended to eliminate this residual deformation. Tremblay et al. (2008a) performed nonlinear analytical studies of 2-, 4-, 8-, 12-, and 16-story buildings with SCED braces and BRBs to compare the dynamic response of the two systems. The prototype buildings were located in the Los Angeles area and were subjected to DBE-level and MCE-level ground motions. Figure 2.20 shows the dynamic lateral force-lateral drift response of the 8-story prototype structures to a DBE-level ground motion (Figure 2.20(a)) and the dynamic lateral force-lateral drift response of the 12-story prototype structures to an MCE-level ground motion (Figure 2.20(b)). The residual drift exhibited by frames with the BRBs is significant, particularly for the MCE-level response. The SCED system, however, self-centered after both ground motions. The study performed by Tremblay et al. (2008a) demonstrated that the SCED system is a viable alternative to a BRB frame. The SCED system had no residual drift under DBE-level seismic input and significantly reduced residual drift under MCE-level seismic input, and it offered better resistance to collapse under the MCE due to the self-centering behavior of the system.

Zhu and Zhang (2008) developed a self-centering friction damping brace (SFDB) for use in CBFs. Figure 2.21 shows a schematic of the SFDB. The SFDB is comprised of two main structural elements, Block A and Block B, as indicated in Figure 2.21. The surface between these blocks is precompressed by the bolts, providing a specified level of friction force capacity to enhance the energy dissipation of the SFDB. Superelastic Nitinol wire strands are used to provide a large drift capacity while maintaining the self-centering behavior of the SFDB. Zhu and Zhang (2008) performed full-scale cyclic tests on an SFDB to validate the expected behavior of the member, and performed an analytical comparitive study of the dynamic response of three-story and six-story SFDB frames and BRB frames under DBE-level and MCE-level ground motions. Figure 2.22 shows typical dynamic response of the three systems studied. Figure 2.22(a) shows the hysteretic behavior of a BRB; Figure 2.22(b) shows the hysteretic behavior of an SFDB with friction; and Figure 2.22(c) shows the hysteretic behavior of an SFDB with no friction acting between Block A and Block B, so the energy dissipation is due to the superelastic response of the Nitinol wires. The results of this study indicate that the SFDB frame system is capable of achieving seismic response maxima similar to those of the BRB system; however, the SFDB frames have significantly reduced residual story drifts.

2.1.4.2.2 Rocking Frame Systems

Midorikawa et al. (2006) performed shake table testing on a rocking structural system that uses yielding column base plates to dissipate energy. A schematic of the rocking behavior of this system is shown in Figure 2.23. Figure 2.24 shows a plan view of the yielding base plate. A study was performed to compare the response of the rocking structural system with that of

a conventional (fixed-base) structural system. Experimental results show that the yielding base plate offers a viable method of dissipating energy in a rocking structural system. The peak base shear response of the rocking structural system was significantly less than the peak base shear response of the fixed-base structural system due to the softening of the lateral force-lateral drift response. The peak displacement response, however, was not significantly different for the two structural systems, because of the energy dissipation provided by the yielding column base plates. Figure 2.25 shows a time history of the roof drift response of the rocking system, which shows the total roof drift response and the roof drift response due to rocking. From Figure 2.25, it can be seen that the rocking response dominates the roof drift response of the rocking frame system.

Tremblay et al. (2008b) developed a viscously damped controlled seismic rocking (VDCSR) system to increase the drift capacity prior to damage of a braced frame system in a low-rise building. The VDCSR system is shown in Figure 2.26. Rocking of the VDCSR system dissipates energy through viscous dampers located at the base of the columns; the dampers resist the uplift and gap opening at the base of the columns and slow their return to the foundation. The VDCSR system uses gravity load on the columns to provide a restoring force to close the gaps at the column bases. Shake table testing was performed on a two-story half-scale VDSCR frame at the Structural Engineering Laboratory at École Polytechnique of Montreal, Canada. Time histories of the response of the test structure are shown in Figure 2.27. The first floor displacement and roof displacement are in phase, indicating that the displacement response is driven by rocking behavior of the VDSCR frame. Figure 2.27(c) shows that it is possible for both columns of the VDSCR frame to be uplifted from the foundation at the same time, which is an

undesirable response. Overall, the results of shake-table testing and analytical studies suggest that the VDSCR frame system can significantly reduce column uplift loads and base shear demands compared with those of conventional CBFs.

Eatherton et al. (2010) performed 0.43-scale subassembly tests on a controlled rocking CBF system at the University of Illinois at Urbana-Champaign. A schematic of a controlled rocking CBF system is shown in Figure 2.28. This system employs shear fuses to dissipate energy and vertically-oriented post-tensioning to increase the moment resistance capacity of the system and to provide self-centering capability. Quasi-static cyclic loading was applied to the test structure to determine the overturning moment-roof drift response of the system, shown in Figure 2.29. The experimental results suggest that the controlled rocking CBF system is able to concentrate structural damage into replaceable elements and eliminate residual drift after unloading.

Ma et al. (2010) performed shake table testing of a controlled rocking CBF system at 0.68-scale on the E-Defense shake table facility in Miki, Japan. Figure 2.30 shows a drawing of the test specimen. Figure 2.30(a) shows an overall elevation view. Figure 2.30(b) shows a detail of the fuse assembly at the base of the CBF. The dynamic response of the test specimen to the JMA Kobe ground motion scaled to MCE-level is shown in Figure 2.31. The time history of uplift ratio (the ratio of column base uplift displacement to the frame bay width) is shown in Figure 2.31(a). The overturning moment-uplift ratio response is shown in Figure 2.31(b). The uplift ratio roughly coincides with roof drift (Ma et al. 2010). Results from the shake table tests suggest that the controlled rocking

CBF system is a viable lateral-load resisting system that can self-center after an earthquake and can control damage in the structural members.

2.1.5 Ductility Demands for Self-Centering Systems

Seo and Sause (2005) studied the ductility demands on self-centering systems. Ductility, μ, is defined as:

$$\mu = \frac{u_{\max}^{nl}}{u_y} \tag{2.10}$$

where,

$u_{\max}^{nl}$ = the peak nonlinear displacement from time-history analysis

$$u_y = \frac{F_y}{k_i} \tag{2.11}$$

F_y = the effective linear limit force corresponding to the beginning of a noticeable reduction in the lateral stiffness of the system

k_i = the initial stiffness of the system

For SC systems, F_y is controlled by gap-opening response rather than inelasticity in the structural members.

Seo and Sause (2005) present a parametric study of SC systems to determine the effect that several variables have on μ. The studied parameters are: (1) the strength reduction factor, R; (2) the stiffness of the system after decompression, k_{pd}; (3) the hysteretic energy

dissipation capacity, β_E (discussed further in Section 5.3.3 of this dissertation); and (4) the site soil conditions. Seo (2005) developed a μ-R-T relationship based on these parameters to determine a median design value of μ for SC systems. This relationship is discussed further in Section 6.3 of this dissertation.

2.2 Summary

SC systems are intended to reduce damage in primary structural members (i.e., beams, columns, and braces) and to eliminate residual drift in the system after lateral loading is removed. Permitting gaps to open in selected connections in the structure under earthquake loading softens the lateral force-lateral drift response, thereby reducing the force demands in the system. Self-centering behavior is achieved through the use of post-tensioning forces and/or gravity forces acting across the gaps in these connections. Energy dissipation elements can be incorporated into SC systems to reduce the peak response.

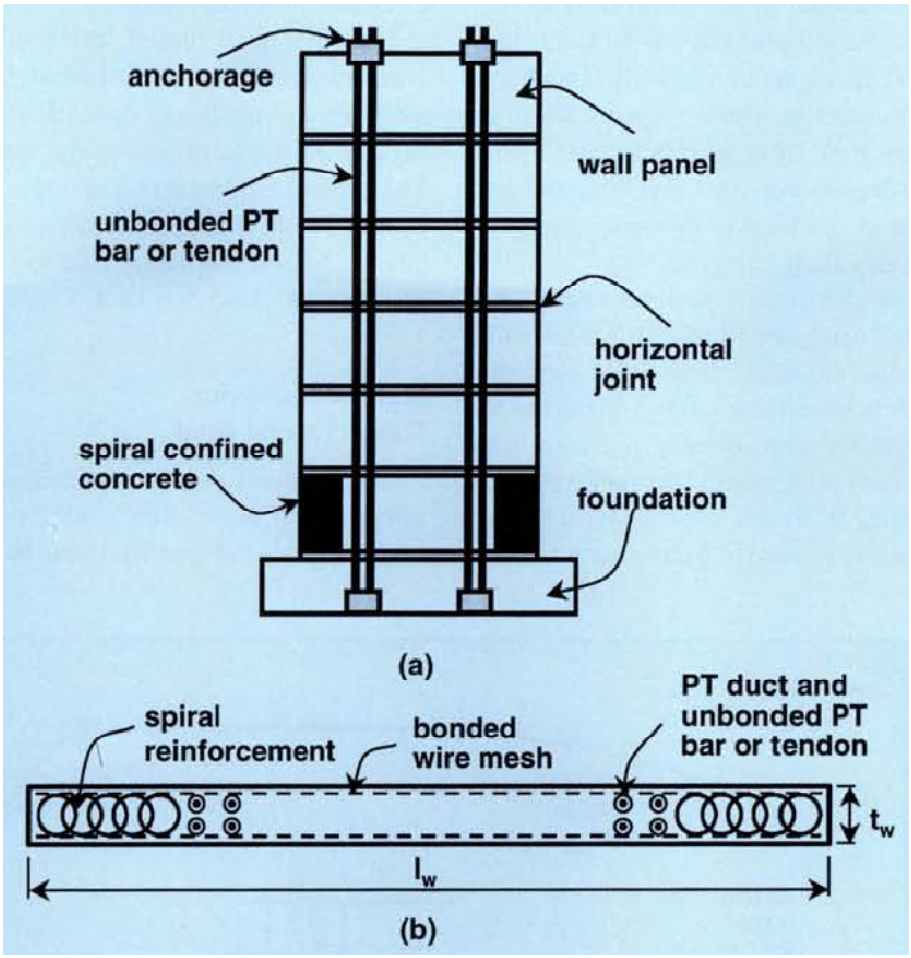

Figure 2.1 – Unbonded post-tensioned precast wall: (a) elevation; (b) enlarged cross section near base (Kurama et al. 1999a)

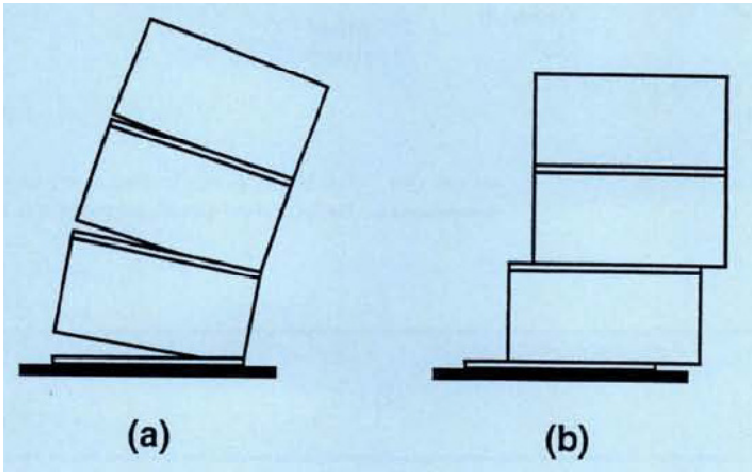

Figure 2.2 – Behavior of unbonded post-tensioned precast wall along horizontal joints: (a) gap opening; (b) shear slip (Kurama et al. 1999a)

(a)

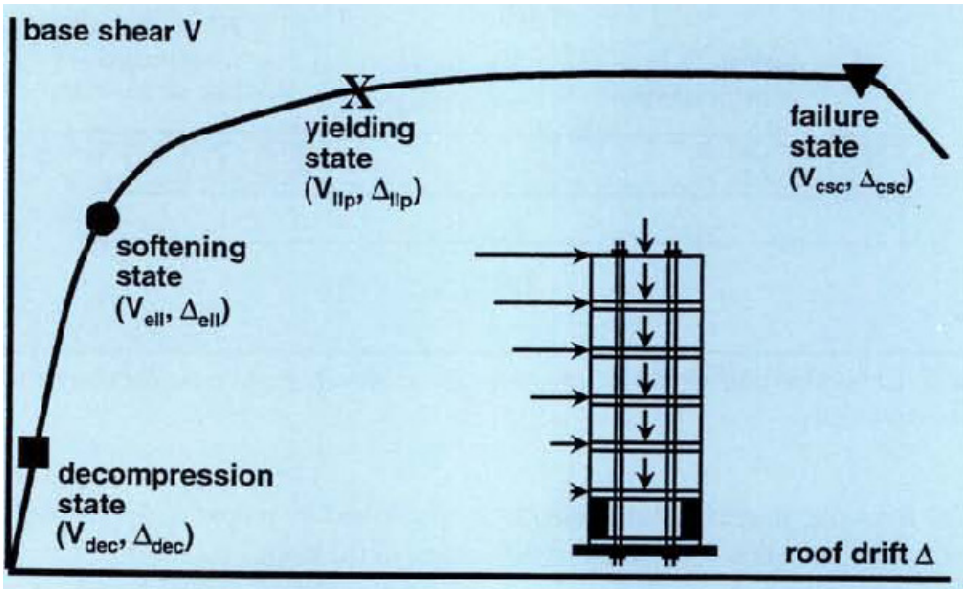

(b)

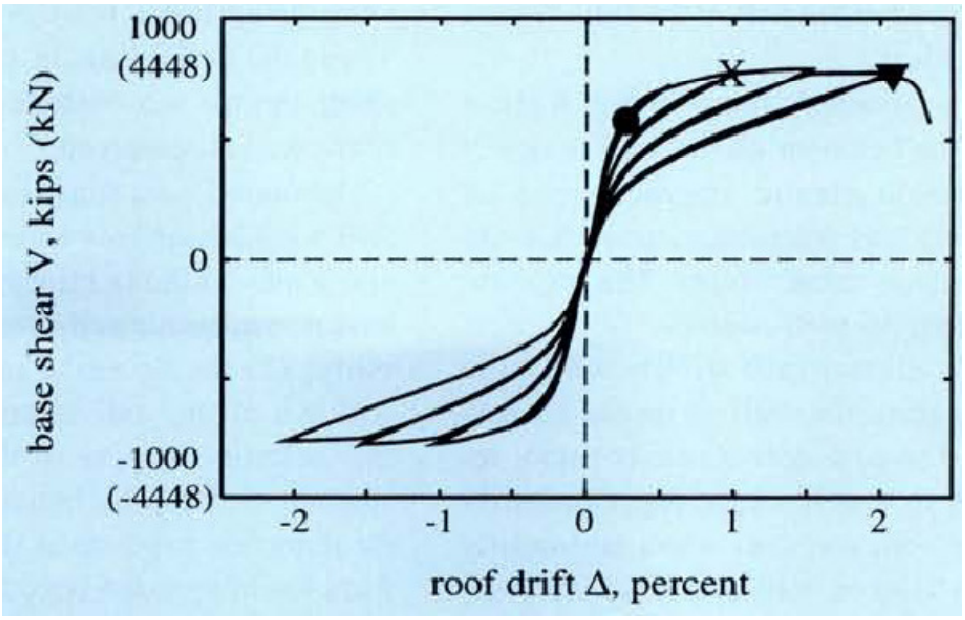

Figure 2.3 – Base shear-roof drift relationship of unbonded post-tensioned shear wall: (a) schematic indicating limit states; (b) hysteretic behavior under lateral load (Kurama et al. 1999a)

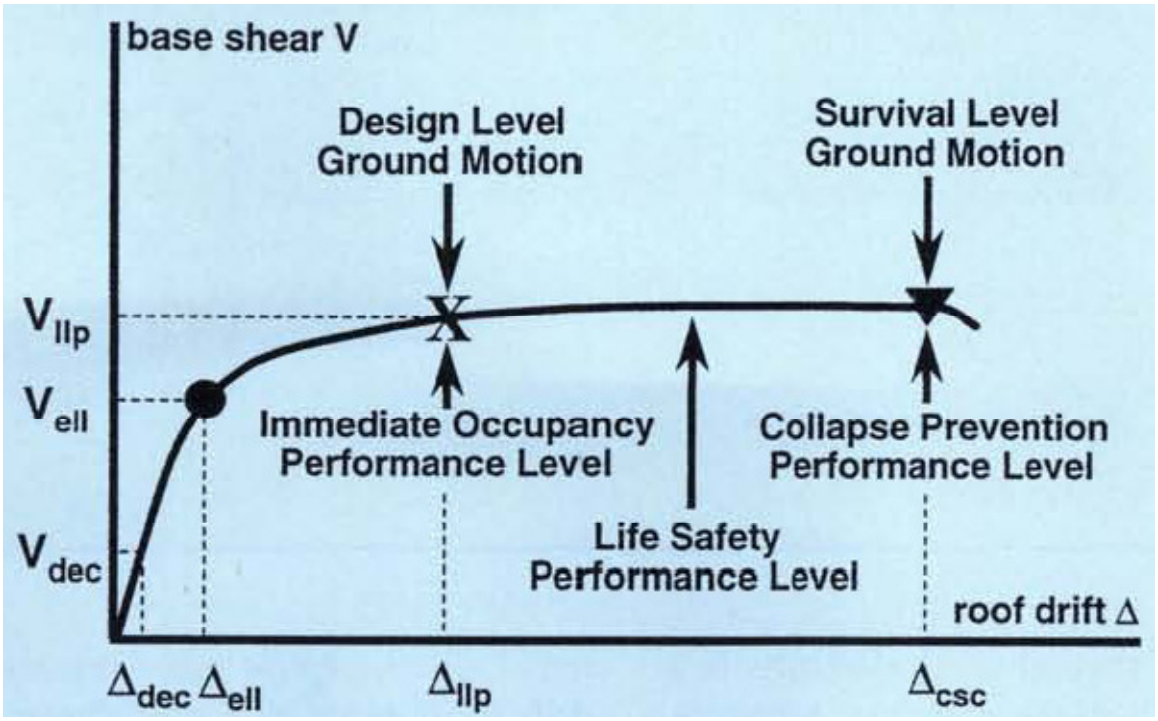

Figure 2.4 – Performance-based design objectives for an unbonded post-tensioned precast concrete wall (Kurama et al. 1999a)

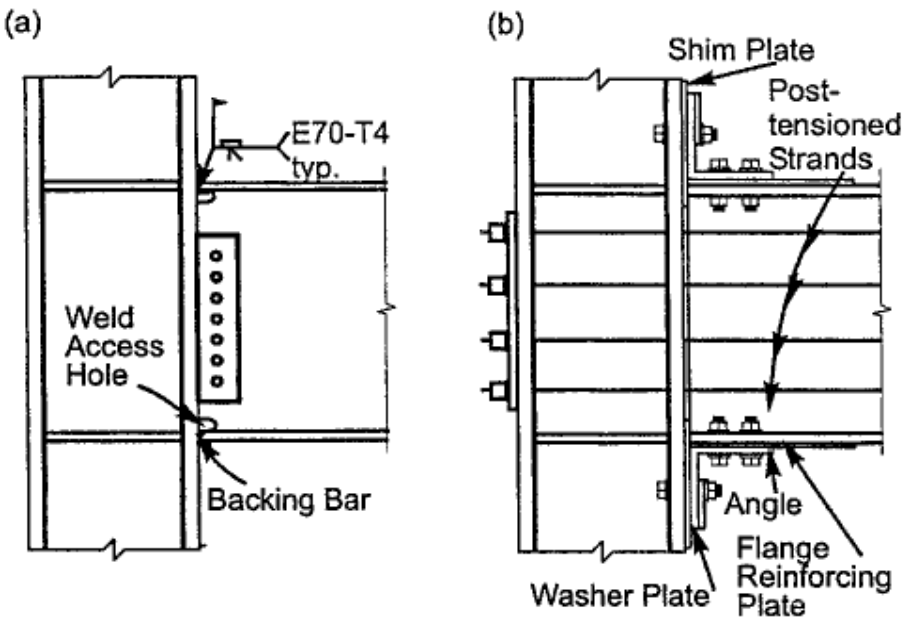

Figure 2.5 – Moment-resisting connections: (a) conventional; (b) post-tensioned (Ricles et al. 2001)

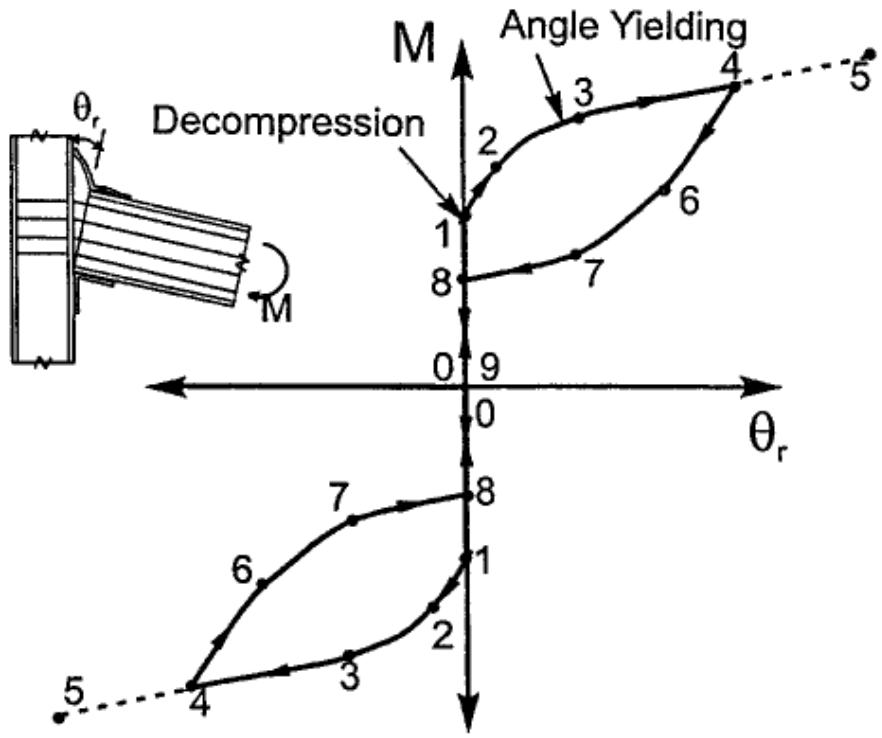

Figure 2.6 – Idealized moment-rotation behavior of post-tensioned MRF connection (Ricles et al. 2001)

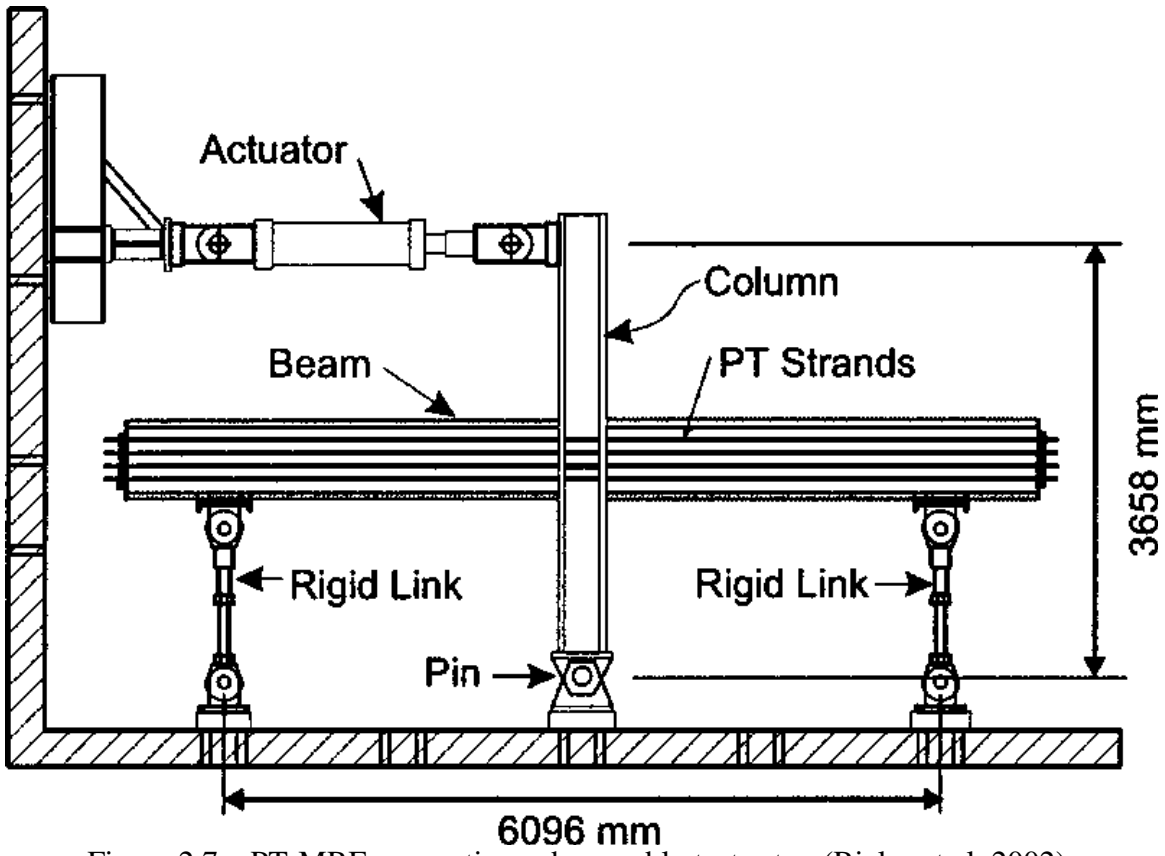

Figure 2.7 – PT-MRF connection subassembly test setup (Ricles et al. 2002)

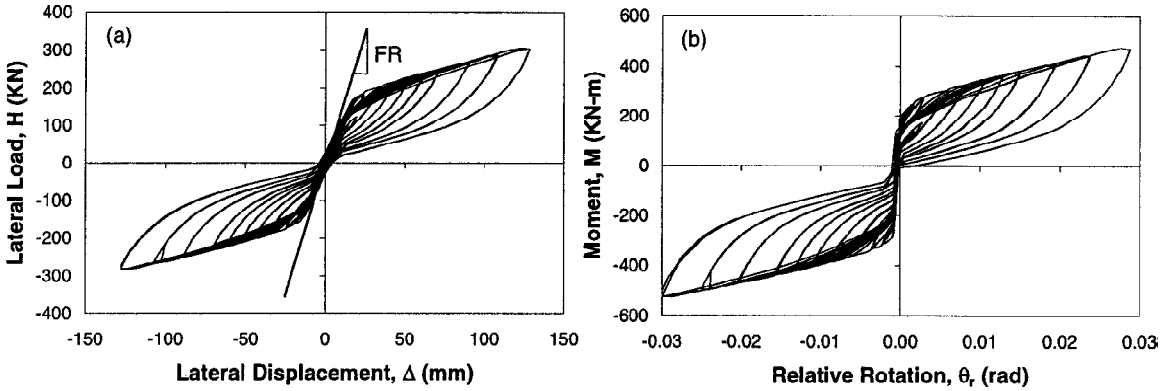

Figure 2.8 – Typical response of PT-MRF subassembly test: (a) lateral load-lateral displacement; (b) moment-rotation (Ricles et al. 2002)

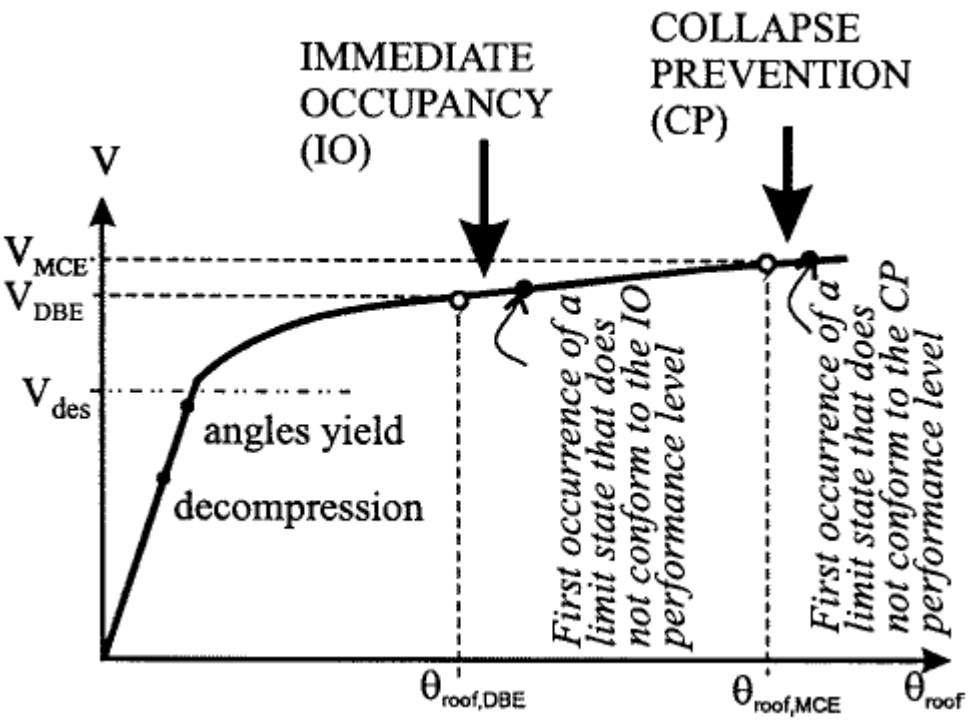

Figure 2.9 – Design objectives related to global response of PT MRF system (Garlock et al. 2007)

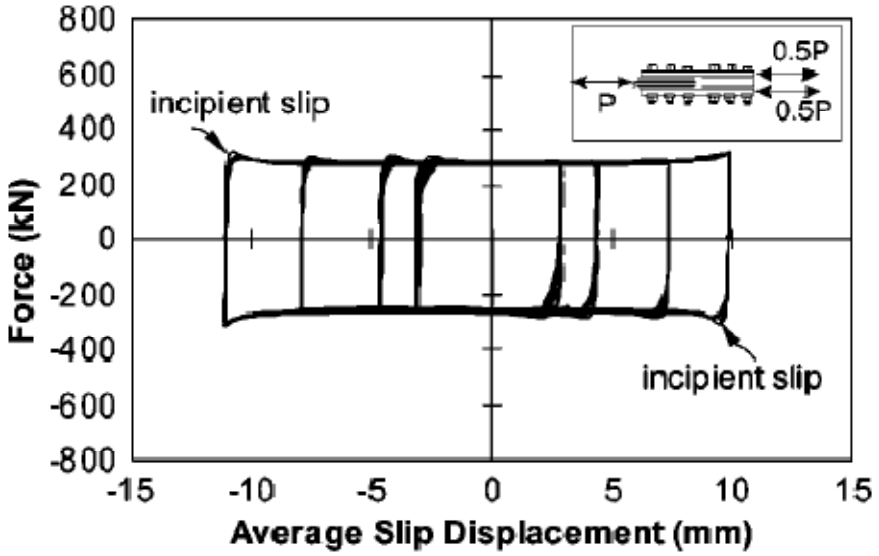

Figure 2.10 – Cyclic behavior of lap connection friction device (Petty 1999)

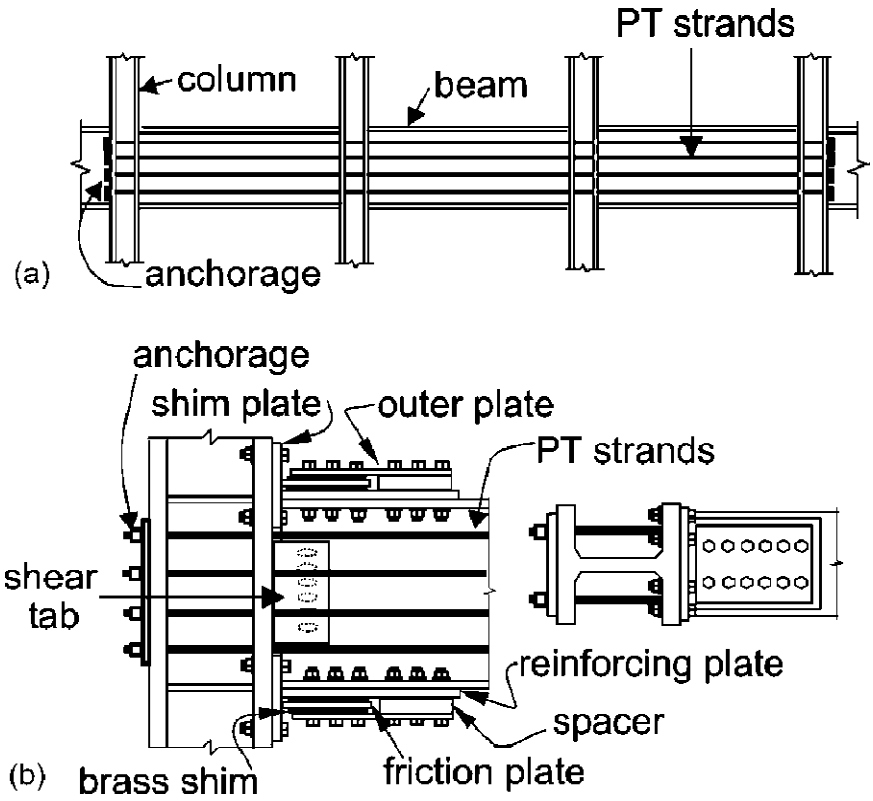

Figure 2.11 – PT-MRF connection with PFDC: (a) elevation view of a multi-bay PT-MRF; (b) connection details of a PT connection (Rojas et al. 2005)

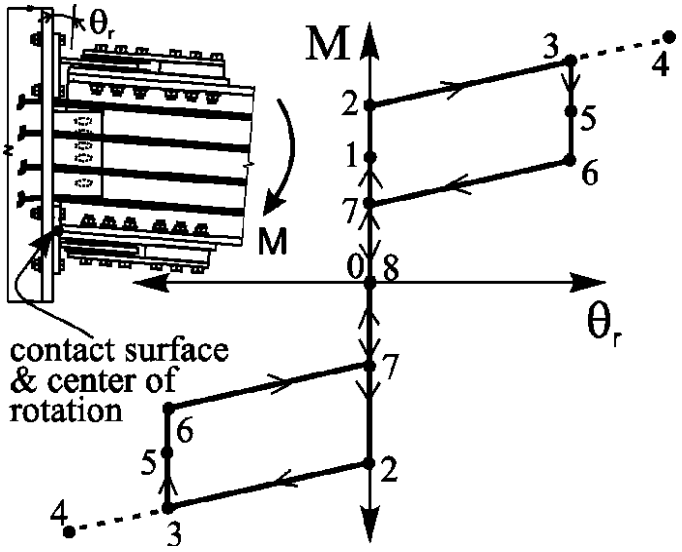

Figure 2.12 – Idealized moment-rotation behavior of PFDC (Rojas et al. 2005)

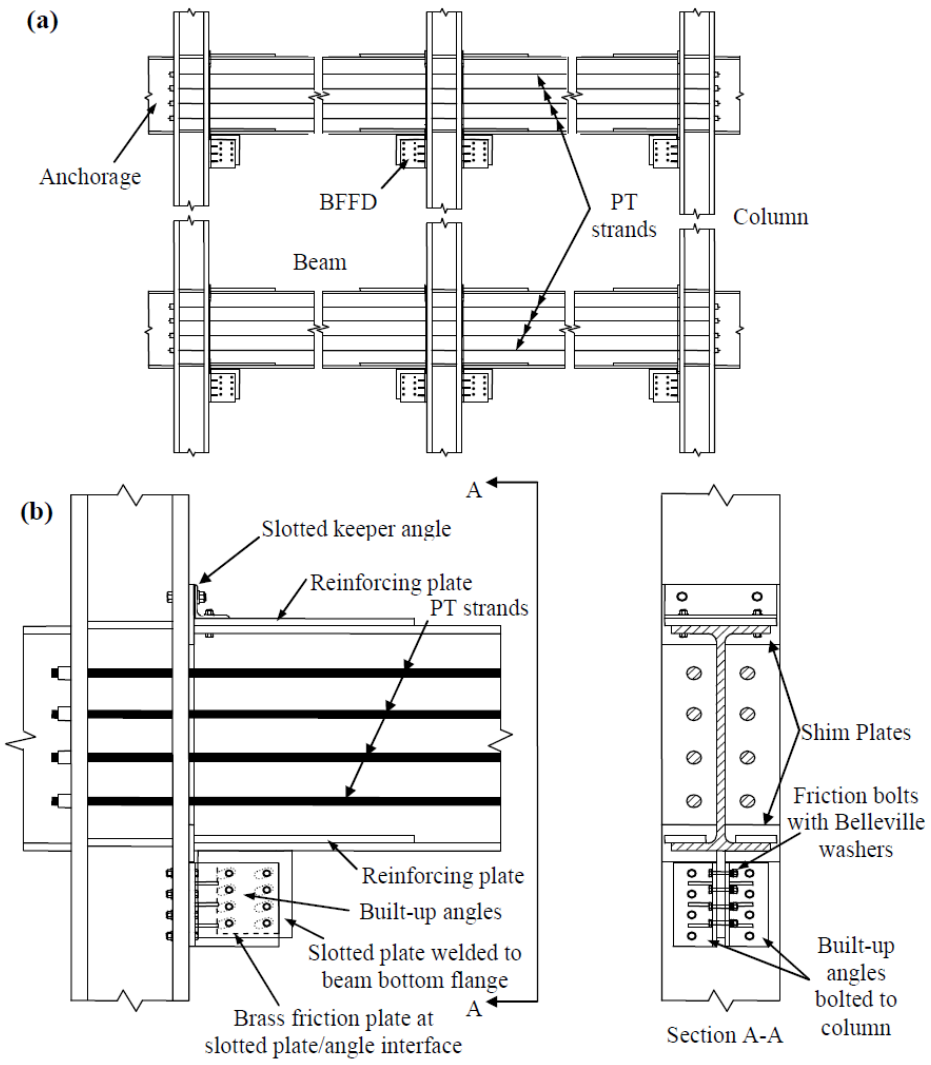

Figure 2.13 – PT-MRF connection with BFFD: (a) elevation view of a multi-bay PT-MRF; (b) connection details of a PT connection (Wolski 2006)

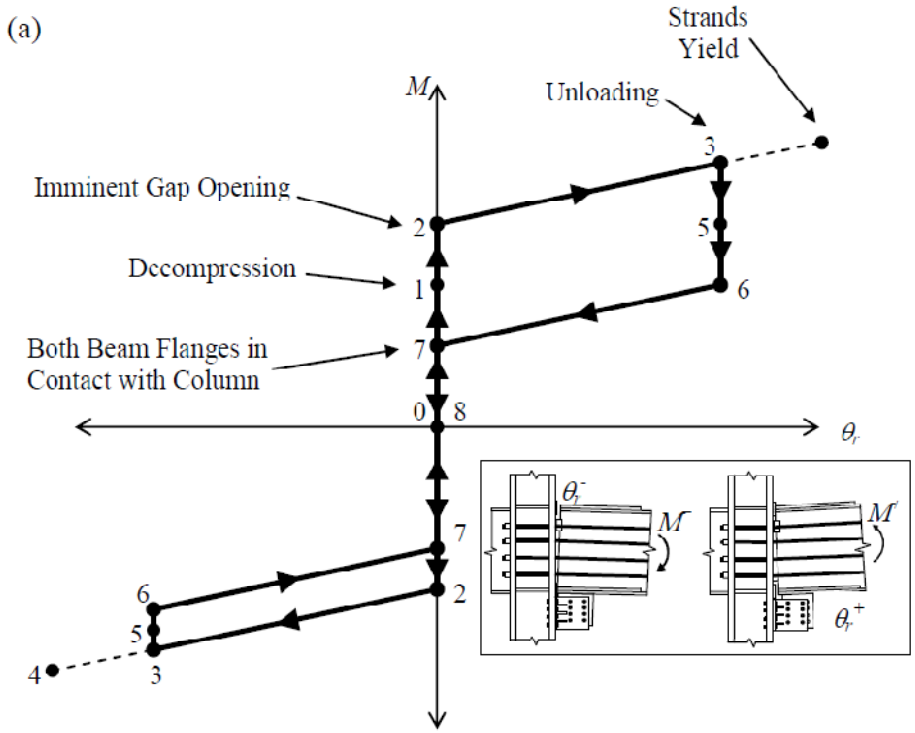

Figure 2.14 – Idealized moment-rotation behavior of a PT-MRF connection with BFFD (Wolski 2006)

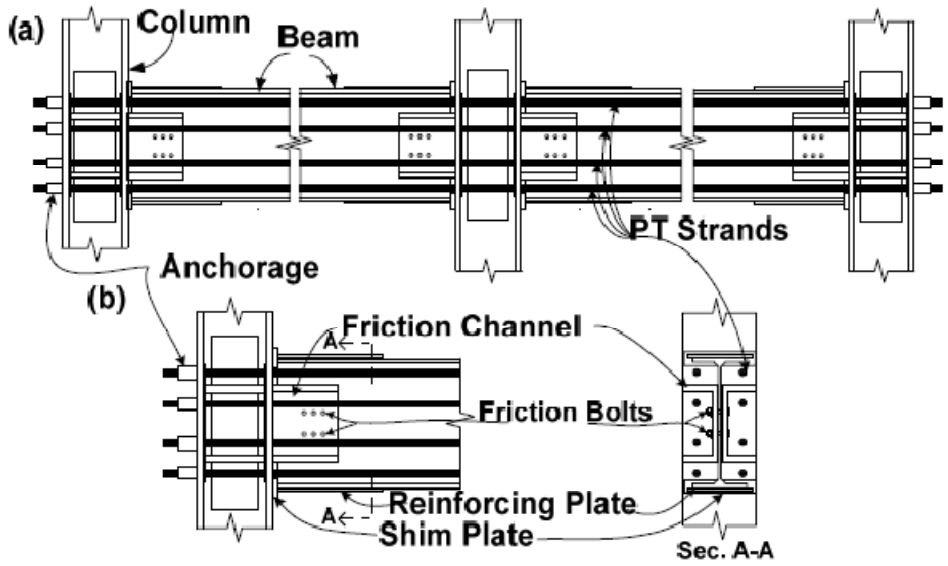

Figure 2.15 – SC-MRF connection with WFD: (a) elevation view of a multi-bay SC-MRF; (b) connection details of a PT connection (Lin et al. 2008)

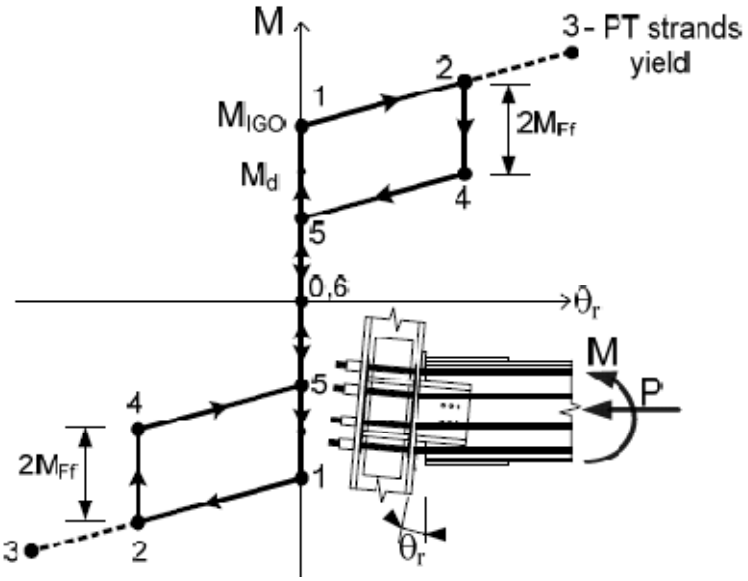

Figure 2.16 – Idealized moment-rotation behavior of an SC-MRF connection with WFD (Lin et al. 2008)

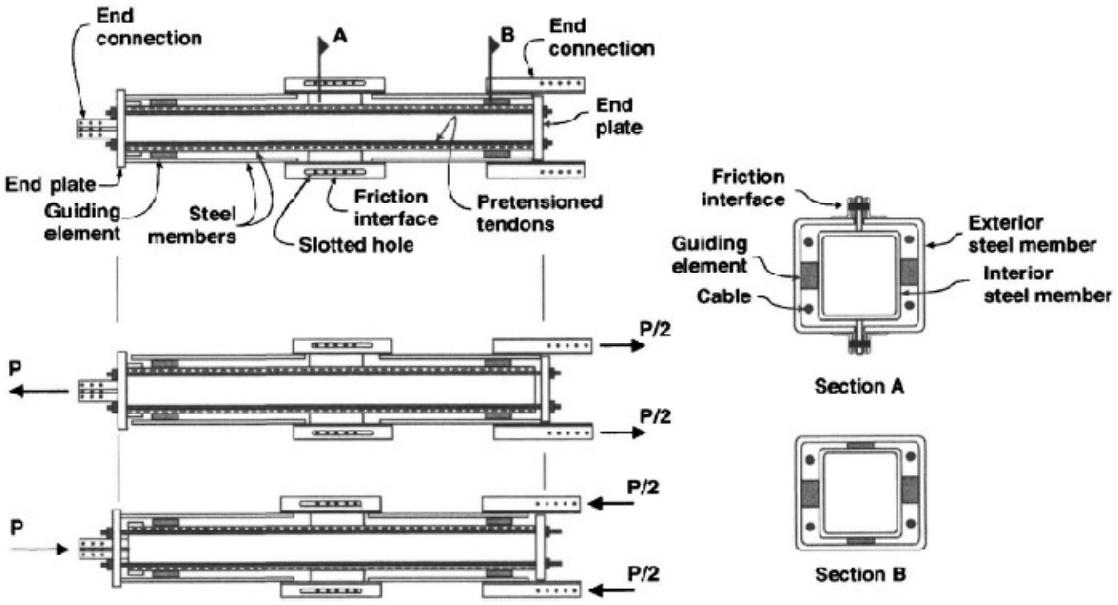

Figure 2.17 – Schematic of SCED system with steel tubes, tendons, and friction dissipative mechanism (Christopoulos et al. 2008)

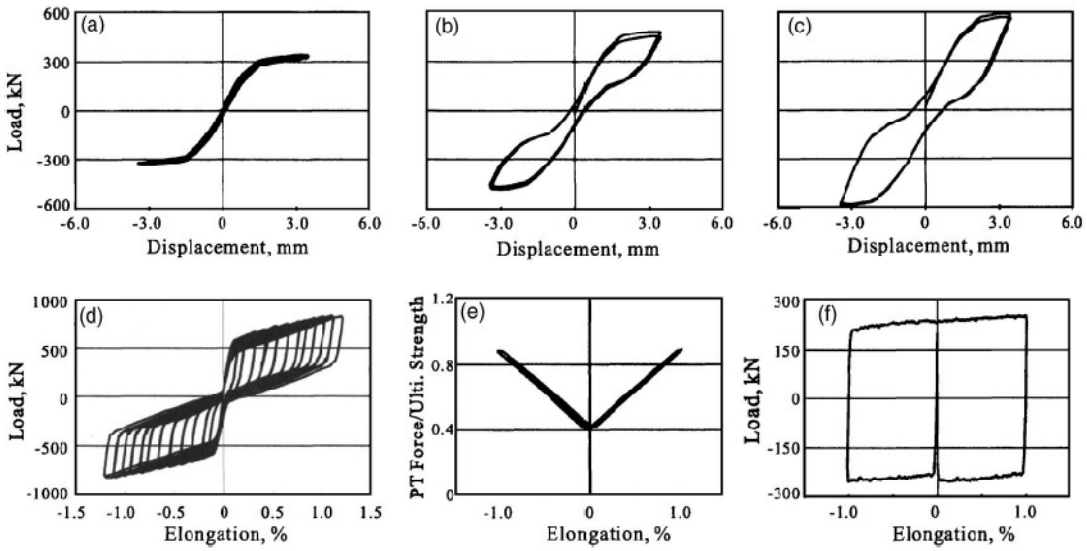

Figure 2.18 – Response of SCED prototype under quasi-static axial loading: (a) only PT applied; (b) PT + two bolt friction mechanism; (c) PT + four bolt friction mechanism; (d) full SCED brace; (e) force in PT elements; (f) friction device only (Christopoulos et al. 2008)

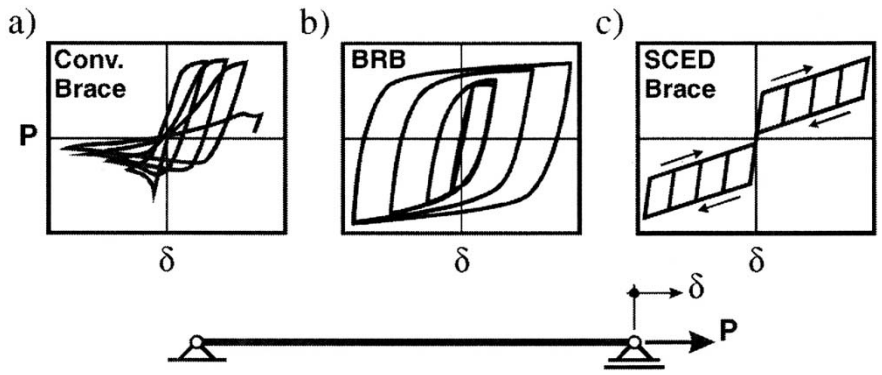

Figure 2.19 – Brace hysteretic response: (a) conventional brace; (b) buckling restrained brace; (c) SCED brace (Tremblay et al. 2008a)

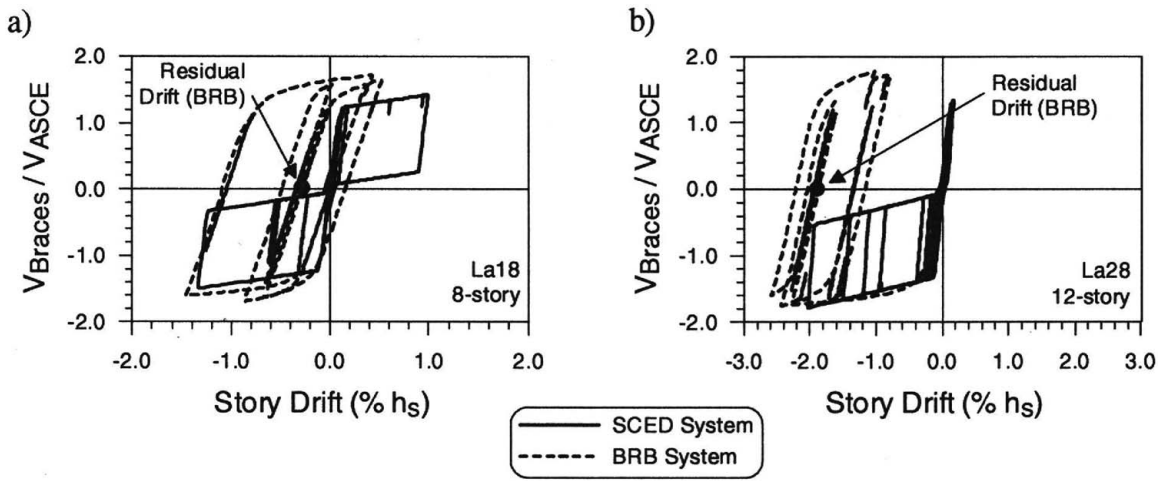

Figure 2.20 – First story lateral load-lateral deformation response: (a) 8-story frames under record LA18 (DBE); (b) 12-story frames under record LA28 (MCE) (Tremblay et al. 2008a)

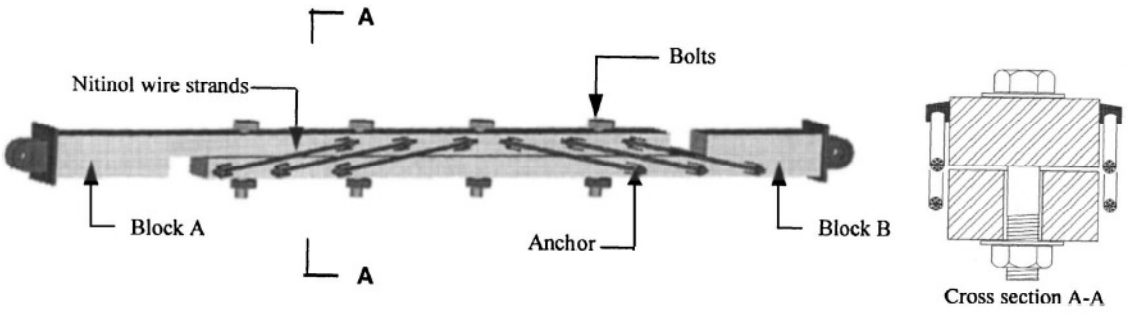

Figure 2.21 – Schematic of configuration of SFDB (Zhu and Zhang 2008)

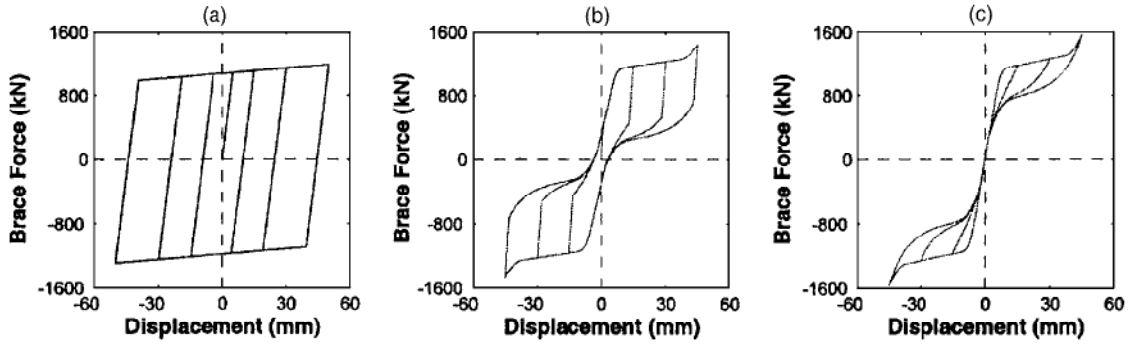

Figure 2.22 – Typical hysteresis of single brace in sixth story of prototype building: (a) BRB; (b) SFDB; (c) SFDB-NF (Zhu and Zhang 2008)

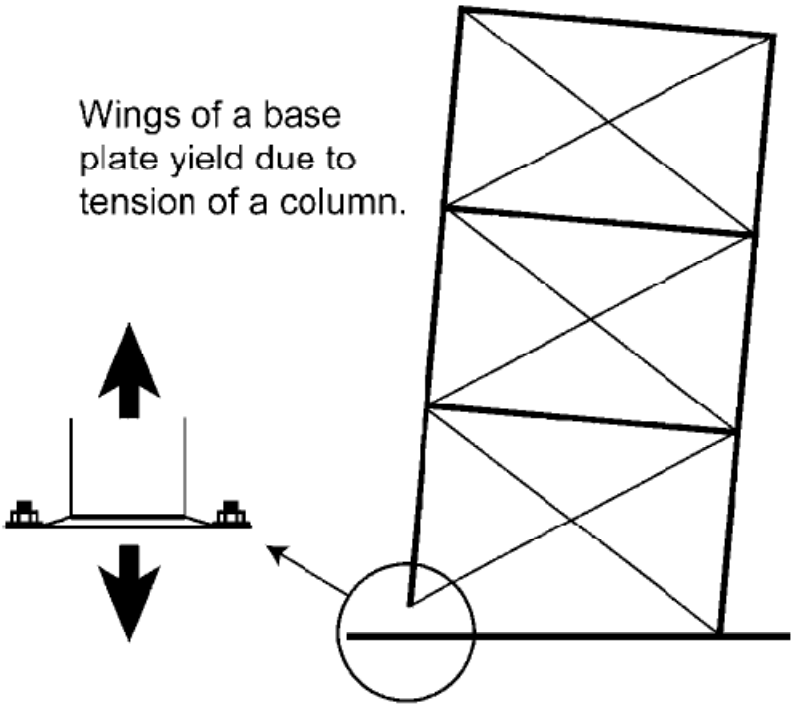

Figure 2.23 – Structural rocking system with yielding base plate (Midorikawa et al. 2006)

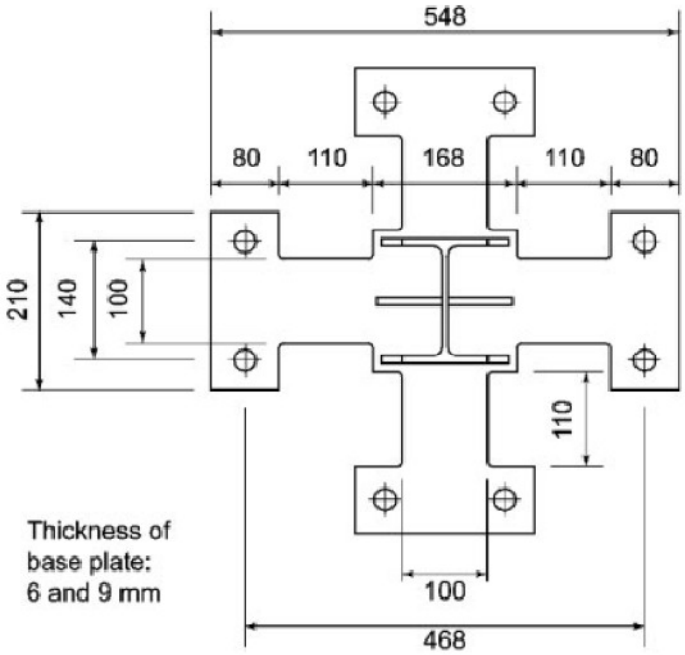

Figure 2.24 – Plan of yielding base plate (Midorikawa et al. 2006)

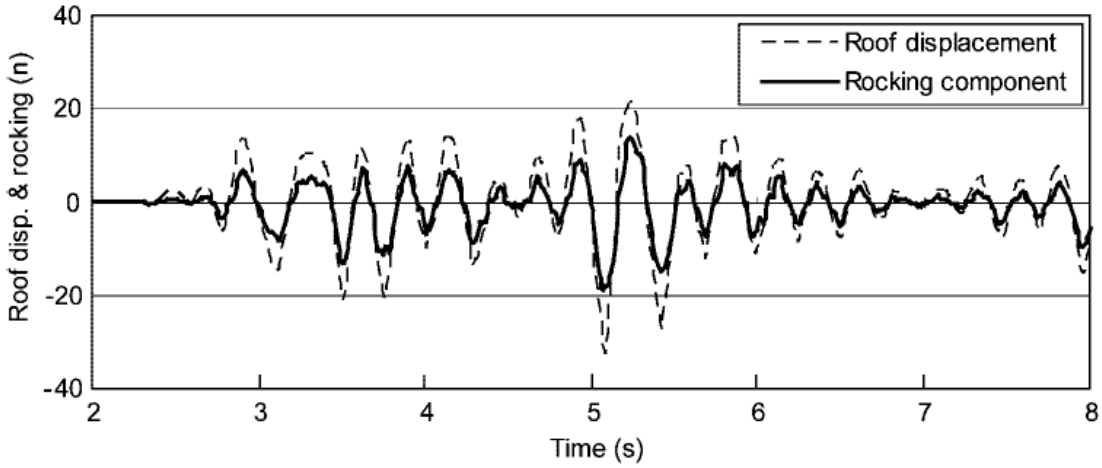

Figure 2.25 – Time history of roof displacement for BP9-2 model (Midorikawa et al. 2006)

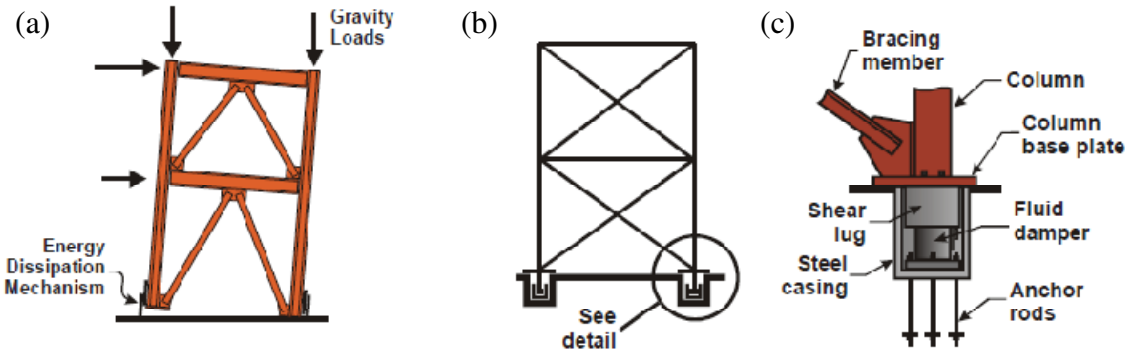

Figure 2.26 – VDCSR system: (a) rocking behavior; (b) schematic of braced frame and viscous dampers at the column bases; (c) details of viscous dampers (Tremblay et al. 2008b)

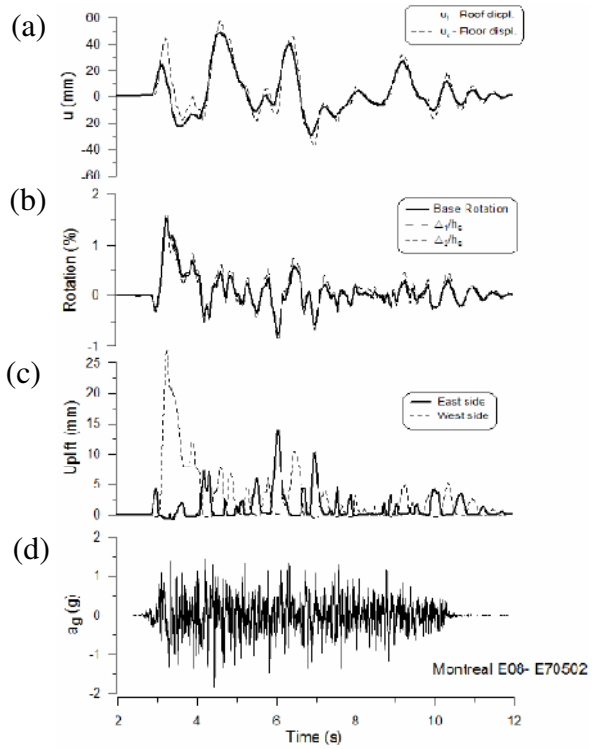

Figure 2.27 – Results of a shake table test of VDCSR system under a magnitude 7.0 earthquake at a distance of 50 km for a Montreal site: (a) lateral displacement; (b) base rotation; (c) column base uplift; (d) ground acceleration (Tremblay et al. 2008b)

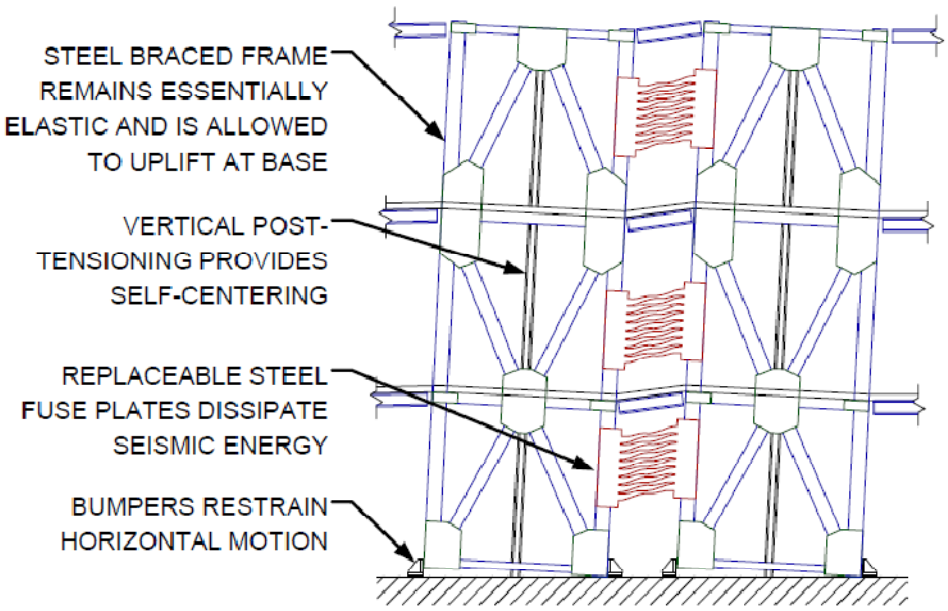

Figure 2.28 – Schematic of controlled rocking system in its rocked position (Eatherton et al. 2010)

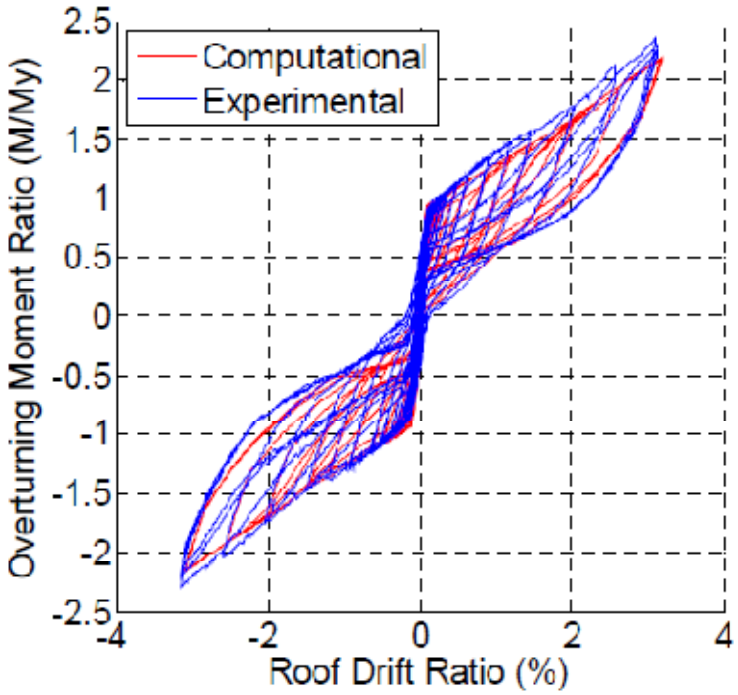

Figure 2.29 – Overturning moment-roof drift response of controlled rocking system (Eatherton et al. 2010)

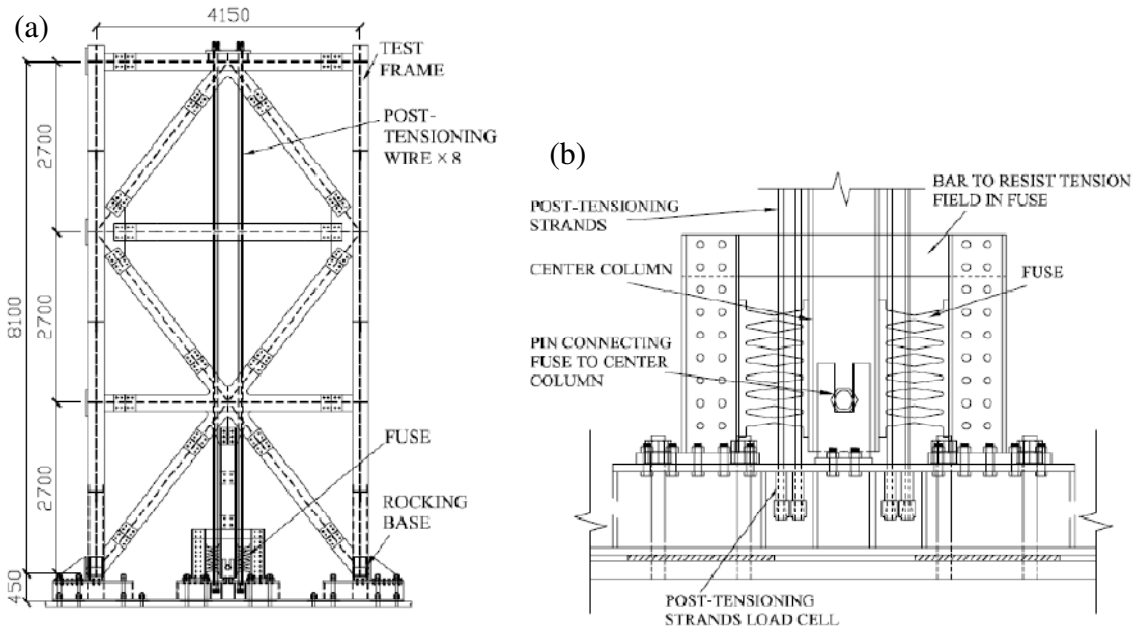

Figure 2.30 – Drawings of controlled rocking frame used for shake-table testing: (a) overall view; (b) detail at fuse (Ma et al. 2010)

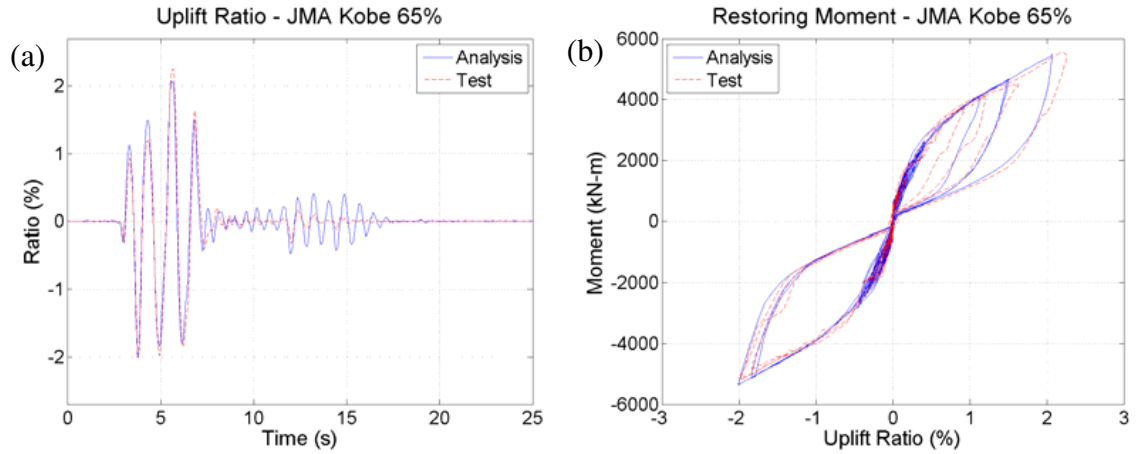

Figure 2.31 – Dynamic response of controlled rocking system: (a) time history of uplift ratio (ratio of column uplift displacement to frame bay width); (b) overturning moment-uplift ratio (Ma et al. 2010)

CHAPTER 3

BEHAVIOR OF PROPOSED SYSTEM

As previously mentioned, a conventional concentrically-braced frame (CBF) is a stiff and economical lateral-load resisting system. However, a CBF will sustain permanent damage at relatively low levels of drift, due to yielding and subsequent buckling of the brace members. The self-centering CBF (SC-CBF) system has been developed to provide increase drift capacity before damage initiates, while maintaining the stiffness of the CBF system.

3.1 Description of System

An SC-CBF system is shown schematically in Figure 3.1. The system consists of beams, columns, and braces in a conventional arrangement, with column base details that permit the columns to decompress and uplift at the foundation. Gravity loads ($F_{g,i}$) and post-tensioning (PT) forces (from PT bars arranged vertically at midbay in the system shown in Figure 3.1) resist column uplift and provide a restoring force after uplift occurs. Energy dissipation elements, shown at the base of the columns in Figure 3.1, can be included to dissipate energy under cyclic loading.

Idealized SC-CBF behavior under lateral loading is shown in Figure 3.2. Figure 3.2(a) shows the elastic deformation of the SC-CBF under a low level of lateral load. This deformation is similar to that of a conventional CBF system. Under higher levels of

lateral load, the overturning moment at the base of the SC-CBF becomes large enough for the "tension" column to decompress and uplift, and the frame "rocks," as shown in Figure 3.2(b). After column decompression and uplift, the roof drift consists of two components: (1) elastic deformation of the SC-CBF, and (2) rigid-body rotation (i.e., rocking) of the SC-CBF about the base of the compression column.

The PT bars elongate from the uplift of the column and rocking of the SC-CBF, which leads to an increase in PT force and provides a positive stiffness to the lateral force-lateral drift behavior. This post-decompression stiffness is much less than the elastic stiffness of the SC-CBF, and the rigid-body rotation dominates the post-decompression lateral force-lateral drift response.

3.2 Limit States

Four primary structural limit states of an SC-CBF are considered: (1) decompression and uplift of the "tension" column at the base of the SC-CBF; (2) yielding of the vertically-oriented PT bars; (3) yielding of the beams, columns, or braces of the SC-CBF; and (4) failure of the beams, columns, or braces of the SC-CBF. These limit states are shown schematically in Figure 3.3, which shows the idealized overturning moment-roof drift response of an SC-CBF system.

3.2.1 Column Decompression

Decompression and the subsequent uplift of the base of the SC-CBF columns is the most significant feature of the SC-CBF system behavior. This behavior occurs when the tension force demand due to the overturning moment from the lateral forces exceeds the

initial compressive force in one of the SC-CBF columns, at which point the "tension" column decompresses and uplifts from the foundation. This uplift opens a gap between the foundation and the column base and permits a rigid-body rotation (or "rocking") of the SC-CBF.

Proper structural detailing must permit this column decompression and the associated rocking to occur without structural damage. As the SC-CBF rocks, the vertically-oriented PT bars elongate, providing a restoring force that tends to self-center the SC-CBF (i.e., return it to its initial position) after column decompression and rocking occur.

3.2.2 PT Bar Yielding

The PT bars elongate after column decompression. As long as the total strain demand in the PT bars (due to initial strain in the bars from post-tensioning plus the strain demand from rocking) is less than the yield strain capacity of the PT bars, the initial PT bar force should be preserved and the SC-CBF will self-center. Yielding of the PT bars is a limit state that produces structural damage (that requires repair); however, the strain demand on the PT bars will be small and the PT bars are relatively ductile, so it is expected that the initial condition of the system can be easily restored by restressing (i.e., repeating the post-tensioning operation on) the PT bars.

3.2.3 Member Yielding

The limited lateral drift capacity before the braces yield and become damaged is a major shortcoming of conventional CBF systems. One of the primary objectives in developing the SC-CBF system is to increase the drift capacity before damage initiates in the braces.

To that end, the rocking behavior of the SC-CBF system is introduced to limit the member forces that develop in the beams, columns, and braces.

Rocking tends to reduce the rate at which the member forces increase with increasing lateral drift; however, the member forces will increase with increasing lateral drift. Therefore, the members will eventually yield. This limit state will lead to permanent deformation and residual drift in the SC-CBF.

3.2.4 Member Failure

Failure of the beams, columns, or braces of the SC-CBF is defined as the loss of force capacity in the member due to excessive member deformation (e.g., member buckling or local buckling). A certain amount of post-yield deformation (ductility) capacity before failure will be available if the members are properly designed and detailed. However, eventually the member ductility capacity will be exhausted and the members will fail, which may lead to instability and collapse of the system.

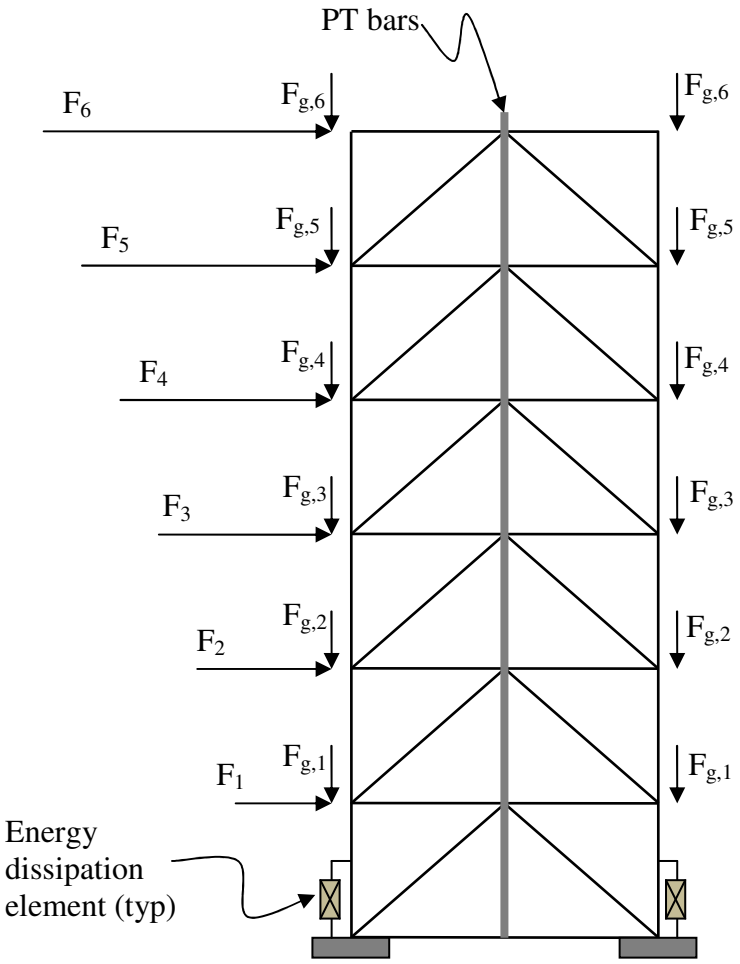

Figure 3.1 – Schematic of SC-CBF system

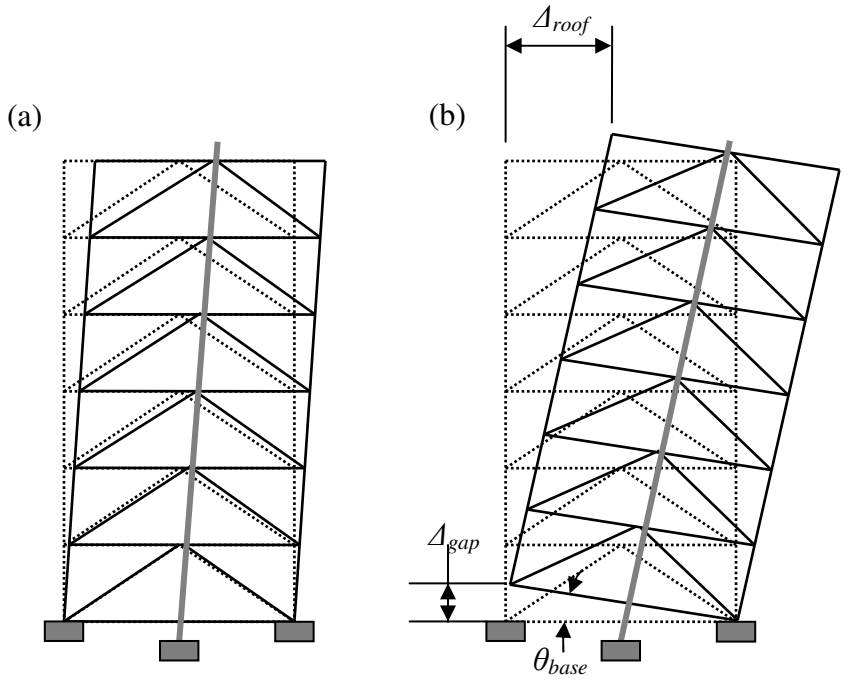

Figure 3.2 – SC-CBF behavior under lateral loading: (a) elastic response prior to column decompression; (b) rigid-body rotation due to rocking

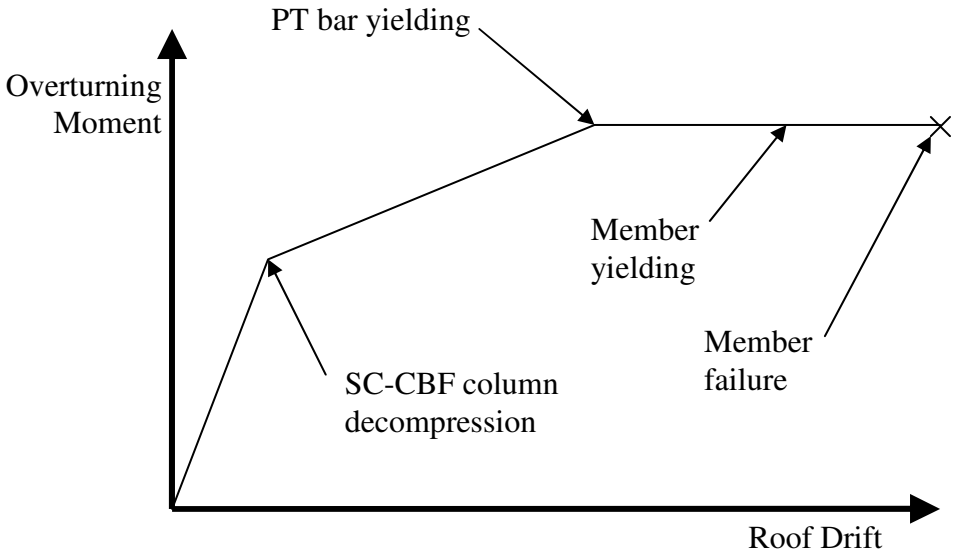

Figure 3.3 – Idealized overturning moment-roof drift response of an SC-CBF

CHAPTER 4

PERFORMANCE-BASED DESIGN

A performance-based seismic design (PBD) approach is an alternative to conventional strength-based seismic design methods in which performance objectives are established and achieved by controlling the occurrence of important structural limit states. Performance objectives are defined by establishing the performance level to be achieved for each seismic input level (seismic hazard level) that is considered. A performance level is defined in terms of the damage that is acceptable for the given performance level. The damage is defined by specific structural (or non-structural) limit states (e.g., member yielding). To develop PBD criteria for the SC-CBF system, performance levels and seismic hazard levels were identified from FEMA 450 (BSSC 2003). Important structural limit states for the SC-CBF system were defined in Chapter 3. The PBD criteria are based on associating each limit state with a performance level, and determining the seismic hazard (earthquake input) level at which each limit state is permitted to occur.

4.1 Seismic Performance Levels and Limit States

Seismic performance levels are used to categorize the structural response to an earthquake ground motion based on the state of the structure and the degree of damage after the earthquake. Four seismic performance levels are defined in FEMA 450 (BSSC

2003): operational (O), immediate occupancy (IO), life safety (LS), and collapse prevention (CP). This section presents definitions of these performance levels and relates them to the limit states defined in Chapter 3.

4.1.1 Operational (O)

FEMA 450 (BSSC 2003) defines the operational (O) performance level as follows:

> *"[T]he operational level represents the least level of damage to the structure. Structures meeting this level when responding to an earthquake are expected to experience only negligible damage to their structural systems and minor damage to nonstructural systems. The structure will retain nearly all of its pre-earthquake strength and stiffness and all mechanical, electrical, plumbing, and other systems necessary for the normal operation of the structure are expected to be functional. If repairs are required, these can be conducted at the convenience of the occupants.*
>
> *"The risk to life safety during an earthquake in a structure meeting this performance level is negligible. Note, that in order for a structure to meet this level, all utilities required for normal operation must be available, either through standard public service or emergency sources maintained for that purpose. Except for very low levels of ground motion, it is generally not practical to design structures to meet this performance level."*

As implied above, no structural damage can occur at the O performance level. With proper detailing of the column base, the limit state of column decompression (and uplift) should occur without structural damage, as previously mentioned. Since column

decompression is the only limit state that does not involve some degree of structural damage, only this limit state is permitted to occur within the O performance level.

4.1.2 Immediate Occupancy (IO)

FEMA 450 (BSSC 2003) defines the immediate occupancy (IO) performance level as follows:

> *"The immediate occupancy level is similar to the operational level although somewhat more damage to nonstructural systems is anticipated. Damage to the structural systems is very slight and the structure retains all of its pre-earthquake strength and nearly all of its stiffness. Nonstructural elements, including ceilings, cladding, and mechanical and electrical components, remain secured and do not represent hazards. Exterior nonstructural wall elements and roof elements continue to provide a weather barrier, and to be otherwise serviceable. The structure remains safe to occupy; however, some repair and clean-up is probably required before the structure can be restored to normal service. In particular, it is expected that utilities necessary for normal function of all systems will not be available, although those necessary for life safety systems would be provided. Some equipment and systems used in normal function of the structure may experience internal damage due to shaking of the structure, but most would be expected to operate if the necessary utility service was available. Similar to the operational level, the risk to life safety during an earthquake in a structure meeting this performance level is negligible. Structural repair may be completed at the occupants' convenience, however, significant nonstructural repair and cleanup is probably required before normal function of the structure can be restored."*

Since the IO performance level requires that the structure "retains all of its pre-earthquake strength and nearly all of its stiffness," this damage level is the minimum damage level considered in the proposed PBD approach. As discussed previously, the column base decompression limit state should occur without structural damage. As noted above, IO performance permits some structural damage, as long as it does not significantly reduce the original strength and stiffness of the system. Minor PT bar yielding that causes small losses of the initial force in the PT bars will not significantly reduce the strength of the SC-CBF, and is therefore permissible within the IO performance level.

4.1.3 Life Safety (LS)

FEMA 450 (BSSC 2003) defines the life safety (LS) performance level as follows:

> *"At the life safety level, significant structural and nonstructural damage has occurred. The structure may have lost a substantial amount of its original lateral stiffness and strength but still retains a significant margin against collapse. The structure may have permanent lateral offset and some elements of the seismic-force-resisting system may exhibit substantial cracking, spalling, yielding, and buckling. Nonstructural elements of the structure, while secured and not presenting falling hazards, are severely damaged and cannot function. The structure is not safe for continued occupancy until repairs are instituted as strong ground motion from aftershocks could result in life threatening damage. Repair of the structure is expected to be feasible, however, it may not be economically attractive to do so. The risk to life during an earthquake, in a structure meeting this performance level is very low."*

The limit states that are permitted within LS performance are column decompression, PT steel yielding, and member yielding. As previously mentioned, column decompression is a damage-free limit state that is permitted for all performance levels. PT bar yielding is the onset of structural damage; loss of initial PT bar force reduces the lateral force level at which column decompression occurs, but this loss in "strength" is permissible at the LS performance level. Additionally, LS performance permits elements of the seismic-force-resisting system to sustain yielding and buckling, as long as a significant margin against collapse is maintained.

4.1.4 Collapse Prevention (CP)

FEMA 450 (BSSC 2003) defines the collapse prevention (CP) performance level as follows:

> *"At the collapse prevention level a structure has sustained nearly complete damage. The seismic-force-resisting system has lost most of its original stiffness and strength and little margin remains against collapse. Substantial degradation of the structural elements has occurred including extensive cracking and spalling of masonry and concrete elements and buckling and fracture of steel elements. The structure may have significant permanent lateral offset. Nonstructural elements of the structure have experienced substantial damage and may have become dislodged creating falling hazards. The structure is unsafe for occupancy as even relatively moderate ground motion from aftershocks could induce collapse. Repair of the structure and restoration to service is probably not practically achievable."*

The limit states that are permissible at the CP performance level are column decompression, PT bar yielding, and member yielding. Member failure is not permitted due to the limited redundancy of the CBF system. If a compressive brace in one story of the SC-CBF were to fail, the tensile brace may be insufficient to carry the lateral force demand, and collapse would be possible.

4.2 Seismic Hazard Levels

Three seismic hazard levels are defined in FEMA 450 (BSSC 2003). These hazard levels are the maximum considered earthquake (MCE); the design basis earthquake (DBE); and the maximum probable event, which is often called the frequently occurring earthquake (FOE).

4.2.1 Maximum Considered Earthquake (MCE)

FEMA 450 (BSSC 2003) defines the MCE as a ground motion intensity that has a 2% probability of exceedance in 50 years, corresponding to a 2500-year return period. This intensity level is intended to be "reasonably representative of the most severe ground motion ever likely to affect a site."

4.2.2 Design Basis Earthquake (DBE)

The DBE is defined in FEMA 450 (BSSC 2003) as a ground motion intensity that is two-thirds that of the MCE. The DBE corresponds approximately to a ground motion intensity that has a return period of several hundred years.

4.2.3 Frequently Occurring Earthquake (FOE)

FEMA 450 (BSSC 2003) defines a "maximum probable event," or frequently occurring earthquake (FOE), as a ground motion intensity that has a 50% probability of exceedance in 50 years, corresponding to a 72-year return period. The FOE is used to establish the performance of structures under earthquake ground motions that are less severe but occur more frequently than the MCE or DBE.

4.3 Performance Objectives

4.3.1 Structural System

The performance objectives for the SC-CBF system are to achieve IO performance under DBE-level ground motions and to achieve CP performance under MCE-level ground motions. In comparison, the performance objectives for conventional seismic-resistant structural systems are to achieve LS performance under DBE-level ground motions and CP performance under MCE-level ground motions (BSSC 2003), so the intended performance of the SC-CBF system is better than that of conventional systems. In this section, these relationships between the performance levels and the seismic input levels will be described.

Figure 4.1 schematically illustrates the expected lateral force versus lateral roof drift behavior of an SC-CBF system. The performance levels and limit states are indicated on the figure as they are expected to occur.

There is significant uncertainty in the roof drift demand for DBE-level and MCE-level seismic input. There is also uncertainty in the limit state capacities (e.g., the roof drift at which the PT bars yield). However, the uncertainty in the capacities is significantly less than the uncertainty in the demands, as illustrated schematically in Figure 4.2, which shows the median demands and capacities as well as schematic probability density functions for those quantities. Since the dispersion in the demands is known to be significantly greater than the dispersion in the capacities, only the dispersion in the demand is explicitly considered in the PBD approach, as described later in Chapters 6 and 7.

FOE performance is not explicitly addressed by the performance objectives for the SC-CBF system. The intensity of the FOE is less than that of the DBE (BSSC 2003); therefore, it is reasonable to expect the performance of the SC-CBF under FOE-level ground motions to be better than the IO performance that is intended for DBE-level ground motions.

Under DBE-level ground motions, the performance objective for an SC-CBF system is to achieve IO performance. As discussed in Section 4.1, column decompression and minor PT bar yielding are permitted. Column decompression should produce no damage and minor PT bar yielding produces only minor damage (loss in initial PT force) that can be easily repaired. As discussed in Chapter 7, the PBD criteria developed for SC-CBFs do not permit PT bar yielding under median DBE-level seismic response, but PT bar yielding may occur under greater than median DBE response. That is, the probability of

PT bar yielding under DBE-level ground motions is intended to be less than 50%, but is not intended to be small (e.g., 5%).

Under MCE-level ground motions, the performance objective for an SC-CBF system is to achieve CP performance. As discussed in Section 4.1, the limit states permitted within the CP performance level are column decompression, PT bar yielding, and member yielding.

Table 4.1 summarizes the limit states that are permissible for each performance level and the corresponding seismic input levels according to the above performance objectives. The performance objectives are also shown schematically in Figure 4.3. Note that the seismic input levels shown in Figure 4.3 indicate the median response for each seismic input level. The significant uncertainties in the seismic responses (i.e., the seismic demands) are accounted for in the PBD procedure presented in Chapters 6 and 7.

4.3.2 Nonstructural Elements

The objective of the SC-CBF system is to achieve damage-free response under DBE-level seismic input, and to limit the damage under MCE-level seismic input. To fully quantify damage to the building, however, both structural and nonstructural elements must be considered. The structural damage is addressed by the performance-based design objectives outlined above. Damage to the nonstructural elements is addressed in this section.

To limit damage in nonstructural elements, both the story drifts and floor accelerations must be controlled. Story drifts must be controlled to limit the deformation demands on the partition, façade, piping, and HVAC systems. Accelerations must be controlled to

limit the acceleration felt by building occupants, and to limit the forces in mechanical equipment, their anchorages, and other building contents.

There are two components of story drift: elastic story drift due to deformations in the beams, columns, and braces, and the story drift due to the rocking of the SC-CBF. As previously mentioned, one performance objective for the SC-CBF system is to maintain elastic behavior in the structural members under DBE-level seismic input. The stiffness of the brace members tends to limit the elastic roof drift of the system. The story drift due to the rocking of the SC-CBF is controlled by the amount of PT steel used in the system, which affects the slope of the lateral force-roof drift response of the system after column decompression, as will be discussed in Chapter 7. For a conventional CBF system, the specified maximum story drift for the DBE is 2% (ASCE 2005). As shown later, SC-CBF systems can be designed to have substantially less drift than 2% under the DBE.

Rocking of the SC-CBF system tends to limit the floor accelerations in the structure by softening the lateral force versus roof drift response, which lengthens the fundamental period of the structure. The peak floor accelerations are controlled by the yield strength of the system (i.e., the lateral force level at which PT bar yielding occurs). The relationship between the yield strength and the design strength (e.g., the design base shear from an equivalent lateral force procedure) is the overstrength factor, Ω_0. For a conventional CBF system, Ω_0 is equal to 2.0 (ASCE 2005).

The story drift, floor accelerations, and overstrength of the prototype SC-CBF described later in the dissertation are evaluated in Chapter 12.

Table 4.1 – Summary of performance-based design objectives

Performance Level	Limit States				Input Levels	
	Column Decompression	PT Bar Yielding	Member Yielding	Member Failure	DBE	MCE
IO	X	X*			X	
CP	X	X	X			X

X = permitted for this performance level
X* = minor PT bar yielding permitted for IO performance level

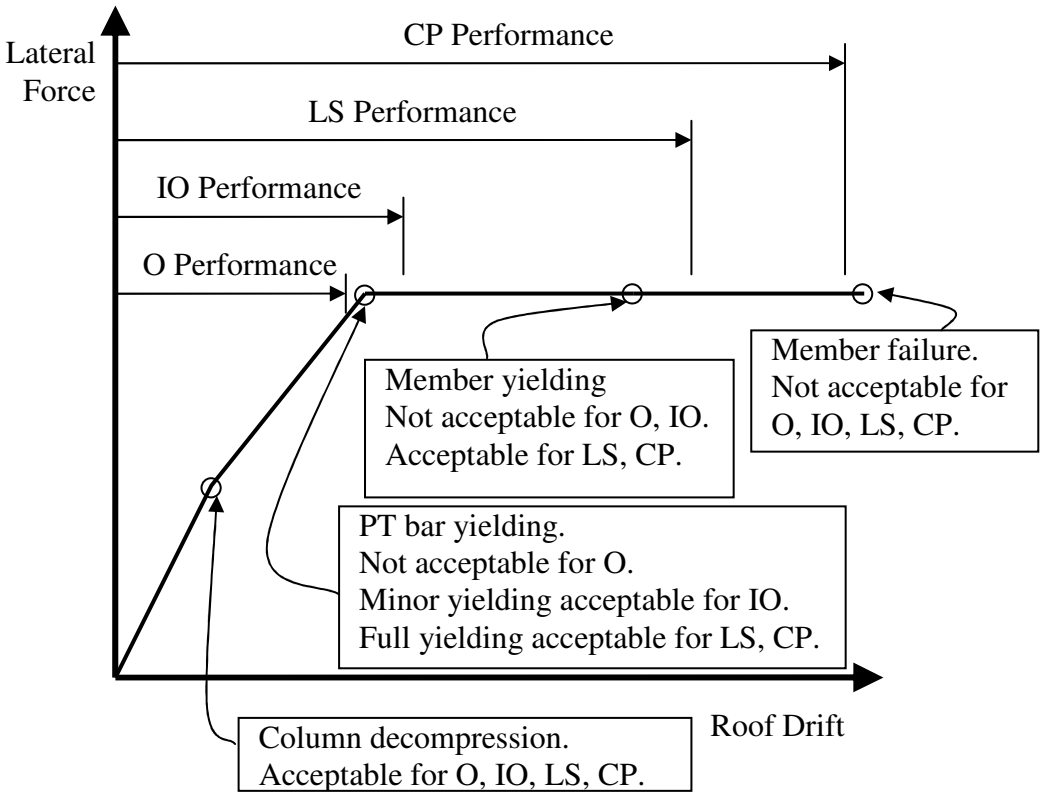

Figure 4.1 – Schematic of seismic performance levels

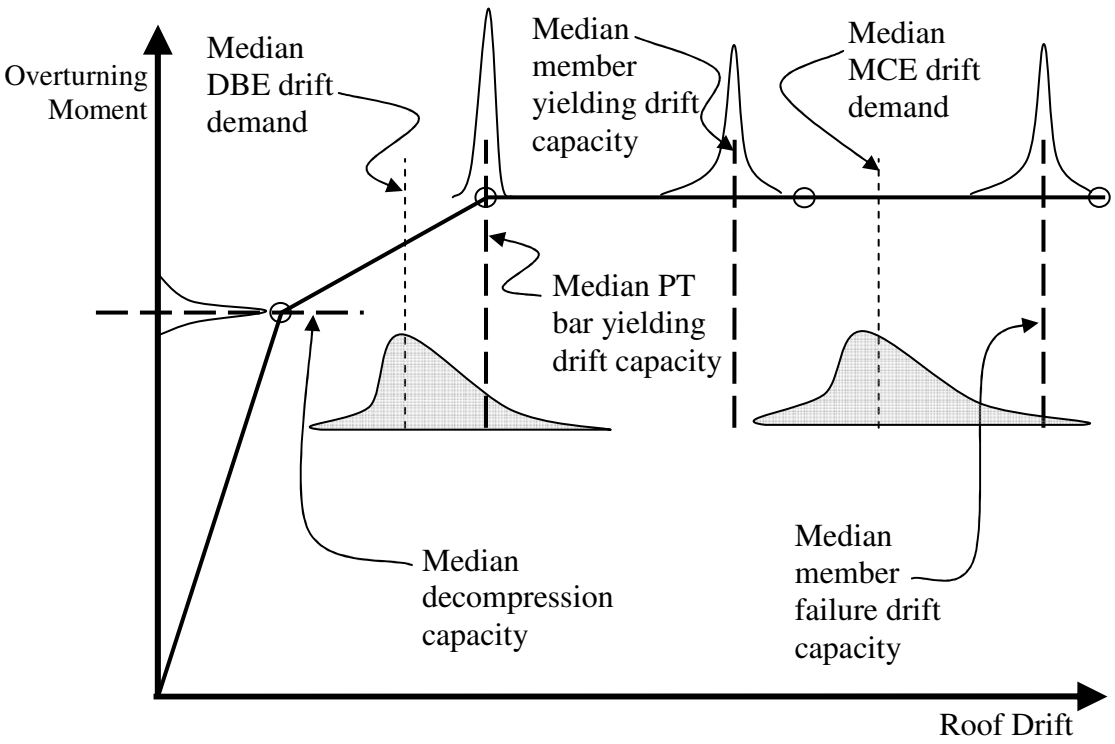

Figure 4.2 – Schematic of overturning moment versus roof drift response for the SC-CBF system, showing the dispersion of capacities and demands

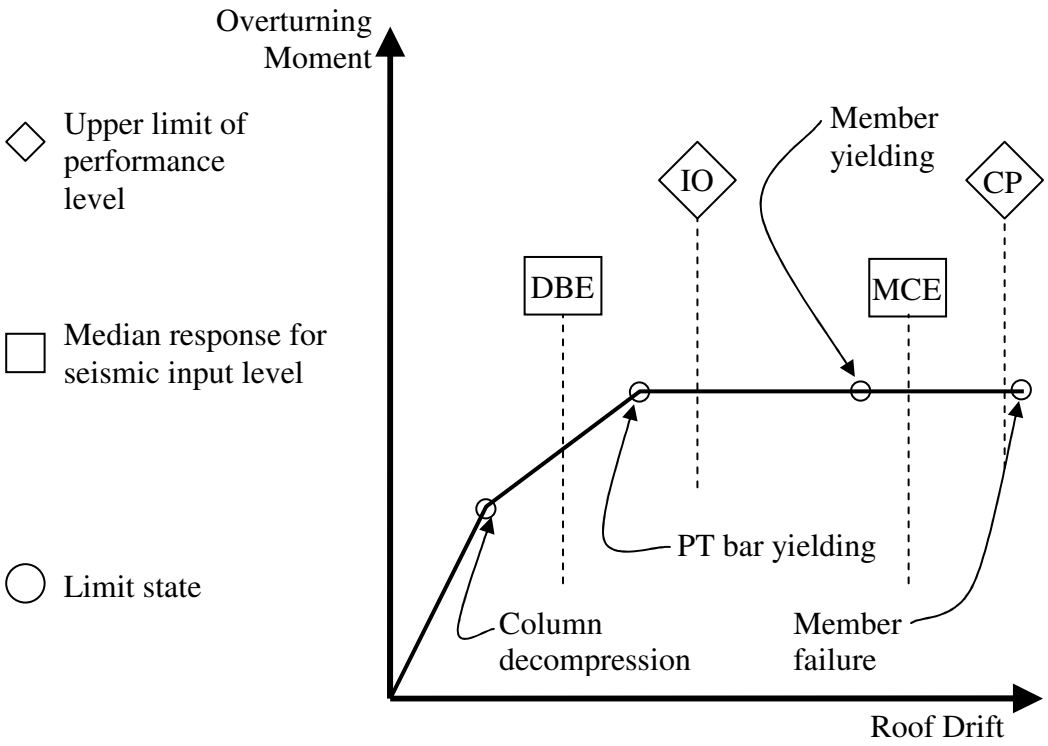

Figure 4.3 – Schematic of performance-based design criteria

CHAPTER 5

SC-CBF CONFIGURATION STUDY

As an initial step in developing the SC-CBF system, a study of several possible SC-CBF configurations was undertaken. This configuration study considers different arrangements of PT bars, different arrangements of SC-CBF members, and different energy dissipation elements. The results of the SC-CBF configuration study are presented in this chapter.

5.1 Prototype Building

To provide a practical context for this research, a prototype building was designed using SC-CBFs as the lateral-force resisting system. The prototype building is a six-story office building designed for a stiff-soil site (Site Class D (ASCE 2005)) in Van Nuys, California.

The floor plan and elevation of the prototype building are shown in Figure 5.1. The floor plan is a simple, 6-bay by 6-bay configuration with 30 ft bay widths. Four SC-CBFs are located in each direction of the building. The arrangement of the SC-CBFs avoids having a column included in more than one SC-CBF.

The assumed dead loads acting at each floor level of the prototype building are shown in Table 5.1. The dead loads include a concrete slab with a two-hour fire rating consisting of

3½ inches of lightweight concrete on a 2-in deep metal floor deck. Carpet is the assumed floor finish. The total gravity load at each floor is 90 psf. The total roof dead load is 110 psf, which accounts for the possibility of heavy mechanical equipment on the roof. The roof dead load conservatively includes a roof slab and roofing materials, leading to roof dead loads that are greater than typical values.

The assumed live loads acting in the building are 50 psf per floor (ASCE 2005), as shown in Table 5.2. The roof live load is also assumed to be 50 psf for consistency with the other floor loads, though this is higher than the roof live load specified by ASCE (2005). The conservatism in the roof loading is not expected to affect the results of the SC-CBF configuration study. The partition load (which is part of the live load) is assumed to be equal to 20 psf. The seismic mass is calculated based on the dead loads and the partition loads for the area of the prototype building for which the inertia forces are resisted by one SC-CBF (i.e., the tributary area for one SC-CBF, equal to one quarter of the total area shown in Figure 5.1). A summary of gravity loads for the tributary area for one SC-CBF column and seismic masses is provided in Tables 5.3 and 5.4.

5.2 Frame Configurations

The goal of this study is to understand the behavior of the SC-CBF system under seismic loading and to determine the effects of several parameters on that behavior. A series of SC-CBF configurations were considered to study the effects of a variety of parameters, including PT steel location, CBF member arrangement, energy dissipation elements, and interaction with the gravity load system.

5.2.1 Frame A

Frame A, shown in Figure 5.2, is the simplest SC-CBF configuration. The beams, columns, and braces of the system are arranged similarly to those of a conventional CBF system; however, details at the column bases permit column decompression and rocking of the SC-CBF. Vertical PT bars, aligned along the column lines, provide resistance to rocking and self-center the system.

Due to the arrangement of the PT bars along the column lines and the resulting column axial forces, the columns are expected to be heavier than those of a conventional CBF. The beams and braces, however, are not expected to differ in weight from those of a conventional CBF.

5.2.2 Frame B

Frame B is shown in Figure 5.3(a). Like Frame A, this configuration is similar to a conventional CBF. Again, the column bases are detailed to permit column decompression and rocking of the SC-CBF. Unlike in Frame A, the PT bars in Frame B are aligned at midbay, so the force in the PT bars is resisted by compressive axial forces in the braces in the uppermost story. Compared to Frame A, this realignment of the PT bars is expected to reduce the axial force demand in the upper story columns while increasing the axial force demand in the uppermost story braces.

The advantage of the midbay location of the PT bars is that for a given amplitude of column uplift and rocking, the PT bars in Frame B are subjected to half the elongation

demand of the PT bars in Frame A. This reduces the probability that the PT bar force demand will exceed the PT bar yield force during rocking.

5.2.3 Frame B_{ED}

Frame B_{ED}, shown in Figure 5.3(b), is nearly identical to Frame B. Frame B_{ED}, however, includes energy dissipation (ED) elements that deform (and dissipate energy) as a result of the rocking behavior of the SC-CBF. These ED elements have a number of effects: they add to the overturning moment resistance, they reduce the rocking response and the associated roof drift response of the system after column decompression, and they add to the energy dissipation capacity of the SC-CBF.

5.2.4 Frame C

Frame C, shown in Figure 5.4, is comprised of two CBFs in one bay, where each CBF can undergo column decompression and rocking behavior. Each CBF is similar in arrangement to Frame A, with the PT steel aligned along the column lines. ED elements are distributed at each floor level along the interface between the two CBFs. The ED elements are located at each floor to take advantage of any relative vertical displacements between the CBFs that are caused by higher mode response. The goal is to increase the energy dissipation during response with or without rocking, including response in the higher modes.

5.2.5 Frame D

Frame D is shown in Figure 5.5(a). In this configuration, two gravity-load-bearing columns (i.e., "gravity columns") are included with the SC-CBF in a single bay. The gravity columns do not decompress and uplift, avoiding the need to detail the floor system to carry vertical loads into columns that displace vertically. The PT bars are located at midbay for Frame D, as in Frame B. ED elements are located between the gravity columns and the SC-CBF, similar to the arrangement in Frame C. These ED elements are deformed by the relative vertical displacement between the gravity columns (which do not uplift) and the SC-CBF columns (which uplift when the SC-CBF rocks).

5.2.6 Frame D_{DIST}

Frame D_{DIST} is shown in Figure 5.5(b). Frame D_{DIST} is nearly identical to Frame D; the only difference is the addition of distribution struts in the upper stories to distribute the PT force over multiple stories. The distribution struts reduce the axial forces in the uppermost story braces and allow for more uniform sizes of the brace members over the height of the SC-CBF.

5.3 Initial Design Procedure

The initial design procedure used to design the SC-CBFs for the configuration study is summarized in this section.

The primary strength parameter for the SC-CBF system is the overturning moment. As noted in Chapter 3, the applied overturning moment will eventually cause column

decompression. After column decompression and uplift, large amplitude rocking response may cause PT bar yielding. The overturning moment capacities at these limit states are denoted OM_D (decompression) and OM_Y (yielding), respectively. The overturning moment demand determined from the equivalent lateral force (ELF) procedure described in ASCE-7 (2005), denoted OM_{ELF}, is a benchmark from which the design demand is determined. OM_D and OM_Y are determined from free-body diagrams of the SC-CBF system. These values are then compared against OM_{ELF} to determine the relative strength of the system at decompression and at PT bar yielding.

The PBD objectives for the SC-CBF system, presented in Chapter 4, require member yielding to occur after PT bar yielding, with the intention that PT bar yielding will help limit the force demands in the SC-CBF members. To achieve this, the member force design demands are based on the lateral forces that develop at OM_Y. The capacities of the members are then determined using AISC-LRFD criteria (AISC 2005b).

5.3.1 Equivalent Lateral Force Procedure

An ELF procedure (ASCE 2005) is used to determine lateral forces for the design of the SC-CBF system. The first step in the ELF procedure is to approximate the fundamental period of the prototype building. The approximate period is given as (ASCE 2005):

$$T_a = C_t \cdot h_n^x \tag{5.1}$$

where,

$C_t = 0.02$

x = 0.75 (ASCE7-05 Table 12.8-2 (ASCE 2005))

h_n = the total height of the structure

The seismic response coefficient is determined as follows (ASCE 2005):

$$C_S = \frac{S_{DS}}{\left(\frac{R}{I}\right)} \tag{5.2}$$

where,

R = the response modification coefficient, assumed to be 8 for SC-CBF systems

I = the importance factor, equal to 1.0 for Occupancy Category II (ASCE 2005)

Maximum and minimum values for the seismic response coefficient are (ASCE 2005):

$$C_{S,max} = \begin{cases} \dfrac{S_{D1}}{T_a \cdot \left(\frac{R}{I}\right)} & if\ T_a \le T_L \\ \dfrac{S_{D1} \cdot T_L}{T_a^2 \cdot \left(\frac{R}{I}\right)} & if\ T_a > T_L \end{cases} \tag{5.3}$$

$$C_{S,min} = \begin{cases} 0.01 & \\ \dfrac{0.5 \cdot S_1}{\left(\frac{R}{I}\right)} & if\ S_1 \ge 0.6g \end{cases} \tag{5.4}$$

Using C_S, the design base shear V is (ASCE 2005):

$$V = C_S \cdot W \tag{5.5}$$

where,

W = the total dead weight of the building, equal to the dead load plus the partition load

The individual lateral forces at each floor level are calculated as follows (ASCE 2005):

$$F_x = C_{vx} \cdot V \tag{5.6}$$

$$C_{vx} = \frac{w_x \cdot h_x^k}{\sum_{i=1}^{n} w_i \cdot h_i^k} \tag{5.7}$$

where,

F_x = lateral seismic force at the xth floor level

C_{vx} = vertical distribution factor for floor x

w_i and w_x = weight assigned to floor level i or x

h_i and h_x = height from the base of the building to floor level i or x

k = 1 for buildings with a fundamental period of 0.5 s or less, k = 2 for buildings with a fundamental period of 2.5 s or more; k is linearly interpolated between 1 and 2 for buildings with a fundamental period between 0.5 s and 2.5 s

The lateral forces from Equation 5.6 are distributed among the SC-CBFs acting in one direction of the building. In the case of the prototype building, there are four SC-CBFs oriented in each direction, as shown in Figure 5.1(a). These SC-CBFs are assumed to be identical; therefore, each SC-CBF is assumed to carry one fourth of the lateral force, and the equivalent lateral force vector $\{F_{ELF}\}$ for one six-story prototype SC-CBF is:

$$\{F_{ELF}\} = \frac{1}{4}\{F_{ELF,1} \quad F_{ELF,2} \quad F_{ELF,3} \quad F_{ELF,4} \quad F_{ELF,5} \quad F_{ELF,6}\}^T \tag{5.8}$$

For SC-CBF design, the ELF overturning moment is determined as follows:

$$OM_{ELF} = \{h\}^T \{F_{ELF}\} \tag{5.9}$$

where,

$\{h\}$ = vector of heights from the base of the SC-CBF to each floor level

5.3.2 Limit States Considered in Design

This section discusses the global SC-CBF design parameters that determine the occurrence of the limit states of column decompression, PT bar yielding, and member yielding.

5.3.2.1 Column Decompression

When the initial overturning moment resistance of the SC-CBF is overcome by the applied overturning moment, the "tension" column decompresses. The resulting column

uplift is referred to as gap-opening behavior. The overturning moment at column decompression is referred to as OM_D.

For the initial design procedure, the overturning moment demand at decompression is expressed in terms of OM_{ELF} as follows:

$$OM_{D,demand} = \alpha_{D,required} \cdot OM_{ELF} \tag{5.10}$$

For the SC-CBF configuration study, $\alpha_{D,required}$ was arbitrarily set to approximately 0.80. This means that column decompression will occur at an overturning moment that is no less than approximately 80% of OM_{ELF}.

The decompression overturning moment capacity, OM_D, is calculated from a free-body diagram of the SC-CBF, including the base overturning moment resistance from the weight of the SC-CBF ($W_{SC\text{-}CBF}$), the initial PT bar force (PT_0), and any ED elements (V_{ED}). For example, Figure 5.6 shows a free-body diagram of Frame D_{DIST} at decompression. From this figure, OM_D is calculated by considering the resistance to the overturning moment as follows:

$$OM_D = \left(PT_0 + W_{SC-CBF}\right) \cdot \frac{b_{SC-CBF}}{2} + \sum_{i=1}^{N} V_{ED,i} \cdot b_{bay} \tag{5.11}$$

where,

b_{bay} = center-to-center spacing of the gravity columns

$b_{SC\text{-}CBF}$ = center-to-center spacing of the SC-CBF columns

N = number of ED elements

$V_{ED,i}$ = yield force of ED element i

PT_0 = initial force in PT bars

$W_{SC\text{-}CBF}$ = total weight of SC-CBF members

Equation 5.11 is written for Frame D_{DIST}. Each frame configuration is different, so the calculation of OM_D must be adjusted to account for the geometry and resisting forces present. Note that for Frame D_{DIST}, the ED forces are shown to act along the centerlines of the gravity columns in Figure 5.6, and the overturning moment contribution of the ED elements is included accordingly in Equation 5.11. The geometry of Frame D_{DIST} (Figure 5.5(b)) has the ED elements located between the gravity column and the SC-CBF column, that is, $\Sigma V_{ED,i}$ acts eccentrically from each column. The gravity columns are assumed to be relatively flexible in bending compared to the lateral stiffness of the SC-CBF. The moment produced by the eccentricity from each gravity column to the line of action of $\Sigma V_{ED,i}$ is expected to be resisted by a redistribution of the lateral forces between the gravity column and the SC-CBF, as shown in Figure 5.7(a). Figure 5.7(b) shows free-body diagrams in which ΣV_{ED} is assumed to act along the centerline of the gravity column, resulting in statically equivalent forces acting on the SC-CBF, including a known distribution of lateral forces acting on the SC-CBF. Therefore, ΣV_{ED} is assumed to act along the centerline of the gravity columns for Frames D and D_{DIST}.

Equation 5.11 shows that OM_D is a function of the initial PT bar force PT_0 (which is equal to the area of the PT steel, A_{PT}, times the initial stress in the bars, σ_0) and ΣV_{ED}. The

overturning moment capacity at decompression for Frame D_{DIST} can be readily adjusted by changing A_{PT}, σ_0, or ΣV_{ED}.

5.3.2.2 PT Bar Yielding

The limit state of PT bar yielding occurs when the overturning moment capacity of the SC-CBF at PT yield is reached by the overturning moment demand. The overturning moment capacity at PT yield is referred to as OM_Y.

OM_Y is calculated from a free-body diagram of the SC-CBF, including the base overturning moment resistance from the weight of the SC-CBF ($W_{SC\text{-}CBF}$), the PT bar yield force (PT_Y), and any ED elements (V_{ED}). For example, Figure 5.8 shows a free-body diagram of Frame D_{DIST} at PT bar yield. From this figure, OM_Y is calculated by considering the resistance to overturning moment when the PT bars yield, as follows:

$$OM_Y = \left(PT_Y + W_{SC-CBF}\right) \cdot \frac{b_{SC-CBF}}{2} + \sum_{i=1}^{N} V_{ED,i} \cdot b_{bay} \tag{5.12}$$

where,

PT_Y = yield force of PT bars

Equation 5.12 is similar to Equation 5.11; the only difference is the value of the PT bar force. As with Equation 5.11, Equation 5.12 applies for Frame D_{DIST} and requires modification for other frame configurations.

The ratio of OM_Y to OM_{ELF} is used to relate the strength of the SC-CBF system at PT yield to the strength of conventional frame systems. $\alpha_{Y,ELF}$ is defined as:

$$\alpha_{Y,ELF} = \frac{OM_Y}{OM_{ELF}} \tag{5.13}$$

Equation 5.12 shows that OM_Y is a function of the PT bar yield force PT_Y (which is equal to the area of the PT steel, A_{PT}, times the yield stress in the bars, σ_Y) and ΣV_{ED}. Assuming that the yield stress of the PT bars is constant, the value of OM_Y for Frame D_{DIST} can be adjusted by changing A_{PT} or ΣV_{ED}.

5.3.2.3 Member Design

This section explains the calculation of the member force design demands in the initial design procedure used for the configuration study. The member force design demands are determined from a nonlinear pushover analysis as discussed in this section.

5.3.2.3.1 Determination of Member Force Design Demands

A nonlinear analytical model of the SC-CBF was developed using the nonlinear structural analysis software OpenSEES (Mazzoni et al. 2009) and was used to determine the member force design demands. A different model was created for each SC-CBF configuration. The analytical model for Frame D_{DIST} is shown in Figure 5.9. The SC-CBF column base behavior is modeled using compression-only gap elements. The PT steel is modeled using bilinear elastic-plastic truss elements with a yield strength equal to the nominal yield stress of the PT bars (120 ksi) multiplied by the PT bar area and a post-yielding stiffness equal to 2% of the initial stiffness. The nodes in the analytical model are located at the working points of the connections between structural members. Note that the gravity column bases are pinned; these pins are at the same height as the base of

the SC-CBF columns, but are offset in Figure 5.9 for clarity. The connections between the SC-CBF members are assumed to be rigid. Cross-section properties of the elements are based on the cross-section properties of the members. The finite dimensions of the joint regions are neglected (i.e., centerline dimensions are used to define the element lengths). The SC-CBF members and the gravity columns are modeled as linear-elastic to enable the member force demands to be determined. P-Δ effects are included in the elements that model the SC-CBF members.

The SC-CBF member force design demands in the configuration study were determined from a static pushover analysis of the OpenSEES model. The pushover analysis was taken up to the point of PT bar yielding (i.e., the applied lateral forces are scaled until OM_Y is reached). The lateral force profile used in this pushover analysis is $\{F_{ELF}\}$, scaled by $\alpha_{Y,ELF}$ to be in equilibrium with OM_Y. Figure 5.10 shows the forces applied to the analytical model and the vertical resisting forces that develop in the energy dissipation elements. The member forces at this state were taken as the member force design demands, $F_{x,Y}$. The models and applied forces for the other frame configurations are similar.

5.3.2.3.2 SC-CBF Member Selection

The SC-CBF connections were assumed to transmit bending moment. Therefore, the members were selected to satisfy the AISC-LRFD criteria (AISC 2005b) for axial force-bending moment interaction:

$$\frac{P_r}{\phi_c P_n} + \frac{8}{9} \cdot \left(\frac{M_{rx}}{\phi_b M_{nx}} + \frac{M_{ry}}{\phi_b M_{ny}} \right) \leq 1.0 \text{ for } \frac{P_r}{\phi_c P_n} \geq 0.2 \quad (5.14)$$

$$\frac{P_r}{2 \cdot \phi_c P_n} + \left(\frac{M_{rx}}{\phi_b M_{nx}} + \frac{M_{ry}}{\phi_b M_{ny}} \right) \leq 1.0 \text{ for } \frac{P_r}{\phi_c P_n} < 0.2 \quad (5.15)$$

where,

P_r = factored design axial force demand determined from second-order analysis (AISC 2005b)

ϕ_c = compression resistance reduction factor, equal to 0.9

P_n = nominal compressive strength of the member

M_{rx} = factored design strong axis bending moment demand determined from second-order analysis (AISC 2005b)

M_{ry} = factored design weak axis bending moment, assumed to be zero

ϕ_b = flexural bending resistance reduction factor, equal to 0.9

M_{ny} and M_{nx} = nominal flexural strength about each cross-sectional axis of the member

As mentioned previously, P-Δ effects are included in the elements modeling the SC-CBF structural members. P-δ effects were neglected in determining P_r and M_{rx}, which were set equal to $F_{x,Y}$.

5.3.3 Hysteretic Energy Dissipation Ratio, β_E

The hysteretic energy dissipation ratio, β_E, is defined as the ratio of the energy dissipated by the hysteresis loop of an SC system to the energy dissipated by a bilinear elasto-plastic system with the same strength under cyclic loading to the same peak displacement (Seo and Sause 2005). The force-displacement behavior for SC systems with various values of β_E is shown in Figure 5.11. The maximum β_E for the types of SC systems shown in Figure 5.11 is 0.50 (see Figure 5.11(d)). The design value of β_E must, therefore, be less than 0.50. Figure 5.12 shows the expected overturning moment-roof drift (i.e., OM vs θ) response for an SC system, indicating critical values of the overturning moment. Note that PT bar yielding affects the energy dissipation of the system; the hysteresis loop shown in Figure 5.12 is valid only while the PT bars remain linear elastic. From Figure 5.12, β_E is calculated as:

$$\beta_E = \frac{OM_{ED}}{OM_D} \tag{5.16}$$

The overturning moment resistance provided by the ED elements, OM_{ED}, can be calculated based on a free-body diagram of the SC-CBF. For example, a free-body diagram of Frame B_{ED} at column decompression is presented in Figure 5.13.

From Figure 5.13, for Frame B_{ED}, OM_D can be written as:

$$OM_D = \sum_{i=1}^{N} F_{g,i} \cdot b_{bay} + \left(PT_0 + W_{SC-CBF}\right) \cdot \frac{b_{bay}}{2} + V_{ED} \cdot b_{bay} \tag{5.17}$$

where,

$F_{g,i}$ = gravity load acting at floor level i

and OM_{ED} for Frame B_{ED} can be written as:

$$OM_{ED} = V_{ED} \cdot b_{bay} \tag{5.18}$$

β_E for Frame B_{ED} can then be determined from Equation 5.16.

5.3.4 Frame Configuration Design Summary

Each frame was designed iteratively using the procedure outlined above. For the frame configuration study, $W_{SC\text{-}CBF}$ was neglected in determining OM_D and OM_Y. The column sizes were varied every three stories. The member selections for each configuration are shown in Figures 5.14 – 5.19. The weights of the structural components for each frame are summarized in Table 5.5. The six natural periods for each frame are summarized in Table 5.6, based on the analytical model discussed in Section 5.4.1. The energy dissipation properties (modal damping ratios ζ_n, and energy dissipation ratio β_E) of each frame are summarized in Table 5.7. The values of $\alpha_{Y,ELF}$ are summarized in Table 5.8.

As previously mentioned, the value of $\alpha_{D,required}$ used for the design of these frames was approximately 0.80. For Frame A, this was achieved using PT bars with an initial stress equal to 20% of their yield capacity (i.e., $\sigma_0 = 0.20\sigma_Y$). The required area of the PT bars at each column line (15.0 in^2 per location) was determined from the initial stress σ_0 and the required initial force PT_0. The overall strength of the system, OM_Y, was controlled by the PT bar area and the PT bar yield stress (120 ksi).

Frame B was designed using the PT bar area from one column line of Frame A (15.0 in^2) as the total bar area, located at midbay. σ_0 was $0.20 \cdot \sigma_Y$. As a result, the actual OM_D of Frame B was less than $0.80 \cdot OM_{ELF}$. Frame B_{ED} has the same PT bar area and σ_0 as Frame B, but the energy dissipation elements increase OM_D of the system, increasing OM_D to $0.80 \cdot OM_{ELF}$ for Frame B_{ED}.

Frame C was designed with σ_0 equal to $0.30 \cdot \sigma_Y$. For comparison with Frame A, the same total PT steel area (30.0 in^2) was used resulting in 7.5 in^2 for each of the four PT bar locations in Frame C. The energy dissipation elements were selected so that OM_D for Frame C was similar to that of Frame B.

Frames D and D_{DIST} were designed to achieve an overall strength, OM_Y, that is the same as that of Frame B_{ED}. Since the gravity loads on the columns no longer contribute to the overturning moment resistance for these configurations, more PT steel was needed, resulting in a total PT bar area of 25.0 in^2. σ_0 was equal to $0.43 \cdot \sigma_Y$.

5.4 Analysis Results

Two types of analyses were performed in this study: static analyses and dynamic analyses. The static analyses included nonlinear monotonic pushovers and nonlinear cyclic pushovers. The dynamic analyses are nonlinear time history analyses of the response of the SC-CBF systems to a suite of ground motions scaled to the DBE level.

5.4.1 Preliminary Nonlinear Analytical Model for 6-Story Prototypes

Nonlinear analytical models were created in OpenSEES (Mazzoni et al. 2009) to study these frame configurations. The global behavior of the system is the focus at this stage of the research rather than local responses, so the analytical models used for the frame configuration study are relatively simple. In particular, the beams, columns, and braces of the SC-CBF (i.e., SC-CBF members) are modeled as linear-elastic to enable the force demands on these members to be determined. As previously mentioned, $W_{SC\text{-}CBF}$ was disregarded for the frame configuration study. Additionally, only the six stories of the superstructure are modeled, and there is no consideration of the flexibility of the foundation or the basement level. The nodes in the analytical model are located at the working points of the connections between structural members. The connections between SC-CBF members were assumed to be rigid.

The seismic masses (based on the tributary area for one SC-CBF) are modeled as lumped masses at each floor level. For Frames A, B, B_{ED}, D, and D_{DIST}, the masses are located at the intersection of the braces. For Frame C, the masses are located at the intersection of the braces in the left SC-CBF, and the nodes at the intersection of the braces in the right SC-CBF are constrained to the nodes in the left SC-CBF so that the two SC-CBFs have identical horizontal displacements. For nonlinear static analyses, the lateral forces are applied on the nodes with the lumped masses. The gravity loads (based on the tributary area for one SC-CBF column) are modeled as concentrated vertical loads on the columns. The preliminary SC-CBF analytical model does not incorporate a lean-on column for P-Δ effects due to the total gravity load of the tributary area for one SC-CBF; P-Δ effects are

included in the elements that model the SC-CBF members (for all SC-CBF configurations) and the adjacent gravity columns (for Frames D and D_{DIST}).

Nonlinearities in the preliminary SC-CBF analytical model are included in three elements: (1) the ED elements, (2) the elements that model the PT bars, and (3) the elements that model decompression and uplift at the base of the SC-CBF columns. The ED elements are assumed to be Coulomb-friction elements modeled as elastic-plastic elements with a fixed yield force (i.e., the friction slip force). The PT bars were modeled as bilinear truss-bar elements with a post-yielding stiffness equal to 2% of the initial stiffness. These elements were in series with tension-only gap elements. These gap elements permit the PT bars to yield in tension but do not permit the bars to resist compressive forces. This series of elements models the behavior of the PT bars as they lose their initial force (i.e., their prestress) after yielding. The column base decompression is modeled using compression-only gap elements located at the base of the columns. These elements permit uplift of the column base while providing a linear-elastic compressive resistance when the column base is in contact with the foundation. Horizontal force (i.e., base shear force) resistance is provided only when the column is in contact; therefore, only the column that is in contact resists the base shear. Sliding at the base due to slip is not permitted in the preliminary SC-CBF analytical model.

Rayleigh damping is included in the model for the dynamic analyses. The damping ratios in the first and third modes are 5% to match the design spectrum (ASCE 2005). The resulting damping ratios in the other modes vary for the different frame configurations, as shown in Table 5.7. Damping was applied to the beams, columns, braces, and masses of

the system. The column base gap elements were left undamped due to the large localized relative velocities that were expected for these elements. Similarly, the PT bar elements were left undamped.

Figure 5.20 shows a schematic of the analytical model for Frame B. In this figure, the PT bars are shown out of alignment to clearly show the element connectivity. In the model, these elements have a straight line geometry.

5.4.2 Static Analysis

Static analyses were conducted using force patterns proportional to $\{F_{ELF}\}$. Two types of static analyses were performed on the structure: nonlinear monotonic pushovers and nonlinear cyclic pushovers. The monotonic pushovers were intended to determine the stiffness and strength of each frame configuration and to verify the occurrence of the limit states. The cyclic pushovers were intended to quantify the energy dissipation capacity of each frame configuration.

5.4.2.1 Monotonic Pushover

Figure 5.21 summarizes the results of the monotonic pushover analyses.

The initial (pre-decompression) stiffness of each frame configuration is a function of the geometry of the frame and the sizes of the structural members. The sizes of the structural members are governed by the member force demands that develop as OM_Y is reached (i.e., at PT bar yield), as discussed in Section 5.3.2.3.

As previously mentioned, the decompression point (i.e., OM_D) for each frame configuration is a function of the geometry of the SC-CBF (e.g. location of PT steel and bay width of the SC-CBF), the initial force in the PT bars (PT_0), and the force capacity of any ED elements.

The ultimate strength of the system (i.e., overturning moment strength, OM_Y) is a function of the yield force of the PT steel (i.e., σ_Y times the PT steel area A_{PT}) and the geometry of the SC-CBF. The overturning moment resistance contribution from the PT bars is also a function of the perpendicular distance from the compression column to the PT bars. For this reason, Frame A has greater ultimate strength than Frame B, even though the A_{PT} along one column of Frame A (i.e., $A_{PT,A}$ / 2) is equal to A_{PT} in Frame B (i.e., $A_{PT,B}$). This effect can be seen in Equation 5.12, where ($b_{SC\text{-}CBF}$ / 2) is the perpendicular distance from the compression column to the PT bars for Frame D_{DIST}.

Figure 5.21 indicates that there is a significant P-Δ effect in the pushover response of the SC-CBFs, although only the gravity load tributary to the SC-CBF columns is included in the model (rather than the entire gravity load tributary to the SC-CBF). This is due to the limited stiffness of the system after PT yielding. After column decompression, the PT bars provide the only resistance to roof drift. As previously mentioned, the post-yielding stiffness of the PT bars is only 2% of the initial stiffness. The negative stiffness due to P-Δ effects is greater than the stiffness provided by the yielded PT bars; therefore, the stiffness of the SC-CBF after PT bar yielding is negative.

5.4.2.2 Cyclic Pushover

Cyclic pushover analyses were performed to determine the energy dissipation capacity of the frame configurations with ED elements. Figure 5.22 summarizes the results of the cyclic pushover analyses. Figures 5.23 through 5.28 show the response to two cycles of loading for each frame configuration.

Figure 5.22(a) shows that the cyclic loading behavior of Frame A and Frame B exhibits hysteresis only after PT yielding. As shown in Figure 5.23(a) (Frame A) and Figure 5.24(a) (Frame B), multiple cycles of loading below PT yield dissipate no energy. Figures 5.23(b) and 5.24(b) show energy dissipation after PT bar yielding. Note the decrease in lateral force resistance at decompression (decompression strength) from the partial loss of the initial PT bar force after PT bar yielding (i.e., the PT bar force at zero lateral drift is reduced after yielding). The loading curve for the second cycle of loading follows the unloading curve for the first cycle of loading. The second cycle of loading to the same roof drift does not yield the bars further.

Frame B_{ED} has only one active ED element (i.e., one element that is deformed as a result of the rocking of the SC-CBF) in the cyclic pushover. Therefore, the hysteresis loop for Frame B_{ED} (Figure 5.22(b)) is controlled by the force-reversal behavior of the ED element. Figure 5.25(a) shows two cycles of loading for Frame B_{ED}, showing the repeatability of the hysteresis when only a single ED element is involved. Figure 5.25(b) shows two cycles of loading beyond PT bar yielding for Frame B_{ED}. The response is similar to that of Frames A and B, where the decompression strength decreases due to a

partial loss of the initial PT bar force, and the second cycle of response unloads along the unloading curve from the first cycle.

Frames D (Figure 5.22(b)), C, and D_{DIST} (Figure 5.22(c)) have multiple active ED elements (i.e., multiple elements are deformed by the rocking behavior) in the cyclic pushover. The ED elements at different floor levels are subjected to force reversal at different levels of lateral drift during unloading; therefore, the hysteresis loops are rounded compared to the hysteresis loop for Frame B_{ED}. Note that Frame D and Frame D_{DIST} have nearly identical responses. The cyclic pushover response is not influenced much by the individual SC-CBF members when they remain elastic. The only difference between the responses of Frames D and D_{DIST} is the initial elastic stiffness.

Frames C, D, and D_{DIST} have residual roof drift at the end of the cyclic pushover. The residual forces in the ED elements distributed over the height of the structure create a distribution of internal forces that causes elastic deformation of the SC-CBF. Frame B_{ED} exhibits no notable residual drift because it has only a single ED element at the base of the SC-CBF, which does not cause elastic deformation of the SC-CBF.

Figures 5.26, 5.27, and 5.28 show the response of Frames C, D, and D_{DIST}, respectively, to two cycles of loading. Figures 5.26(a), 5.27(a), and 5.28(a) show the response to cyclic loading to 1% roof drift. For these frames, the second cycle of loading response is different from the first cycle due to the forces in the ED elements distributed over the height of the structure. After the ED elements are fully yielded, however, the second cycle loading curve joins the first cycle loading curve. Figures 5.26(b), 5.27(b), and

5.28(b) show the response to cyclic loading after PT bar yielding. As with Frames A and B, a partial loss of the initial PT bar force from PT bar yielding reduces the decompression strength. The second cycle of response unloads along the unloading curve from the first cycle of response.

5.4.3 Dynamic Analysis

5.4.3.1 Ground Motions

A suite of 12 ground motions was selected for the dynamic analyses used in the frame configuration study. The ground motions were selected because they have pseudo-acceleration response spectrum shapes similar to that of the DBE design spectrum (ASCE 2005). Each ground motion was scaled to the DBE hazard level according to the method proposed by Seo (2005). Seo's expression for the scale factor is:

$$SF = \exp\left(\frac{\sum_{k}^{m}\left(\ln\left(SA_{design}\left(T_k\right)/SA_{GM}\left(T_k\right)\right)+\ln\left(SA_{design}\left(T_{k+1}\right)/SA_{GM}\left(T_{k+1}\right)\right)\right).\frac{\Delta T_k}{2}}{\sum_{k}^{m}\Delta T_k}\right) \qquad (5.19)$$

This scaling method minimizes the difference between the natural log of the design spectral acceleration and the natural log of the ground motion spectral acceleration (i.e., natural log of the ground motion pseudo-acceleration) over a selected period range. The ratios of the natural log of the spectral acceleration at selected periods T_k are weighted by one-half the period range defined by $\Delta T_k = T_{k+1} - T_k$. A scaling procedure that considers a range of periods is advantageous for the frame configuration study because the structures with the various frame configurations have different natural periods. Note that the natural

periods are determined from the seismic mass tributary to a single SC-CBF (i.e., one quarter of the total mass for the prototype building shown in Figure 5.1).

For the configuration study, the periods used to determine the scale factor were: 0.1 s, 1.0 s, 2.0 s, and 4.0 s. The scale factor based on these periods can be written as:

$$SF = \left(\frac{SA_{design}(0.1)}{SA_{GM}(0.1)} \right)^{0.1154} \left(\frac{SA_{design}(1.0)}{SA_{GM}(1.0)} \right)^{0.2436} \left(\frac{SA_{design}(2.0)}{SA_{GM}(2.0)} \right)^{0.3846} \left(\frac{SA_{design}(4.0)}{SA_{GM}(4.0)} \right)^{0.2564} \quad (5.20)$$

where,

$SA_{design}(t)$ = design spectral acceleration at period t

$SA_{GM}(t)$ = spectral acceleration for the unscaled ground motion at period t

The ground motions used for the frame configuration study are summarized in Table 5.9. Figure 5.29 shows the design spectrum (ASCE 2005) and the spectral accelerations (i.e., the pseudo-acceleration spectra) for each of the scaled ground motions used in this study.

5.4.3.2 Dynamic Analysis Results

Typical dynamic responses for the SC-CBF system are shown in Figures 5.30 through 5.35. Figures 5.30(a) through 5.35(a) show the roof drift response and the column base gap-opening response of the various frame configurations to the DBE-level ground motion nr0ccy270. In these figures, roof drift to the right is considered positive and gap-opening at the base of the left SC-CBF column is considered positive. Roof drift to the left is considered negative and gap-opening at the base of the right SC-CBF column is considered negative. These figures show that roof drift response is closely related to the

gap-opening (i.e., rocking) response. Note that there is a minimum roof drift at which the column decompresses and a gap opens, which depends on the elastic (pre-decompression) stiffness of the SC-CBF. For the response of Frame C (Figure 5.33), the response shown is for the left CBF in Figure 5.4. The left exterior column is at the far left of Figure 5.4, and the left interior column is the column directly to the left of the ED elements.

In Figures 5.30(a) through 5.35(a), the lengthening of the structural period due to SC-CBF rocking is shown. That is, during rocking (when one column has decompressed), the effective period of the roof drift response is lengthened with respect to the period when both columns are in contact with the foundation. This period elongation is due to the softening of the overturning moment versus roof drift behavior after column decompression. The degree to which the period is lengthened is a function of the initial elastic stiffness of the frame, the frame configuration, and A_{PT}, which affect the post-decompression stiffness (as discussed in Section 5.4.2.1).

The relationship between gap-opening and PT force can be seen in Figures 5.30(b) through 5.35(b). For Frame A (Figure 5.30(b)), the left PT bar force is plotted. For Frame C (Figure 5.33(b), the left exterior PT bar force is plotted. The PT force response of Frame A and Frame C depends upon which column decompresses; when column decompression occurs at the column line where the PT bars are located, the PT bars extend and their force increases. When column decompression occurs at the opposite column, the PT bars shorten and their forces decrease. For the other frame configurations, the PT bars are located at midbay, so the PT force response is independent of which column decompresses.

Figures 5.30(c) through 5.35(c) show the typical time history response of the first story south brace force demand for each frame configuration. The horizontal lines in the figures show the axial force design demand, which was determined as described in Section 5.2.2.3. At many times during the response, the brace force demand from the nonlinear dynamic analyses is significantly greater than the design demand. Note that, as discussed in Section 5.4.1, the braces are modeled as linear elastic elements, so the observed response does not include nonlinear behavior (i.e., yielding) within the member.

The peak responses of each frame configuration and mean values of the peak responses are summarized in Figure 5.36. Figure 5.36(a) shows the peak dynamic roof drift responses (i.e., the peak response from the nonlinear dynamic analyses under each of the DBE-level ground motions) for each frame configuration. Figure 5.36(b) shows the peak dynamic PT force responses normalized by the PT yield force capacity for each frame configuration. Figure 5.36(c) shows the peak dynamic brace force response for each story of each frame configuration, normalized by the axial force design demand for the braces in that story. These figures illustrate the large dispersion (as a function of the ground motion) in the dynamic response, as mentioned in Chapter 4.

The peak roof drift responses of the different frame configurations, shown in Figure 5.36(a), illustrate the effects of changing the design parameters. The PT steel for Frame A is located along the column line, whereas the PT steel for Frame B is located at midbay. As a result of the larger post-decompression stiffness of Frame A, Frame A has a smaller mean roof drift response when compared with Frame B. The effect of adding ED elements can be seen when comparing the roof drift responses of Frame B and Frame

B_{ED}, where the mean roof drift response of Frame B_{ED} is less than that of Frame B. Frames D and D_{DIST} have similar configuration, though they have slightly different elastic stiffnesses; the similarity in their mean peak roof drift response indicates that the roof drift demand is not very sensitive to small differences in elastic stiffness.

The peak PT force responses, normalized by the PT yield force capacity for each configuration, are summarized in Figure 5.36(b). Locating the PT steel along the column lines, as in Frame A and Frame C, tends to produce large PT bar force response due to the increased elongation demand. The effect of moving the PT bars to midbay is shown by comparing the results for Frame A and Frame B; the mean PT bar force response is greatly reduced by locating the PT bars at midbay. As expected, the addition of ED elements also reduces the mean dynamic PT force response. The mean PT force response for Frame B_{ED} is much less than that for Frame B.

The initial stress in the PT bars, σ_{PT0}, also affects the dynamic PT bar force response. Frames B_{ED} and D both have energy dissipation elements and midbay PT bars. Figure 5.36(a) shows that Frame B_{ED} has greater mean roof drift response than Frame D. However, Figure 5.36(b) shows that Frame D has greater mean normalized PT force response than Frame B_{ED}. Frame D has a larger σ_0 ($\sigma_{0,D} = 0.43\sigma_Y$ versus $\sigma_{0,BED} = 0.20\sigma_Y$), which increases the normalized PT force response.

Figure 5.36(c) shows the peak dynamic brace force response in each story of each frame configuration, normalized by the design demand. As noted in the discussion of the brace force time histories, the peak dynamic response tends to be greater than the design

demand. This is typical for each of the frame configurations studied, which indicates that the method for estimating member force design demands must be re-evaluated; a modified method for estimating design demands is presented in Chapter 6. Note that the dynamic brace force response in the uppermost story for Frame B, B_{ED}, and D tend to be less than the design demands for those braces, because the PT force dominates the force demand in those braces. The distribution struts used in Frame D_{DIST} distribute this effect to the upper four stories. The design demands were calculated at the PT bar yielding limit state; therefore, the braces that directly resist the PT bar force have relatively high design demands, and the normalized brace force response for those braces is relatively low.

5.5 Frame D_{DF}

This section describes one final frame configuration, Frame D_{DF}, which was developed from Frame D_{DIST}. Frame D_{DIST} was developed without considering how the lateral inertial forces are transferred from the floor diaphragm to the SC-CBF. Recall that for Frame D_{DIST}, the floor system is supported by the gravity columns adjacent to the SC-CBF, but the floor system is not directly connected to the SC-CBF columns, to avoid the need to detail such connections to accommodate the uplift of the SC-CBF. Therefore, the lateral inertia forces in the floor diaphragms must be transferred from the adjacent gravity columns to the SC-CBF. Frame D_{DF}, shown schematically in Figure 5.37, is a modified version of Frame D_{DIST} that includes lateral-load bearings at the floor levels to transmit the lateral inertia forces into the SC-CBF. These lateral-load bearings develop friction forces (in the vertical direction), due to the relative vertical motion between the SC-CBF columns and the adjacent gravity columns (as the SC-CBF columns uplift) in the

presence of normal forces from the lateral inertia forces. In Frame D_{DF}, the friction forces in the lateral-load bearing elements are the only added energy dissipation mechanism in the system. Unlike the previously studied frame configurations, the ED forces in Frame D_{DF} increase and decrease with the lateral inertia forces that are transmitted as normal force in the lateral-load bearings.

Figure 5.38 shows a free-body diagram at decompression of a six-story prototype of Frame D_{DF}. Note that, as for Frames D and D_{DIST}, the energy dissipation forces are shown along the centerline of the gravity columns (see Figure 5.7), as explained in Section 5.3.2.1.

The friction force at each lateral-load bearing can be written as:

$$F_{ED,i} = \mu \cdot F_i \tag{5.21}$$

and the total friction force is:

$$F_{ED} = \sum_{i=1}^{N} F_{ED,i} = \mu \cdot \sum_{i=1}^{N} F_i = \mu \cdot V_b \tag{5.22}$$

where,

μ = coefficient of friction at the lateral-load bearings

F_i = lateral force at floor i

N = number of floors

V_b = base shear

OM_D for Frame D_{DF} can be written as follows:

$$OM_D = \left(PT_0 + W_{SC-CBF}\right) \cdot \frac{b_{SC-CBF}}{2} + F_{ED} \cdot b_{ED} \tag{5.23}$$

where b_{ED} is the distance between the point of contact of the compression column and the centerline of the gravity column along which F_{ED} acts, as shown in Figure 5.38.

Substituting Equation 5.22 into Equation 5.23 for OM_D results in:

$$OM_D = \left(PT_0 + W_{SC-CBF}\right) \cdot \frac{b_{SC-CBF}}{2} + \mu \cdot V_{b,D} \cdot b_{ED} \tag{5.24}$$

where $V_{b,D}$ is the base shear at OM_D, equivalent to $\sum_{i=1}^{N} F_{D,i}$, where $F_{D,i}$ is the inertia force at floor i at column decompression (Figure 5.38). Similarly, OM_Y can be written as:

$$OM_Y = \left(PT_Y + W_{SC-CBF}\right) \frac{b_{SC-CBF}}{2} + \mu \cdot V_{b,Y} \cdot b_{ED} \tag{5.25}$$

where $V_{b,Y}$ is the base shear at OM_Y, equivalent to $\sum_{i=1}^{N} F_{Y,i}$, where $F_{Y,i}$ is the inertia force at floor i at PT bar yield.

Figure 5.39 shows hysteresis loops for an SC-CBF with constant OM_{ED} (e.g., Frame D_{DIST}) and an SC-CBF with lateral-load bearing friction elements providing OM_{ED} (e.g., Frame D_{DF}), where OM_D is the same for the two frames. OM_{ED} for an SC-CBF like Frame D_{DIST} is calculated using an equation similar to Equation 5.18. As previously mentioned, OM_{ED} for an SC-CBF like Frame D_{DF} is a function of the lateral forces (e.g., see Equations 5.24 and 5.25), and therefore varies from a minimum at OM_D ($OM_{ED,D}$) to a maximum at OM_Y ($OM_{ED,Y}$). OM_{ED} for Frame D_{DF}, as a function of the base shear, is:

$$OM_{ED} = F_{ED} \cdot b_{ED} = \mu \cdot V_b \cdot b_{ED} = \mu \cdot \frac{OM}{h^*} \cdot b_{ED} \tag{5.26}$$

where,

OM = the applied overturning moment from the lateral forces

h^* = the effective height of the lateral forces (i.e., the ratio of OM to V_b)

$$h^* = \frac{\{h\}^T \{F\}}{\{i\}^T \{F\}} \tag{5.27}$$

where,

$\{F\}$ = vector of lateral forces

$\{i\}$ = influence vector = $\{1\ 1\ 1\ 1\ 1\ 1\}^T$ for a six-degree-of-freedom system

The value of β_E for Frame D_{DF}, when the peak response is OM_Y, can then be written as:

$$\beta_E = \frac{\frac{1}{2}\left(OM_{ED,D} + OM_{ED,Y}\right)}{OM_D} \tag{5.28}$$

where the numerator represents the trapezoidal area within the hysteresis loop shown in Figure 5.39.

The expected peak response for the DBE will be greater than OM_D but will not necessarily reach OM_Y, since the PBD objective is to avoid PT bar yielding under the DBE. Therefore, it is desirable to determine β_E for a peak overturning moment demand that is less than OM_Y:

$$\beta_E = \frac{\frac{1}{2}\left(2 \cdot OM_{ED,D} + \lambda \cdot \left(OM_{ED,Y} - OM_{ED,D}\right)\right)}{OM_D} \tag{5.29}$$

$$\lambda = \frac{OM_{\max} - OM_D}{OM_Y - OM_D} \tag{5.30}$$

where λ ranges from 0 (peak demand is OM_D) to 1 (peak demand is OM_Y, as in Equation 5.28). β_E, as calculated from Equation 5.28 or Equation 5.29, is the ratio of the energy dissipated by the hysteresis loop of Frame D_{DF} to the energy dissipated by a bilinear elasto-plastic system with the same strength (OM_D) under cyclic loading to the same peak displacement (Seo and Sause 2005). For an SC-CBF with constant OM_{ED} (e.g., Frame D_{DIST}), Equation 5.16 can be used to calculate β_E. For an SC-CBF with constant OM_{ED} to self-center (i.e., eliminate residual drift), β_E must be less than or equal to 50%, as discussed previously. For Frame D_{DF}, however, β_E is a function of the peak OM demand; at high OM demands, β_E can exceed 50% and the system can still self-center, as shown in Figure 5.39. Therefore, to maintain self-centering for Frame D_{DF}, the value of β_E for a peak demand equal to OM_D, $\beta_{E,D}$, must be less than or equal to 50%.

$$\beta_{E,D} = \frac{OM_{ED,D}}{OM_D} \tag{5.31}$$

For an SC-CBF with constant OM_{ED}, $\beta_{E,D}$ is equal to β_E.

Figures 5.40 and 5.41 show cyclic pushover responses for Frame D_{DF}. Frame D_{DF} has the same members as Frame D_{DIST}, but the only energy dissipation is through friction at the

lateral-load bearings. The modeling of the friction elements at the lateral-load bearings is discussed in detail in Chapter 8.

Figure 5.40(a) shows the response of Frame D_{DF} subjected to two cycles of loading to 1% roof drift. As the lateral force is removed from the SC-CBF, there is a change in the distribution of the lateral gaps at the lateral-load bearings, causing some bearings to have residual friction forces where the gaps are closed. This change in the contact condition causes a redistribution of lateral forces between the gravity columns and the SC-CBF in subsequent cycles of lateral loading. Figure 5.40(b) shows the response to two cycles of loading past PT yield. As with the other frame configurations, the lateral force at decompression is decreased in the second cycle of response due to a partial loss of the initial PT bar force after PT bar yielding.

Figure 5.41 compares the hysteresis loops of Frame D_{DF} and Frame D_{DIST}. Figure 5.41(a) shows that at low drift demands, Frame D_{DF} dissipates less energy than Frame D_{DDIST}. However, the post-decompression slope of the lateral force-roof drift response is greater for Frame D_{DF} than for Frame D_{DIST}. This is because the friction in the lateral-load bearings (i.e., the energy dissipation for Frame D_{DF}) is proportional to the applied lateral force. Figure 5.41(b) shows that the width of the hysteresis loop for Frame D_{DF} is less than that of Frame D_{DIST} at column decompression, but greater than that of Frame D_{DIST} at PT bar yielding.

One advantage of Frame D_{DF} is that no additional ED elements are required, reducing fabrication and erection costs. Additionally, since the ED forces are proportional to the

applied loads, the ED forces will not produce notable residual drift. As the lateral forces acting on the SC-CBF become zero as the earthquake ground shaking subsides, the friction in the lateral-load bearings becomes zero and there is no residual force acting on the SC-CBF to prevent it from returning to its initial position (i.e., self-centering), as shown in Figures 5.39, 5.40, and 5.41.

5.6 Summary

The frame configuration study results show that the SC-CBF system can perform as described in Chapter 3. Column decompression works to soften the lateral force-roof drift response of the structure as intended. The results show that PT bar yielding can occur without creating significant residual drift.

Altering the configuration of the SC-CBF system permits the behavior of the system to be controlled. Locating the PT bars at midbay rather than at the column lines decreases the likelihood of PT bar yielding; the drift response may be greater, but the PT force response is less.

The dynamic response of the SC-CBF system indicates that the estimated design demands for the frame members are unconservative and were frequently exceeded during response to DBE-level seismic input. Chapter 6 investigates the design demands for the member forces and for the roof drift.

Based on the results of this frame configuration study, Frame D_{DIST} had the most advantages of the studied frames (A, B, B_{ED}, C, D, D_{DIST}). Frame D_{DF}, which incorporates friction at the lateral-load bearings to provide energy dissipation, has the

same advantages and also provides a mechanism for transmitting lateral inertia forces into the SC-CBF. For these reasons, Frame D_{DF} is used as the basis for the SC-CBF test structure described later in this dissertation.

Table 5.1 – Design dead loads at each floor level

Dead Loads	Floors 1-5 (psf)	Roof (psf)
Floor/roof slab	43	43
Floor/roof deck	3	3
Roofing material	0	5
Mechanical weight	10	30
Ceiling material	5	5
Floor finish	2	0
Steel fireproofing	2	2
Structural steel	15	15
Exterior wall (per sq. ft. of floor area)	10	7
Total	90	110

Table 5.2 – Design live loads at each floor level

Live Loads	Floors 1-5 (psf)	Roof (psf)
Office	50	0
Partitions	20	0
Roof live load	0	50

Table 5.3 – Summary of gravity loads per column and tributary seismic mass for one SC-CBF (Frames A, B, B_{ED}, D, and D_{DIST})

Floor	Dead Load (kip)	Live Load (kip)	Mass (kip-s^2/in)
1	99	11.25	2.306
2	99	11.25	2.306
3	99	11.25	2.306
4	99	11.25	2.306
5	99	11.25	2.306
6	99	11.25	2.306

Table 5.4 – Summary of gravity loads per column and tributary seismic mass for one SC-CBF (Frame C)

	Exterior Columns		Interior Columns		
Floor	Dead Load (kip)	Live Load (kip)	Dead Load (kip)	Live Load (kip)	Mass (kip-s^2/in)
1	74.25	8.44	24.75	2.81	2.306
2	74.25	8.44	24.75	2.81	2.306
3	74.25	8.44	24.75	2.81	2.306
4	74.25	8.44	24.75	2.81	2.306
5	74.25	8.44	24.75	2.81	2.306
6	74.25	8.44	24.75	2.81	2.306

Table 5.5 – Design summary of the various frame configurations

	Frame A		Frame B		Frame B_{ED}		Frame C		Frame D		Frame D_{DIST}	
	Weight (kip)	**% of total**	**Weight (kip)**	**% of total**	**Weight (kip)**	**% of total**	**Weight (kip)**	**% of total**	**Weight (kip)**	**% of total**	**Weight (kip)**	**% of total**
Braces	18.0	27.4	19.3	29.9	19.5	28.9	16.6	24.5	19.2	29.4	18.0	28.5
Columns	31.8	48.4	29.5	45.8	31.4	46.4	43.0	63.5	30.6	46.9	27.6	43.8
Beams	13.2	20.1	13.1	20.4	14.0	20.7	6.7	9.9	13.3	20.4	11.0	17.4
Struts	2.7	4.1	2.5	3.8	2.7	4.0	1.5	2.2	2.2	3.3	6.5	10.2
Total	65.8	100	64.4	100	67.7	100	67.7	100	65.2	100	63.1	100

Table 5.6 – Natural periods (sec) for frame configurations

Mode	Frame A	Frame B	Frame B_{ED}	Frame C	Frame D	Frame D_{DIST}
1	0.913	1.019	0.994	1.762	1.063	1.007
2	0.309	0.334	0.325	0.552	0.344	0.332
3	0.180	0.185	0.181	0.301	0.186	0.175
4	0.136	0.138	0.135	0.217	0.140	0.132
5	0.115	0.116	0.114	0.178	0.115	0.109
6	0.100	0.105	0.103	0.149	0.100	0.098

Table 5.7 – Energy dissipation properties for frame configurations, including modal damping ratio (ζ_n) and energy dissipation ratio (β_E), expressed as percentages

Property	Frame A	Frame B	Frame B_{ED}	Frame C	Frame D	Frame D_{DIST}
ζ_1	5.0	5.0	5.0	5.0	5.0	5.0
ζ_2	3.8	3.7	3.7	3.7	3.7	3.7
ζ_3	5.0	5.0	5.0	5.0	5.0	5.0
ζ_4	6.1	6.3	6.3	6.4	6.2	6.2
ζ_5	7.0	7.2	7.2	7.7	7.3	7.3
ζ_6	8.0	7.9	7.9	9.0	8.3	8.0
β_E	--	--	19.2	30.7	41.3	41.3

Table 5.8 – Values of $\alpha_{Y,ELF}$ for frame configurations

	Frame A	Frame B	Frame B_{ED}	Frame C	Frame D	Frame D_{DIST}
$\alpha_{Y,ELF}$	1.9	1.1	1.3	1.0	1.2	1.2

Table 5.9 – Summary of ground motions used for frame configuration study

Event	Station	Record	Component	SF
1999 Chi-Chi	CHY036	ch0chy036270	270	1.082
	TCU038	ch0tcu038000	000	2.038
	TCU042	ch0tcu042270	270	2.103
1992 Landers	Yermo Fire Station	ld0yer270	270	1.730
1989 Loma Prieta	Hollister Diff. Array	lp0hd1165	165	1.637
	Hollister Diff. Array	lp0hd1255	255	1.859
	Hollister South & Pine	lp0hsp090	090	1.992
1994 Northridge	Canyon Country – W Lost Canyon	nr0ccy270	270	1.175
	Canoga Park – Topanga Canyon	nr0cpc106	106	1.772
	Hollywood – Willoughby	nr0hlc090	090	3.455
	Northridge – Saticoy	nr0nrg090	090	1.939
1987 Superstition Hills	Westmoreland Fire Station	sh0wsm090	090	2.470

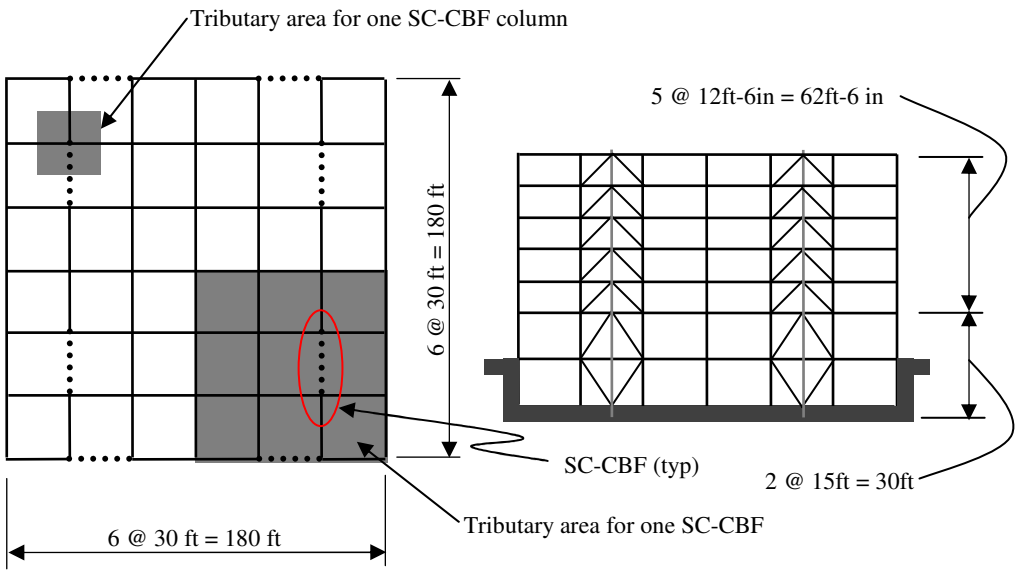

Figure 5.1 – Prototype building used for the frame configuration study: (a) floor plan; (b) elevation

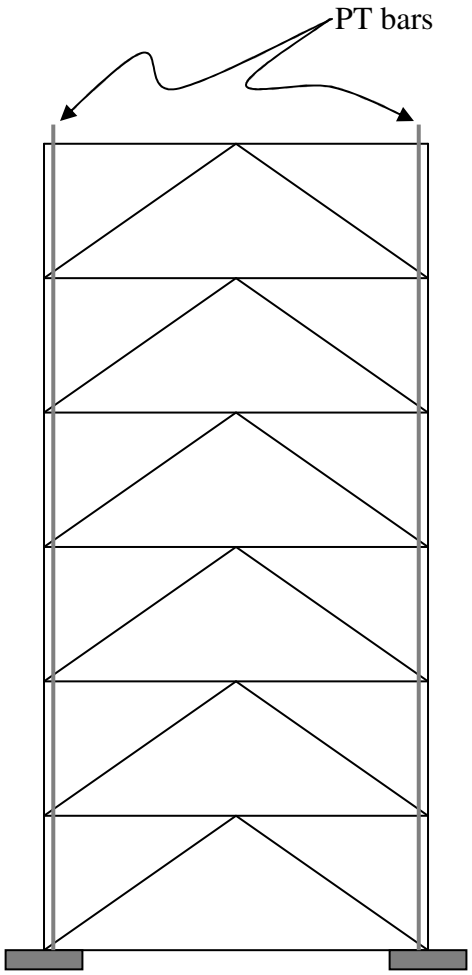

Figure 5.2 – Frame configuration: Frame A

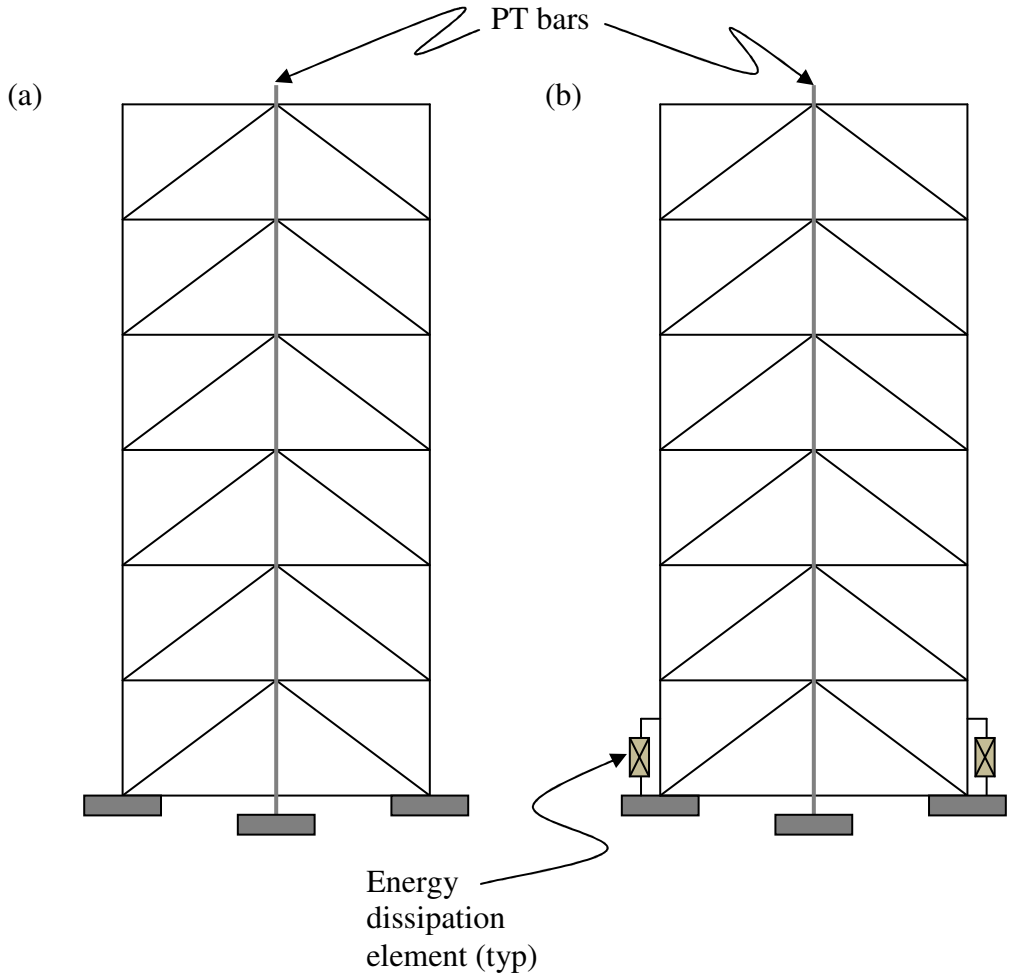

Figure 5.3 – Frame configurations: (a) Frame B; (b) Frame B_{ED}

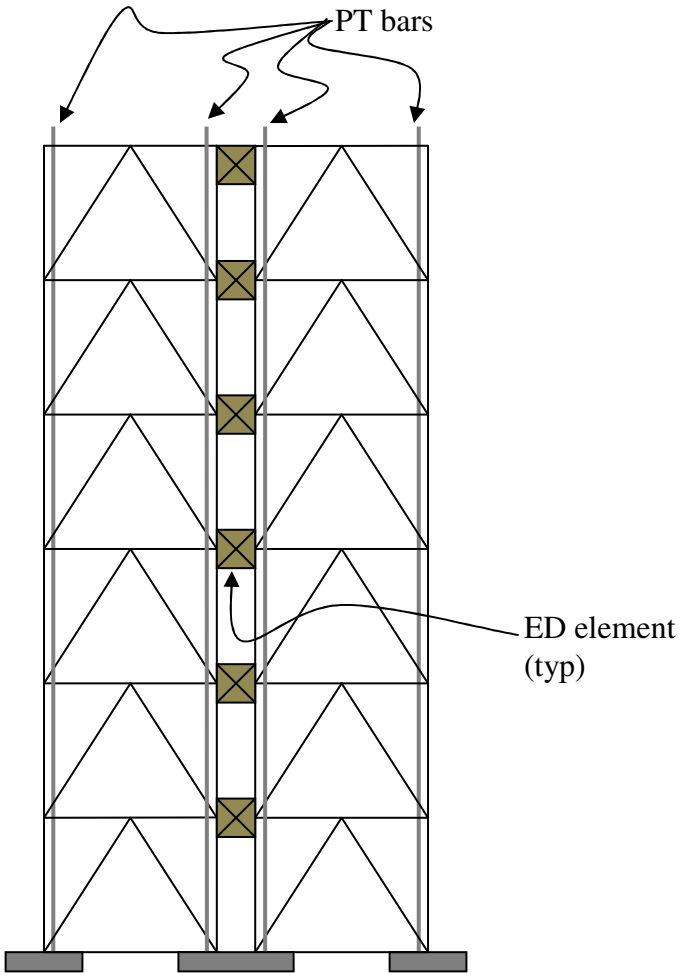

Figure 5.4 – Frame configuration: Frame C

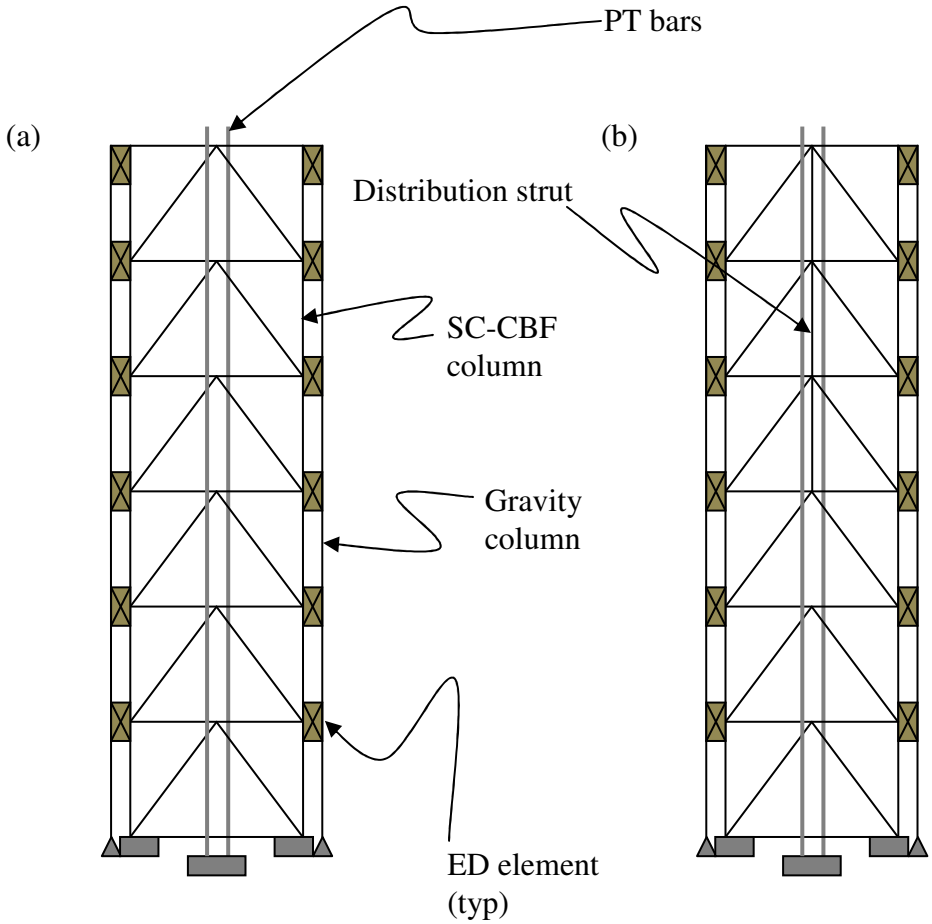

Figure 5.5 – Frame configurations: (a) Frame D; (b) Frame D_{DIST}

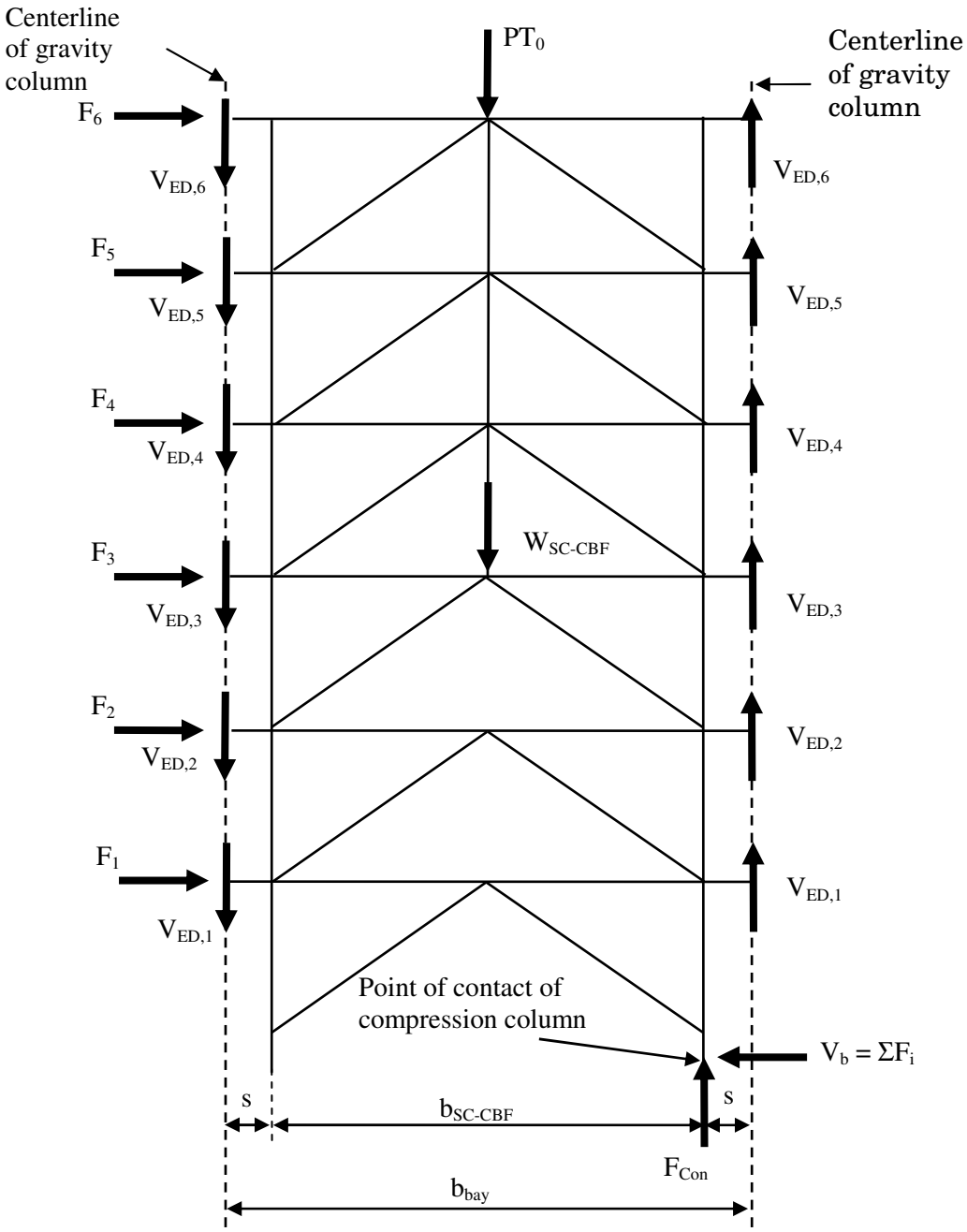

Figure 5.6 – Free-body diagram of Frame D_{DIST} at decompression

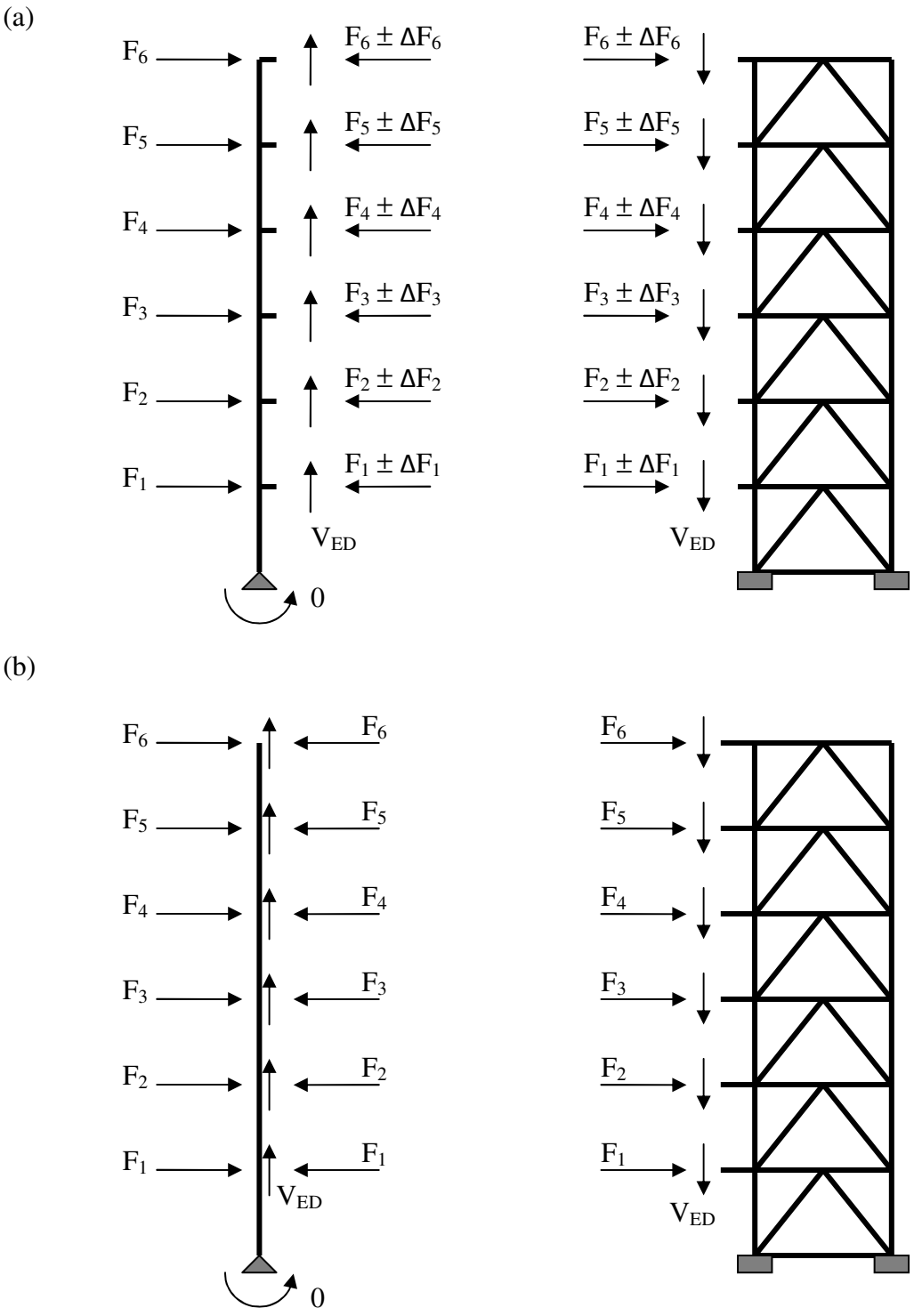

Figure 5.7 – Free-body diagrams of SC-CBF and adjacent gravity column: (a) assumed actual distribution of lateral forces; (b) statically-equivalent distribution of lateral forces

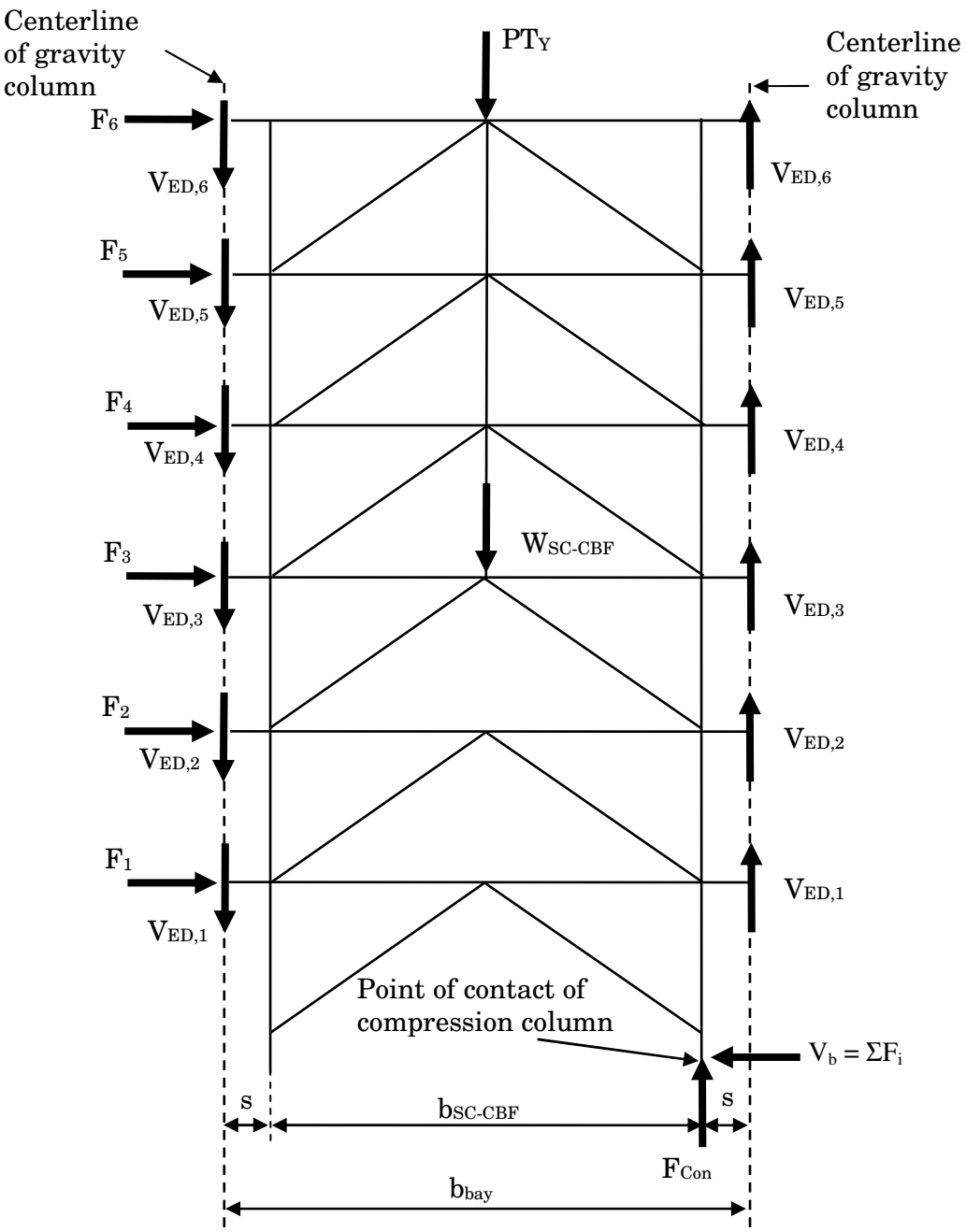

Figure 5.8 – Free-body diagram of Frame D_{DIST} at PT bar yielding

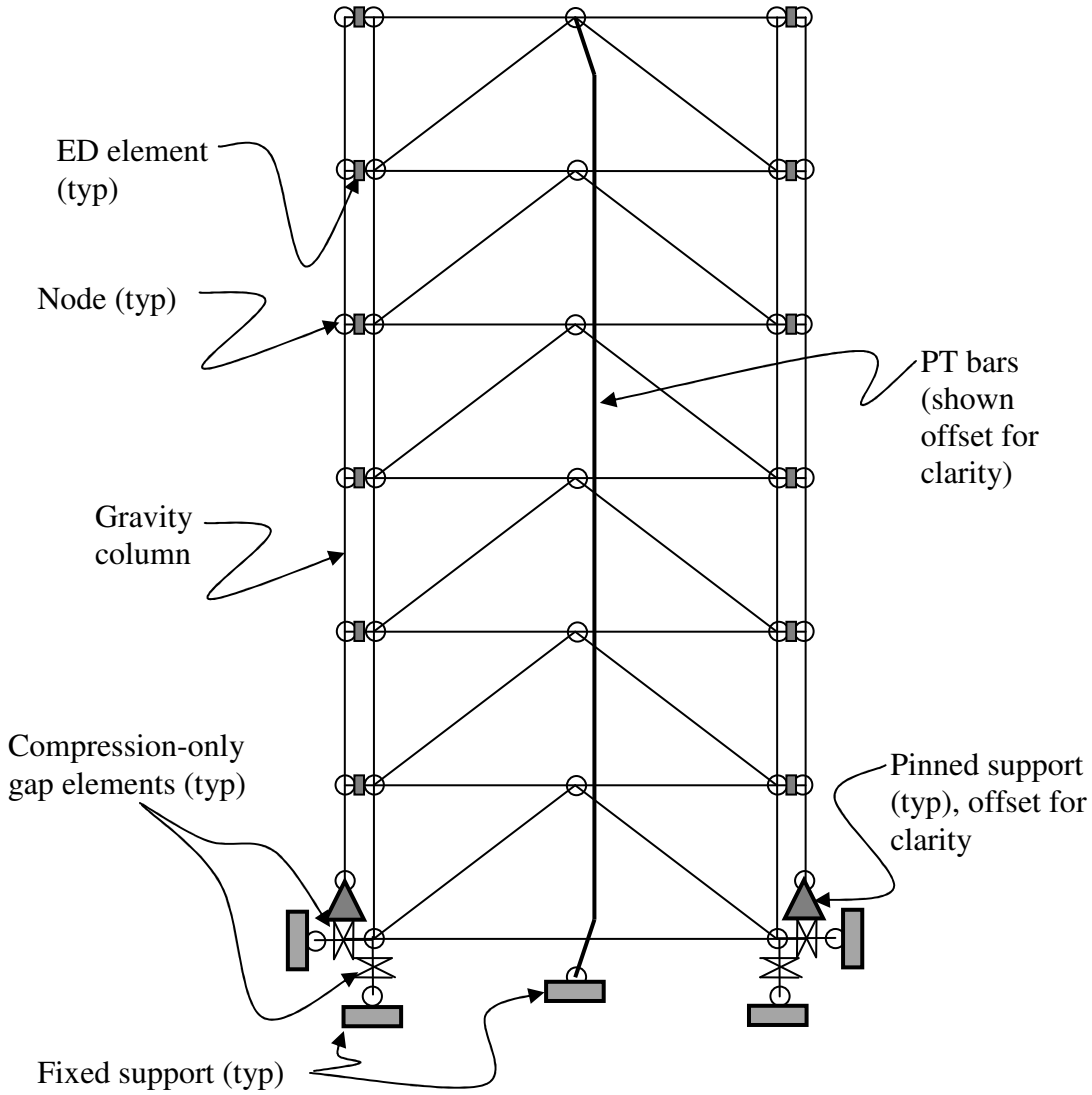

Figure 5.9 – Schematic of nonlinear analytical model for design of Frame D_{DIST}

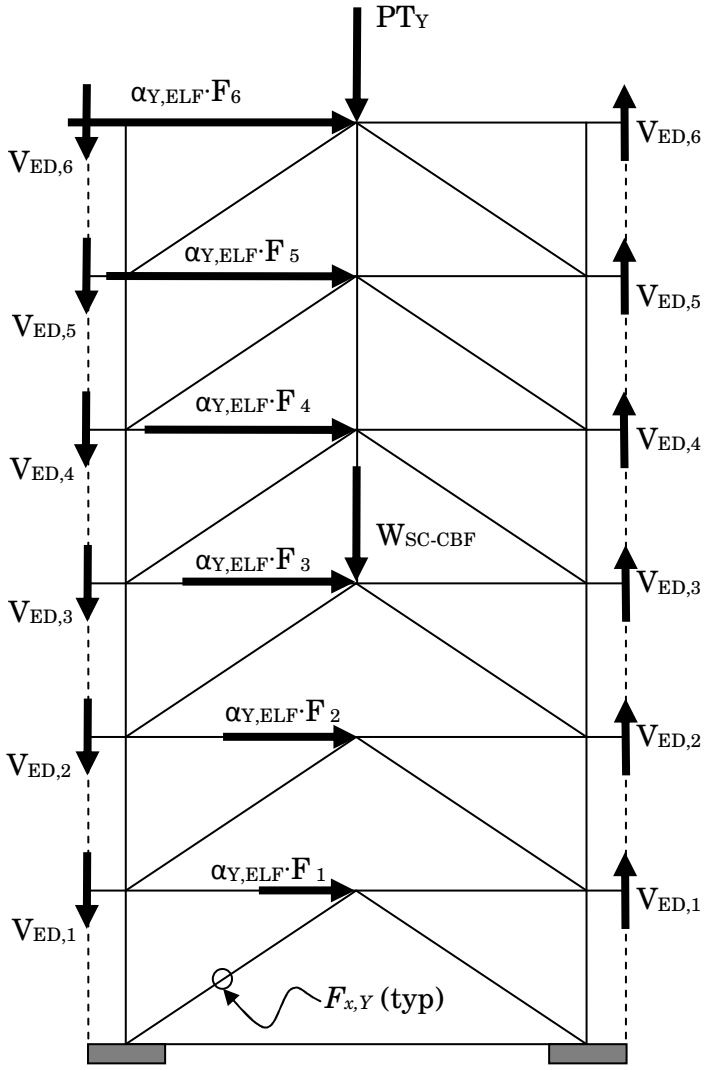

Figure 5.10 – Forces that develop in the nonlinear analytical model of Frame D_{DIST} subjected to $\{F_{ELF}\}$ scaled to be in equilibrium with OM_Y

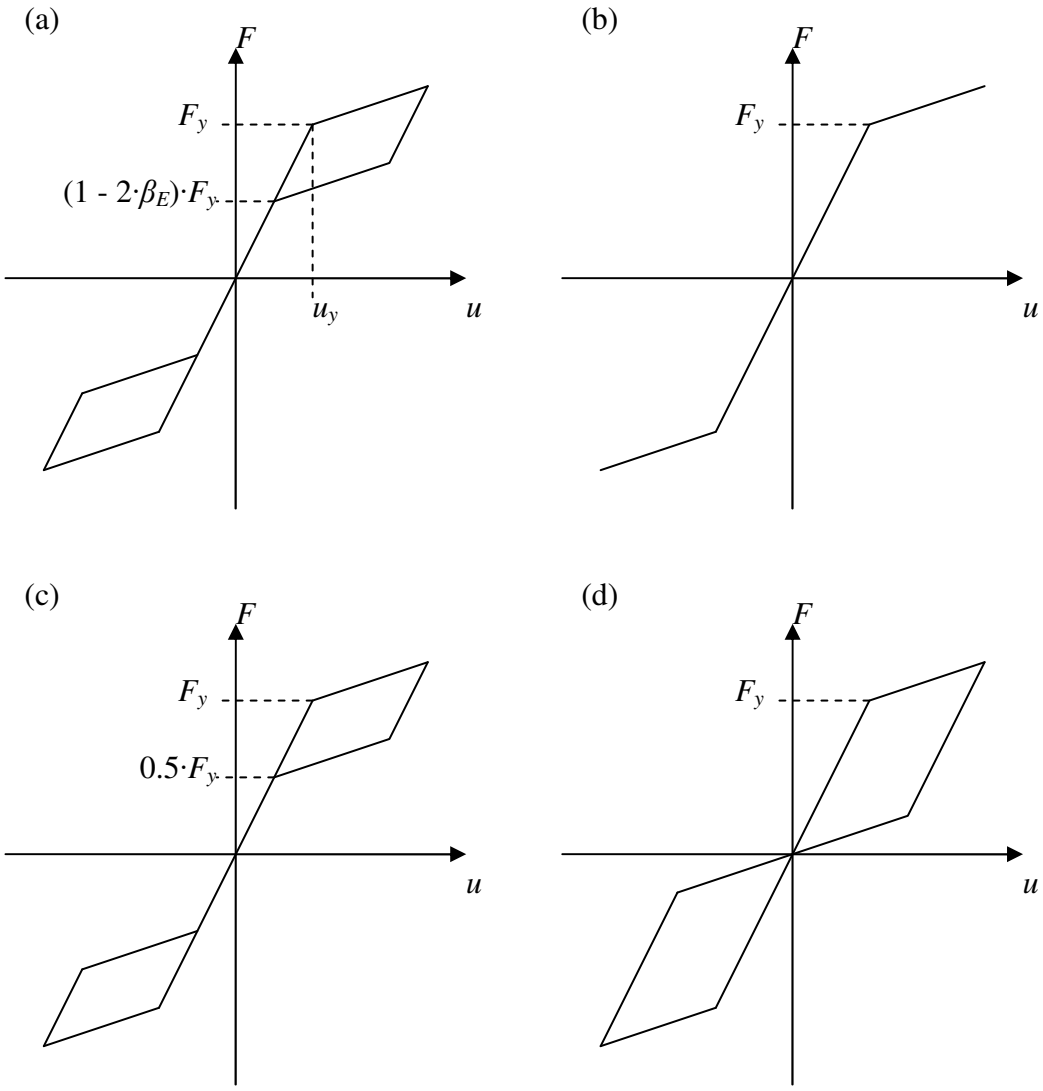

Figure 5.11 – Force-displacement (F-u) behavior of SC systems with varying β_E (Seo and Sause 2005): (a) SC model with β_E; (b) $\beta_E = 0\%$; (c) $\beta_E = 25\%$; (d) $\beta_E = 50\%$

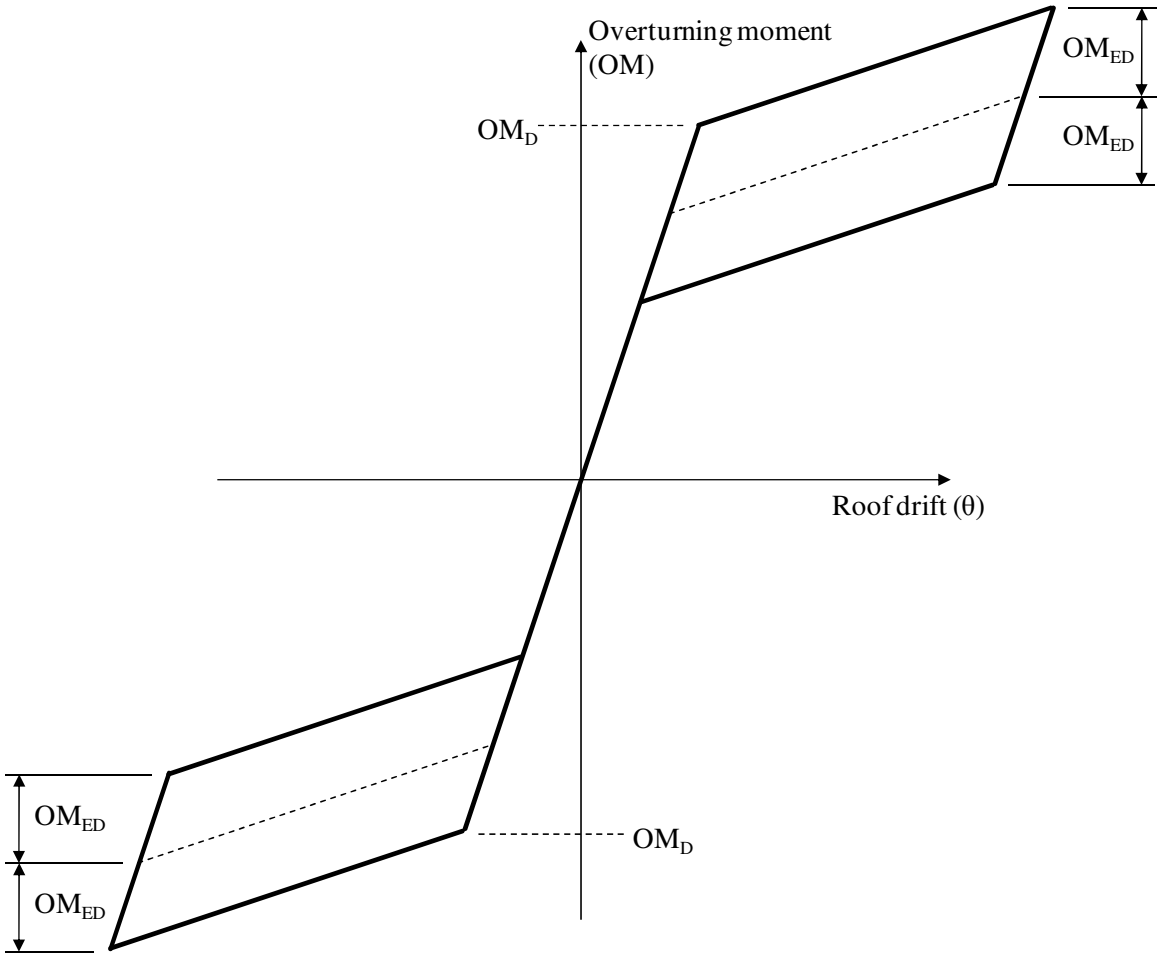

Figure 5.12 – Overturning moment-roof drift (OM-θ) relationship for an SC-CBF with constant OM_{ED}

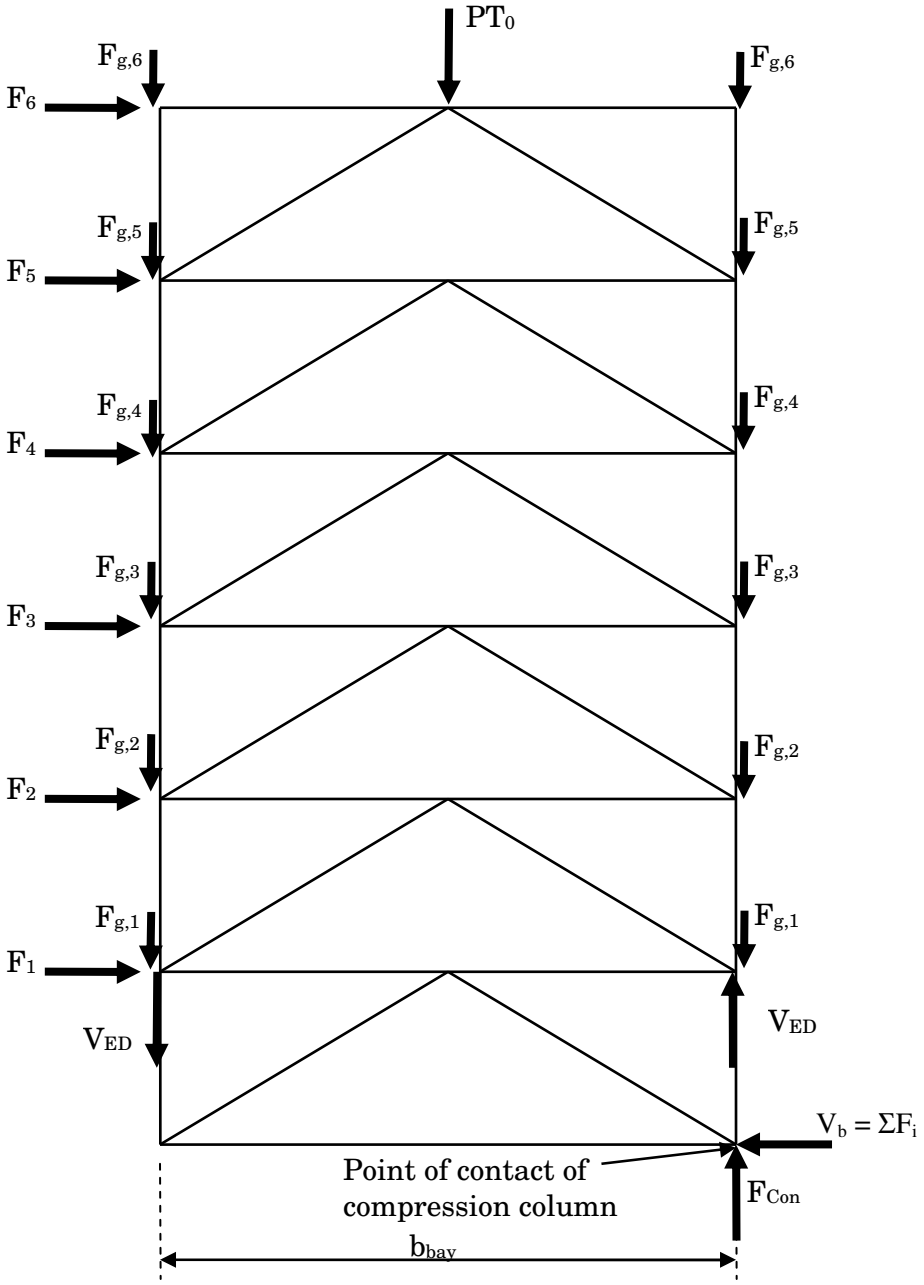

Figure 5.13 – Free-body diagram of Frame B_{ED} at column decompression

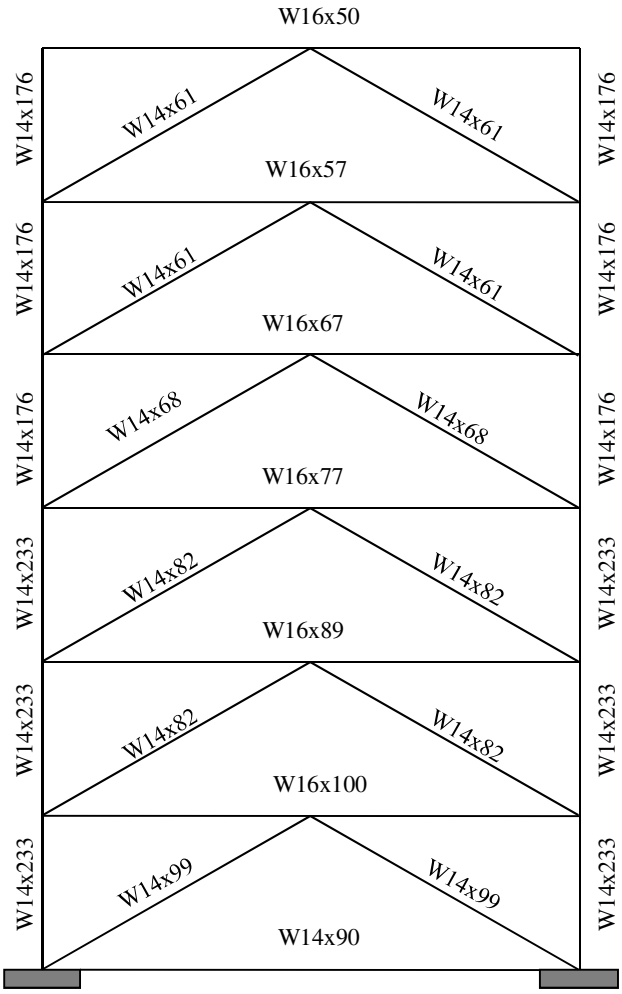

Figure 5.14 – Member selections for Frame A

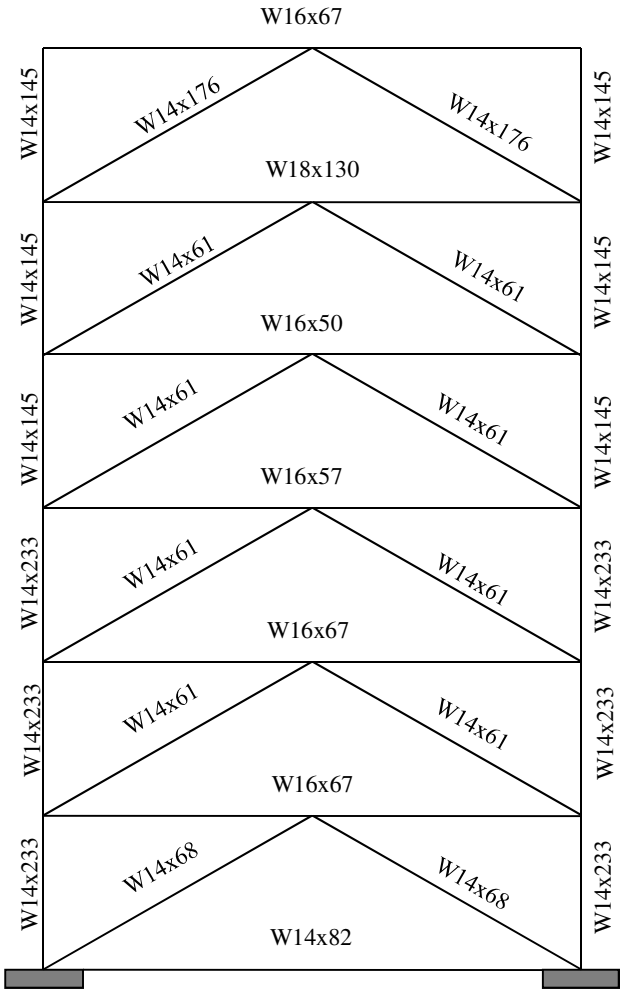

Figure 5.15 – Member selections for Frame B

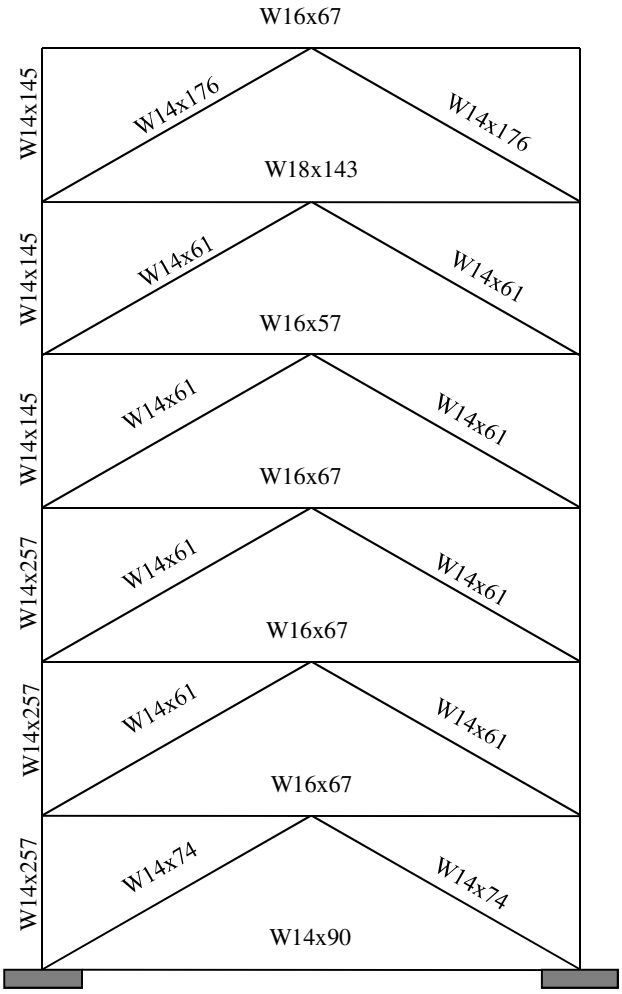

Figure 5.16 – Member selections for Frame B_{ED}

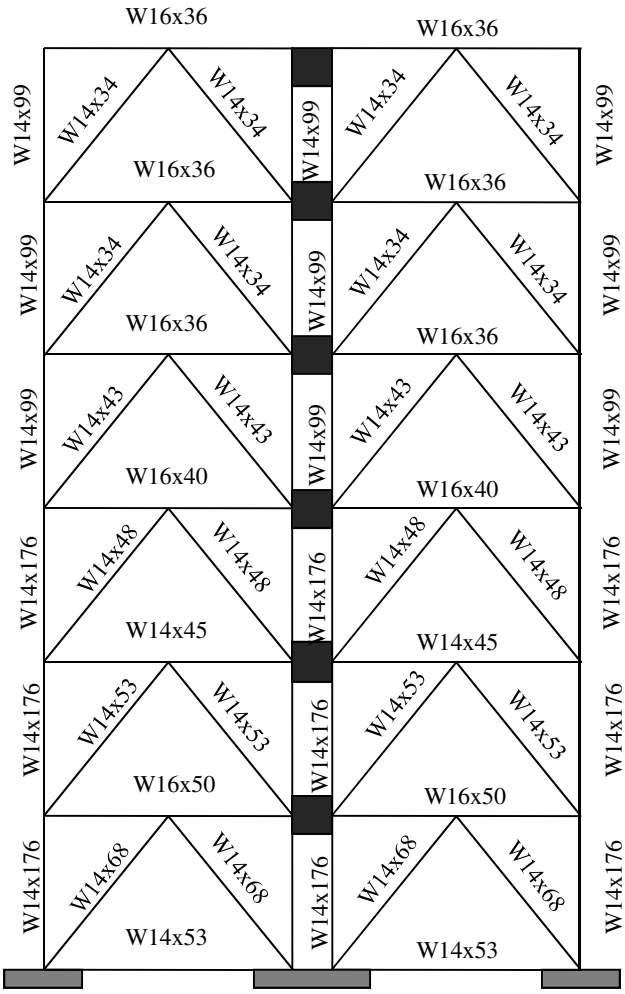

Figure 5.17 – Member selections for Frame C

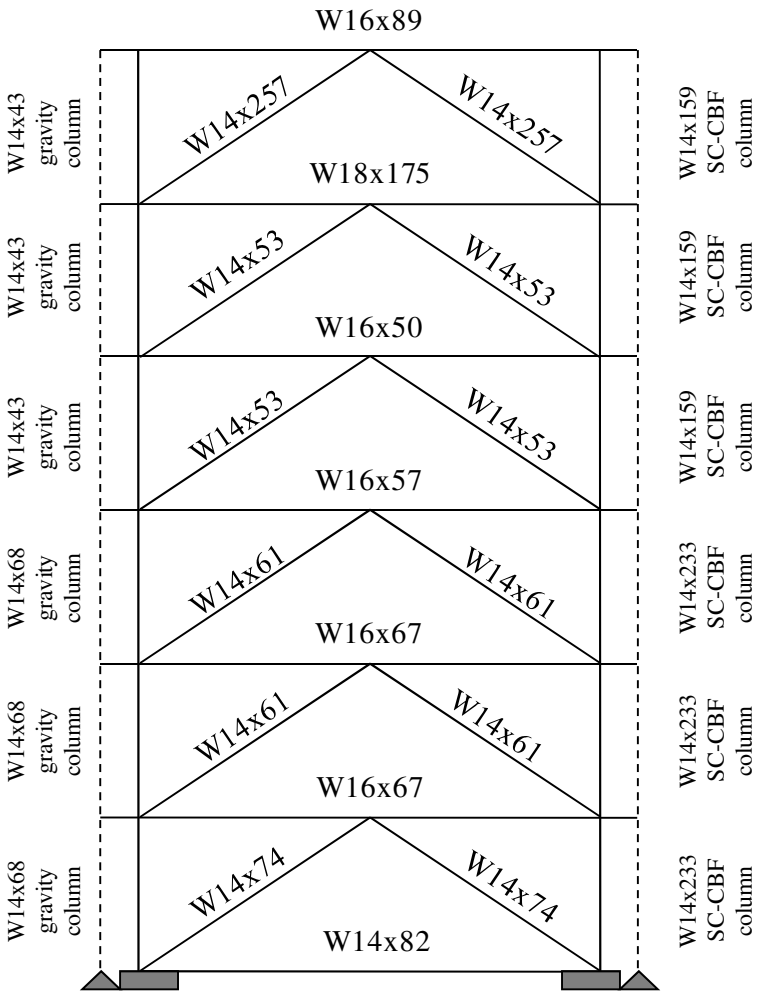

Figure 5.18 – Member selections for Frame D

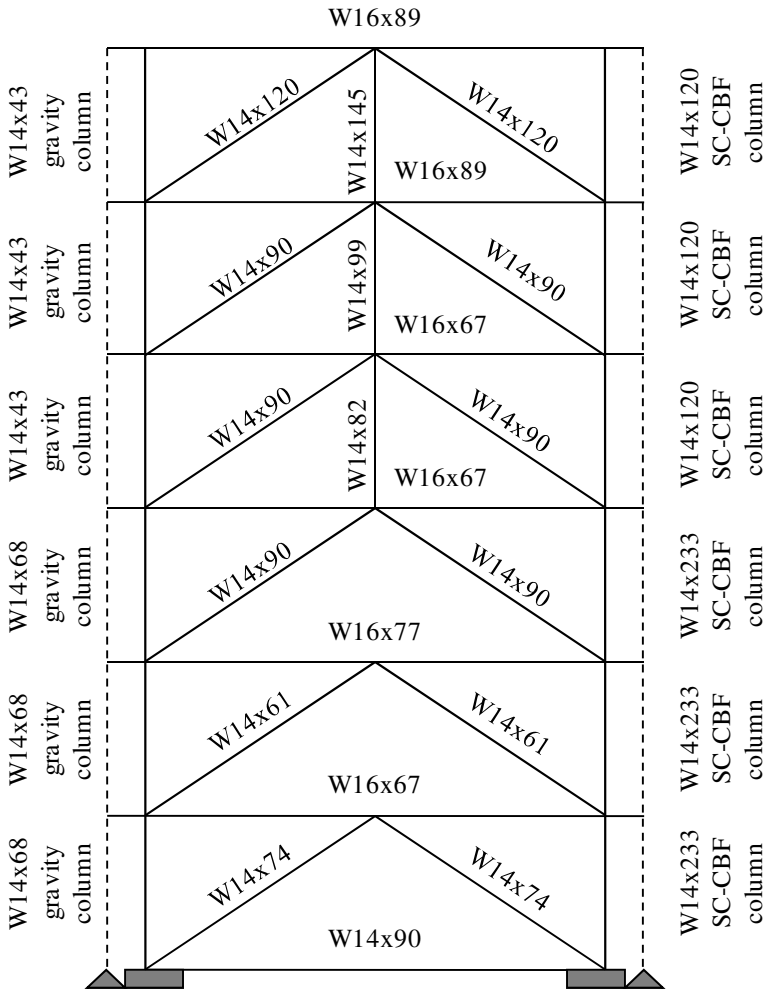

Figure 5.19 – Member selections for Frame D_{DIST}

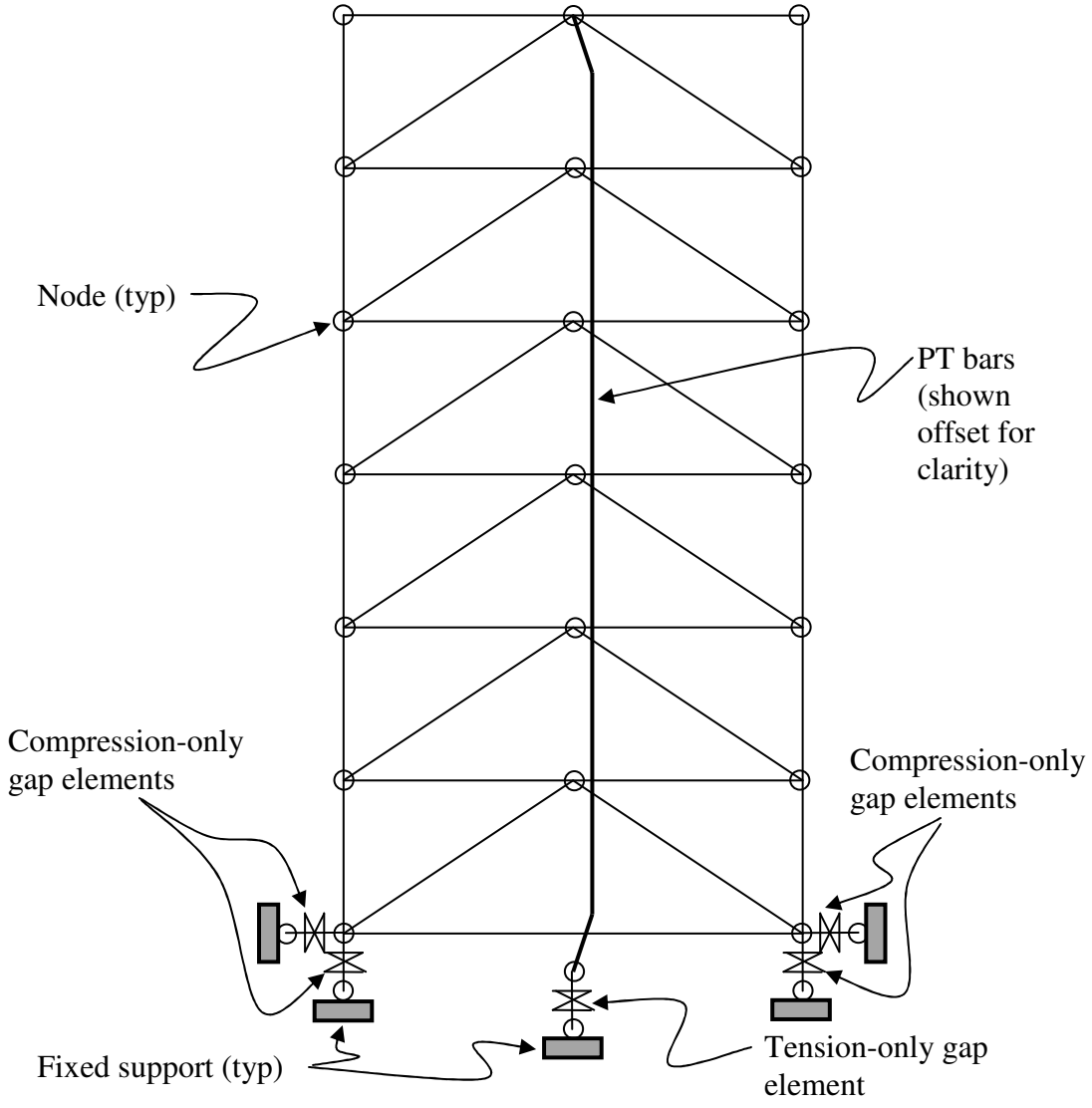

Figure 5.20 – Schematic of preliminary analytical model for Frame B

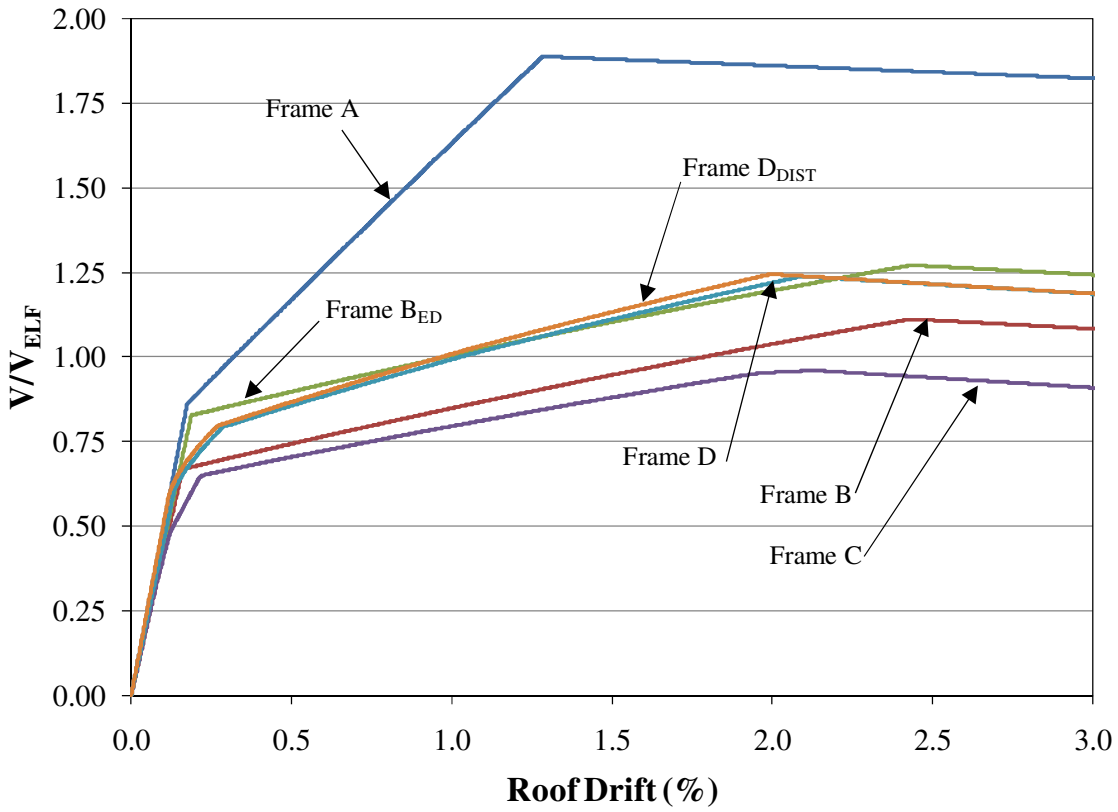

Figure 5.21 – Monotonic pushover results

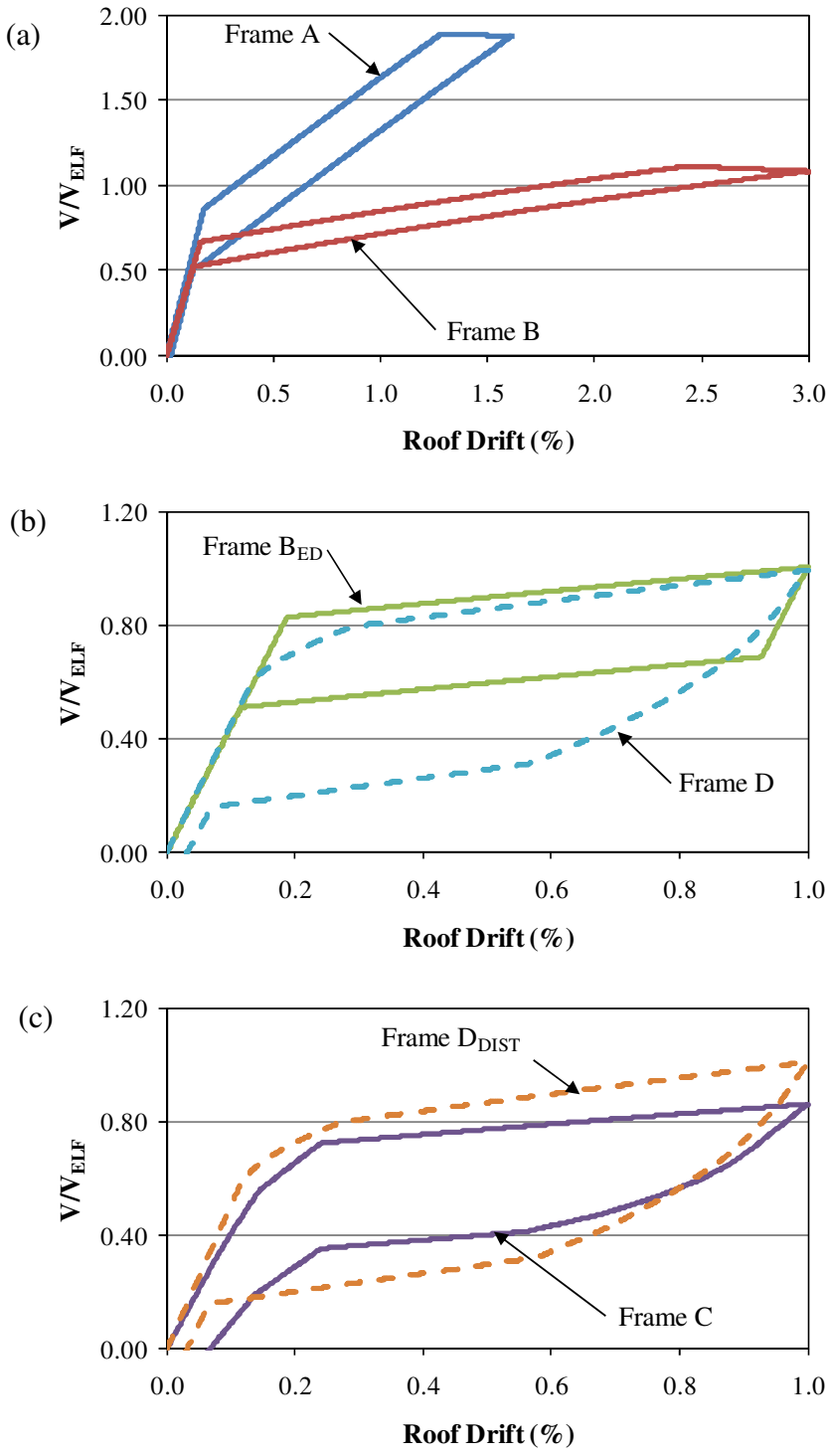

Figure 5.22 – Cyclic pushovers: (a) Frames A and B after PT bar yielding; (b) Frames B_{ED} and D to 1% roof drift; (c) Frames C and D_{DIST} to 1% roof drift

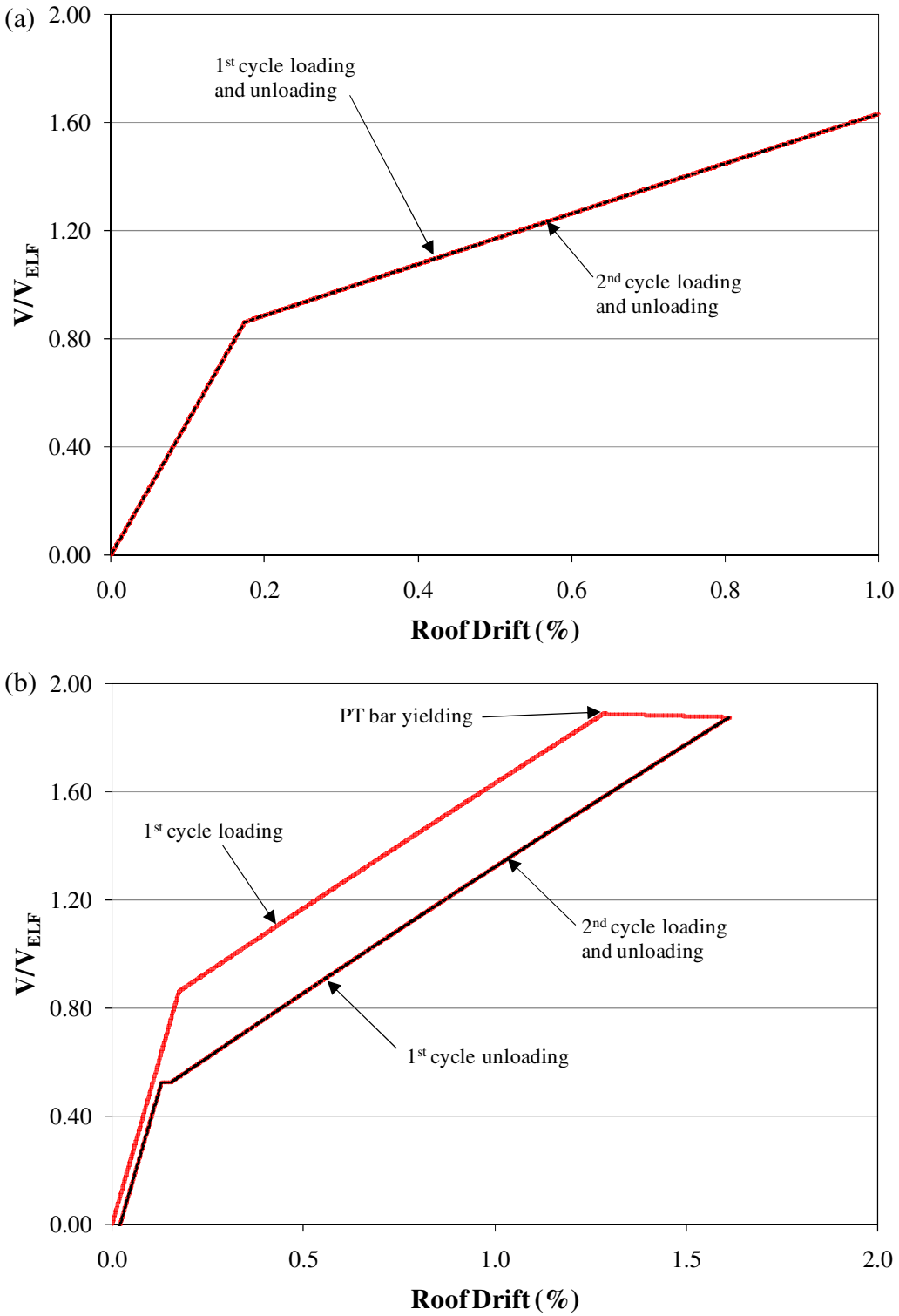

Figure 5.23 – Cyclic pushover of Frame A: (a) to 1% roof drift; (b) after PT bar yielding

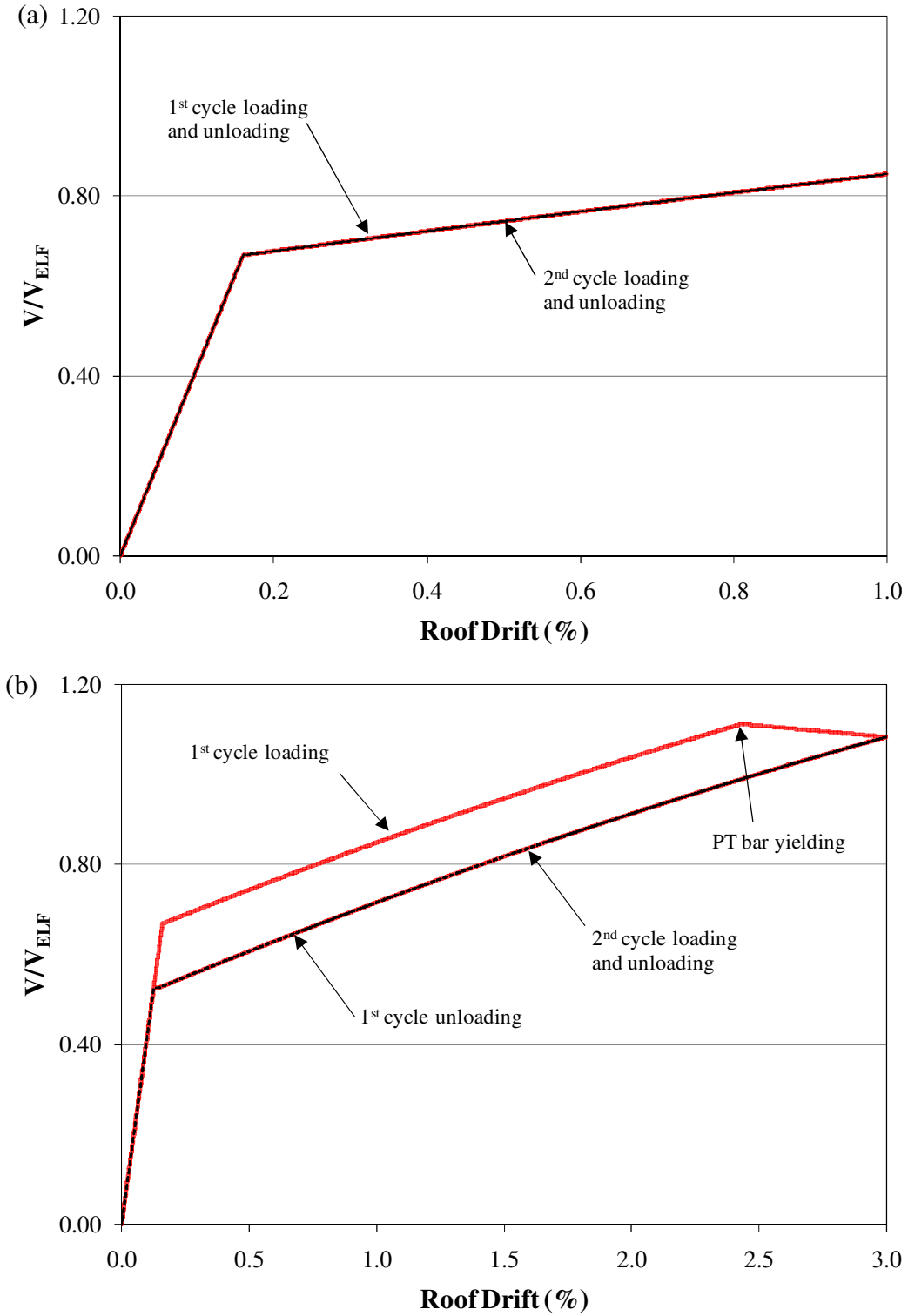

Figure 5.24 – Cyclic pushover of Frame B: (a) to 1% roof drift; (b) after PT bar yielding

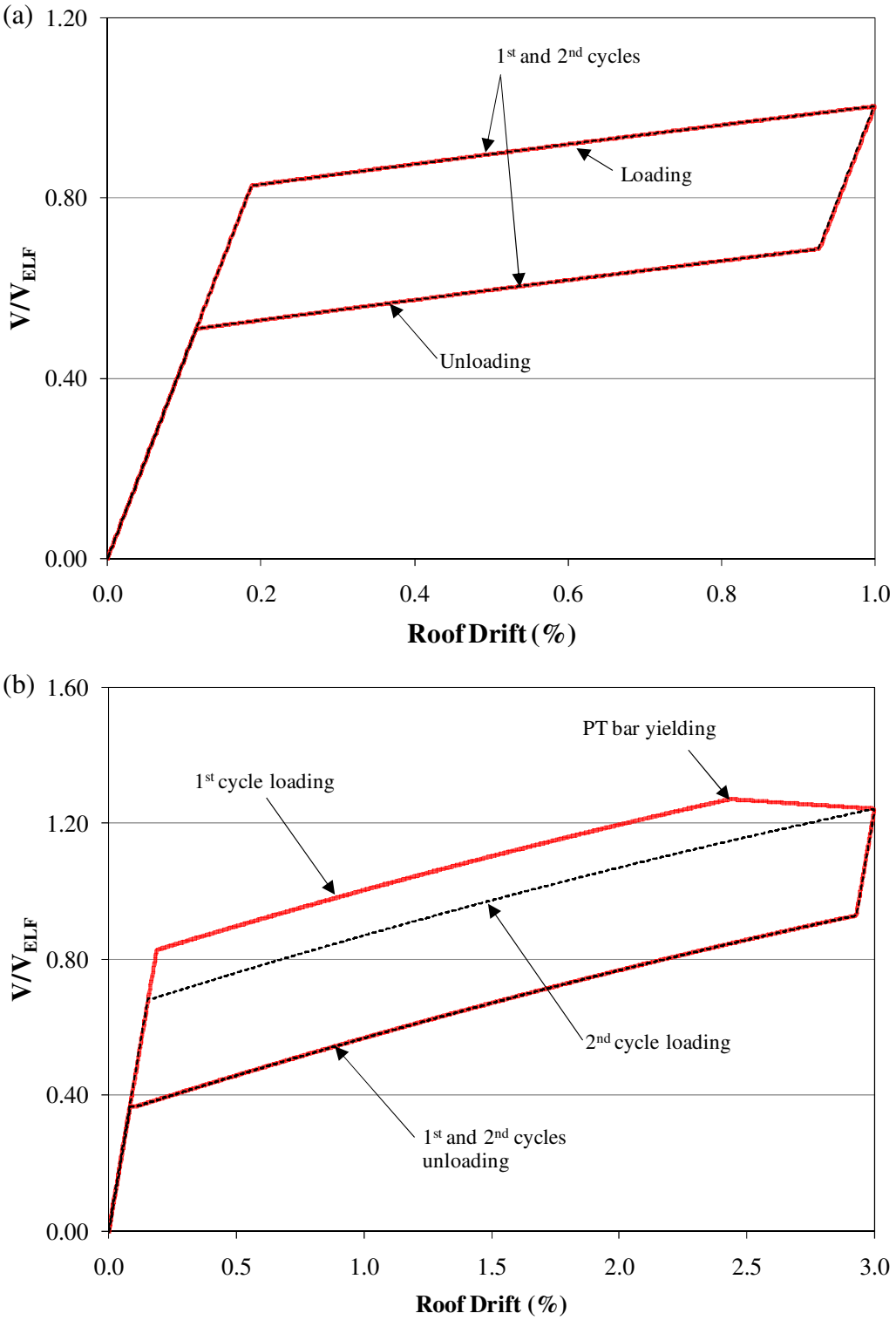

Figure 5.25 – Cyclic pushover of Frame B_{ED}: (a) to 1% roof drift; (b) after PT bar yielding

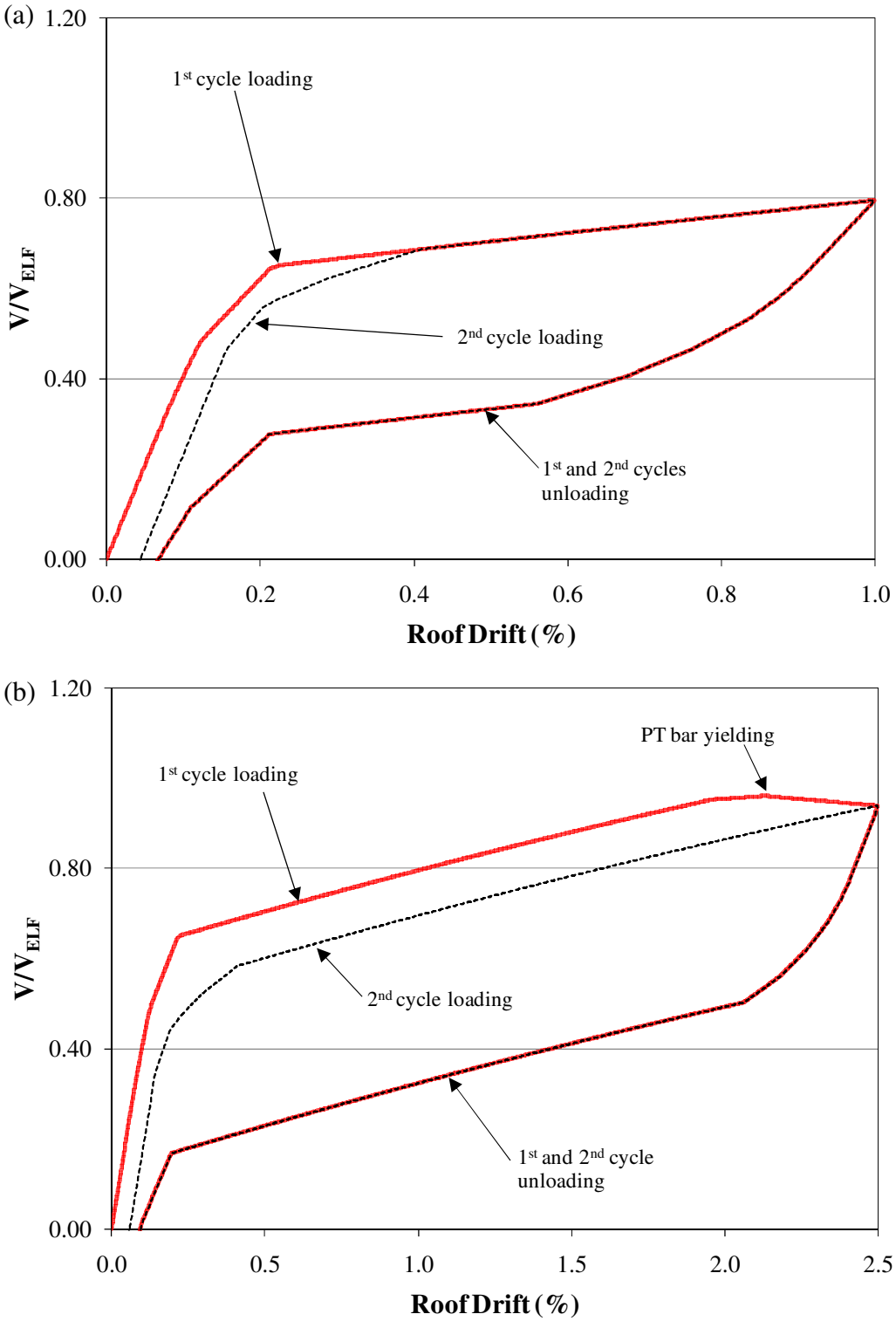

Figure 5.26 – Cyclic pushover of Frame C: (a) to 1% roof drift; (b) after PT bar yielding

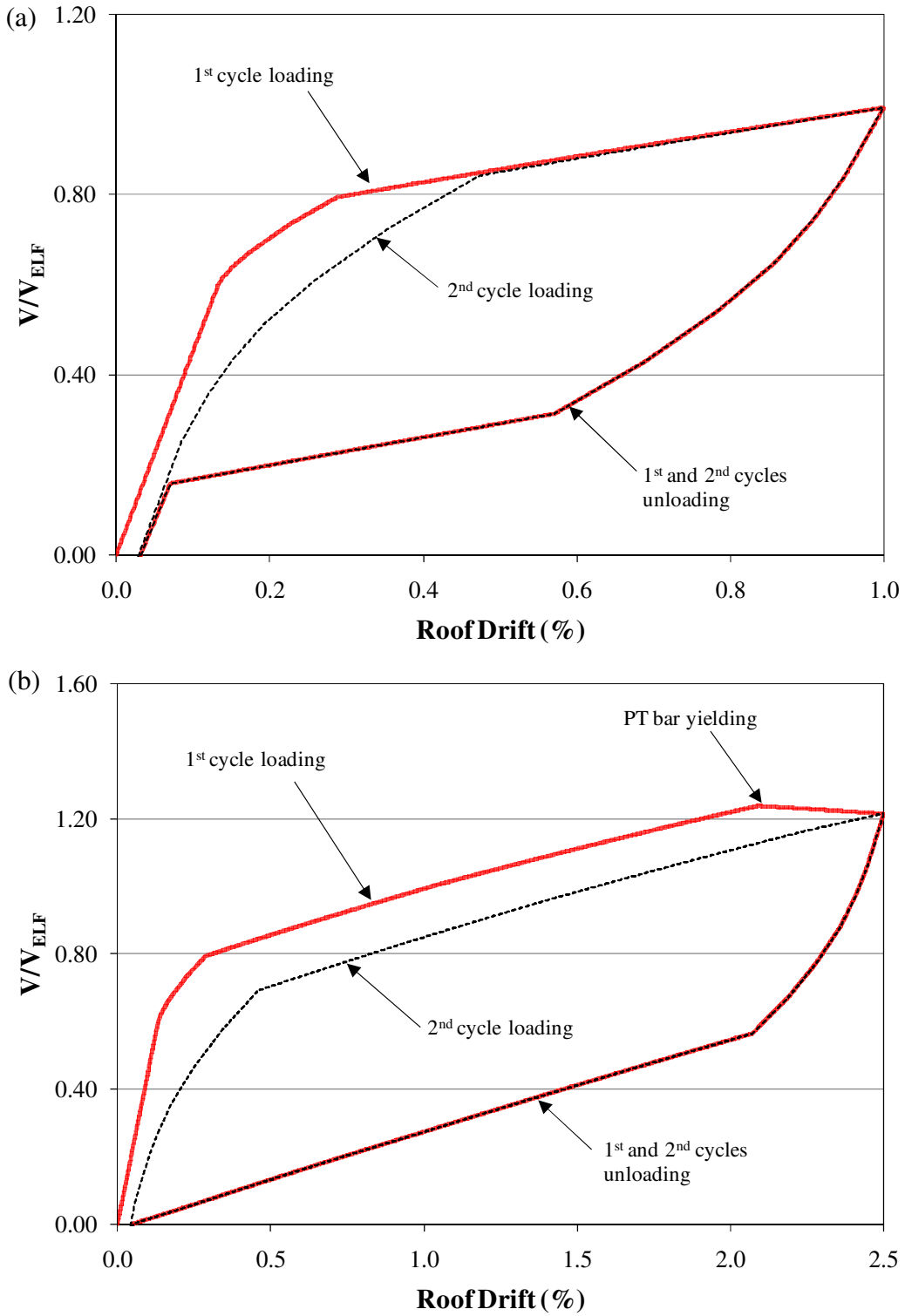

Figure 5.27 – Cyclic pushover of Frame D: (a) to 1% roof drift; (b) after PT bar yielding

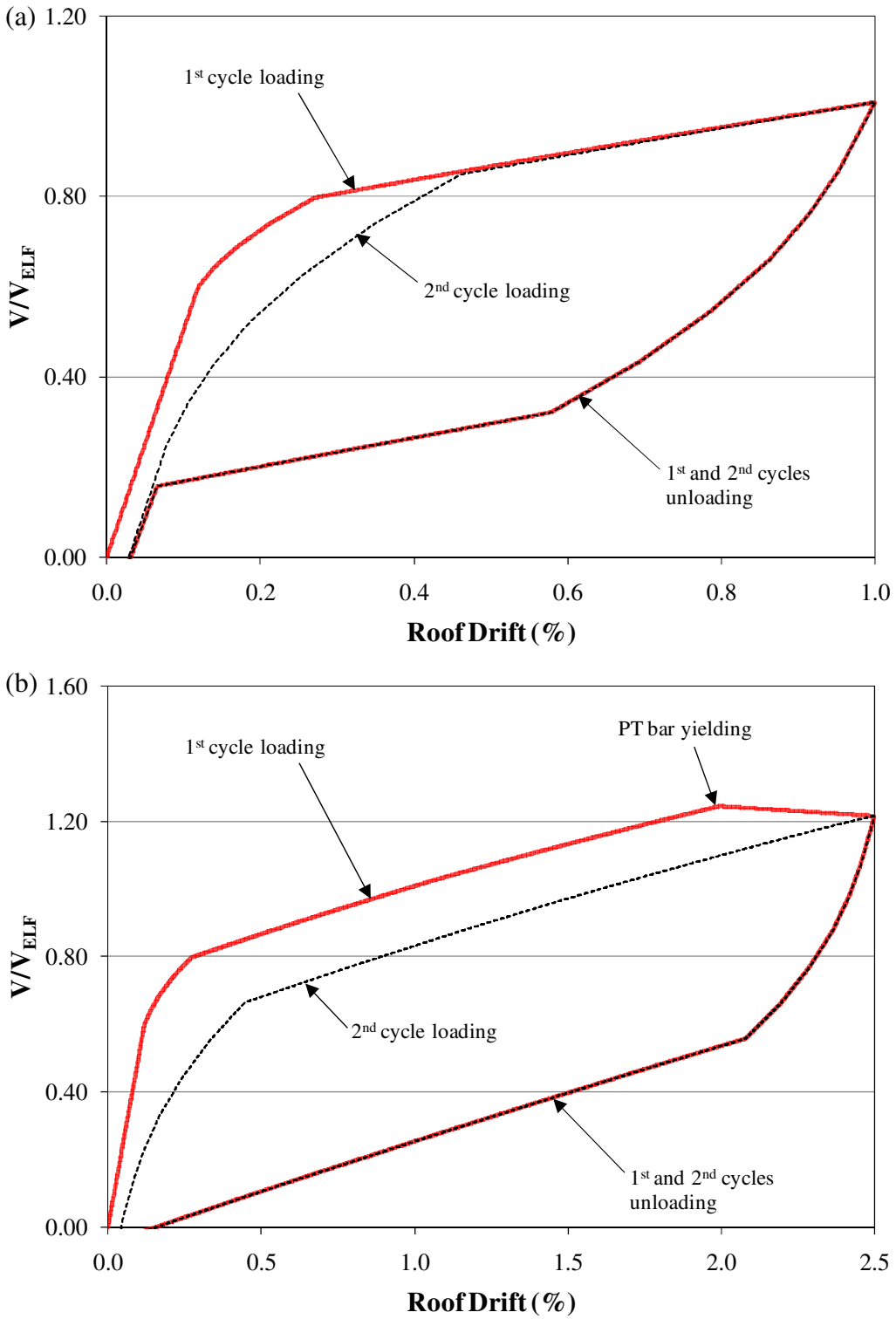

Figure 5.28 – Cyclic pushover of Frame D_{DIST}: (a) to 1% roof drift; (b) after PT bar yielding

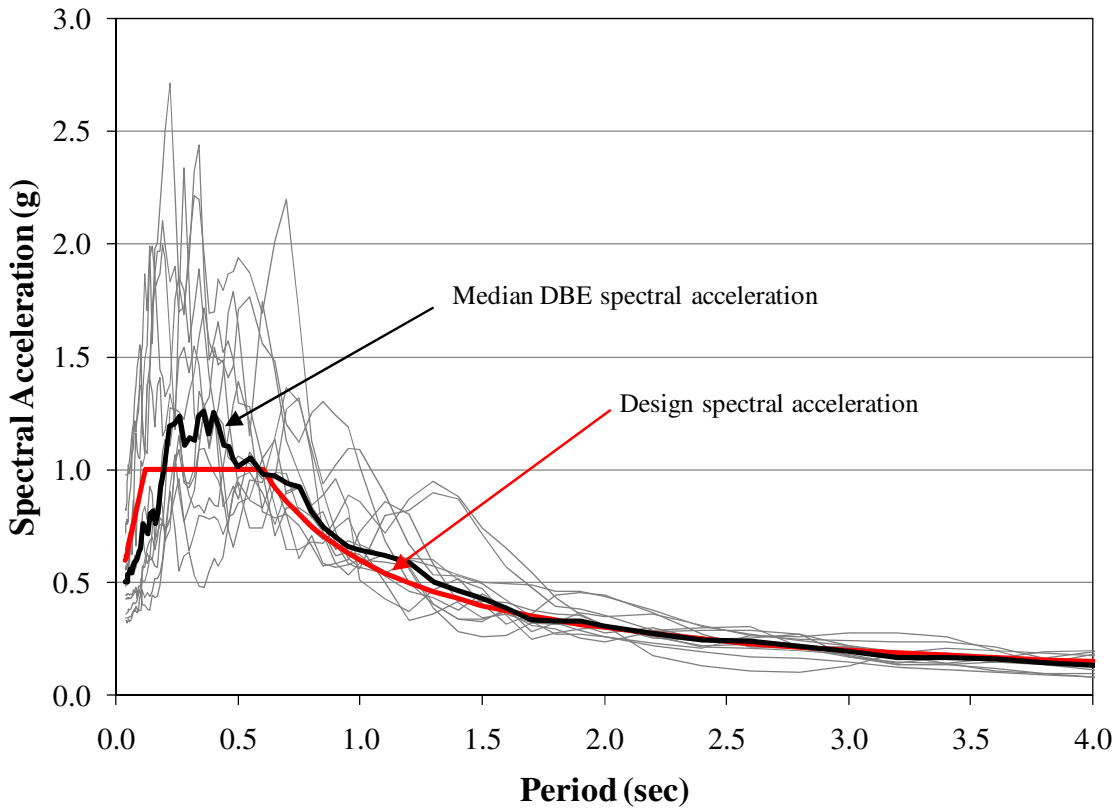

Figure 5.29 – Spectral accelerations of ground motions used for SC-CBF configuration study

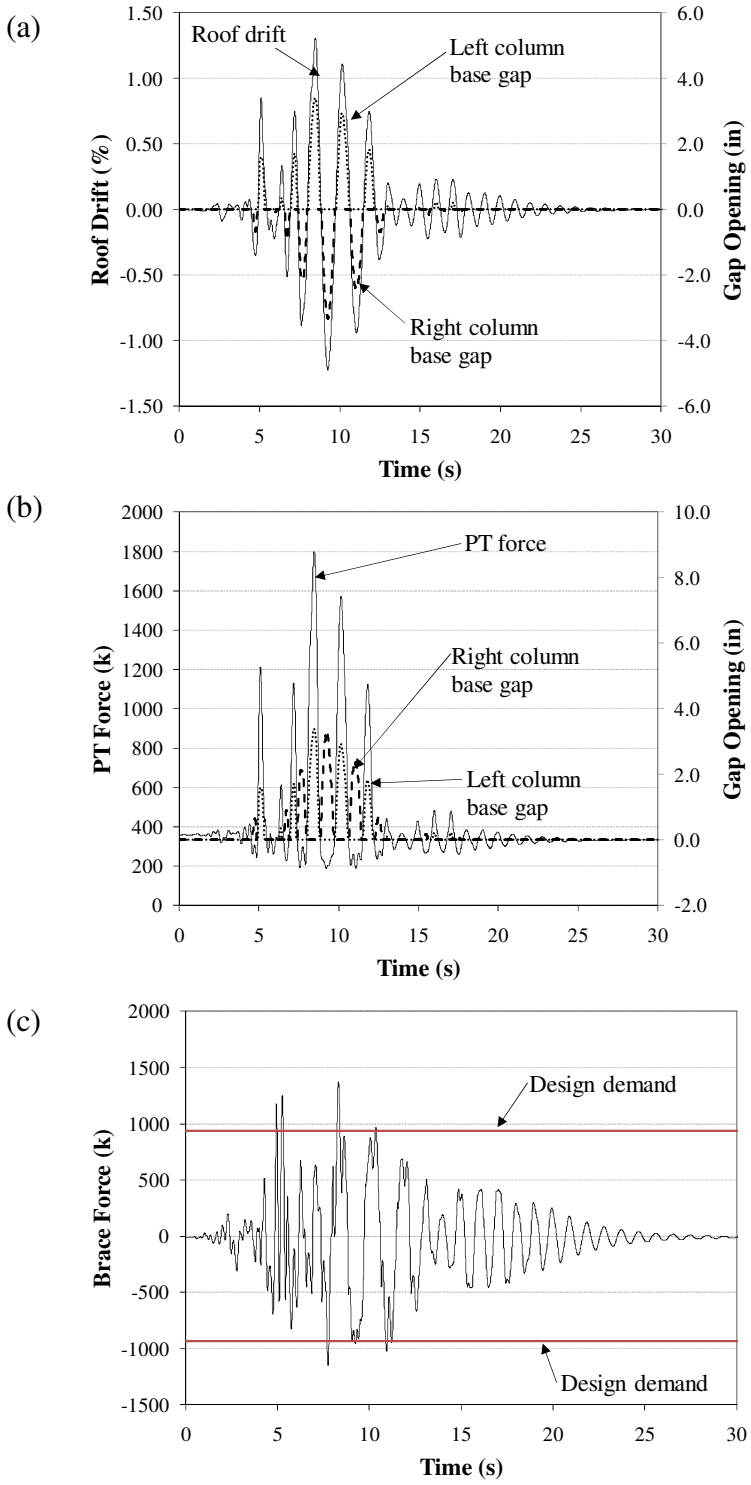

Figure 5.30 – Frame A dynamic response to nr0ccy270 scaled to DBE-level: (a) roof drift and gap-opening; (b) PT force and gap-opening; (c) first story brace force

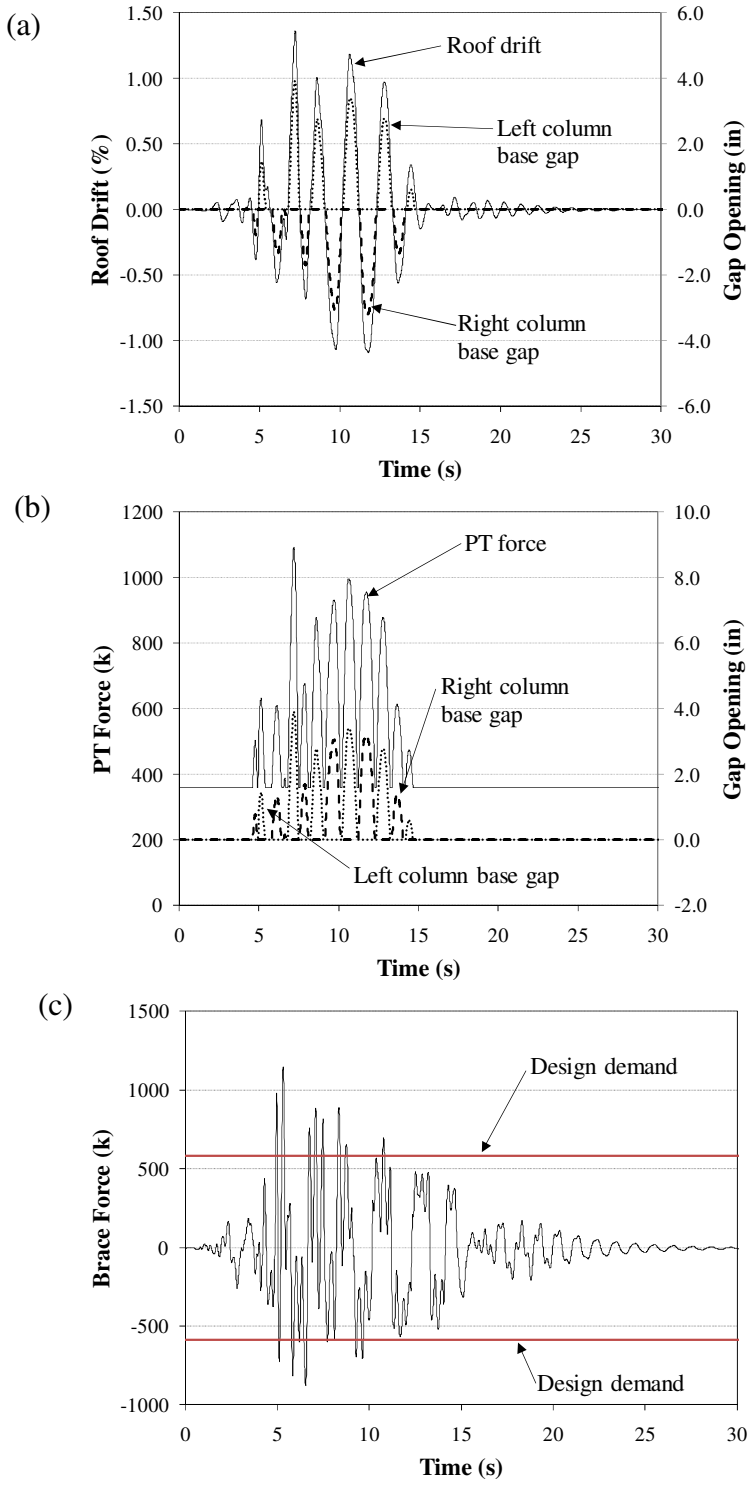

Figure 5.31 – Frame B dynamic response to nr0ccy270 scaled to DBE-level: (a) roof drift and gap opening; (b) PT force and gap opening; (c) first story brace force

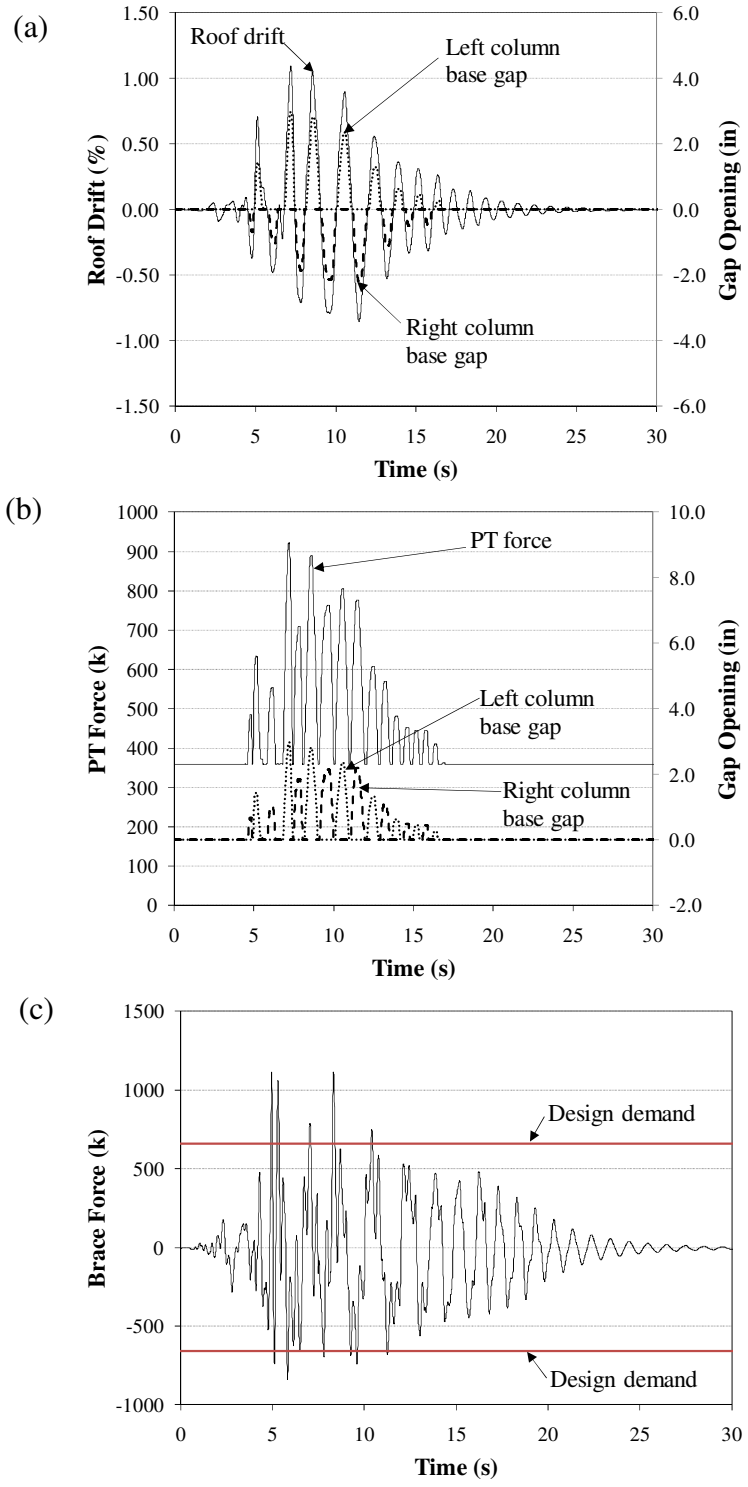

Figure 5.32 – Frame B_{ED} dynamic response to nr0ccy270 scaled to DBE-level: (a) roof drift and gap-opening; (b) PT force and gap opening; (c) first story brace force

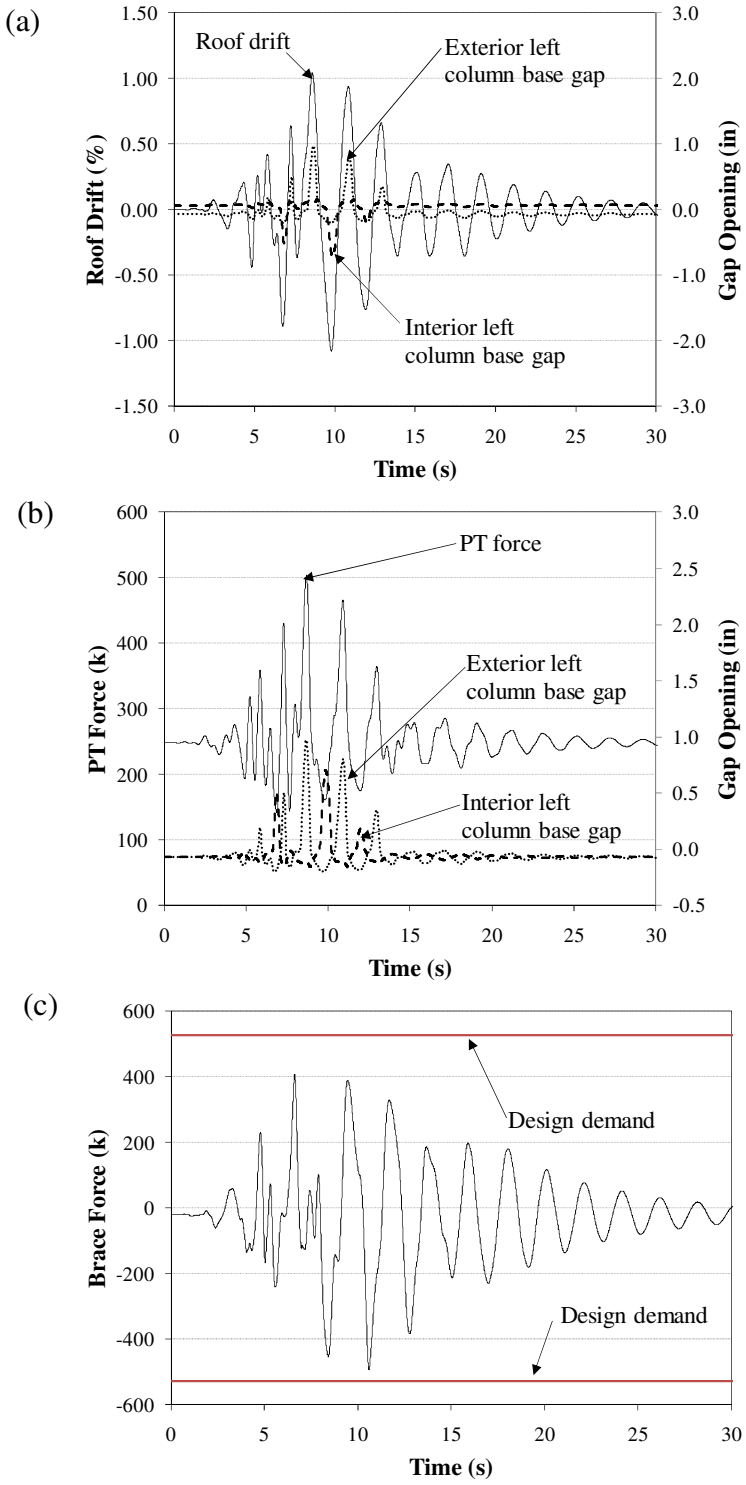

Figure 5.33 – Frame C dynamic response to nr0ccy270 scaled to DBE-level: (a) roof drift and gap-opening; (b) PT force and gap opening; (c) first story brace force

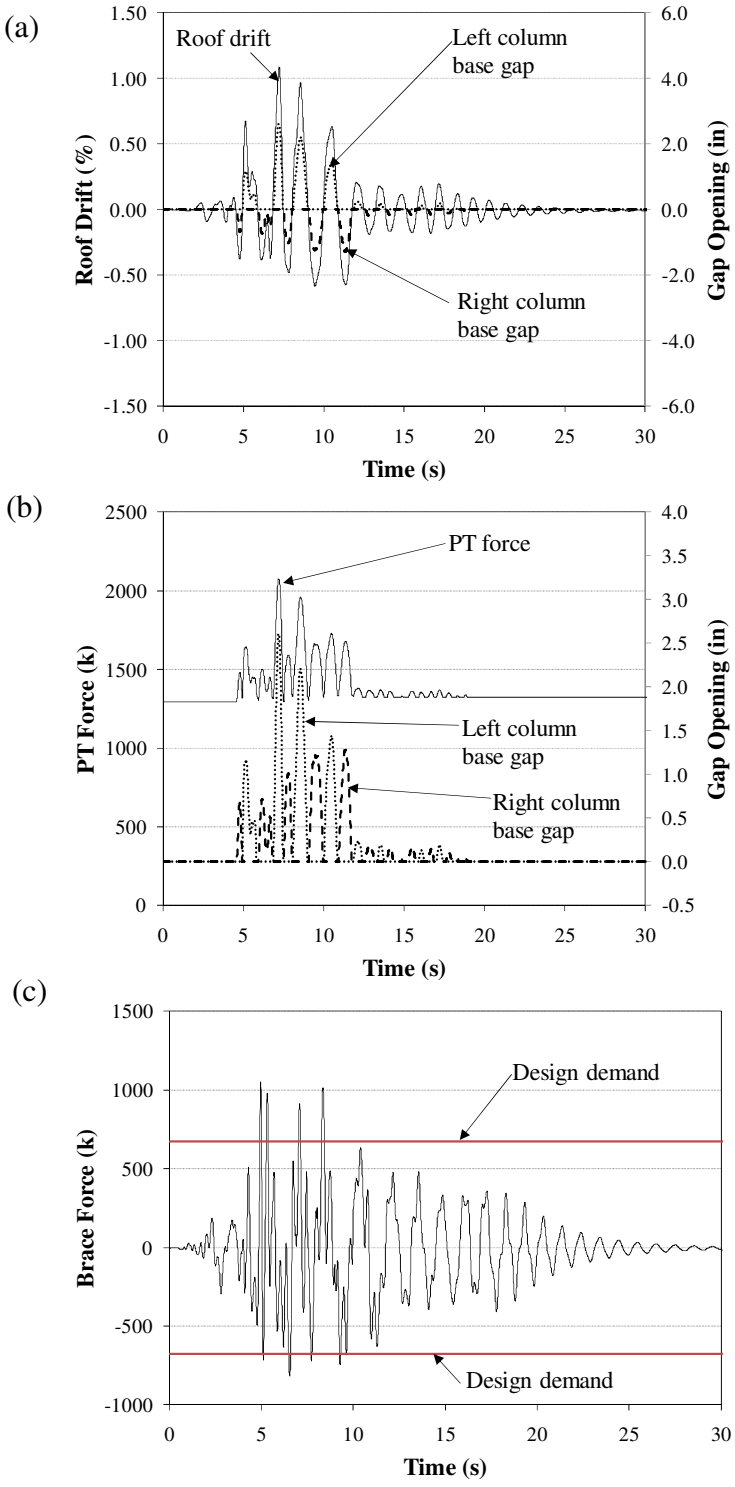

Figure 5.34 – Frame D dynamic response to nr0ccy270 scaled to DBE-level: (a) roof drift and gap-opening; (b) PT force and gap opening; (c) first story brace force

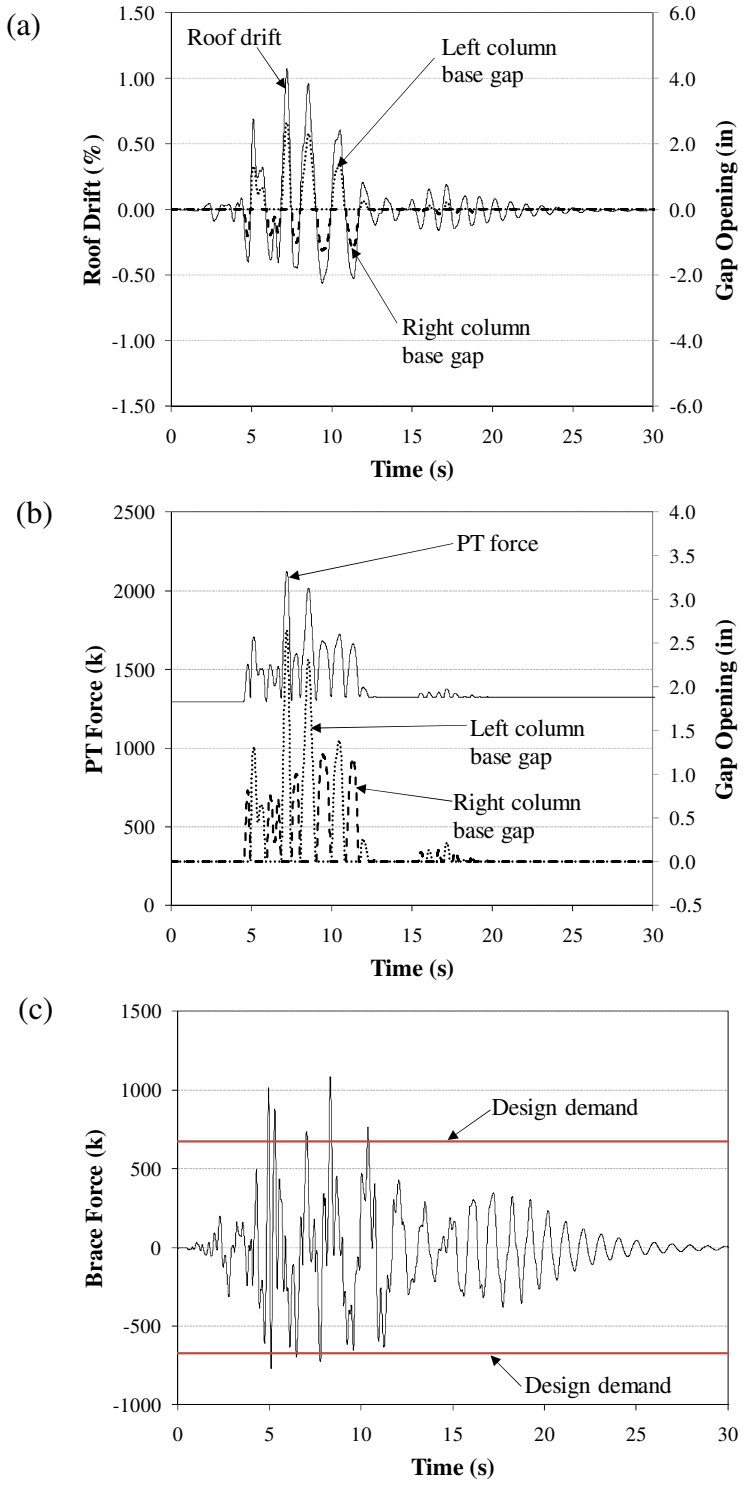

Figure 5.35 – Frame D_{DIST} dynamic response to nr0ccy270 scaled to DBE-level: (a) roof drift and gap-opening; (b) PT force and gap opening; (c) first story brace force

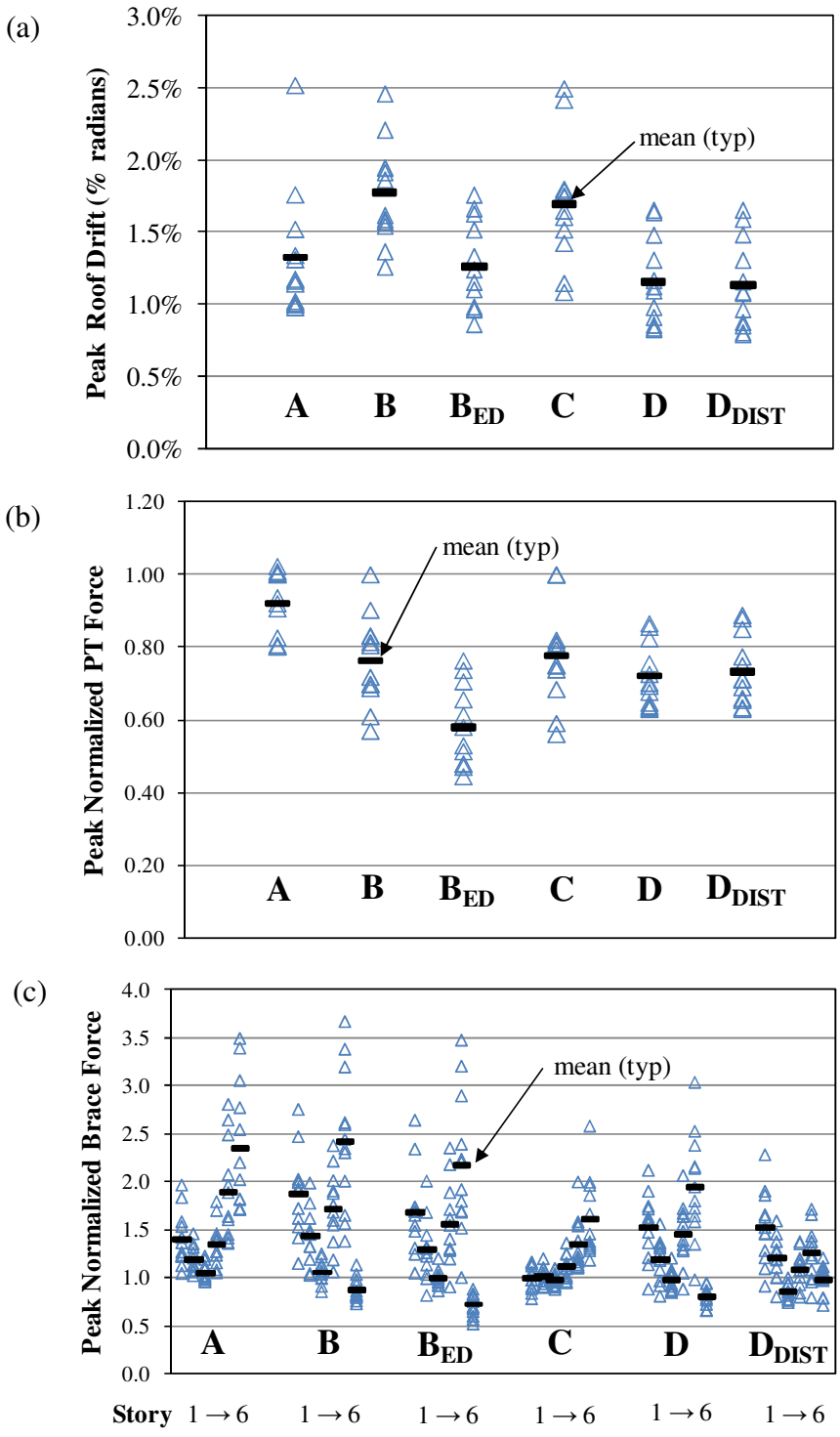

Figure 5.36 – Dynamic response by frame for 12 DBE-level ground motions: (a) peak roof drift; (b) peak PT force normalized by PT yield force capacity; (c) peak dynamic brace force normalized by design demand

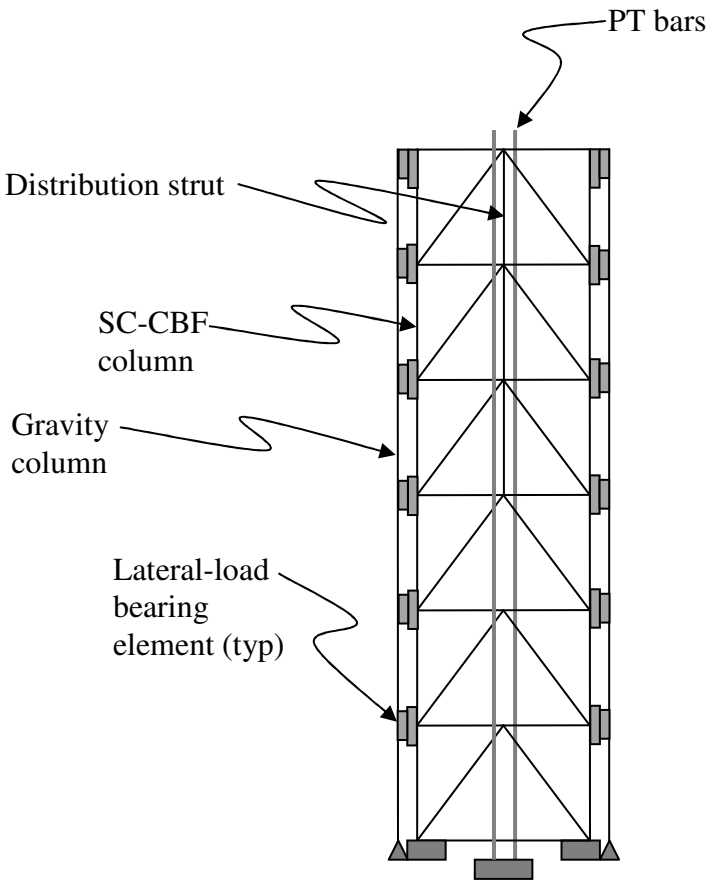

Figure 5.37 – Frame configuration: Frame D_{DF}

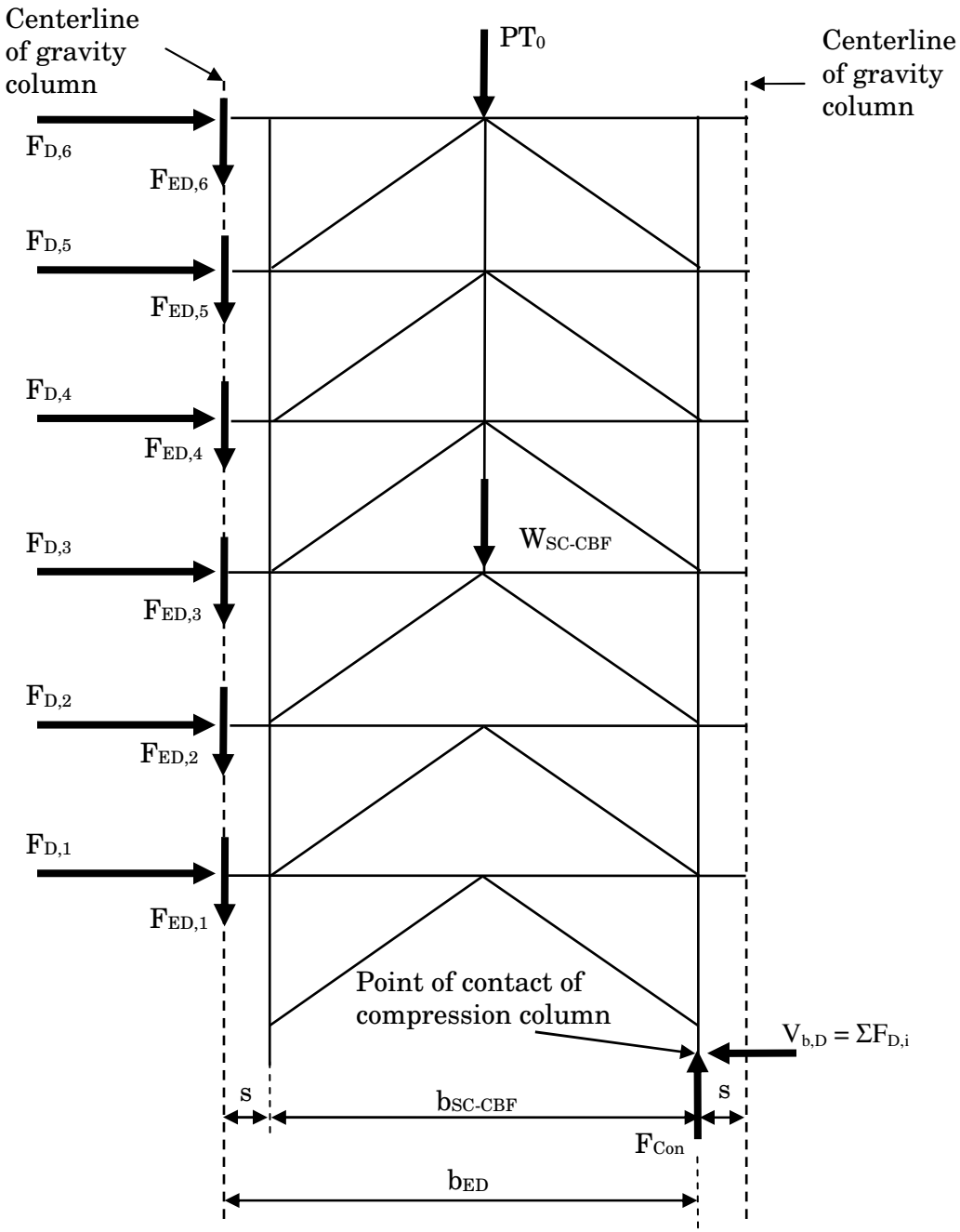

Figure 5.38 – Free-body diagram of Frame D_{DF} at decompression

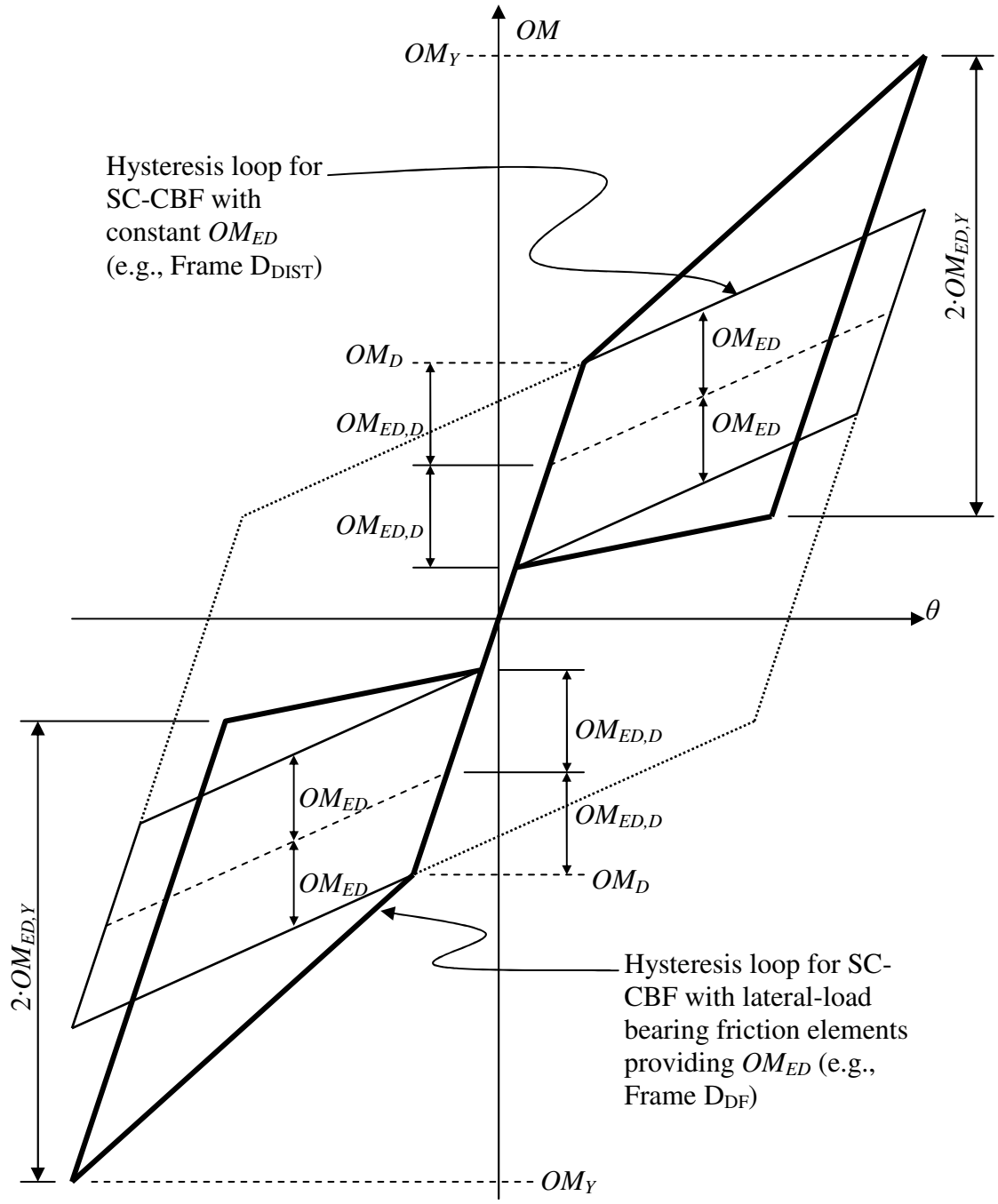

Figure 5.39 – Schematic overturning moment-roof drift relationship for an SC-CBF with lateral-load bearing friction elements providing OM_{ED}

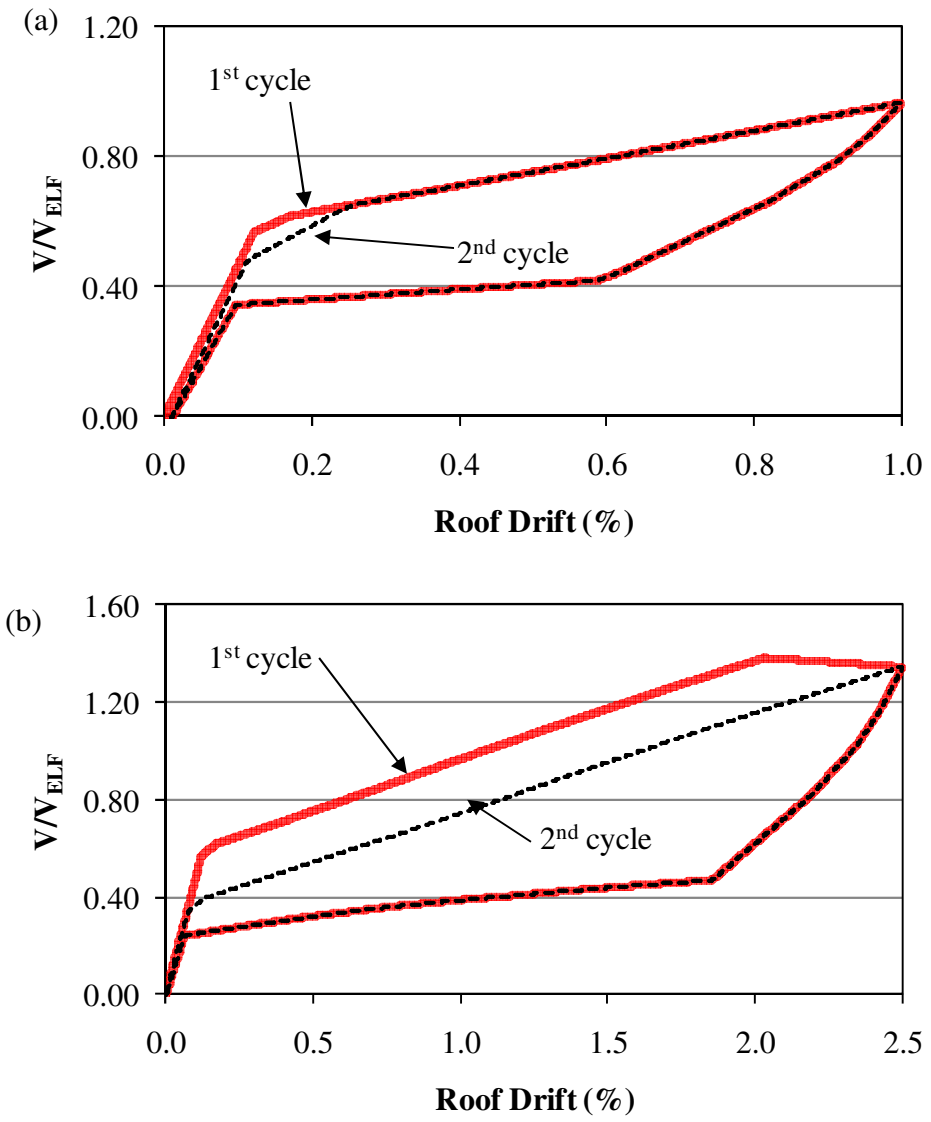

Figure 5.40 – Cyclic pushover response of Frame D_{DF}: (a) to 1% roof drift; (b) after PT bar yielding

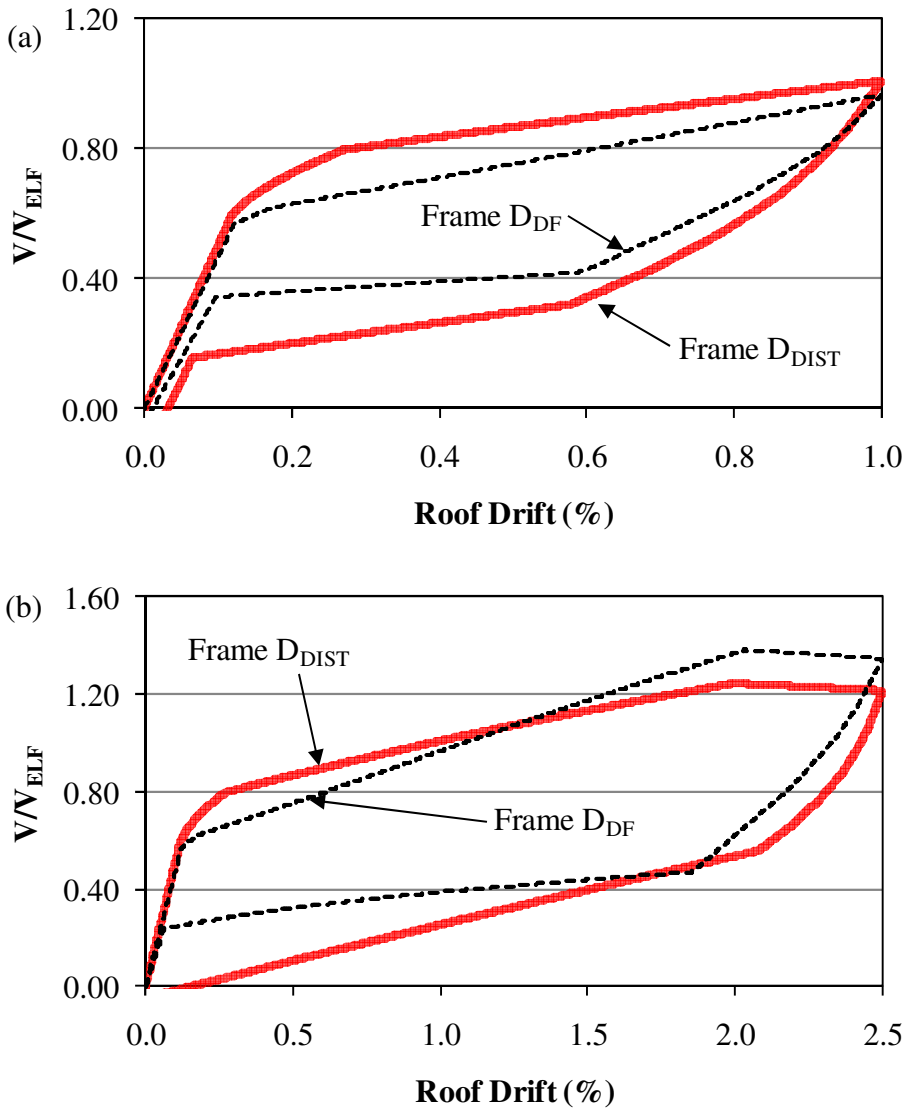

Figure 5.41 – Cyclic pushover response of Frame D_{DIST} and Frame D_{DF}: (a) first cycle to 1% roof drift; (b) first cycle after PT bar yielding

CHAPTER 6

DESIGN DEMAND ANALYSIS

The results of the SC-CBF configuration study presented in Chapter 5 show that the response of the SC-CBF system from nonlinear dynamic analysis is consistent with the behavior discussed in Chapter 3. However, the limit states of PT bar yielding and member yielding were frequently reached under DBE-level ground motions, so the SC-CBF systems studied did not meet the performance-based design (PBD) objectives discussed in Chapter 4. Assessment of the results shows that the SC-CBF member force design demands from the initial approach described in Chapter 5 underestimate the response from nonlinear dynamic analysis. In addition, an analytical method to determine design demands for the PT bar yielding limit state is needed.

This chapter presents analytical methods for estimating SC-CBF design demands that are consistent with the PBD objectives discussed in Chapter 4. A linear-elastic analytical model intended for the design of the SC-CBF system is discussed. The demands related to the limit states of decompression, PT bar yielding, and member yielding are discussed. The limit state of member failure is not addressed here but is discussed in Section 7.2. The uncertainty in the demands and the consequences of the limit states being reached are considered when calculating the design demands associated with the considered limit

states. Chapter 7 will address the capacities associated with these limit states and present a summary of the SC-CBF design procedure.

6.1 Analytical Model for SC-CBF Design

To produce a PBD approach that is compatible with typical design office practice, a linear elastic analysis model of the SC-CBF is used to estimate the design demands for each limit state. The analytical model of a four-story version of Frame D_{DF} (see Section 5.5) is shown schematically in Figure 6.1. This is a simplified model of the SC-CBF; only the main structural members (i.e., the beams, columns, braces, and distribution strut) are included. The gravity columns are neglected; the PT bars and lateral-load bearings (Section 5.5) are modeled by forces at their interface with the SC-CBF.

Member-to-member connections in the SC-CBF are modeled (and designed) as rigid moment-resisting connections. Therefore, the structural members are designed for axial force-bending moment interaction. The column bases have fixed boundary conditions. The SC-CBF structural members are modeled including P-Δ effects.

Lateral forces and the corresponding friction forces that develop in the friction bearings are applied at nodes A, B, C, D, F, G, H, and I. As indicated in Figure 6.1 and discussed in Section 5.3.2.1, these points are offset from the SC-CBF column and aligned with the gravity column centerlines to account for the eccentricity of the friction forces in the lateral-load bearings from the columns. Lateral forces are applied as compressive forces to simulate the load path of the inertia forces in the system, where the floor diaphragms

are connected to the gravity columns, and the inertial forces are transferred through the lateral-load bearings. The PT force is applied vertically at node E.

6.2 Decompression Limit State

Decompression of the "tension" column of the SC-CBF occurs when the overturning moment from the lateral forces overcomes the overturning moment resistance of the SC-CBF based on the initial PT force (PT_0), the gravity loads acting on the SC-CBF (e.g., the weight of the SC-CBF members, $W_{SC\text{-}CBF}$, the gravity load acting at each floor level, $F_{g,i}$), and the energy-dissipation (ED) element forces (e.g., ΣV_{ED} or F_{ED}).

As discussed in Section 5.3.2.1 (see Equation 5.10), the decompression overturning moment demand, $OM_{D,demand}$, is expressed in terms of OM_{ELF} as follows:

$$OM_{D,demand} = \alpha_{D,required} \cdot OM_{ELF} \tag{6.1}$$

where $\alpha_{D,required}$ is a factor used to express the required strength of the system relative to the strength of a conventional lateral force resisting system and OM_{ELF} is the overturning moment caused by $\{F_{ELF}\}$, as determined in Section 5.3.1. The decompression strength of the SC-CBF, OM_D, must be greater than $OM_{D,demand}$.

The roof drift at decompression is used later in calculating the DBE roof drift design demand. A static analysis that simulates the conditions at the decompression limit state can be conducted using the analytical model discussed in Section 6.1. Any ED forces acting on the SC-CBF (e.g., the forces in the ED elements in Frames B_{ED}, C, D, and D_{DIST}, or the friction forces in the lateral-load bearings in Frame D_{DF}) are assumed to be

fully developed at decompression. The PT force is assumed to be PT_0 because the PT bars do not elongate until significantly after decompression.

The decompression demand for the SC-CBF system is based upon the applied overturning moment, which is primarily a first mode response. Therefore, the lateral forces used in the decompression analysis are based on the first mode force distribution, $\{F_1\}$, scaled to be in equilibrium with $OM_{D,demand}$. The first mode forces are scaled by α_{D1}, determined as follows:

$$\alpha_{D1} = \frac{OM_D}{OM_1} \tag{6.2}$$

where,

OM_D = decompression strength of the SC-CBF, calculated from a free-body diagram of the SC-CBF at decompression, as discussed in Section 5.3.2.1

$$OM_1 = \{h\}^T \{F_1\} \tag{6.3}$$

$$\{F_1\} = \{s_1\} g = \Gamma_1 [m] \{\phi_1\} g \tag{6.4}$$

$$\Gamma_1 = \frac{\{\phi_1\}^T [m] \{i\}}{M_1} \tag{6.5}$$

$$M_1 = \{\phi_1\}^T [m] \{\phi_1\} \tag{6.6}$$

$[m]$ = matrix of seismic masses tributary to the SC-CBF

$\{i\}$ = influence vector = $\{1\ 1\ 1\ 1\}^T$ for a four story SC-CBF

The forces applied in the decompression analysis of Frame D_{DF} are shown in Figure 6.2 and include: lateral forces, $\{F_D\} = \alpha_{DI} \cdot \{F_I\}$; friction forces, $\{F_{ED}\} = \mu \cdot \{F_D\}$; PT_0; and $W_{SC\text{-}CBF}$. The static analysis determines the roof displacement at decompression, Δ_D, which is used in the design procedure as described later. The decompression roof drift is:

$$\theta_D = \frac{\Delta_D}{h} \tag{6.7}$$

where,

h = the total height of the structure

6.3 PT Bar Yielding Limit State

For design, the PT bar yielding limit state is quantified in terms of a global response quantity, namely the roof drift. The overturning moment-roof drift response of the SC-CBF system becomes nonlinear at decompression, as shown in Figure 3.3. The PBD objectives discussed in Chapter 4 state that the PT bars should not yield under median DBE-level seismic response. PT bar yielding is a limit state that has modest consequences, since IO performance is achieved even if the PT bars undergo minor yielding under the DBE, and the repair effort required to restress the PT bars (i.e., repeat the post-tensioning operation on the PT bars) is not significant. Therefore, the median DBE roof drift demand is taken as the design demand for the PT bar yielding limit state, thereby permitting as much as a 50% probability that the design demand will be exceeded under the DBE.

Figure 6.3 shows the idealized overturning moment versus roof drift response of an SC-CBF system. This figure indicates that the DBE roof drift design demand, $\theta_{DBE,dd}$, can be estimated as:

$$\theta_{DBE,dd} = \mu_{DBE} \cdot \theta_D \tag{6.8}$$

where μ_{DBE} is the ductility demand for the DBE. In the calculation of μ_{DBE}, a coefficient $R_{A,D}$ is used instead of the code-based response modification coefficient, R. $R_{A,D}$ is the ratio of the required strength of the structure for it to remain elastic during median DBE-level response over the actual strength of the structure. The required strength of the structure to remain elastic is calculated from the code-based design spectrum (with R = 1). The actual strength of the SC-CBF system is taken as the strength at decompression (OM_D). $R_{A,D}$ is based on first mode response because the roof drift demand is dominated by the first mode. $R_{A,D}$ is used only to estimate μ_{DBE} and $\theta_{DBE,dd}$.

$R_{A,D}$ is calculated as follows:

$$R_{A,D} = \frac{OM_{elastic,1}}{OM_D} \tag{6.9}$$

where $OM_{elastic,1}$ is the required elastic strength of the structure, considering only the first mode effective modal mass as follows:

$$OM_{elastic,1} = \frac{M_1^*}{M_{total}} \cdot OM_{elastic} \tag{6.10}$$

and $OM_{elastic}$ is the required elastic strength of the structure from the design spectrum:

$$OM_{elastic} = R \cdot OM_{ELF} \tag{6.11}$$

The first mode effective modal mass M_1^* is calculated as follows (Chopra 2007):

$$M_1^* = \frac{\left(\{\phi_1\}^T [m]\{i\}\right)^2}{\{\phi_1\}^T [m]\{\phi_1\}} = \Gamma_1 \left(\{\phi_1\}^T [m]\{i\}\right) \tag{6.12}$$

The total tributary mass for the SC-CBF, M_{total}, is:

$$M_{total} = \{i\}^T [m]\{i\} \tag{6.13}$$

μ_{DBE} can be calculated from standard relationships between R and μ, determined from single-degree-of-freedom nonlinear analyses and published in the literature (e.g, Seo and Sause 2005). Such relationships, known as μ-R-T relationships, account for the effect of period and energy dissipation on the ductility demand expressed as a function of the strength of the structure (R). The μ-R-T relationship should be specific to self-centering (SC) systems. Seo (2005) established the following μ-R-T relationship for SC systems:

$$\mu_{DBE} = R_{A,D}^{\,p(T_1)} \tag{6.14}$$

where,

$$p(T_1) = \exp\left(\frac{c_1}{T_1^{c_2}}\right) \tag{6.15}$$

and

$$c_1 = \left(a - b\sqrt{\alpha_k}\right)^2 \tag{6.16}$$

$$c_2 = \left(c - d\sqrt{\alpha_k}\right)^2 \tag{6.17}$$

α_k is the ratio of the post-decompression stiffness of the SC-CBF to the initial stiffness. The coefficients a, b, c, and d are functions of the hysteretic energy dissipation ratio for the structure, β_E, and the site soil conditions (site class). Values of these coefficients are given in Table 6.1, based on the secant frequency damping model (Seo 2005). This μ-R-T relationship for SC systems is a function of two design parameters: β_E and α_k. These parameters are discussed below.

6.3.1 Hysteretic Energy Dissipation Ratio, β_E

The hysteretic energy dissipation ratio, β_E, is defined in Section 5.3.3 as the ratio of the energy dissipated by the hysteresis loop of an SC system to the energy dissipated by a bilinear elasto-plastic system with the same strength under cyclic loading to the same peak displacement (Seo and Sause 2005).

From Figure 5.12 (see Equation 5.16) for an SC-CBF system with constant OM_{ED}, β_E is:

$$\beta_E = \frac{OM_{ED}}{OM_D} \tag{6.18}$$

This expression is valid for configurations such as Frames B_{ED}, C, D, and D_{DIST}, which have constant ED element force values. Frame D_{DF}, as discussed in Section 5.5, has friction-based ED elements in the lateral-load bearings, in which the friction forces are proportional to the lateral inertia forces. From Figure 5.39 (see Equation 5.29), β_E for Frame D_{DF} is defined as:

$$\beta_E = \frac{\frac{1}{2}\left(2 \cdot OM_{ED,D} + \lambda\left(OM_{ED,Y} - OM_{ED,D}\right)\right)}{OM_D} \tag{6.19}$$

As previously discussed, the strength of an SC-CBF system is expressed in terms of the overturning moment. The first mode lateral force distribution $\{F_1\}$ is used to calculate θ_D and $R_{A,D}$. Therefore, $\{F_1\}$ and OM_1 should be used in the calculation of β_E. Equation 6.19 requires the calculation of OM_{ED} at two conditions: at column decompression ($OM_{ED,D}$) and at PT bar yielding ($OM_{ED,Y}$). In Section 5.5, Equation 5.26 expressed OM_{ED} for Frame D_{DF} as a function of the applied overturning moment:

$$OM_{ED} = \mu \cdot \frac{OM}{h^*} \cdot b_{ED} \tag{6.20}$$

Using the first mode lateral force distribution, $OM_{ED,D}$ and $OM_{ED,Y}$ can be written as:

$$OM_{ED,D} = \eta \cdot OM_D \tag{6.21}$$

$$OM_{ED,Y} = \eta \cdot OM_Y \tag{6.22}$$

where the constant dimensionless parameter η is defined as:

$$\eta = \mu \cdot \frac{b_{ED}}{h_1^*} \tag{6.23}$$

where,

$$h_1^* = \frac{OM_1}{V_{b1}} = \frac{\{h\}^T\{F_1\}}{\{i\}^T\{F_1\}} \tag{6.24}$$

where V_{b1} is the base shear for the first mode lateral force distribution.

Using Equations 6.19, 6.21, 6.22, and 6.23, β_E can be written as:

$$\beta_E = \eta \cdot \left(1 + \frac{\lambda}{2} \cdot (\alpha_Y - 1)\right) \tag{6.25}$$

where,

$$\alpha_Y = \frac{OM_Y}{OM_D} \tag{6.26}$$

$$\lambda = \frac{OM_{\max} - OM_D}{OM_Y - OM_D} \tag{6.27}$$

6.3.2 SC-CBF Stiffness Ratio, α_k

There are two distinct ranges of elastic behavior for the SC-CBF system: (1) the elastic behavior prior to column decompression and (2) the elastic behavior after column decompression but prior to yielding of the PT bars. Prior to column decompression, the lateral drift is due to the elastic deformation of SC-CBF structural members. The stiffness prior to column decompression is expressed as:

$$k_{elastic} = \frac{OM_D}{\theta_D} \tag{6.28}$$

where θ_D is determined from Equation 6.7.

After decompression, the elastic member deformation contributes little to the lateral drift, which is dominated by rigid-body rotation (i.e., rocking) about the base of the

compression column. The "post-decompression" stiffness, k_{pd}, of the SC-CBF system depends upon the frame configuration, and, in particular, k_{pd} depends mostly upon the stiffness of the PT bars. For an SC-CBF system with constant (or zero) V_{ED} and PT bars located at midbay, k_{pd} can be estimated as:

$$k_{pd} = \frac{A_{PT} \cdot E}{L_{PT}} \cdot \left(\frac{b_{SC-CBF}}{2} \right)^2 \tag{6.29}$$

For Frame D_{DF}, however, k_{pd} is dependent upon the stiffness of the PT bars and the friction in the lateral-load bearings, and can be estimated as:

$$k_{pd} = \frac{A_{PT} \cdot E}{L_{PT}} \cdot \left(\frac{b_{SC-CBF}}{2} \right)^2 \cdot \left(\frac{1}{1-\eta} \right) \tag{6.30}$$

For structures in which η equals 1 (i.e., $\mu \cdot b_{ED}$ equals h_1^*), k_{pd} equals ∞. In other words, when η equals 1, the friction in the lateral-load bearings prevents column decompression and rocking of the SC-CBF.

The ratio of k_{pd} to $k_{elastic}$ is defined as α_k:

$$\alpha_k = \frac{k_{pd}}{k_{elastic}} \tag{6.31}$$

k_{pd} for Frame D_{DIST} (Equation 6.29) is dependent upon the stiffness of the PT bars. k_{pd} for Frame D_{DF} (Equation 6.30) is dependent upon the stiffness of the PT bars and η, which is a function of μ and h_1^* (Equation 6.23).

6.3.3 Factored Roof Drift Design Demand for PT Bar Yielding

Figure 6.4 shows a schematic of the probability density function for the maximum roof drift response to DBE-level ground motions. Three values of roof drift response under the DBE, θ_{DBE}, are shown in this figure: the roof drift design demand, $\theta_{DBE,dd}$; the median roof drift response, $\theta_{DBE,m}$; and the factored roof drift design demand, $\theta_{DBE,fdd}$. $\theta_{DBE,fdd}$ is defined in this section.

$\theta_{DBE,dd}$ is intended to be an estimate of the median roof drift demand for the DBE (Seo 2005); therefore, $\theta_{DBE,dd}$ is assumed to be equal to $\theta_{DBE,m}$ (i.e., the bias shown in Figure 6.4 is assumed to be zero) and the probability of θ_{DBE} exceeding $\theta_{DBE,dd}$ is assumed to be 50%.

Using a factored design demand, $\theta_{DBE,fdd}$, in design enables the probability that θ_{DBE} exceeds the factored design demand to be controlled, where $\theta_{DBE,fdd}$ is:

$$\theta_{DBE,fdd} = \gamma_{\theta} \cdot \theta_{DBE,dd} \tag{6.32}$$

Assuming that $\theta_{DBE,m}$ is equal to $\theta_{DBE,dd}$ (i.e., there is no bias), and assuming that θ_{DBE} follows a lognormal distribution, the probability of θ_{DBE} exceeding $\theta_{DBE,fdd}$ can be written as:

$$P\left(\theta_{DBE} > \theta_{DBE,fdd}\right) = 1 - \Phi\left(\frac{\ln\left(\theta_{DBE,fdd}\right) - \ln\left(\theta_{DBE,m}\right)}{\sqrt{\ln\left(1+\delta_\theta^2\right)}}\right)$$
$$= 1 - \Phi\left(\frac{\ln\left(\gamma_\theta \cdot \theta_{DBE,dd}\right) - \ln\left(\theta_{DBE,dd}\right)}{\sqrt{\ln\left(1+\delta_\theta^2\right)}}\right) \quad (6.33)$$
$$= 1 - \Phi\left(\frac{\ln\left(\gamma_\theta\right)}{\sqrt{\ln\left(1+\delta_\theta^2\right)}}\right)$$

where δ_θ is the coefficient of variation of the roof drift response and Φ is the cumulative distribution function for a standard normal variate (Ang and Tang 2007).

The value of γ_θ required to achieve a target probability of θ_{DBE} exceeding $\theta_{DBE,fdd}$, $P(\theta_{DBE} > \theta_{DBE,fdd})$, can be determined as follows:

$$\gamma_\theta = exp\left[\left(\sqrt{ln\left(1+\delta_\theta^2\right)}\right) \cdot \left(\Phi^{-1}\left[1 - P\left(\theta_{DBE} > \theta_{DBE,fdd}\right)\right]\right)\right] \quad (6.34)$$

Again, assuming that $\theta_{DBE,dd}$ equals $\theta_{DBE,m}$ and with γ_θ equal to 1.0, the probability of θ_{DBE} exceeding $\theta_{DBE,fdd}$ is 50%, which is consistent with the PBD objectives for DBE-level seismic input as discussed in Chapter 4.

6.4 Member Yielding Limit State

The PBD objectives discussed in Chapter 4 require that the SC-CBF members do not yield under DBE-level seismic input. The member yielding limit state is not consistent with IO performance since it can result in permanent drift. Therefore, the member force design demands must have a small probability of being exceeded under the DBE. Also, as discussed previously, PT bar yielding should occur prior to member yielding; therefore,

the member force design demands should be estimated assuming that the PT bars have yielded.

This section discusses the member force design demands and how they are estimated from a modal analysis of the SC-CBF system. These design demands account for both the large dispersion in the dynamic demands shown in Figure 5.36(c) and correlation of the modal responses due to the rocking response of the SC-CBF.

6.4.1 Rocking Behavior

The column uplift and rocking behavior of the SC-CBF system is unlike the behavior of a conventional CBF system. As such, estimates of the member force design demands should consider the rocking behavior.

6.4.1.1 Modal Expansion of the Rocking Displaced Shape

The rocking displaced shape is assumed to be a rigid-body rotation about the base, where the floor displacements are proportional to the floor heights. For example, an approximate normalized rocking displaced shape for a six-story SC-CBF can be written as:

$$\{u_{rock}\} = \left\{ \frac{h_1}{h} \quad \frac{h_2}{h} \quad \frac{h_3}{h} \quad \frac{h_4}{h} \quad \frac{h_5}{h} \quad \frac{h_6}{h} \right\}^T \tag{6.35}$$

where,

h_i = height of floor i

This rocking displaced shape can be expanded into its modal components as follows (Chopra 2007):

$$\{u_{rock}\} = \sum_{n=1}^{N} \{\phi_n\} q_n \tag{6.36}$$

$$q_n = \frac{\{\phi_n\}^T [m] \{u_{rock}\}}{\{\phi_n\}^T [m] \{\phi_n\}} \tag{6.37}$$

where,

q_n = nth mode component amplitude

$\{\phi_n\}$ = nth mode shape

The rocking displaced shape and its modal components are shown in Figure 6.5 for the first four modes of Frame D, where the modal displaced shape (i.e., the modal component of the rocking displaced shape $\{u_{rock}\}$) for mode n is $\{\phi_n\} \cdot q_n$. Rocking of the SC-CBF is driven by applied overturning moment; it is therefore assumed that the rocking behavior is a first-mode dominated response, since overturning moment is a first-mode dominated response. The modal expansion of the rocking displaced shape shows that the higher modes are also excited by rocking, leading to larger higher-mode response for an SC-CBF than for a conventional system. The member force design demand calculation must therefore account for higher mode demands as well as the first mode demands.

6.4.1.2 Effective Pseudo-Acceleration

The restoring force vector for dynamic response can be expressed as the sum of the modal restoring force vectors:

$$\{f_r(t)\} = \sum_{n=1}^{N} \{f_{r,n}(t)\} \tag{6.38}$$

For a linear structural system, the modal restoring forces (i.e., equivalent static forces (Chopra 2007)) can be written as:

$$\{f_{r,n}(t)\} = \{s_n\} A_n(t) = \Gamma_n [m] \{\phi_n\} A_n(t) \tag{6.39}$$

$$\Gamma_n = \frac{\{\phi_n\}^T [m] \{i\}}{M_n} \tag{6.40}$$

$$M_n = \{\phi_n\}^T [m] \{\phi_n\} \tag{6.41}$$

where,

$\{f_{r,n}(t)\}$ = restoring force (i.e., equivalent static force) vector for mode n

$A_n(t)$ = modal pseudo-acceleration

Equation 6.38 is valid only for linear dynamic response to seismic loading. To extend this concept to nonlinear response, the modal effective pseudo-acceleration, $\alpha_n(t)$, is introduced. For a nonlinear structure, the modal restoring forces can be written as:

$$\{f_{r,n}(t)\} = \{s_n\} \alpha_n(t) = \Gamma_n [m] \{\phi_n\} \alpha_n(t) \tag{6.42}$$

Using only the mass orthogonality of the modes and no assumptions regarding the linearity of the response, $\alpha_n(t)$ can be determined as:

$$\alpha_n(t) = \frac{\{\phi_n\}^T \{f_r(t)\}}{\Gamma_n \cdot M_n} \tag{6.43}$$

Note that for linear dynamic response, $\alpha_n(t)$ is equal to $A_n(t)$.

Figure 6.6 shows response of Frame D from nonlinear dynamic analysis under the DBE-level ground motion nr0ccy270, introduced in Chapter 5. Figure 6.6(a) shows $\alpha_1(t)$ and the column base gap-opening (i.e., rocking) response, which shows that the rocking is in phase with the first mode response, as expected. Furthermore, as the first mode response amplitude increases, the rocking response amplitude also increases. Figure 6.6(b) shows $\alpha_2(t)$ and the column base gap-opening response, which shows that higher amplitude second mode response also occurs at the time of rocking.

6.4.2 Member Force Demands for Each Mode

To develop member force design demands that are accurate estimates of the member force demands during dynamic response, the member force demands for each mode are estimated initially using simple analytical models and the maximum values of the effective pseudo-acceleration, α_n. A linear elastic analysis model of the SC-CBF is used to estimate the member force demand for each mode.

6.4.2.1 First Mode Member Force Estimation

In Chapter 5, the member force design demands were determined using the ELF lateral force profile scaled until OM_Y was reached. As previously mentioned, the ELF lateral force profile is similar to the first mode lateral force profile. Here, the first mode lateral force profile will be used in calculating the member force design demands, with higher mode response considered in Section 6.4.2.2.

To estimate the first mode member force demands, a procedure similar to the one discussed in Chapter 5 will be used; the first mode lateral forces are scaled until OM_Y is reached. The overturning moment demand for each of the higher modes is small compared to the demand for the first mode; therefore, the forces used in the analysis of the first mode member forces include the weight of the SC-CBF ($W_{SC\text{-}CBF}$), and PT force (PT_Y), and the ED forces (V_{ED}) due to their contribution to the overturning moment resistance of the system. The forces applied to the analysis model are shown in Figure 6.7, which shows the forces applied to Frame D_{DIST} at PT yield.

The ratio of OM_Y to OM_1 represents a limit on effective pseudo-acceleration for the first mode, because the overturning moment demand cannot exceed the yield overturning moment of the SC-CBF.

$$\alpha_{Y,1} = \frac{OM_Y}{OM_1} \tag{6.44}$$

The applied forces in Figure 6.7 can then be calculated as:

$$\{F_{Y,1}\} = \alpha_{Y,1}\{F_1\} = \{F_{Y,1} \quad F_{Y,2} \quad F_{Y,3} \quad F_{Y,4} \quad F_{Y,5} \quad F_{Y,6}\}^T \tag{6.45}$$

The first mode member force design demands for each member x, $F_{1,x,dd}$, in Frame D_{DIST} are then determined from a linear elastic analysis of the loading shown in Figure 6.7.

6.4.2.2 Higher Mode Member Force Estimation

The higher mode member force demands can be estimated by applying the modal force distributions to the linear elastic model. The member force demand in member x for a unit spectral acceleration, $F_{n,x,unit}$, is determined by applying the force distribution $\{F_n\}$ to the elastic model (Chopra 2007). This force distribution can be written as:

$$\{F_n\} = \{s_n\}g = \Gamma_n[m]\{\phi_n\}g \tag{6.46}$$

The loads used in the analysis of higher mode member forces for a six-story SC-CBF are shown schematically in Figure 6.8.

$F_{n,x,unit}$ for member x can be determined from the results of the linear elastic analysis. These demands are for a unit acceleration in each mode. To determine the design demands for a linear system, these demands are multiplied by the pseudo-acceleration (Chopra 2007); for the nonlinear SC-CBF system, however, these demands should be multiplied by the effective pseudo-acceleration for each mode, as follows:

$$F_{n,x,dd} = \alpha_n \cdot F_{n,x,unit} \tag{6.47}$$

where α_n is the peak value of the time-varying effective pseudo acceleration for mode n, $\alpha_n(t)$. It is important to note that while α_n can be determined from the nonlinear response

of an SC-CBF to a given earthquake ground motion, α_n is not known during design of the SC-CBF. A nominal value of the modal member force design demand can be estimated by replacing α_n with the spectral acceleration value from the DBE design spectrum as follows:

$$F_{n,x,dd} = SA_n \cdot F_{n,x,unit} \tag{6.48}$$

where,

SA_n = DBE design spectral acceleration for the n^{th} mode

However, it is expected that Equation 6.48 will underestimate the higher mode response of an SC-CBF due to the rocking response. Therefore, modal load factors γ_n are introduced to account for the potential bias and dispersion in the higher mode response, where the bias exists because SA_n may not be an accurate estimate of the median value of α_n, $\alpha_{n,m}$. The factored modal member force design demands are defined as:

$$F_{n,x,fdd} = \gamma_n \cdot SA_n \cdot F_{n,x,unit} \tag{6.49}$$

where $\gamma_n \cdot SA_n$ represents the upper bound to α_n with a low probability of exceedance. The factors γ_n are discussed further in Section 6.4.3.2.

6.4.2.3 Modal Truncation

To streamline the design process, it may be possible to reduce the number of modes considered in the member force design demand calculation. The effective modal mass

indicates how much mass participates in the response of each mode (Chopra 2007), and is calculated as:

$$M_n^* = \Gamma_n \{\phi_n\}^T [m]\{i\} = \frac{\left(\{\phi_n\}^T [m]\{i\}\right)^2}{M_n} \tag{6.50}$$

The total mass tributary to the SC-CBF is:

$$M_{total} = \{i\}^T [m]\{i\} = \sum_{n=1}^{N} M_n^* \tag{6.51}$$

The number of modes needed for an accurate estimate of the member force design demand is a function of the cumulative effective modal mass. That is, if $\sum_{n=1}^{J} M_n^*$ is sufficiently close to M_{total}, the modes above mode J can be truncated. Truncating the highest modes such that most of the total mass is accounted for in the cumulative effective modal mass of the retained modes ($\sum_{n=1}^{J} M_n^*$) will have a negligible effect on the estimated design demands. Using the smallest J, with $\sum_{n=1}^{J} M_n^* \geq 0.95 \cdot M_{total}$, should be sufficient to capture the higher mode contributions to the member force design demands. For example, Table 6.2 shows the calculation of M_n^* for Frame D_{DIST}v2, where Frame D_{DIST}v2 is a second version of Frame D_{DIST}, as described in Section 6.5. Note that the mode shapes used in these calculations were mass-normalized and $\Gamma_n = \{\phi_n\}^T[m]\{i\}$; in general, $\Gamma_n \neq \{\phi_n\}^T[m]\{i\}$. The first three modes include more than 95% of the total mass of the structure; therefore, only the first three modes are needed to estimate the member force design demands.

6.4.3 Reliability of Factored Member Force Design Demands

In Section 6.4.2.2, modal load factors γ_n were introduced to factor the design response spectral accelerations, SA_n, to $\gamma_n \cdot SA_n$ to provide upper bound estimates of the modal response. This section discusses the use of γ_n to control the probability of the member force demands under the DBE exceeding the factored member force design demands. First, the design response spectrum is established. Then, the probability of α_n exceeding $\gamma_n \cdot SA_n$ is used to select values of γ_n. The effect of γ_n will be reviewed in Section 6.4.6.

6.4.3.1 Design Response Spectrum

The design response spectrum for the DBE is defined based on ASCE-7 (2005) as:

$$SA(T) = \begin{cases} S_{DS}\left(0.4 + 0.6 \cdot \dfrac{T}{T_0}\right) & T \le T_0 \\ S_{DS} & T_0 < T \le T_S \\ \dfrac{S_{D1}}{T} & T_S < T \le T_L \\ \dfrac{S_{D1} \cdot T_L}{T^2} & T_L < T \end{cases} \tag{6.52}$$

where,

S_{DS}, S_{D1} = spectral response acceleration parameters for short periods and a period of 1 sec., respectively (ASCE 2005)

T_0, T_S, and T_L = transition periods (ASCE 2005)

The DBE-level design response spectrum given by Equation 6.52 is shown in Figure 6.9.

As mentioned in Section 6.4.2.2, SA_n values from the design spectrum will be factored to estimate an upper bound for the higher mode response of an SC-CBF.

6.4.3.2 Modal Load Factors

Figure 6.10 shows the distribution of α_n for Frame D_{DIST} and for Frame D_{DIST}v2 from nonlinear dynamic analyses. α_n is the peak value of the time varying modal effective pseudo-acceleration $\alpha_n(t)$ calculated using Equation 6.43. The dynamic analysis results for Frame D_{DIST} were presented in Chapter 5. Frame D_{DIST}v2 was designed using the factored modal member force design demands presented in this chapter (see Section 6.5), and then analyzed using the nonlinear analysis model and ground motions presented in Chapter 5. The median α_n for each mode, $\alpha_{n,m}$, is also shown in Figure 6.10. Assuming that values of α_n follow a lognormal distribution, $\alpha_{n,m}$ is estimated from the α_n data as follows (Ang and Tang 2007):

$$\alpha_{n,m} = \exp(\lambda_\alpha) \tag{6.53}$$

where,

$$\lambda_\alpha = \ln(\mu_\alpha) - \frac{1}{2}\zeta_\alpha^2 \tag{6.54}$$

$$\zeta_\alpha = \sqrt{\ln(1+\delta_\alpha^2)} \tag{6.55}$$

μ_α = mean value of α_n

δ_α = coefficient of variation of $\alpha_n = \sigma_\alpha / \mu_\alpha$

σ_α = standard deviation of α_n

Figure 6.10 also shows the spectral accelerations, SA_n, from the DBE design spectrum for each of the higher modes. The first mode spectral acceleration, SA_1, is not determined from the design spectrum, but is set equal to $\alpha_{Y,1}$, because the first mode force and acceleration responses, including the first mode effective pseudo-acceleration, are limited by PT bar yielding (i.e., OM_1 is limited by OM_Y). Figure 6.10 shows that the higher mode responses from dynamic analysis have high dispersion, while the first mode response is close to $\alpha_{Y,1}$. The first mode has less dispersion due PT bar yielding, which limits the response, while the higher modes are (in many cases) excited beyond SA_n by the rocking response. Note that α_1 can exceed $\alpha_{Y,1}$ if the higher mode contribution to the overturning moment opposes the first mode contribution to the overturning moment at the time when the peak value of $\alpha_1(t)$ is reached.

Figure 6.11 shows a schematic of the assumed probability density function for α_n response to DBE-level seismic input. α_n is assumed to follow a lognormal distribution. Table 6.3 gives values of α_n for Frame D_{DIST} and Frame D_{DIST}v2 from nonlinear response to the suite of 12 DBE-level ground motions introduced in Section 5.4.3.1. The mean, standard deviation, coefficient of variation, and median values of α_n (μ_α, σ_α, δ_α, and $\alpha_{n,m}$, respectively), T_n, as well as SA_n are presented in Table 6.4, where SA_n equals $\alpha_{Y,1}$ for the first mode and SA_n equals the spectral acceleration from the DBE design spectrum for the higher modes, are presented in Table 6.4. The probability that α_n exceeds $\alpha_{Y,1}$ or SA_n is calculated as follows:

$$P(\alpha_n > SA_n) = 1 - \Phi\left(\frac{\ln(SA_n) - \ln(\alpha_{n,m})}{\sqrt{\ln(1+\delta_\alpha^2)}}\right) \tag{6.56}$$

The probabilities of α_n exceeding $\alpha_{Y,1}$ or SA_n for Frame D_{DIST} and Frame D_{DIST}v2 are shown in Table 6.4. α_n frequently exceeds SA_n; for example, α_2 has a 69.0% probability of exceeding SA_2 for Frame D_{DIST} and a 76.0% probability of exceeding SA_2 for Frame D_{DIST}v2. There are two significant reasons why α_n frequently exceeds SA_n: (1) the bias in the α_n data (i.e., $\alpha_{n,m}$ is often larger than SA_n), and (2) the dispersion of the α_n data (i.e., δ_α). Modal load factors, γ_n, that account for both the bias and the dispersion are applied to SA_n for use in design. Values of γ_n were determined such that the probability of α_n exceeding $\gamma_n \cdot SA_n$ is approximately 5%, as follows:

$$\gamma_n = exp\left[\left(\sqrt{ln(1+\delta_\alpha^2)}\right) \cdot \left(\Phi^{-1}[1 - P(\alpha_n > \gamma_n \cdot SA_n)]\right)\right] \tag{6.57}$$

The modal load factors chosen were 1.15 for the first mode and 2.0 for the higher modes. These values of γ_n were chosen to be uniform and general (not specific for the data given in Table 6.4), so the probability of α_n exceeding $\gamma_n \cdot SA_n$ is actually in the range of 0.1% to 11%, as seen in Table 6.4. Figures 6.10 and 6.11 graphically illustrate the reduced probability of α_n exceeding $\gamma_n \cdot SA_n$. Note that the large bias and dispersion for the second mode α_n response leads to the relatively high probabilities of α_2 exceeding $\gamma_2 \cdot SA_2$.

6.4.4 Combination of Factored Modal Member Force Design Demands

To satisfy the PBD objectives for member yielding, the member force design demands for the DBE should provide an upper bound to the peak member force responses from

nonlinear dynamic analysis. The peak member force responses from dynamic analysis would be overestimated by the sum of the factored modal member force design demands. Therefore, a mode combination method is used to approximate the peak dynamic member force responses from the factored modal member force design demands. The complete quadratic combination method is used.

6.4.4.1 Complete Quadratic Combination (CQC) Method

The CQC method combines modal responses considering the correlation between each pair of modes. The CQC method equation is written as:

$$r_{design} = \left(\sum_{i=1}^{N} \sum_{n=1}^{N} \rho_{in} \cdot r_{i0} \cdot r_{n0} \right)^{\frac{1}{2}} \tag{6.58}$$

where,

r_{i0} = the peak response of quantity r (e.g., member force) in mode i

r_{n0} = the peak response of quantity r (e.g., member force) in mode n

ρ_{in} = correlation coefficient between modes i and n

The CQC method accounts for the correlation between the modes and also maintains the sign of the response quantities (Chopra 2007).

6.4.4.2 Correlation Coefficients

The correlation coefficients used in Equation 6.55 must be determined for the SC-CBF system. Correlation coefficients that are widely used for linear elastic structures are (Der Kiureghian 1980):

$$\rho_{in} = \frac{8\sqrt{\zeta_i \cdot \zeta_n}\left(\beta_{in} \cdot \zeta_i + \zeta_n\right)\beta_{in}^{3/2}}{\left(1-\beta_{in}^2\right)^2 + 4 \cdot \zeta_i \cdot \zeta_n \cdot \beta_{in} \cdot \left(1+\beta_{in}^2\right) + 4\left(\zeta_i^2 + \zeta_n^2\right)\beta_{in}^2} \tag{6.59}$$

where,

ζ_i = damping ratio in mode i

ζ_n = damping ratio in mode n

β_{in} = ratio of natural frequencies in modes i and n, ω_i / ω_n

These coefficients are dependent upon the relative proximity of the natural frequencies and the damping of the modes. As β approaches 1, ρ approaches 1 and the modal responses are strongly correlated. As β approaches 0 or ∞, ρ approaches zero and the modal responses are independent. Rocking of the SC-CBF appears to excite the higher modes regardless of their frequencies, so the correlation coefficients for the SC-CBF system are not expected to depend so directly on the frequency ratios β_{in}.

The correlation between α_n from the rocking response of Frame D_{DIST}v2 was calculated to provide estimates of ρ_{in} for an SC-CBF. To determine these correlations, the time history of the rocking response was studied and the duration of significant rocking was identified, as indicated in Figures 6.12 and 6.13, which show the response of Frame

D_{DIST}v2 to the DBE-level ground motion nr0ccy270 (see Section 5.4.3.1). Figure 6.12 shows the time history of gap-opening response due to rocking at the base of the SC-CBF columns. Figure 6.13 shows the time history of α_2. Figures 6.12(a) and 6.13(a) show the full time history; Figures 6.12(b) and 6.13(b) show the time history during significant rocking response. The correlation between the values of α_n for the different modes was studied during significant rocking response because the rocking behavior appears to increase the higher mode responses.

The correlation between two random variables X and Y can be calculated from the covariance of those variables, Cov(X,Y), as follows (Ang and Tang 2007):

$$\rho = \frac{Cov(X,Y)}{\sigma_X \cdot \sigma_Y} \tag{6.60}$$

where,

$$Cov(X,Y) = E[(X-\mu_X)(Y-\mu_Y)] = E[XY] - E[X]E[Y] \tag{6.61}$$

σ_X = standard deviation of X

σ_Y = standard deviation of Y

E[XY] = the expected value of X times Y

E[X] = the expected value (mean) of X

E[Y] = the expected value (mean) of Y

Table 6.5 shows the results of this analysis for the first four modes of Frame D_{DIST}v2, from the dynamic response to the DBE-level ground motions introduced in Section 5.4.3.1. The variation of the coefficients between the ground motions is high, indicating that the correlation is highly dependent upon the characteristics of the ground motion input.

Table 6.6 shows the mean values of the correlation coefficients for α_n between all modes during the rocking response of Frame D_{DIST}v2. Table 6.7 shows the correlation coefficients determined from Equation 6.59 (Der Kiureghian 1980). Note that for the lowest few modes, the coefficients calculated from Equation 6.59 are an order of magnitude smaller than the coefficients determined from the time-history analysis of Frame D_{DIST}v2. Therefore, new coefficients are required for the SC-CBF system.

The correlation coefficients used for the design of SC-CBF systems are intended to apply to a variety of configurations and designs. Therefore, it is desirable to select a uniform and general set of coefficients for use in design. Based on the coefficients determined from the time-history analysis of Frame D_{DIST}v2 (and considering that only the first three modes will be used in design for this frame), the selected correlation coefficients are:

$$\rho_{ij} = \begin{Bmatrix} 1.0 & if\ i = j \\ 0.25 & if\ i \neq j \end{Bmatrix} \tag{6.62}$$

6.4.5 Calculation of Factored Member Force Design Demands

The factored member force design demands are based on factored member axial force and moment design demands for each mode, including the appropriate spectral

accelerations and modal load factors for each mode (i.e., $\gamma_n \cdot SA_n$, where SA_1 equals $\alpha_{Y,1}$ for the first mode and SA_n equals the spectral acceleration from the DBE design spectrum), as discussed in the previous sections. For an SC-CBF system in which the first three modes are considered for design, the factored modal member force design demands (e.g., axial force or moment) for each member can be expressed in vector form as:

$$\begin{Bmatrix} F_{1,x,fdd} \\ F_{2,x,fdd} \\ F_{3,x,fdd} \end{Bmatrix} = \begin{Bmatrix} \gamma_1 \cdot F_{1,x,dd} \\ \gamma_2 \cdot F_{2,x,dd} \\ \gamma_3 \cdot F_{3,x,dd} \end{Bmatrix} \tag{6.63}$$

where the mode number is denoted by the subscript.

The factored member force design demands are then determined using the complete quadratic combination of the factored modal member force design demands:

$$F_{x,fdd} = \left(\sum_{i=1}^{N} \sum_{j=1}^{N} \rho_{ij} \cdot F_{i,x,fdd} \cdot F_{j,x,fdd} \right)^{\frac{1}{2}} \tag{6.64}$$

where,

$F_{x,fdd}$ = factored member force (axial force or bending moment) design demand

ρ_{ij} = correlation coefficient between modes i and j, from Equation 6.62

$F_{i,x,fdd}$ = factored modal member force design demand in mode i

$F_{j,x,fdd}$ = factored modal member force design demand in mode j

6.4.6 Probability of Exceeding Factored Member Force Design Demands

The probability of the maximum DBE-level member force response for member x, F_x, exceeding $F_{x,fdd}$ is controlled by limiting $P(\alpha_n > \gamma_n \cdot SA_n)$ and by introducing the correlation coefficients ρ_{ij} shown in Equation 6.62. F_x is assumed to follow a lognormal distribution. Figure 6.14 shows a schematic of the probability density function for F_x, including the median DBE-level demand, $F_{x,m}$, and $F_{x,fdd}$. The probability of F_x exceeding $F_{x,fdd}$ can be estimated as:

$$P\left(F_x > F_{x,fdd}\right) = 1 - \Phi\left(\frac{\ln\left(F_{x,fdd}\right) - \ln\left(F_{x,m}\right)}{\sqrt{\ln\left(1+\delta_{F_x}^2\right)}}\right) \tag{6.65}$$

where δ_{Fx} is the coefficient of variation of F_x. Table 6.8 shows the peak brace force response in story i (F_{bri}, where i = 1 to 6) for Frame D_{DIST} and Frame D_{DIST}v2 from nonlinear dynamic analysis under the suite of 12 DBE-level ground motions introduced in Section 5.4.3.1. Table 6.9 shows the mean, standard deviation, and coefficient of variation of F_x (μ_{Fx}, σ_{Fx}, and δ_{Fx}, respectively). Table 6.9 also shows the design demands for each story of Frame D_{DIST} ($F_{x,Y}$, as described in Chapter 5) and Frame D_{DIST}v2 ($F_{x,fdd}$, as described in Section 6.4.5) and the probability of F_x exceeding these values. The dynamic analysis results discussed in Section 5.4.3.2 show that $F_{x,Y}$ is unconservative; Table 6.9 shows that the probability of F_x exceeding $F_{x,Y}$ is 94.1% for the first story braces in Frame D_{DIST} while the probability of F_x exceeding $F_{x,fdd}$ (i.e., based on the approach presented in this chapter) is 0.7% for the first story braces in Frame D_{DIST}v2. F_x for the third floor braces has a low probability of exceeding both $F_{x,Y}$ and $F_{x,fdd}$, due to the

small higher mode effects in that story. The following section considers the differences between the original frames designed using $F_{x,Y}$ and the redesigned frames using $F_{x,fdd}$.

6.5 Effect of Modified Member Force Design Demands

To demonstrate the improved performance of SC-CBFs with members designed for the factored member force design demands from the analysis procedures presented in this chapter ($F_{x,fdd}$) rather than the unfactored design demands from the initial design procedure presented in Chapter 5 ($F_{x,Y}$), Frames A, D, and D_{DIST} were redesigned. The redesigned SC-CBFs are designated Frame Av2, Frame Dv2, and Frame D_{DIST}v2, respectively. The member selections for these redesigned SC-CBFs are presented in Figures 6.15 through 6.17.

The effect of the higher mode design demands on the brace axial force design demands is shown in Table 6.10. The difference between the unfactored member force design demands obtained from a static pushover up to PT yield, $F_{x,Y}$ (Frames A, D, and D_{DIST}), and $F_{x,fdd}$ (Frames Av2, Dv2, and D_{DIST}v2) are significant. For example, for the first story braces, $F_{br1,fdd}$ for each frame configuration is more than double $F_{br1,Y}$. Note that γ_1 is 1.15, so the first mode design demands presented in Chapter 6 are expected to be approximately 15% greater than $F_{x,Y}$ from Chapter 5 since both are established at PT yield. The majority of the difference is, therefore, due to the higher mode demands. The increase in design demand is small for the third story of Frame D_{DIST}v2 since the higher mode effects are small for that story of that frame configuration.

Table 6.11 compares the weights of Frames A, D, and D_{DIST} with those of Frames Av2, Dv2, and D_{DIST}v2, respectively. As expected, the larger member force demands require larger members, regardless of the configuration. Frame Av2 is 60% heavier than Frame A. Frame Dv2 is 49% heavier than Frame D. Frame D_{DIST}v2 is 61% heavier than Frame D_{DIST}. Overall, however, the weight of the braces, beams, columns, and struts as a percentage of the total weight of steel in a building (including the gravity load framing) will not be significantly changed by the new design demand calculation procedure.

Figure 6.18 summarizes the responses obtained from nonlinear dynamic analyses of Frames A, D, and D_{DIST} for the suite of 12 DBE-level ground motions introduced in Section 5.4.3.1. The nonlinear model presented in Section 5.4.1 was used. The response of the original SC-CBF designs from Chapter 5 is compared with that of the redesigned SC-CBFs. Figure 6.18(a) shows the peak roof drift response for each SC-CBF for the 12 DBE-level ground motions. With the exception of the largest peak drift response for Frame A, the designs based on the new member force design demands have similar, but slightly smaller, global response. Figure 6.18(b) shows the maximum PT force response, normalized by the PT yield force, for each frame. As with the roof drift, this response is largely unchanged by designing for the larger factored member force design demands $F_{x,fdd}$ estimated by the methods proposed in this chapter. These results suggest that the peak roof drift and PT force are primarily functions of frame configuration, not member size.

Figure 6.18(c) shows the peak dynamic brace force response normalized by the appropriate design demands (e.g., $F_{x,Y}$ for Frames A, D, and D_{DIST}; $F_{x,fdd}$ for Frames Av2,

Dv2, and D_{DIST}v2). The member force design demands from static pushover up to PT yield, $F_{x,Y}$, used in the initial design procedure for Frames A, D, and D_{DIST} are unconservative, as shown in Chapter 5. The factored member force design demands from the method proposed in this chapter, $F_{x,fdd}$, used for Frames Av2, Dv2, and D_{DIST}v2, are conservative. The maximum normalized response for each ground motion is less than 1.0; however, as seen in Table 6.9, the dispersion in this data, δ_{Fx}, for the redesigned SC-CBFs is not significantly different from that of the original SC-CBF designs. The conservatism in this improved design demand calculation (i.e., $F_{x,fdd}$) leads to a significantly reduced probability of the brace force response exceeding the brace force design demands under the DBE.

The results in this section validate the proposed analytical approach for calculating factored member force design demands for the SC-CBF system. However, this study used a very limited data set to estimate γ_n and $[\rho]$, and further study of γ_n and $[\rho]$ is required. The preliminary values presented in this chapter, however, are conservative and will be used to design the large-scale SC-CBF test structure discussed in Chapter 8.

Chapter 7 will discuss the capacities for the limit states of decompression, PT bar yielding, and member yielding, and will summarize the proposed design procedure for SC-CBFs.

Table 6.1 – Regression coefficients *a*, *b*, *c*, and *d* for Equations 6.15 and 6.16 (Seo 2005)

Site Class	β_E (%)	*a*	*b*	*c*	*d*
C	0	0.636	0.306	0.713	0.111
	12.5	0.569	0.264	0.769	0.115
	25	0.515	0.222	0.816	0.113
	100	0.412	0.498	0.904	-0.415
D	0	0.729	0.399	0.624	0.0657
	12.5	0.657	0.327	0.678	0.0756
	25	0.597	0.288	0.728	0.0677
	100	0.457	0.500	0.872	-0.305

Table 6.2 – Calculation of the effective modal mass for Frame $D_{DIST}v2$

Mode	Γ_n	$\{\phi_n\}^T[m]\{i\}$	M_n^*	M_n^*/M_{total}	$\Sigma M_n^*/M_{total}$
1	3.261	3.261	10.631	0.768	0.768
2	1.470	1.470	2.162	0.156	0.925
3	-0.756	-0.756	0.571	0.041	0.966
4	-0.535	-0.535	0.286	0.021	0.987
5	-0.412	-0.412	0.170	0.012	0.999
6	-0.126	-0.126	0.016	0.001	1.000

Table 6.3 – Effective modal pseudo-accelerations for Frames D_{DIST} and D_{DIST}v2

Record	Frame D_{DIST}						Frame D_{DIST}v2					
	α_1 (g)	α_2 (g)	α_3 (g)	α_4 (g)	α_5 (g)	α_6 (g)	α_1 (g)	α_2 (g)	α_3 (g)	α_4 (g)	α_5 (g)	α_6 (g)
ch0chy036270	0.153	0.488	0.375	0.335	0.841	0.779	0.170	0.522	0.463	0.343	0.465	0.385
ch0tcu038000	0.173	1.120	0.459	0477	1.291	1.005	0.184	1.057	0.665	0.420	0.542	0.454
ch0tcu042270	0.158	1.586	0.717	0.566	0.769	0.861	0.172	1.505	0.771	0.571	0.555	0.646
ld0yer270	0.186	0.893	0.764	0.535	1.537	1.164	0.201	0.920	0.731	0.511	0.472	0.626
lp0hd1165	0.181	1.037	0.758	0.638	1.629	1.561	0.186	0.926	0.647	0.500	0.614	0.570
lp0hd1255	0.163	1.412	0.922	0.639	1.219	0.837	0.191	1.255	0.876	0.674	0.727	0.776
lp0hsp090	0.150	0.861	0.861	0.535	1.528	1.129	0.169	1.154	0.563	0.467	0.487	0.435
nr0ccy270	0.167	2.168	1.820	1.471	1.873	1.289	0.192	1.729	1.254	1.111	0.893	0.998
nr0cpc106	0.174	1.219	1.391	0.924	1.424	1.399	0.199	1.749	1.132	1.064	0.910	0.939
nr0hlc090	0.151	1.759	1.520	1.079	1.829	1.126	0.167	2.033	1.677	1.008	0.973	0.944
nr0nrg090	0.165	2.429	1.711	1.275	1.914	1.425	0.201	1.897	1.119	1.077	0.865	0.921
sh0wsm090	0.153	0.996	1.122	0.924	1.088	1.045	0.171	1.273	1.092	0.787	0.527	0.581

Table 6.4 – Statistics for α_n and probability of exceedance of SA_n for Frames D_{DIST} and D_{DIST}v2

	Mode	μ_α (g)	σ_α (g)	δ_α	$\alpha_{n,m}$ (g)	T_n (s)	SA_n (g)	$\alpha_{n,m}/SA_n$	$P(\alpha_n>SA_n)$ (%)	γ_n	$\gamma_n \cdot SA_n$ (g)	$P(\alpha_n>\gamma_n \cdot SA_n)$ (%)
Frame D_{DIST}	**1***	0.165	0.012	0.074	0.164	1.007	0.180	0.910	10.0	1.15	0.207	0. 1
	2	1.331	0.567	0.426	1.224	0.332	1.000	1.224	69.0	2.00	2.000	11.5
	3	1.035	0.477	0.461	0.940	0.175	1.000	0.940	44.4	2.00	2.000	4.3
	4	0.783	0.350	0.447	0.715	0.132	1.000	0.715	21.6	2.00	2.000	0.8
	5	1.412	0.383	0.271	1.363	0.109	0.947	1.439	91.4	2.00	1.894	10.8
	6	1.135	0.248	0.218	1.109	0.098	0.890	1.246	84.6	2.00	1.779	1.4
Frame D_{DIST}v2	**1***	0.184	0.013	0.072	0.183	0.745	0.184	0.993	46.1	1.15	0.212	2.1
	2	1.335	0.455	0.341	1.263	0.239	1.000	1.263	76.0	2.00	2.000	8.3
	3	0.916	0.348	0.380	0.856	0.135	1.000	0.856	33.6	2.00	2.000	1.0
	4	0.711	0.286	0.402	0.660	0.101	0.907	0.727	20.5	2.00	1.814	0.4
	5	0.669	0.193	0.288	0.643	0.085	0.824	0.781	19.0	2.00	1.648	0.0
	6	0.690	0.219	0.318	0.657	0.080	0.799	0.823	26.4	2.00	1.598	0.2

* – For the first mode, $SA_1 = \alpha_{1,Y}$ and SA_1 is not from the DBE design spectrum

Table 6.5 – Correlation coefficients during rocking response for Frame $D_{DIST}v2$

Record	ρ_{12}	ρ_{13}	ρ_{14}	ρ_{23}	ρ_{24}	ρ_{34}
ch0chy036270	0.026	0.063	0.048	0.506	0.601	0.760
ch0tcu038000	0.071	0.027	0.055	0.527	0.607	0.764
ch0tcu042270	0.133	0.046	0.066	0.585	0.627	0.787
ld0yer270	0.078	0.013	0.070	0.384	0.550	0.659
lp0hd1165	0.081	0.025	0.075	0.393	0.497	0.753
lp0hd1255	0.193	0.125	0.171	0.495	0.587	0.732
lp0hsp090	0.061	0.028	0.005	0.406	0.515	0.743
nr0ccy270	0.236	0.173	0.227	0.458	0.485	0.746
nr0cpc106	0.160	0.087	0.101	0.337	0.447	0.603
nr0hlc090	0.116	0.058	0.083	0.203	0.313	0.577
nr0nrg090	0.130	0.067	0.110	0.387	0.482	0.625
sh0wsm090	0.078	0.019	0.01	0.248	0.301	0.414

Table 6.6 – Mean correlation coefficients for Frame $D_{DIST}v2$ from analysis during rocking response

Mode	1	2	3	4	5	6
1	1	0.113	0.061	0.086	0.081	0.091
2	0.113	1	0.411	0.501	0.512	0.494
3	0.061	0.411	1	0.680	0.661	0.651
4	0.086	0.501	0.680	1	0.846	0.880
5	0.081	0.512	0.661	0.846	1	0.850
6	0.091	0.494	0.651	0.880	0.850	1

Table 6.7 – Correlation coefficients for Frame $D_{DIST}v2$ determined using method of Der Kiureghian (1980)

Mode	1	2	3	4	5	6
1	1	0.004	0.002	0.002	0.001	0.001
2	0.004	1	0.022	0.012	0.010	0.009
3	0.002	0.022	1	0.133	0.063	0.053
4	0.002	0.012	0.133	1	0.358	0.248
5	0.001	0.010	0.063	0.358	1	0.859
6	0.001	0.009	0.053	0.248	0.859	1

Table 6.8 – Brace axial force response for Frames D_{DIST} and $D_{DIST}v2$ from nonlinear dynamic analysis

Record	Frame D_{DIST}						Frame $D_{DIST}v2$					
	F_{br1} (k)	F_{br2} (k)	F_{br3} (k)	F_{br4} (k)	F_{br5} (k)	F_{br6} (k)	F_{br1} (k)	F_{br2} (k)	F_{br3} (k)	F_{br4} (k)	F_{br5} (k)	F_{br6} (k)
ch0chy036270	610.3	442.5	638.5	634.9	605.5	742.9	713.1	562.6	621.6	723.3	787.4	840.8
ch0tcu038000	860.4	655.3	814.6	802.2	829.5	1015.7	876.0	580.4	776.5	734.8	779.1	944.0
ch0tcu042270	1250.2	806.9	666.5	942.6	1102.1	1127.0	1277.0	758.2	636.3	852.7	1005.7	951.5
ld0yer270	733.8	555.0	810.9	917.4	948.9	1115.0	896.6	601.1	874.7	831.3	948.9	1085.3
lp0hd1165	1022.8	703.2	862.5	855.9	923.8	1044.5	965.4	683.5	775.5	792.0	874.6	987.6
lp0hd1255	1095.8	716.9	704.6	905.7	1009.3	1078.5	1192.0	757.3	670.1	968.8	1071.7	1048.2
lp0hsp090	809.7	553.1	660.5	668.6	732.5	827.0	1129.8	737.4	646.0	805.8	952.2	955.0
nr0ccy270	1112.5	703.6	811.8	1081.6	1318.3	1265.5	1261.2	792.6	717.8	989.9	1214.7	1167.1
nr0cpc106	977.2	661.3	806.4	957.7	1060.3	1170.5	1485.3	753.1	818.3	1000.6	1149.4	1093.3
nr0hlc090	1277.3	763.7	659.8	859.6	1053.6	1028.1	1239.2	779.1	680.1	970.2	1089.9	984.6
nr0nrg090	1533.8	882.5	740.6	1098.3	1275.2	1168.6	1299.5	791.5	759.4	1004.9	1189.2	1175.6
sh0wsm090	982.3	612.9	732.3	737.2	757.1	822.4	1092.8	718.3	728.6	729.0	894.8	969.4

Table 6.9 – Statistics for F_x and probability of exceedance of brace force design demands for Frames D_{DIST} and D_{DIST}v2

	Method for Determining Design Demand	**Story**	μ_{Fx} **(k)**	σ_{Fx} **(k)**	δ_{Fx}	$F_{x,m}$ **(k)**	***Design Demand (k)***	**P($F_x > x$) (%)**
Frame D_{DIST}	$F_{x,Y}$ - member forces from static pushover to PT yield (Chapter 5)	**1**	1022.2	255.9	0.250	991.6	674.4	94.1
		2	671.4	120.3	0.179	660.9	557.0	83.2
		3	742.4	76.8	0.103	738.5	869.1	5.7
		4	871.8	145.1	0.166	860.0	802.0	66.3
		5	968.0	214.3	0.221	945.1	772.2	82.2
		6	1033.8	159.6	0.154	1021.7	1055.1	41.7
Frame D_{DIST}v2	$F_{x,fdd}$ - factored modal member force design demands (Chapter 6)	**1**	1119.0	219.4	0.196	1098.1	1775.0	0.7
		2	709.6	83.4	0.118	704.7	1191.6	0.0
		3	725.4	78.3	0.108	721.2	1160.3	0.0
		4	866.9	113.2	0.131	859.6	1218.4	0.4
		5	996.5	148.6	0.149	985.6	1428.3	0.6
		6	1016.9	99.0	0.097	1012.1	1592.3	0.0

Table 6.10 – Brace axial force design demands

Frame	Method for Determining Design Demand*	*Brace Force Design Demands*					
		Story 1 **(k)**	***Story 2*** **(k)**	***Story 3*** **(k)**	***Story 4*** **(k)**	***Story 5*** **(k)**	***Story 6*** **(k)**
A	$F_{x,Y}$	935.8	787.4	712.2	593.0	434.3	250.1
Av2	$F_{x,fdd}$	2041.5	1462.7	1076.9	974.3	1034.1	875.1
D	$F_{x,Y}$	675.5	561.1	508.9	427.9	359.5	2284.3
Dv2	$F_{x,fdd}$	1900.3	1278.7	864.5	851.2	1006.1	2905.7
D_{DIST}	$F_{x,Y}$	674.4	557.0	869.1	802.0	772.2	1055.1
D_{DIST}v2	$F_{x,fdd}$	1775.0	1191.6	1160.3	1218.4	1428.3	1592.3

* $F_{x,Y}$ = member design forces from static pushover to PT yielding (Chapter 5)

$F_{x,fdd}$ = factored member force demands (Chapter 6)

Table 6.11 – Summary of redesigns of Frames A, D, and D_{DIST}

	Frame A		Frame Av2		Frame D		Frame Dv2		Frame D_{DIST}		Frame D_{DIST}v2	
	Weight (k)	% of total	Weight (k)	% of total	Weight (k)	% of total	Weight (k)	% of total	Weight (k)	% of total	Weight (k)	% of total
Braces	18.0	27.4	31.7	30.0	19.2	29.4	32.3	33.1	18.0	28.5	29.0	28.6
Columns	31.8	48.4	46.6	44.2	30.6	46.9	44.2	45.3	27.6	43.8	41.8	41.2
Beams	13.2	20.1	24.0	22.8	13.3	20.4	18.6	19.1	11.0	17.4	16.6	16.6
Struts	2.7	4.1	3.3	3.1	2.2	3.3	2.4	2.4	6.5	10.2	14.1	14.1
Total	65.8	100	105.6	100	65.2	100	97.4	100	63.1	100	101.6	100

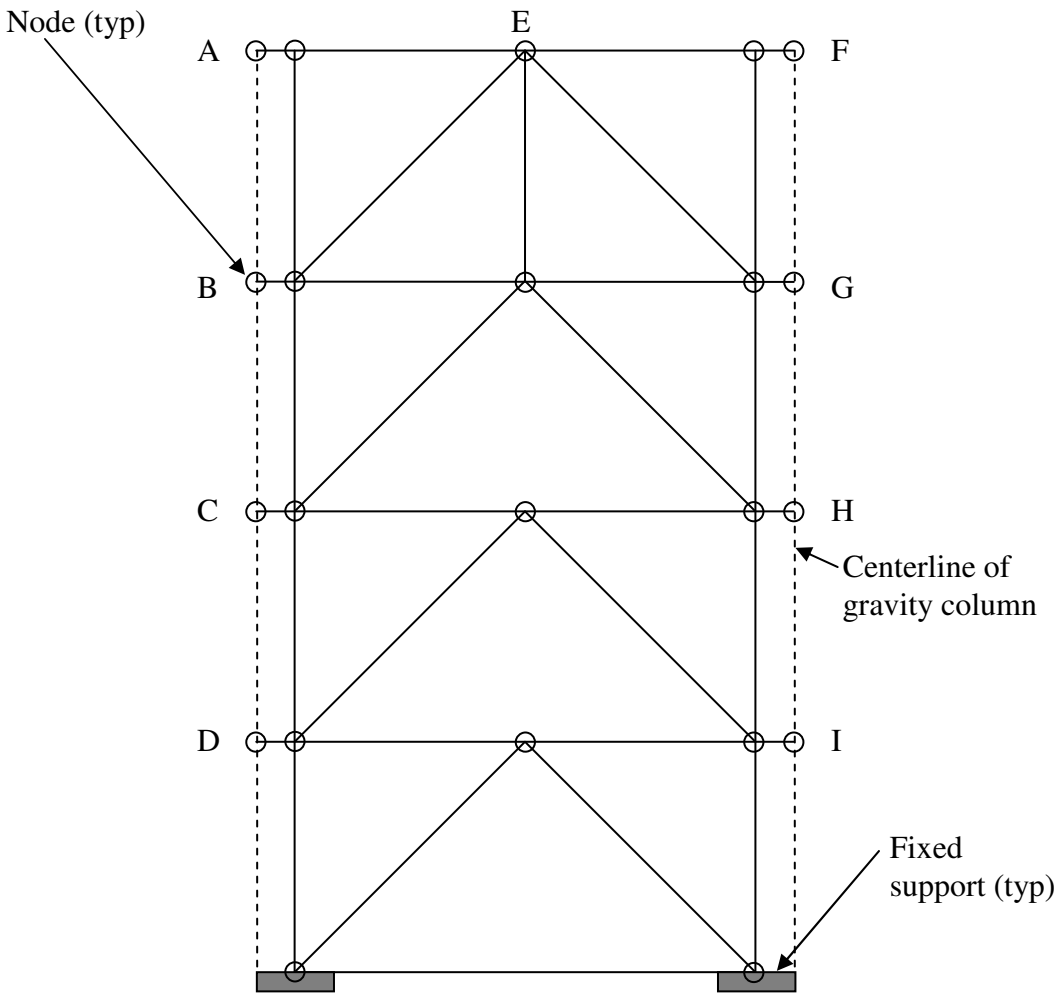

Figure 6.1 – Schematic of analytical model for design of four-story Frame D_{DF}

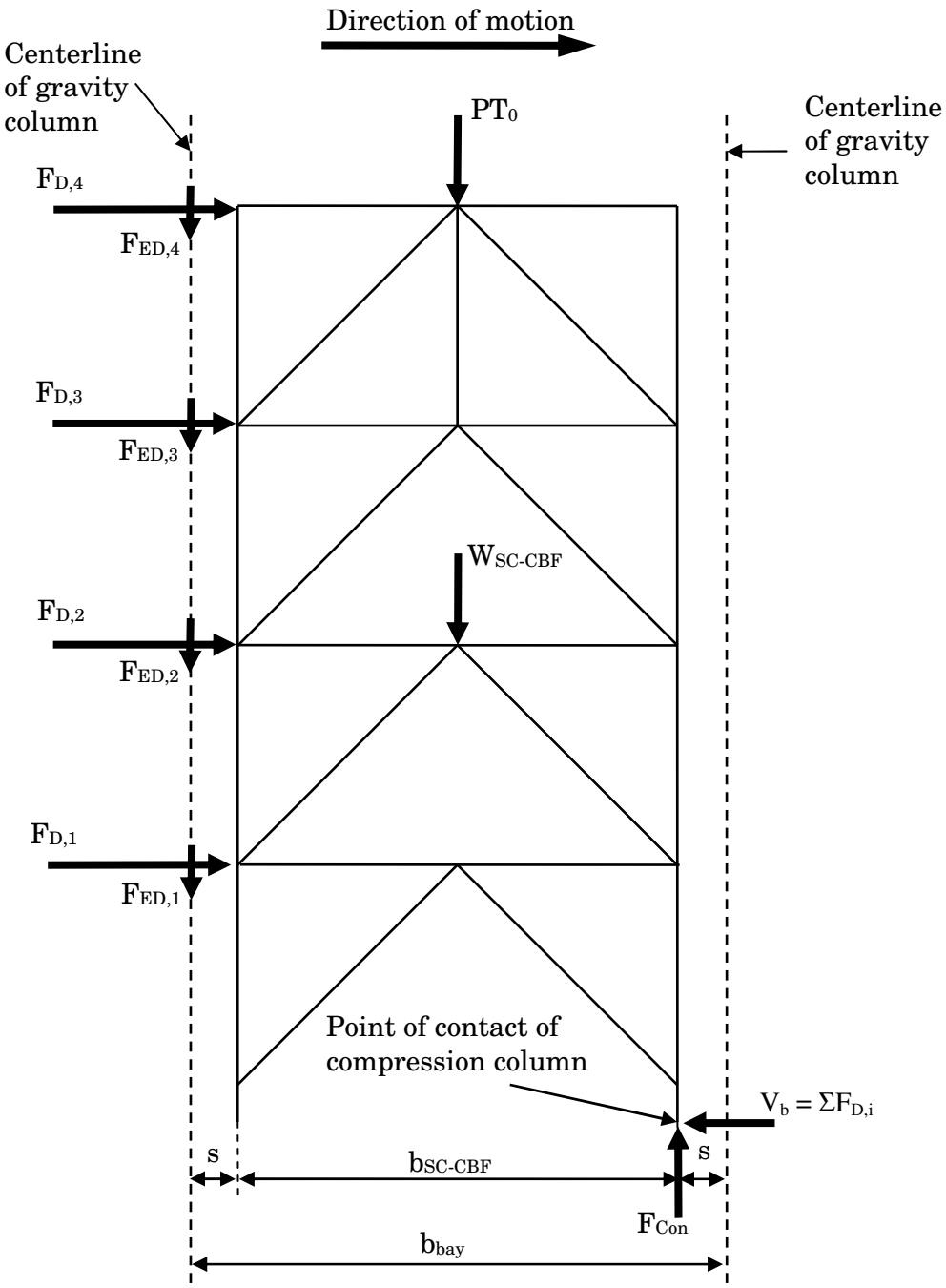

Figure 6.2 – Applied forces for decompression analysis of a four-story Frame D_{DF}

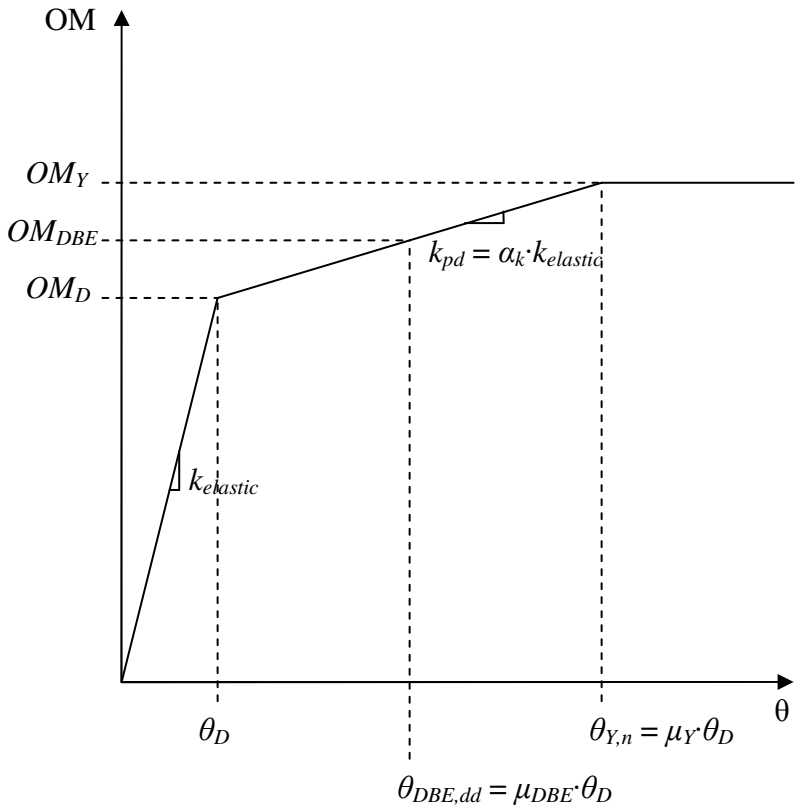

Figure 6.3 – Schematic of idealized overturning moment versus roof drift response of an SC-CBF system

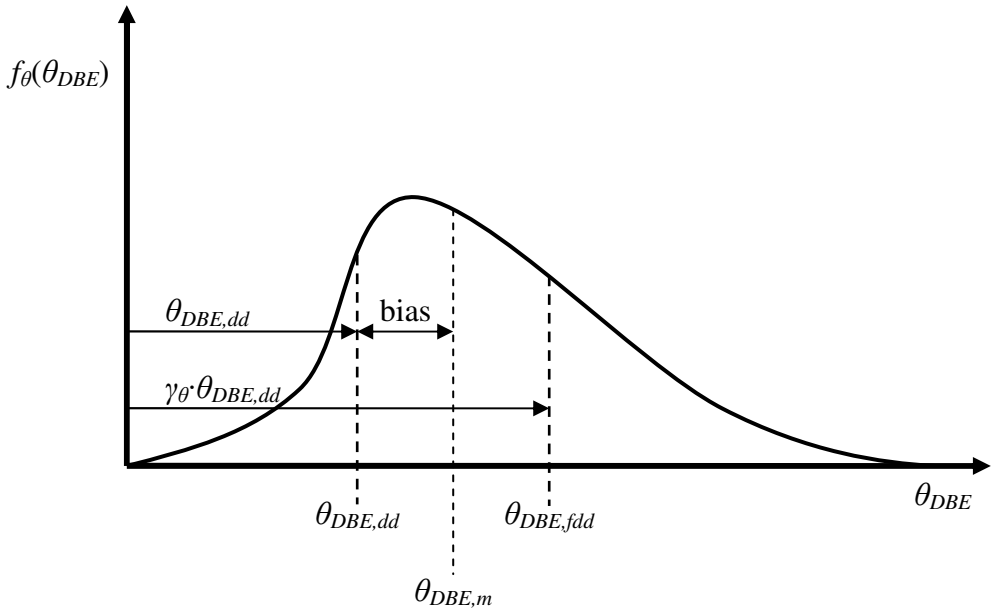

Figure 6.4 – Schematic of probability density function for DBE-level roof drift response

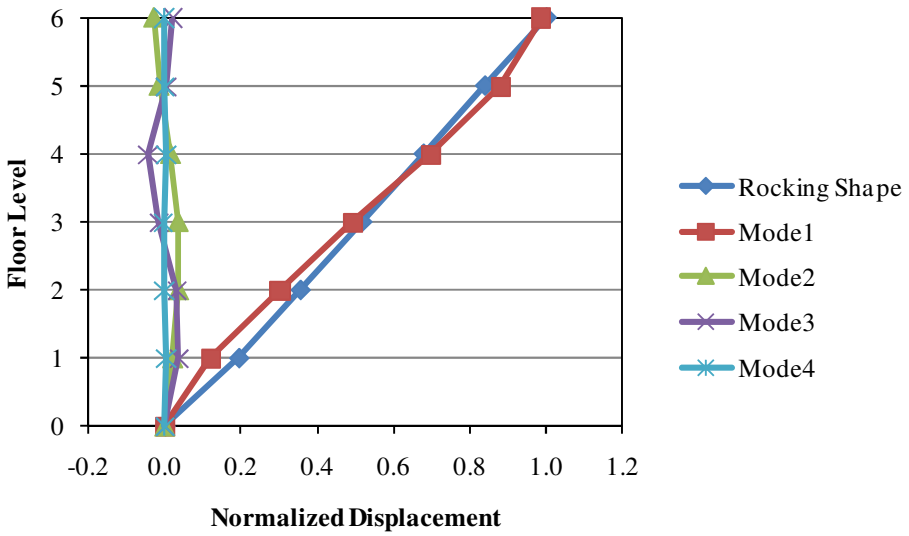

Figure 6.5 – Modal expansion of the rocking deformed shape for Frame D

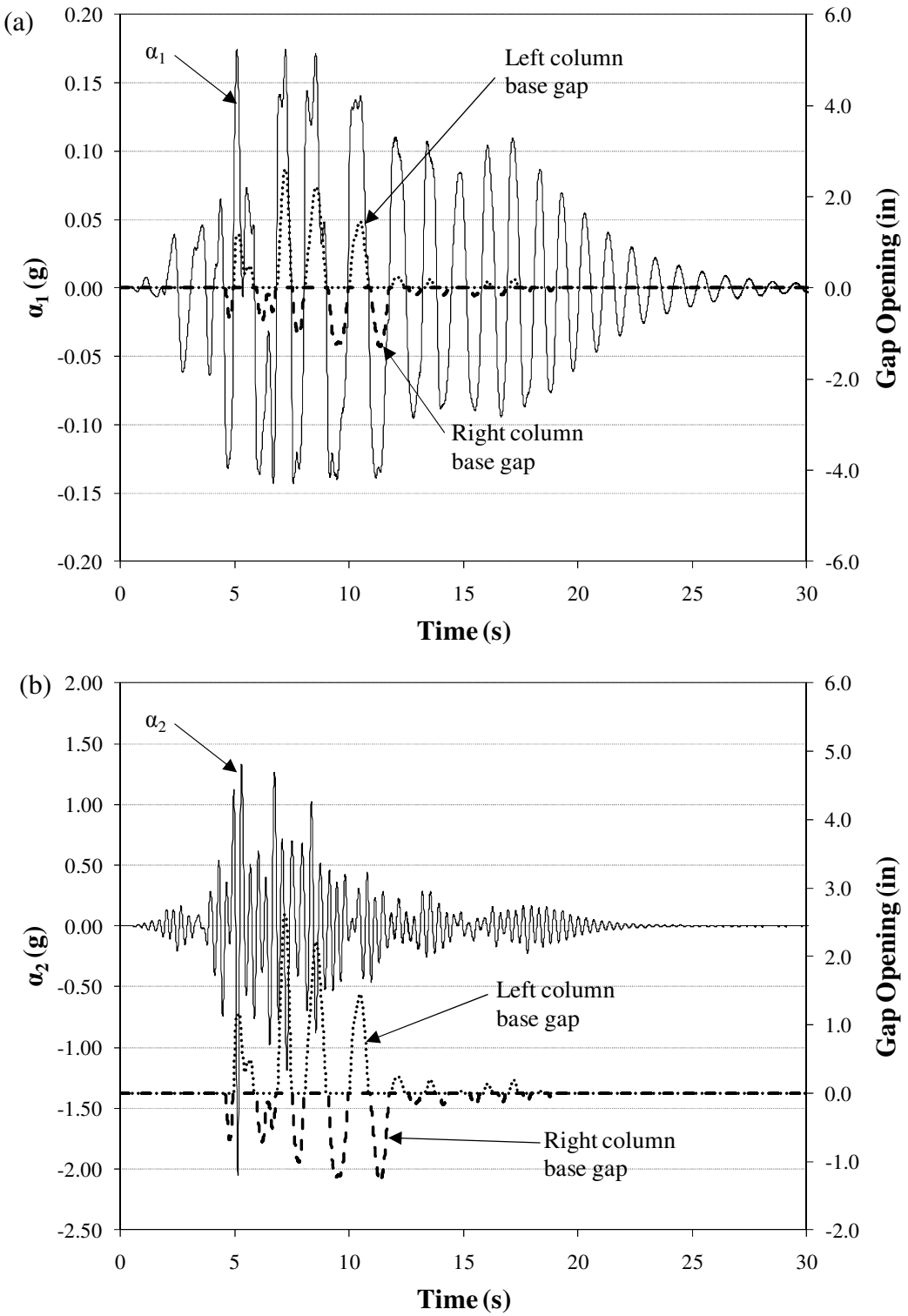

Figure 6.6 – Frame D dynamic response to DBE-level ground motion nr0ccy270: (a) α_1 with column-base gap-opening displacements; (b) α_2 with column-base gap-opening displacements

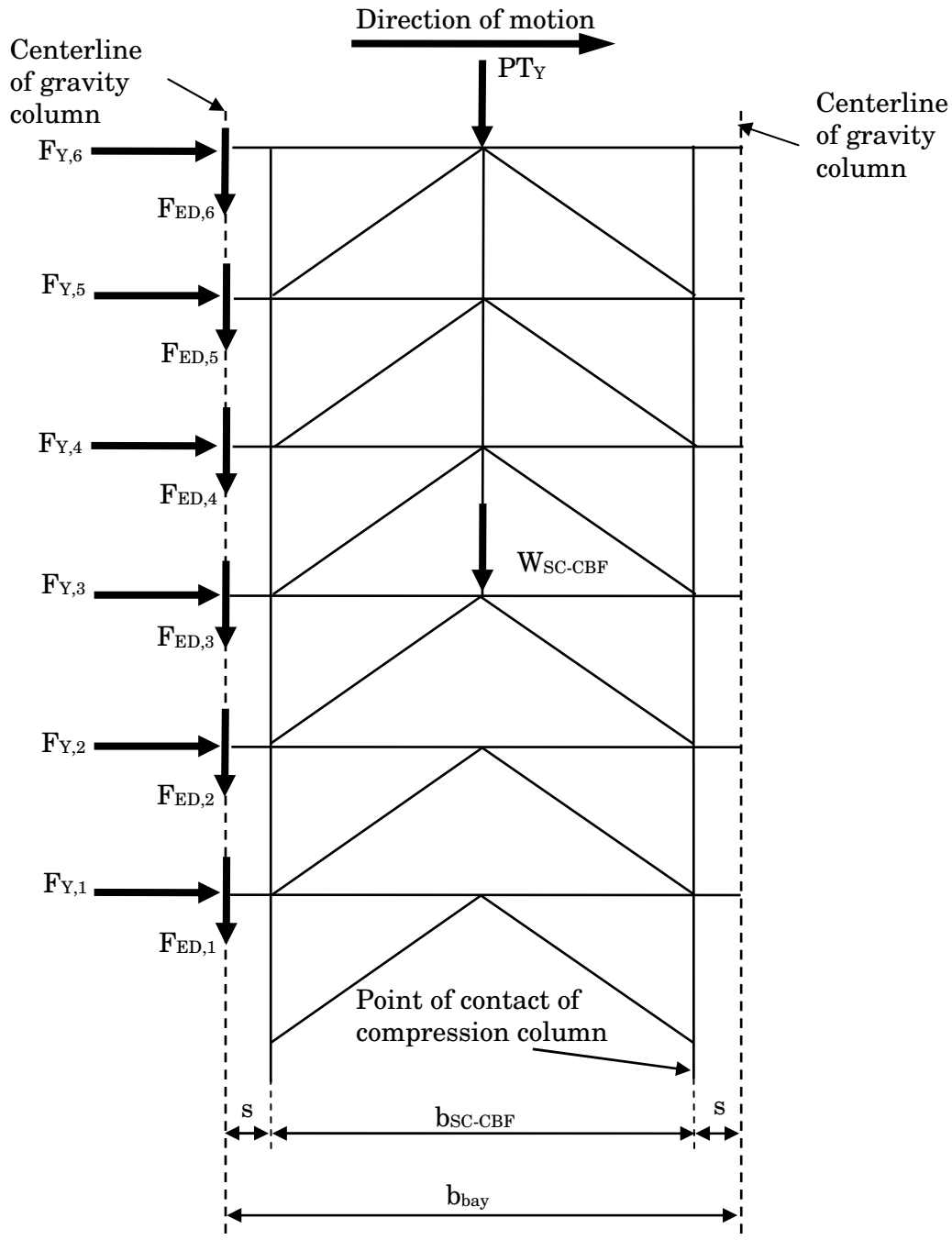

Figure 6.7 – First mode forces applied to Frame D_{DIST} at PT bar yielding

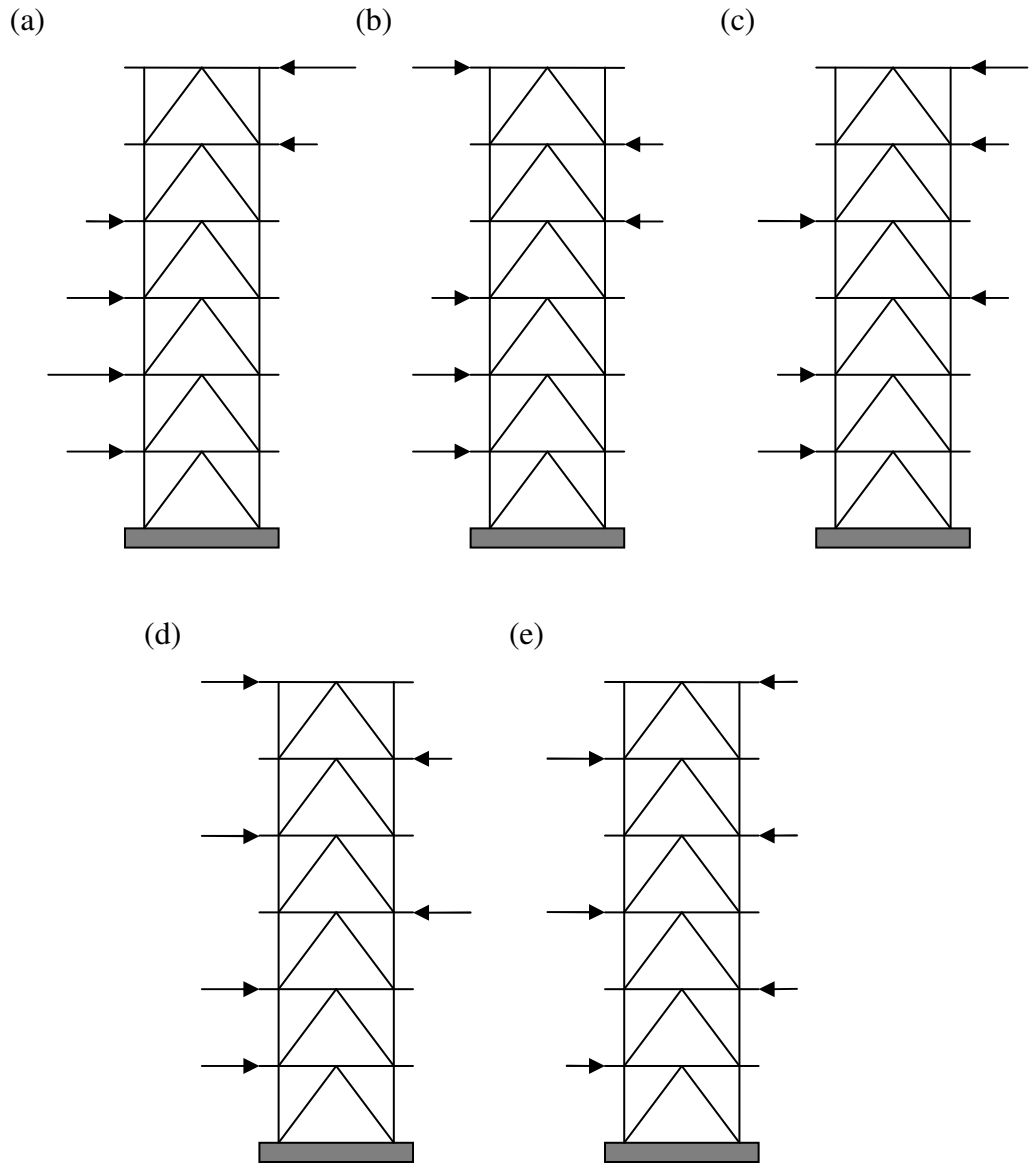

Figure 6.8 – Schematic of higher mode load cases: (a) 2nd mode; (b) 3rd mode; (c) 4th mode; (d) 5th mode; (e) 6th mode

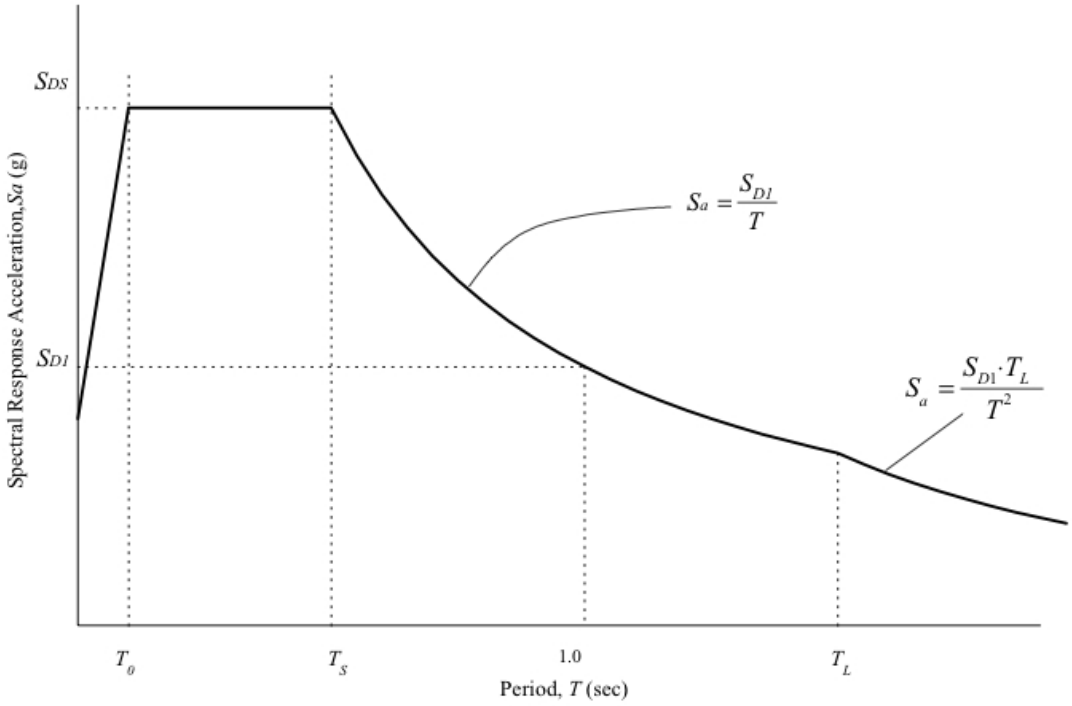

Figure 6.9 – Design response spectrum (ASCE 2005)

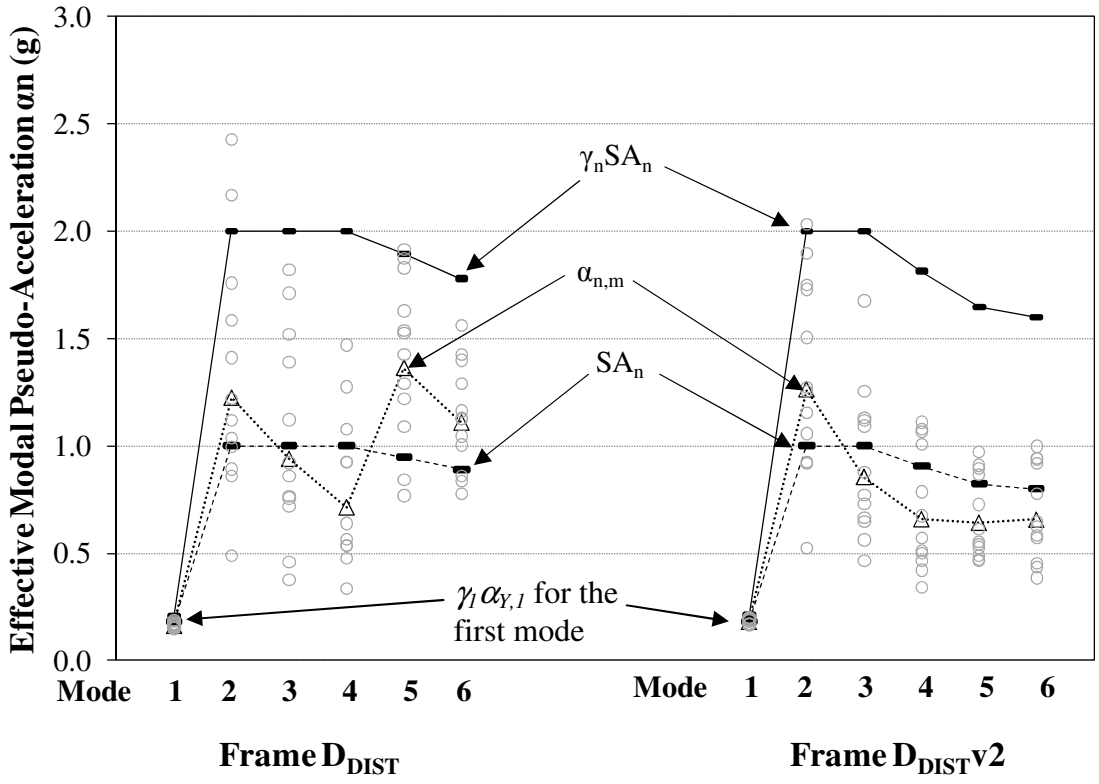

Figure 6.10 – Distribution of effective modal pseudo-accelerations for Frames D_{DIST} and $D_{DIST}v2$

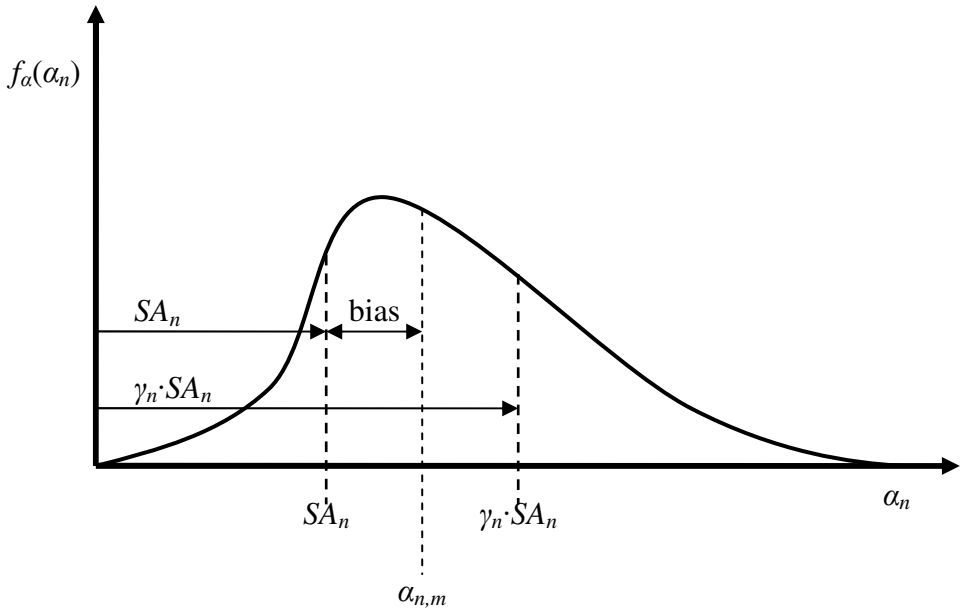

Figure 6.11 – Schematic of probability density function for effective modal pseudo-acceleration

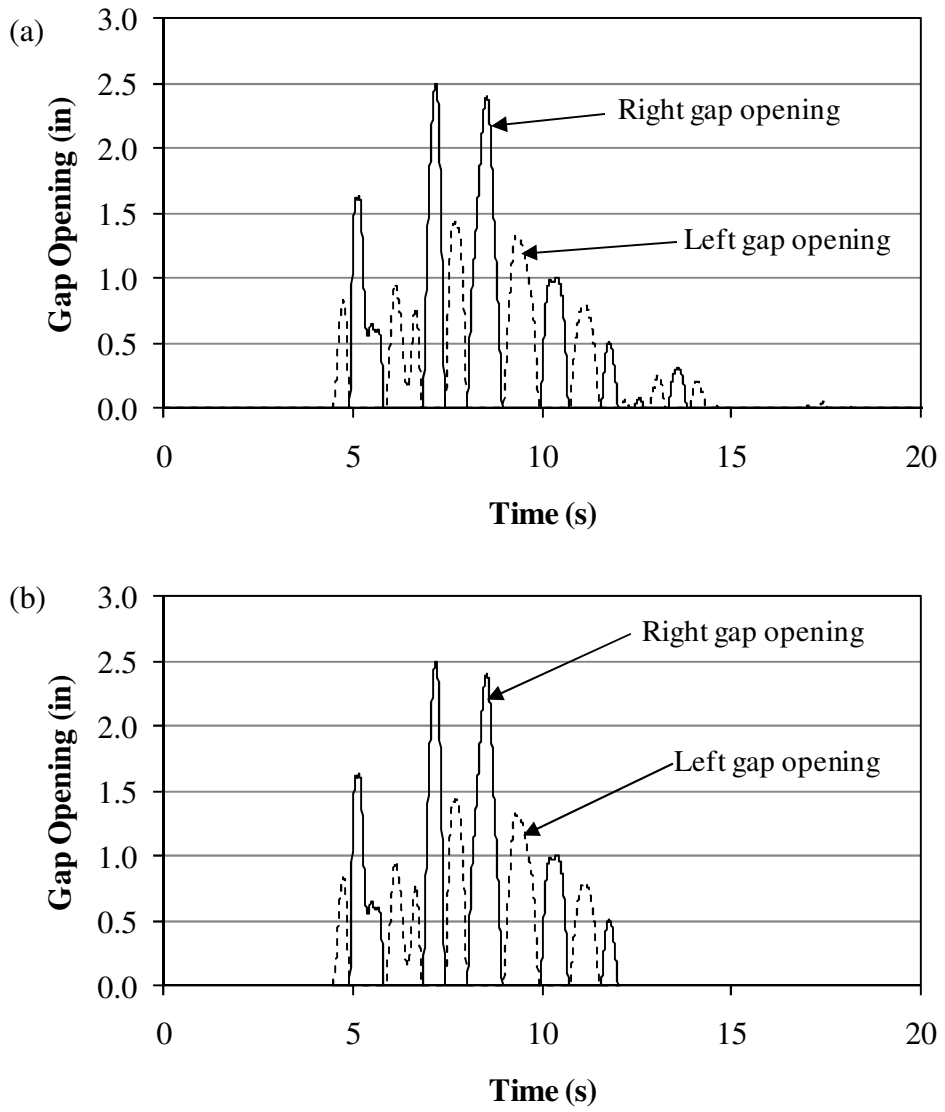

Figure 6.12 – Time history of gap-opening displacement response of Frame D_{DIST}v2 under nr0ccy270 ground motion: (a) full time history; (b) time history during significant rocking response

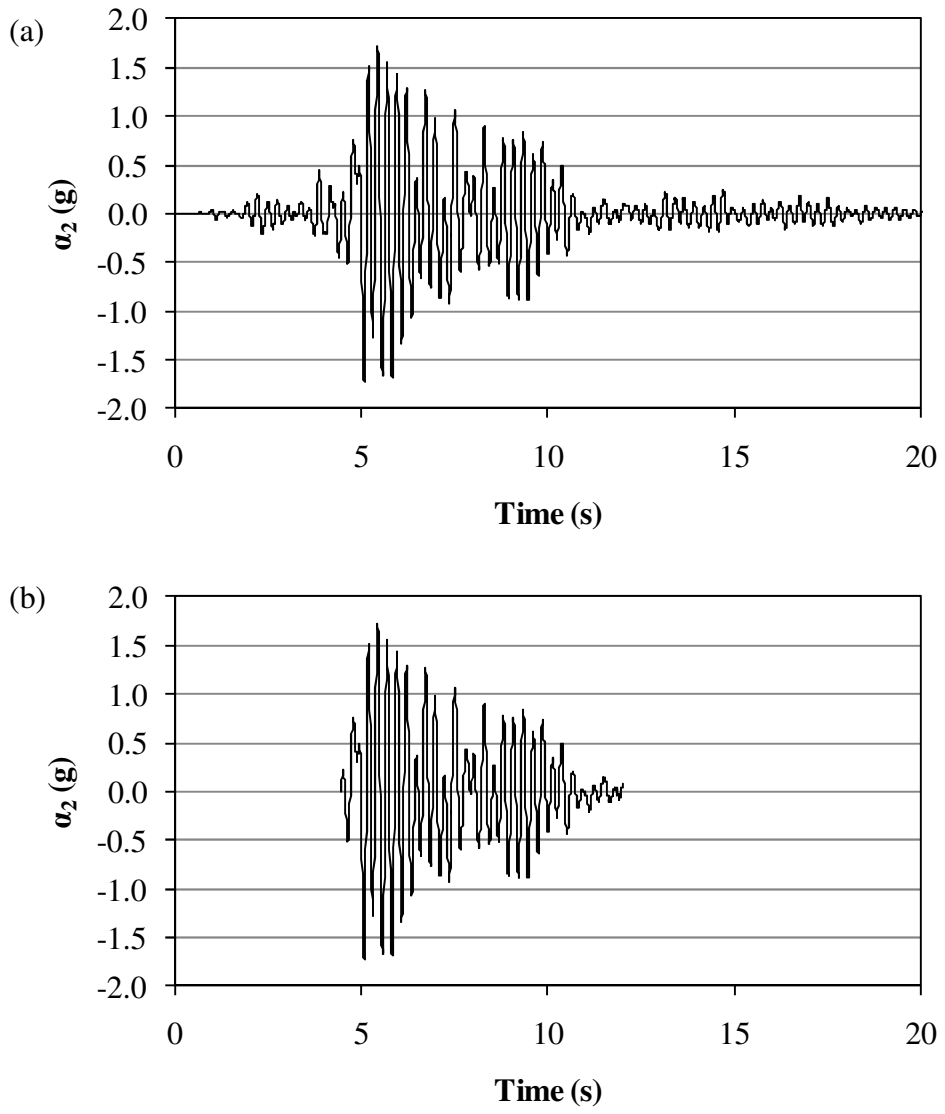

Figure 6.13 – Time history of α_2 response for Frame $D_{DIST}v2$ under nr0ccy270 ground motion: (a) full time history; (b) time history during significant rocking response

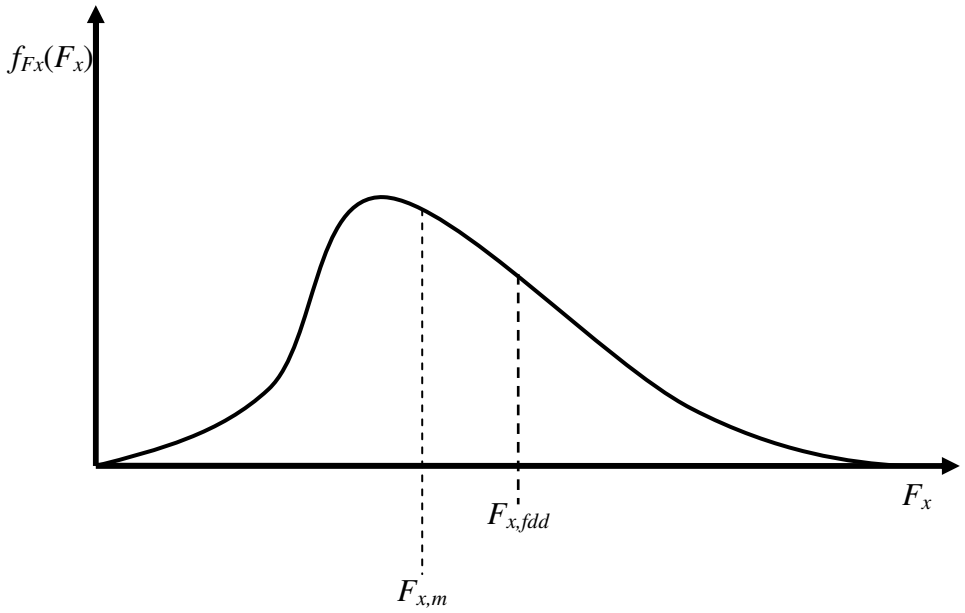

Figure 6.14 – Schematic of probability density function for DBE-level member force response

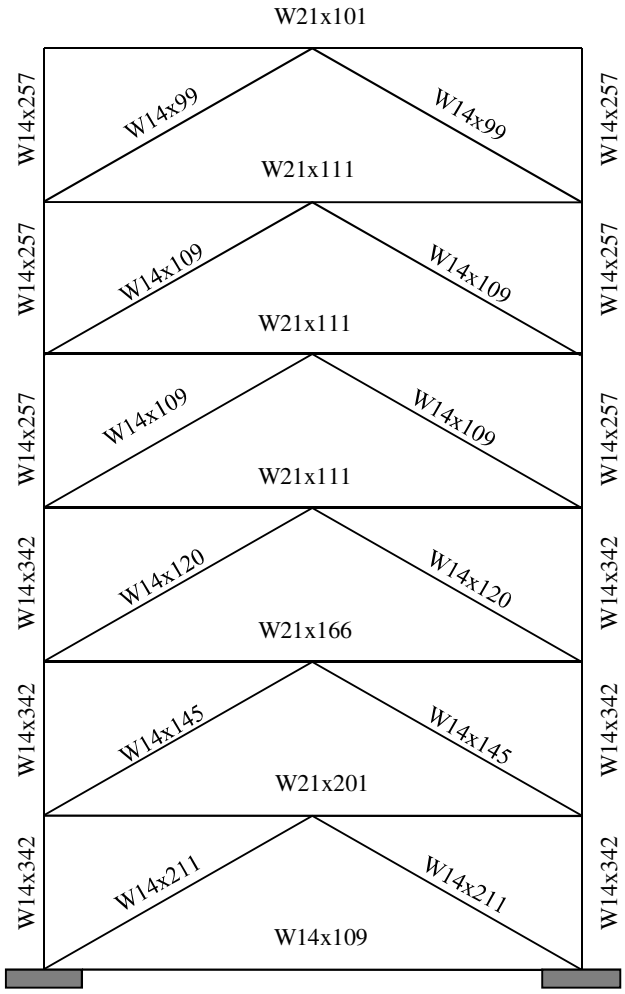

Figure 6.15 – Member selections for Frame Av2

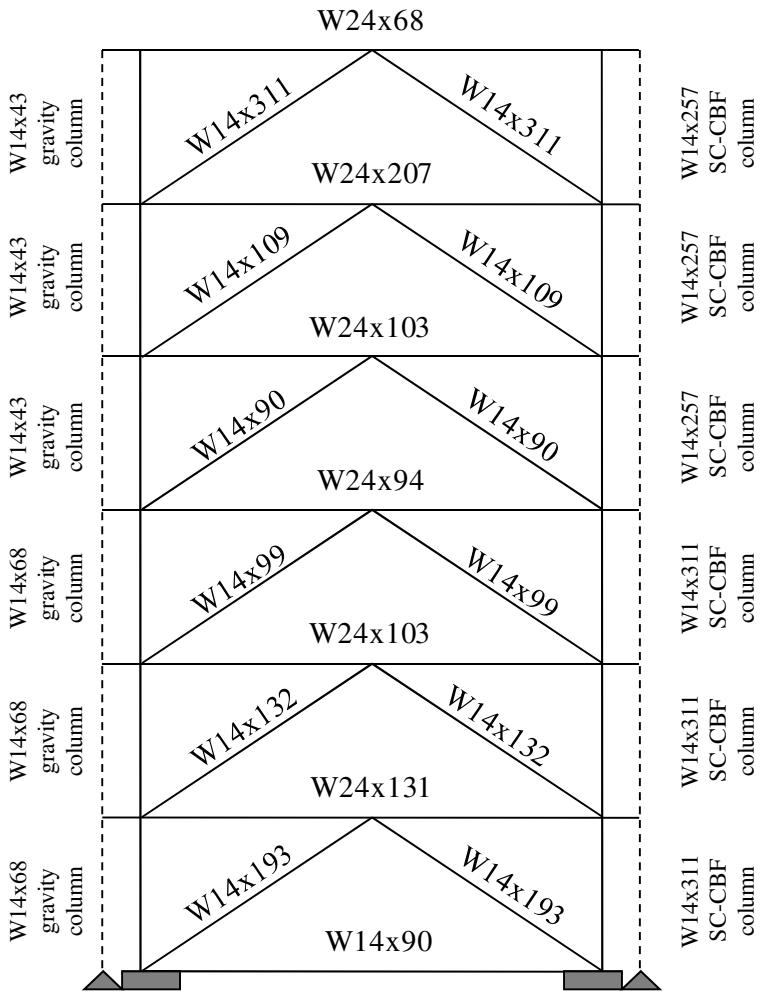

Figure 6.16 – Member selections for Frame Dv2

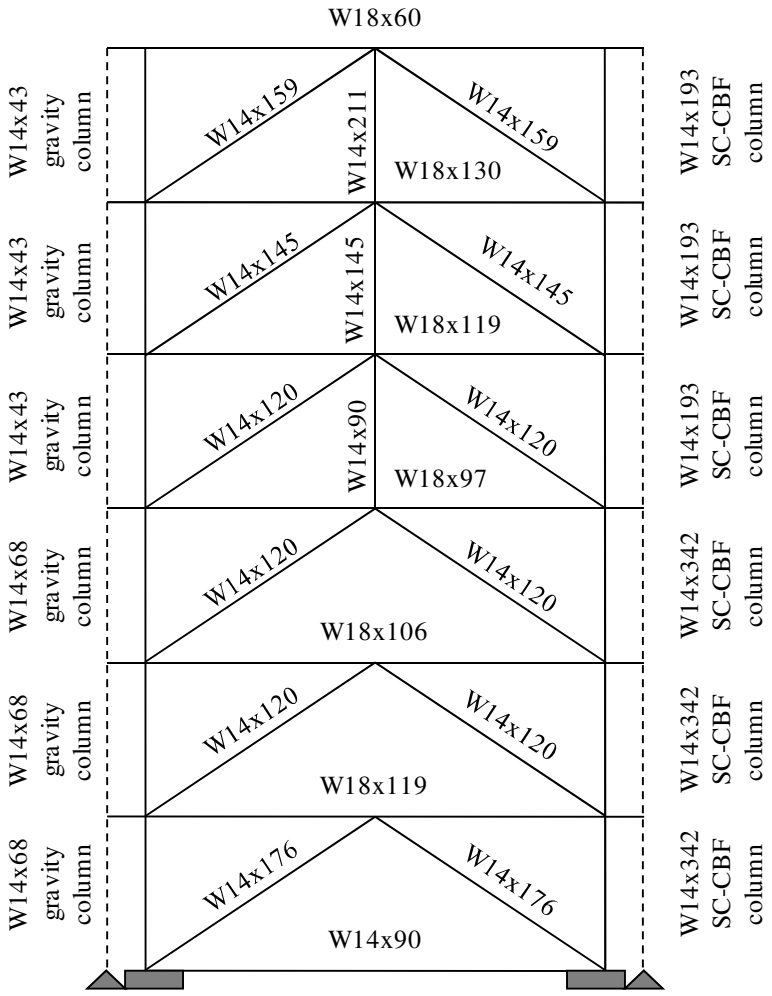

Figure 6.17 – Member selections for Frame $D_{DIST}v2$

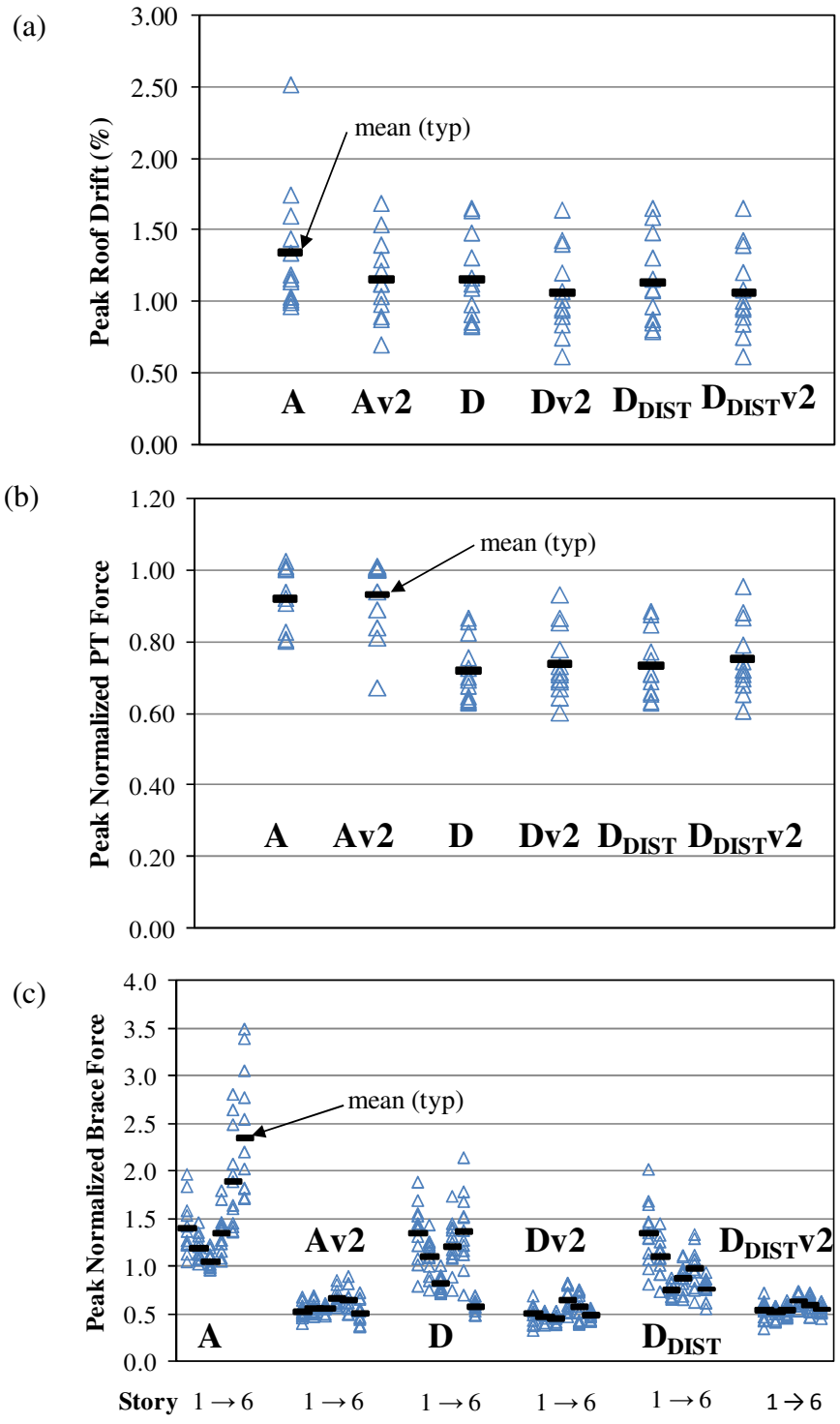

Figure 6.18 – Dynamic response by frame for 12 DBE-level ground motions: (a) maximum roof drift; (b) maximum PT force normalized by PT yield force; (c) maximum dynamic brace force normalized by design demand appropriate for each SC-CBF (e.g., $F_{x,Y}$ for Frames A, D, and D_{DIST}; $F_{x,fdd}$ for Frames Av2, Dv2, and $D_{DIST}v2$)

CHAPTER 7

SC-CBF PERFORMANCE-BASED SEISMIC DESIGN PROCEDURE

This chapter presents a performance-based seismic design (PBD) procedure for the SC-CBF system. As described in the preceding chapters, specific limit states are considered, namely column decompression, PT bar yielding, and member yielding. The limit state of member failure is not directly addressed; however, designing and detailing the SC-CBF members and connections to satisfy the AISC seismic design criteria (AISC 2005a) ensures that the members have adequate ductility to create a large margin between the limit states of member yielding and member failure.

Chapter 6 presented the design demands associated with the limit states of column decompression, PT bar yielding, and member yielding. This chapter presents the capacity associated with each limit state and the required relationship between the capacity and the design demand. There are four distinct phases of design for an SC-CBF system: the preliminary design phase, the structural member design phase, the PT steel design phase, and the detail design phase. Figure 7.1 shows the relationships between these phases of the design procedure.

The preliminary design phase determines where the SC-CBFs will be located in the building and which SC-CBF configuration (see Chapter 5) will be used. The gravity load

resisting system in the building is designed in this phase. Values of initial design parameters (energy dissipation capacity, initial sizes of structural members, the area of PT bars, and the initial force in the PT bars) are also selected in this phase of design. The preliminary design phase is discussed in Section 7.1.

After an SC-CBF configuration is selected, the design of the SC-CBF consists of two interrelated design phases: the selection of the sizes of the SC-CBF structural members (i.e., the beams, columns, and braces) and the selection of the appropriate area and initial force of the PT bars. The required size of the SC-CBF structural members is a function of the inertia forces that develop for each mode and the PT bar yield force, while the PT bars are designed to satisfy the drift demand for the DBE, which is a function of the lateral stiffness of the SC-CBF, the decompression strength OM_D, the energy dissipation ratio β_E, and the post-decompression stiffness k_{pd}. The design procedure, therefore, is iterative, as shown in Figure 7.1.

Section 7.2 discusses the structural member design phase. This design phase consists of estimating the modal dynamic characteristics of the SC-CBF, determining applied forces for the analysis of the modal member force design demands (as discussed in Section 6.4.2), estimating the factored member force design demands $F_{x,fdd}$ (as discussed in Section 6.4.5), and selecting members to satisfy the design criteria with respect to the limit state of member yielding.

Section 7.3 discusses the PT steel design phase. The limit states of column decompression and PT yield are considered in this phase. The factored DBE roof drift

demand, $\theta_{DBE,fdd}$, is used as the PT steel design demand. The roof drift capacity at PT yield must be greater than this demand.

The detail design phase is discussed in Section 7.4. This phase develops the structural details of the SC-CBF system (e.g., SC-CBF member connection details, the PT anchorages, and details of the lateral-load bearings).

7.1 Preliminary Design Phase

The preliminary design phase has four aspects: selecting the location, number, and overall dimensions of the SC-CBFs in the building; selecting the SC-CBF configuration; designing the gravity load bearing system; and estimating initial design values for the SC-CBF. If feasible and economical members, PT bars, and design details cannot be developed in later design phases, this phase of design must be revisited. The iterative nature of the design procedure is indicated in Figure 7.1.

7.1.1 Location and Number of SC-CBFs

The location and number of SC-CBFs in the building are functions of the geometry and layout of the floor plan of the building. The SC-CBFs should be located such that columns are not included in more than one SC-CBF. Including more SC-CBFs in each direction reduces the tributary mass of each SC-CBF, thereby reducing the inertia forces that act on each SC-CBF.

If the later design phases do not produce feasible and economical SC-CBF members, PT bars, and design details, it may be necessary to reevaluate the number of SC-CBFs in the building and their overall dimensions.

7.1.2 Selection of SC-CBF Configuration

The configuration study discussed in Chapter 5 shows that the configuration of the SC-CBF has a significant effect on the response of the system. The choice of SC-CBF configuration also determines whether or not supplemental energy dissipation devices must be designed, as mentioned in Section 7.1.4.1.

Each SC-CBF configuration has advantages and disadvantages. If feasible and economical members, PT bars, and design details cannot be developed in later design phases, it may be possible to use a different SC-CBF configuration without changing the number of SC-CBFs in the building.

7.1.3 Design of Gravity Load Bearing System

In general, the gravity load bearing system can be designed independently of the SC-CBF. For a frame configuration like Frame D, D_{DIST}, or D_{DF}, however, it is important to consider the uplift demand on the gravity columns adjacent to the SC-CBF columns.

7.1.4 Estimating Initial Design Values for the SC-CBF

Four design parameters must be estimated for use in the next phase of design: the capacity of any supplemental energy dissipation elements (depending on the selected SC-

CBF configuration), the initial sizes of the structural members, the initial area of the PT bars, and the initial force in the PT bars.

7.1.4.1 Capacity of Supplemental Energy Dissipation Elements

As shown in Section 5.3.3, the force capacity of the ED elements determines the energy dissipation ratio β_E of the SC-CBF system. β_E is a measure of the degree to which the SC-CBF dissipates energy, and is needed to estimate the roof drift design demand, as shown in Section 6.3. Therefore, a value of V_{ED} must be estimated for the first iteration of design.

There are two methods for estimating the initial value of V_{ED}: a target force capacity can be selected (i.e., $V_{ED} = V_{ED,t}$), or a target energy dissipation ratio can be selected (i.e., $\beta_E = \beta_{E,t}$). Based on the discussion in Section 5.3.3, for the first iteration of design, $\beta_{E,t}$ can be expressed as:

$$\beta_{E,t} = \frac{OM_{ED}}{OM_{D,demand}} \tag{7.1}$$

where,

$$OM_{D,demand} = \alpha_{D,required} \cdot OM_{ELF} \tag{7.2}$$

Note that, as discussed in Section 5.3.3, OM_{ED} is dependent upon the frame configuration. For example, from Figure 5.13, OM_{ED} for Frame B_{ED} can be written as:

$$OM_{ED} = V_{ED} \cdot b_{bay} \tag{7.3}$$

For Frame B_{ED}, then, V_{ED} can be determined as a function of $\beta_{E,t}$ as follows:

$$V_{ED} = \frac{\alpha_{D,required} \cdot OM_{ELF}}{b_{bay}} \cdot \beta_{E,t} \tag{7.4}$$

After the first iteration of design, OM_D may be greater than $\alpha_{D,required} \cdot OM_{ELF}$; to maintain $\beta_{E,t}$, V_{ED} must be recalculated as follows:

$$V_{ED} = \frac{OM_D}{b_{bay}} \cdot \beta_{E,t} \tag{7.5}$$

If the later design phases do not produce feasible and economical SC-CBF members, PT bars, and design details, increasing the value of $\beta_{E,t}$ is a simple change that can be made in the preliminary design phase to improve the performance of the system. This iteration is shown in Figure 7.1.

7.1.4.2 Structural Members for First Design Iteration

As shown in Chapter 6, the member force design demands are a function of the natural periods and mode shapes of the SC-CBF. To determine these modal dynamic characteristics, the member sizes are estimated prior to the first iteration of the structural member design phase.

7.1.4.3 PT Bars for First Design Iteration

The total area of the PT bars, A_{PT}, and the initial stress in the bars, σ_0, directly affect the overturning moment capacity and roof drift capacity at column decompression and PT

bar yielding, as shown by the configuration study results in Chapter 5. Section 7.3 explains how A_{PT} and σ_0 are selected for the preliminary design phase.

7.2 Structural Member Design Phase

The structural member design phase determines the SC-CBF factored member force design demands (i.e., axial force and bending moment) and selects the member sizes based on AISC-LRFD criteria (AISC 2005b). The AISC-LRFD criteria address only the limit state of member yielding (i.e., reaching the member force or moment capacity). To create a margin between the limit states of member yielding and member failure, the seismic design criteria (AISC 2005a) for special concentrically-braced frames (SCBFs) should be considered when selecting the structural members. The seismic design criteria for SCBFs ensure that the members have adequate ductility capacity so that the global drift of the SC-CBF at the limit state of member failure will be much larger than the global drift at member yielding.

7.2.1 Factored Member Force Design Demands

The analyses required to estimate the factored modal member force design demands were presented in Section 6.4.2. The analytical model used for these analyses is discussed in Section 6.1. The factored modal member force design demands, $F_{i,x,fdd}$, are combined to determine the factored member force design demands, $F_{x,fdd}$, as shown in Equation 6.64 (see Section 6.4.5):

$$F_{x,fdd} = \left(\sum_{i=1}^{N} \sum_{j=1}^{N} \rho_{ij} \cdot F_{i,x,fdd} \cdot F_{j,x,fdd} \right)^{\frac{1}{2}} \tag{7.6}$$

7.2.2 Member Capacity and Selection Criteria

The SC-CBF structural members are selected such that their capacities are greater than the factored member force design demands. The members are selected to satisfy the AISC-LRFD criteria (AISC 2005b) for axial force-bending moment interaction:

$$\frac{P_r}{\phi_c P_n} + \frac{8}{9} \cdot \left(\frac{M_{rx}}{\phi_b M_{nx}} + \frac{M_{ry}}{\phi_b M_{ny}} \right) \leq 1.0 \text{ for } \frac{P_r}{\phi_c P_n} \geq 0.2 \tag{7.7}$$

$$\frac{P_r}{2 \cdot \phi_c P_n} + \left(\frac{M_{rx}}{\phi_b M_{nx}} + \frac{M_{ry}}{\phi_b M_{ny}} \right) \leq 1.0 \text{ for } \frac{P_r}{\phi_c P_n} < 0.2 \tag{7.8}$$

where,

P_r = factored design axial force demand determined from second-order analysis (AISC 2005b)

ϕ_c = compression resistance reduction factor, equal to 0.9

P_n = nominal compressive strength of the member

M_{rx} = factored design strong axis bending moment demand determined from second-order analysis (AISC 2005b)

M_{ry} = factored design weak axis bending moment, assumed to be zero

ϕ_b = flexural bending resistance reduction factor, equal to 0.9

M_{ny} and M_{nx} = nominal flexural strength about each cross-sectional axis of the member

P_r and M_{rx} are determined from second-order analysis. As mentioned previously, P-Δ effects are included in the elements modeling the SC-CBF structural members. P-δ effects are less significant than the P-Δ effects; in this research, P-δ effects were neglected in determining P_r and M_{rx}, which were set equal to $F_{x,fdd}$. Alternatively, a more rigorous analysis (AISC 2005b) can be used to include the P-δ effects.

It is important to also consider the seismic design criteria (AISC 2005a) for SCBF systems to ensure adequate ductility of the SC-CBF structural members. In particular, limitations are set on the slenderness of the braces and the width-thickness ratios of the columns and braces.

7.2.3 Reliability of Member Design

As discussed in Chapter 4 and shown in Chapters 5 and 6, there is significant uncertainty in the member force response from nonlinear dynamic analysis, F_x (considered to be the actual seismic demands), due to variability in ground motion characteristics, even when ground motions are scaled to a specific hazard level (e.g., DBE). The PBD criteria for member yielding address this uncertainty in three ways: the use of modal load factors γ_n, the proposed CQC correlation matrix [ρ], and the resistance factors ϕ (AISC 2005b).

As discussed in Section 6.4.3.2, the values of γ_n were determined such that the probability of α_n exceeding $\gamma_n SA_n$ was small (i.e., approximately 5%), where, for the first mode, $SA_1 = \alpha_{1Y}$ and for higher modes, SA_n equals the spectral acceleration from the DBE design spectrum. These factored design spectral accelerations were used to determine the factored modal member force design demands, $F_{i,x,fdd}$. Since the probability of α_n exceeding $\gamma_n SA_n$ is small (in the range of 0.1% to 11%, as shown in Section 6.4.3.2) the probability of the member force response F_x exceeding $F_{x,fdd}$ is similarly small.

Due to the rocking response of the SC-CBF after column decompression, the modal responses appear to be more highly correlated than those of a conventional structural system. Therefore, the CQC method, with a correlation matrix $[\rho]$ that reflects the greater correlation of the peak modal responses, is used to calculate the factored member force design demands, $F_{x,fdd}$.

As previously mentioned in Section 4.3, the capacity has less uncertainty than the demands. Member selection is based on the AISC-LRFD criteria (AISC 2005b), which uses ϕ factors to account for uncertainty and bias in the capacity of structural members. The ϕ factors and the need to select members from discrete sizes of structural shapes increase the margin between the member force design demands and the actual member force capacity. Figure 7.2 shows a schematic of the probability density functions for the DBE-level member force response (demand) and the member force capacity. The bias in the factored capacity ϕF_n reflects the bias between the mean capacity, $\mu_{capacity}$, and the

nominal capacity, F_n, as well as the ϕ factor (AISC 2005b). The difference between $F_{x,fdd}$ and ϕF_n reflects the effect of selecting members from the discrete structural shapes.

In Section 6.4.6, the probability of the member force dynamic response F_x exceeding $F_{x,fdd}$ was estimated. For a lognormal distribution (e.g., the distribution assumed for the dynamic member force demands, F_x), the probability of F_x exceeding F_n is estimated as:

$$P\left(F_x > F_{x,fdd}\right) = 1 - \Phi\left(\frac{ln\left(F_{x,fdd}\right) - ln\left(F_{x,m}\right)}{\sqrt{ln\left(1+\delta_{F_x}^2\right)}}\right) \tag{7.9}$$

where $F_{x,m}$ is the median value of F_x.

Note that due to the difference between $F_{x,fdd}$ and F_n, the probability of F_x exceeding F_n is less than the probability of F_x exceeding $F_{x,fdd}$. Furthermore, due to the capacity factor ϕ and the bias in capacity (difference between F_n and median capacity $\mu_{capacity}$), the probability of F_x exceeding the actual capacity is far smaller than the probability of F_x exceeding $F_{x,fdd}$.

The reliability of the structural member design phase of the proposed design procedure will be evaluated in Chapter 12.

7.3 PT Steel Design Phase

The PT steel design phase considers the limit states of column decompression and PT bar yielding. This section presents a review of the design demands, a discussion of the capacities associated with these limit states, and a discussion of the reliability of the PT steel design.

7.3.1 Column Decompression Limit State

7.3.1.1 Design Demand

At the column decompression limit state, two response quantities are considered: the decompression overturning moment ($OM_{D,demand}$) and the roof drift (θ_D). The decompression overturning moment, $OM_{D,demand}$, is expressed in terms of OM_{ELF} (see Section 5.3.2.1).

$$OM_{D,demand} = \alpha_{D,required} \cdot OM_{ELF} \tag{7.12}$$

$\alpha_{D,required}$ expresses the required strength relative to the strength of a conventional seismic-resistant system. For a conventional system, the response modification factor R is used to relate the minimum system strength (OM_{ELF}) to the force demands based on linear elastic response to the DBE ($OM_{elastic}$), as follows (ASCE 2005):

$$R = \frac{OM_{elastic}}{OM_{ELF}} \tag{7.13}$$

where OM_{ELF} reflects the code-required minimum strength of the conventional structure. As noted in Section 5.3.1, R is assumed to be 8 for the SC-CBF system. Similarly, for an SC-CBF, the parameter $R_{d,max}$ can be written as:

$$R_{d,max} = \frac{OM_{elastic}}{OM_{D,demand}} = \frac{R \cdot OM_{ELF}}{\alpha_{D,required} \cdot OM_{ELF}} = \frac{R}{\alpha_{D,required}} \tag{7.14}$$

To avoid decompression under wind loading or other non-seismic loading, $R_{d,max}$ is limited to a maximum value of 10; therefore, with R equal to 8, $\alpha_{D,required}$ must be greater

than or equal to 0.80. For the preliminary design phase, before the first design iteration, $\alpha_{D,required}$ is equal to 0.80. Note that $\alpha_{D,required}$ and $R_{d,max}$ could be determined from a rational analysis of the building under wind loading or other non-seismic loading conditions.

The roof drift demand at column decompression, θ_D, is determined, as discussed in Section 6.2, as follows:

$$\theta_D = \frac{\Delta_D}{h} \tag{7.15}$$

where Δ_D is the roof drift determined from analyzing the simple linear-elastic analytical model discussed in Section 6.1 under the lateral forces discussed in Section 6.2: $\{F_D\} = \alpha_{D1} \cdot \{F_1\}$; friction forces, $\{F_{ED}\} = \mu \cdot \{F_D\}$; PT_0; and the weight of the SC-CBF, $W_{SC\text{-}CBF}$. θ_D is used to determine the DBE roof drift demand, θ_{DBE}.

7.3.1.2 Capacity

The overturning moment capacity of the SC-CBF at column decompression, OM_D, is a function of the configuration of the SC-CBF, as shown in Chapter 5. For example, Figure 7.3 shows a free-body diagram of a four-story version of Frame D_{DF}. The loading condition shown in the free-body diagram is at column decompression. The applied lateral loads, $\{F_D\}$ (as defined in Section 6.2), produce an applied overturning moment, OM_D, about the contact point of the compression column. To satisfy equilibrium, the overturning moment resistance equals OM_D. At decompression, the PT force equals PT_0, because the PT steel elongates only after column decompression occurs. The overturning

moment resistance OM_D for Frame D_{DF} can be computed from the free-body diagram in Figure 7.3 as a function of PT_0, as follows:

$$OM_D = \left(PT_0 + W_{SC-CBF}\right) \cdot \frac{b_{SC-CBF}}{2} + OM_{ED,D} \tag{7.16}$$

where, as described in Section 6.3.1,

$$OM_{ED,D} = \eta \cdot OM_D \tag{7.17}$$

$$\eta = \mu \cdot \frac{b_{ED}}{h_1^*} \tag{7.18}$$

As shown in Section 6.2, the design parameter $\alpha_{D,required}$ is used to set the required strength of the SC-CBF relative to the strength of a conventional seismic-resistant system in the preliminary design phase, before the first design iteration. Using $\alpha_{D,required}$, PT_0 can be determined for Frame D_{DF} from the free-body diagram in Figure 7.3 as follows:

$$PT_0 = \alpha_{D,required} \cdot OM_{ELF} \cdot \left(\frac{2}{b_{SC-CBF}}\right) - OM_{ED,D} \cdot \left(\frac{2}{b_{SC-CBF}}\right) - W_{SC-CBF} \tag{7.19}$$

For subsequent design iterations, PT_0 is selected according to the PT bar yielding criteria as discussed in Section 7.3.2.2.

Two parameters that characterize the decompression capacity (i.e., the decompression "strength," OM_D) of an SC-CBF relative to the DBE demands for a linear elastic structure are R_A and $R_{A,D}$. R_A is similar to the response modification coefficient, R (ASCE 2005), in

that it expresses the strength of the system with respect to the force demands based on linear elastic response. R_A can be written as:

$$R_A = \frac{OM_{elastic}}{OM_D} = \frac{R \cdot OM_{ELF}}{\alpha_D \cdot OM_{ELF}} = \frac{R}{\alpha_D} \tag{7.20}$$

where the value of R is the value used to determine $\{F_{ELF}\}$ from the design spectrum, as discussed in Section 5.3.1. If α_D equals 1.0, then R_A equals R. OM_D must be greater than $OM_{D,demand}$; therefore, R_A is less than or equal to $R_{d,max}$. Note that α_D is the ratio of the actual OM_D to OM_{ELF}:

$$\alpha_D = \frac{OM_D}{OM_{ELF}} \tag{7.21}$$

$R_{A,D}$, as defined in Section 6.3, expresses the strength of the system relative to the force demands based on elastic response considering only the effective mass of the first mode. The following expression can be written for $R_{A,D}$:

$$R_{A,D} = \frac{OM_{1,elastic}}{OM_D} = \frac{M_1^*}{M_{total}} \cdot \frac{OM_{elastic}}{OM_D} = \frac{M_1^*}{M_{total}} \cdot R_A = \frac{M_1^*}{M_{total}} \cdot \frac{R}{\alpha_D} \tag{7.22}$$

As mentioned in Section 6.3, $R_{A,D}$ is used to determine the DBE drift demand.

7.3.2 PT Bar Yielding Limit State

7.3.2.1 Factored Design Demand

As discussed in Section 6.3, the DBE roof drift demand is the design demand used to control the PT bar yielding limit state in the design process. The calculation of this design

demand is explained in Section 6.3. The median ductility demand under the DBE is given as:

$$\mu_{DBE} = R_{A,D}{}^{p(T_1)} \tag{7.23}$$

where $p(T_1)$ is described in Section 6.3.

The ductility demand is then applied to the decompression roof drift demand, θ_D, to approximate the nominal roof drift demand under the DBE as follows:

$$\theta_{DBE,dd} = \mu_{DBE} \cdot \theta_D \tag{7.24}$$

As discussed in Section 6.3.3, the factor γ_θ can be used to reduce the probability that the DBE roof drift demand θ_{DBE} exceeds the factored design demand $\theta_{DBE,fdd}$, where $\theta_{DBE,fdd}$ is:

$$\theta_{DBE,fdd} = \gamma_\theta \cdot \theta_{DBE,dd} \tag{7.25}$$

7.3.2.2 Capacity

There are two capacities associated with the PT bar yielding limit state that are important for an SC-CBF system: the yield strength of the system (OM_Y), and the nominal roof drift capacity at PT yield ($\theta_{Y,n}$).

The overturning moment capacity of the SC-CBF at PT bar yielding, OM_Y, is a function of the configuration of the SC-CBF, as shown in Chapter 5. For example, Figure 7.4 shows a free-body diagram of a four-story version of Frame D_{DF} at PT bar yielding. The applied lateral loads, $\{F_{Y,1}\}$ (as defined in Section 6.4.2.1), produce an applied

overturning moment, OM_Y, about the contact point of the compression column. To satisfy equilibrium, the overturning moment resistance equals OM_Y. By definition, at OM_Y, the force in the PT bars equals PT_Y. The overturning moment resistance OM_Y can be computed for Frame D_{DF} from the free-body diagram in Figure 7.4 as a function of PT_Y:

$$OM_Y = \left(PT_Y + W_{SC-CBF}\right) \cdot \frac{b_{SC-CBF}}{2} + OM_{ED,Y} \tag{7.26}$$

where,

$$OM_{ED,Y} = \eta \cdot OM_Y \tag{7.27}$$

The value of PT_Y required for the initial iteration of design can be determined by introducing the design parameter $\alpha_{Y,init}$:

$$\alpha_{Y,init} = \frac{OM_Y}{OM_{ELF}} \tag{7.28}$$

where $\alpha_{Y,init}$ specifies the initial overstrength of the SC-CBF (OM_Y) relative to the code-based required strength from $\{F_{ELF}\}$ (OM_{ELF}). Using $\alpha_{Y,init}$, $PT_{Y,req,init}$ can be determined for Frame D_{DF} from the free-body diagram in Figure 7.4 as follows:

$$PT_{Y,req,init} = \alpha_{Y,init} \cdot OM_{ELF} \cdot \left(\frac{2}{b_{SC-CBF}}\right) - OM_{ED,Y} \cdot \left(\frac{2}{b_{SC-CBF}}\right) - W_{SC-CBF} \tag{7.29}$$

Here, for the first design iteration, $\alpha_{Y,init}$ is set equal to 1.2 (i.e., OM_Y is set equal to $1.2 \cdot OM_{ELF}$). The required area of the PT steel for the first design iteration can then be determined as follows:

$$A_{PT,req,init} = \frac{PT_{Y.req,init}}{\sigma_Y} \tag{7.30}$$

where,

σ_Y = nominal yield stress of PT bars, 120 ksi

PT bars are only available in discrete sizes; therefore, the actual area of the PT bars, A_{PT}, must determined and the actual PT_Y is calculated as:

$$PT_Y = A_{PT} \cdot \sigma_Y \tag{7.31}$$

The actual value of PT_Y is then used to determine the actual value of OM_Y, for example, using Equation 7.26 for Frame D_{DF}. This value is then used to determine the ratio of the yield strength of the SC-CBF system, OM_Y, to the decompression strength, OM_D:

$$\alpha_Y = \frac{OM_Y}{OM_D} \tag{7.32}$$

A_{PT} for further iterations of the design procedure is determined by changing the number and size of the PT bars. PT_Y, OM_Y, and α_Y are then determined as described above.

The overturning moment versus roof drift response of the SC-CBF system is shown schematically in Figure 7.5. As discussed in Section 6.3.2, there are two distinct ranges of linear elastic behavior for the SC-CBF system: the linear elastic behavior prior to column decompression and linear elastic behavior after column decompression but prior to PT bar yielding. The ratio of these stiffnesses is:

$$\alpha_k = \frac{k_{pd}}{k_{elastic}} \tag{7.33}$$

where,

$$k_{elastic} = \frac{OM_D}{\theta_D} \tag{7.34}$$

Note that k_{pd} depends upon the SC-CBF configuration, as discussed in Section 6.3.2.

From Figure 7.5, the following relationships can be established:

$$\theta_{Y,n} = \mu_Y \cdot \theta_D \tag{7.35}$$

$$\theta_{elastic,Y} = \frac{OM_Y}{k_{elastic}} \tag{7.36}$$

$$OM_Y = \theta_D \cdot k_{elastic} + \left(\theta_{Y,n} - \theta_D\right) \cdot k_{pd} \tag{7.37}$$

where,

μ_Y = ductility capacity at PT yield

$\theta_{elastic,Y}$ = roof drift at OM_Y that is due to the elastic deformation of the structural members

Substituting Equations 7.32, 7.33, 7.34, and 7.35 into Equation 7.37, and solving for μ_Y results in:

$$\mu_Y = \frac{\alpha_Y + \alpha_k - 1}{\alpha_k} \tag{7.38}$$

Dividing Equation 7.37 by $k_{elastic}$ and using Equation 7.36 gives:

$$\theta_{elastic,Y} = \frac{\theta_D \cdot k_{elastic} + (\theta_{Y,n} - \theta_D) \cdot k_{pd}}{k_{elastic}} \tag{7.39}$$

Substituting Equations 7.33 and 7.35 into Equation 7.39 gives:

$$\theta_{elastic,Y} = \theta_D [1 + \alpha_k \cdot (\mu_Y - 1)] \tag{7.40}$$

Note that the estimate of $\theta_{elastic,Y}$ assumes that deformation patterns of the SC-CBF members after decompression are the same as those before decompression. $\theta_{elastic,Y}$ does not include rigid-body motion (rocking) of the SC-CBF or other member deformations due to the elongation of the PT bars.

The remaining component of $\theta_{Y,n}$ is due to rocking, which lengthens the PT bars. The elongation capacity of the PT bars at yield can be defined as:

$$\Delta L_{PT,Y} = L_{PT} \cdot \left(\frac{\sigma_Y - \sigma_0}{E} \right) \tag{7.41}$$

The rigid body rocking capacity at PT yield is obtained by dividing $\Delta L_{PT,Y}$ by the distance from the PT steel to the contact point of the compression column, which varies based on the location of the PT bars for each SC-CBF configuration (for example, $b_{SC\text{-}CBF}$ / 2 for Frame D_{DIST} in Figure 7.4).

$$\theta_{rock,PT,Y} = \frac{\Delta L_{PT,Y}}{\left(\frac{b_{SC-CBF}}{2} \right)} \tag{7.42}$$

Note that Equation 7.42 is valid for Frame D_{DF}. The distance from the PT steel to the contact point of the compression column varies with the frame configuration, so $\theta_{rock,PT,Y}$ must be calculated accordingly.

Figure 7.6 shows the two components of roof drift at $\theta_{Y,n}$. The first component is $\theta_{rock,PT,Y}$ and the second component is $\theta_{elastic,Y.}$ The nominal drift capacity at PT yield is the sum of $\theta_{rock.PT,Y}$ and $\theta_{elastic,Y}$:

$$\theta_{Y,n} = \theta_{rock,PT,Y} + \theta_{elasticY} \tag{7.43}$$

The PT bars must be selected such that:

$$\theta_{Y,n} \geq \theta_{DBE,fdd} \tag{7.44}$$

7.3.2.3 Reliability of PT Steel Design

$\theta_{DBE,dd}$, as discussed in Section 6.3 and calculated from Equation 7.24, is an estimate of the median DBE-level response, and $\theta_{Y,n}$ from Equation 7.43 is the nominal value of the roof drift capacity at PT yield, θ_Y. Partial safety factors γ_θ and ϕ_θ may be used to account for both bias and uncertainty in the demand and the capacity, respectively, to provide a margin of safety against PT yield at the DBE. γ_θ was introduced in Section 6.3 and mentioned in Section 7.3.2.1. The uncertainty in the demand is large (Seo 2005) compared to the uncertainty in the capacity, so ϕ_θ is set equal to 1.0 for simplicity. Further research on the uncertainty in the roof drift capacity at PT yield is needed.

In Section 6.3.3, an expression for estimating the probability that the roof drift response under the DBE, θ_{DBE}, exceeds $\theta_{DBE,fdd}$ is given. Figure 7.7 shows a schematic of the probability density functions for DBE roof drift response (demand) and roof drift capacity at PT yield. Here the reliability of the SC-CBF with respect to the PT bar yielding limit state is estimated using the following assumptions. The bias in the roof drift capacity at PT bar yielding (the difference between $\theta_{Y,n}$ and the median roof drift capacity at PT yield, $\mu_{capacity}$) is assumed to be negligible. Similarly, the dispersion in the roof drift capacity at PT yield, θ_Y, is neglected. The reliability of the SC-CBF system with respect to the PT bar yielding limit state is then estimated as the probability of θ_{DBE} exceeding $\theta_{Y,n}$. Assuming a lognormal distribution for the maximum roof drift response θ_{DBE}, and assuming that the median value of θ_{DBE}, $\theta_{DBE,m}$, is approximately $\theta_{DBE,dd}$ (see Section 6.3.3), the probability that θ_{DBE} will exceed $\theta_{Y,n}$ can be expressed as:

$$P(\theta_{DBE} > \theta_{Y,n}) = 1 - \Phi\left(\frac{ln(\theta_{Y,n}) - ln(\theta_{DBE,m})}{\zeta_\theta}\right) = 1 - \Phi\left(\frac{ln(\theta_{Y,n}) - ln(\theta_{DBE,dd})}{\zeta_\theta}\right) \quad (7.45)$$

where,

Φ = cumulative distribution function of the standard normal variate (Ang and Tang 2007)

ζ_θ = lognormal parameter of $\theta_{DBE} = (ln(1+\delta_\theta^2))^{1/2}$

δ_θ = coefficient of variation of θ_{DBE}

It is important to note that the assumption in this formulation is that the capacity is treated deterministically. The PBD criteria discussed in Chapter 4 permit a 50% probability of PT bar yielding under the DBE.

7.4 Detail Design Phase

After the structural members and the PT bars have been selected to meet the PBD objectives outlined in Chapter 4, the details of the SC-CBF system must be designed. These details include, but are not limited to, the PT anchorages at the top and bottom of the SC-CBF, the connections between the SC-CBF members, the SC-CBF column base details, and the lateral-load bearings (for Frame D_{DF}).

The structural members should be selected according to the AISC-LRFD criteria (2005b) for strength and the seismic design criteria (AISC 2005a) for ductility. It is important, therefore, to design the connections between the SC-CBF structural members to accommodate the strength and ductility demands of the members. Gonner et al. (2010) provides a discussion of the detailed design of the SC-CBF test structure.

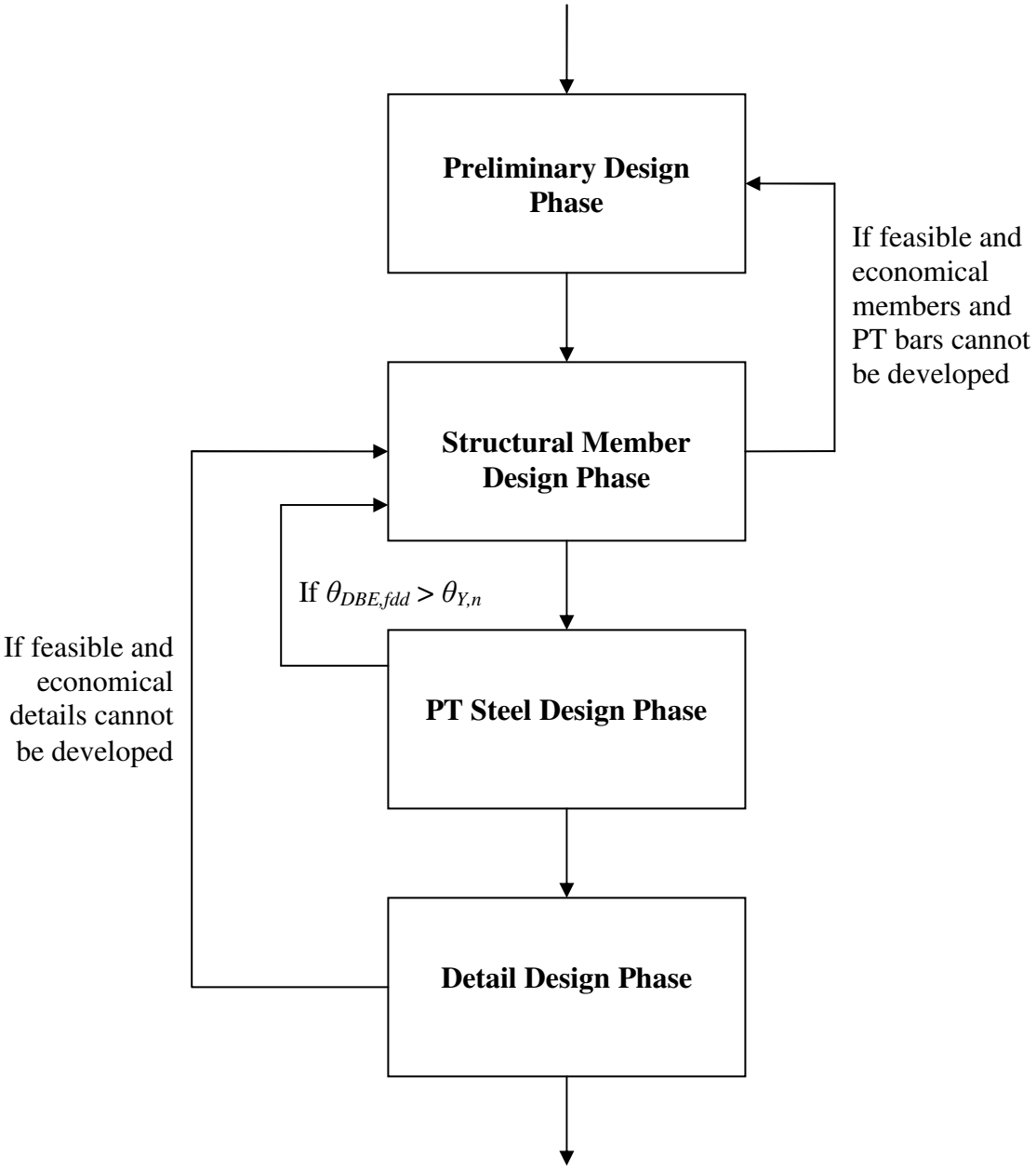

Figure 7.1 – Phases of PBD procedure for SC-CBF system (after Gonner 2009)

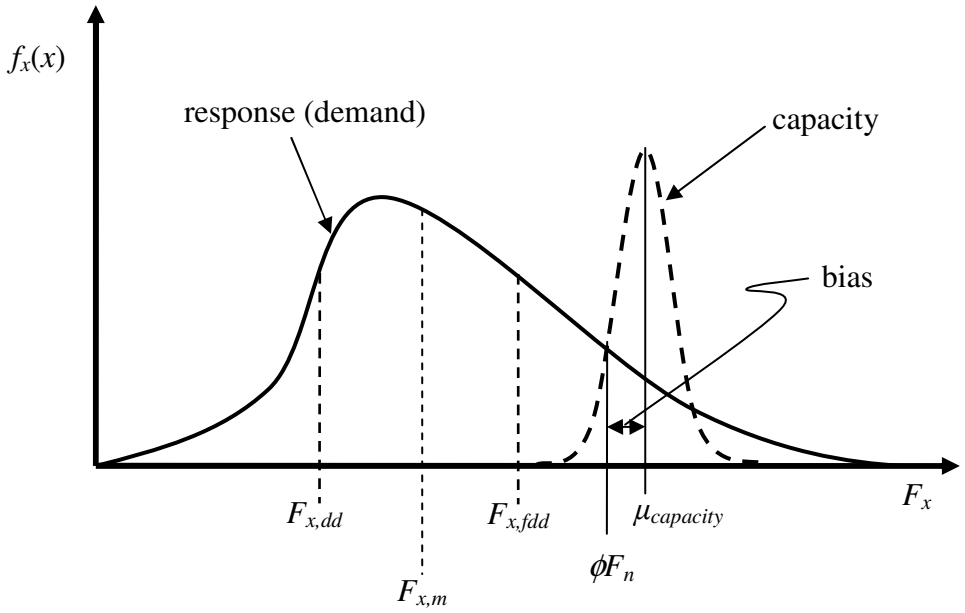

Figure 7.2 – Schematic of probability density function for DBE-level member force response and member force capacities

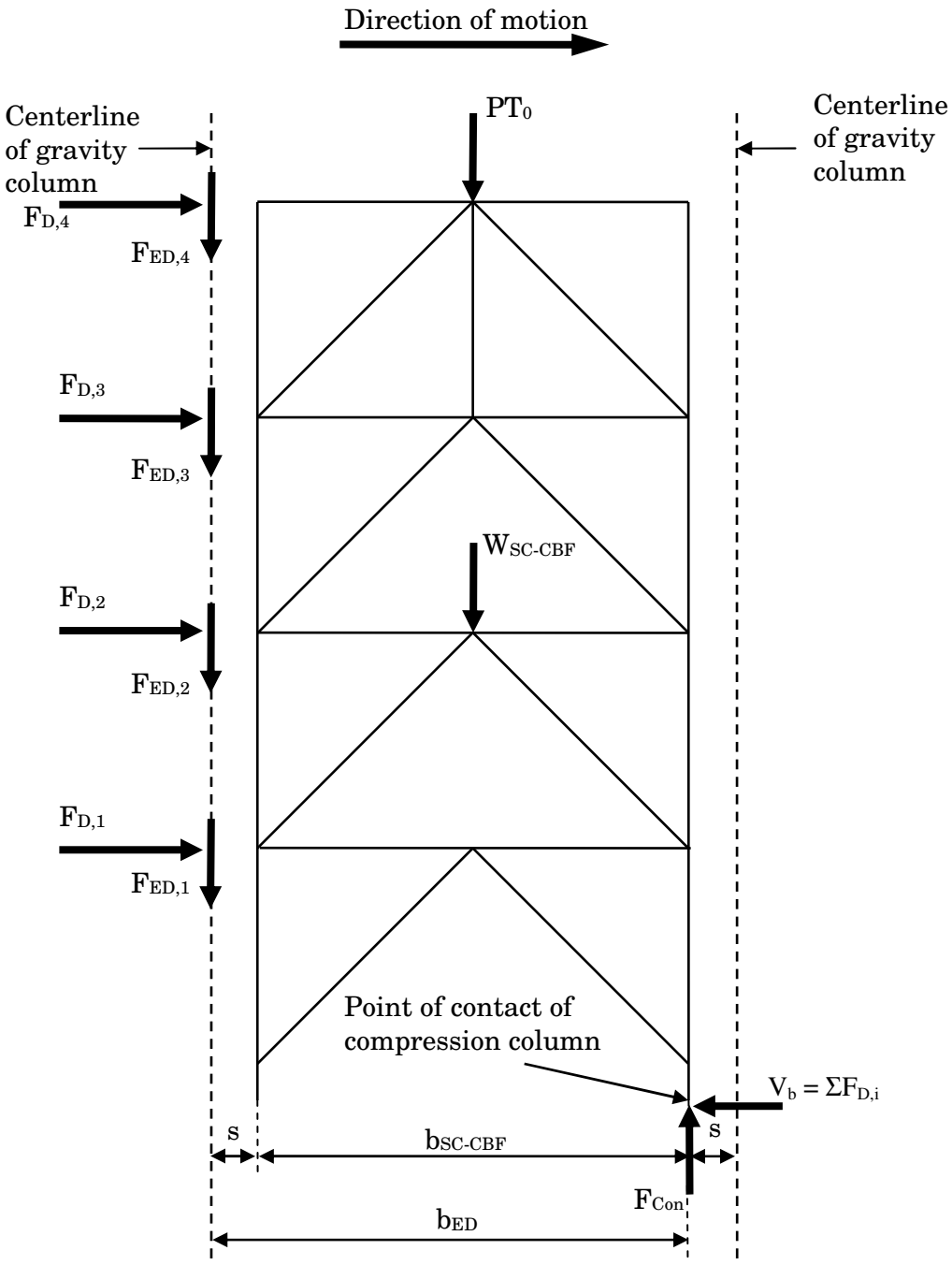

Figure 7.3 – Free-body diagram of Frame D_{DF} at decompression

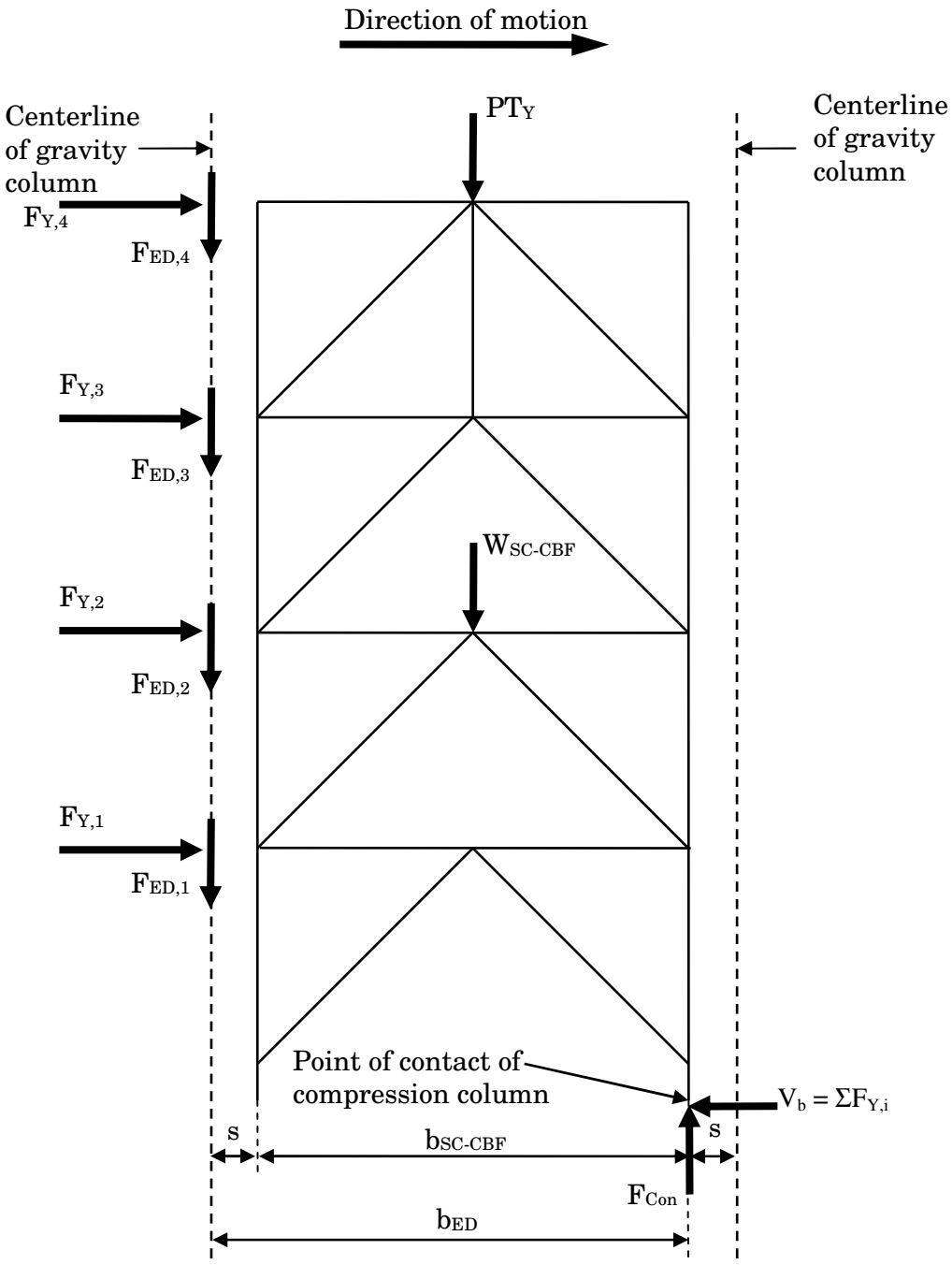

Figure 7.4 – Free-body diagram of Frame D_{DF} at PT bar yielding

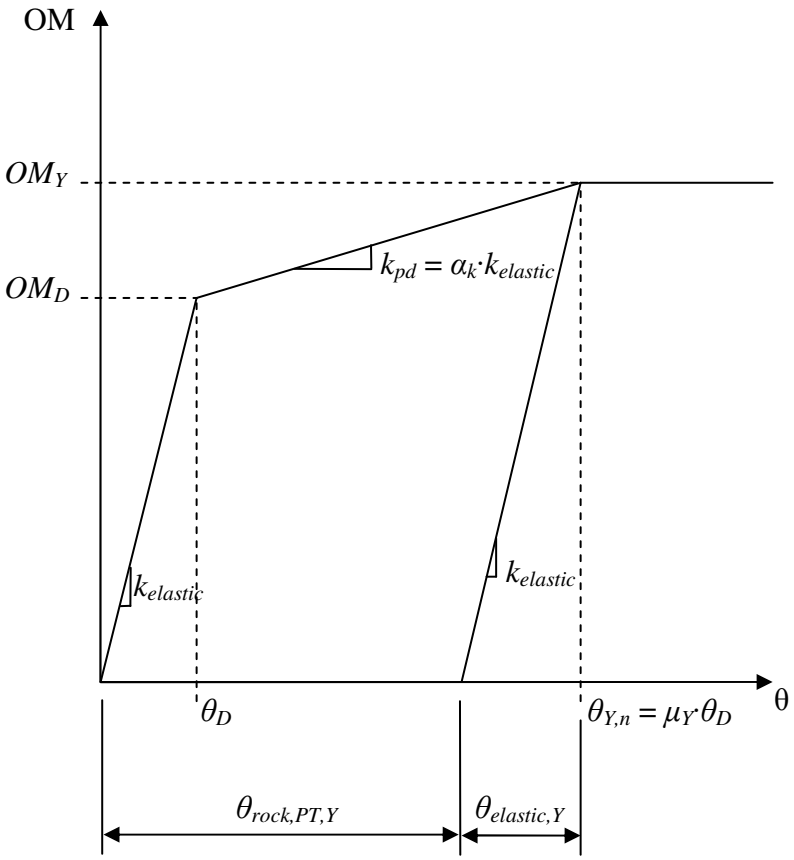

Figure 7.5 – Schematic of idealized overturning moment versus roof drift response of an SC-CBF system

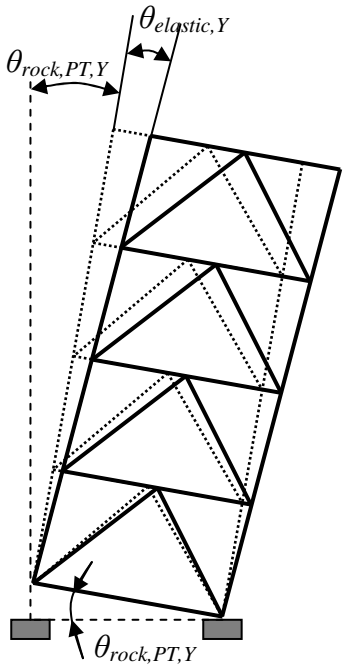

Figure 7.6 – Schematic of assumed rocking behavior: (a) at OM_D; (b) beyond OM_D

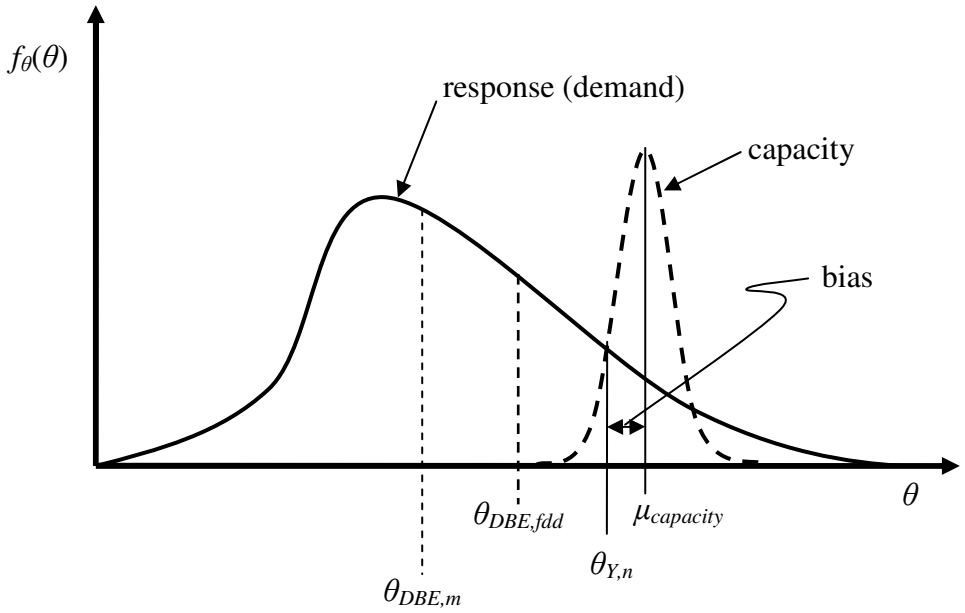

Figure 7.7 – Schematic of probability density function for DBE-level roof drift response and roof drift capacity at PT bar yielding

CHAPTER 8

DESIGN AND MODELING OF THE SC-CBF TEST STRUCTURE

The design procedure discussed in Gonner (2009) was used to design a large-scale SC-CBF test structure. The test structure was fabricated and erected in the ATLSS Center laboratory at Lehigh University and was studied experimentally using the Real-Time Multi-Dimensional (RTMD) Earthquake Simulation Facility, which is part of the NSF-funded Network for Earthquake Engineering Simulation (NEES). The SC-CBF test structure was subjected to simulated earthquake loading using the hybrid simulation method. Other experiments were performed on the test structure to determine its stiffness characteristics. These experiments were conducted to establish the performance of the SC-CBF system (as discussed in Chapters 3 and 4) and to validate the nonlinear analytical model and related numerical simulations of the SC-CBF test structure (as discussed in Chapters 9, 10, and 11).

This chapter summarizes the SC-CBF test structure, as well as the procedure used to design it (Gonner 2009). First, the prototype building used for the SC-CBF test structure is discussed. Then the design of the SC-CBF test structure is discussed. The demand and capacity calculations for each iteration of design are considered.

Next, the components of the SC-CBF test structure are discussed. The arrangement of these components and the relationship of the components to the prototype building are explained.

The analytical model used to predict the behavior of the SC-CBF test structure is discussed next. The analytical model was built using OpenSEES (Mazzoni et al. 2009), a nonlinear analysis program for static and dynamic loading, including earthquake loading simulations. An introduction to the OpenSEES program is presented, followed by a discussion of the properties of the analytical model.

Next, the structural response quantities of interest, the methods of measuring these quantities in the SC-CBF test structure, and the techniques used to model them are discussed. Finally, results of the preliminary static tests on the test frame used to calibrate the stiffness of certain elements of the analytical model are presented.

8.1 Scaled Prototype Building for SC-CBF Test Structure

The prototype building for the SC-CBF test structure is a four-story office building designed for a site in Van Nuys, CA with stiff soil conditions (Site Class D (ASCE 2005)). The test SC-CBF was designed and constructed at 0.6-scale to fit in the ATLSS laboratory; therefore, the prototype building was designed at 0.6-scale. Figure 8.1(a) shows a typical floor plan of the scaled prototype building, which is 6 bays by 6 bays. The bay spacing is 18 ft from column centerline to column centerline (30 ft at full scale). Figure 8.1(b) shows an elevation of the prototype SC-CBF. The first story height is 9 ft

(15 ft at full scale), and the upper story heights are 7.5 ft (12.5 ft at full scale). The below-grade basement level has the same story height as the first story.

SC-CBFs are arranged symmetrically as indicated in Figure 8.1(a). Four SC-CBFs act along each axis of the building. Similar to the prototype building used for the frame configuration study presented in Chapter 5, the arrangement of the SC-CBFs avoids having any columns included in more than one SC-CBF.

Tables 8.1 and 8.2 show the dead loads and live loads, respectively, used for the design of the SC-CBF test structure. As in the prototype structure for the SC-CBF configuration study discussed in Section 5.1, the roof live load is conservatively taken to be the same as the total live load at a typical floor. The roof live load is greater than the value specified by ASCE (2005), and the roof dead load is conservatively assumed to be comprised of a roof slab and roofing materials. One quarter of the live load, as well as the full dead load, within the area of the prototype building for which the inertia forces are resisted by one SC-CBF (i.e., the tributary area for the SC-CBF, equal to one quarter of the total floor area as indicated in Figure 8.1) is applied to the lean-on column to generate the P-Δ effect. One quarter of the live load is used to approximate the live load that can be expected to be acting on the structure at the time of an earthquake.

The dead loads and live loads summarized in Tables 8.1 and 8.2 are slightly different from those used in the frame configuration study, as summarized in Tables 5.1 and 5.2 and discussed in Section 5.1. The differences are: (1) the distribution of the weight of the roofing material and the mechanical weight at the roof has changed, but the total of the

two components remains the same; (2) the assumed exterior wall weights at each floor are slightly less for the SC-CBF test structure than they were for the frame configuration study; and (3) the roof live load for the SC-CBF test structure has been conservatively considered as 65 psf rather than 50 psf. Table 8.3 summarizes the seismic masses at each floor level, taking into account the dead loads and partition loads (ASCE 2005) within the tributary area for one SC-CBF.

8.2 Design of the SC-CBF Test Structure

The SC-CBF test structure was designed using the configuration of Frame D_{DIST} by Gonner (2009). This design procedure assumed a constant value of OM_{ED}; however, Gonner also developed details for the lateral-load bearings to provide controlled friction (i.e., to behave as discussed in Section 5.5). The SC-CBF test structure was studied experimentally using the configuration of Frame D_{DF}. The design procedure outlined in Chapter 7 is a general procedure that can be used for any frame configuration, including Frame D_{DIST} and Frame D_{DF}.

Table 8.4 summarizes the properties of the SC-CBF test structure at each iteration of the design of the test structure. Each design iteration is presented using member section sizes, PT bar areas, and initial PT bar forces selected by Gonner (2009) at each iteration. Three data sets are presented: (1) Frame D_{DIST} designed by Gonner (2009), (2) Frame D_{DIST} using the procedure from Chapter 7, and (3) Frame D_{DF} using the procedure from Chapter 7. The tabulated properties are: the weight of the SC-CBF members, $W_{SC\text{-}CBF}$; the area of the PT bars, A_{PT}; the energy dissipation ratio, β_E, as calculated from Equation 5.16 for

Frame D_{DIST} and Equation 5.28 for Frame D_{DF}; the energy dissipation ratio at decompression, $\beta_{E,D}$, as calculated from Equation 5.16 for Frame D_{DIST} and Equation 5.31 for Frame D_{DF}; the total ED device force, which equals V_{ED} for Frame D_{DIST} and equals $(F_{ED,D} + F_{ED,Y})/2$ for Frame D_{DF}; OM_{ED} at decompression for each frame, which equals OM_{ED} calculated from Equation 5.18 for Frame D_{DIST} and equals $OM_{ED,D}$ calculated from Equation 6.21 for Frame D_{DF}; the decompression strength of the system, OM_D; and the yield strength of the system, OM_Y.

The changes in the values of $W_{SC\text{-}CBF}$, A_{PT}, and V_{ED} for each iteration show the changes in the design of the SC-CBF test structure. As discussed in Chapter 7, the initial member sizes (and the corresponding value of $W_{SC\text{-}CBF}$) are arbitrary; Gonner (2009) based the initial member selections on scaled-down member sizes from a full-scale prototype structure. A_{PT} for the first iteration is determined based on $A_{PT,req,init}$ as discussed in Section 7.3.2.2. V_{ED} for the first iteration of design was based on a value of $\beta_{E,t}$ (as discussed in Section 7.1.4.1) of 45%. For the second and fourth iterations of design, A_{PT} was increased to satisfy the PT steel design criteria. For the third and fifth iterations of design, the SC-CBF members were reselected to satisfy the member yielding design criteria. Through the fifth iteration of design, β_E was equal to $\beta_{E,t}$ (45%), and V_{ED} was determined as discussed in Section 7.1.4.1. For the sixth iteration of design, after the PT yielding design criteria and member yielding design criteria were satisfied, the value of V_{ED} was set equal to the nominal capacity of the ED element that was designed for the SC-CBF test structure. The final iteration of design was necessary to ensure that the design criteria would be satisfied with the actual value of V_{ED}.

Frame D_{DIST} has a constant ED force; therefore, $\beta_{E,D}$ equals β_E. For Frame D_{DF}, however, β_E is a function of the applied force; therefore, β_E is greater than $\beta_{E,D}$. For Frame D_{DF}, if $\beta_{E,D}$ is less than 50%, the system should self-center regardless of the value of β_E.

8.2.1 PT Bar Yielding Limit State

Table 8.5 presents a summary of design parameters relevant to the PT bar yielding limit state: the value of the response modification coefficient R used to calculate the factored DBE roof drift demand (R_{actual} (Gonner 2009) or $R_{A,D}$); the ductility demand under the DBE, μ_{DBE}, from Equation 6.14; the factored DBE roof drift demand, $\theta_{DBE,fdd}$, from Equation 6.8; the nominal roof drift capacity at PT bar yield, $\theta_{Y,n}$, from Equation 7.43; and the probability that the DBE roof drift demand exceeds the nominal roof drift capacity at PT bar yield, $P(\theta_{DBE} > \theta_{Y,n})$, as discussed in Section 7.3.2.3 (Equation 7.45). $P(\theta_{DBE} > \theta_{Y,n})$ is calculated assuming a lognormal distribution of roof drift demand, assuming that the median response is equal to the design demand and the coefficient of variation is 0.30. Design iterations 1, 3, 4, 5, and 6 are presented; in the second iteration of design, the PT bar yielding limit state was not checked. Three data sets are presented: Frame D_{DIST} designed by Gonner (2009), Frame D_{DIST} designed using the procedure from Chapter 7, and Frame D_{DF} designed using the procedure from Chapter 7.

The final value of $\theta_{Y,n}$ for the two frame configurations is similar regardless of design procedure. The slight difference in $\theta_{Y,n}$ is due to the elastic deformation of the SC-CBF members, $\theta_{elastic,Y}$ (from Section 7.3.2.2, Equation 7.40). $\theta_{elastic,Y}$ is a function of α_k, which changes due to the friction in the lateral-load bearings, as discussed in Section 6.3.2.

Since $\theta_{Y,n}$ is similar for each configuration, the differences in the results for $P(\theta_{DBE} > \theta_{Y,n})$ are primarily due to the difference in $\theta_{DBE,fdd}$, because $\theta_{DBE,fdd}$ is assumed to be the median roof drift response (with $\gamma_\theta = 1.0$). $\theta_{DBE,fdd}$ is a function of μ_{DBE}, which is a function of R_{actual} (Gonner 2009) or $R_{A,D}$ (as shown in Equation 7.23). R_{actual} for Frame D_{DIST} from Gonner (2009) is greater than $R_{A,D}$ calculated using the design procedure from Chapter 7 for Frame D_{DIST}, because Gonner used the total tributary mass, whereas the design procedure in Chapter 7 uses the first mode effective modal mass. Due to the use of the total tributary mass, the values of μ_{DBE} from Gonner (2009) are greater than the values of μ_{DBE} calculated using the design procedure from Chapter 7. As a result, the design roof drift demand (based on the procedure presented in Chapter 7) is less than the drift capacity at the third iteration, rather than the sixth iteration, and the final design is quite conservative, with only a 7.2% probability of PT bar yielding in the D_{DIST} configuration.

Comparing the two designs based on the procedure discussed in Chapter 7, Frame D_{DIST} has a smaller value of μ_{DBE} for each iteration of design (see Table 8.4) than Frame D_{DF}. This is primarily due to the difference in $R_{A,D}$; as shown in Equation 6.9, $R_{A,D}$ is inversely proportional to OM_D. OM_D for Frame D_{DF} is only 74% of OM_D for Frame D_{DIST}; therefore, $R_{A,D}$ and μ_{DBE} for Frame D_{DF} will be higher than $R_{A,D}$ and μ_{DBE} for Frame D_{DIST}. For both configurations, $\theta_{DBE,fdd}$ is less than $\theta_{Y,n}$. Although Frame D_{DF} has a higher value of $\theta_{DBE,fdd}$ than Frame D_{DIST}, $P(\theta_{DBE} > \theta_{Y,n})$ is only 23.9%.

The values of $P(\theta_{DBE} > \theta_{Y,n})$ indicate that both frame configurations designed using the procedure from Chapter 7 are expected to achieve the performance objective for the PT bar yielding limit state under the DBE, as presented in Chapter 4. The design criteria

presented in Chapter 7 limit the probability of yielding the PT bars to less than 50%. The final design of Frame D_{DIST}, using the procedure discussed in Chapter 7, exceeds the design criteria. The effect of the higher value of OM_D for Frame D_{DIST} compared to that for Frame D_{DF} is significant, suggesting that for Frame D_{DF}, increasing the initial force in the PT bars or adding supplemental ED elements similar to those used in Frame D_{DIST} could be considered, if needed, to increase the decompression strength of the system and reduce $\theta_{DBE,dd}$.

8.2.2 Member Yielding Limit State

Table 8.6 summarizes the final values of $F_{bri,fdd}$ (the factored axial force design demand for the brace in story *i*) for the SC-CBF braces for each of the three frame designs: Frame D_{DIST} designed by Gonner (2009), Frame D_{DIST} using the procedure from Chapter 7, and Frame D_{DF} using the procedure from Chapter 7. These data indicate that $F_{bri,fdd}$ is not very sensitive to the differences between the two frame configurations and the two design procedures. The factored higher mode member force design demands are identical for any given set of SC-CBF members; therefore, the difference in $F_{bri,fdd}$ stems from the first mode member force design demands, $F_{1,bri,dd}$. As discussed in Section 6.4.2.1, $F_{1,bri,dd}$ is determined at OM_Y; Table 8.4 shows that OM_Y differs slightly between Frame D_{DIST} and Frame D_{DF}. The difference in OM_Y does not cause a significant change in $F_{bri,fdd}$, however; this suggests that both frame configurations designed using the procedure from Chapter 7 will satisfy the performance objective for the member yielding limit state under the DBE presented in Chapter 4.

The fourth column of Table 8.6 shows the nominal yield force of the brace in each story i, $F_{bri,n}$. The fifth column of Table 8.6 shows the values of $F_{bri,n}$ divided by $F_{bri,fdd}$. These data show that there is a significant margin between $F_{bri,fdd}$ and $F_{bri,n}$. There are three primary sources of the margin between $F_{bri,fdd}$ and $F_{bri,n}$: (1) the need to select from discrete sizes of structural shapes, (2) the use of interaction equations (AISC 2005b) to select the members rather than designing for axial forces alone, (3) the resistance factor ϕ in the capacity calculations (AISC 2005b). The second story braces show the highest margin; the section sizes for these braces were increased to make the member selections more uniform to reduce fabrication and erection costs.

8.3 SC-CBF Test Structure Components for Hybrid Simulations

For the hybrid simulations on the SC-CBF test structure, the test structure is divided into two substructures, an experimental substructure and an analytical substructure, as indicated in Figure 8.2. Figure 8.2(a) shows the experimental substructure, which consists of all elements of the SC-CBF test structure that were located in the laboratory, including the SC-CBF, the adjacent gravity columns, the basement substructure, the PT bars, the loading beams, the lateral-load bearings, and the actuators. Figure 8.2(b) shows the analytical substructure, which consists of the lean-on column, the seismic mass, and the damping substructure. The experimental and analytical substructure are connected to one another at the degrees of freedom indicated in Figure 8.2 (i.e., the two substructures have the same horizontal displacement degrees of freedom). The components of the SC-CBF test structure will be discussed in more detail in the following sections.

Figure 8.3 shows a drawing of the SC-CBF test structure, excluding the loading beams and the actuators. The components of the SC-CBF test structure shown in Figure 8.3 were fabricated and erected to directly represent the associated components of the prototype building.

Figure 8.4 shows a photograph of the SC-CBF test structure in the laboratory. The SC-CBF test structure is located within a test fixture (the bracing frame indicated in Figure 8.4) to provide out-of-plane bracing. The loading beams are not visible in this picture; the loading beams are located at each floor level between the bracing frame and the SC-CBF, and are used to simulate the action of the floor diaphragm in the prototype building. Actuators are attached to the experimental substructure as shown in Figure 8.2(a) and are used to impose target displacements on the adjacent north gravity column, as discussed later.

The SC-CBF test structure is located in the laboratory such that the right side of Figures 8.2, 8.3, and 8.4 is to the north; therefore, structural members and response quantities will be described as "north" and "south" instead of "right" and "left" (e.g., the north gravity column, roof drift to the north).

8.3.1 Experimental Substructure

8.3.1.1 SC-CBF

The SC-CBF includes the beams, columns, braces, and struts of the SC-CBF. Figure 8.5 shows a drawing of the SC-CBF test structure. Note that since the SC-CBF test structure has the Frame D_{DF} configuration, the SC-CBF is not directly attached to the floor

diaphragm. To make the inertia forces from the floor diaphragm concentric with the centroidal axes of the beams in the SC-CBF, the centroidal axes of the SC-CBF beams are aligned with the top-of-steel of the gravity system. The dimensions shown in Figure 8.5 reflect this alignment.

Figure 8.6(a) shows a typical connection between a column, beam, and brace in the SC-CBF test structure. At each end of the braces, lap plates are used to transfer forces from the wide-flange brace section to the gusset plates. The gusset plates then transfer these forces into the beams and columns. An explanation of the design of the connections and details of the SC-CBF is presented by Gonner et al. (2010).

At the base of the SC-CBF columns, there are points at which forces are transferred from the SC-CBF to the basement substructure. These points are the half-round reaction point and the vertical load reaction point, as indicated in Figure 8.7. The half-round reaction point provides a horizontal reaction to transmit lateral force (i.e., base shear) from the SC-CBF to the basement substructure. The vertical load reaction point provides a vertical reaction to transmit vertical load into the basement substructure, and also provides a horizontal reaction through friction between the column base and the basement substructure.

Since Frame D_{DF} separates the gravity load bearing system from the SC-CBF, the only gravity load acting on the SC-CBF is the self-weight of the structural members (the beams, columns, and braces of the SC-CBF).

8.3.1.2 Adjacent Gravity Columns

In the prototype building, the adjacent gravity columns of the SC-CBF test structure would support gravity loads for the tributary area for each SC-CBF column, as described in Chapter 5. However, the full tributary gravity loads were not recreated in the laboratory; the actual gravity loads carried by the adjacent gravity columns in the laboratory are shown in Table 8.7. The only gravity loads acting on the gravity columns are the self-weight of the columns themselves and the weight of the loading beams (Section 8.3.1.5) and the actuators (Section 8.3.1.7). The remainder of the tributary gravity loads for these columns is included in the gravity load applied to the lean-on column, which will be discussed in Section 8.3.2.1.

A pin was used at the base of the adjacent gravity columns (i.e., at ground level of the prototype building, as indicated in Figure 8.8) to ensure that the column base has the rotation capacity to accommodate a large first story drift demand without damaging the gravity column.

8.3.1.3 Basement Substructure

The basement substructure of the SC-CBF test structure is defined as the set of members located below the level at which the rocking occurs (i.e., below ground level of the prototype building). A drawing of the basement substructure is shown in Figure 8.9. The basement substructure includes a foundation beam, a W36x230 used to support the SC-CBF and resist the PT force from the basement PT anchorage. So-called side plates are used to transfer the lateral force from the SC-CBF at the half-round reaction point (shown

in Figure 8.10) into the ground links (shown schematically in Figure 8.9 as reaction forces F_{GLS} and F_{GLN}, and shown in the drawing in Figure 8.10). The basement columns are extensions of the gravity columns, extending from the base of the basement substructure to the pins in the adjacent gravity columns near ground level (i.e., the top of the foundation beam).

The basement substructure is supported at four points: two pins at the base of the basement columns and the two ground links indicated by F_{GLS} and F_{GLN} in Figure 8.9. The pins at the base of the basement columns are intended to approximate the point of inflection in the columns at the basement level of the prototype building (see Figure 8.1(b)). The ground links are intended to approximate the base shear reaction provided at the ground level of the prototype building. The reactions from these boundary conditions are indicated in Figure 8.9. The south and north vertical reactions at the pins at the column bases are labeled F_{Sy} and F_{Ny}, respectively, and the south and north horizontal reactions at the pins are labeled F_{Sx} and F_{Nx}. The south and north ground link reactions are labeled F_{GLS} and F_{GLN}, respectively.

The location of the half-round reaction point is eccentric to the ground links. The side plates are used to resist the moment due to this eccentricity, to transfer the lateral force into the ground links and to transfer the moment due to the eccentricity between the half-round and the ground links into the foundation beam. Figure 8.10 shows the relationship between the side plate, the half-round reaction point, and the ground link. Figure 8.11 shows the connection between the side plates and the ground link clevis connection plate. Figure 8.12 shows how the side plates are connected to the flanges of the foundation

beam; flange plates are welded to each flange of the foundation beam and to each side plate. These flange plates transmit moment due to the eccentricity of the ground link and the half-round reaction point from the side plates into the foundation beam.

As shown in Figure 8.10, the side plates extend over a segment of the foundation beam. The flange plates connecting the side plates to the foundation beam cause these components to act as a unit; therefore, the cross-section of this segment of the foundation beam is a combined section of the W36x230 and the side plates, as shown in Figure 8.13.

8.3.1.4 PT Bars

For the SC-CBF test structure, there are three PT bar locations in the plane of the frame (Gonner 2009): at midbay, 8 inches north of midbay, and 8 inches south of midbay. These three locations are indicated in the schematic shown in Figure 8.2. At each of these locations, one PT bar is located on each side of the SC-CBF (i.e., one bar to the east and one bar to the west). The PT bars are anchored at the roof PT bar anchorage and the basement PT bar anchorage, shown in Figure 8.5 and Figure 8.9, respectively.

8.3.1.5 Loading Beams

Loading beams were used in the SC-CBF test structure to model the action of the floor diaphragm that connects the adjacent gravity columns in the prototype building. Elastic deformations within the floor diaphragm permit displacements of the adjacent north and south gravity columns of the SC-CBF relative to each other (i.e., differential displacements between the two adjacent gravity columns). As discussed later in Section 8.3.1.7, the DOFs for the north gravity column are assumed to be identical to those of the

lean-on column. The loading beams approximate the flexibility of the floor diaphragm between the adjacent gravity columns; forces are transmitted through the loading beams, but the displacements of the two adjacent gravity columns at each floor level are not identical.

Figure 8.14 shows the arrangement of the loading beams with respect to the SC-CBF. The loading beams are attached to the north gravity column by the actuator loading plate and to the south gravity column by a spreader beam. Further details of the loading beam system are presented by Gonner et al. (2010).

8.3.1.6 Lateral-Load Bearings

The inertia forces are transferred from the adjacent gravity columns to the SC-CBF columns through the lateral-load bearings acting in compression only. The loading beams transfer lateral load into the south gravity column. Therefore, when the actuators are in compression, they directly load the north gravity column, as seen in Figure 8.2; when the actuators are in tension, the loading beams transfer the load to the south gravity column. Lateral loads are then transmitted from the gravity columns to the SC-CBF columns through the lateral-load bearings.

Each lateral-load bearing consists of a brass friction plate on the SC-CBF column and a steel bearing on the adjacent gravity column. As a compressive load is applied between the two surfaces, a friction force develops. The coefficient of friction for steel on brass is about 0.45 (Petty 1999). This friction dissipates energy during dynamic response of an SC-CBF in the Frame D_{DF} configuration, as discussed in Section 5.5.

During erection of the SC-CBF test structure, small lateral gaps were left at the lateral-load bearings, between the steel bearing and the brass friction plate. These gaps were on the order of 0.01 inches. Gaps at the lateral-load bearings were considered to be necessary to eliminate friction at the bearings when no lateral loads are acting on the SC-CBF.

8.3.1.7 Actuators

Actuators were used to impose target displacements in the hybrid simulations, determined by the integration algorithm discussed in Chapter 10, at the degrees of freedom (DOFs) of the experimental substructure. The DOFs used for the experimental substructure were the horizontal displacements of the north gravity column at the floor levels. For the SC-CBF test structure, these DOFs were assumed to be identical to the horizontal displacement DOFs of the lean-on column, which is part of the analytical substructure.

8.3.2 Analytical Substructure

8.3.2.1 Lean-On Column

The analytical lean-on column used for the hybrid simulations in the laboratory accounts for the gravity columns that are within the tributary area for one SC-CBF in the prototype building. Figure 8.1(a) shows the floor plan of the scaled prototype building, with the SC-CBF and its tributary area indicated. There are two column types that must be accounted for in the lean-on column: 8¼ typical gravity columns (W8x35) and the two gravity columns adjacent to the out-of-plane SC-CBF (W8x67). The axial force and bending moment resistance of these columns are modeled in the lean-on column. To estimate the

properties of the lean-on column, it is assumed that the typical gravity columns are arranged such that half are oriented with their strong axis in the same plane as the SC-CBF and half are oriented with their weak axis in the same plane as the SC-CBF.

The lean-on column is modeled as a continuous column with a pinned base. The base of the lean-on column is at the same elevation as the base of the SC-CBF columns (i.e., the top of steel of the foundation beam at which gap opening occurs). The gravity loads applied at each floor level are summarized in Table 8.7. The properties of the lean-on column are summarized in Table 8.8.

8.3.2.2 Seismic Mass

The seismic mass included in the hybrid simulation on the SC-CBF test structure is modeled as a series of concentrated masses at each floor level, representing the mass within the tributary area for one SC-CBF. These concentrated masses are placed at the floor-level nodes of a lean-on column. Table 8.3 summarizes the mass at each floor level.

8.3.2.3 Damping

Rayleigh damping was used in the hybrid simulations. As indicated in Figure 8.2, four DOFs are considered for the SC-CBF test structure. This results in a 4x4 damping matrix. The damping coefficients for the Rayleigh damping matrix were determined using the mass and stiffness matrices for the SC-CBF test structure. The modal damping ratios used to determine the damping coefficients were 2% damping for the first mode and 5% damping for the third mode, based on the stiffness matrix from the SC-CBF test structure experimental substructure. Including the elastic stiffness of the lean-on column and the P-

D effect from the vertical loads on the lean-on column, the effective damping ratios were calculated to be 2.6% for the first mode, 4.8% for the second mode, 6.1% for the third mode, and 6.9% for the fourth mode.

8.4 Analytical Model for SC-CBF Test Structure

This section describes the modeling techniques and assumptions used to develop an analytical model of the SC-CBF test structure. The analytical model includes certain components of the SC-CBF test structure that are described in Section 8.3. The analytical model is intended to represent the earthquake response of a single SC-CBF along with its tributary area in the prototype building shown in Figure 8.1. To enable the analytical model to be correlated with the experimental results from hybrid simulations, care was taken to model the basement substructure used in the laboratory rather than a typical basement structure for the prototype building. Figure 8.15 shows a schematic of the analytical model developed for the SC-CBF test structure; this figure shows the components of the model that represent the components of the SC-CBF test structure shown in Figure 8.3.

8.4.1 Overview of OpenSEES Program

To predict the behavior of the SC-CBF test structure, nonlinear analytical models were created using the OpenSEES program (Mazzoni et al. 2009). OpenSEES is a structural analysis program that is capable of nonlinear static (e.g., static pushover or support settlement) or dynamic (e.g., response to earthquake ground motion input) analysis of two- or three-dimensional structures. The SC-CBF test structure was modeled as a two-

dimensional structure. Nodes are used to define the geometry of the structure. For a two-dimensional structure, each node has three degrees of freedom: two orthogonal displacements and one in-plane rotation. Linear or nonlinear elements are used to connect the nodes, and can include P-Δ effects.

OpenSEES (Mazzoni et al. 2009) permits the use of a variety of integration algorithms and numerical solution algorithms. For dynamic analysis, the available integration algorithms include the central difference method, the Newmark method, the Hilber-Hughes-Taylor method, the generalized alpha method, and the TRBDF2 method. The Newmark method with constant average acceleration, which is an unconditionally stable implicit method, was used for dynamic analysis. Nonlinear static analyses can be conducted using force control, displacement control, or arc-length control. Both load control and displacement control were used.

The solution algorithms permitted by OpenSEES (Mazzoni et al. 2009) include a linear algorithm, the Newton method, the Newton method with line search, the modified Newton method, the Krylov-Newton method, the Broyden-Fletcher-Goldfarb-Shanno method, and the Broyden method. The solution algorithm used for the both the nonlinear static analysis and the nonlinear dynamic analyses of the SC-CBFs for this research is the Krylov-Newton algorithm (Carlson and Miller 1998), which "uses a modified Newton method with Krylov subspace acceleration to advance to the next time step" (Mazzoni et al. 2009), thereby achieving convergence more quickly than the modified Newton method alone.

8.4.2 Model for SC-CBF

The beams, columns, braces, and distribution struts of the SC-CBF are modeled using fiber elements. The fiber element cross-sections represent the cross-sectional geometry of the members and connection regions as follows. Figure 8.6 shows a typical connection between a column, beam, and brace in the SC-CBF test structure. Figure 8.6(a) shows the geometry of the wide flange section brace member and the lap plates and gusset plates used to connect the brace member to the beams and columns. To approximate the various cross-sections of the members and the connected lap and gusset plates, the working-point-to-working-point length of the member is discretized into a series of segments, as indicated in Figure 8.6(b). Each segment is assumed to be prismatic (with constant cross-sectional properties over its length) as shown schematically in Figure 8.6(c). For fiber element segments used to model the SC-CBF members, the cross-sectional properties are based on the nominal dimensions of the steel section and any plate material (e.g., gusset plates or lap plates) attached to the member. For the segments that model the gusset plates, the prismatic sections are based on the Whitmore section (AISC 2005c); the average width of the Whitmore section over the length of the segment is used to determine the cross-section properties for the segment, as indicated in Figure 8.6(c). P-Δ effects were included in the elements used to model the structural members.

Continuity between segments and members is assumed; that is, the connections in the SC-CBF are modeled as moment-resisting connections rather than the pinned truss-type connections that are typically used for braced frames. The connections between the

members are stiffened by large gusset plates, as shown in Figure 8.6. These connections will, therefore, transfer moments as well as axial forces into the members.

Several SC-CBF column base details, shown in Figure 8.7, required special consideration: the half-rounds used to transfer lateral force above the column base, the vertical gap opening behavior at the column base, and the friction at the column base that transfers lateral force into the foundation beam.

The half-round elements at the base of the SC-CBF columns were modeled in OpenSEES using a rigid beam element to connect the half-round to the centerline of the SC-CBF column. The contact between the half-round and the bearing plate on the basement substructure is modeled using a horizontally oriented gap element, which transfers force via compression but has zero tensile force capacity. The stiffness of the gap element is listed in Table 8.9. The final stiffness value was determined from correlation of global response quantities (i.e., displacements u_1 through u_4, as indicated in Figure 8.2) between analytical and experimental pushover results.

Vertical gap opening at the column base is modeled using a vertically oriented gap-friction element. Gap-friction elements are zero-length springs that resist compressive forces and develop friction forces perpendicular to the normal force. Gap-friction elements provide no resistance to tensile forces. The expected behavior of the SC-CBF is to rock about a point at the base of the SC-CBF column. The assumed center of rotation is at the extreme outer fiber of the flange of the SC-CBF column, between the extreme fiber of the flange and the column flange reinforcing plate. Therefore, the vertical gap

element is located between the SC-CBF column and the foundation beam at the interface of the column flange and the column flange reinforcing plate, as indicated in Figure 8.7. A rigid beam element is used to connect the node for this vertical gap element to the element along the centerline of the SC-CBF column. This vertical gap element includes a friction component that resists lateral force (i.e., base shear of the SC-CBF). The friction force capacity of the element is proportional to the compressive force in the element times the user-defined coefficient of friction. The contact stiffness, friction stiffness, and coefficient of friction of the gap element are listed in Table 8.9.

The base plates between the SC-CBF column base and the foundation beam, as seen in Figure 8.7, are not included in the analytical model. The section properties of the SC-CBF column are based on the nominal section dimensions (AISC 2005c).

The only gravity load acting on the SC-CBF is self-weight of the structural members (i.e., the beams, columns, braces, and struts). The member self-weights were modeled using concentrated nodal loads at the working points of the structural members.

8.4.3 Model for Adjacent Gravity Columns

The gravity columns are continuous from the pin at ground level to the fourth floor level. Nodes are located at the floor levels. The gravity columns do not have significant changes in geometry, and are therefore modeled using a single fiber element for each story. The nominal dimensions of the gravity column section (AISC 2005c) are used to determine the geometry of the fiber element section. P-Δ effects are included in these fiber elements.

A pin is located in the gravity columns close to ground level, as shown in Figure 8.8, to approximate the pinned connection at the base of these columns in the prototype building. The pin is modeled using stiff horizontally- and vertically-oriented zero-length springs between the node at the base of the gravity column and the node at the top of the basement substructure column.

The gravity loads acting on the adjacent gravity columns, shown in Table 8.7, are included in the analytical model.

8.4.4 Model for Basement Substructure

As previously mentioned, the basement substructure is composed of a W36x230 foundation beam, basement columns connected to pins at the base, ground links, and a substantial amount of connection material.

The foundation beam is modeled in three segments, as indicated in Figure 8.16. The outermost of these regions is a rigid beam element within the width of the basement column. The next segment is a short region over which the side plates act compositely with the foundation beam, as discussed in Section 8.3.3. The remainder of the foundation beam is modeled as a W36x230, with section properties given by AISC (2005c). As shown in Figure 8.16, below the vertical gap element at the base of each SC-CBF column, a rigid beam element connects the lower node of the gap element to the centerline of the foundation beam. The lower node of the gap element is also attached to the side plate elements via a spring element described later.

Vertically-oriented side plate elements are used to transfer the force from the half-rounds on the SC-CBF columns to the ground links, and to transfer the moment due to the eccentricity between the half round reaction point and the ground link into the foundation beam. These side plates are aligned along the basement columns, as shown in Figure 8.16. The side plates are not directly connected to the basement columns, as shown in Figures 8.11 and 8.12, but are connected instead to both flanges of the foundation beam with flange attachment plates (as shown in Figure 8.12) to transfer moment from the side plates to the foundation beam. As previously mentioned, horizontally oriented gap elements are used to transfer the lateral forces from the half-rounds on the SC-CBF columns to the basement substructure; the basement substructure nodes of these elements are connected to the centerline of the side plate elements with rigid beam elements. In the laboratory, the side plates are connected to the ground links at the outer flange of the basement columns. A rigid beam element is used between the node for the ground link element and the centerline of the side plate elements.

The flange attachment plates (shown in Figure 8.12) transfer the moment between the foundation beam and the side plates. The flange attachment plates are modeled as horizontal springs that connect the side plate elements to the foundation beam flanges. These springs allow lateral forces to be transferred from the base of the SC-CBF columns to the side plates following either of two load paths: (1) through the flange attachment plates; or (2) through the foundation beam.

The side plates, the foundation beam, and the basement columns are modeled using fiber elements. The side plate element section properties are based on the dimensions of the

plates. As previously mentioned, the foundation beam is modeled in three segments: a rigid end segment, a short segment consisting of the foundation beam and side plates, and the W36x230 beam itself. Figure 8.13 shows a section through the foundation beam and side plates; this cross-section is used to determine the fiber element properties for this segment. The fiber element section properties for the W36x230 are based on the nominal dimensions of the section (AISC 2005c). The fiber element section properties for the basement columns are based on the nominal dimensions of the W8x67 section (AISC 2005c). P-Δ effects were considered in the elements used to model the basement substructure.

The reaction points at the base of the basement substructure and the ground links are modeled using zero-length spring elements. The stiffnesses of these springs were determined from correlation of experimental and analytical static loading results. Lateral forces were applied at each floor level and the displacements of the basement substructure in the analytical model were compared to the measured basement substructure displacements in the laboratory as follows.

Figures 8.17 through 8.20 show the vertical displacement of the foundation beam (measured at the stiffeners below (i.e., just beneath) the SC-CBF columns) at the south and north ends versus roof the displacement under the application of lateral force at each floor. It was desirable to match the behavior at larger values of overturning moment; therefore, correlation with the results from applying loads at the third and fourth floor levels was considered to be more important than correlation with the first and second floor applied loads.

Figures 8.21 through 8.24 show the ground link force-deformation behavior. The experimental behavior of the ground links is nearly linear, without any nonlinearities due to tolerances in the clevis pins because the ground links were precompressed to 300 kip in compression. The experimental behavior does show a small level of hysteresis due to friction in the ground link clevises. In the analytical model, the ground links were modeled as simple linear elastic springs. Correlation is strong regardless of which floor was loaded because the lateral displacement of the basement substructure is related to the base shear, not the applied overturning moment.

The weight of the basement substructure does not affect the response of the SC-CBF; therefore, these gravity loads are neglected in the model.

8.4.5 Model for PT Bars

The PT bars in the analytical model are modeled as bilinear yielding beam-column elements with negligible flexural stiffness. The yield stress of the PT bars was the average yield force of the bars determined from tension tests (Gonner et al. 2010) divided by the nominal bar area. The stiffness of the PT bar elements (104 kip/in) was determined based on the nominal area of the PT bars, the modulus of elasticity of the PT bars (29700 ksi), and the length of the PT bars. The actual PT bars, due to their unsupported length, are incapable of resisting compressive forces without buckling (elastically). To model this behavior, tension-only zero-length springs are located in series with the PT bar elements. The stiffness of these springs is equal to 29700 kip/in. This permits the PT bar elements to yield and captures the loss of PT force due to yielding.

In the analytical model, a single PT bar element is used to model each pair of PT bars at the south, center, and north PT bar locations. Therefore, three PT bar elements are used to model the six PT bars in the SC-CBF test structure.

8.4.6 Model for Loading Beams

The loading beams are modeled using beam-column elements joining the gravity column nodes at each floor level. The stiffnesses of the loading beams were determined from loading each floor in tension and determining the actuator force and the relative displacement of the two gravity columns. The results of these tests are shown in Figures 8.25 through 8.28. Note that the stiffnesses determined from these tests account for the loading beams as well as the connecting material at each end (i.e., the spreader beam at the south gravity column and the actuator plate at the north gravity column).

The self-weight of the loading beams is divided evenly between the two adjacent gravity columns, and the actuator self-weight is applied only to the north gravity column. These differences are reflected in the data presented in Table 8.7.

8.4.7 Lateral-Load Bearings

The elements used to model the lateral-load bearings at each floor level are horizontally oriented gap-friction elements like those discussed in Section 8.4.2. The lateral-load bearing elements transfer the inertia forces from the gravity columns to the SC-CBF columns, and the friction developed during compression provides energy dissipation. As mentioned in Section 8.3.1.6, the lateral-load bearings consist of a steel bearing and a

brass friction plate; the coefficient of friction used for steel-on-brass was 0.45 (Petty 1999).

Initial gaps are input to the lateral-load bearing elements to model the gaps at the lateral-load bearings in the test structure.

8.4.8 Model for Lean-On Column

As with the gravity columns, the lean-on column is modeled using a single element for each story. Nodes are located at the same elevation as the floor levels. The lean-on column section properties are determined by combining the section properties of the gravity columns included in the tributary area for one SC-CBF in the prototype building, as discussed previously in Section 8.3.2.1 for the analytical substructure for the hybrid simulations.

8.4.9 Damping Substructure Model

Rayleigh damping was used for the experimental hybrid simulations, as discussed in Section 8.3.2.3. The damping ratios were 2.6% for the first mode, 4.8% for the second mode, 6.1% for the third mode, and 6.9% for the fourth mode.

OpenSEES (Mazzoni et al. 2009) allows the use of Rayleigh damping with a damping factor a_0 applied to the mass matrix and a damping factor a_1 applied to the stiffness matrix on an element-by-element basis. Due to the expected large relative velocities in certain elements of the SC-CBF system (e.g., in the gap elements at the base of the SC-CBF columns and in the PT bars), applying the damping factor a_1 to each element of the

system opened the possibility of unrealistically large damping forces in certain elements. Therefore, Rayleigh damping was implemented using a special substructure called a "damping substructure," placed in parallel with the model of the SC-CBF test structure, and connected to the nodes of the lean-on columns. Figure 8.29 shows the four sub-substructures that comprise the damping substructure.

To determine the properties of the damping substructure, a damping matrix $[\bar{c}]$ was calculated assuming Rayleigh damping. The Rayleigh damping matrix for a four-degree-of-freedom structure is written as (Chopra 2007):

$$[\bar{c}] = a_0[m] + a_1[k] = \begin{bmatrix} \bar{c}_{11} & \bar{c}_{12} & \bar{c}_{13} & \bar{c}_{14} \\ \bar{c}_{21} & \bar{c}_{22} & \bar{c}_{23} & \bar{c}_{24} \\ \bar{c}_{31} & \bar{c}_{32} & \bar{c}_{33} & \bar{c}_{34} \\ \bar{c}_{41} & \bar{c}_{42} & \bar{c}_{43} & \bar{c}_{44} \end{bmatrix} \tag{8.1}$$

where,

$[m]$ = matrix of seismic masses within the tributary area for one SC-CBF

$[k]$ = stiffness matrix of SC-CBF

To input this $[\bar{c}]$ matrix in the model, four parallel damping sub-substructures were connected to the lean-on column as shown in Figure 8.29. The damping coefficients, $\bar{c}_{ij}$, shown in Equation 8.1 can be written in terms of the coefficients for the dashpots of the damping sub-substructures, c_{ij}, shown in Figure 8.29 as follows:

$$[\bar{c}] = \begin{bmatrix} c_{11}+c_{12}+c_{13}+c_{14} & -c_{12} & -c_{13} & -c_{14} \\ -c_{12} & c_{12}+c_{22}+c_{23}+c_{24} & -c_{23} & -c_{24} \\ -c_{13} & -c_{23} & c_{13}+c_{23}+c_{33}+c_{34} & -c_{34} \\ -c_{14} & -c_{24} & -c_{34} & c_{14}+c_{24}+c_{34}+c_{44} \end{bmatrix} \quad (8.2)$$

The values of the dashpot coefficients associated with the off-diagonal terms are determined from Equations 8.1 and 8.2 as follows:

$$c_{in} = -\bar{c}_{in}, \text{ for } n > i \quad (8.3)$$

Note that the minus sign is used so that the coefficients for most of the dashpots are positive. For cases where an off-diagonal term in $[\bar{c}]$ is positive, the dashpot coefficient in the damping sub-substructure will be negative. The remaining coefficients associated with the diagonal terms can be determined from Equations 8.1 and 8.2 as follows:

$$c_{ii} = \bar{c}_{ii} - \sum_{n \neq i} c_{in} \quad (8.4)$$

8.4.10 Model for SC-CBF Restoring Forces

In the hybrid simulations, the restoring forces in the experimental substructure, which represent the resistance of the SC-CBF to lateral forces, are measured using the load cells in the actuators. To enable comparisons between the measured restoring forces from the experimental substructure in the hybrid simulations and the corresponding restoring forces in the analytical model of the SC-CBF test structure, zero-length spring elements were placed between the north gravity column and the lean-on column. These spring elements were used to determine the restoring forces in the analytical model, and were

made stiff to maintain nearly equal displacements between the north gravity column DOFs and the lean-on column DOFs.

8.5 Response Quantities for Correlation

To determine the correlation of the analytical model with the experimental data, it is necessary to select measurements that will be used to quantify the response of the structure. The selected response quantities, and the techniques used to measure them in the laboratory and to determine them from the model, are discussed here.

8.5.1 Floor Displacements

The floor displacements are a measure of the global response of the SC-CBF system. To maintain consistency between measurements from the test structure and results from the analytical model, and to account for lateral gaps at the lateral-load bearings between the gravity columns and the SC-CBF columns, the floor-level displacements of the north gravity column are considered to be the floor displacements. Due to physical constraints, two displacements are measured in the laboratory, one above the actuator attachment and one below; these displacements are averaged to determine the actual floor displacement (Gonner et al. 2010). In the model, however, the displacements of the gravity column nodes at each floor level are directly output by the OpenSEES program (Mazzoni et al. 2009).

8.5.2 Column Base Gap-Opening Displacements

Column base gap opening is an important feature of SC-CBF response. In the laboratory, two measurements are necessary to determine the gap opening displacement. One measurement on the east side and one measurement on the west side of the web of the SC-CBF column. These results are averaged. The two measurements are taken along the centerline of the column. In the analytical model, the column base gap is located at the outer flange of the SC-CBF column, as this is the point on the compression column about which the frame is expected to rock. The column base gap-opening displacements are determined directly from the deformation of these gap-friction elements.

8.5.3 PT Bar Forces

The initial PT bar forces are an important aspect of the initial conditions of the SC-CBF. Yielding of the PT bars is an important limit state. In the laboratory, the force in each of the six PT bars is directly measured by a load cell. In the analytical model, as discussed earlier, only three elements are used to model the PT bars. Therefore, the loads from the two bars located at each PT bar location (i.e., south, center, or north) are added together to compare with the results of the analytical model.

8.5.4 SC-CBF Restoring Forces

The restoring forces of the SC-CBF are the lateral forces resisted by the SC-CBF and adjacent gravity columns. These forces are used to determine the applied base shear and the applied overturning moment. As noted previously, in the laboratory, the applied forces are determined from the load cells in the actuators, whereas the restoring forces

from the analytical model are determined from the forces in the stiff springs between the north gravity column and the lean-on column.

The applied base shear is taken as the summation of the applied forces. To determine the applied overturning moment, each force is multiplied by its height above the base of the SC-CBF (i.e. the top of steel of the foundation beam).

8.5.5 Effective Modal Pseudo-Accelerations α_n

$\alpha_n(t)$, as defined in Chapter 6, is derived from the restoring force vector. In the laboratory, the hybrid simulation method determines the restoring force vector for the entire structure by adding the restoring force vectors from the analytical substructure and the experimental substructure. The total restoring force vector for the analytical model is determined from restoring forces at the lumped masses at the lean-on column nodes.

8.5.6 Brace Axial Forces

The primary member force of concern is the axial force in the braces. This axial force response is measured in the laboratory using a full bridge arrangement of strain gauges. In the analytical model, the axial forces in the members are determined from the element internal force output.

8.6 Dynamic Properties of SC-CBF Test Structure

The best measure of the accuracy of the analytical model is a direct comparison of responses. To determine the accuracy of the analytical model with respect to the SC-CBF test structure, a series of static "unit force" tests of the SC-CBF experimental substructure

was conducted in the laboratory. In each test, a single lateral force was applied at a selected floor level. By normalizing the displacement by the change in applied force over a range of response, the displacement profile under a unit force at each floor level was determined.

Similarly, the analytical model was subjected to the same series of static loads. For these analyses, the lean-on column was assumed to have negligible stiffness and no vertical loads were applied to the lean-on column, to simulate the conditions of the SC-CBF experimental substructure in the laboratory. For both the laboratory and the analytical model, static forces were applied in the south direction and the north direction as separate load cases; the results presented here (and used for the hybrid simulations) considered only the loading to the north. Due to the flexibility of the loading beams, the stiffness matrix of the SC-CBF test structure is a function of the direction of loading.

The results of these "unit force" tests are shown in Figures 8.30 through 8.45. The response to a force applied at the first floor level is shown in Figures 8.30 though 8.33. Figures 8.34 through 8.37 show the response to a force applied at the second floor level. The response to a force applied at the third floor level is shown in Figures 8.38 through 8.41. Figures 8.42 through 8.45 show the response to a force applied at the fourth floor level.

These figures compare the results of the laboratory tests to those of the analytical model. A trendline is drawn on the data over a range of linear response. The slope of the trendline represents the flexibility coefficient for the degrees of freedom indicated on the

abscissa and the ordinate of each plot. Once the flexibility matrix is obtained from these coefficients, it is inverted to calculate the stiffness matrix. The slopes of the data from the laboratory tests are used to determine the stiffness matrix of the SC-CBF test structure. The slopes of the data from the analytical model are used to determine the stiffness matrix of the analytical model. The stiffness matrices for the test structure and the analytical model are shown in Tables 8.10 and 8.11, respectively. There is some variation from symmetry of the off-diagonal terms due to the nonlinearity of the system – as the force is applied at different floor levels, the lateral gaps open and close differently. The stiffness matrices shown in Tables 8.10 and 8.11 are symmetric; the off-diagonal terms were averaged to obtain symmetric stiffness matrices.

The natural periods of the SC-CBF test structure can be determined from the system stiffness matrix and the mass matrix. The system stiffness matrix is determined by adding the elastic and geometric stiffness matrices for the lean-on column to the SC-CBF stiffness matrices presented in Tables 8.10 and 8.11. Table 8.12 shows the natural periods calculated based on the stiffness matrix for the experimental SC-CBF ($T_{n,E}$) and for the analytical model ($T_{n,M}$). There is a large difference in the first mode period; however, the higher mode periods are very close. The difference in the first mode period is likely due to differences in the contact conditions at the lateral-load bearings and the difference in the diagonal terms of the stiffness matrices shown in Tables 8.10 and 8.11 (e.g., the differences between the values of k_{33} and k_{44}).

The fourth column of Table 8.12 shows the periods used for the design of the SC-CBF test structure (i.e., the periods from the linear elastic analytical model for design

discussed in Section 6.1), $T_{n,d}$. The values of $T_{n,d}$ are significantly smaller than the values of $T_{n,E}$ or $T_{n,M}$; the linear elastic model has fixed-base columns, and is therefore stiffer than the test structure.

The fifth column of Table 8.12 shows the periods determined from an eigenvalue analysis of the OpenSEES model, $T_{n,OS}$. Due to the initial gaps at the lateral-load bearings and their effect on the initial stiffness of the model, the OpenSEES model was modified for this analysis. The lateral-load bearing elements were removed from the model, and the south gravity column nodes at each floor level were connected to the south SC-CBF column nodes at each floor level using rigid horizontal springs. $T_{1,OS}$ is between $T_{1,E}$ and $T_{1,M}$, suggesting that the contact conditions at the lateral-load bearings are significant when determining the fundamental period of the SC-CBF. The higher mode values of $T_{n,OS}$ are smaller than the higher mode values of $T_{n,E}$ or $T_{n,M}$. The rigid horizontal springs used to determine $T_{n,OS}$ provide both tensile and compressive resistance, while the lateral-load bearings only provide compressive resistance. This affects the periods of the higher modes.

Figures 8.46 through 8.49 compare the stiffness matrices of the SC-CBF test structure experimental substructure from the laboratory unit force testing and from the analytical model. The results are calculated by applying a 100 kip force at a given floor level and determining the corresponding displacements. These figures show that although the coefficients in the two stiffness matrices (Tables 8.10 and 8.11) seem to be very different and the first mode periods are different, the elastic displacements are similar for the SC-CBF test structure and the analytical model.

Table 8.1 – Dead loads at each floor level for SC-CBF test structure

Dead Load	Floor 1 (psf)	Floors 2-3 (psf)	Roof (psf)
Floor/roof slab	43	43	43
Floor/roof deck	3	3	3
Roofing material	0	0	10
Mechanical weight	10	10	25
Ceiling material	5	5	0
Floor finish	2	2	0
Steel fireproofing	2	2	2
Structural steel	15	15	15
Exterior wall (per sq. ft. of floor area)	7.9	6.9	5.1
Total	87.9	86.9	103.1

Table 8.2 – Live loads at each floor level for SC-CBF test structure

Live Load	Floors 1-3 (psf)	Roof (psf)
Office	50	0
Partitions	15	0
Roof live load	0	65

Table 8.3 – Summary of tributary seismic masses for SC-CBF test structure

Floor	Mass ($k\text{-}s^2/in$)
1	0.776
2	0.770
3	0.770
4	0.812

Table 8.4 – Summary of SC-CBF design iterations

Frame	Design Iteration	$W_{SC\text{-}CBF}$ (kip)	A_{PT} (in^2)	β_E [§] (%)	$\beta_{E,D}$ [◊] (%)	*Total ED Force* [†] (kip)	OM_{ED} *at decom-pression* [‡] (kip·ft)	OM_D (kip·ft)	OM_Y (kip·ft)
D_{DIST} [*]	1	15.80	3.16	45.0	45.0	73.5	1323	2940	4286
	2	15.80	5.00	45.0	45.0	87.2	1570	3488	6188
	3	13.64	5.00	45.0	45.0	87.2	1570	3459	6172
	4	13.64	5.10	45.0	45.0	88.1	1586	3524	6278
	5	14.88	5.10	45.0	45.0	88.1	1586	3541	6287
	6	14.88	5.10	48.5	48.5	88.5	1593	3783	6295
D_{DIST} [**]	1	15.80	3.16	45.0	45.0	73.5	1323	2940	4286
	2	15.80	5.00	45.0	45.0	87.2	1570	3488	6188
	3	13.64	5.00	45.0	45.0	87.2	1570	3459	6172
	4	13.64	5.10	45.0	45.0	88.1	1586	3524	6278
	5	14.88	5.10	45.0	45.0	88.1	1586	3541	6287
	6	14.88	5.10	48.5	48.5	88.5	1593	3783	6295
D_{DF} [**]	1	15.80	3.16	42.4	30.0	59.4	980	2309	4230
	2	15.80	5.00	51.1	30.0	84.8	1399	2739	6595
	3	13.64	5.00	51.2	30.0	84.4	1392	2716	6572
	4	13.64	5.10	51.3	30.0	86.0	1419	2768	6700
	5	14.88	5.10	51.4	30.1	86.8	1433	2787	6728
	6	14.88	5.10	51.4	30.1	86.9	1433	2787	6728

[*] – Designed by Gonner (2009)

[**] – Designed according to design procedure presented in Chapter 7

§ – Determined from Equation 5.16 for Frame D_{DIST} and Equation 5.28 for Frame D_{DF}

◊ – Determined from Equation 5.16 for Frame D_{DIST} and Equation 5.31 for Frame D_{DF}

† – Equals the specified value of V_{ED} for Frame D_{DIST}, and equals ($F_{ED,D}$ + $F_{ED,Y}$)/2 for Frame D_{DF}

‡ – OM_{ED} for Frame D_{DIST}, $OM_{ED,D}$ for Frame D_{DF}

Table 8.5 – Summary of SC-CBF design values for the PT bar yielding limit state

Frame	Design Iteration	*R value used to calculate* $\theta_{DBE,fdd}$ §	μ_{DBE}	$\theta_{DBE,fdd}$ (% rad)	$\theta_{Y,n}$ (% rad)	$P(\theta_{DBE} > \theta_{Y,n})$ (%)
D_{DIST}*	**1**	10.0	34.1	1.589	1.100	89.5
	3	8.5	22.8	1.511	1.427	57.7
	4	8.3	22.1	1.494	1.429	56.0
	5	8.3	22.5	1.443	1.423	51.9
	6	7.8	19.4	1.404	1.434	47.2
D_{DIST}**	**1**	8.2	25.4	1.137	1.097	54.8
	3	7.0	17.3	1.081	1.421	17.6
	4	6.9	16.8	1.069	1.423	16.5
	5	6.9	17.3	1.046	1.417	15.1
	6	6.9	15.2	0.921	1.414	7.2
D_{DF}**	**1**	10.5	38.5	1.345	1.096	75.7
	3	8.9	25.0	1.220	1.427	29.6
	4	8.8	24.2	1.205	1.430	28.0
	5	8.8	24.9	1.180	1.423	26.1
	6	8.8	24.4	1.156	1.423	23.9

* – Designed by Gonner (2009)

** – Designed according to design procedure presented in Chapter 7

§ – R_{actual} (Gonner 2009) for Frame D_{DIST}*, $R_{A,D}$ for Frames D_{DIST}** and D_{DF}**

Table 8.6 – Summary of SC-CBF design values for the member yielding limit state

Frame	Story	$F_{bri,fdd}$ (kip)	$F_{bri,n}$ (kip)	$F_{bri,n} / F_{bri,fdd}$
D_{DIST}*	1	384.9	520.1	1.35
	2	231.7	536.1	2.31
	3	376.0	536.1	1.43
	4	479.1	668.7	1.40
D_{DIST}**	1	384.9	520.1	1.35
	2	231.7	536.1	2.31
	3	376.0	536.1	1.43
	4	479.1	668.7	1.40
D_{DF}**	1	388.1	520.1	1.34
	2	239.8	536.1	2.24
	3	386.0	536.1	1.39
	4	471.8	668.7	1.42

* – Designed by Gonner (2009)

** – Designed according to design procedure presented in Chapter 7

Table 8.7 – Summary of dead loads for SC-CBF test structure

Floor	Lean-on Column (kip)	North Gravity Column (kip)	South Gravity Column (kip)	Total (kip)
1	290.71	9.75	3.43	303.89
2	288.47	9.65	3.33	301.45
3	288.47	9.65	3.33	301.45
4	305.18	9.28	2.96	317.42

Table 8.8 – Column properties

Column	A (in^2)	I_x (in^4)	I_y (in^4)	A_{vy} (in^2)	A_{vx} (in^2)
W8x35 (typical)	10.3	127.0	42.6	2.52	7.94
W8x67	19.7	N/A	88.6	N/A	15.48
Lean-on Column	124.38	876.80	N/A	N/A	74.10

N/A – Not applicable

Table 8.9 – Properties of gap elements in the analytical model

Location	Contact Stiffness (kip/in)	Friction Stiffness (kip/in)	Coefficient of Friction
1st floor lateral-load bearing	20000	10000	0.45
2nd floor lateral-load bearing	8000	10000	0.45
3rd floor lateral-load bearing	10000	10000	0.45
4th floor lateral-load bearing	5000	10000	0.45
Half-round at SC-CBF column base	10000	--	--
Vertical gap at SC-CBF column base	5000	10000	0.60

Table 8.10 – Stiffness matrix for SC-CBF test structure experimental substructure (kip/in), based on unit force loading in the laboratory (Chancellor et al. 2010)

DOF	1	2	3	4
1	1472.0	-656.8	-18.1	-56.2
2	-656.8	1598.2	-670.5	-49.1
3	-18.1	-670.5	1765.5	-857.2
4	-56.2	-49.1	-857.2	885.6

Table 8.11 – Stiffness matrix for analytical model of SC-CBF test structure experimental substructure (kip/in), based on unit force loading

DOF	1	2	3	4
1	1516.8	-667.7	13.1	-74.3
2	-667.7	1575.0	-759.2	12.3
3	13.1	-759.2	1614.6	-757.1
4	-74.3	12.3	-757.1	763.2

Table 8.12 – Estimated full-scale periods of SC-CBF test structure

Mode	$T_{n,E}$ (s)	$T_{n,M}$ (s)	$T_{n,d}$ (s)	$T_{n,OS}$ (s)
1	0.548	0.612	0.502	0.590
2	0.232	0.240	0.171	0.238
3	0.156	0.163	0.103	0.154
4	0.120	0.119	0.081	0.124

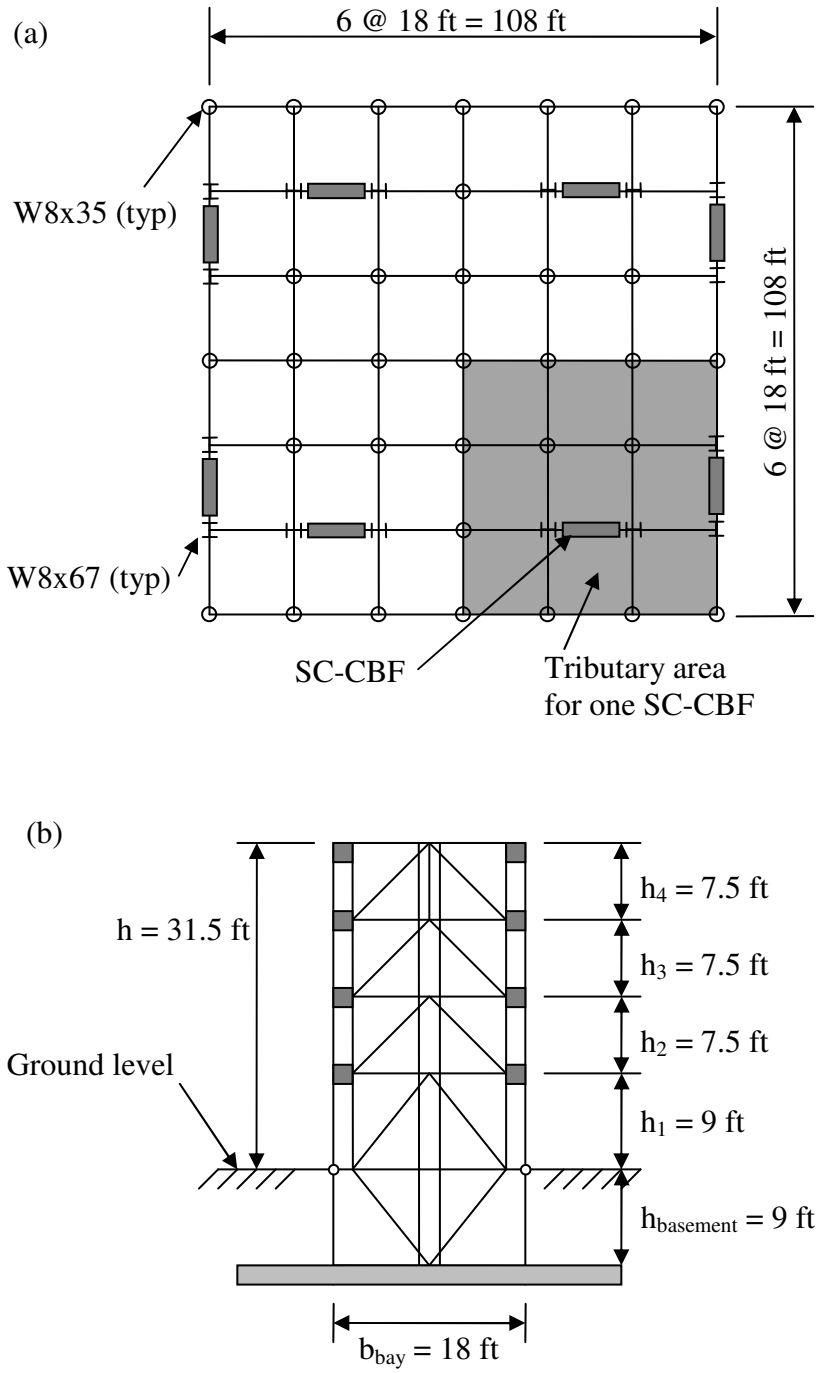

Figure 8.1 – Prototype building: (a) floor plan; (b) elevation of SC-CBF

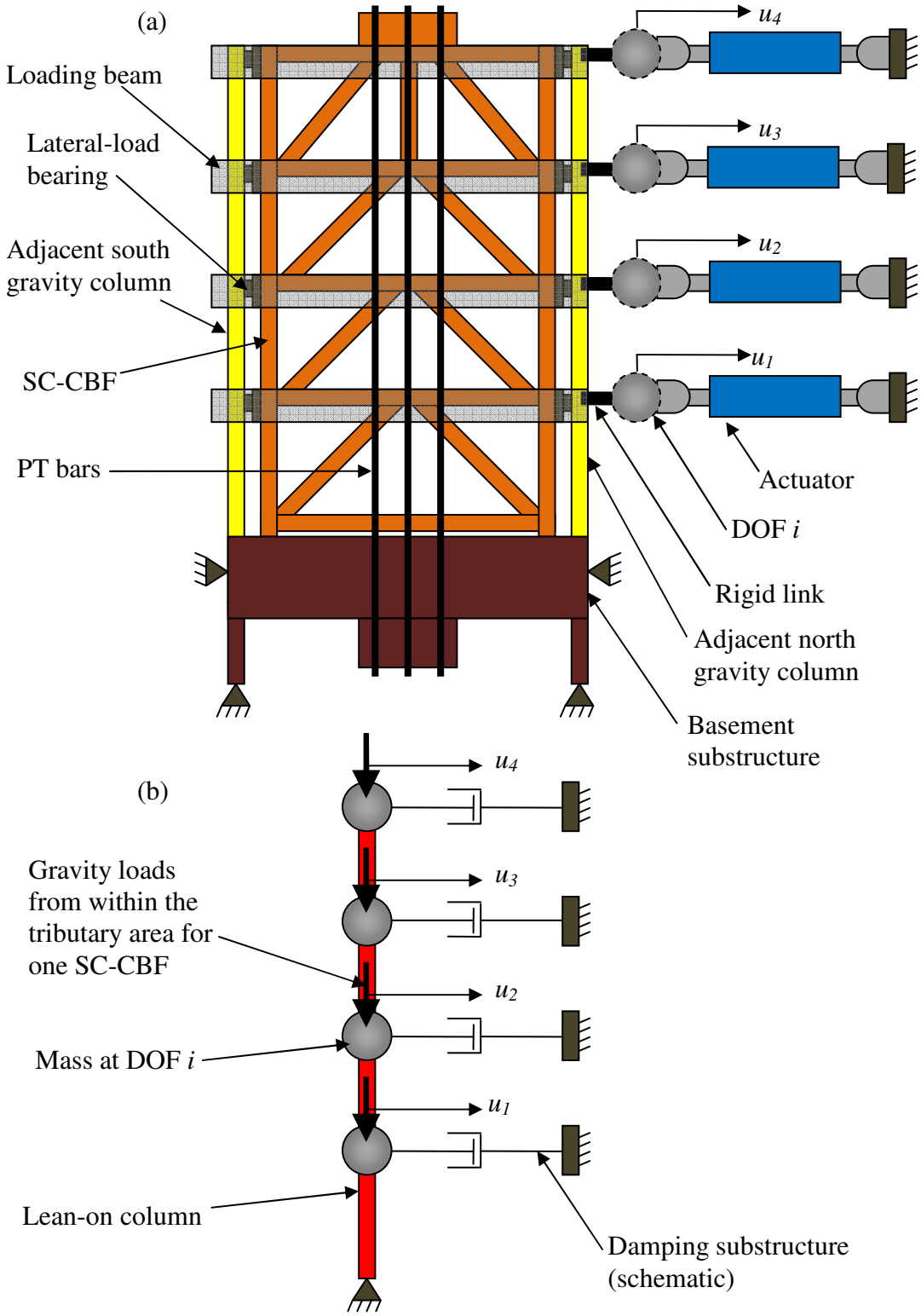

Figure 8.2: SC-CBF test structure: (a) experimental substructure; (b) analytical substructure

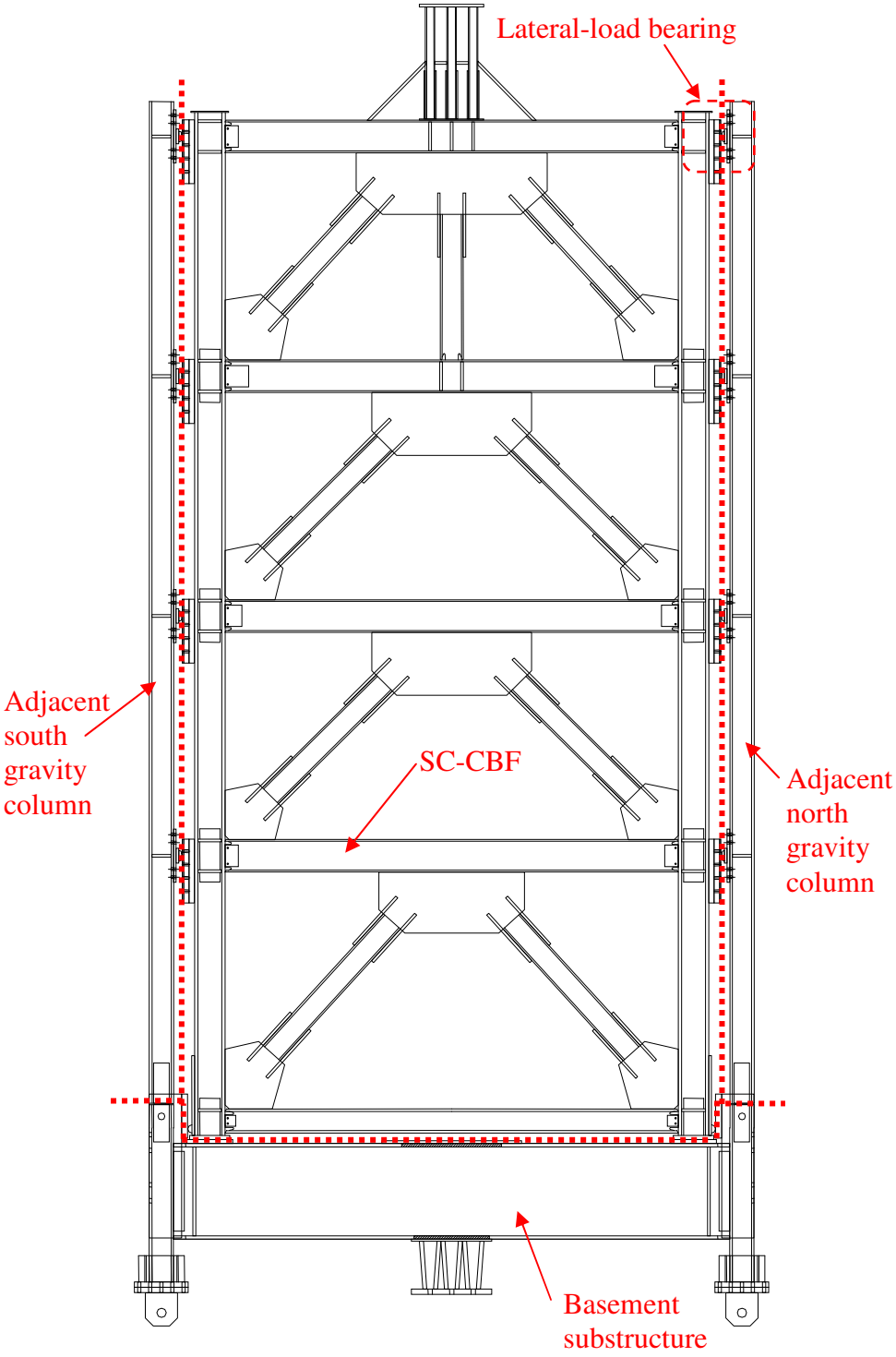

Figure 8.3 – Drawing of SC-CBF test structure, including basement substructure and adjacent gravity columns

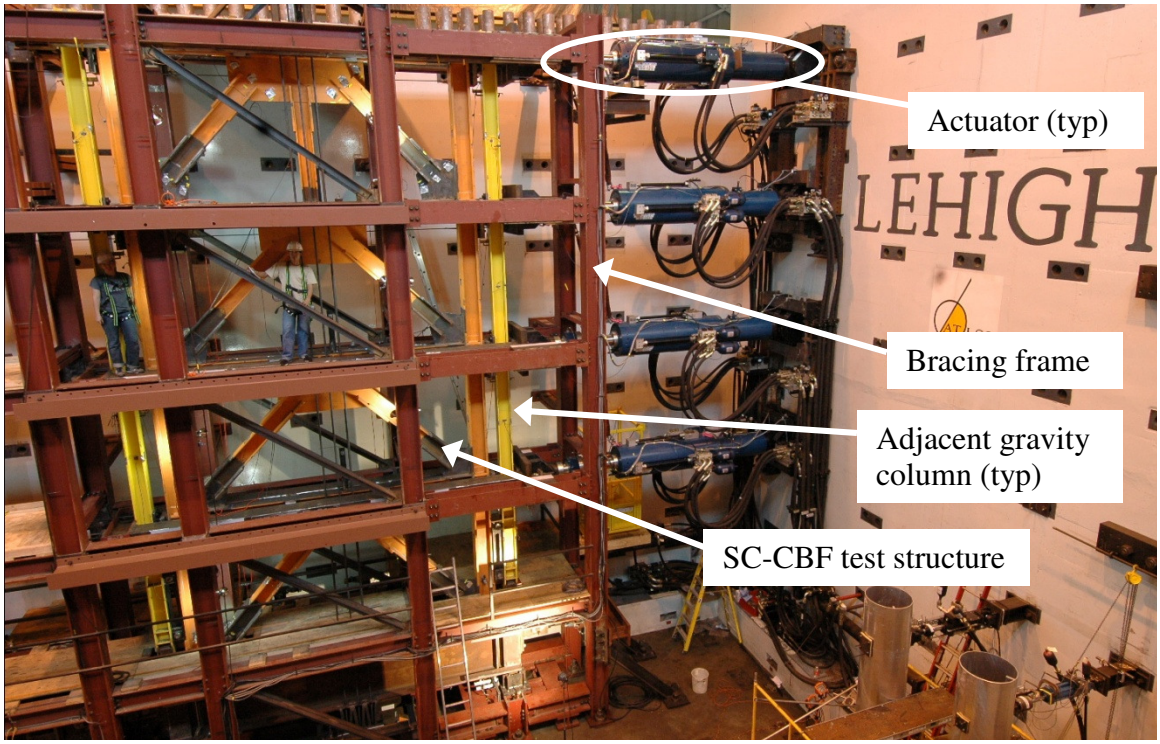

Figure 8.4 – Photograph of SC-CBF test structure

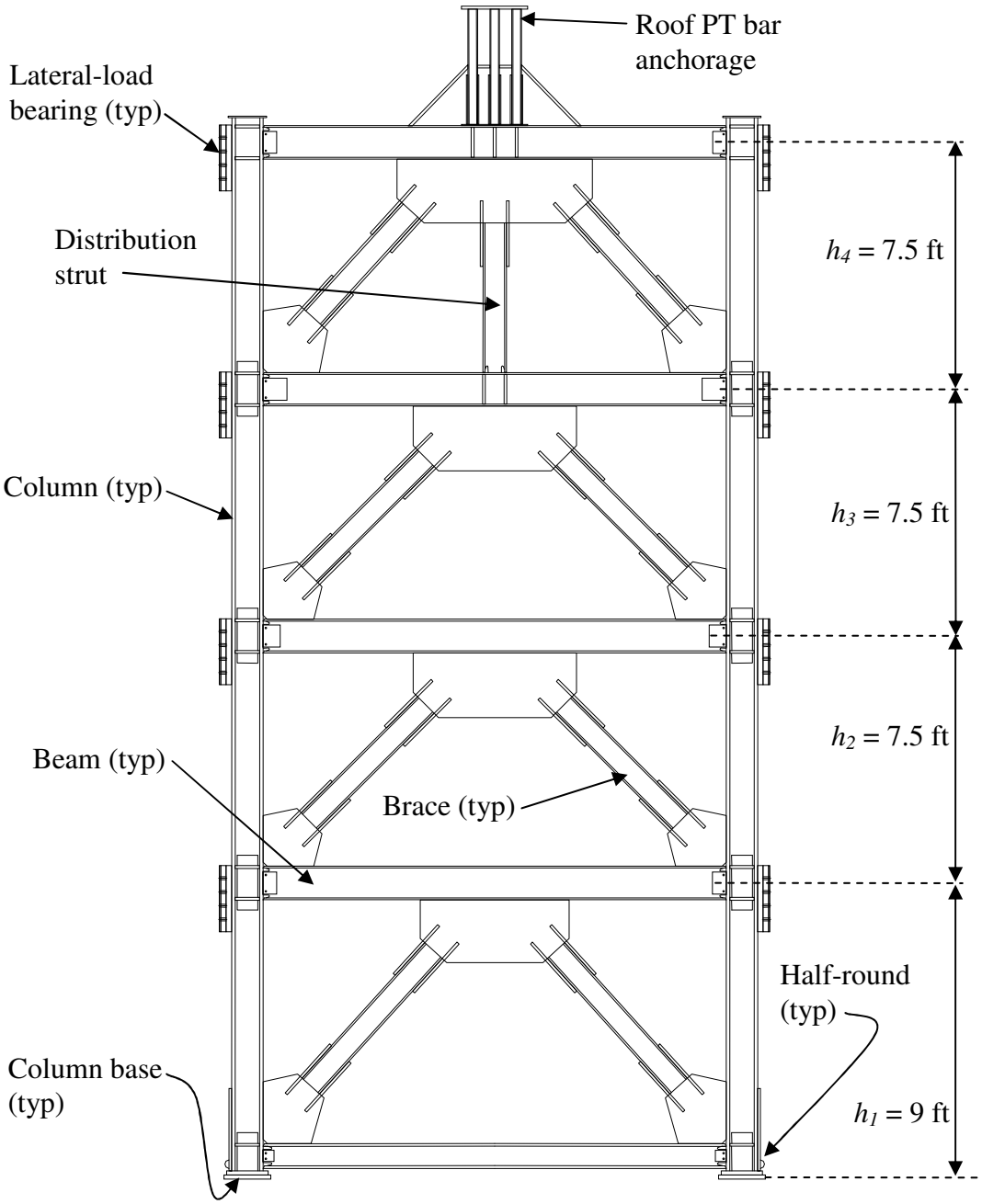

Figure 8.5 – Drawing of SC-CBF test structure

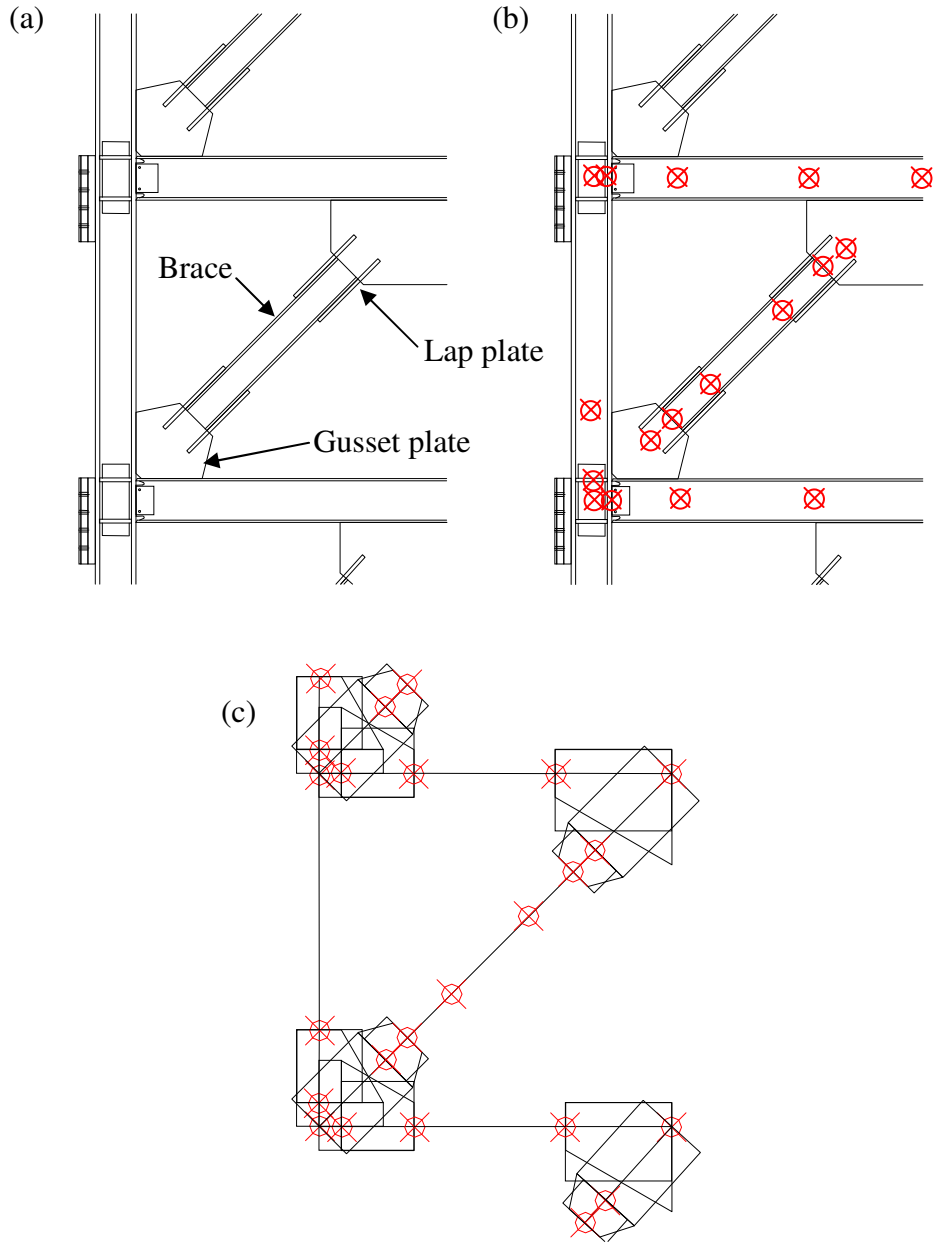

Figure 8.6 – Typical brace connection at SC-CBF column: (a) drawing; (b) drawing with nodes indicated; (c) model

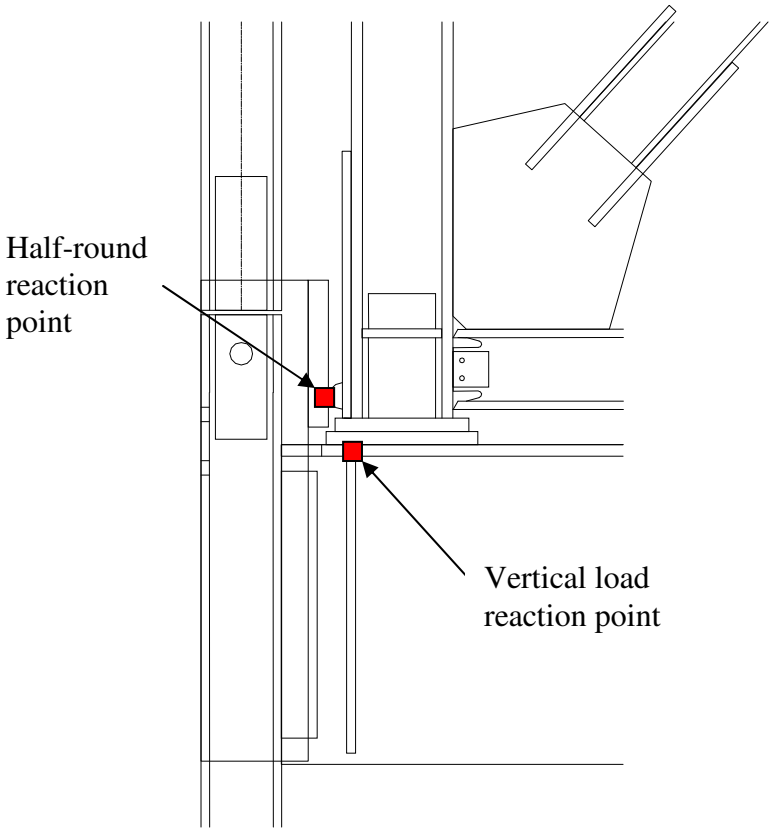

Figure 8.7 – Drawing of SC-CBF column base detail

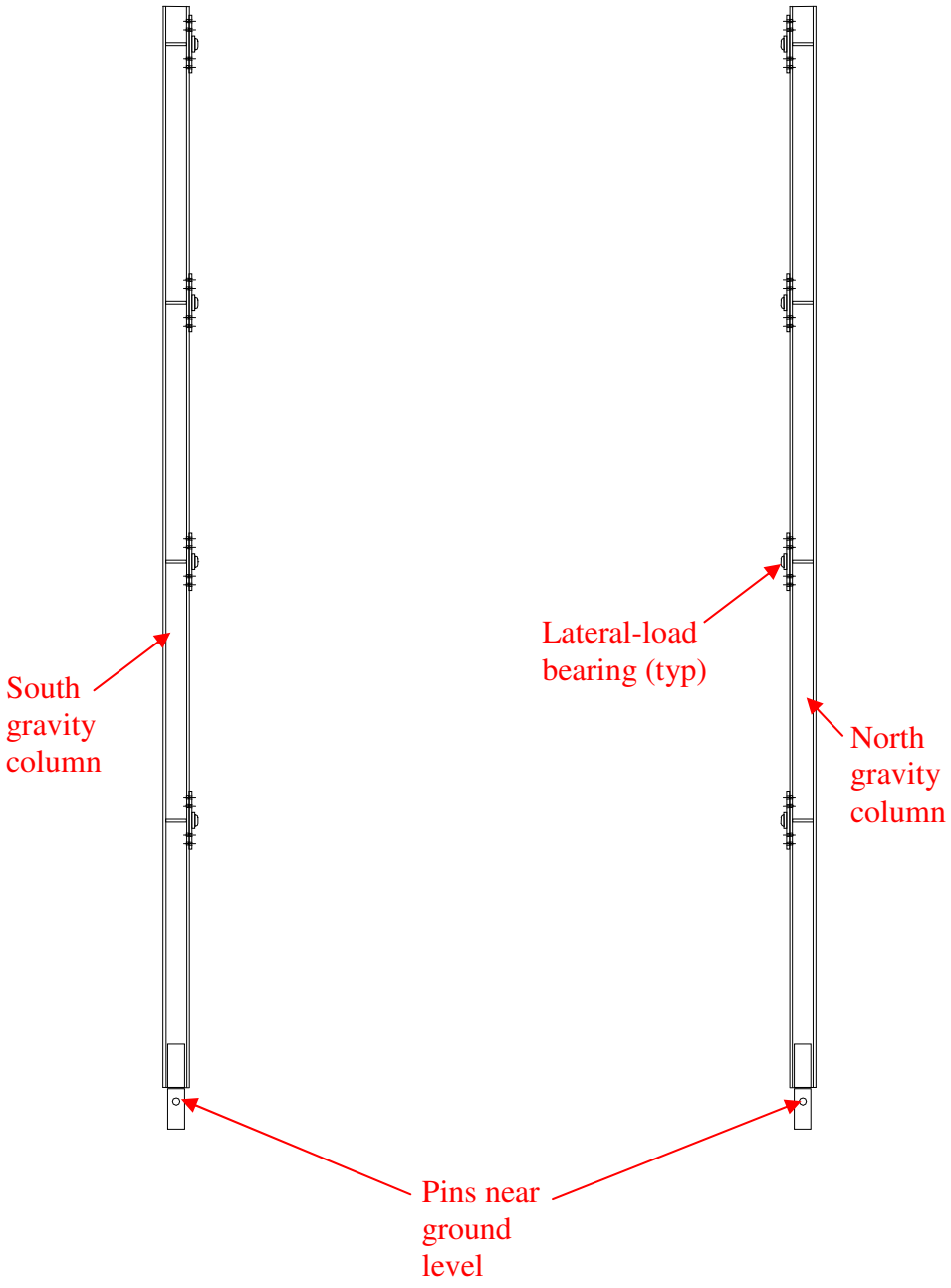

Figure 8.8 – Drawing of adjacent gravity columns for SC-CBF test structure

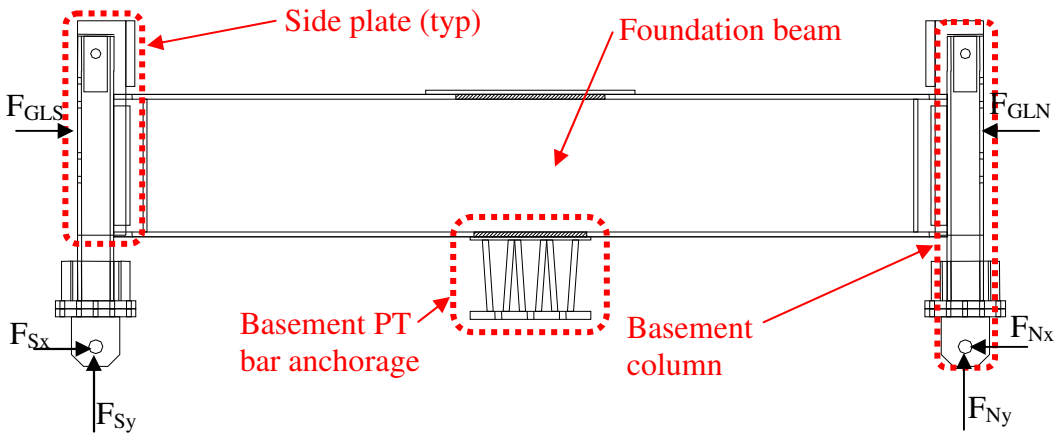

Figure 8.9 – Drawing of basement substructure of SC-CBF test structure

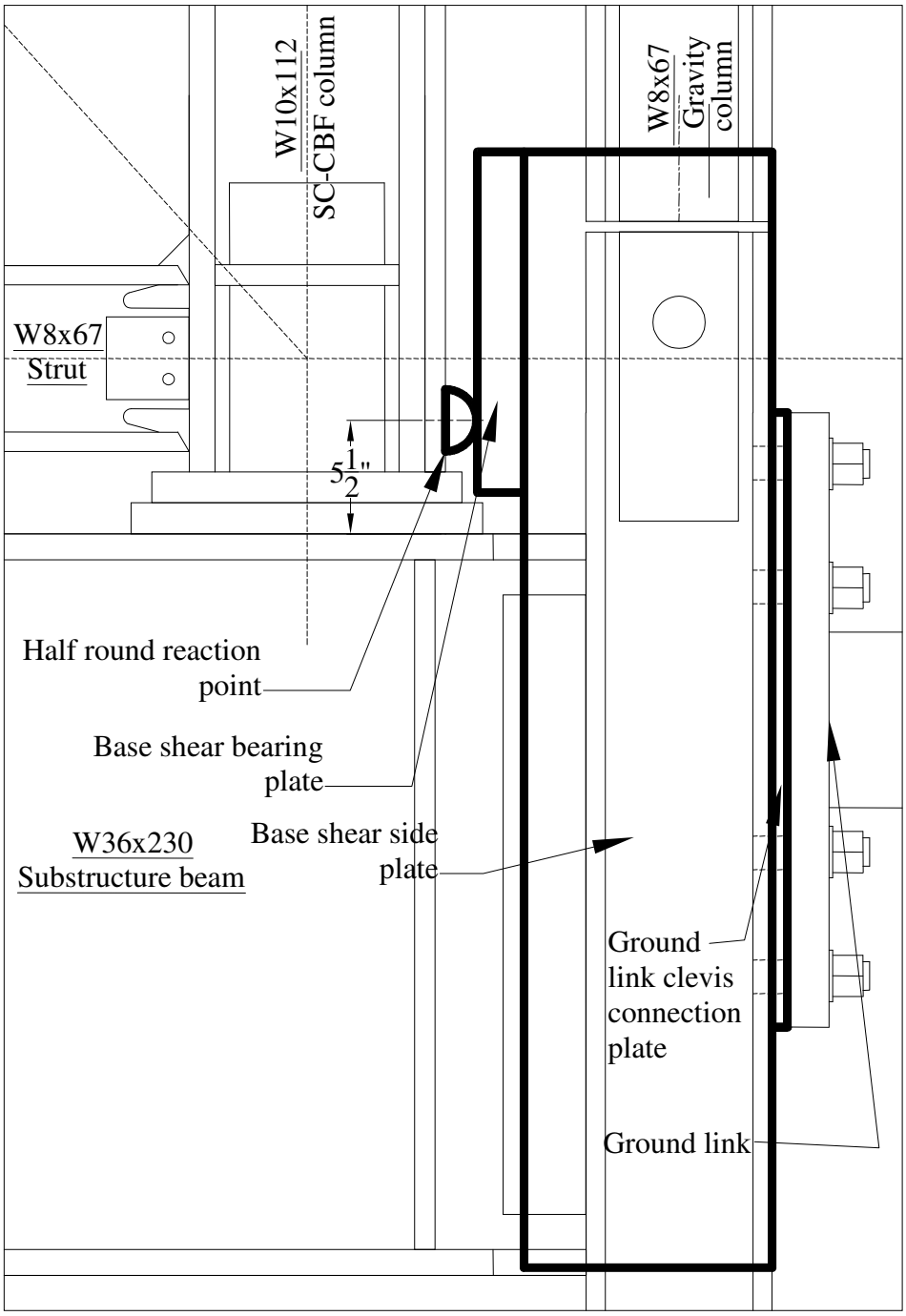

Figure 8.10 – Elevation view of half round reaction point at SC-CBF column base (Gonner et al. 2010)

Figure 8.11 – Base shear transmission assembly (Gonner et al. 2010)

Figure 8.12 – Substructure beam flange attachment plates (Gonner et al. 2010)

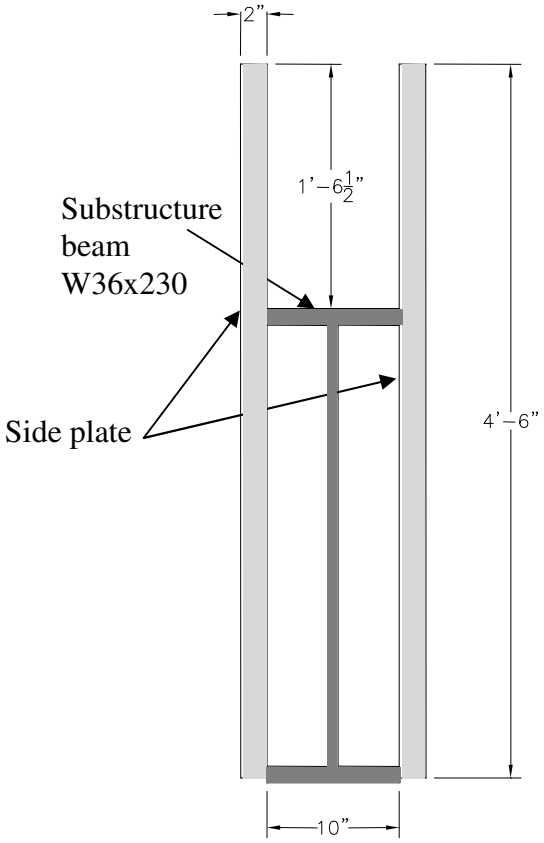

Figure 8.13 – Section through foundation beam and side plates (see Figure 8.12)

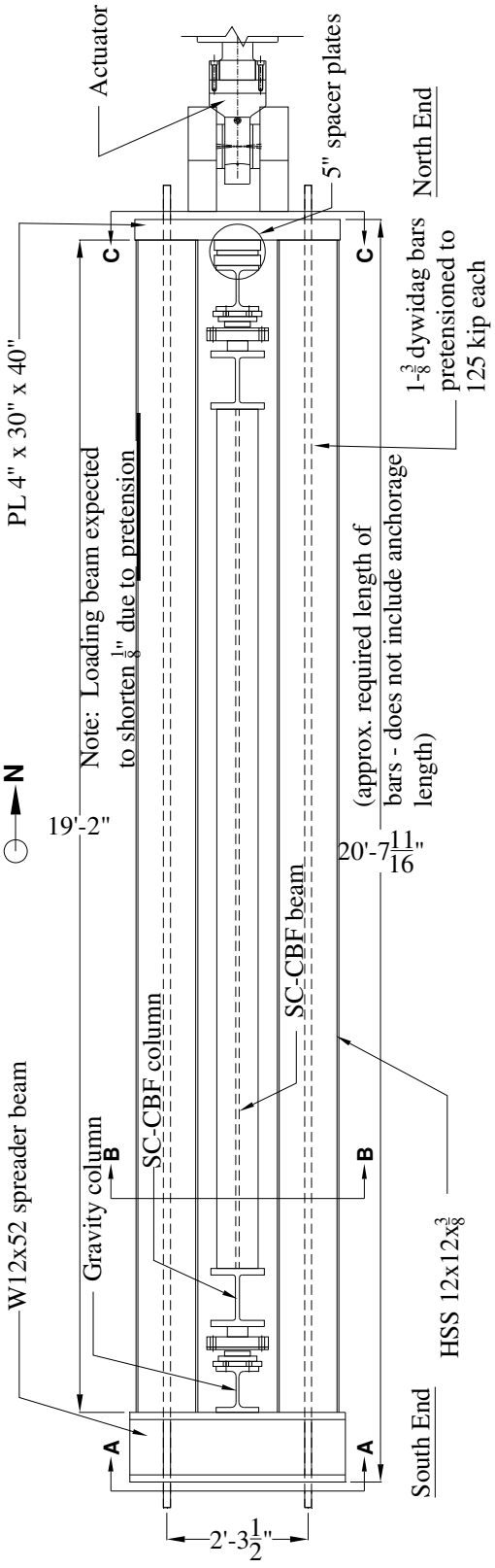

Figure 8.14 – Plan view of loading beam system (Gonner et al. 2010)

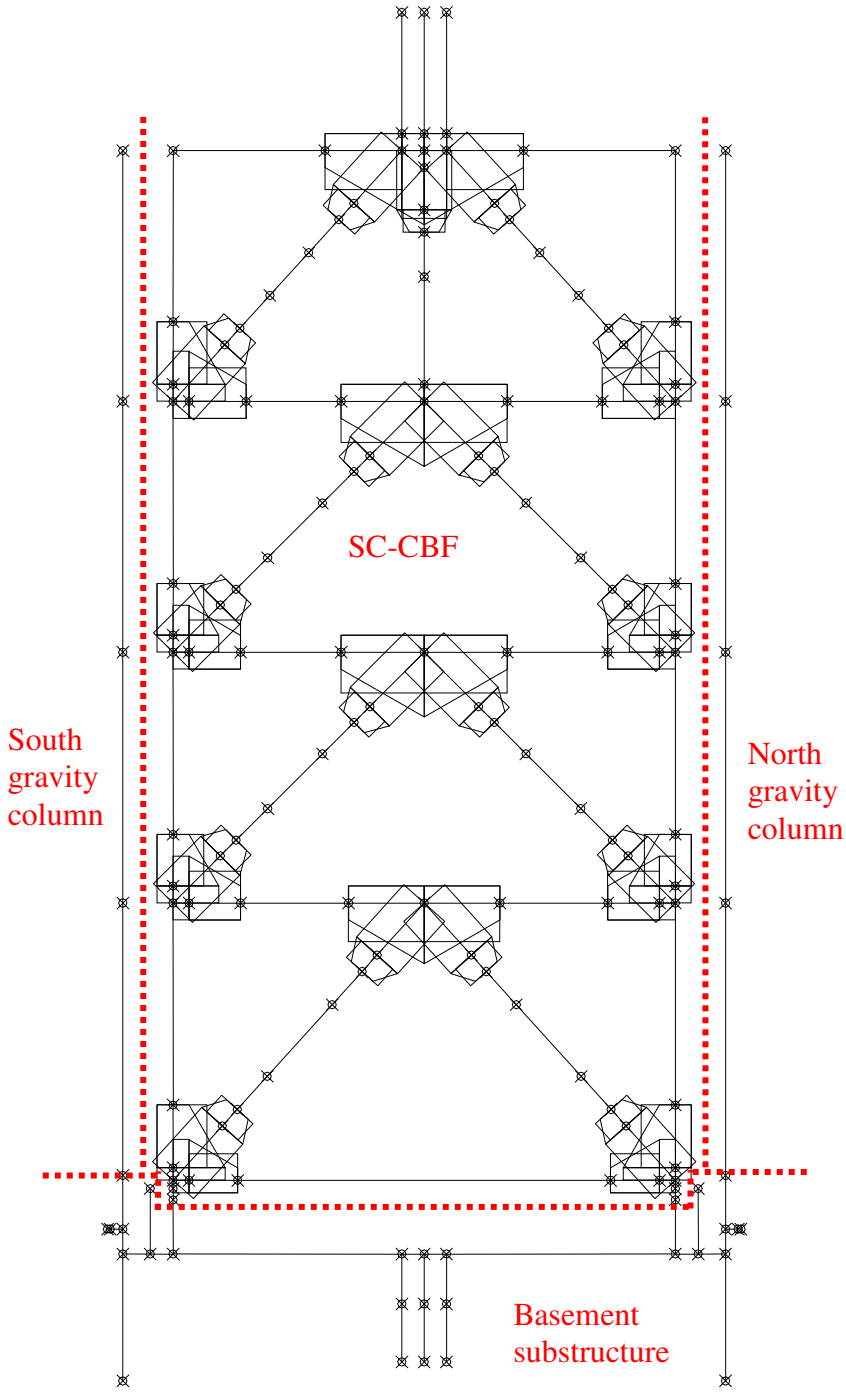

Figure 8.15 – Schematic of analytical model of SC-CBF test structure, including basement substructure and adjacent gravity columns

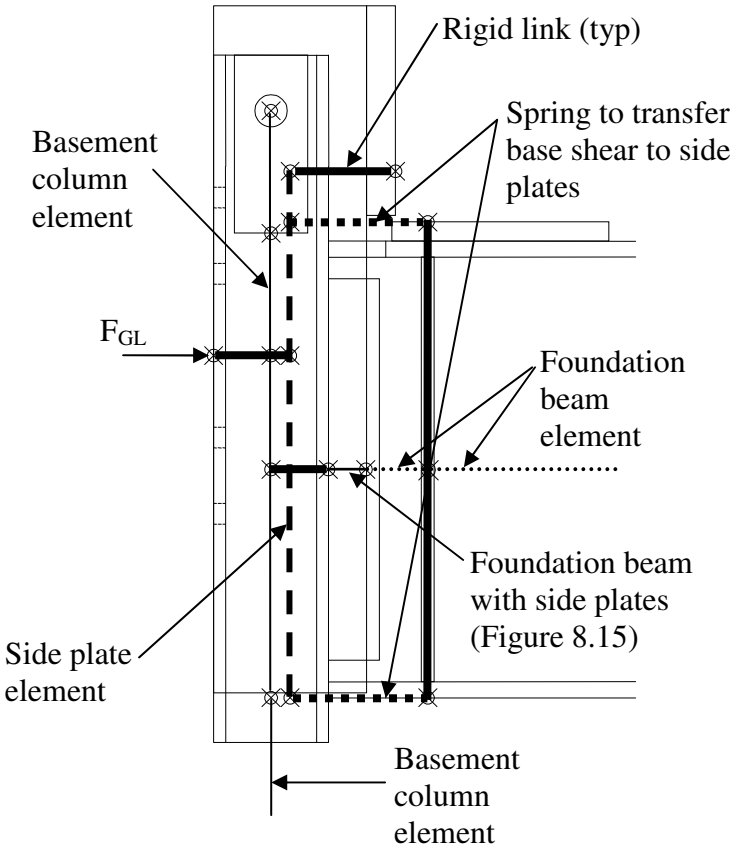

Figure 8.16 – Model of basement substructure

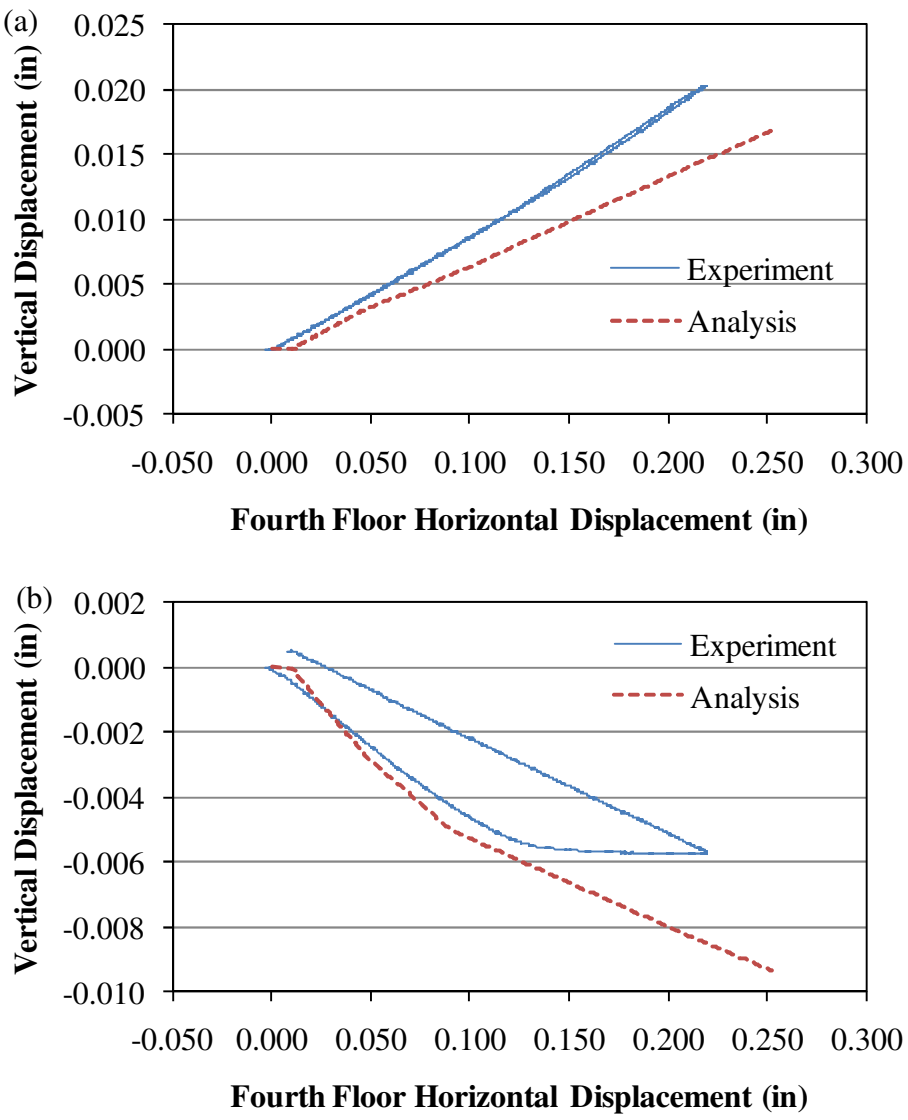

Figure 8.17 – Vertical displacement of foundation beam below SC-CBF columns for loading to the north at the first floor level: (a) below the south column; (b) below the north column

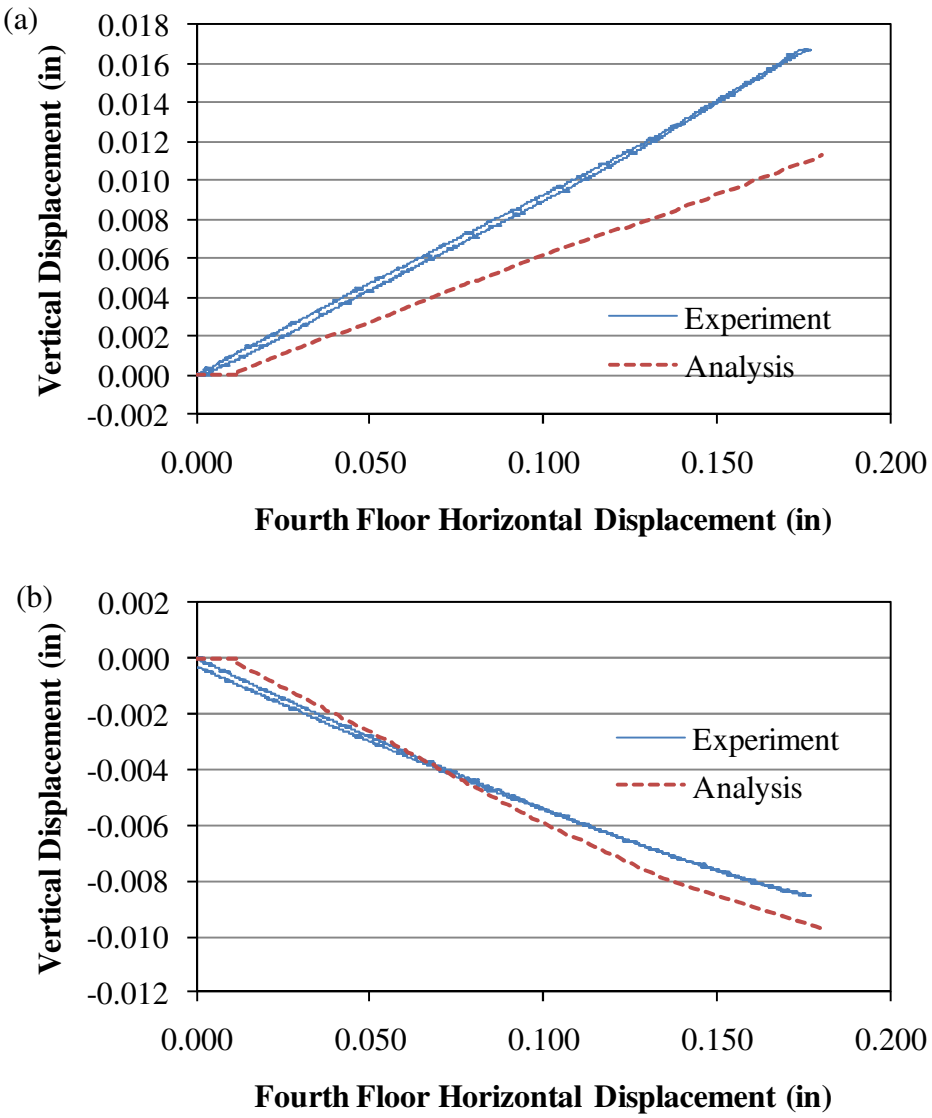

Figure 8.18 – Vertical displacement of foundation beam below SC-CBF columns for loading to the north at the second floor level: (a) below the south column; (b) below the north column

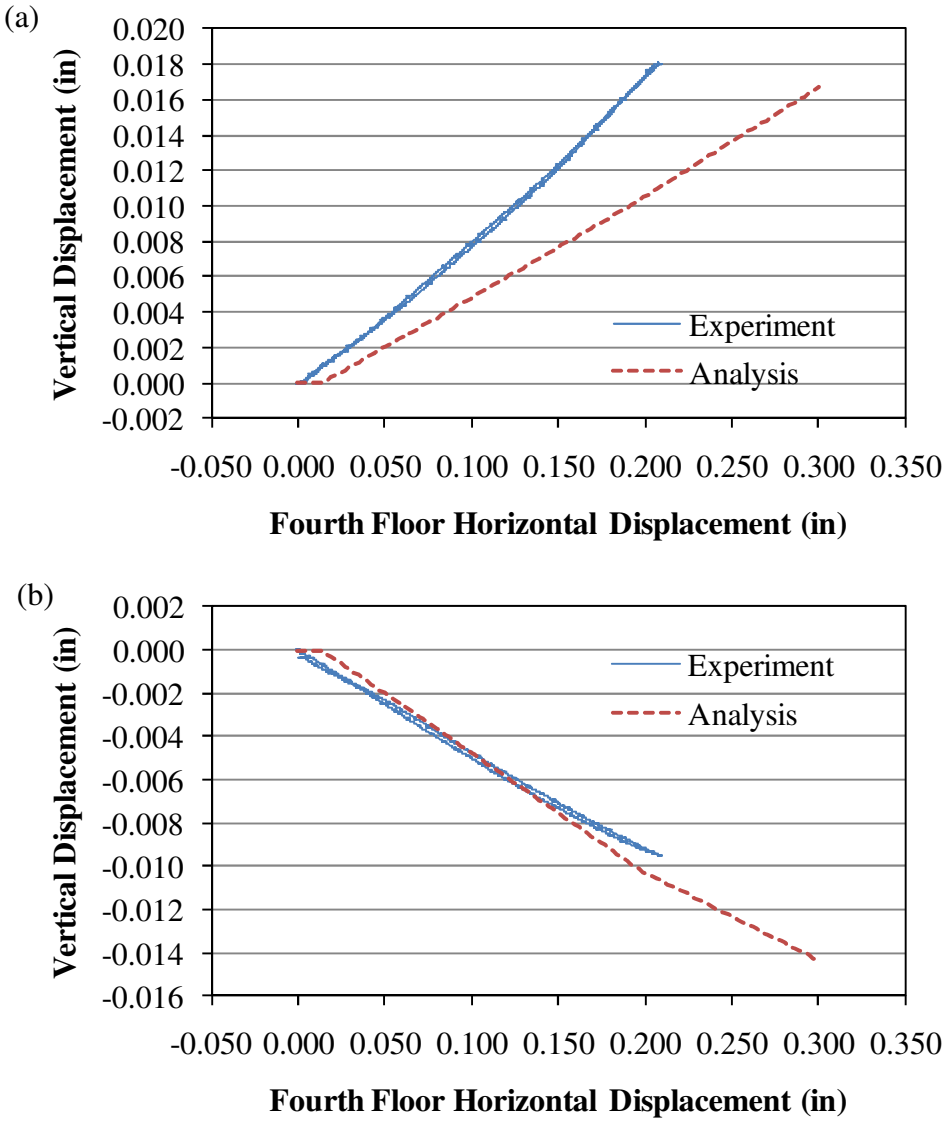

Figure 8.19 – Vertical displacement of foundation beam below SC-CBF columns for loading to the north at the third floor level: (a) below the south column; (b) below the north column

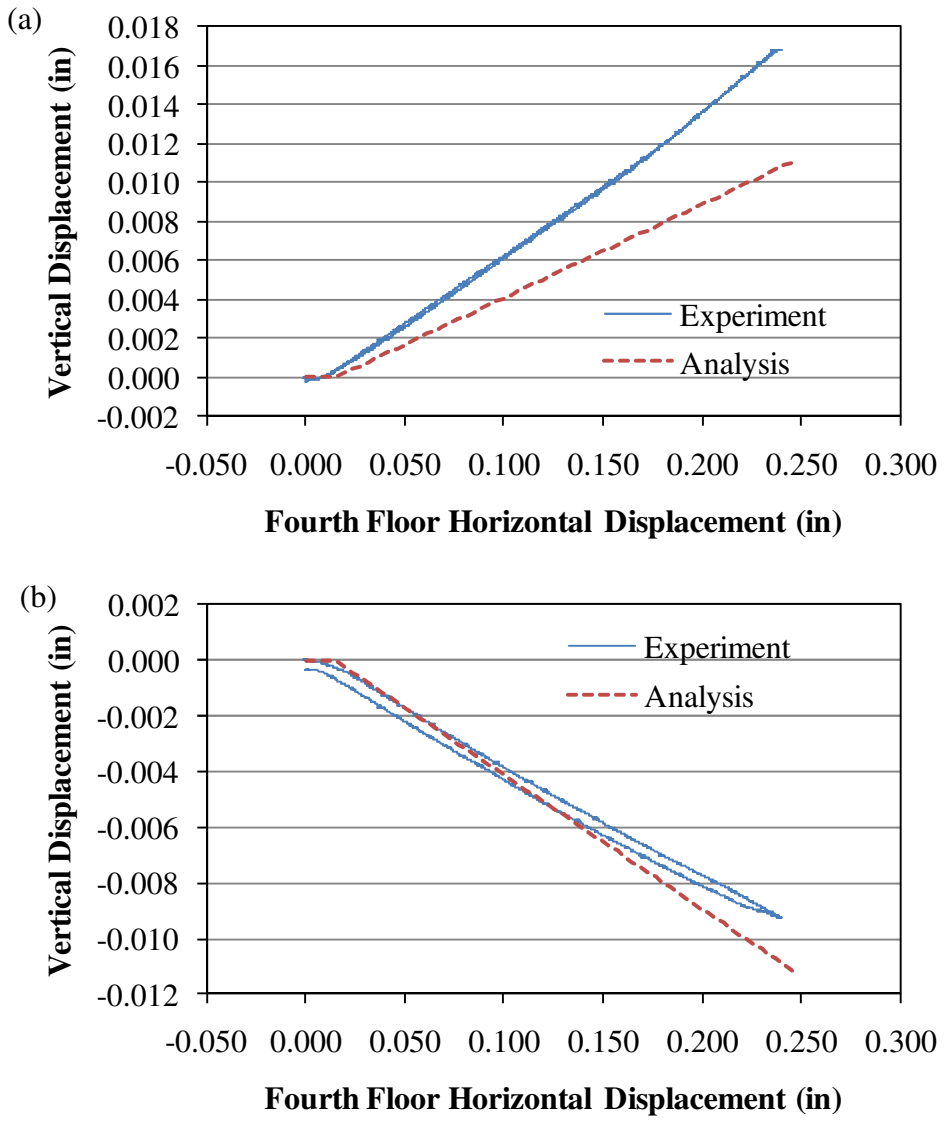

Figure 8.20 – Vertical displacement of foundation beam below SC-CBF columns for loading to the north at the fourth floor level: (a) below the south column; (b) below the north column

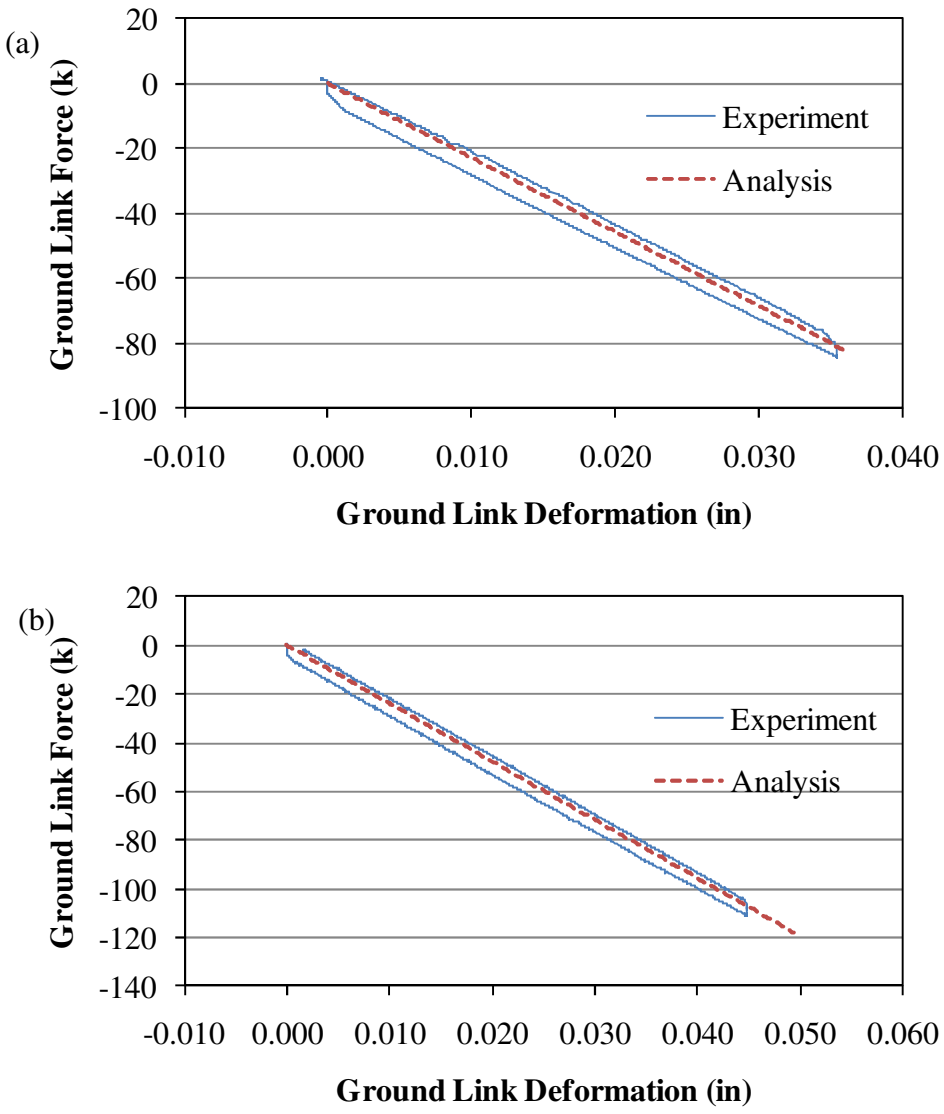

Figure 8.21 – Ground link force-deformation curves for loading to the north at the first floor level: (a) south ground link; (b) north ground link

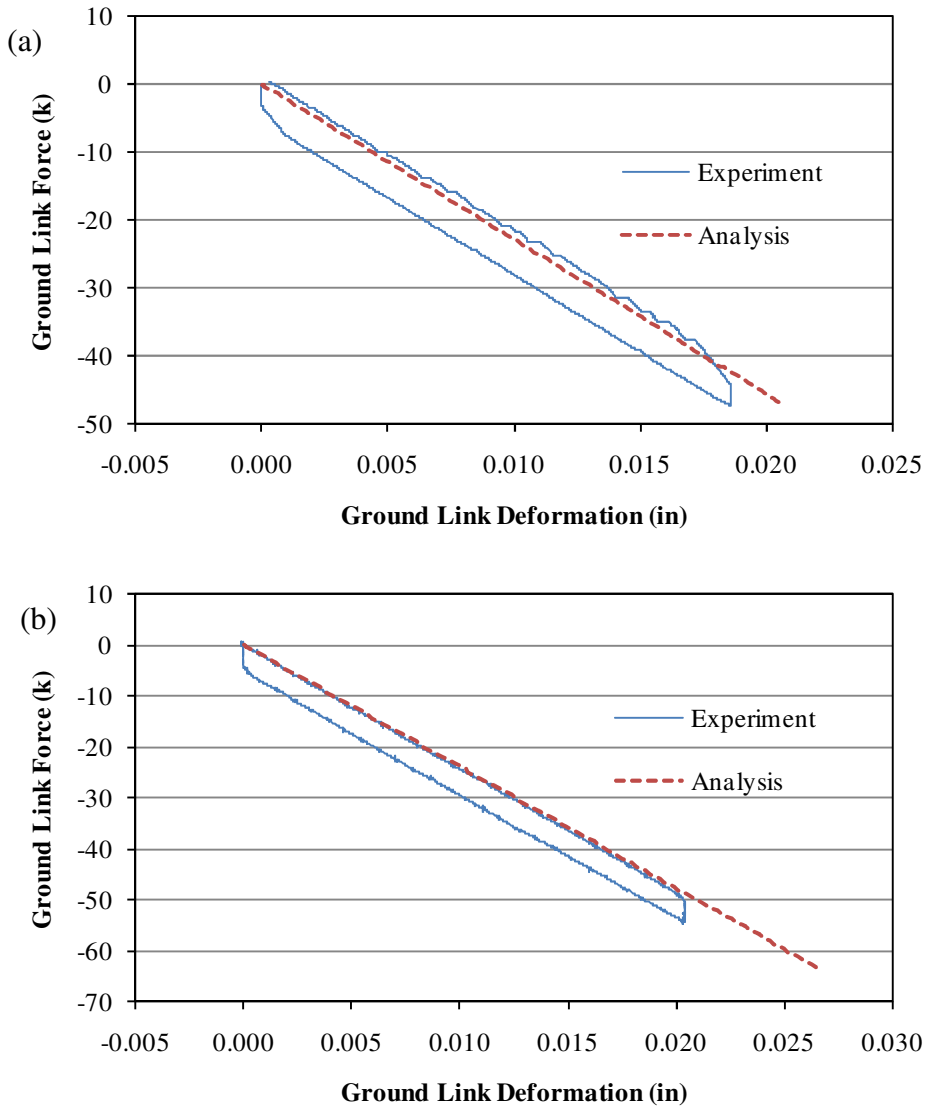

Figure 8.22 – Ground link force-deformation curves for loading to the north at the second floor level: (a) south ground link; (b) north ground link

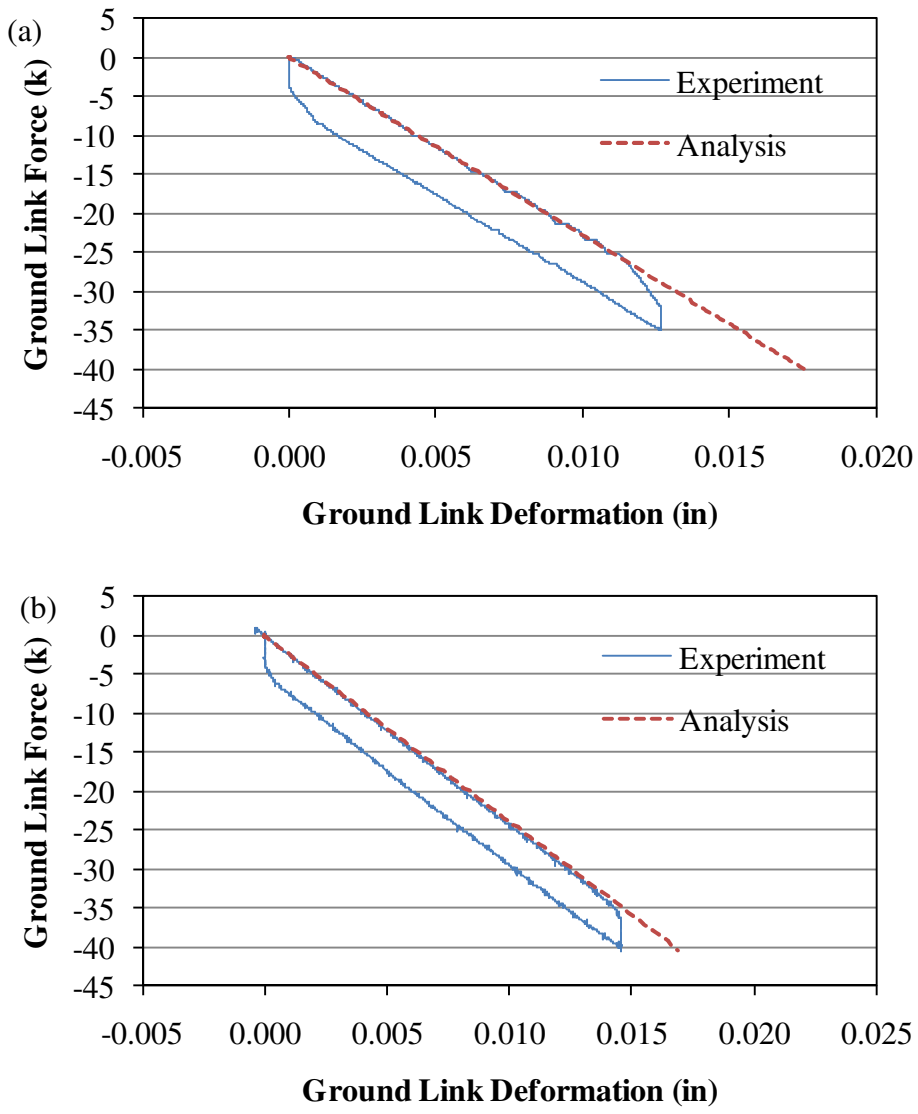

Figure 8.23 – Ground link force-deformation curves for loading to the north at the third floor level: (a) south ground link; (b) north ground link

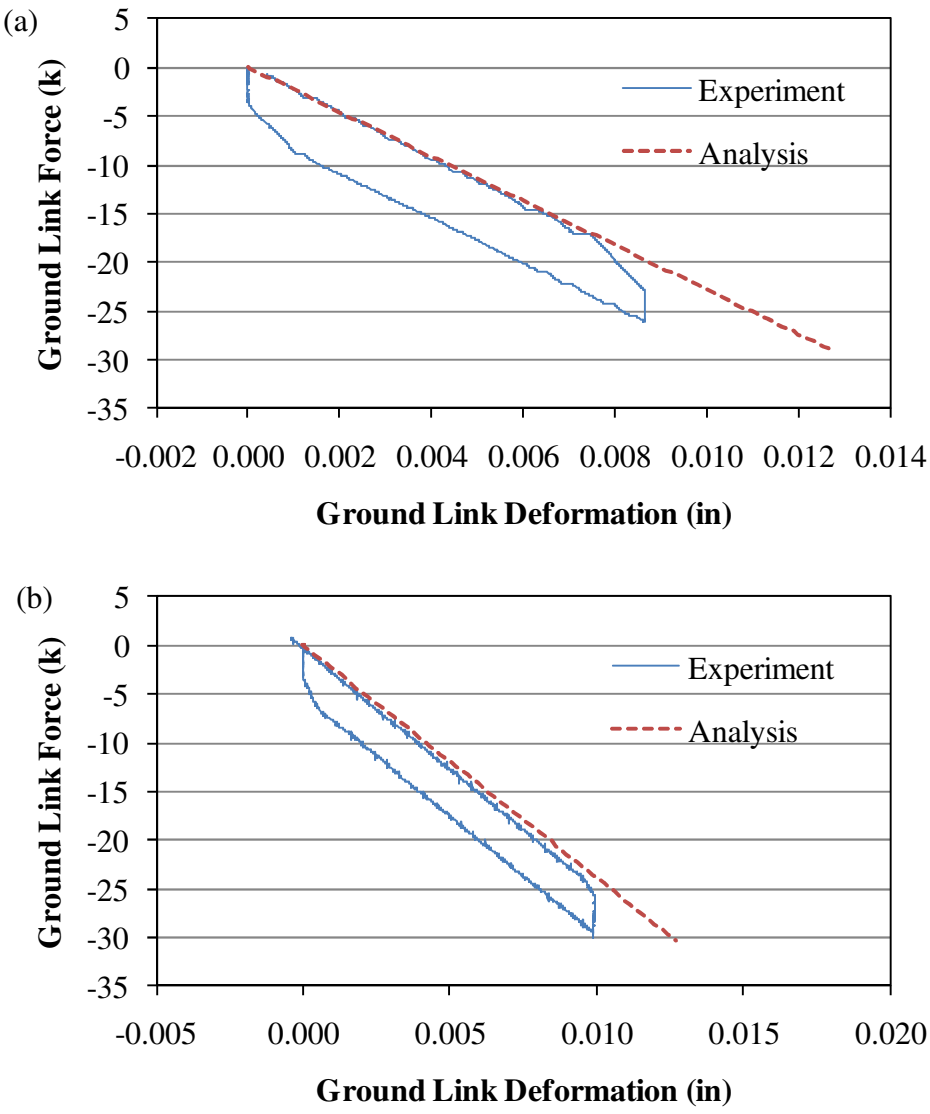

Figure 8.24 – Ground link force-deformation curves for loading to the north at the fourth floor level: (a) south ground link; (b) north ground link

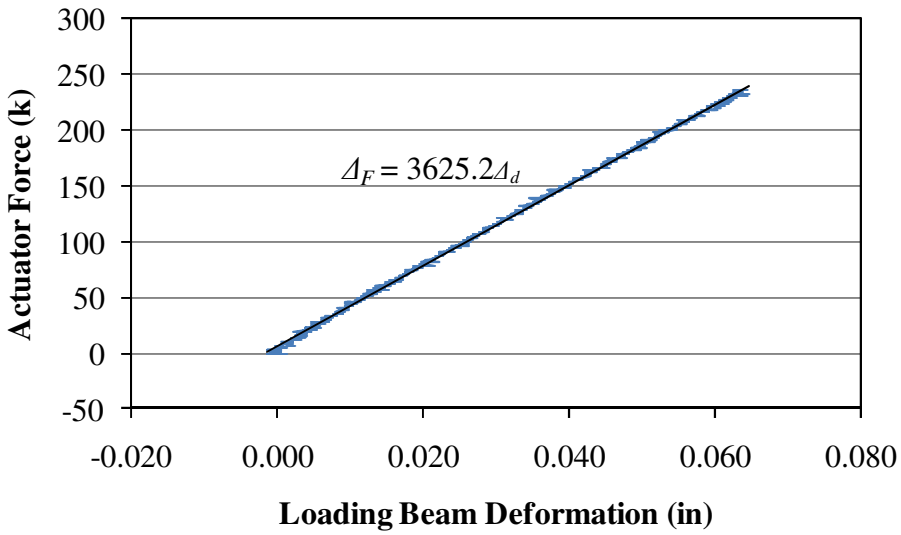

Figure 8.25 – First floor loading beam experimental axial force-deformation response

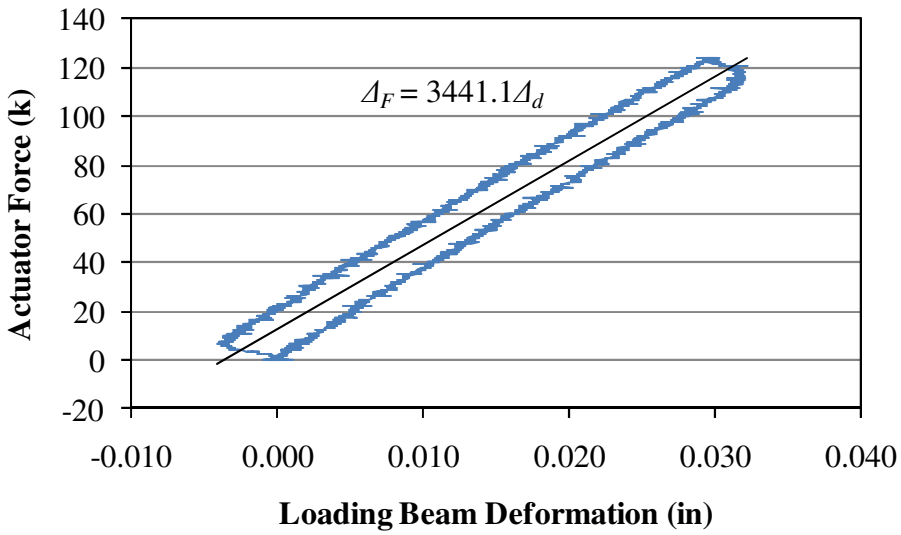

Figure 8.26 – Second floor loading beam experimental axial force-deformation response

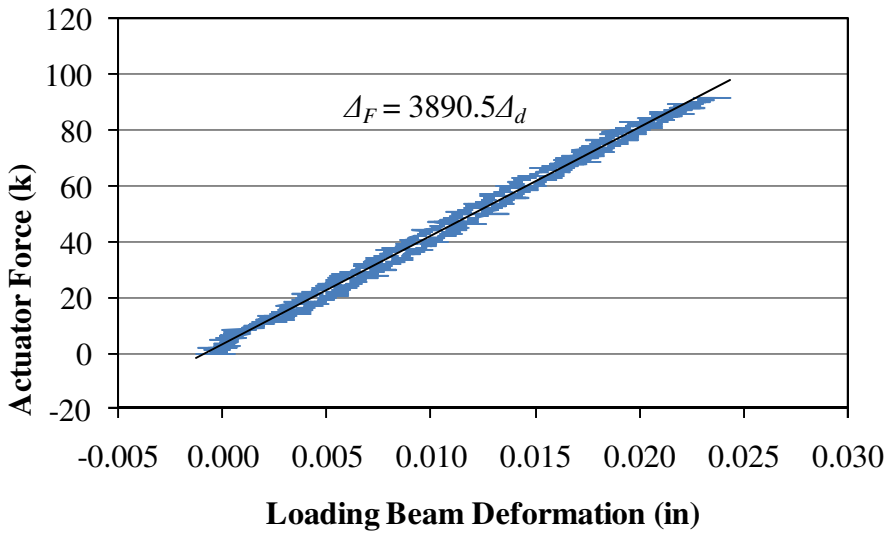

Figure 8.27 – Third floor loading beam experimental axial force-deformation response

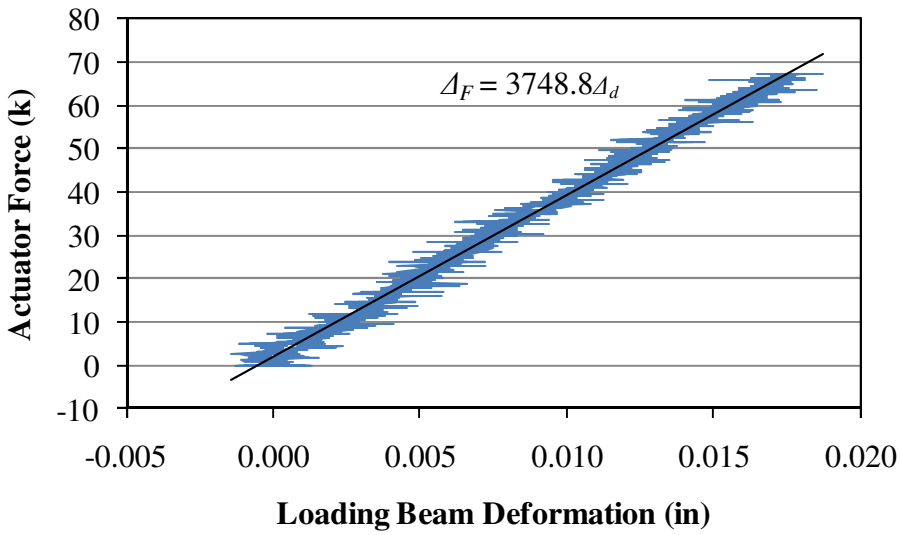

Figure 8.28 – Fourth floor loading beam experimental axial force-deformation response

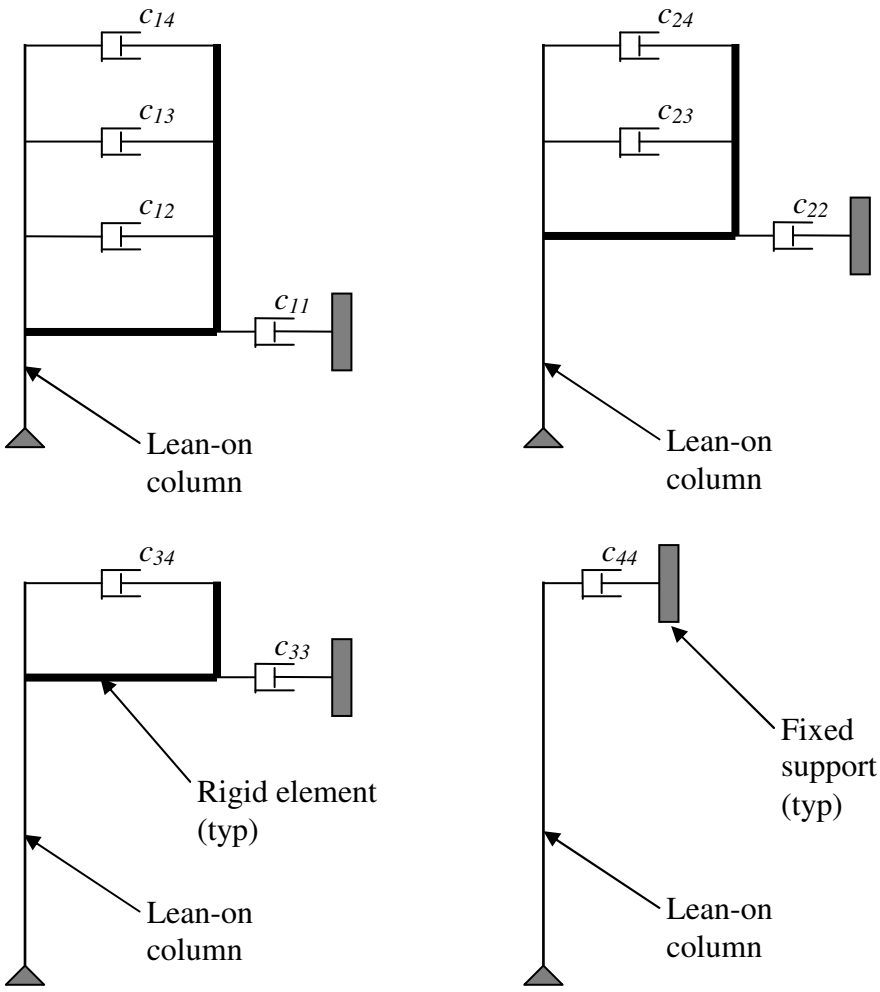

Figure 8.29 – Schematic of the four parallel sub-substructures that comprise the damping substructure used in analytical model

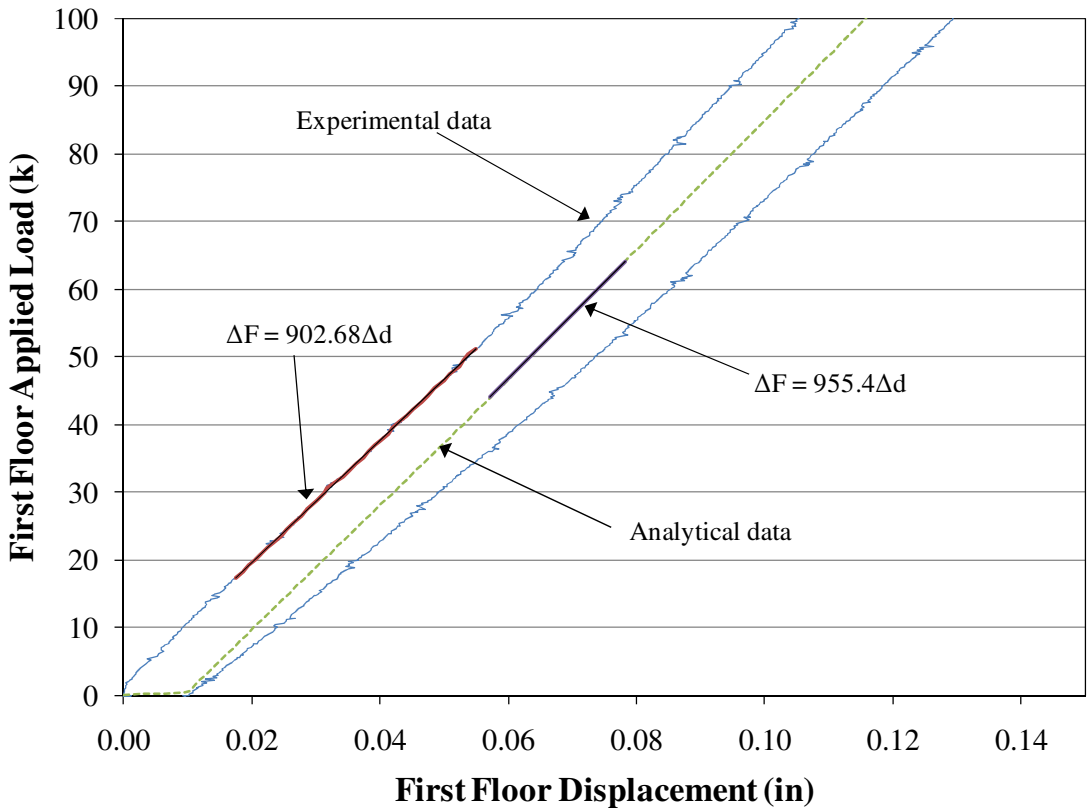

Figure 8.30 – First floor displacement response to a force applied at the first floor level

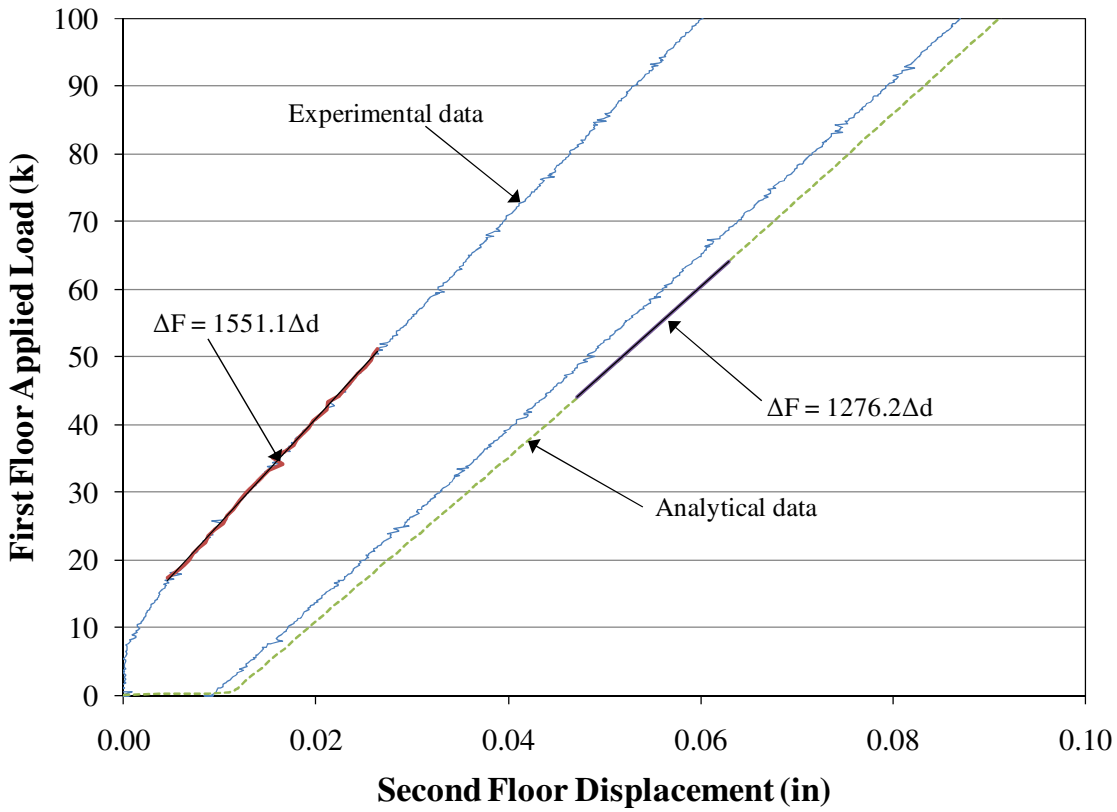

Figure 8.31 – Second floor displacement response to a force applied at the first floor level

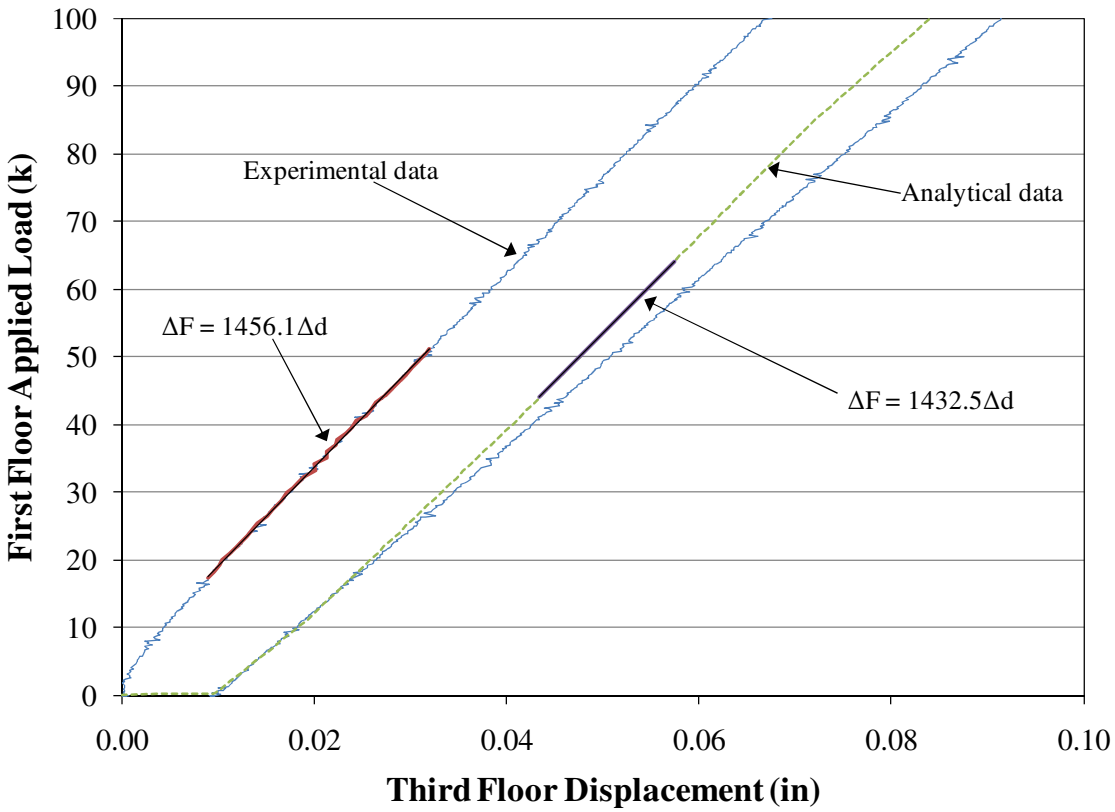

Figure 8.32 – Third floor displacement response to a force applied at the first floor level

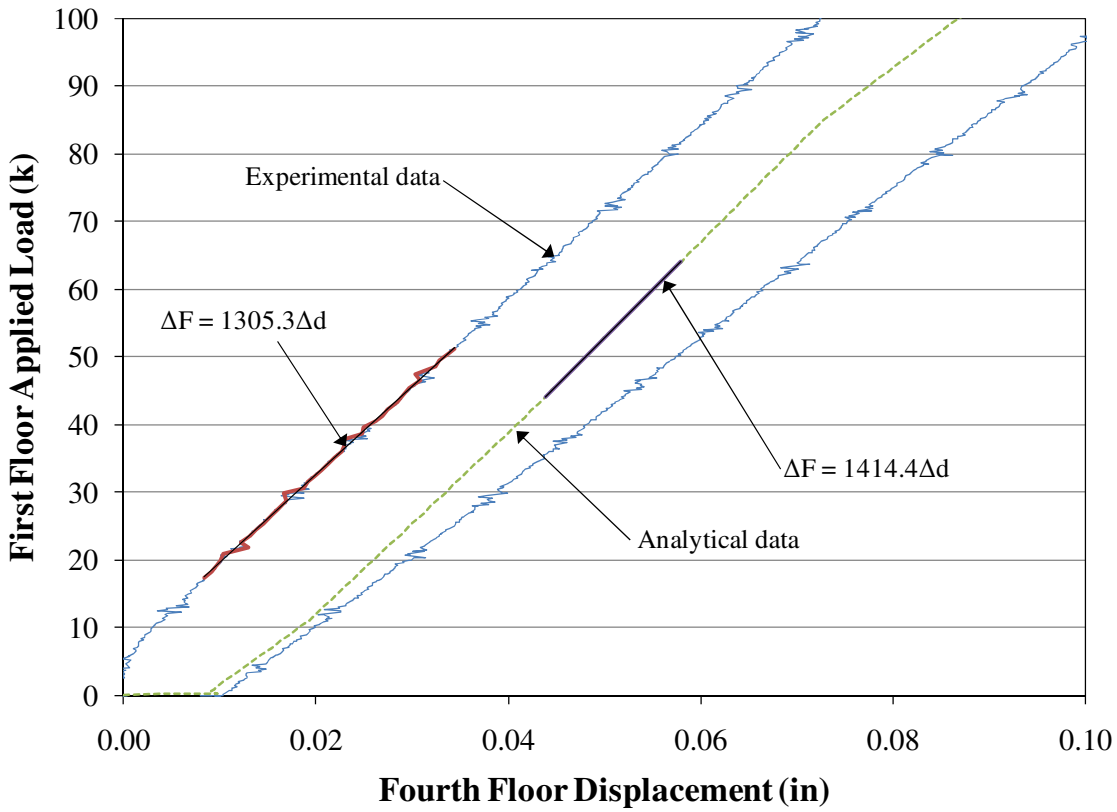

Figure 8.33 – Fourth floor displacement response to a force applied at the first floor level

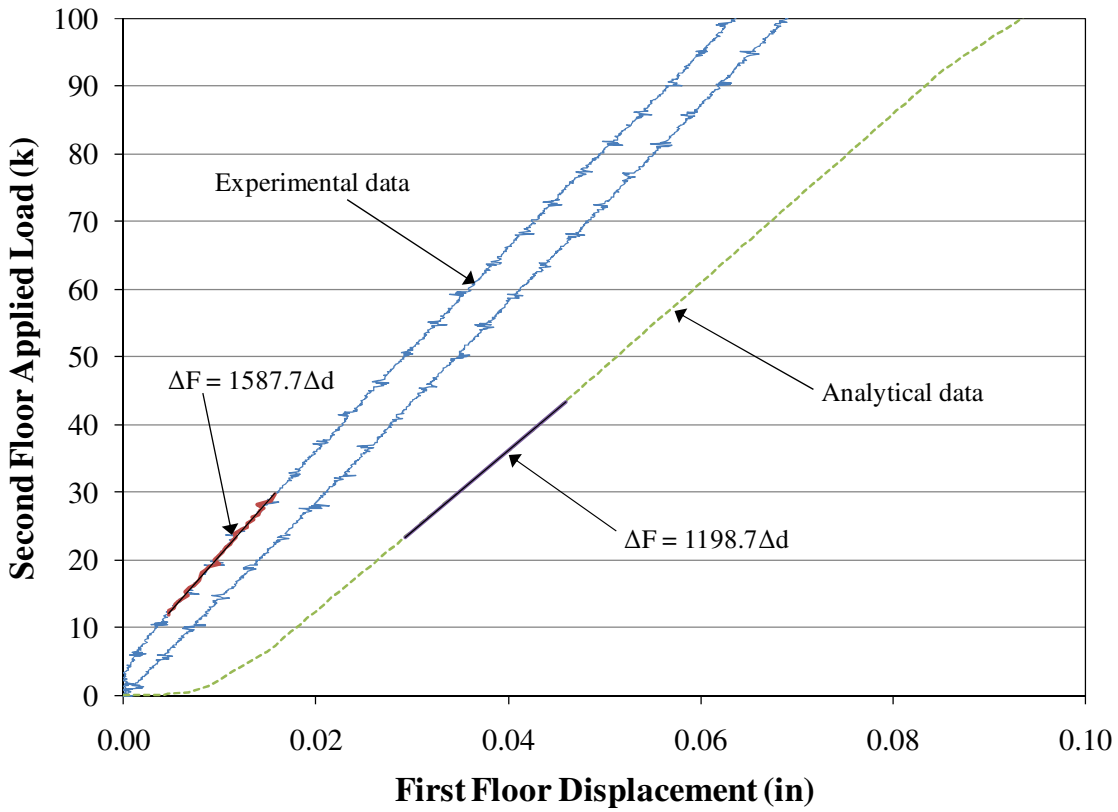

Figure 8.34 – First floor displacement response to a force applied at the second floor level

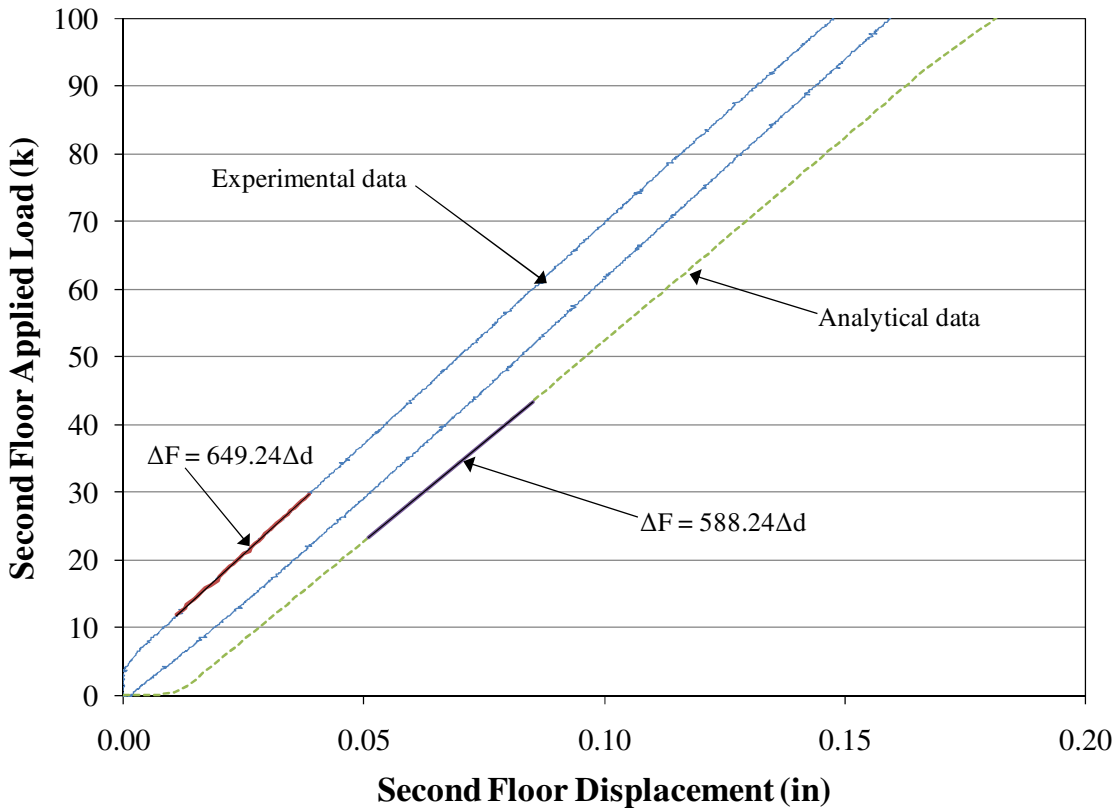

Figure 8.35 – Second floor displacement response to a force applied at the second floor level

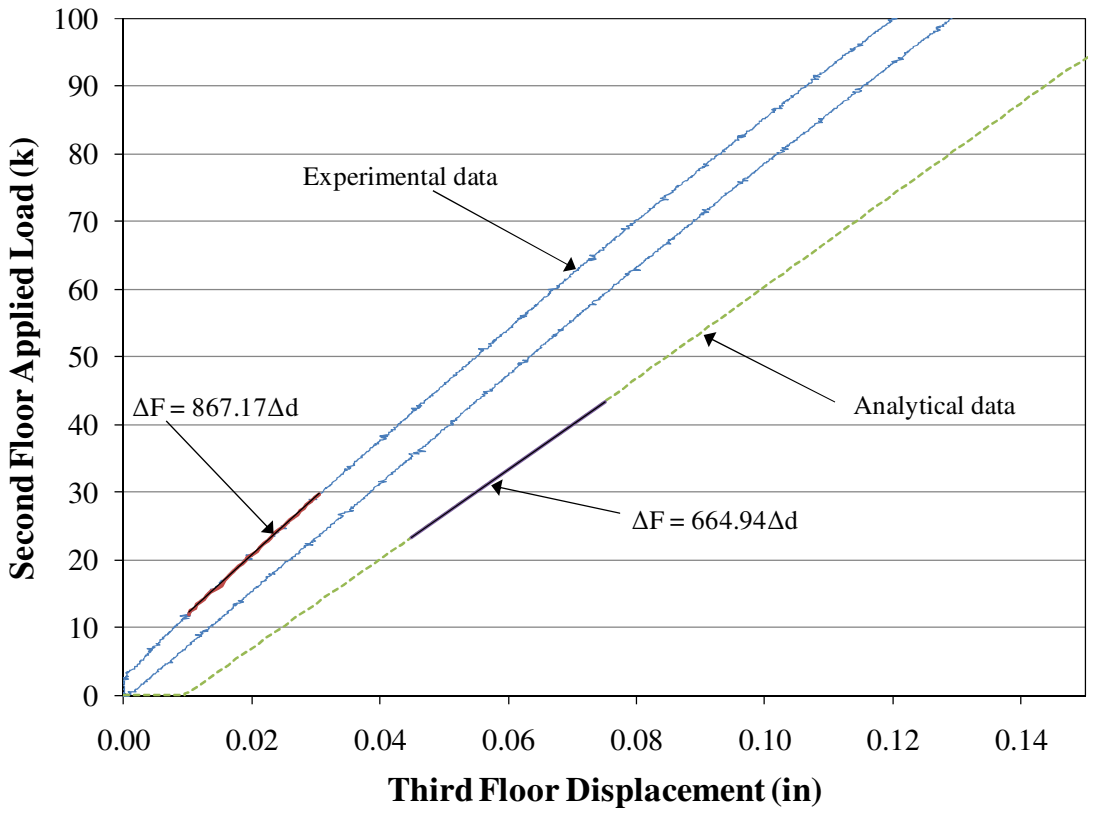

Figure 8.36 – Third floor displacement response to a force applied at the second floor level

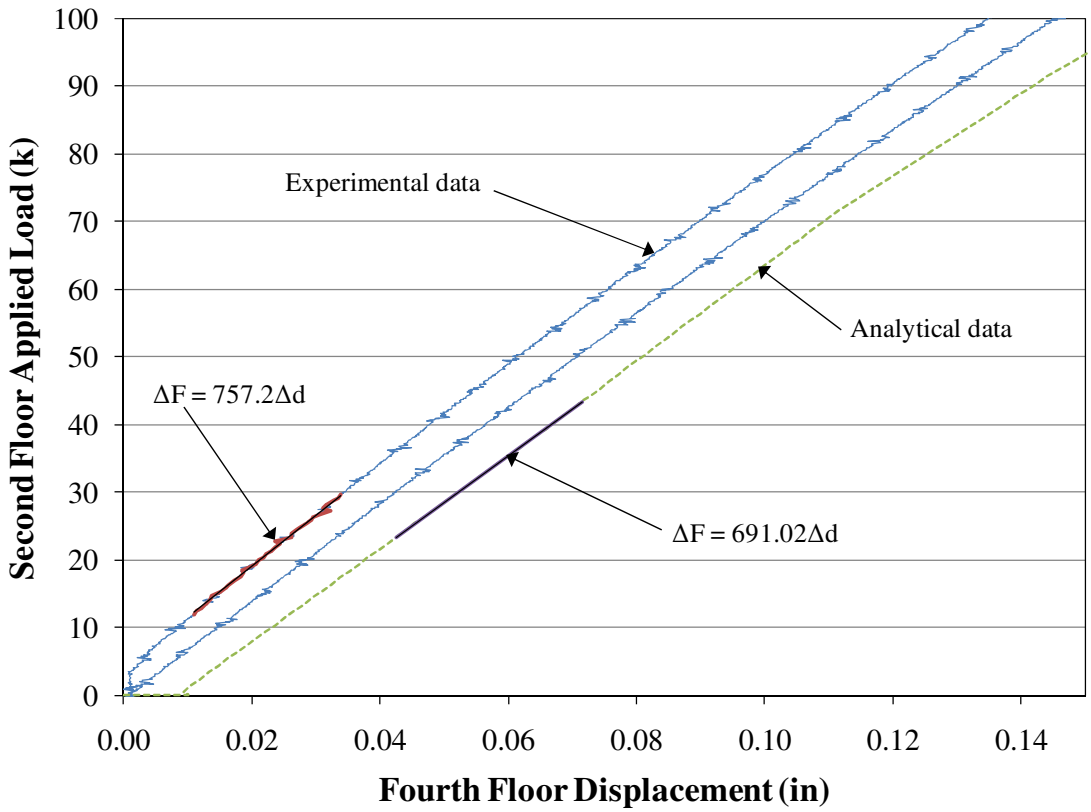

Figure 8.37 – Fourth floor displacement response to a force applied at the second floor level

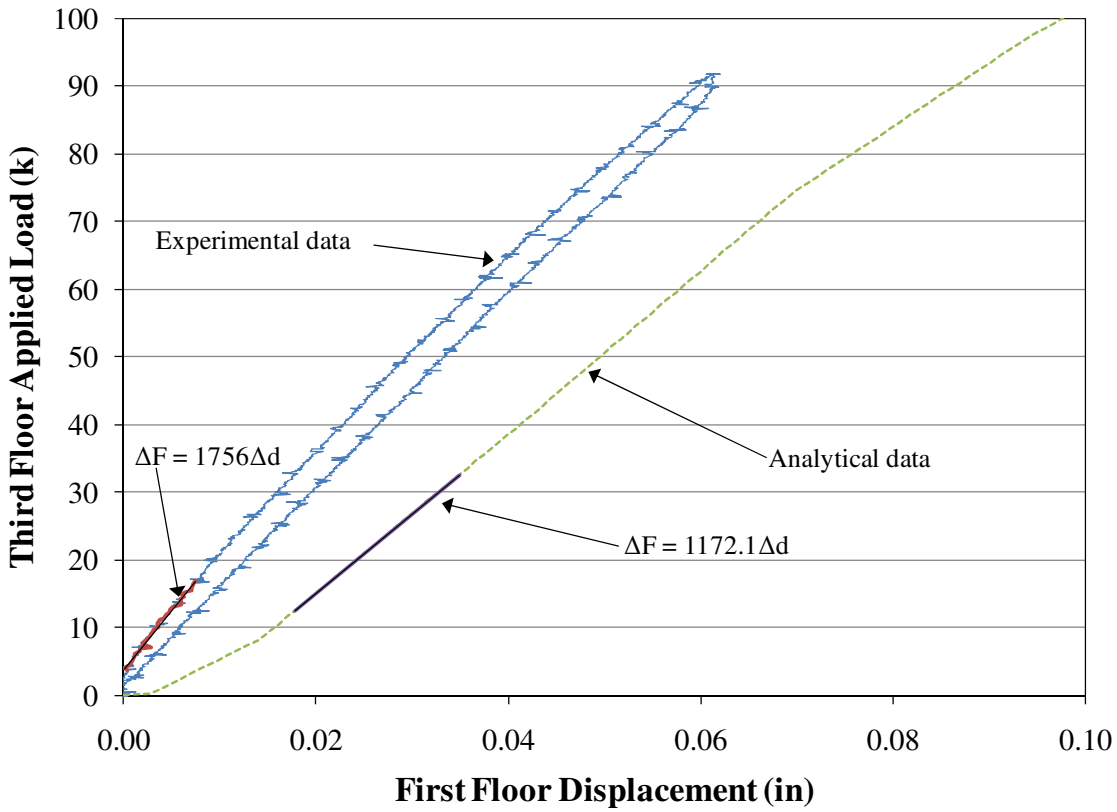

Figure 8.38 – First floor displacement response to a force applied at the third floor level

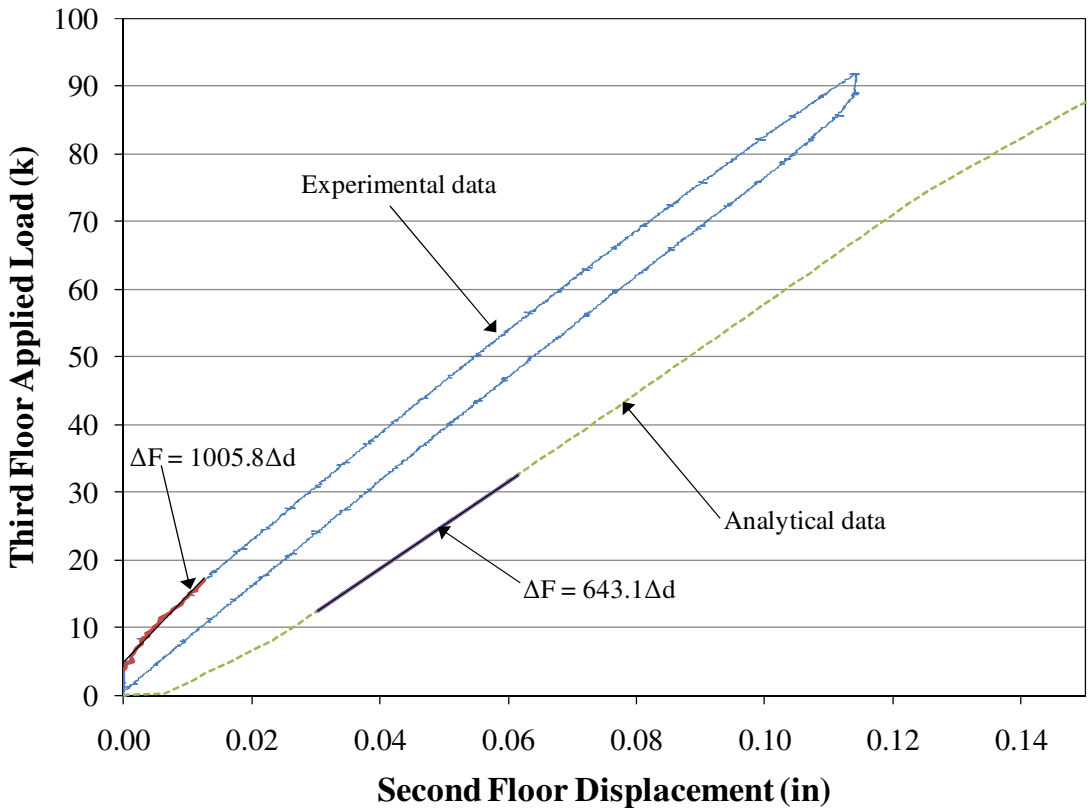

Figure 8.39 – Second floor displacement response to a force applied at the third floor level

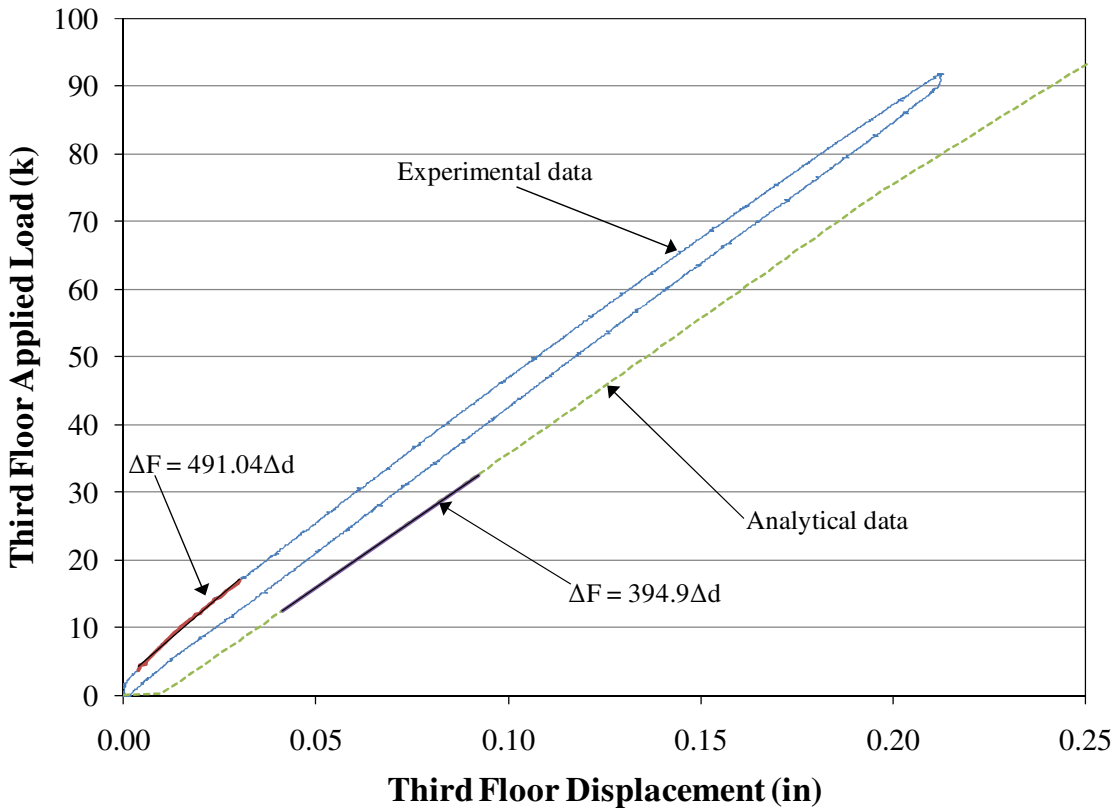

Figure 8.40 – Third floor displacement response to a force applied at the third floor level

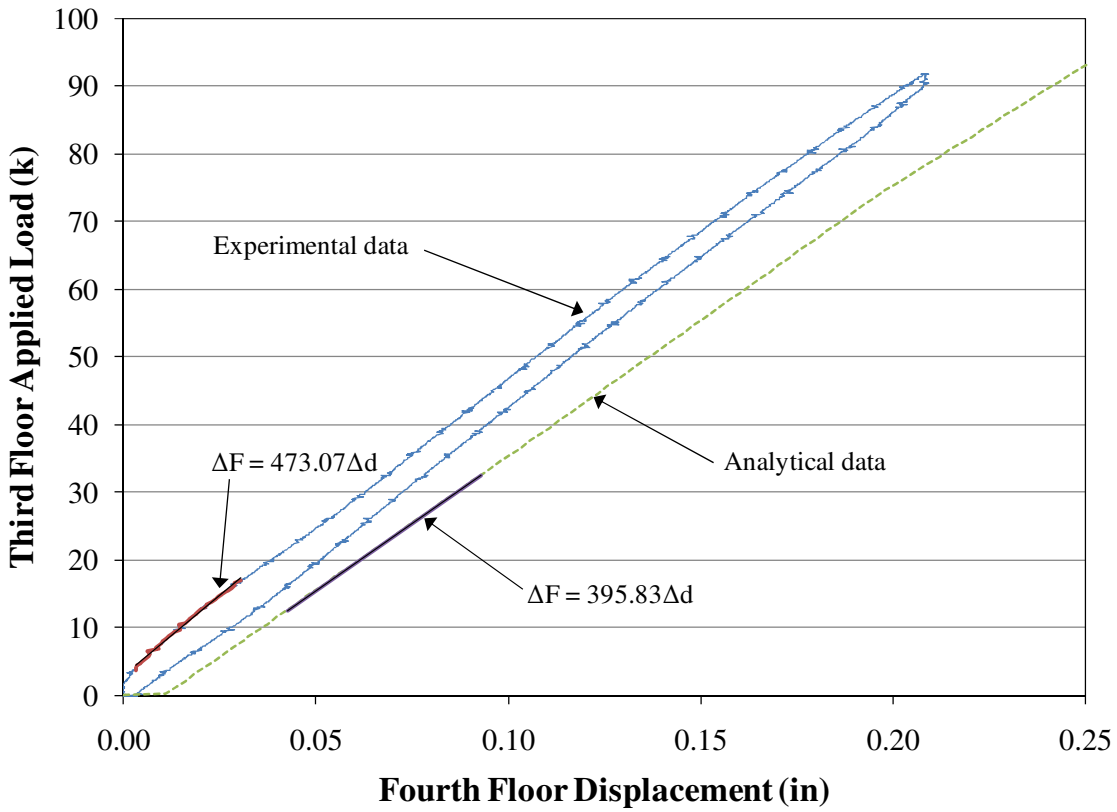

Figure 8.41 – Fourth floor displacement response to a force applied at the third floor level

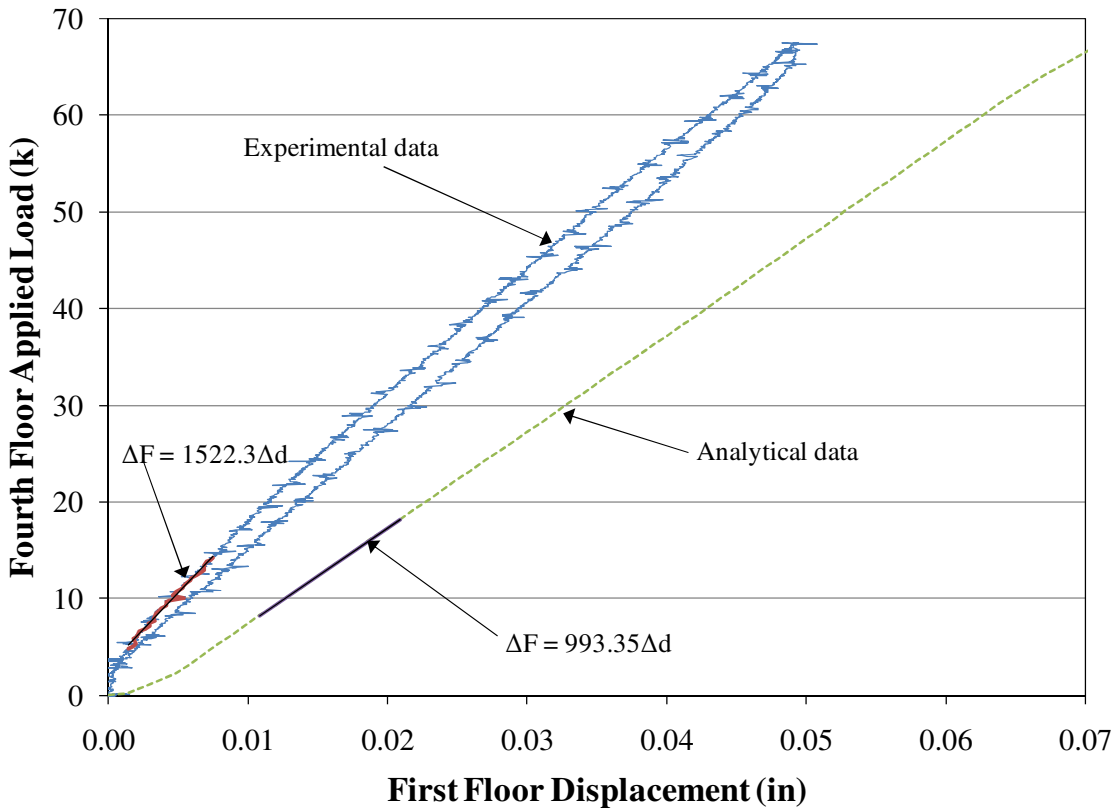

Figure 8.42 – First floor displacement response to a force applied at the fourth floor level

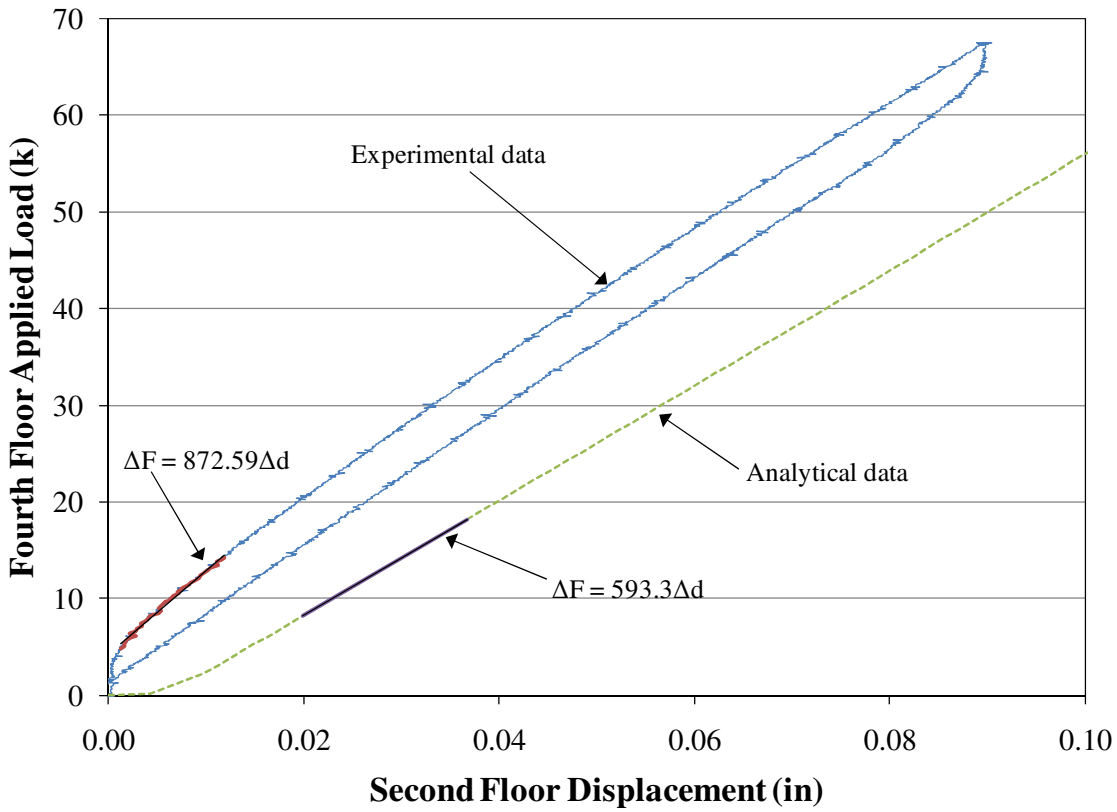

Figure 8.43 – Second floor displacement response to a force applied at the fourth floor level

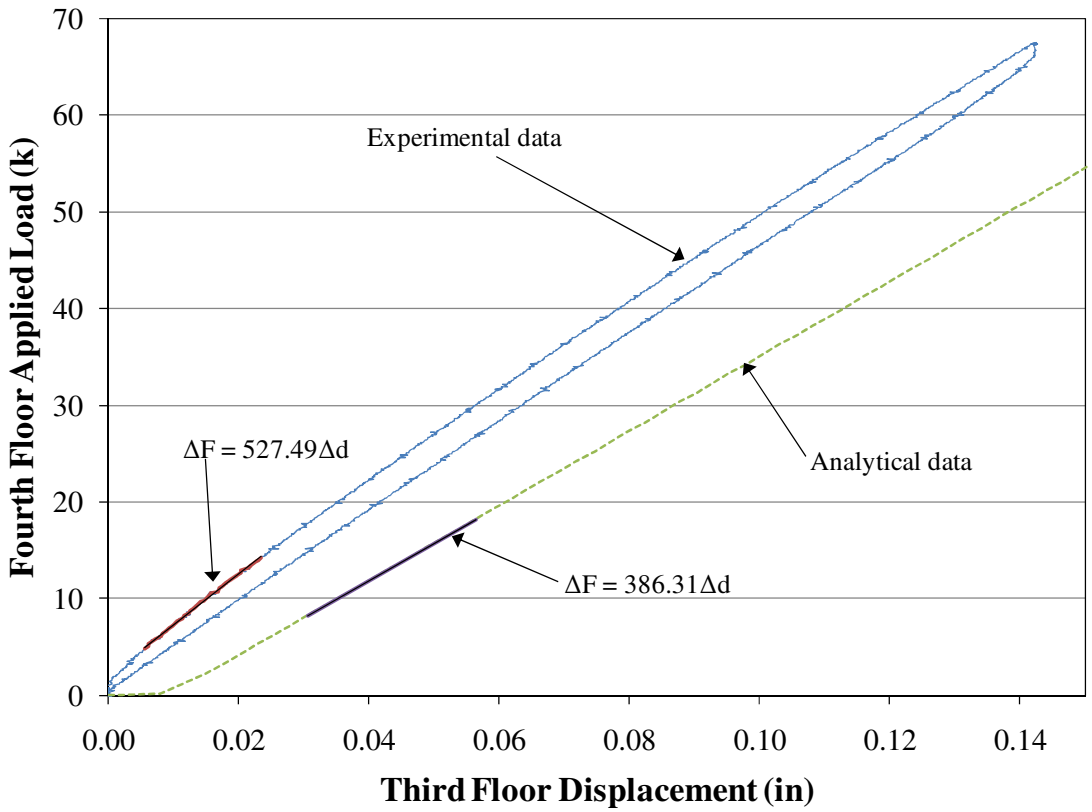

Figure 8.44 – Third floor displacement response to a force applied at the fourth floor level

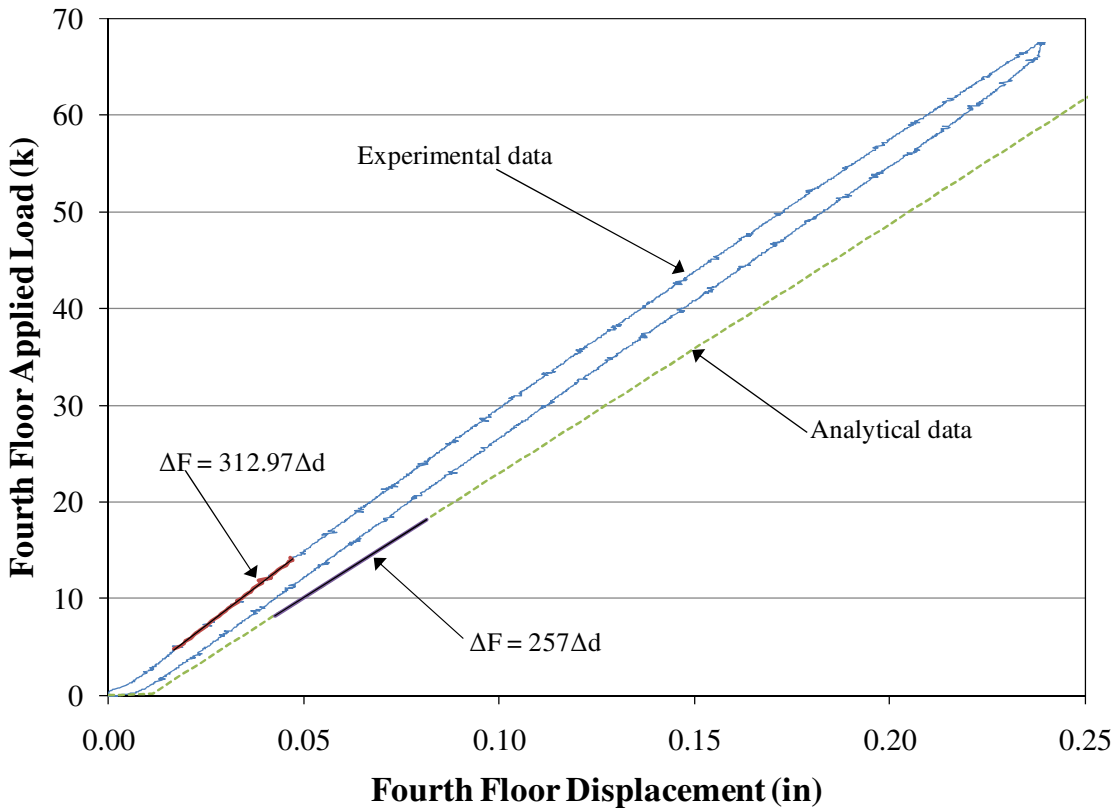

Figure 8.45 – Fourth floor displacement response to a force applied at the fourth floor level

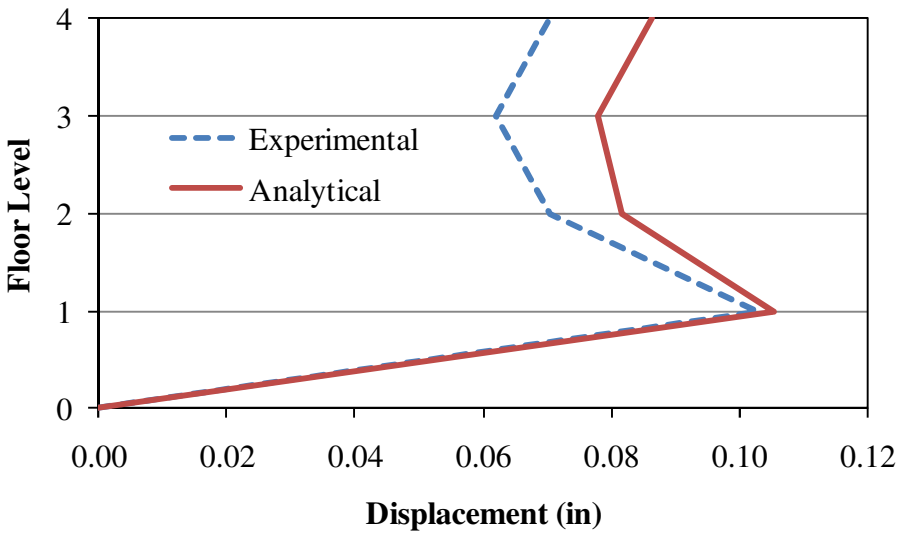

Figure 8.46 – Displacements extrapolated from stiffness matrices for SC-CBF test structure and analytical model subjected to 100 kip force at the first floor level

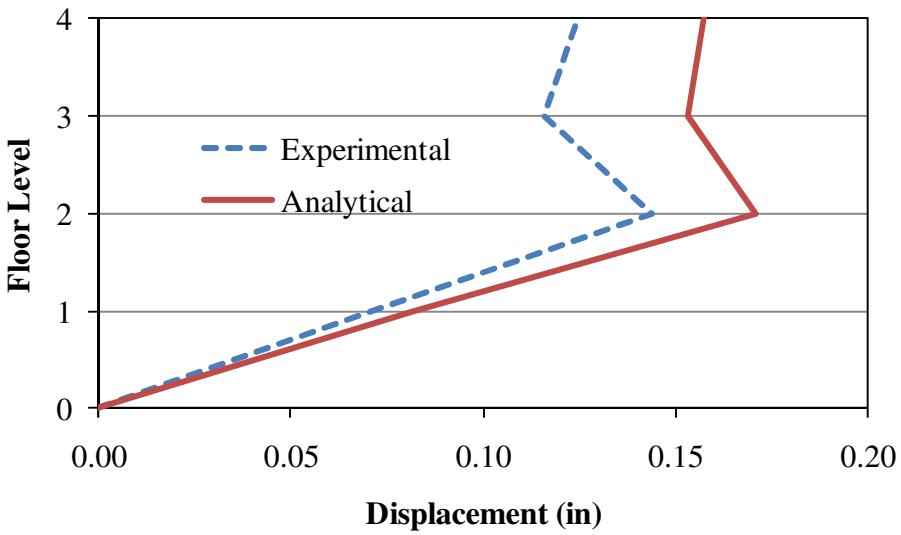

Figure 8.47 – Displacements extrapolated from stiffness matrices for SC-CBF test structure and analytical model subjected to 100 kip force at the second floor level

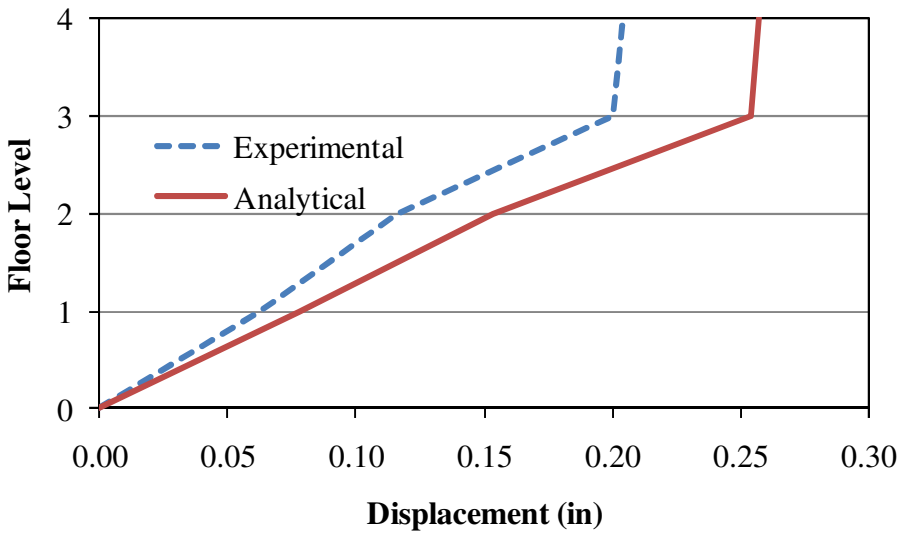

Figure 8.48 – Displacements extrapolated from stiffness matrices for SC-CBF test structure and analytical model subjected to 100 kip force at the third floor level

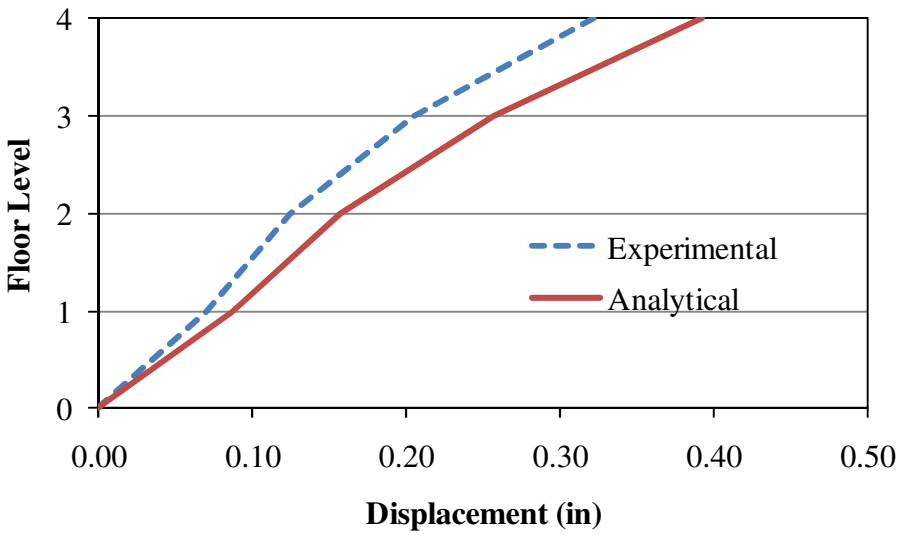

Figure 8.49 – Displacements extrapolated from stiffness matrices for SC-CBF test structure and analytical model subjected to 100 kip force at the fourth floor level

CHAPTER 9

NUMERICAL PREDICTION OF SC-CBF TEST STRUCTURE RESPONSE

Large-scale hybrid (i.e., combined laboratory and numerical) simulations of the seismic response of the SC-CBF test structure were conducted to validate the seismic performance of the SC-CBF system and to validate the analytical model for the SC-CBF test structure. This chapter discusses numerical predictions of the seismic response of the SC-CBF test structure and the selection of the ground motions for the hybrid simulations. First, the predictive analytical model used in the numerical simulation is discussed. Then, the ground motions used in this study are defined and the method used to scale the ground motions is explained. Next, a summary of the nonlinear dynamic response to DBE-level and MCE-level ground motions from the numerical simulations is presented. Finally, detailed results from the predictions of the SC-CBF test structure response are presented for a DBE-level ground motion, an MCE-level ground motion, and an extreme MCE-level ground motion.

9.1 Predictive Analytical Model

The predictive analytical model is based on the nonlinear analytical model of the SC-CBF test structure described in Chapter 8. To make accurate predictions of the test structure response, the values for three important parameters of the analytical model were

considered further in developing the predictive model: (1) the initial horizontal gaps between the gravity columns and the SC-CBF at the lateral-load bearings, (2) the initial PT force in the PT bars (PT_0), and (3) the PT bar yield stress (σ_Y). This section discusses these parameters and how their values were determined for the predictive model.

The initial gaps at the lateral-load bearings were input into the predictive analytical model to be consistent with (e.g., on the same order of magnitude as) measurements made during preliminary testing of the SC-CBF test structure. Two sets of preliminary measurements of the total gaps at each floor level (i.e., the sum of the gaps at the north and south lateral-load bearings) are shown in Table 9.1. The total gaps at the lateral-load bearings for the predictive model were set at 0.010, 0.012, 0.013, and 0.020 inches at the first, second, third, and fourth floor levels, respectively.

The total initial force in the PT bars, PT_0, was determined from the design procedure as 240.8 kip (Gonner 2009); therefore, the initial force at each of the three PT locations was set to 80.3 kip for the predictive model. Note that the beam-column element in the analytical model at each PT bar location represents two 1-in diameter high-strength PT bars. The actual initial force at each PT location in the SC-CBF test structure in the laboratory ranged from 80 kip to 85 kip due to the inexact nature of the stressing process. The predictive model did not include this variation in the initial PT force.

The yield stress of the PT bars was input into the predictive model as the average yield force of the bars determined from tension tests (Gonner et al. 2010) divided by the nominal bar area. The average yield force from the tension tests for a single bar was

122.1 kip, so the average yield stress (based on the nominal bar area of 0.85 in^2) from the tension tests, defined as the "actual" PT bar yield stress, is 143.6 ksi, which was used in the model. This value is substantially larger than the nominal value of the PT bar yield stress, 120 ksi.

9.2 Ground Motion Record Selection

9.2.1 Selection of DBE-Level and MCE-Level Ground Motions

To assess the seismic performance of the SC-CBF test structure under DBE-level and MCE-level seismic input, a suite of 15 pairs of ground motion records was selected at each input level. This section explains the method used to select and scale the suite of ground motions for each seismic input level.

To select ground motion records to represent the DBE and MCE seismic input levels, the seismic hazard for the site of the prototype building in Van Nuys, CA was established (Seo et al. 2010). The hazard is expressed in terms of the spectral acceleration at the first mode period of the test structure at full scale (i.e., $SA(T_{1,fs})$). The first mode period of the test structure at full scale, $T_{1,fs}$, is approximately 0.55 s, as given in Table 8.11, obtained by scaling up the test structure first mode period, T_1 (0.42 s), from 0.6-scale to full scale. The scale factor for time is equal to the square root of the length scale factor λ (Herrera 2005). The seismic hazards for the DBE and MCE levels are expressed as $SA_{DBE}(T_{1,fs})$ = 0.89 g and $SA_{MCE}(T_{1,fs})$ = 1.56 g, which are values of $SA(T_{1,fs})$ with a 10% and 2% probability of exceedance in 50 years, respectively (Seo et al. 2010). The values of

$SA_{DBE}(T_{1,fs})$ and $SA_{MCE}(T_{1,fs})$ were determined from the seismic hazard curve for the Van Nuys site (Seo et al. 2010).

Hazard disaggregation was used to determine the magnitude, M, and distance, D, combinations for ground motions with intensities $SA(T_{1,fs})$ that are greater than or equal to $SA_{DBE}(T_{1,fs})$ or $SA_{MCE}(T_{1,fs})$. McGuire (1995) proposes a disaggregation of the seismic hazard to determine the M and D combinations for ground motions that have intensities $SA(T_{1,fs})$ that are banded around $SA_{DBE}(T_{1,fs})$ or $SA_{MCE}(T_{1,fs})$. The disaggregation method used for this study follows McGuire's method (Seo et al. 2010). For a given M and D, an attenuation function (from Chiou and Youngs (2008)) defines the expected value (geometric mean) and the standard deviation of the spectral acceleration. In particular, it defines the geometric mean and standard deviation of the spectral accelerations for the two orthogonal components of horizontal ground motion. A third parameter, ε, relates the spectral acceleration $SA(T_{1,fs})$ to the expected value as follows: a positive ε indicates how many standard deviations $SA(T_{1,fs})$ is above the expected value and a negative ε indicates how many standard deviations $SA(T_{1,fs})$ is below the expected value. Indirectly, ε characterizes the spectral acceleration for a given ground motion relative to the expected spectral shape; a positive value of ε indicates a high spectral acceleration at $T_{1,fs}$ relative to the spectrum away from $T_{1,fs}$, and a negative value of ε indicates a low spectral acceleration at $T_{1,fs}$ relative to the spectrum away from $T_{1,fs}$.

Ground motions were selected to closely match the disaggregation results for the Van Nuys site in terms of M, D, and ε. In other words, the seismic hazard at the Van Nuys site was first expressed as the relative number (or percentage) of ground motions that

contribute to the hazard and have certain values of M, D, and ε. These results are summarized in Tables 9.2 and 9.3 for the DBE-level and MCE-level ground motions, respectively. Ground motions were then selected to match these values. The ground motions were selected from the PEER-NGA database (Seo et al. 2010). The records were first chosen as a pair of orthogonal ground motion components from an event with the appropriate magnitude M, recorded at a site with the appropriate distance D. Then $SA(T_{1,fs})$ was determined for each of the pair of records, and the geometric mean was determined and compared with the attenuation function results. Due to the limited availability of ground motion records in the database, certain combinations of M, D, and ε were unavailable; in such cases, records with similar values of M, D, and ε were chosen. In all cases, the pair of records was scaled so that the geometric mean of $SA(T_{1,fs})$ for the two records equaled the target $SA(T_{1,fs})$ value of $SA_{DBE}(T_{1,fs})$ or $SA_{MCE}(T_{1,fs})$. The values of M, D, and ε, for each ground motion pair and the scale factor are shown in Tables 9.4 and 9.5 for the DBE-level and MCE-level ground motions, respectively.

The DBE design spectrum and the spectral accelerations for the selected DBE- and MCE-level ground motions are shown in Figure 9.1 and Figure 9.2, respectively. These spectra are plotted for full-scale natural periods (not for the 0.6-scale test structure).

9.2.2 Selection of Extreme MCE-Level Ground Motions

To assess the performance of the SC-CBF system to extreme seismic input, four ground motions that produce response well above the median MCE-level response (extreme MCE-level ground motions) were selected from the 1995 Kobe, Japan earthquake. These

extreme MCE-level ground motions were recorded at two different stations: the KJM station (the kjm000 and kjm090 ground motions) and the Takatori station (the tak000 and tak090 ground motions).

These ground motions were chosen based on the intensity of the ground accelerations and the magnitude of the expected dynamic response. Figure 9.3 shows the spectral accelerations for the four unscaled extreme MCE-level ground motions compared to the DBE design spectrum and the median spectral acceleration for the selected MCE-level ground motions. The spectral accelerations for these ground motions are high with respect to the design spectrum, both in the short period range (higher mode response) and in the long period range (first mode and rocking response). These high spectral accelerations are expected to increase the member force and base shear responses, as well as the roof drift response, respectively.

9.3 Predictions from Numerical Simulations

The predictions of the SC-CBF test structure seismic response, from the predictive model discussed earlier, are presented in two ways: (1) a statistical summary of the results for the ground motions at each hazard level, and (2) a detailed discussion of the prediction of the response to an individual ground motion at the DBE level, at the MCE level, and at the extreme MCE level.

9.3.1 Summary of Maximum Dynamic Response

The dynamic response to the suites of DBE, MCE, and extreme MCE ground motion records is presented in this section. Maxima for the following quantities are used to

characterize the response of the SC-CBF system: the maximum roof drift, (θ_{max}, also denoted as θ_{DBE}, θ_{MCE}, or θ_{xMCE} for the specific levels of ground motion input); the maximum story drift of any story, (θ_s); f_{bri}, which is the maximum brace force in story i, F_{bri}, normalized by the factored member force design demand in story i, $F_{bri,fdd}$; and the maximum base shear ($V_{b,max}$).

Among the member forces, the brace forces, rather than the forces in the beams and columns, are the main focus of the predictive numerical simulations and the subsequent correlation studies in Chapter 10. The brace forces are considered to be more critical to the design and performance of the SC-CBF. Note that in the analytical model, the SC-CBF members (i.e., the beams, columns, braces, and struts) are modeled with linear elastic elements. Therefore, when the member force response exceeds the capacity of the member, the value of the response from the numerical simulation is no longer accurate. The predictive analytical model was not intended to provide the nonlinear deformation demands in the members.

9.3.1.1 Predicted Response to DBE-Level Ground Motions

Table 9.6 summarizes the maximum response to the suite of DBE-level ground motion records. In Table 9.6, the name of each record has the prefix "DBE_" to indicate that the record is selected and scaled to reflect DBE-level seismic input for the Van Nuys site of the prototype building. The mean, μ_{DBE}, and standard deviation, σ_{DBE}, across the suite of DBE-level ground motions for each response quantity is shown in Table 9.7.

The roof drift maxima, θ_{DBE}, range from 0.51% radians to 1.52% radians. These values are 1.26 standard deviations below and 2.21 standard deviations above the mean, respectively. Each ground motion caused column decompression, but no ground motion caused PT bar yielding, suggesting that the PBD criteria set forth in Chapter 4 are satisfied at the DBE level.

Since the maximum drift response under the DBE is expected to be dominated by rocking of the SC-CBF (a rigid-body motion), the maximum story drift is expected to be similar to the maximum roof drift. This is indicated in Table 9.6, where it can be seen that the ground motions that cause large maximum roof drift response tend to produce large maximum story drift response.

Where f_{bri} exceeds 1.0 (shown in bold text in Table 9.6), the f_{bri} data show that the response is not consistent with the PBD criteria for all DBE-level ground motions; F_{bri} exceeds $F_{bri,fdd}$ for the following ground motions: DBE_abbar--l, DBE_abbar--t, DBE_nr-pel360, DBE_ucl090, DBE_ucl360, and DBE_wah090. However, as discussed in Section 8.2.2, the axial capacities of the braces are larger than the factored brace force design demands. The brace axial force design demands and capacities are shown in Table 8.6. As discussed in Chapter 8, the second story brace force capacity is much higher than the design demand because those member sizes were increased to have more uniform brace section sizes over the height of the structure to save fabrication costs. The axial force factored design demand is considered rather than the interaction criteria (AISC 2005b) to determine whether or not member yielding occurs because yielding due to combined axial-flexural loading is expected to cause small plastic deformations in the ends of the

members, whereas yielding due to axial loading is expected to cause large plastic deformations that would have a significant effect on structural response and cause residual drift.

The margin by which the nominal capacity of the first story braces, $F_{br1,n}$, exceeds the factored first story brace force design demand, $F_{br1,fdd}$, is 34%, which suggests that the first story braces would not reach their capacity and undergo nonlinear behavior under the DBE. The probability of F_{bri} exceeding $F_{bri,fdd}$ will be discussed in Chapter 12. Note that the brace force in the first story has a larger coefficient of variation than the brace forces in the other stories due to the larger contribution of the higher modes, which also affects the maximum base shear response, $V_{b,max}$.

$V_{b,max}$ is also tabulated for each ground motion. For the sake of comparison, the design base shear from the ELF forces (see Chapter 7) is 151 kip. The mean base shear demand is 2.7 times the design base shear; that is, the "overstrength" is 2.7. This overstrength is similar to that given in building codes (e.g., ASCE 2005) for conventional CBF systems ($\Omega_0 = 2$), special CBF systems ($\Omega_0 = 2$), BRBF systems with pinned connections ($\Omega_0 = 2$), and BRBF systems with rigid connections ($\Omega_0 = 2.5$) (ASCE 2005). This result indicates that the improved performance of the system is not due to increased system strength.

9.3.1.2 Predicted Response to MCE-Level Ground Motions

Table 9.8 summarizes the maximum response to the suite of MCE-level ground motion records. In Table 9.8, the name of each record has the prefix "MCE_" to indicate that the record is selected and scaled to reflect MCE-level seismic input for the Van Nuys site of

the prototype building. The mean, μ_{MCE}, and standard deviation, σ_{MCE}, across the suite of MCE-level ground motions for each response quantity are shown in Table 9.7.

The roof drift maxima, θ_{MCE}, range from 0.58% radians to 2.64% radians. These values are 1.74 standard deviations below and 2.27 standard deviations above the mean, respectively. As previously mentioned, since the rocking behavior dominates the response at the time of maximum drift response, the maximum story drift is similar to the maximum roof drift. Table 9.8 shows that ground motions that cause large maximum roof drift response also tend to produce large maximum story drift response.

The f_{bri} data indicate that F_{bri} exceeds $F_{bri,fdd}$ for the following ground motions: MCE_5082-235, MCE_5082-325, MCE_a-tmz000, MCE_cap000, MCE_dzc270, MCE_h-cpe237, MCE_lp-hda165, MCE_mrp090, MCE_mrp180, MCE_nr-pel360, and MCE_stn110. As shown in Table 8.6, $F_{bri,n}$ is greater than $F_{bri,fdd}$, creating a margin of safety between the design nominal capacities and the factored design demands. Despite this margin of safety, the dynamic demands for the following records would cause the first floor braces to reach their nominal capacity (i.e., F_{br1} exceeds $F_{br1,n}$), resulting in nonlinear behavior that is not accounted for in the predictive model: MCE_5082-235 and MCE_dzc270. As with the DBE response, the first floor braces have the largest coefficient of variation due to the large higher mode contributions. The third and fourth floor braces have the smallest mean value of f_{bri} due to the effects of the PT force and distribution strut, as discussed in Chapter 5.

The $V_{b,max}$ values tabulated in Table 9.7 indicate that the mean base shear response for the MCE (493 kip) is only about 20% greater than that for the DBE (406 kip), although by definition the MCE seismic input level is 50% greater than the DBE level (BSSC 2003). This suggests that the base shear response is being limited by the rocking behavior of the system. Therefore, it appears that the rocking behavior provides some control over the forces that develop in the SC-CBF system, as well as the base shear and overturning moment input to the foundation.

9.3.1.3 Predicted Response to Extreme MCE-Level Ground Motions

Table 9.9 summarizes the maximum response to the extreme MCE-level ground motions. These ground motion records are labeled "us" in Table 9.9 to denote that they are the unscaled records. The responses to the extreme MCE-level ground motions are not included in the calculation of the mean response for the MCE-level ground motions shown in Table 9.7, but will be compared against the mean MCE response.

The roof drift maxima for the extreme MCE-level ground motions, θ_{xMCE}, tend to be high relative to the MCE maxima, as expected. The responses to the ground motions recorded at the KJM station (kjm000 and kjm090) are similar to the MCE responses discussed in the previous section (within two standard deviations of the mean responses), while the responses to the ground motions recorded at the Takatori station (tak000 and tak090) are significantly greater than the MCE responses.

The maximum brace force response is also high for these records, exceeding the design demands for three of the four ground motions: kjm000_us, tak000_us, and tak090_us.

Due to the margin between $F_{bri,fdd}$ and $F_{bri,n}$, however, the braces do not reach their nominal capacity and do not undergo nonlinear behavior during these extreme MCE-level ground motions.

9.3.2 Selection of Ground Motion Records for Hybrid Simulations

To assess the experimental performance of the SC-CBF test structure and to validate the analytical model of the SC-CBF test structure, large scale hybrid simulations were performed on a subset of the ground motions presented in this chapter. The ground motions were selected for the hybrid simulations to reflect the full range of structural response. Records were selected to produce below the mean (low-level), near the mean (mid-level), and above the mean (high-level) response for the DBE and MCE earthquake input levels. One extreme MCE-level ground motion was also selected for the hybrid simulations. The basis of the selection of each record is explained later. The limitations of the test setup for the experimental substructure in the laboratory were considered; in particular, there is a maximum floor-level inertial force that can be applied due to the force capacities of the actuators, a maximum base shear due to the reaction capacity of the test fixture, and maximum floor displacements due to both the clearance from the test fixture to the test specimen and the available stroke of the displacement transducers.

9.3.2.1 DBE Level

Five DBE-level ground motion records were selected from the suite of DBE records. One low-level DBE record (DBE_cls000), two mid-level DBE records (DBE_5108-090 and DBE_h-shp270), and two high-level DBE records (DBE_arl090 and DBE_nr0pel360)

were selected. The maximum responses to these records are summarized in Table 9.10. Table 9.11 expresses these maxima as multiples of the corresponding standard deviations above and below the mean DBE response.

DBE_cls000 was selected as a low-level DBE record because each maximum response for this record is below the mean DBE response. DBE_5108-090 and DBE_h-shp270 were selected as mid-level DBE records because their θ_{DBE} and θ_s responses are close to the mean DBE drift responses. DBE_arl090 was selected as a high-level DBE because its θ_{DBE} is well above the mean value of θ_{DBE}. DBE_nr-pel360 was selected as a high-level DBE because f_{bri} is consistently more than one standard deviation above the mean value of f_{bri}.

9.3.2.2 MCE Level

Five MCE records were selected for use in laboratory simulations. Three mid-level MCE records (MCE_a-tmz270, MCE_lp-hda255, and MCE_stn110) and two high-level MCE records (MCE_cap000 and MCE_h-cpe237) were selected. No low-level MCE records were chosen, as the responses were similar to the DBE-level responses. The maximum responses to the selected MCE records are summarized in Table 9.10. Table 9.11 expresses the maximum responses of the selected MCE records as multiples of corresponding standard deviations above the mean MCE response.

MCE_a-tmz270 was selected as a mid-level MCE because f_{bri} and $V_{b,max}$ are near the mean MCE response; θ_{MCE} and θ_s, however, are below the mean. MCE_lp-hda255 was selected as a mid-level MCE response because θ_{MCE} and θ_s are nearly identical to the

mean MCE responses. MCE_stn110 was selected as a mid-level MCE record because θ_{MCE} and f_{bri} are generally close to the mean MCE response. MCE_cap000 was selected as a high-level MCE because θ_{MCE} and θ_s are more than one standard deviation above the mean MCE responses. MCE_h-cpe237 was selected as a high-level MCE because $V_{b,max}$ is close to the nominal base shear capacity of the test setup (i.e., 600 kip).

9.3.2.3 Extreme MCE Level

One extreme MCE-level ground motion, xMCE_tak090, was selected for laboratory simulations of the response of the SC-CBF test structure to an extreme ground motion input. Both the maximum roof displacement and the base shear were considered in selecting this ground motion.

As shown in Table 9.9, θ_{xMCE} for both components of the ground motion recorded at the Takatori station is very high; these values are greater than that which could be accommodated by the test setup. In particular, the displacement capacity of the displacement transducers measuring the floor displacements would be reached. To overcome this limitation, a ground motion denoted xMCE_tak090 was established, which is equal to the tak090_us ground motion scaled by 0.9. θ_{xMCE} for xMCE_tak090 is within the displacement limits of the test setup; therefore, this ground motion was selected for laboratory simulation of the extreme MCE response. In addition, $V_{b,max}$ for xMCE_tak090 is about 1% greater than the nominal base shear capacity of the test setup.

The maximum responses to xMCE_tak090 are included in Table 9.10 for comparison with the maximum responses to the DBE- and MCE-level ground motions selected for

laboratory simulations. Table 9.11 expresses the response maxima for xMCE_tak090 as a number of standard deviations above the mean MCE response. As previously mentioned, the xMCE response is not included in the calculation of the mean MCE response, but is compared against it. The maximum roof drift for xMCE_tak090 is more than five standard deviations above the mean MCE response, while the base shear is less than one standard deviation above the mean MCE response, which suggests that the base shear is controlled to some extent by the rocking response.

9.3.3 Response to Individual Ground Motion Records

Eleven total ground motions were selected for use in the laboratory hybrid simulations. The responses from numerical simulation of three of these ground motions will be presented in greater detail here: one DBE-level record (DBE_arl090), one MCE-level record (MCE_h-cpe237), and the xMCE_tak090 record. The numerical simulation response results presented in this section are typical of the expected seismic response of the SC-CBF test structure.

9.3.3.1 DBE_arl090

Figures 9.4 to 9.11 show the response of the SC-CBF to DBE_arl090. Figure 9.4 shows the displacement response of the north gravity column at each floor level. Figure 9.5 shows the column base gap opening response at each SC-CBF column base. Figure 9.6 shows the hysteretic response of the system; Figure 9.6(a) shows the overturning moment plotted against the roof drift, while Figure 9.6(b) shows the overturning moment plotted against the column base gap opening displacement. Figure 9.7 shows the PT force at each

of the PT bar locations. The PT force plotted is the sum of the forces in the two bars at each location. Figure 9.8(a) shows the base shear response of the system, determined by summing the forces acting between the lean-on column and the north gravity column. Figure 9.8(b) shows the overturning moment response of the system, determined by multiplying each of the forces acting between the lean-on column and the north gravity column by the height of the corresponding floor level above the base of the SC-CBF. Figure 9.9 shows the effective modal pseudo-accelerations for the system. Figures 9.10 and 9.11 show the brace axial force response of the south and north braces, respectively. The horizontal lines in Figures 9.10 and 9.11 shows the factored brace force design demand $F_{bri,fdd}$ for the braces in each story.

The floor displacement response is shown in Figure 9.4. There are two distinct response segments that represent significant response: from t = 2 s to t = 5 s, and from t = 6 s to t = 12 s. The first range, from 2 to 5 seconds, is an asymmetric response in which the negative displacement is larger than the positive displacement. The second range of significant response, from 6 to 12 seconds, is a more symmetric response, in which the peak displacements in the negative and positive directions are nearly equal. At the end of the earthquake, the SC-CBF has self-centered.

Figure 9.5 shows the column base gap opening response of the frame. Symmetry, or asymmetry, of the response is readily visible here. In the first range of large response, the north column base gap opening (shown in Figure 9.5(b)) is clearly larger than the south column base gap opening (shown in Figure 9.5(a)). The second range of significant response is more symmetric, as mentioned previously.

Figure 9.6 shows the hysteretic behavior of the SC-CBF. Figure 9.6(a) shows the overturning moment response plotted against the roof drift. Note the flag-shaped hysteresis loops that are characteristic of SC systems. There is some deviation from consistent bilinear behavior that is particularly noticeable in the direction of negative roof drift; this nonlinearity in the hysteresis loop shape is likely due to higher mode effects on the overturning moment. Figure 9.6(b) shows the overturning moment response plotted against the opening of the two column base gaps. The shapes of these hysteresis loops closely approximate the shapes of the loops in Figure 9.6(a), illustrating the close relationship between gap opening displacement and roof drift.

Figure 9.7 shows the PT bar force response of the system. The yield force of the PT bars at one location, determined as the mean value from tension tests (Gonner et al. 2010), is 244.2 kip (i.e., 122.1 kip per PT bar). The peak force demands occur during the time of the largest response discussed above, but do not approach the yield force.

The base shear response of the system is shown in Figure 9.8(a). The base shear is driven primarily by the first mode; however, higher-mode effects (higher frequency content in the response) are seen throughout the response history, particularly early in the record when the response is greatest. The same trend is seen in the overturning moment response, shown in Figure 9.8(b), though the higher-mode effects are, as expected, less prevalent.

Figure 9.9 shows the effective modal pseudo-acceleration response of the SC-CBF. The first mode response, shown in Figure 9.9(a), closely resembles the overturning moment

plotted in Figure 9.8(b) because the first mode response drives the overturning moment. Note that gap opening response (Figure 9.5) occurs most significantly between t = 3s and t = 12s; the higher-mode effective pseudo-accelerations (Figure 9.9(b), (c), and (d)) are significantly higher in this range than throughout the rest of the response history. This appears to corroborate the assertion made in Chapter 6, that the higher-mode responses are excited by the column base gap opening.

Figures 9.10 and 9.11 show the axial force response in the south and north braces in each story, respectively. None of the dynamic brace force demands are predicted to reach their factored design demands, which is consistent with the PBD objectives discussed in Chapter 4. Due to the configuration of the SC-CBF and the initial PT bar force, the third- and fourth-story braces have initial compression, and remain in compression, as seen in Figures 9.10(c), 9.10(d), 9.11(c), and 9.11(d).

9.3.3.2 MCE_h-cpe237

Figures 9.12 to 9.19 show the response of the SC-CBF to MCE_h-cpe237. Figure 9.12 shows the displacement response of the north gravity column at each floor level. Figure 9.13 shows the column base gap opening response at each SC-CBF column base. Figure 9.14 shows the hysteretic response of the system; Figure 9.14(a) shows the overturning moment plotted against the roof drift, while Figure 9.14(b) shows the overturning moment plotted against the column base gap opening displacement. Figure 9.15 shows the PT force at each of the PT bar locations. The bar force plotted is the sum of the forces in the two bars at each location. Figure 9.16(a) shows the base shear response of the

system. Figure 9.16(b) shows the overturning moment response of the system. Figure 9.17 shows the effective modal pseudo-accelerations for the system. Figures 9.18 and 9.19 show the brace axial force response of the south and north braces, respectively. The horizontal lines in Figures 9.18 and 9.19 shows the factored brace force design demand $F_{bri,fdd}$ for the braces in each story.

Figure 9.12 shows the floor displacement response of the SC-CBF to MCE_h-cpe237. Unlike the response to DBE_arl090, this response is generally symmetric. The range over which the displacement response is most significant is from t = 12s to t = 28 s.

The column base gap opening response is shown in Figure 9.13. For this ground motion, gap opening occurs consistently throughout the entire record. This is different from the response to DBE_arl090, in which there were durations where the column base gaps remained closed during a large part of the response history (as shown in Figure 9.5). This result is expected due to the difference in the level of seismic input.

Figure 9.14 shows the hysteretic behavior of the SC-CBF. The overturning moment is plotted against the roof drift in Figure 9.14(a). Again, the SC-CBF exhibits the flag-shaped hysteresis that is characteristic of SC systems. Figure 9.14(b) shows the overturning moment plotted against the column base gap opening. As in the DBE response, these hysteresis loops resemble the loops plotted in Figure 9.14(a), indicating the relationship between the column base gap opening and the roof drift.

The PT bar force response is plotted in Figure 9.15. As previously mentioned, gap opening occurs consistently throughout the response to this record; therefore, the PT

force demand is usually greater than the initial force in the bars. As was the case for the DBE response, however, the bars maintain their initial force to the end of the record because the bars did not yield.

Applied base shear and overturning moment are plotted in Figures 9.16(a) and 9.16(b), respectively. The base shear response shows significant higher mode contributions, seen as high-frequency oscillation in the response, whereas the overturning moment response is primarily a first-mode response. This is corroborated by Figure 9.17(a), which shows the first mode effective pseudo-acceleration response of the SC-CBF. The shape of this plot closely resembles that of Figure 9.16(b), indicating that the first mode response is closely related to the overturning moment response.

Figures 9.17(b), 9.17(c), and 9.17(d) show the second, third, and fourth mode effective pseudo-accelerations. The value of α_n, for each mode, is less for the second half of the response (t = 25 s or more) than for the first half of the response (t = 25 s or less). This is due to the ground motion input, which is greater for the first 25 s than it is for the rest of the record. The amplification of the higher modes due to rocking is not observed in this response because the rocking occurs continuously throughout the response history; therefore, the response without the amplification cannot be observed.

Figures 9.18 and 9.19 show the brace force demands in each story in the south and north braces, respectively. The first story brace force response reaches 106% of the factored design demands (see Table 9.8); however, the margin between the nominal capacity $F_{br1,n}$

and the factored design demand $F_{br1,fdd}$ allows this dynamic response to occur without yielding the member (see Table 8.6).

9.3.3.3 xMCE_tak090

Figures 9.20 to 9.27 show the response of the SC-CBF to xMCE_tak090. Figure 9.20 shows the displacement response of the north gravity column at each floor level. Figure 9.21 shows the column base gap opening response at each SC-CBF column base. Figure 9.22 shows the hysteretic response of the system; Figure 9.22(a) shows the overturning moment plotted against the roof drift, while Figure 9.22(b) shows the overturning moment plotted against the column base gap opening displacement. Figure 9.23 shows the PT force at each of the PT bar locations. The bar force plotted is the sum of the forces in the two bars at each location. Figure 9.24(a) shows the base shear response of the system. Figure 9.24(b) shows the overturning moment response of the system. Figure 9.25 shows the effective modal pseudo-accelerations for the system. Figures 9.26 and 9.27 show the brace axial force response of the south and north braces, respectively. The horizontal lines in Figures 9.26 and 9.27 shows the factored brace force design demand $F_{bri,fdd}$ for the braces in each story.

Figure 9.20 shows the floor displacement response for xMCE_tak090. These displacement demands are much greater than those for the other records studied; there are five peak responses with greater roof-level displacement than any of the responses to the other ground motions selected for the laboratory simulations. The absolute peak response is in the negative direction close to t = 5 s.

The column base gap opening response, shown in Figure 9.21, is also much greater for this record than for the other records included in the study. The peak gap opening displacement is 7.73 inches at the north column base.

Figure 9.22 shows the hysteretic response. The applied overturning moment is plotted against the roof drift in Figure 9.22(a) and against the column base gap opening in Figure 9.22(b). Note that the flag-shaped hysteresis loops in the positive and negative directions in Figure 9.22 exhibit a reduction in the overturning moment at decompression (approaching zero), unlike the behavior seen in Figures 9.6 and 9.14. This reduction is due to the loss of PT force in the system from PT bar yielding, which reduces the decompression strength of the system such that at decompression only the gravity load acting on the SC-CBF test structure, $W_{SC\text{-}CBF}$, and the friction at the lateral-load bearings resist overturning of the frame. After decompression, any slack in the bars due to permanent elongation from yielding is taken up and the PT bars elongate elastically and contribute to overturning moment resistance.

Figure 9.23 shows the PT bar force response to xMCE_tak090. As the PT bars yield, the plastic elongation reduces the force that remains in the PT bars at the times of zero column uplift (zero column base gap opening). The amount of plastic elongation is so large that each PT bar is observed to lose its entire initial force.

Figure 9.24 shows the base shear and overturning moment response. As seen in the prior responses, the base shear response shows significant contributions from the higher

modes. The overturning moment response, however, is dominated by first mode response.

The effective modal pseudo-accelerations are plotted in Figure 9.25. The first mode response, shown in Figure 9.25(a), closely follows the overturning moment response, as expected. The higher mode responses, shown in Figure 9.25(b), 9.25(c), and 9.25(d), are greatest over the first 10 seconds of response, when gap opening response is greatest. This indicates the amplification of the higher mode response due to rocking behavior.

The brace force responses are shown in Figures 9.26 and 9.27. The response of the first, second, and third story braces (Figures 9.26(a), 9.27(a), 9.26(b), 9.27(b), 9.26(c), and 9.27(c)) exceeds the factored design demands. The brace force demands normalized by the factored design demands for these stories are 1.09, 1.18, and 1.02, respectively. These values are less than the margin between the factored design demand and the nominal member capacity (see Table 8.6), so these demands occur without yielding of the members.

Table 9.1 – Measured gaps at lateral-load bearings during preliminary testing

Floor	11/18/2009 Total Gap (in)	12/27/2009 Total Gap (in)
1	0.0135	0.0305
2	0.0095	0.0170
3	0.0060	0.0160
4	0.0100	0.0335

Table 9.2 – Results of DBE-level hazard disaggregation for Van Nuys site

D **(km)**	***M***	***ε***	**Contribution to Hazard (%)**	**Target Number of Ground Motions**
5 – 10	5.0 – 5.5	1.0 – 2.0	1.1	0
5 – 10	5.5 – 6.0	1.0 – 2.0	1.5	0
5 – 10	6.0 – 6.5	0.5 – 1.0	2.3	0
5 – 10	6.5 – 7.0	0.0 – 0.5	27.4	4
5 – 10	7.0 – 7.5	-0.5 – 0.0	2.7	0
10 – 15	5.0 – 5.5	2.0 – 3.0	0.2	0
10 – 15	5.5 – 6.0	1.0 – 2.0	0.8	0
10 – 15	6.0 – 6.5	1.0 – 2.0	3.1	1
10 – 15	6.5 – 7.0	0.5 – 1.0	30.5	5
10 – 15	7.0 – 7.5	0.5 – 1.0	0.5	0
15 – 20	5.5 – 6.0	2.0 – 3.0	0.3	0
15 – 20	6.0 – 6.5	1.0 – 2.0	2.7	1
15 – 20	6.5 – 7.0	1.0 – 2.0	4.0	1
15 – 20	7.0 – 7.5	1.0 – 2.0	3.6	1
15 – 20	7.5 – 8.0	1.0 – 2.0	0.1	0
20 – 25	6.0 – 6.5	2.0 – 3.0	1.2	0
20 – 25	6.5 – 7.0	1.0 – 2.0	2.7	1
20 – 25	7.0 – 7.5	1.0 – 2.0	1.1	0
25 – 30	6.0 – 6.5	2.0 – 3.0	0.3	0
25 – 30	6.5 – 7.0	1.0 – 2.0	1.6	0
25 – 30	7.0 – 7.5	1.0 – 2.0	0.8	0
30 – 35	6.5 – 7.0	2.0 – 3.0	0.5	0
30 – 35	7.0 – 7.5	1.0 – 2.0	1.9	0
30 – 35	7.5 – 8.0	1.0 – 2.0	0.8	0
35 – 40	6.5 – 7.0	2.0 – 3.0	0.9	0
35 – 40	7.0 – 7.5	2.0 – 3.0	0.5	0
40 – 45	6.5 – 7.0	2.0 – 3.0	0.1	0
40 – 45	7.0 – 7.5	2.0 – 3.0	0.0	0
45 – 50	7.0 – 7.5	2.0 – 3.0	0.5	0
45 – 50	7.5 – 8.0	1.0 – 2.0	4.6	1
45 – 50	8.0 – 8.5	1.0 – 2.0	1.4	0
50 – 55	7.0 – 7.5	2.0 – 3.0	0.1	0
50 – 55	7.5 – 8.0	2.0 – 3.0	0.1	0
70 – 75	7.5 – 8.0	2.0 – 3.0	0.0	0
85 – 90	7.5 – 8.0	2.0 – 3.0	0.3	0

Table 9.3 – Results of MCE-level hazard disaggregation for Van Nuys site

D **(km)**	***M***	ε	**Contribution to Hazard (%)**	**Target Number of Ground Motions**
5 – 10	5.0 – 5.5	2.0 – 3.0	0.4	0
5 – 10	5.5 – 6.0	1.0 – 2.0	1.3	0
5 – 10	6.0 – 6.5	1.0 – 2.0	2.7	1
5 – 10	6.5 – 7.0	1.0 – 2.0	44.9	7
5 – 10	7.0 – 7.5	0.5 – 1.0	6.6	1
10 – 15	5.5 – 6.0	2.0 – 3.0	0.2	0
10 – 15	6.0 – 6.5	2.0 – 3.0	2.4	0
10 – 15	6.5 – 7.0	1.0 – 2.0	29.5	5
10 – 15	7.0 – 7.5	1.0 – 2.0	0.7	0
15 – 20	6.0 – 6.5	2.0 – 3.0	0.9	0
15 – 20	6.5 – 7.0	2.0 – 3.0	2.2	0
15 – 20	7.0 – 7.5	2.0 – 3.0	2.8	1
15 – 20	7.5 – 8.0	1.0 – 2.0	0.1	0
20 – 25	6.5 – 7.0	2.0 – 3.0	1.0	0
20 – 25	7.0 – 7.5	2.0 – 3.0	0.7	0
25 – 30	6.5 – 7.0	2.0 – 3.0	0.1	0
25 – 30	7.0 – 7.5	2.0 – 3.0	0.2	0
30 – 35	7.0 – 7.5	2.0 – 3.0	0.6	0
30 – 35	7.5 – 8.0	2.0 – 3.0	0.5	0
45 – 50	7.5 – 8.0	2.0 – 3.0	1.3	0
45 – 50	8.0 – 8.5	2.0 – 3.0	0.8	0

Table 9.4 – Summary of DBE-level ground motion characteristics

Event	Station	Components	*M*	*D* (km)	*ε*	Scale Factor
1994 Northridge	**Santasusana**	090, 360	6.69	16.74	0.95	2.49
1990 Manjil, Iran	**Manjil**	L, T	7.37	12.56	1.00	1.36
1994 Northridge	**Arleta**	090, 360	6.69	8.66	0.23	1.40
1976 Friuli, Italy	**Tolmezzo**	000, 270	6.50	15.82	1.25	1.46
1989 Loma Prieta	**Capitola**	000, 090	6.93	15.23	1.30	0.83
1989 Loma Prieta	**Corralitos**	000, 090	6.93	3.85	0.26	0.73
1980 Victoria, Mexico	**Cerro Prieto**	045, 315	6.33	14.37	1.96	1.28
1979 Imperial Valley	**Sahop Casa Flores**	000, 270	6.53	9.64	0.39	1.75
1999 Chi-Chi	**HWA059**	E, N	7.62	49.15	1.29	2.26
1994 Northridge	**Hollywood Storage FF**	090, 360	6.69	24.03	1.31	1.55
1994 Northridge	**Sun Valley – Roscoe**	000, 090	6.69	10.05	0.49	1.28
1995 Kobe	**Shin-Osaka**	000, 090	6.90	19.15	1.17	1.37
1989 Loma Prieta	**San Jose-Santa Teresa Hills**	225, 315	6.93	14.69	0.75	1.79
1994 Northridge	**UCLA Grounds**	090, 360	6.69	22.49	0.80	2.35
1989 Loma Prieta	**Waho**	000, 090	6.93	17.47	0.63	1.55

Table 9.5 – Summary of MCE-level ground motion characteristics

Event	Station	Components	*M*	*D* (km)	*ε*	Scale Factor
1994 Northridge	**Wadsworth VA**	235, 325	6.69	23.60	1.55	2.71
1976 Friuli, Italy	**Tolmezzo**	000, 270	6.50	15.82	1.26	2.55
1989 Loma Prieta	**Capitola**	000, 090	6.93	15.23	1.28	1.45
1999 Duzce	**Duzce**	180, 270	7.14	6.58	0.76	1.69
1994 Northridge	**Faring Road**	000, 090	6.69	20.81	1.43	2.10
1994 Northridge	**Fletcher**	144, 234	6.69	27.26	1.52	3.16
1979 Imperial Valley	**Cerro Prieto**	147, 237	6.53	15.19	1.23	3.85
1994 Northridge	**Canyon Country – W Lost Canyon**	000, 270	6.69	12.44	1.44	1.33
1989 Loma Prieta	**Hollister Diff. Array**	165, 255	6.93	24.82	1.23	2.24
1995 Kobe	**Morigawachi**	000, 090	6.90	24.78	1.51	2.42
1994 Northridge	**Moorpark**	090, 180	6.69	24.76	1.04	3.80
1992 Landers	**Morango Valley**	000, 090	7.28	17.32	0.96	2.26
1994 Northridge	**Hollywood Storage FF**	090, 360	6.69	24.03	1.55	2.71
1995 Kobe	**Shin-Osaka**	000, 090	6.90	19.15	1.17	2.39
1994 Northridge	**Saturn**	020, 110	6.69	27.01	1.98	1.98

Table 9.6 - Summary of predicted responses to DBE-level ground motions

Ground Motion	θ_{DBE} (% rad)	θ_s (% rad)	f_{br1}	f_{br2}	f_{br3}	f_{br4}	$V_{b,max}$ (kip)
DBE_5108-090	0.84	0.92	0.84	0.74	0.86	0.60	455
DBE_5108-360	0.66	0.80	0.84	0.84	0.79	0.65	458
DBE_a-tmz000	0.53	0.62	0.62	0.68	0.60	0.49	330
DBE_a-tmz270	0.76	0.88	0.52	0.63	0.69	0.52	287
DBE_abbar--l	0.79	0.85	**1.07**	0.96	0.75	0.65	576
DBE_abbar--t	1.48	1.62	**1.14**	0.99	**1.03**	0.77	612
DBE_arl090	1.38	1.50	0.83	0.79	0.83	0.68	450
DBE_arl360	0.75	0.86	0.76	0.71	0.67	0.52	422
DBE_cap000	1.18	1.25	0.67	0.78	0.61	0.53	365
DBE_cap090	0.51	0.58	0.44	0.51	0.49	0.36	237
DBE_cls000	0.65	0.73	0.51	0.60	0.69	0.50	277
DBE_cls090	0.76	0.77	0.47	0.58	0.53	0.43	252
DBE_cpe045	1.25	1.38	0.81	0.89	0.79	0.64	439
DBE_cpe315	0.55	0.57	0.57	0.55	0.57	0.45	304
DBE_h-shp000	0.56	0.65	0.85	0.69	0.66	0.55	458
DBE_h-shp270	0.92	1.04	0.86	0.85	0.83	0.65	471
DBE_hwa059-e	0.76	0.78	0.43	0.55	0.50	0.41	228
DBE_hwa059-n	0.61	0.64	0.49	0.56	0.46	0.39	262
DBE_nr-pel090	0.81	0.93	0.61	0.66	0.51	0.44	334
DBE_nr-pel360	0.95	1.16	**1.01**	0.94	0.94	0.73	548
DBE_ro3000	0.63	0.70	0.60	0.62	0.55	0.43	317
DBE_ro3090	1.52	1.67	0.84	0.96	0.79	0.66	471
DBE_shi000	1.18	1.26	0.49	0.72	0.62	0.51	270
DBE_shi090	0.82	0.93	0.51	0.61	0.51	0.42	283
DBE_sjte225	0.56	0.64	0.81	0.67	0.65	0.49	440
DBE_sjte315	0.79	0.81	0.76	0.66	0.63	0.48	415
DBE_ucl090	0.97	1.12	**1.02**	0.88	0.93	0.66	537
DBE_ucl360	1.25	1.47	**1.18**	**1.18**	1.00	0.75	645
DBE_wah000	0.80	0.88	0.75	0.75	0.81	0.57	403
DBE_wah090	1.18	1.39	**1.17**	1.00	0.95	0.70	641

Table 9.7 – Mean and standard deviation of predicted responses to DBE- and MCE-level ground motions

	θ_{max} (% rad)	θ_s (% rad)	f_{br1}	f_{br2}	f_{br3}	f_{br4}	$V_{b,max}$ (kip)
μ_{DBE}	0.88	0.98	0.75	0.75	0.71	0.56	406
σ_{DBE}	0.29	0.33	0.23	0.17	0.16	0.12	123
μ_{MCE}	1.47	1.59	0.91	0.93	0.89	0.70	493
σ_{MCE}	0.52	0.52	0.24	0.18	0.18	0.14	130

Table 9.8 - Summary of predicted responses to MCE-level ground motions

Ground Motion	θ_{MCE} (% rad)	θ_s (% rad)	f_{br1}	f_{br2}	f_{br3}	f_{br4}	$V_{b,max}$ (kip)
MCE_5082-235	1.71	1.74	**1.37**	**1.23**	**1.01**	0.89	752
MCE_5082-325	0.97	1.23	**1.20**	**1.01**	**1.20**	0.98	648
MCE_a-tmz000	1.22	1.36	**1.08**	**1.01**	0.93	0.79	584
MCE_a-tmz270	1.13	1.26	0.97	0.81	0.91	0.71	543
MCE_cap000	2.05	2.21	0.92	**1.03**	0.86	0.75	511
MCE_cap090	1.05	1.15	0.66	0.67	0.69	0.51	354
MCE_dzc180	1.68	1.79	0.76	0.87	0.71	0.60	419
MCE_dzc270	2.64	2.81	**1.38**	**1.14**	**1.06**	0.90	754
MCE_far000	0.58	0.67	0.55	0.57	0.66	0.50	293
MCE_far090	1.23	1.34	0.77	0.77	0.85	0.70	423
MCE_fle144	0.65	0.70	0.78	0.78	0.59	0.51	421
MCE_fle234	1.18	1.29	0.83	0.77	0.80	0.64	450
MCE_h-cpe147	0.92	1.00	0.93	0.87	0.74	0.59	494
MCE_h-cpe237	1.75	1.84	**1.06**	0.93	0.87	0.72	574
MCE_los000	1.21	1.33	0.87	0.80	0.86	0.67	474
MCE_los270	1.01	1.16	0.69	0.76	1.00	0.73	376
MCE_lp-hda165	2.63	2.75	0.89	**1.09**	0.88	0.74	492
MCE_lp-hda255	1.48	1.58	0.94	1.00	0.88	0.75	524
MCE_mrg000	1.85	1.91	0.79	0.93	0.78	0.66	442
MCE_mrg090	1.68	1.71	0.65	0.79	0.74	0.64	358
MCE_mrp090	2.23	2.32	**1.27**	**1.09**	**1.14**	0.90	686
MCE_mrp180	1.52	1.72	**1.31**	**1.13**	**1.20**	0.98	718
MCE_mvh000	0.84	0.87	0.59	0.57	0.57	0.48	325
MCE_mvh090	1.38	1.49	0.66	0.81	0.65	0.57	368
MCE_nr-pel090	1.58	1.66	0.80	0.88	0.74	0.64	441
MCE_nr-pel360	1.52	1.81	**1.27**	**1.19**	**1.23**	0.98	685
MCE_shi000	1.90	1.97	0.79	0.99	0.90	0.77	440
MCE_shi090	1.87	1.99	0.81	0.91	0.79	0.65	453
MCE_stn020	1.15	1.27	0.64	0.75	0.78	0.59	351
MCE_stn110	1.60	1.73	0.84	0.86	**1.03**	0.78	454

Table 9.9 – Summary of predicted response to extreme MCE-level ground motions

Ground Motion	θ_{xMCE} (% rad)	θ_s (% rad)	f_{br1}	f_{br2}	f_{br3}	f_{br4}	$V_{b,max}$ (kip)
kjm000_us	2.36	2.61	**1.17**	**1.16**	**1.05**	0.82	661
kjm090_us	1.57	1.59	0.62	0.83	0.77	0.66	343
tak000_us	5.36	5.50	**1.13**	**1.21**	**1.02**	0.85	636
tak090_us	4.95	5.07	**1.24**	**1.21**	**1.11**	0.90	680
xMCE_tak090	4.33	4.46	**1.09**	**1.18**	**1.02**	0.84	607

Table 9.10 - Summary of predicted responses for ground motions used for laboratory simulations

Input Level	Ground Motion	θ_{max} (% rad)	θ_s (% rad)	f_{br1}	f_{br2}	f_{br3}	f_{br4}	$V_{b,max}$ (kip)
Low DBE	DBE_cls000	0.65	0.73	0.51	0.58	0.67	0.51	277
Mid DBE	DBE_5108-090	0.84	0.92	0.84	0.72	0.84	0.61	455
	DBE_h-shp270	0.92	1.04	0.86	0.82	0.80	0.66	471
High DBE	DBE_arl090	1.38	1.50	0.83	0.76	0.81	0.69	450
	DBE_nr-pel360	0.95	1.16	1.00	0.91	0.91	0.74	548
Mid MCE	MCE_a-tmz270	1.13	1.26	0.97	0.81	0.91	0.71	543
	MCE_lp-hda255	1.48	1.58	0.94	1.00	0.88	0.75	524
	MCE_stn110	1.60	1.73	0.84	0.86	1.03	0.78	454
High MCE	MCE_cap000	2.05	2.21	0.92	**1.03**	0.86	0.75	511
	MCE_h-cpe237	1.75	1.84	**1.06**	0.93	0.87	0.72	574
Extreme MCE	xMCE_tak090	4.33	4.46	**1.06**	**1.18**	**1.02**	0.84	607

Table 9.11 – Summary of predicted responses for ground motions used for laboratory simulations, expressed as a multiplier of standard deviations above (+) or below (-) the mean

Input Level	Ground Motion	θ_{max}	θ_s	f_{br1}	f_{br2}	f_{br3}	f_{br4}	$V_{b,max}$
Low DBE	DBE_cls000	-0.79	-0.78	-1.03	-0.92	-0.10	-0.47	-1.05
Mid DBE	DBE_5108-090	-0.15	-0.19	0.41	-0.07	0.94	0.37	0.39
	DBE_h-shp270	0.12	0.18	0.50	0.58	0.72	0.82	0.52
High DBE	DBE_arl090	1.71	1.60	0.37	0.23	0.74	1.05	0.36
	DBE_nr-pel360	0.24	0.54	1.14	1.14	1.41	1.47	1.15
Mid MCE	MCE_a-tmz270	-0.67	-0.64	0.28	-0.55	0.24	0.00	0.38
	MCE_lp-hda255	0.00	-0.01	0.17	0.58	0.08	0.27	0.23
	MCE_stn110	0.25	0.27	-0.27	-0.23	0.91	0.51	-0.30
High MCE	MCE_cap000	1.12	1.19	0.06	0.79	-0.06	0.28	0.14
	MCE_h-cpe237	0.53	0.48	0.68	0.20	0.02	0.08	0.62
Extreme MCE	xMCE_tak090	5.55	5.52	0.76	1.40	0.69	0.98	0.88

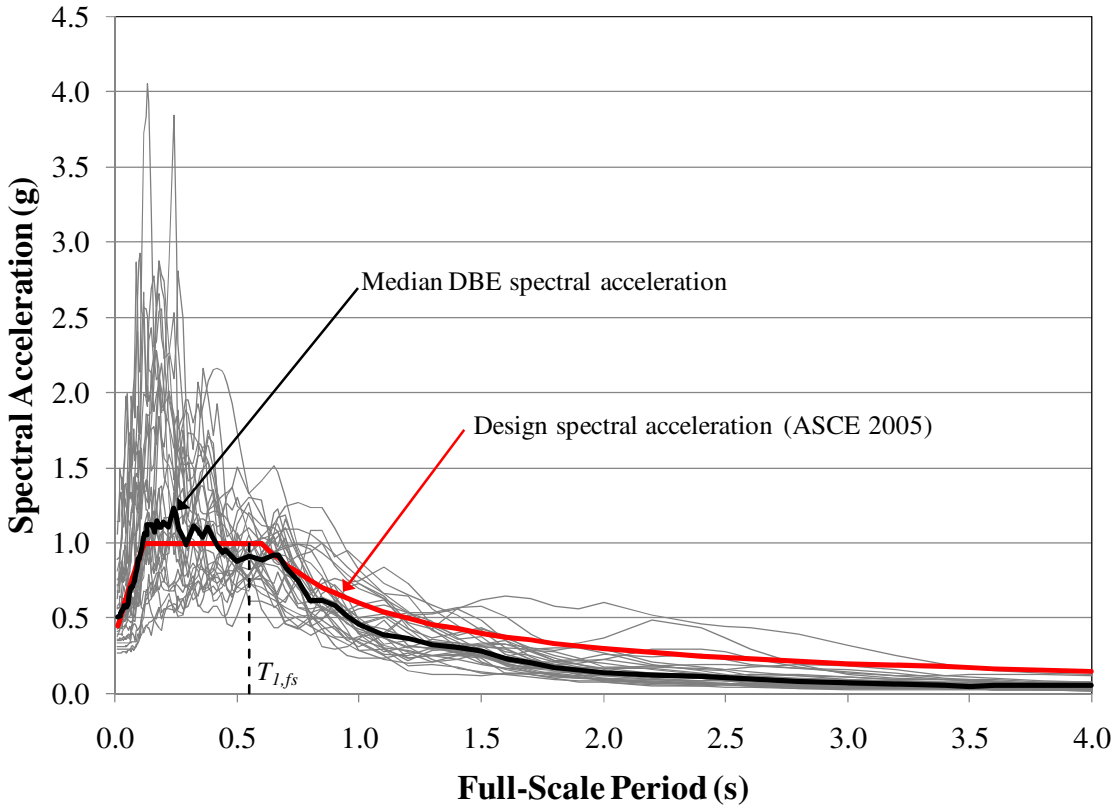

Figure 9.1 – Response spectra for DBE-level ground motions

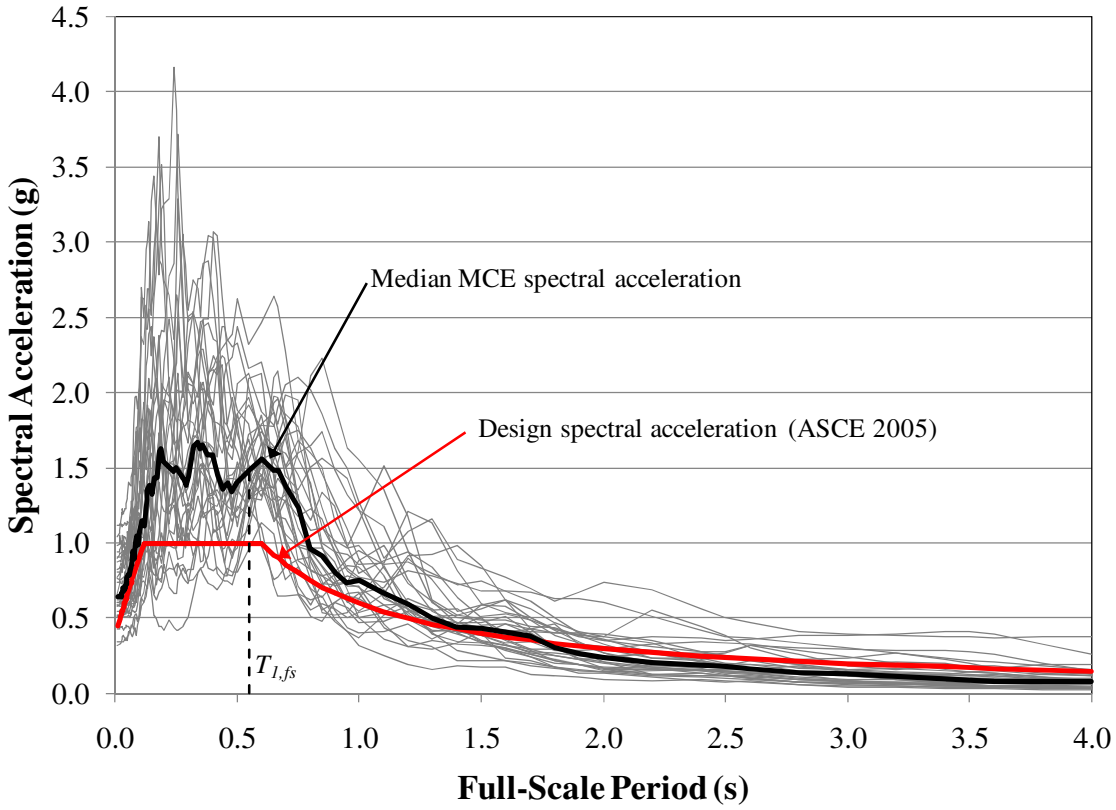

Figure 9.2 – Response spectra for MCE-level ground motions

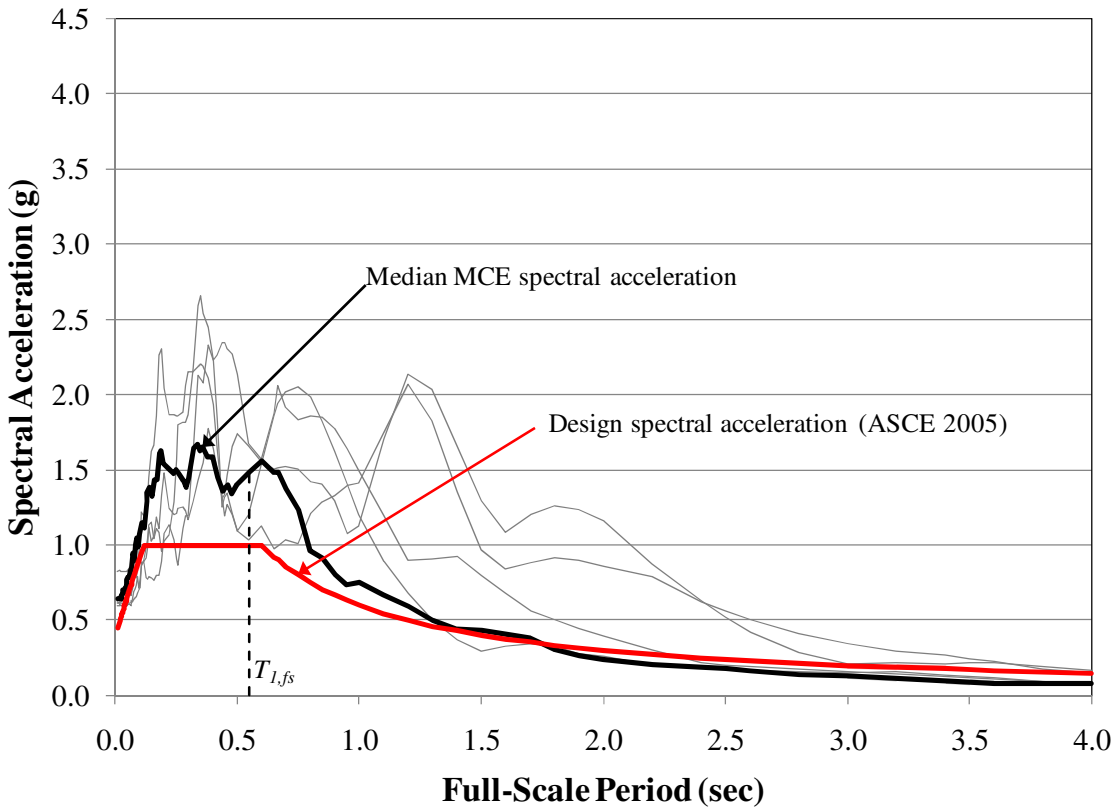

Figure 9.3 – Response spectra for extreme MCE-level ground motions

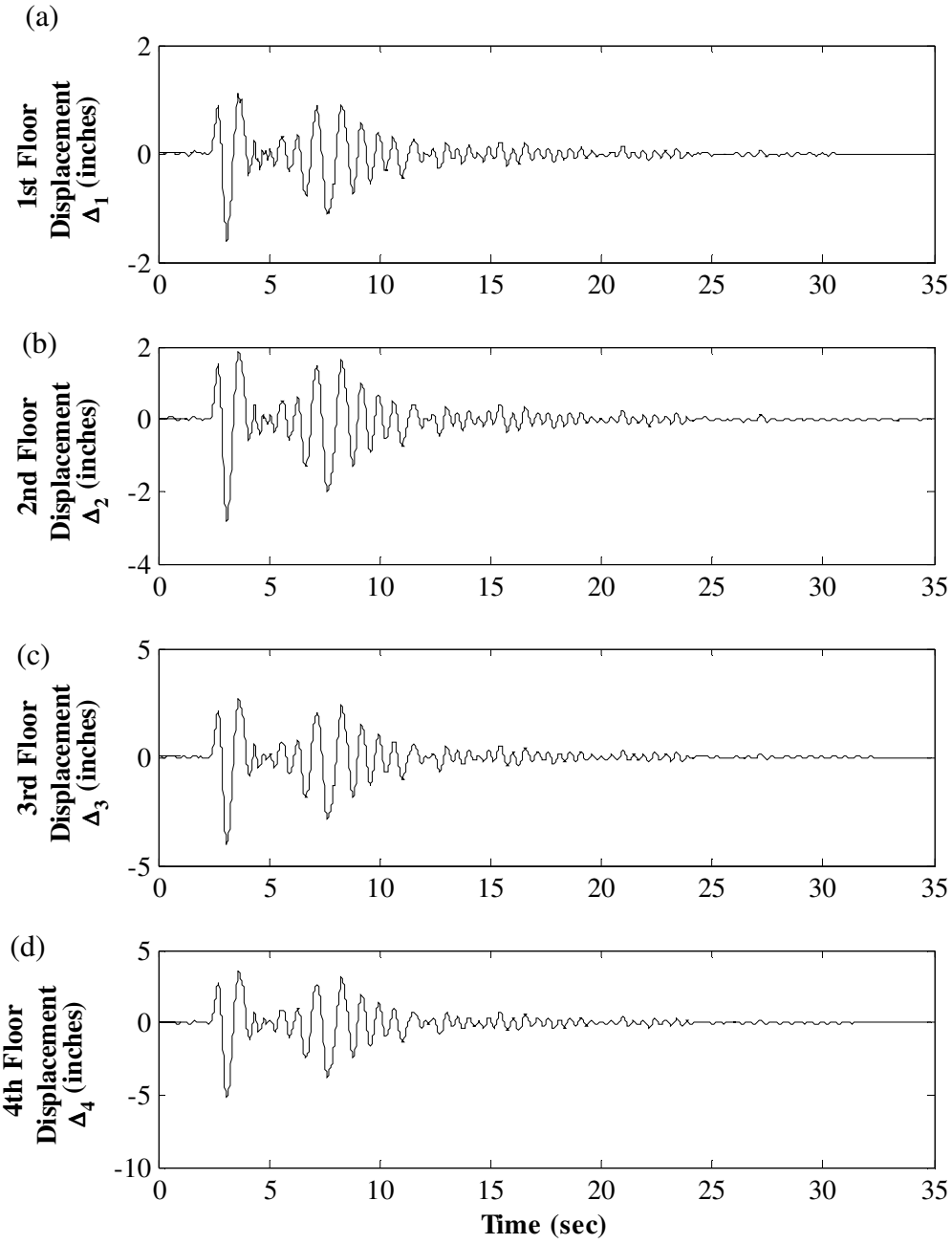

Figure 9.4 – Floor displacement response to DBE_arl090: (a) 1st floor; (b) 2nd floor; (c) 3rd floor; (d) 4th floor

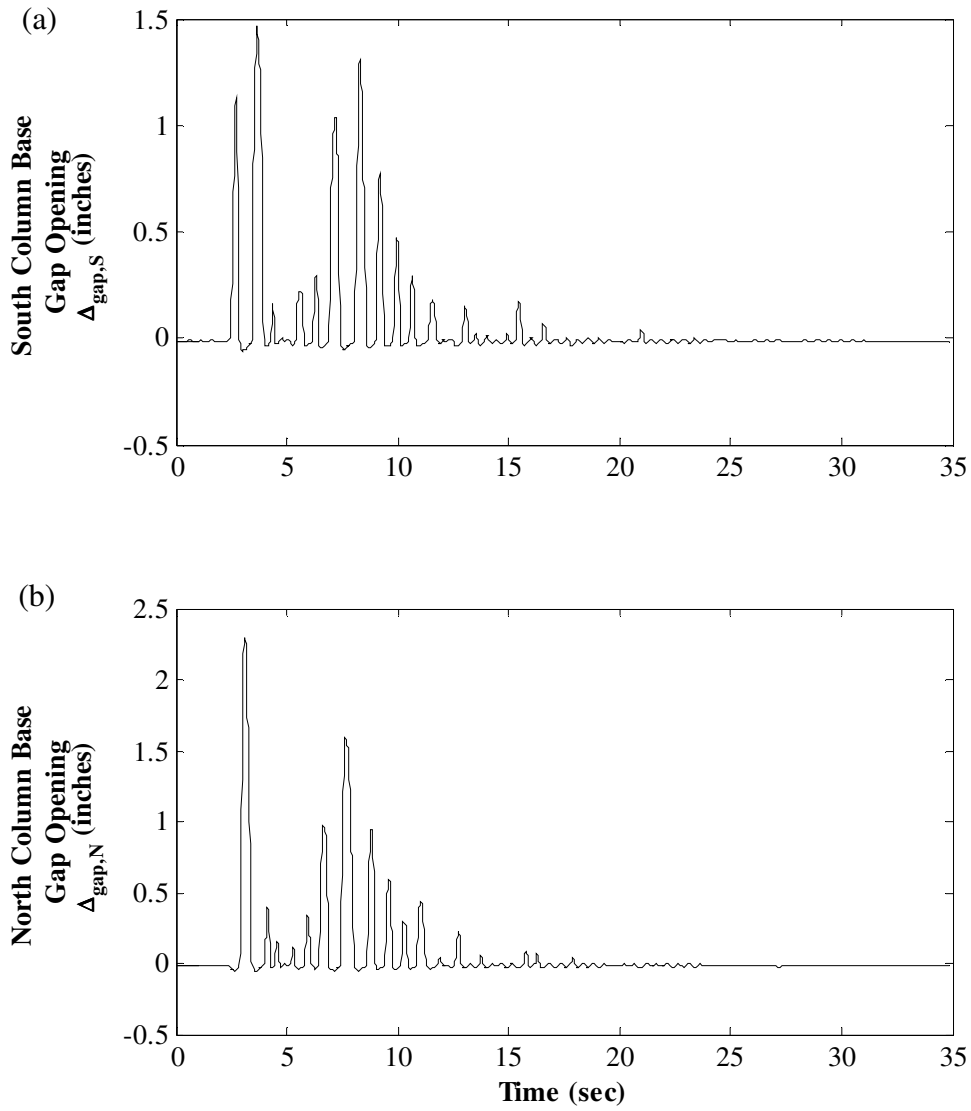

Figure 9.5 – Column base gap opening response to DBE_arl090: (a) at south column base; (b) at north column base

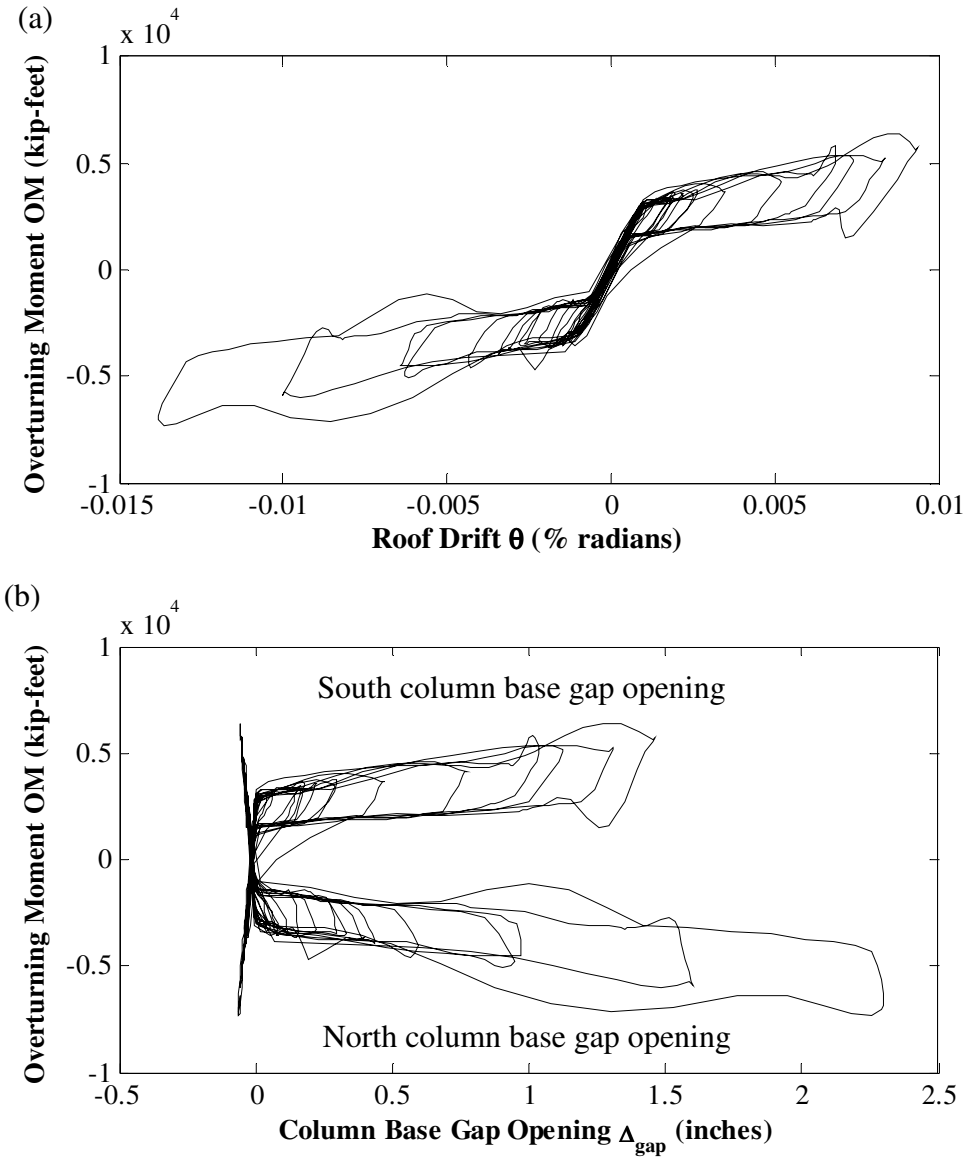

Figure 9.6 – Hysteretic response to DBE_arl090: (a) overturning moment versus roof drift; (b) overturning moment versus gap opening

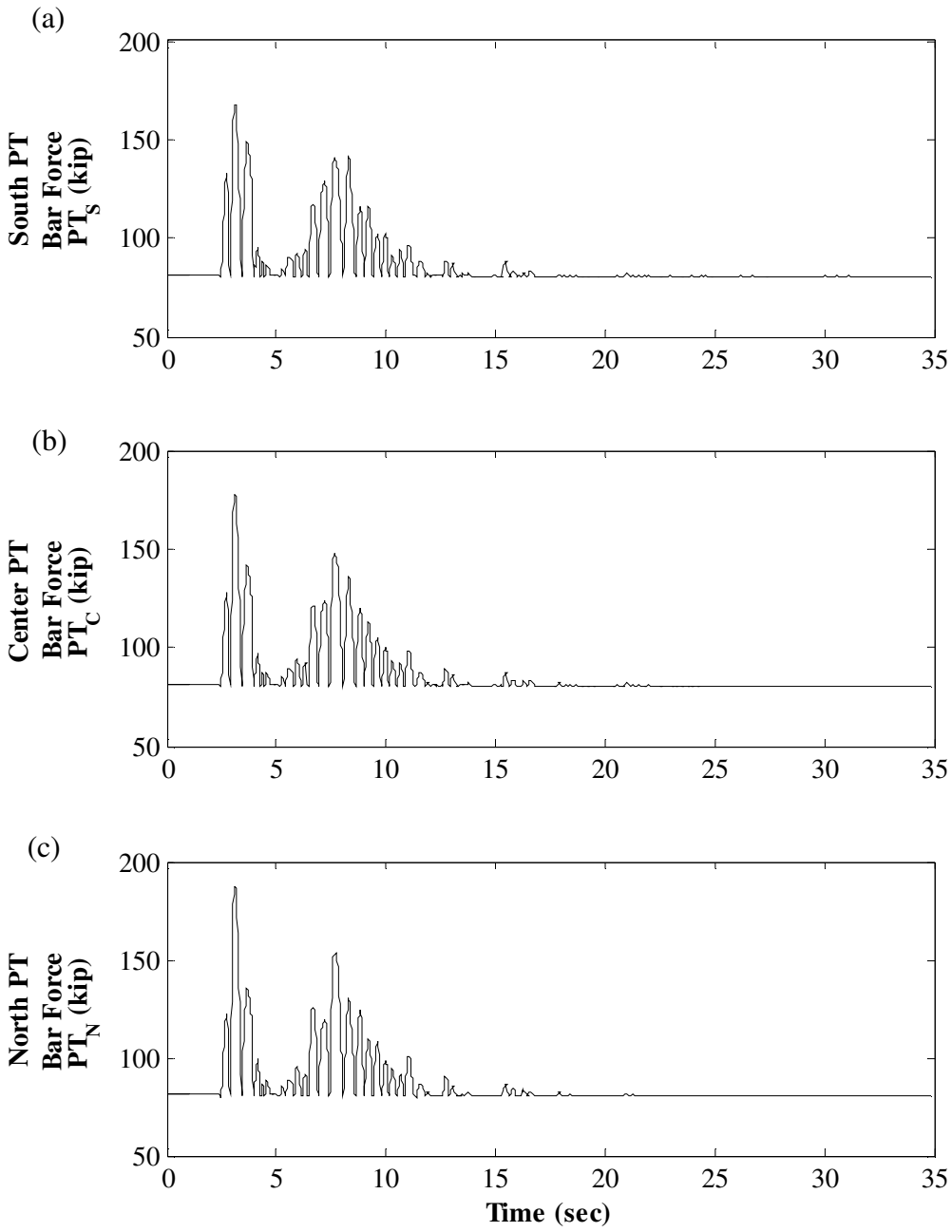

Figure 9.7 – PT force response to DBE_arl090: (a) south PT bars; (b) center PT bars; (c) north PT bars

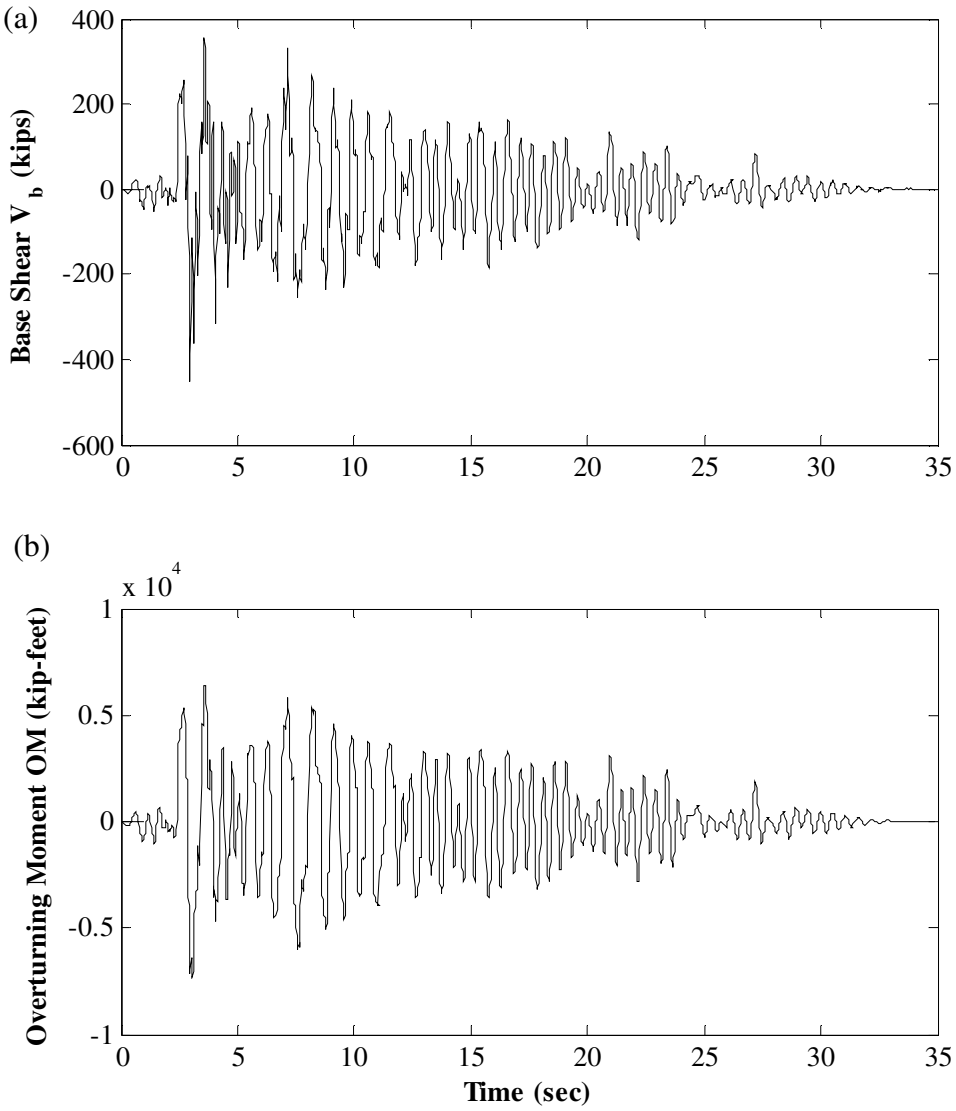

Figure 9.8 – Dynamic time history response to DBE_arl090: (a) base shear; (b) overturning moment

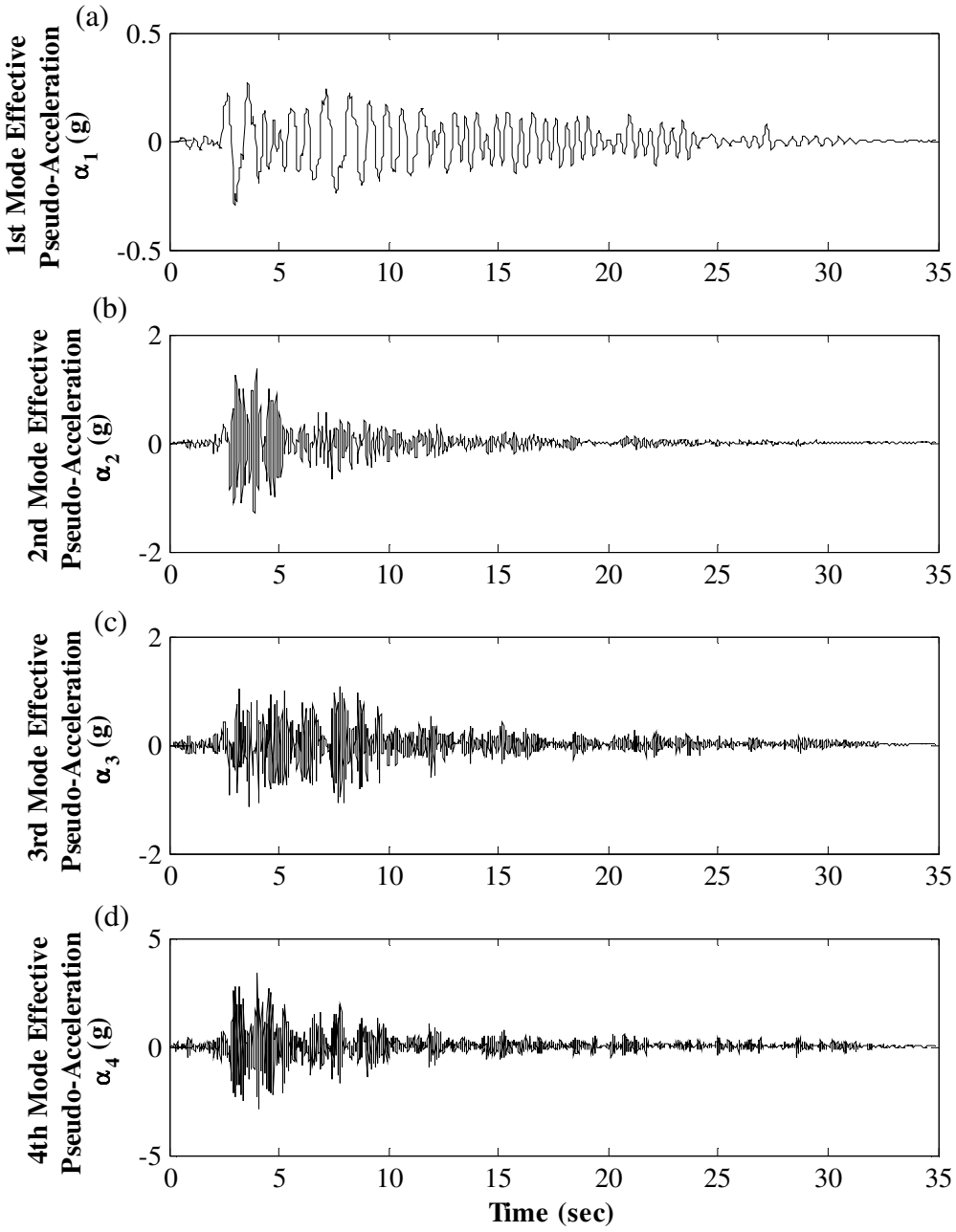

Figure 9.9 – Effective modal pseudo-acceleration response to DBE_arl090: (a) 1st mode; (b) 2nd mode; (c) 3rd mode; (d) 4th mode

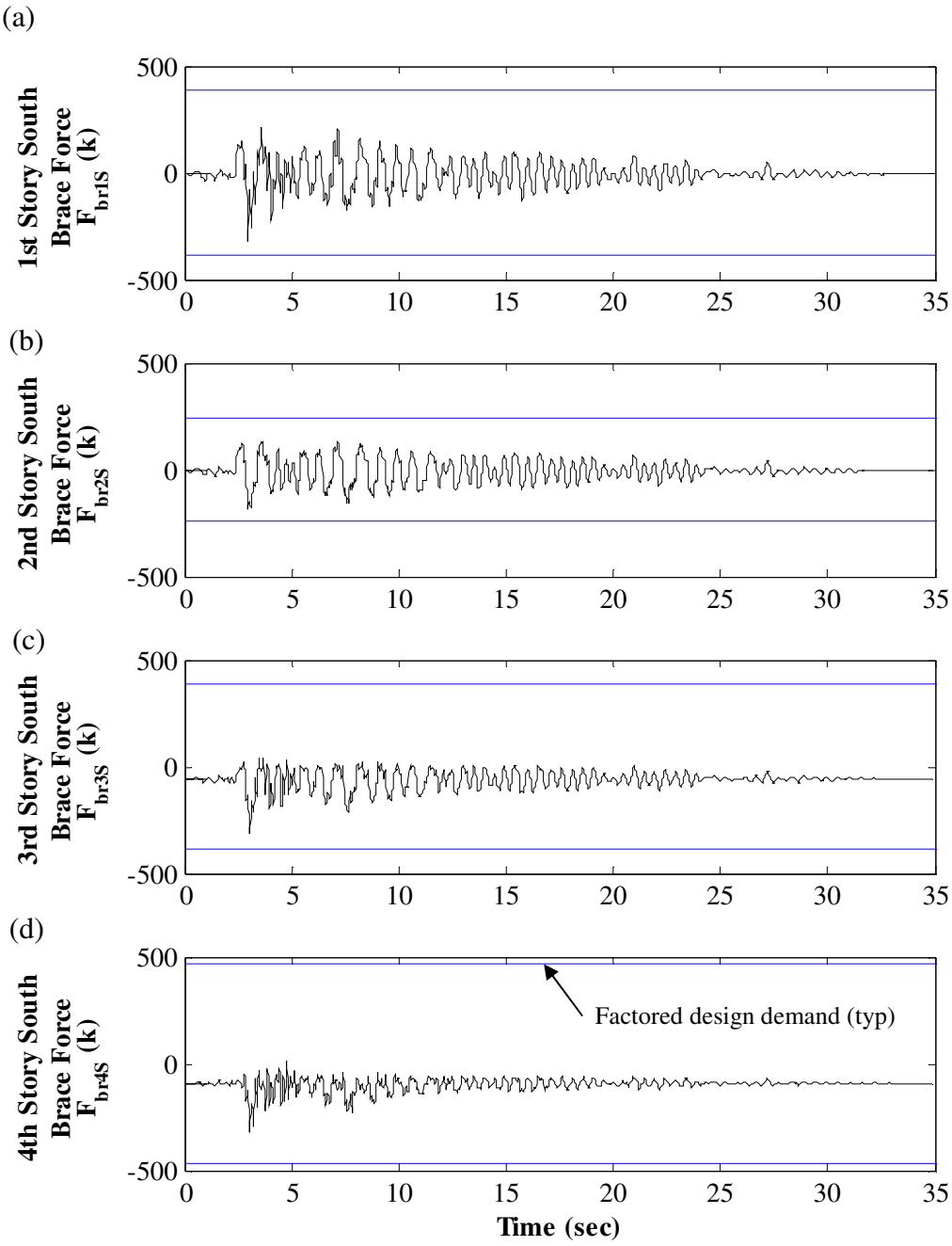

Figure 9.10 – South brace force response to DBE_arl090: (a) 1st story; (b) 2nd story; (c) 3rd story; (d) 4th story

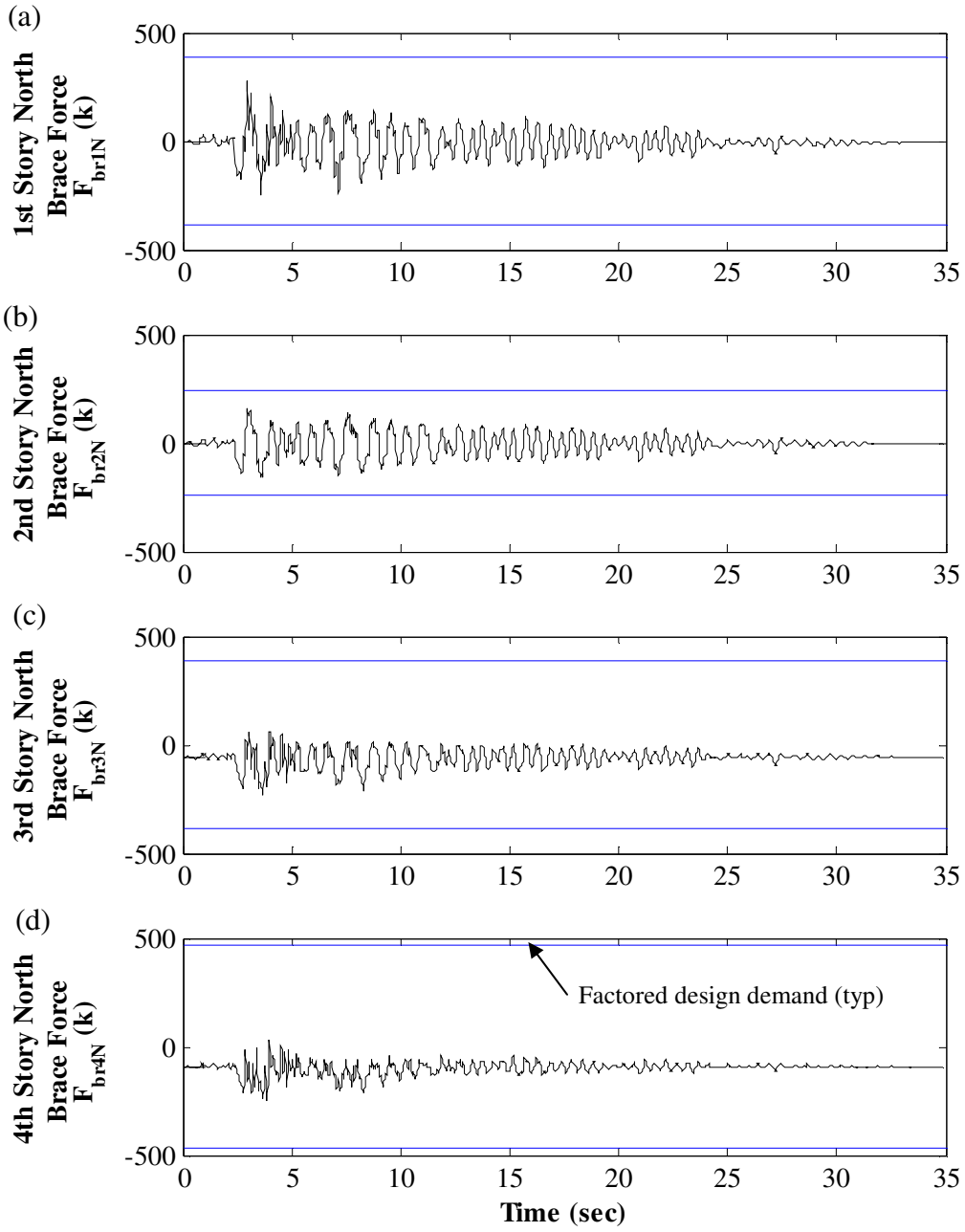

Figure 9.11 – North brace force response to DBE_arl090: (a) 1st story; (b) 2nd story; (c) 3rd story; (d) 4th story

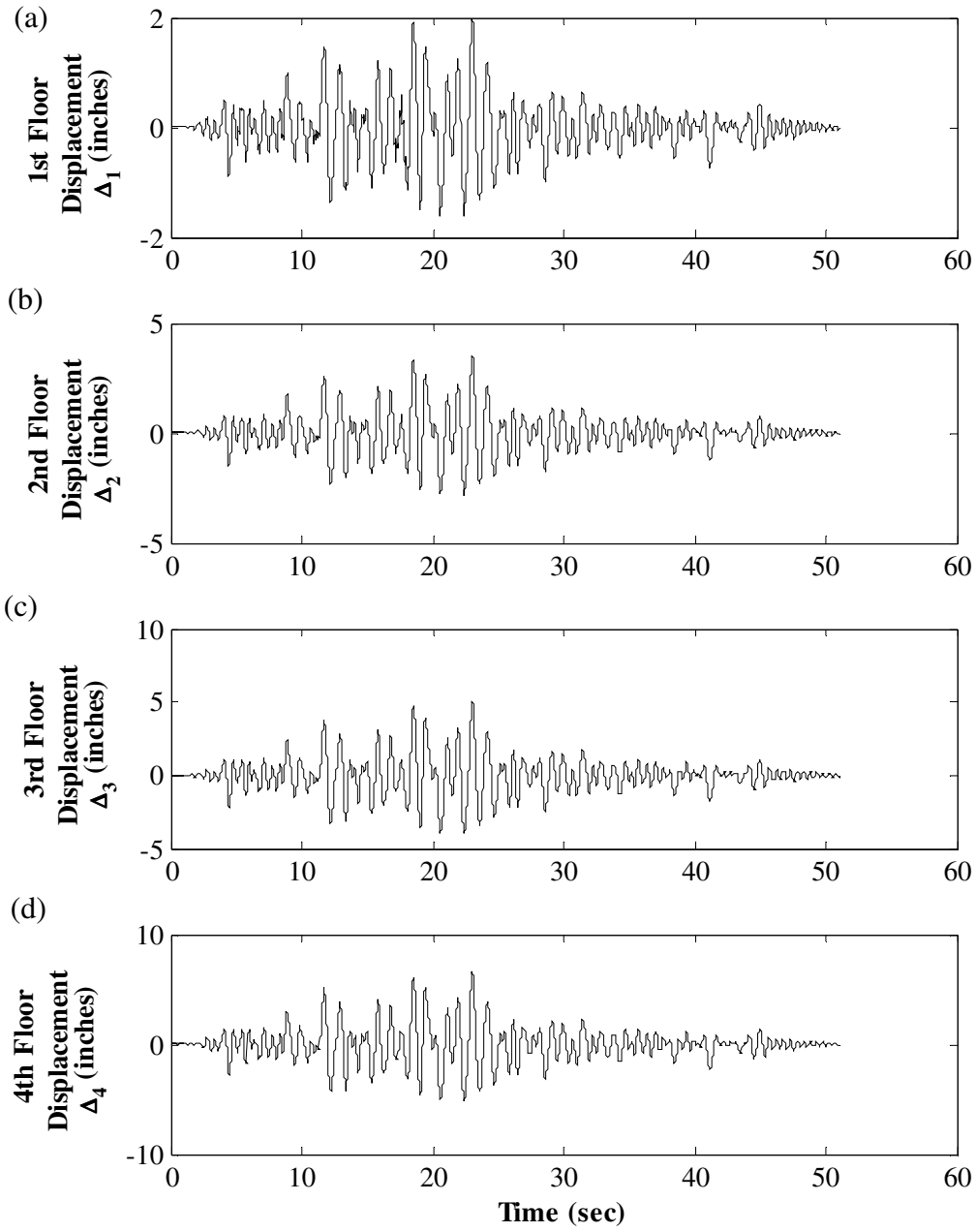

Figure 9.12 – Floor displacement response to MCE_h-cpe237: (a) 1st floor; (b) 2nd floor; (c) 3rd floor; (d) 4th floor

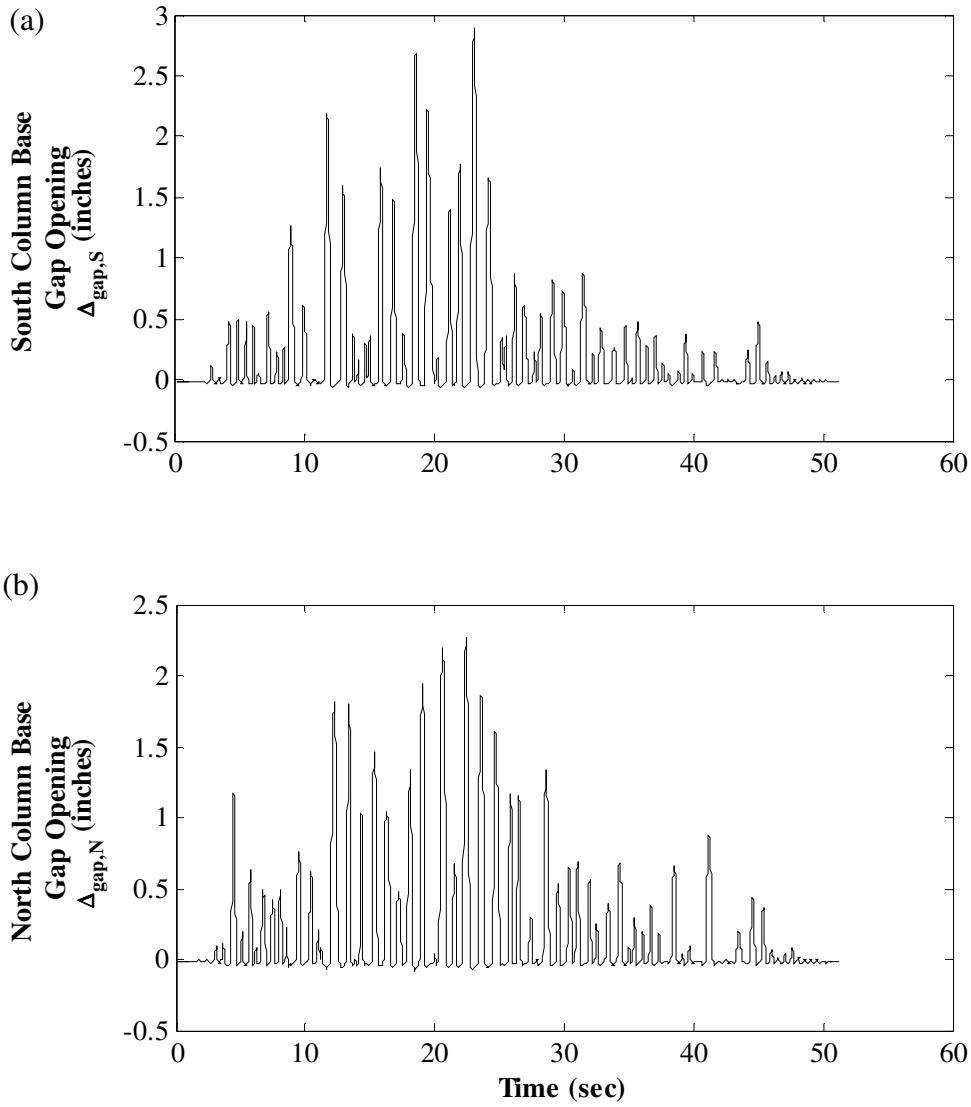

Figure 9.13 – Column base gap opening response to MCE_h-cpe237: (a) at south column base; (b) at north column base

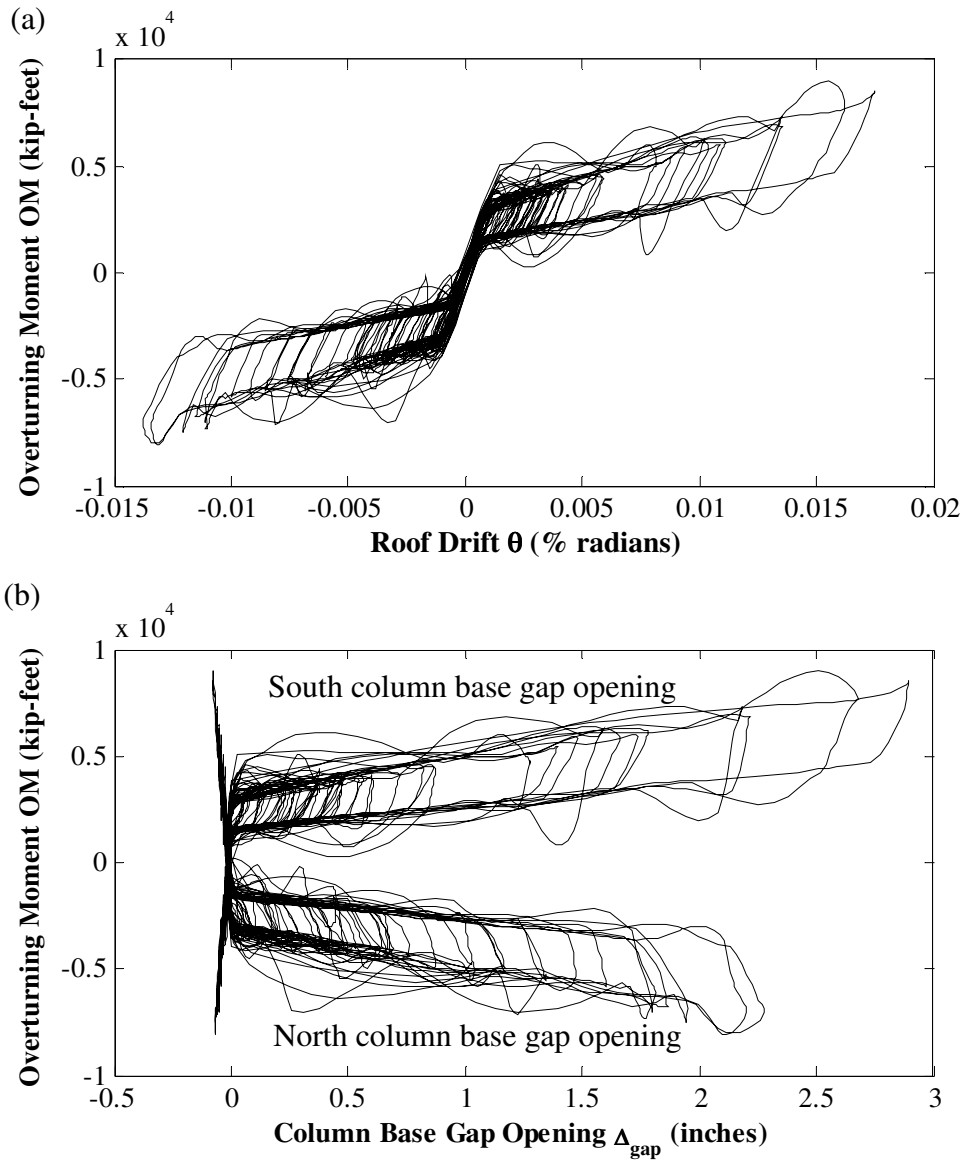

Figure 9.14 – Hysteretic response to MCE_h-cpe237: (a) overturning moment versus roof drift; (b) overturning moment versus gap opening

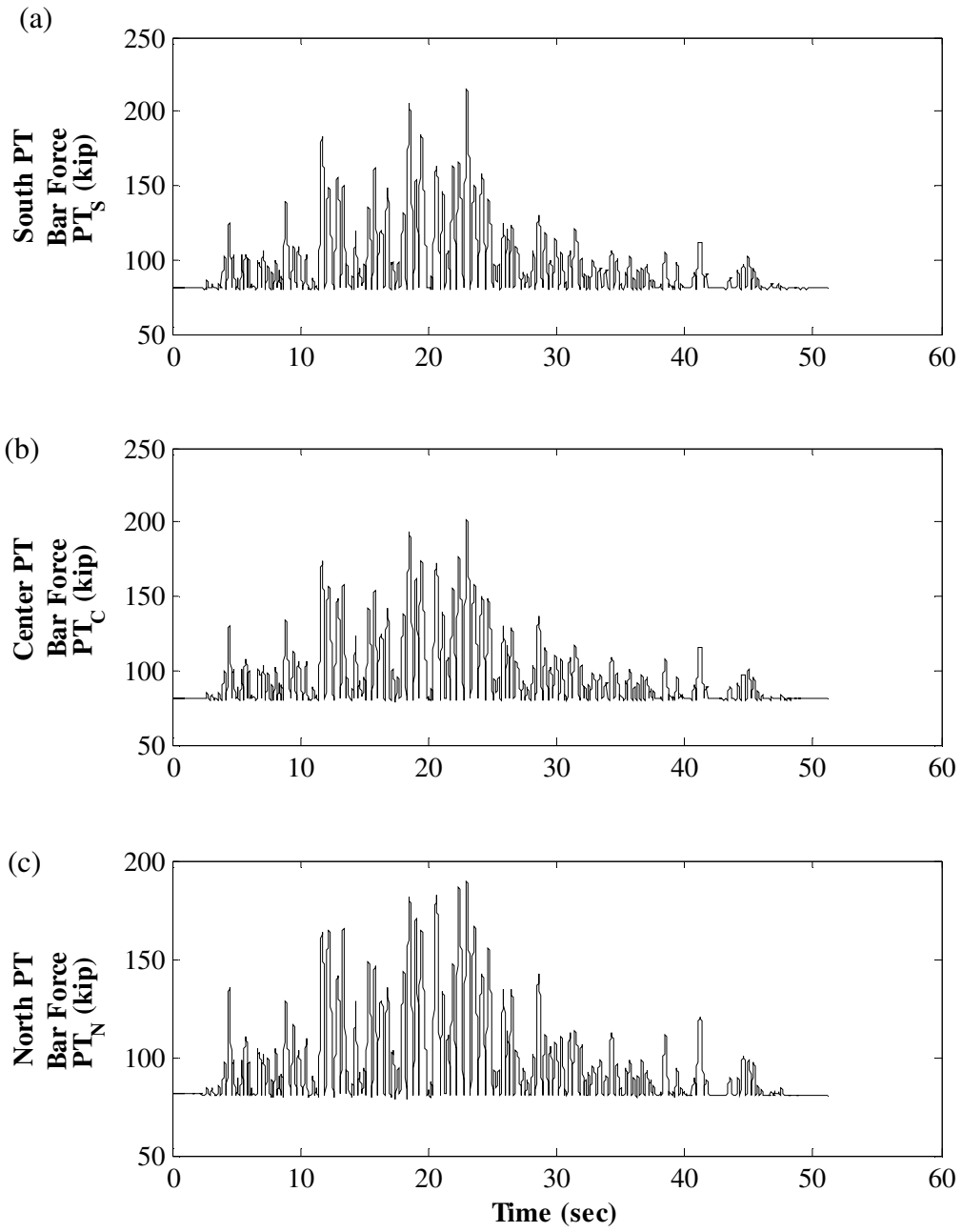

Figure 9.15 – PT force response to MCE_h-cpe237: (a) south PT bars; (b) center PT bars; (c) north PT bars

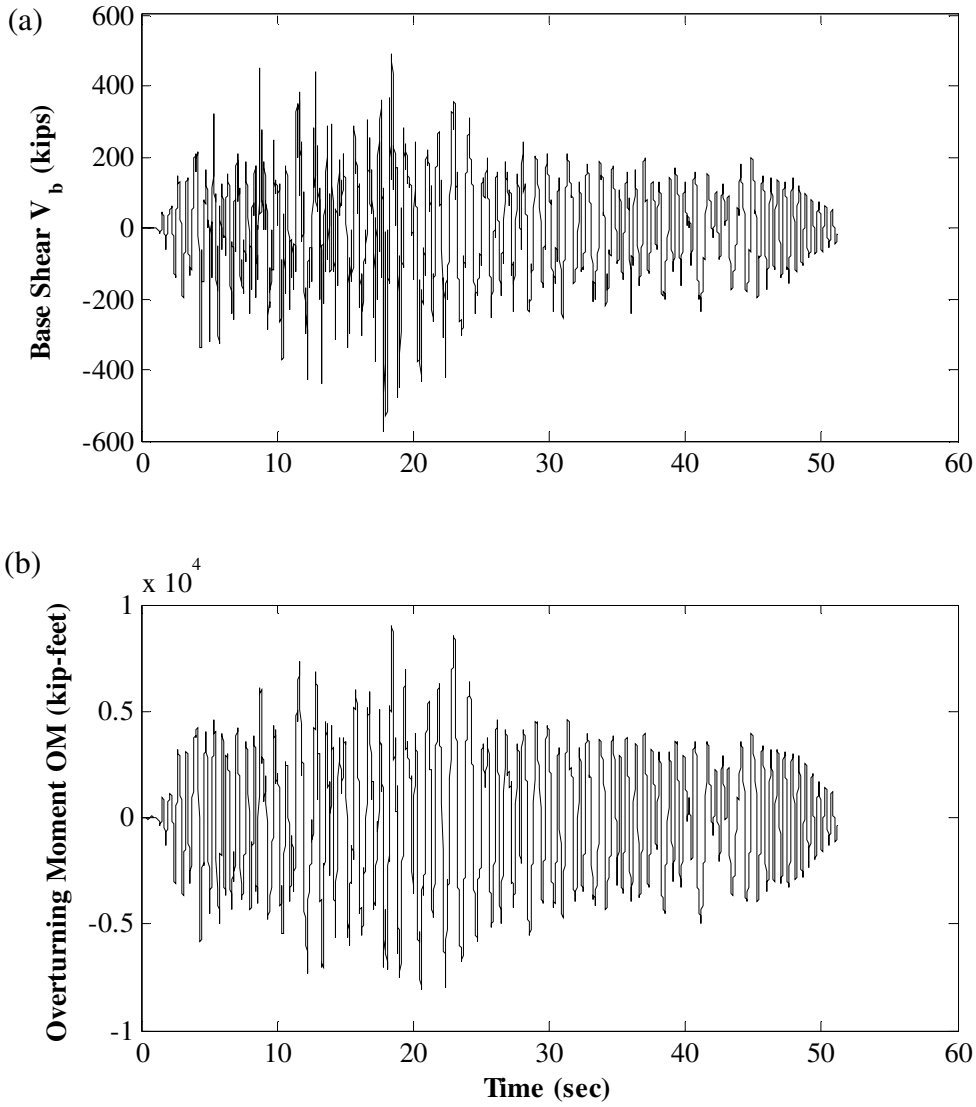

Figure 9.16 – Dynamic time history response to MCE_h-cpe237: (a) base shear; (b) overturning moment

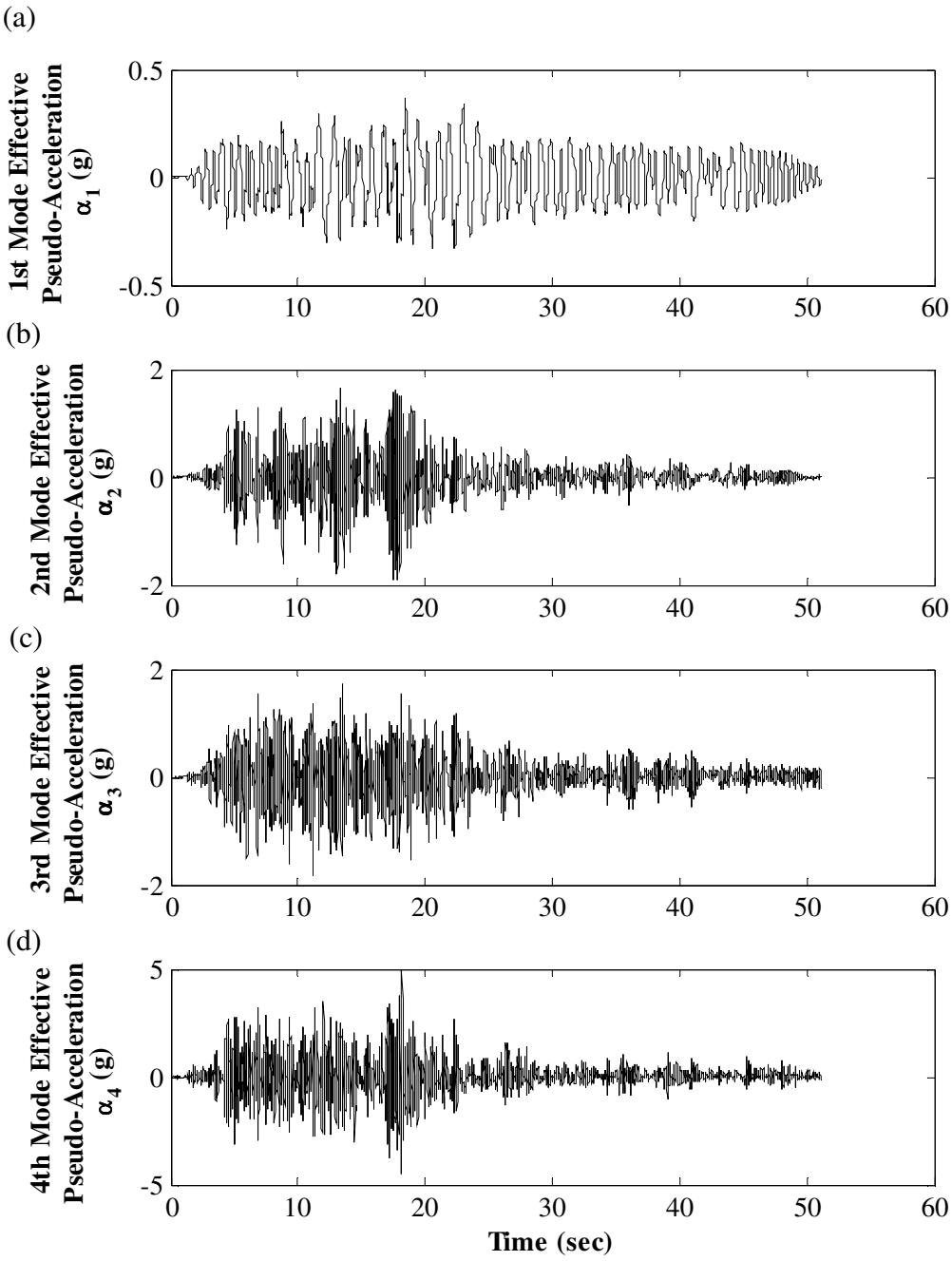

Figure 9.17 – Effective modal pseudo-acceleration response to MCE_h-cpe237: (a) 1st mode; (b) 2nd mode; (c) 3rd mode; (d) 4th mode

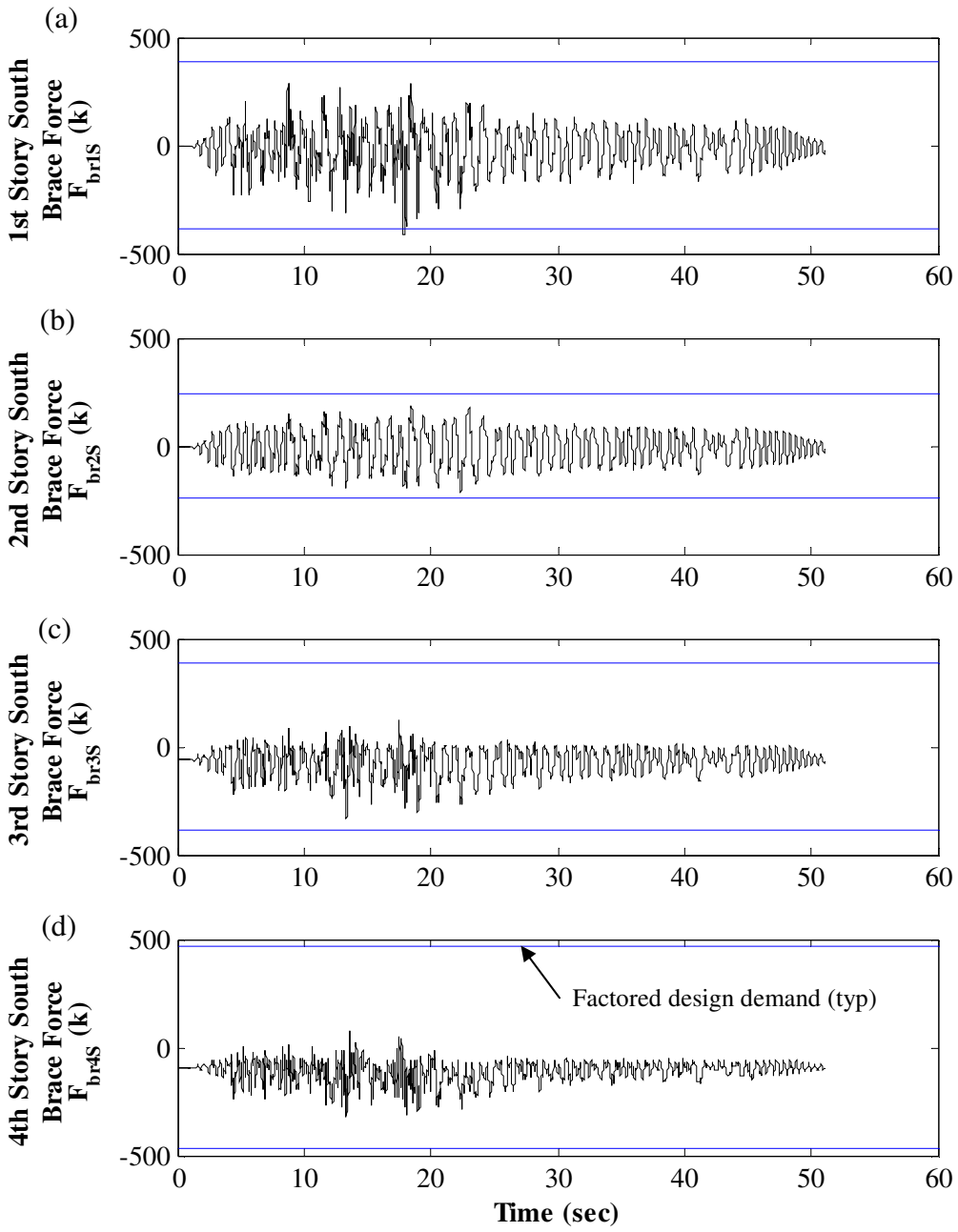

Figure 9.18 – South brace force response to MCE_h-cpe237: (a) 1st story; (b) 2nd story; (c) 3rd story; (d) 4th story

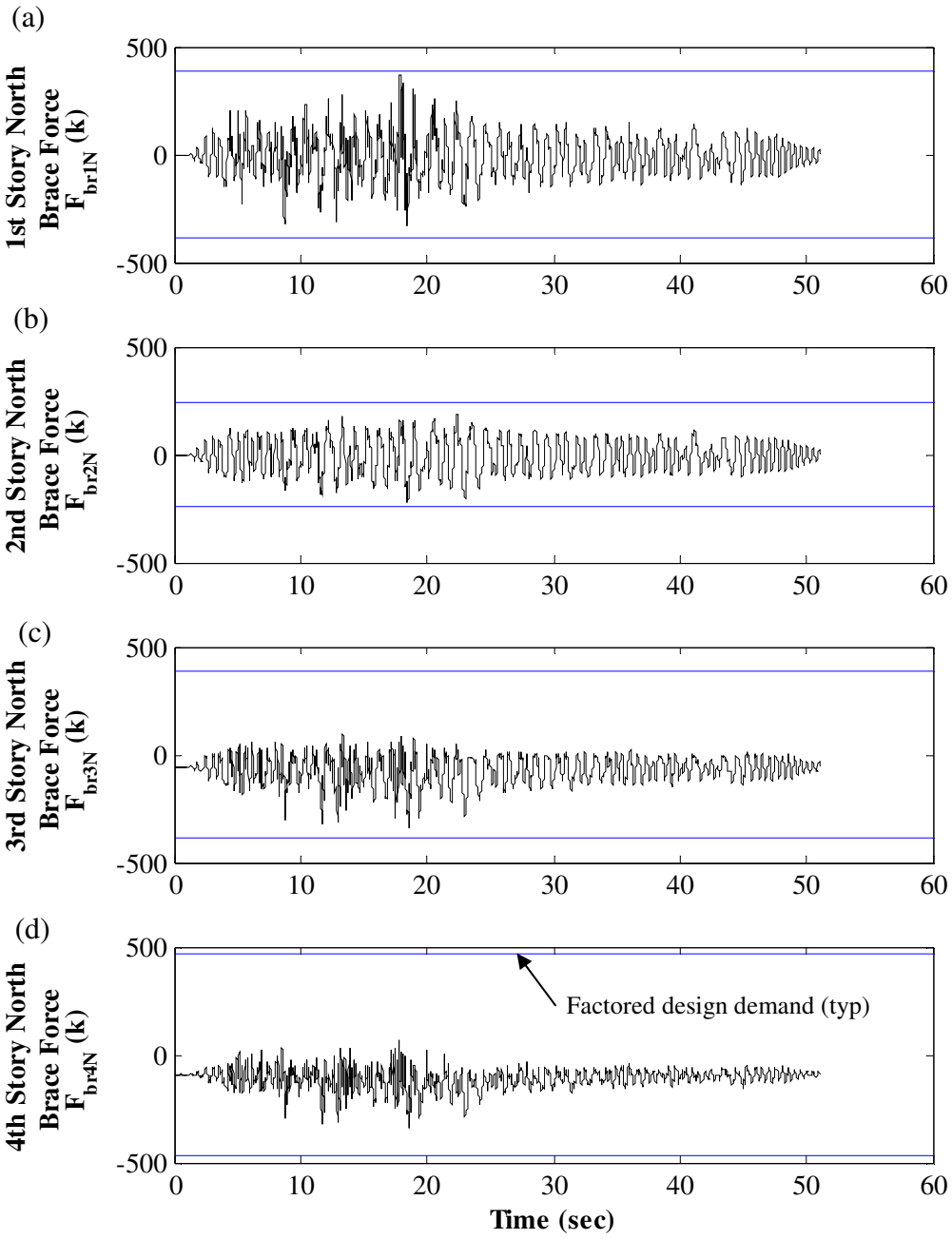

Figure 9.19 – North brace force response to MCE_h-cpe237: (a) 1st story; (b) 2nd story; (c) 3rd story; (d) 4th story

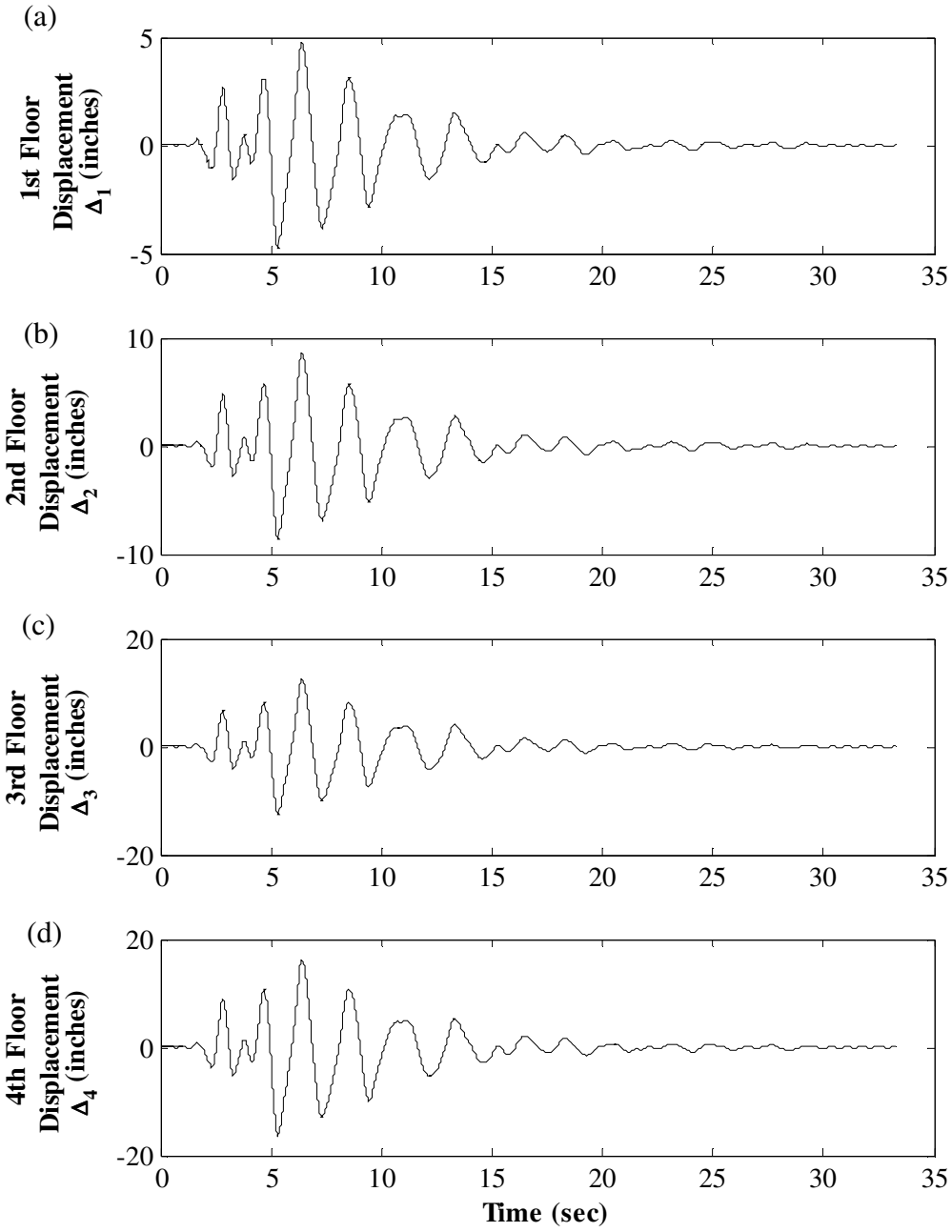

Figure 9.20 – Floor displacement response to xMCE_tak090: (a) 1st floor; (b) 2nd floor; (c) 3rd floor; (d) 4th floor

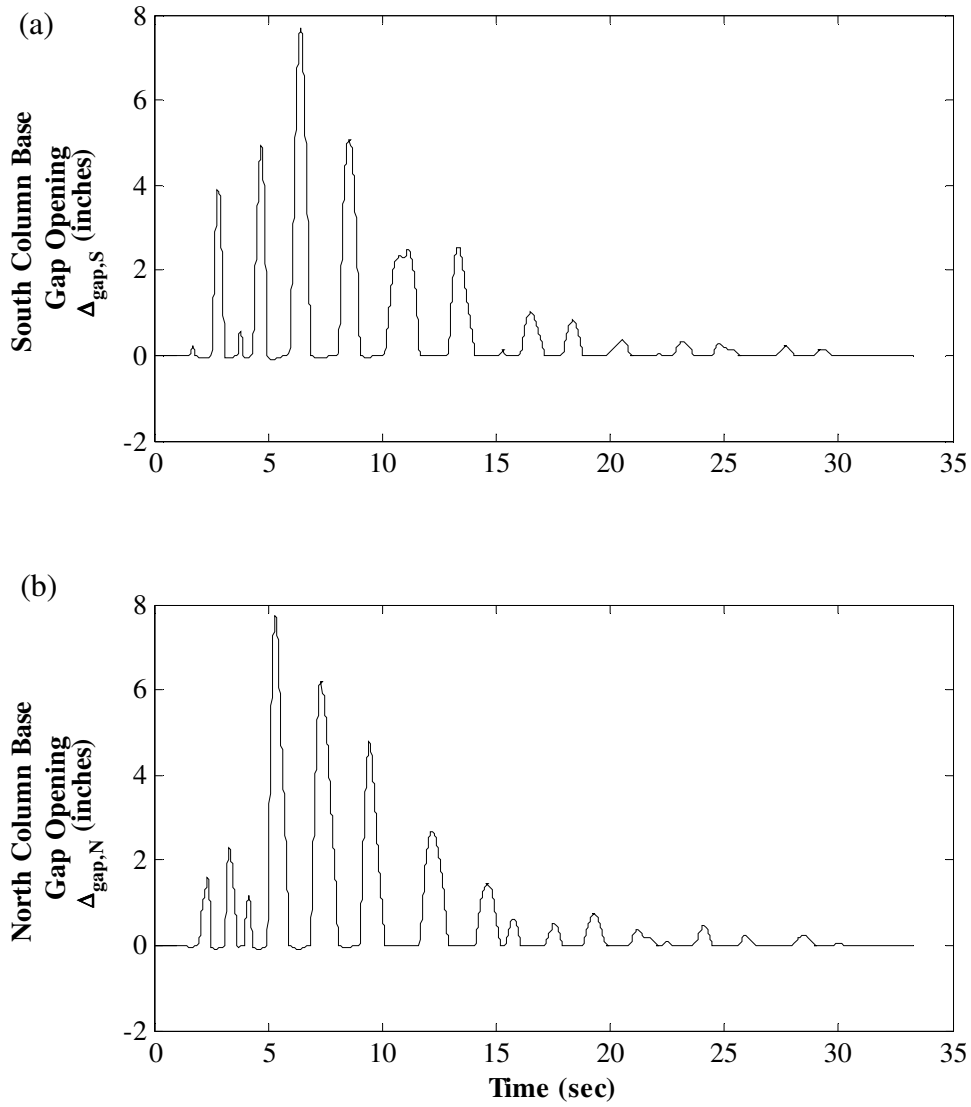

Figure 9.21 – Column base gap opening response to xMCE_tak090: (a) at south column base; (b) at north column base

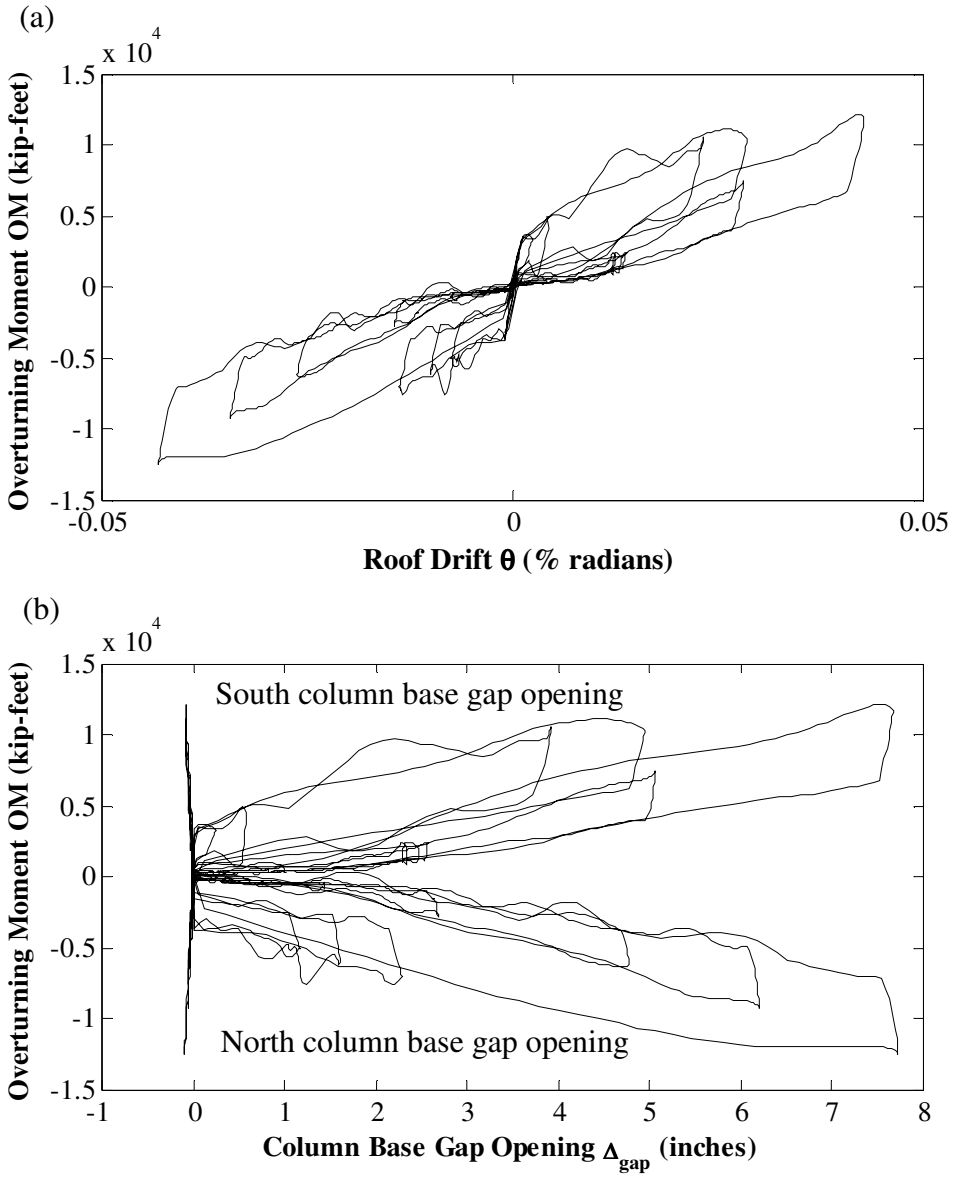

Figure 9.22 – Hysteretic response to xMCE_tak090: (a) overturning moment versus roof drift; (b) overturning moment versus gap opening

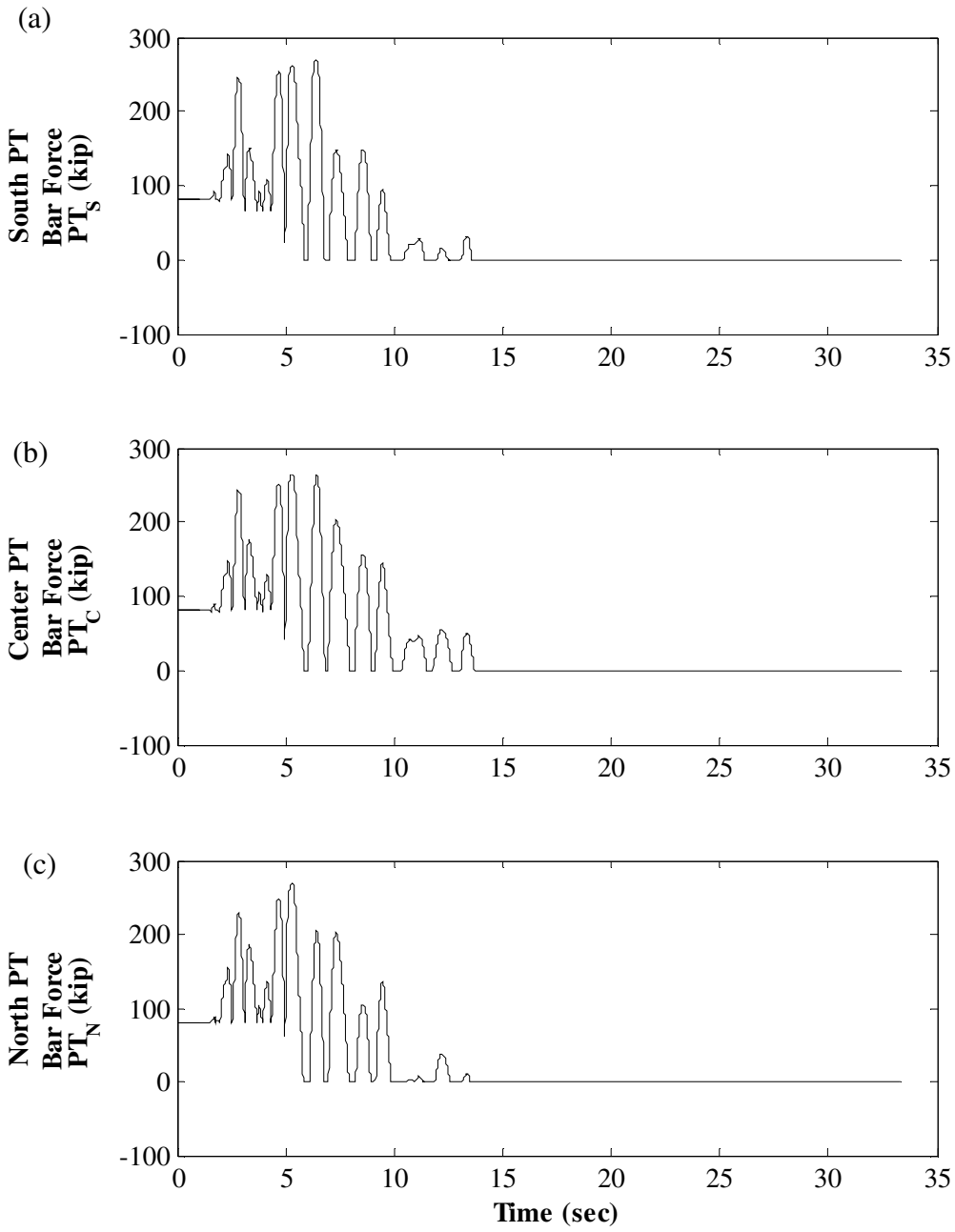

Figure 9.23 – PT force response to xMCE_tak090: (a) south PT bars; (b) center PT bars; (c) north PT bars

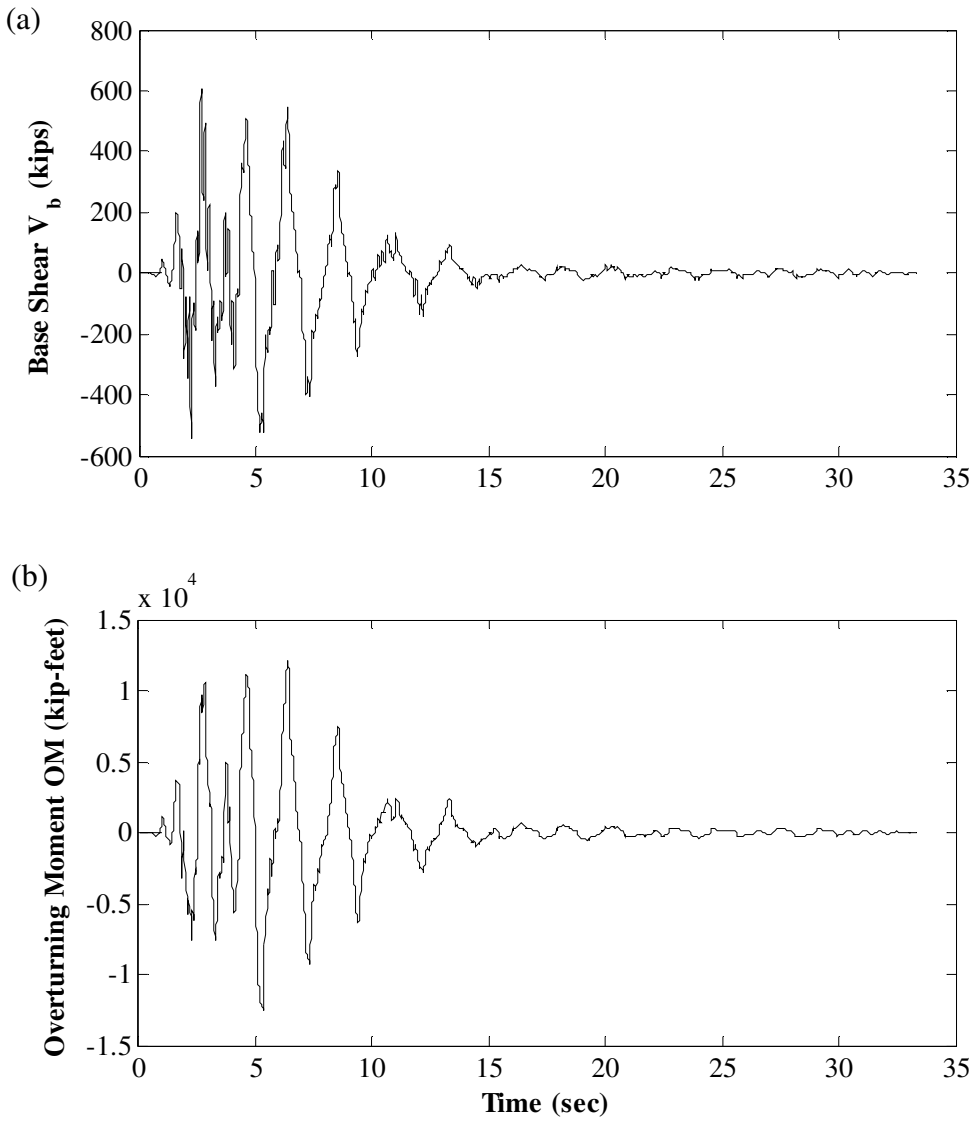

Figure 9.24 – Dynamic time history response to xMCE_tak090: (a) base shear; (b) overturning moment

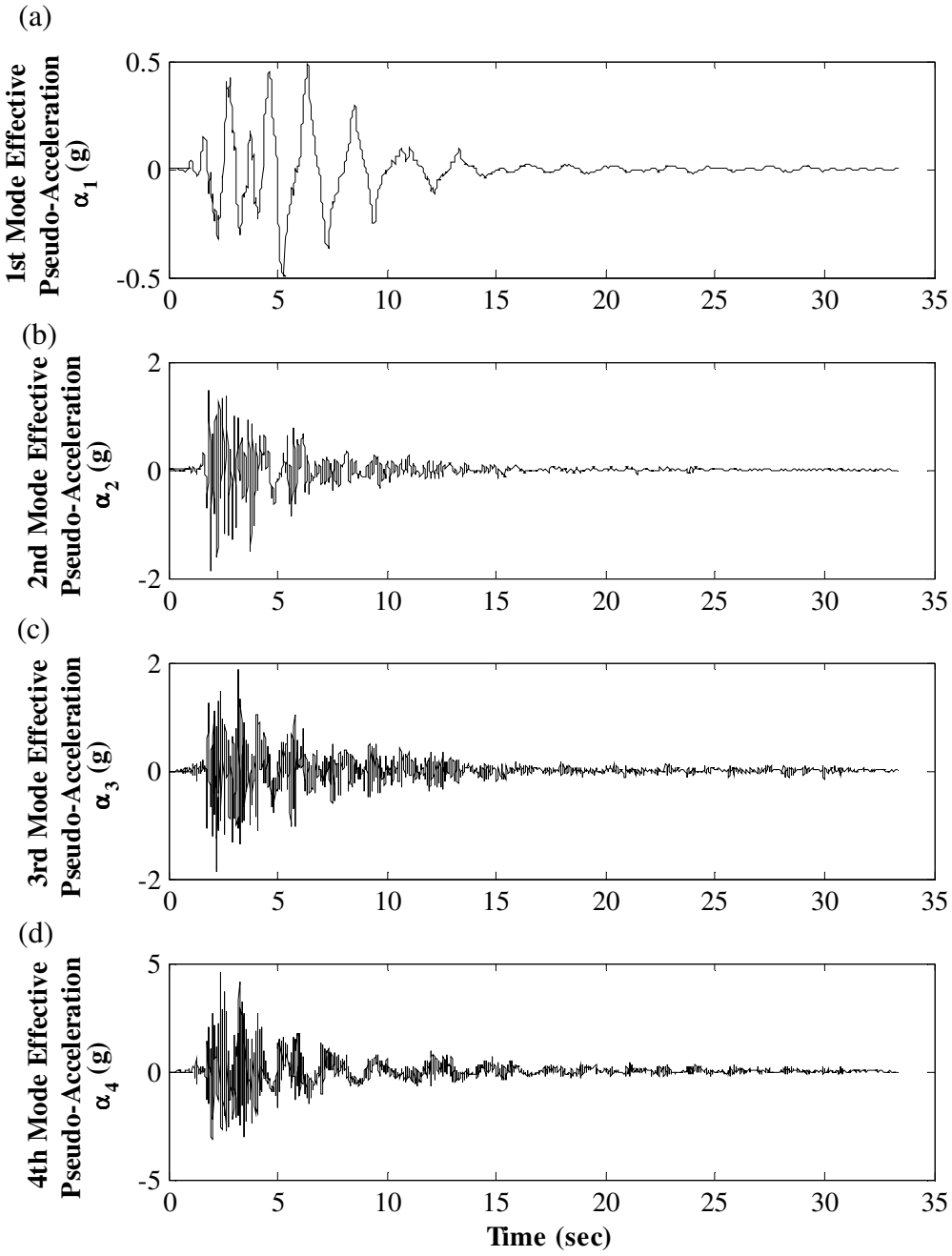

Figure 9.25 – Effective modal pseudo-acceleration response to xMCE_tak090: (a) 1st mode; (b) 2nd mode; (c) 3rd mode; (d) 4th mode

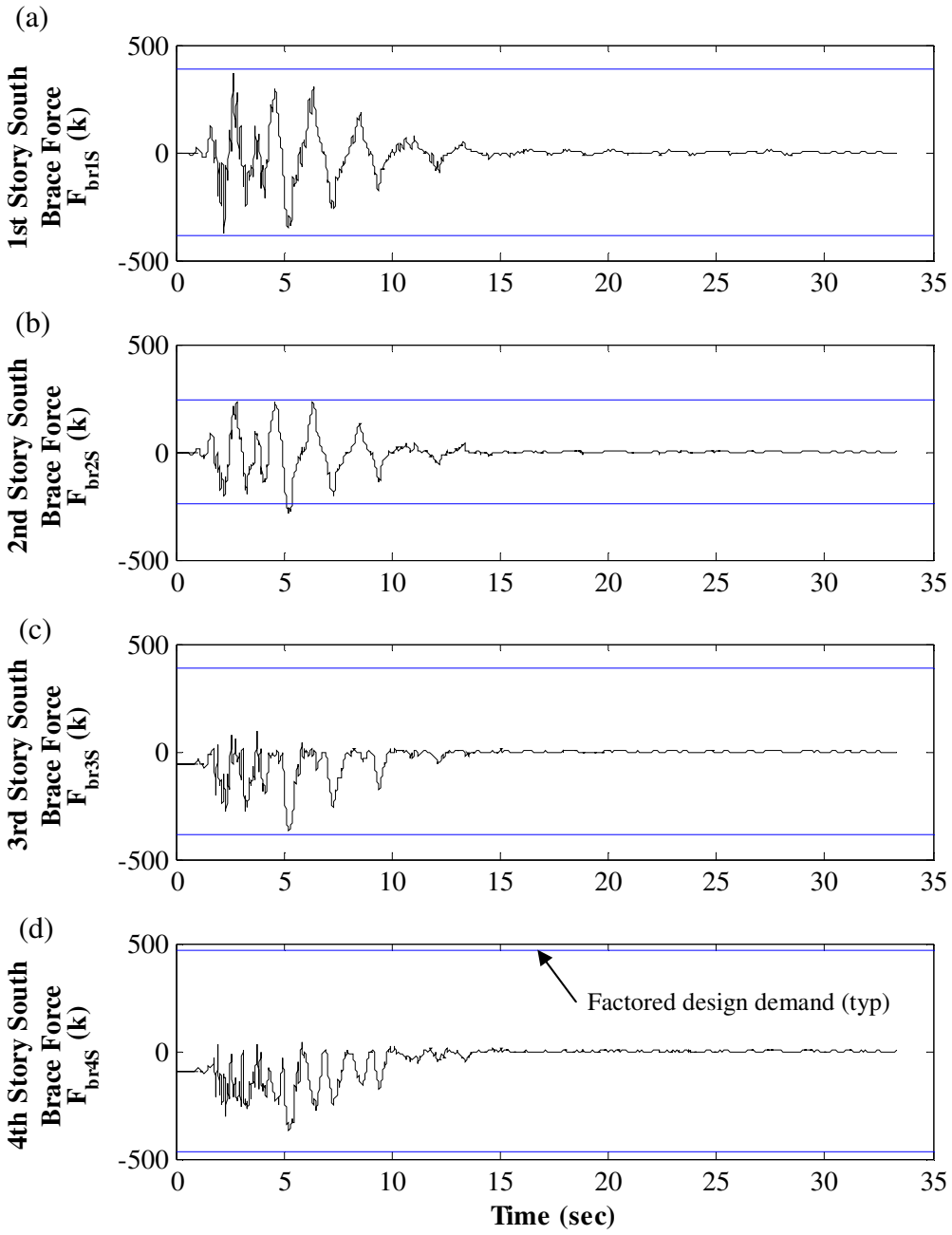

Figure 9.26 – South brace force response to xMCE_tak090: (a) 1st story; (b) 2nd story; (c) 3rd story; (d) 4th story

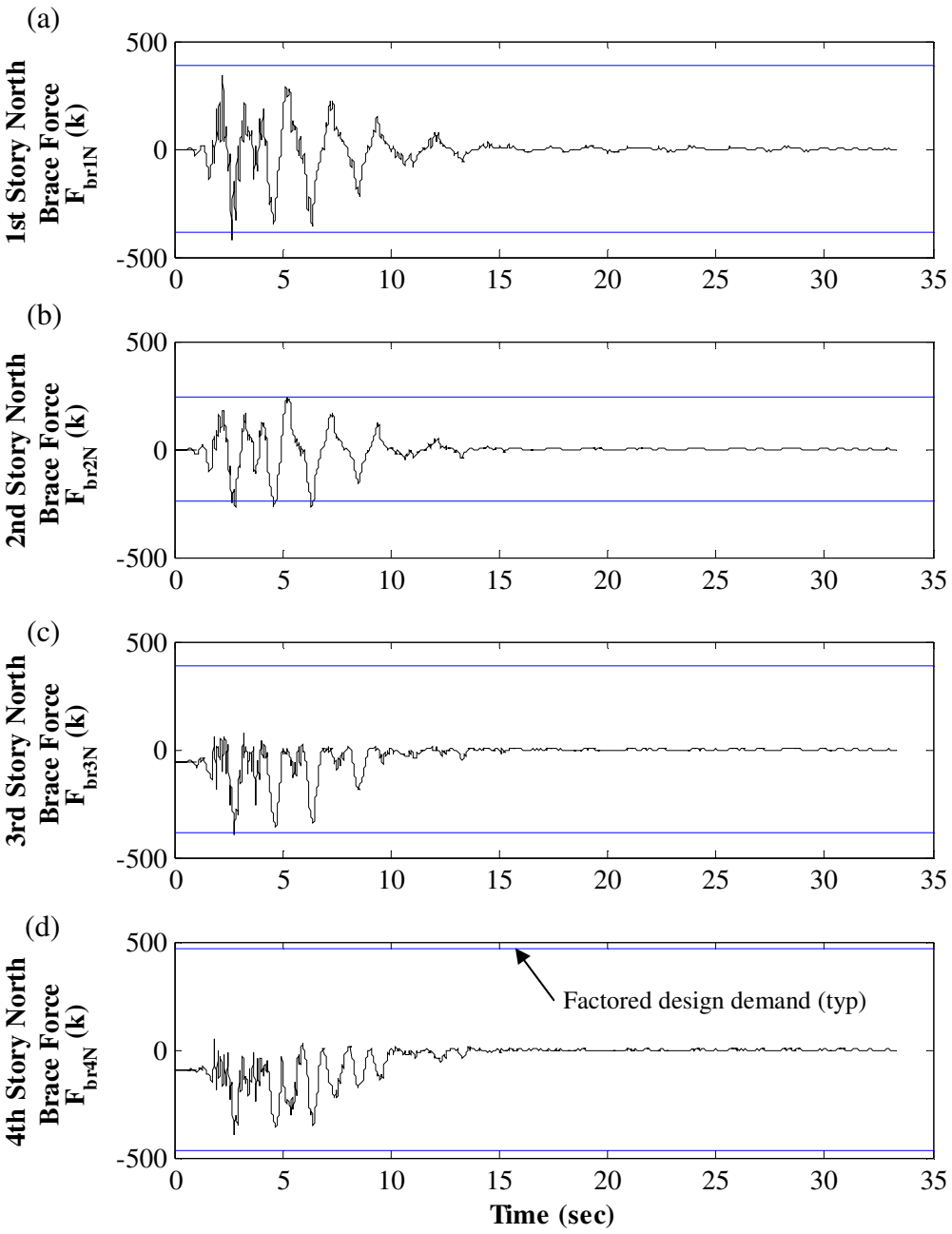

Figure 9.27 – North brace force response to xMCE_tak090: (a) 1st story; (b) 2nd story; (c) 3rd story; (d) 4th story

CHAPTER 10

CORRELATION OF PREDICTIVE NUMERICAL SIMULATION OF SC-CBF TEST STRUCTURE RESPONSE WITH EXPERIMENTAL RESULTS

This chapter discusses the results of the laboratory hybrid simulations and the correlation of these experimental results with the numerical simulation results from the predictive analytical model discussed in Chapter 9. The hybrid simulations were performed at the Real-Time Multi-Dimensional (RTMD) Earthquake Simulation Facility at the Advanced Technology for Large Structural Systems (ATLSS) Center at Lehigh University. The predictive analytical model was developed using OpenSEES (Mazzoni et al. 2009), as discussed in Chapters 8 and 9.

10.1 Experimental Methods

10.1.1 Hybrid Simulation of Earthquake Response

The hybrid simulation method was used to determine the dynamic response of the SC-CBF test structure to a series of DBE-, MCE-, and extreme MCE-level ground motions. The hybrid simulation method uses a model of the structural system that includes two or more substructures. At least one of the substructures is an experimental substructure that exists physically in the laboratory, and at least one of the substructures is an analytical substructure that exists as a simulation model in a computer and describes the remaining

part of the structural system that is not modeled by the experimental substructure. For the SC-CBF test structure, the experimental substructure consists of the SC-CBF, the adjacent gravity columns, the basement substructure, the PT bars, the loading beams, the lateral-load bearings, and the actuators, as discussed in Chapter 8. The analytical substructure consists of a lean-on column, which models the remaining gravity columns and gravity loads that are stabilized by a single SC-CBF; the seismic mass that is tributary to a single SC-CBF; and a damping substructure that models the inherent viscous damping in the system.

In the hybrid simulation method, selected degrees of freedom (DOFs) of the experimental substructure and selected DOFs of the analytical substructure are shared (i.e., are identical). For each time step of the simulated response, restoring forces are calculated at the DOFs of the analytical substructure and are measured from load cells at the DOFs of the experimental substructure. For the SC-CBF test structure, these DOFs are the lateral displacements of the north gravity column of the SC-CBF test structure at the floor levels. The total restoring force is then used to determine the target displacement at each DOF for the following time step.

Displacement commands are input into the hydraulic actuator servo-controller to achieve the target displacement at each DOF for the following time step; substeps may be used until the measured displacement at each DOF reaches the target displacement to be imposed onto the experimental substructure within a specified tolerance. Similarly, the target displacements are imposed on the analytical substructure.

The target displacements at each time step are calculated from the equation of motion using the CR integration algorithm. The equation of motion, discretized at time t_{i+1} is written as:

$$[m]\{\ddot{u}(t_{i+1})\}+[c]\{\dot{u}(t_{i+1})\}+\{r(t_{i+1})\}=\{p(t_{i+1})\} \tag{10.1}$$

where,

$[m]$ = structural mass matrix

$\{\ddot{u}(t_{i+1})\}$ = vector of relative accelerations (second derivative with respect to time of target displacements)

$[c]$ = structural damping matrix

$\{\dot{u}(t_{i+1})\}$ = vector of relative velocities (first derivative with respect to time of target displacements)

$\{r(t_{i+1})\}$ = vector of restoring forces of the structure

$\{p(t_{i+1})\}$ = vector of applied external force

where, for earthquake ground motion input,

$$\{p(t_{i+1})\}=-[m]\cdot\{i\}\cdot\ddot{u}_g(t_{i+1}) \tag{10.2}$$

where,

$\{i\}$ = influence vector = $\{1\ 1\ 1\ 1\}^T$ for a four-degree-of-freedom system

$\ddot{u}_g(t_{i+1})$ = ground acceleration

The unconditionally stable explicit CR integration algorithm (Chen et al. 2009) is used to solve the equations of motion for each time step. Assuming that the target displacement, velocity, and acceleration vectors at time t_i ($\{u(t_i)\}$, $\{\dot{u}(t_i)\}$, and $\{\ddot{u}(t_i)\}$, respectively) are known, the velocity and displacement at time t_{i+1} are determined using the CR integration algorithm as follows:

$$\{\dot{u}(t_{i+1})\} = \{\dot{u}(t_i)\} + \Delta t \cdot [\alpha_1] \cdot \{\ddot{u}(t_i)\} \tag{10.3}$$

$$\{u(t_{i+1})\} = \{u(t_i)\} + \Delta t \cdot \{\dot{u}(t_i)\} + \Delta t^2 \cdot [\alpha_2] \cdot \{\ddot{u}(t_i)\} \tag{10.4}$$

where,

Δt = size of the time step = t_{i+1} - t_i

$$[\alpha_1] = [\alpha_2] = 4 \cdot \left(4 \cdot [m] + 2 \cdot \Delta t \cdot [c] + \Delta t^2 \cdot [k]\right)^{-1} \cdot [m] \tag{10.5}$$

$[m]$ = structural mass matrix

$[c]$ = structural damping matrix

$[k]$ = linear elastic stiffness matrix of the structure, including the stiffness of the analytical substructure and an estimate of the stiffness of the experimental substructure

The target displacement vector $\{u(t_{i+1})\}$ can be decomposed into a displacement vector for the DOFs of the experimental substructure, $\{u^e(t_{i+1})\}$, and a displacement vector for

the DOFs of the analytical substructure, $\{u^a(t_{i+1})\}$. These displacements, referred to as the "target displacements," are imposed upon the experimental substructure and the analytical structure, and the restoring force vector $\{r(t_{i+1})\}$ (which is the sum of subvectors $\{r^e(t_{i+1})\}$ for the experimental substructure and $\{r^a(t_{i+1})\}$ for the analytical substructure) is determined. The equation of motion can then be solved for the unknown acceleration at time t_{i+1} as follows (Chen et al. 2009):

$$\{\ddot{u}(t_{i+1})\} = [m]^{-1}(\{p(t_{i+1})\} - [c]\{\dot{u}(t_{i+1})\} - \{r(t_{i+1})\}) \tag{10.6}$$

For the hybrid simulations of the earthquake response of the SC-CBF test structure, a series of command displacements are applied to the experimental substructure using substeps to smoothly (and monotonically) impose the target displacements. For the first substep, the target displacement, $\{d^{c(1)}(t_{i+1})\}$, is equal to the previous target displacement plus a fraction of the change in the target displacement over the time step i:

$$\{d^{c(1)}(t_{i+1})\} = \{u^e(t_i)\} + \beta \cdot (\{u^e(t_{i+1})\} - \{u^e(t_i)\}) \tag{10.9}$$

where,

β = fraction of the total change in displacement applied in each substep; for this study, $\beta = 0.80$

To limit the duration of the hybrid simulations=, the command displacement for the first substep is applied to the experimental substructure over a duration of one second (i.e., $dt^{(1)} = 1.0$ s). A vector of measured displacements at each DOF at the end of substep j, denoted $\{u^{m(j)}(t_{i+1})\}$, are used to check convergence to the target displacements.

$\{u^{m(j)}(t_{i+1})\}$ is obtained by averaging 16 displacement measurements taken at a frequency of 2048 Hz, for an effective frequency of 128 Hz for the averaged measurements. This averaging is performed to reduce the effect of noise. These low frequency measurements provided reasonable estimates of the actual displacements because the simulations were performed at a slow rate.

For subsequent substeps (i.e., $j = 2$ to n, where n is the number of substeps required for the measured displacements to converge to within a small tolerance (±0.005 inches) of the target displacements $\{u^e(t_{i+1})\}$), the command displacement is:

$$\left\{d^{c(j)}(t_{i+1})\right\} = \left\{u^{m(j-1)}(t_i)\right\} + \beta \cdot \left(\left\{u^e(t_{i+1})\right\} - \left\{u^{m(j-1)}(t_i)\right\}\right) \tag{10.10}$$

The command displacement for the j^{th} substep is applied to the experimental substructure over $dt^{(j)} = (1-\beta)^{(j-1)}$ seconds; this reduction in the duration of the substep is intended to maintain constant velocity during the time the target displacement is imposed on the experimental substructure. A minimum value of $dt^{(j)}$ is set at 25 ms, which limits the duration of the substep if four or more substeps are required.

When $\{u^{m(j)}(t_{i+1})\}$ has converged to within the tolerance of $\{u(t_{i+1})\}$, the experimental restoring forces at each DOF, $\{r^e(t_{i+1})\}$, are then measured.

A schematic representation of the implementation of the CR algorithm is shown in Figure 10.1.

Near the end of each hybrid simulation, as the amplitude of the earthquake ground acceleration record subsided, the damping ratio in the analytical substructure was

artificially increased to damp out the response at the end of the test. Therefore, the final half second to one second of experimental response is not expected to correlate with the results of the numerical simulations.

10.1.2 Static Testing

In addition to the hybrid simulations of earthquake response, static tests were performed to assess the condition of the SC-CBF test structure. Two types of static pushover tests were performed: displacement-controlled pushovers, where a displacement pattern was applied to the structure and scaled up to a target peak displacement, and force-controlled pushovers, where a force was applied at a single floor level and scaled up to a target peak force level. These static tests were intended to determine if the properties (e.g., stiffness and strength) of the SC-CBF test structure were changing due to structural damage or other changes in the condition of the structure. Further details of the static testing are presented by Chancellor et al. (2010).

10.2 Experimental Program

There were three main phases of the experimental program: static calibration, dynamic calibration, and dynamic testing.

The static calibration phase of the experimental program was used to determine the stiffness of the elements of the test fixture and the test structure; data from this phase of testing were used in developing the analytical model, as discussed in Chapter 8.

The dynamic calibration phase of the experimental program was used to estimate the natural periods and damping of the SC-CBF test structure, with its adjacent gravity columns and its associated tributary gravity columns, gravity loads (including the P-Δ effects), seismic mass, and damping substructure. The natural periods were determined based on the system stiffness and the mass at each floor level. Once the periods were estimated, the damping matrix for the hybrid simulations was selected. The damping matrix used for the hybrid simulations is a Rayleigh damping matrix (see Chapter 8) with 2% damping in the first mode and 5% damping in the third mode.

The dynamic testing phase of the experimental program consisted of hybrid simulations of the response of the SC-CBF test structure to the ground motions selected in Chapter 9, as well as the static testing described in Section 10.1.2. In addition to the hybrid simulations reported here, other hybrid simulations were performed, as described by Chancellor et al. (2010).

Table 10.1 summarizes the dynamic testing phase of the SC-CBF experimental program. This table shows the seismic input level and name of each ground motion used for the hybrid simulations, as well as the number of simulations performed (which includes preliminary hybrid simulations conducted during the dynamic calibration phase of the experimental program as well as other hybrid simulations reported by Chancellor et al. (2010)). The predicted peak responses (from Chapter 9) of the SC-CBF test structure to each ground motion are also shown in Table 10.1. The tabulated response quantities are the peak roof drift, θ_{max}; the peak story drift, θ_s; and the peak base shear, $V_{b,max}$. The predicted values of each quantity are presented, as well as the number of standard

deviations above or below the mean response for the input level (e.g., DBE or MCE). The mean responses are shown in Table 10.2.

A subset of the hybrid simulations of the SC-CBF test structure summarized in Table 10.1 are used to validate the analytical model developed in Chapter 8 and are reported in this dissertation. Table 10.3 summarizes the simulations that are used for this purpose. The simulations are listed in the order in which they were performed. This order was selected to gradually increase the maximum response of the SC-CBF test structure, and to minimize the minor repairs of the SC-CBF test structure that might be needed during the experimental program. These minor repairs included retensioning the PT bars as necessary (i.e., after they yielded), replacing the brass friction plates at the lateral-load bearings as necessary, and evaluating the condition of the test fixtures. The naming convention for the hybrid simulations is "SeismicInputLevel_GroundMotion_ DateOfHybridSimulation," as shown in the fourth column of Table 10.3.

10.3 Correlation of Experimental Response with Predictive Numerical Analysis Results

The correlation of the experimental response with the results of the dynamic nonlinear analyses of the predictive model will be discussed in this section. The predictive model is discussed in Chapter 9. The response quantities that will be compared are: floor displacements at the north gravity column at each floor level i (Δ_i); the gap-opening displacement at the base of the SC-CBF columns due to rocking ($\Delta_{gap,S}$ for the south column gaps, $\Delta_{gap,N}$ for the north column gaps); the total PT force in each of the three PT

bar locations (sum of the forces in the two bars at the south location, PT_S; center location, PT_C; and north location, PT_N); the base shear, V_b, determined by summing the actuator forces in the laboratory or by summing the forces in the stiff springs between the lean-on column and the north gravity column in the analytical model; the overturning moment, OM, calculated from the forces in the actuators in the laboratory or the forces in the springs between the lean-on column and the north gravity column in the analytical model; the effective modal pseudo-acceleration, α_n, for each mode; and the axial forces in the south and north braces in story i, F_{briS} and F_{briN}, respectively.

10.3.1 Summary of Experimental Response

The experimental response of the SC-CBF test structure was in accordance with the intended system behavior presented in Chapter 3. In particular, the limit states of column decompression (for DBE-level, MCE-level, and extreme MCE-level seismic input) and PT bar yielding (for MCE-level and extreme MCE-level input) were reached without structural damage, and the limit states of member yielding and member failure were not reached. The SC-CBF test structure self-centered for each ground motion.

During the experimental program, three factors that affect the correlation of the experimental results with the results of the predictive analysis discussed in Chapter 9 became evident: the size of the gaps at the lateral-load bearings at each floor level, the initial force in the PT bars, and the yield force of the PT bars. These factors will be discussed further in Chapter 11.

10.3.2 Correlation of DBE-Level Response

Overall, there is strong correlation between the predictive numerical analysis results and the experimental hybrid simulation results for the DBE-level ground motions. There were some differences between the two results, stemming from two significant differences between the laboratory conditions of the test structure and the conditions of the analytical model. The first of these differences is the initial PT force; in the laboratory, it was difficult to fine-tune the force in each PT bar, leading to some variation in the initial forces for each test. This directly affected the correlation of the PT forces and the axial forces in the upper-story braces. The second difference between the laboratory and analytical conditions was that the horizontal gaps at the lateral-load bearings varied between simulations, while the horizontal gaps for the predictive model were identical for each simulation. This difference had a significant effect on the distribution of the lateral forces, which altered the correlation of the base shear and overturning moment as the effective height of the lateral forces acting between the gravity columns and the SC-CBF columns changed.

An additional difference between the experimental and analytical responses of the SC-CBF test structure can be seen in the gap-opening response (e.g., Figures 10.3 and 10.4(b)). In the analytical model, a negative gap-opening displacement occurs due to elastic deformation of the zero-length gap element used to model the gap opening; negative deformation occurs when the element is compressed (i.e., when the column is in contact). The effect of this additional flexibility at the column bases does not appear to be significant.

10.3.2.1 DBE_cls000_12-31-2009

The correlation of the prediction from numerical analysis of the response to DBE_cls000 and the experimental results from hybrid simulation DBE_cls000_12-31-2009 is shown in Figures 10.2 through 10.9. Figure 10.2 shows the correlation of the displacement response at each floor level. Figure 10.3 shows the correlation of the column base gap-opening displacements. The hysteretic response is shown in Figure 10.4; overturning moment is plotted against roof drift in Figure 10.4(a) and against column base gap opening in Figure 10.4(b). In Figure 10.4(b), positive values of OM correspond to $\Delta_{gap,S}$, and negative values of OM correspond to $\Delta_{gap,N}$. Figure 10.5 shows the correlation of the PT bar forces at each PT bar location. Figure 10.6 shows the correlation of the base shear (Figure 10.6(a)) and the overturning moment (Figure 10.6(b)). Correlation of α_n for each mode of vibration is shown in Figure 10.7. Figures 10.8 and 10.9 show the correlation of the south and north brace force response for each story, as well as the factored design demands $F_{bri,fdd}$.

10.3.2.2 DBE_5108-090_12-31-2009

The correlation of the prediction from numerical analysis of the response to DBE_5108-090 and the experimental results from DBE_5108-090_12-31-2009 is shown in Figures 10.10 through 10.17. Figure 10.10 shows the correlation of the floor displacement response. Figure 10.11 shows the correlation of the column base gap-opening displacements. The hysteretic response is shown in Figure 10.12; overturning moment is plotted against roof drift in Figure 10.12(a) and against column base gap opening in

Figure 10.12(b). In Figure 10.12(b), positive values of *OM* correspond to $\Delta_{gap,S}$, and negative values of *OM* correspond to $\Delta_{gap,N}$. Figure 10.13 shows the correlation of the PT bar forces. Figure 10.14 shows the correlation of the base shear (Figure 10.14(a)) and the overturning moment (Figure 10.14(b)). Correlation of α_n is shown in Figure 10.15. Figures 10.16 and 10.17 show the correlation of the south and north brace force response, as well as the factored design demands $F_{bri,fdd}$.

10.3.2.3 DBE_h-shp270_12-31-2009

The correlation of the prediction from numerical analysis of the response to DBE_h-shp270 and the experimental results from DBE_h-shp270_12-31-2009 is shown in Figures 10.18 through 10.25. Figure 10.18 shows the correlation of the floor displacement response. Figure 10.19 shows the correlation of the column base gap-opening displacements. The hysteretic response is shown in Figure 10.20; overturning moment is plotted against roof drift in Figure 10.20 (a) and against column base gap opening in Figure 10.20(b). In Figure 10.20(b), positive values of *OM* correspond to $\Delta_{gap,S}$, and negative values of *OM* correspond to $\Delta_{gap,N}$. Figure 10.21 shows the correlation of the PT bar forces. Figure 10.22 shows the correlation of the base shear (Figure 10.22(a)) and the overturning moment (Figure 10.22(b)). Correlation of α_n is shown in Figure 10.23. Figures 10.24 and 10.25 show the correlation of the south and north brace force response, as well as the factored design demands $F_{bri,fdd}$.

10.3.2.4 DBE_arl090_01-06-2010

The correlation of the prediction from numerical analysis of the response to DBE_arl090 and the experimental results from DBE_arl090_01-06-2010 is shown in Figures 10.26 through 10.33. Figure 10.26 shows the correlation of the floor displacement response. Figure 10.27 shows the correlation of the column base gap-opening displacements. The hysteretic response is shown in Figure 10.28; overturning moment is plotted against roof drift in Figure 10.28(a) and against column base gap opening in Figure 10.28(b). In Figure 10.28(b), positive values of OM correspond to $\Delta_{gap,S}$, and negative values of OM correspond to $\Delta_{gap,N}$. Figure 10.29 shows the correlation of the PT bar forces. Figure 10.30 shows the correlation of the base shear (Figure 10.30(a)) and the overturning moment (Figure 10.30(b)). Correlation of α_n is shown in Figure 10.31. Figures 10.32 and 10.33 show the correlation of the south and north brace force response, as well as the factored design demands $F_{bri,fdd}$.

10.3.2.5 DBE_nr-pel360_01-08-2010

The correlation of the prediction from numerical analysis of the response to DBE_nr-pel360 and the experimental results from DBE_nr-pel360_01-08-2010 is shown in Figures 10.34 through 10.41. Figure 10.34 shows the correlation of the floor displacement response. Figure 10.35 shows the correlation of the column base gap-opening displacements. The hysteretic response is shown in Figure 10.36; overturning moment is plotted against roof drift in Figure 10.36(a) and against column base gap opening in Figure 10.36(b). In Figure 10.36(b), positive values of OM correspond to

$\Delta_{gap,S}$, and negative values of *OM* correspond to $\Delta_{gap,N}$. Figure 10.37 shows the correlation of the PT force demands. Figure 10.38 shows the correlation of the base shear (Figure 10.38(a)) and the overturning moment (Figure 10.38(b)). Correlation of α_n is shown in Figure 10.39. Figures 10.40 and 10.41 show the correlation of the south and north brace force response, as well as the factored design demands $F_{bri,fdd}$.

10.3.3 Correlation of MCE-Level Response

Overall, there is strong correlation between the predictive numerical analysis results and the experimental hybrid simulation results for the MCE-level ground motions. The differences between the analytical and experimental results are similar to those discussed for the correlation of the DBE-level response: differences in gaps at the lateral-load bearings, differences in initial PT bar force, and a difference in the vertical stiffness at the base of the SC-CBF columns.

10.3.3.1 MCE_stn110_01-07-2010

The correlation of the prediction from numerical analysis of the response to MCE_a-tmz270 and the experimental results from hybrid simulation MCE_a-tmz270_01-07-2010 is shown in Figures 10.42 through 10.49. Figure 10.42 shows the correlation of the displacement response at each floor level. Figure 10.43 shows the correlation of the column base gap-opening displacements. The hysteretic response is shown in Figure 10.44; overturning moment is plotted against roof drift in Figure 10.44(a) and against column base gap opening in Figure 10.44(b). In Figure 10.44(b), positive values of *OM* correspond to $\Delta_{gap,S}$, and negative values of *OM* correspond to $\Delta_{gap,N}$. Figure 10.45 shows

the correlation of the PT bar forces at each PT bar location. Figure 10.46 shows the correlation of the base shear (Figure 10.46(a)) and the overturning moment (Figure 10.46(b)). Correlation of α_n for each mode of vibration is shown in Figure 10.47. Figures 10.48 and 10.49 show the correlation of the south and north brace force response for each story, as well as the factored design demands $F_{bri,fdd}$.

10.3.3.2 MCE_a-tmz270_01-07-2010

The correlation of the prediction from numerical analysis of the response to MCE_a-tmz270 and the experimental results from MCE_a-tmz270_01-07-2010 is shown in Figures 10.50 through 10.57. Figure 10.50 shows the correlation of the floor displacement response. Figure 10.51 shows the correlation of the column base gap-opening displacements. The hysteretic response is shown in Figure 10.52; overturning moment is plotted against roof drift in Figure 10.52(a) and against column base gap opening in Figure 10.52(b). In Figure 10.52(b), positive values of OM correspond to $\Delta_{gap,S}$, and negative values of OM correspond to $\Delta_{gap,N}$. Figure 10.53 shows the correlation of the PT bar forces. Figure 10.54 shows the correlation of the base shear (Figure 10.54(a)) and the overturning moment (Figure 10.54(b)). Correlation of α_n is shown in Figure 10.55. Figures 10.56 and 10.57 show the correlation of the south and north brace force response, as well as the factored design demands $F_{bri,fdd}$.

10.3.3.3 MCE_lp-hda255_02-02-2010

The correlation of the prediction from numerical analysis of the response to MCE_lp-hda255 and the experimental results from MCE_lp-hda255_02-02-2010 is shown in

Figures 10.58 through 10.65. Figure 10.58 shows the correlation of the floor displacement response. Figure 10.59 shows the correlation of the column base gap-opening displacements. The hysteretic response is shown in Figure 10.60; overturning moment is plotted against roof drift in Figure 10.60(a) and against column base gap opening in Figure 10.60(b). In Figure 10.60(b), positive values of *OM* correspond to $\Delta_{gap,S}$, and negative values of *OM* correspond to $\Delta_{gap,N}$. Figure 10.61 shows the correlation of the PT bar forces. Figure 10.62 shows the correlation of the base shear (Figure 10.62(a)) and the overturning moment (Figure 10.62(b)). Correlation of α_n is shown in Figure 10.63. Figures 10.64 and 10.65 show the correlation of the south and north brace force response, as well as the factored design demands $F_{bri,fdd}$.

10.3.3.4 MCE_cap000_01-11-2010

The correlation of the prediction from numerical analysis of the response to MCE_cap000 and the experimental results from MCE_cap000_01-11-2010 is shown in Figures 10.66 through 10.73. Figure 10.66 shows the correlation of the floor displacement response. Figure 10.67 shows the correlation of the column base gap-opening displacements. The hysteretic response is shown in Figure 10.68; overturning moment is plotted against roof drift in Figure 10.68(a) and against column base gap opening in Figure 10.68(b). In Figure 10.68(b), positive values of *OM* correspond to $\Delta_{gap,S}$, and negative values of *OM* correspond to $\Delta_{gap,N}$. Figure 10.69 shows the correlation of the PT bar forces. Figure 10.70 shows the correlation of the base shear (Figure 10.70(a)) and the overturning moment (Figure 10.70(b)). Correlation of α_n is shown in

Figure 10.71. Figures 10.72 and 10.73 show the correlation of the south and north brace force response, as well as the factored design demands $F_{bri,fdd}$.

10.3.3.5 MCE_h-cpe237_01-13-2010

The correlation of the prediction from numerical analysis of the response to MCE_h-cpe237 and the experimental results from MCE_h-cpe237_01-13-2010 is shown in Figures 10.74 through 10.81. Figure 10.74 shows the correlation of the floor displacement response. Figure 10.75 shows the correlation of the column base gap-opening displacements. The hysteretic response is shown in Figure 10.76; overturning moment is plotted against roof drift in Figure 10.76(a) and against column base gap opening in Figure 10.76(b). In Figure 10.76(b), positive values of *OM* correspond to $\Delta_{gap,S}$, and negative values of *OM* correspond to $\Delta_{gap,N}$. Figure 10.77 shows the correlation of the PT bar forces. Figure 10.78 shows the correlation of the base shear (Figure 10.78(a)) and the overturning moment (Figure 10.78(b)). Correlation of α_n is shown in Figure 10.79. Figures 10.80 and 10.81 show the correlation of the south and north brace force response, as well as the factored design demands $F_{bri,fdd}$.

10.3.4 Correlation of Extreme MCE-Level Response: xMCE_tak090_02-05-2010

The correlation of the prediction from numerical analysis of the response to xMCE_tak090 and the experimental results from hybrid simulation xMCE_tak090_02-05-2010 is shown in Figures 10.82 through 10.89. Figure 10.82 shows the correlation of the displacement response at each floor level. Figure 10.83 shows the correlation of the column base gap-opening displacements. The hysteretic response is shown in Figure

10.84; overturning moment is plotted against roof drift in Figure 10.84(a) and against column base gap opening in Figure 10.84(b). In Figure 10.84(b), positive values of *OM* correspond to $\Delta_{gap,S}$, and negative values of *OM* correspond to $\Delta_{gap,N}$. Figure 10.85 shows the correlation of the PT bar forces. Figure 10.86 shows the correlation of the base shear (Figure 10.86(a)) and the overturning moment (Figure 10.86(b)). Correlation of α_n for each mode of vibration is shown in Figure 10.87. Figures 10.88 and 10.89 show the correlation of the south and north brace force response for each story, as well as the factored design demands $F_{bri,fdd}$.

The correlation of the first five seconds of analytically predicted and experimental response is good for this ground motion (i.e., similar to the correlation for the DBE-level and MCE-level ground motions). However, after five seconds of response, the numerical analysis overpredicts the experimental response of the SC-CBF test structure. At the times of the largest roof drift response in each direction, the friction surfaces of the lateral-load bearings (i.e., the brass friction plates) in the test structure in the laboratory became damaged, which increased the coefficient of friction beyond the value of 0.45 used in the predictive analytical model. This damage increased the energy dissipation in the SC-CBF test structure, thereby reducing the response. This result will be discussed further in Chapter 11.

10.4 Summary

As previously mentioned, the predictive analytical model developed in Chapter 9 did not include variations in the initial laboratory conditions of the SC-CBF test structure, which

affected the correlation of the laboratory simulation results with the numerical analysis results. These conditions are the initial force in the PT bars, the size of the gaps at the lateral-load bearings, the vertical stiffness at the base of the SC-CBF columns, and the PT bar yield force.

When the brass friction plates on the friction surfaces of the lateral-load bearings became damaged and were replaced during the experimental program, the PT bars were unstressed and later restressed during the process of replacing these plates. Also, the PT bars were restressed after each simulation in which the PT bars yielded. As a result, the initial PT forces varied slightly throughout the experimental program. Experimental data on the initial PT force are presented in Chapter 11 and were used in calibrated analytical models, as discussed in Chapter 11.

The horizontal gaps in the lateral-load bearings were measured during the experimental program to observe the variation over time in the size of the gaps in the test structure. These data were used in the calibrated models discussed in Chapter 11.

In addition to these initial conditions that affect correlation between experimental and analytical results, damage that occurs during the experiments that is not included in the model can affect the correlation. As the xMCE_tak090_02-05-2010 hybrid simulation was performed in the laboratory, the brass friction plates on the friction surface of the lateral-load bearings were damaged sufficiently to cause an increase in the effective coefficient of friction in the lateral-load bearings during the simulation. This damage significantly affected the correlation of the experimental and analytical response.

A calibrated model is presented in Chapter 11 that addresses some of these differences between the numerical analysis and experimental results.

Table 10.1 – Summary of laboratory hybrid simulations

Input Level	Ground Motion	# of Sims.	θ_{max} (% rad)	θ_s (% rad)	$V_{b,max}$ (kip)	θ_{max} *	θ_s *	$V_{b,max}$ *
Low DBE	DBE_cls000	3	0.65	0.73	277	-0.81	-0.80	-1.04
Median DBE	DBE_5108-090	14	0.84	0.92	455	-0.18	-0.22	0.29
	DBE_h-shp270	1	0.92	1.04	471	0.11	0.13	0.50
High DBE	DBE_arl090	2	1.38	1.50	450	1.74	1.62	0.38
	DBE_nr-pel360	1	0.95	1.16	548	0.20	0.51	1.22
Median MCE	MCE_a-tmz270	2	1.13	1.26	543	0.31	0.32	-0.32
	MCE_lp-hda255	1	1.48	1.58	524	-0.69	-0.66	0.35
	MCE_stn110	3	1.60	1.73	454	0.02	0.01	0.24
High MCE	MCE_cap000	1	2.05	2.21	511	1.19	1.26	0.16
	MCE_h-cpe237	1	1.75	1.84	574	0.55	0.49	0.61
Extreme MCE	xMCE_tak090	2	4.33	4.46	607	5.68	5.66	0.87

* - Given as a multiplier of the standard deviation above (+) or below (-) the mean

Table 10.2 – Summary of mean responses

Input Level	θ_{max} (% rad)	$\theta_{s,max}$ (% rad)	$V_{b,max}$ (kip)
DBE	0.88	0.98	406
MCE	1.47	1.59	493

Table 10.3 – Experimetal program

Date	Test #	Ground Motion	Simulation Name	θ_{max} (% rad)	θ_s (% rad)	$V_{b,max}$ (kip)
12/31/2009	1	DBE_cls000	DBE_cls000_12-31-2009	0.65	0.73	277
12/31/2009	2	DBE_5108-090	DBE_5108-090_12-31-2009	0.84	0.92	455
12/31/2009	3	DBE_h-shp270	DBE_h-shp270_12-31-2009	0.92	1.04	471
1/4/2010	4a	DBE_arl090	DBE_arl090_01-04-2010	1.38	1.50	450
1/6/2010	4b	DBE_arl090	DBE_arl090_01-06-2010	1.38	1.50	450
1/7/2010	5	MCE_stn110	MCE_stn110_01-7-2010	1.60	1.73	454
1/7/2010	6	MCE_a-tmz270	MCE_a-tmz270_01-07-2010	1.13	1.26	543
1/8/2010	7a	MCE_lp-hda255	MCE_lp-hda255_01-08-2010	1.48	1.58	524
1/8/2010	8	DBE_nr-pel360	DBE_nr-pel360_01-08-2010	0.95	1.16	548
1/11/2010	9	MCE_cap000	MCE_cap000_01-11-2010	2.05	2.21	511
1/13/2010	10	MCE_h-cpe237	MCE_h-cpe237_01-13-2010	1.75	1.84	574
1/13/2010	11a	xMCE_tak090	xMCE_tak090_01-13-2010	4.33	4.46	607
1/28/2010	7b	MCE_lp-hda255	MCE_lp-hda255_01-28-2010	1.48	1.58	524
2/2/2010	7c	MCE_lp-hda255	MCE_lp-hda255_02-02-2010	1.48	1.58	524
2/5/2010	11b	xMCE_tak090	xMCE_tak090_02-05-2010	4.33	4.46	607

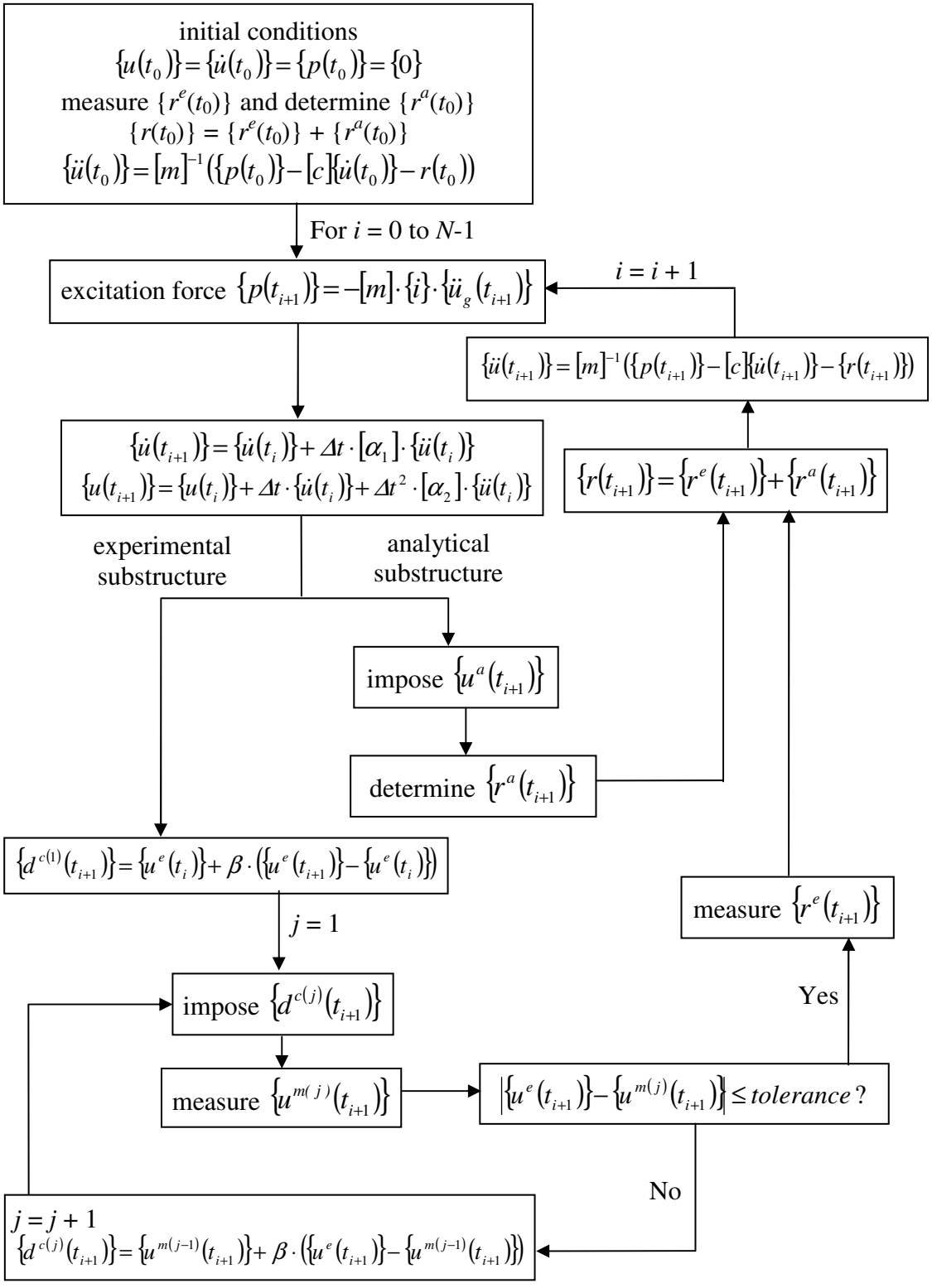

Figure 10.1 – Implementation of CR integration algorithm for hybrid testing for the SC-CBF test structure

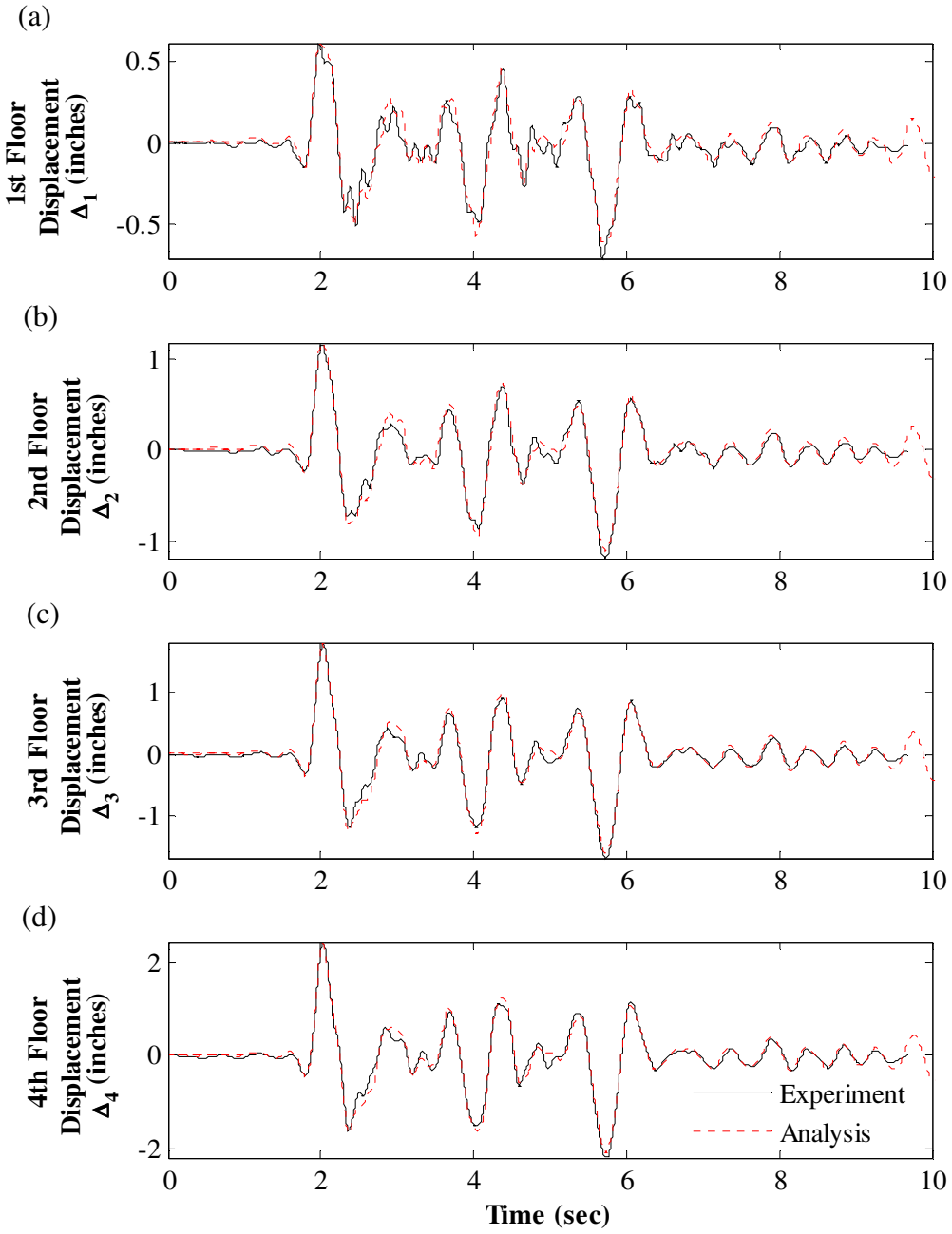

Figure 10.2 – Correlation of floor displacement response to DBE_cls000: (a) 1st floor; (b) 2nd floor; (c) 3rd floor; (d) 4th floor

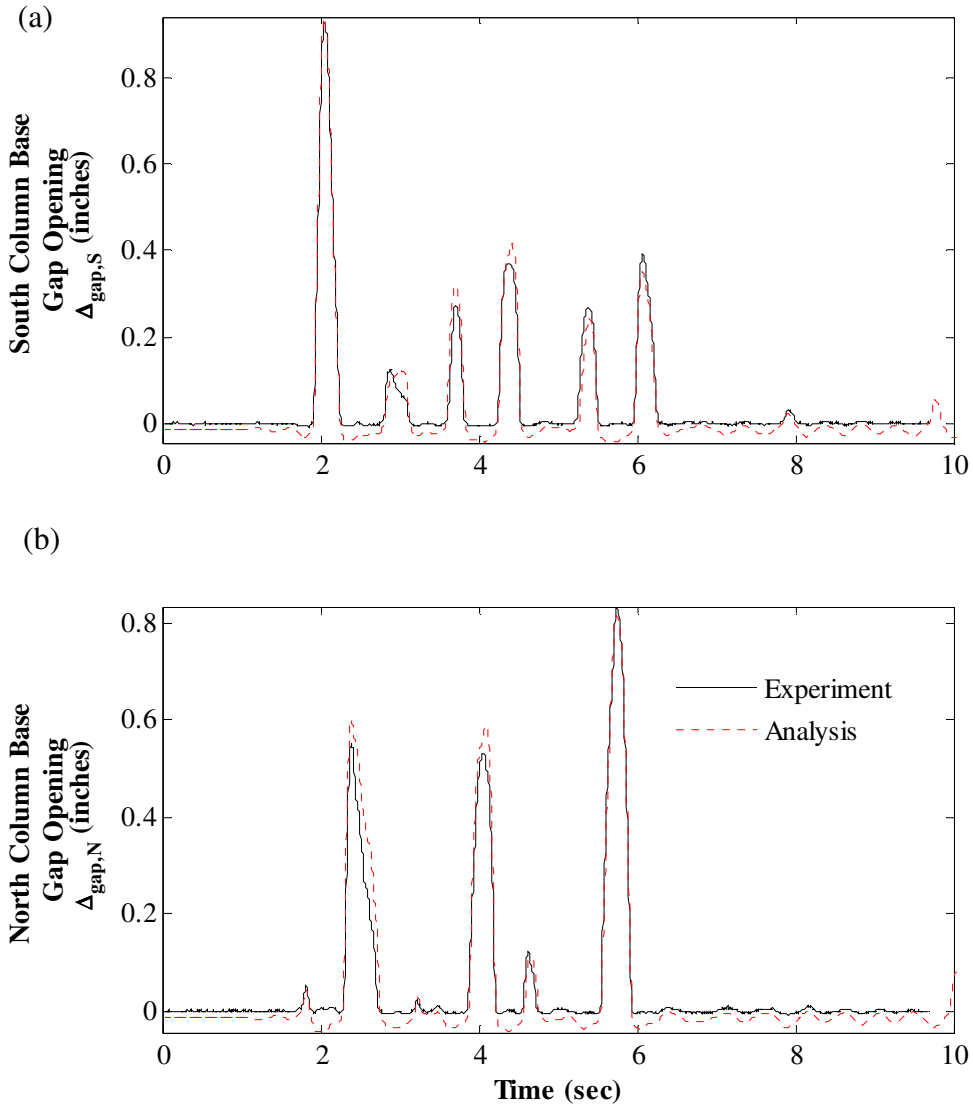

Figure 10.3 – Correlation of column base gap opening response to DBE_cls000: (a) at south column base; (b) at north column base

(a)

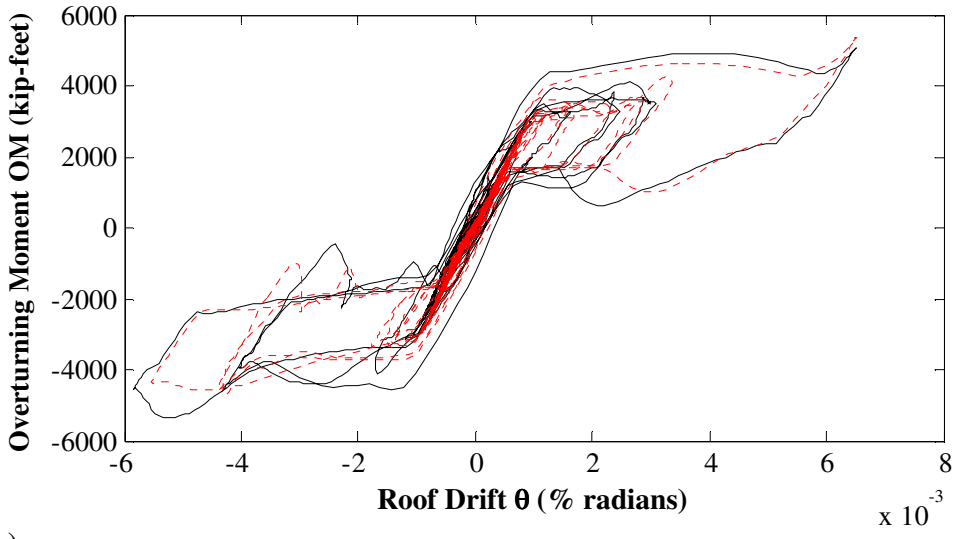

(b)

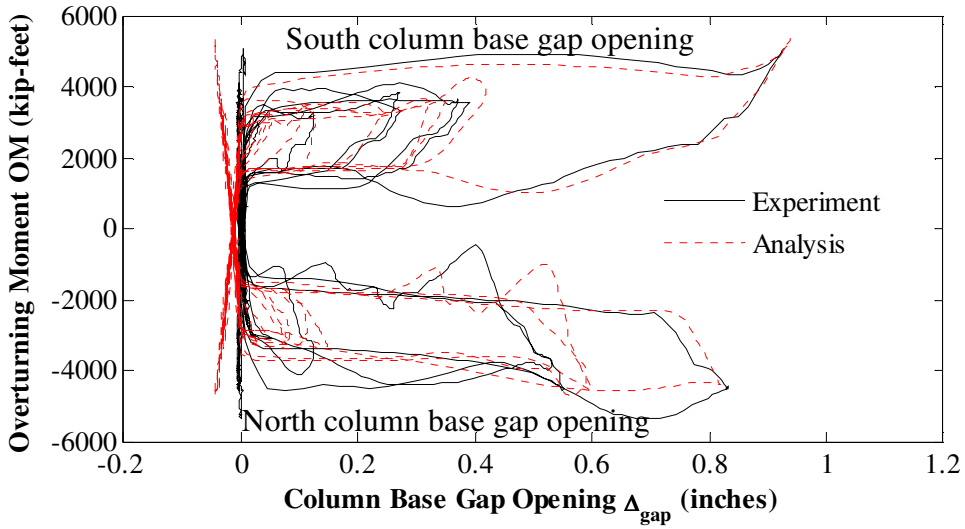

Figure 10.4 – Correlation of hysteretic response to DBE_cls000: (a) overturning moment versus roof drift; (b) overturning moment versus column base gap opening

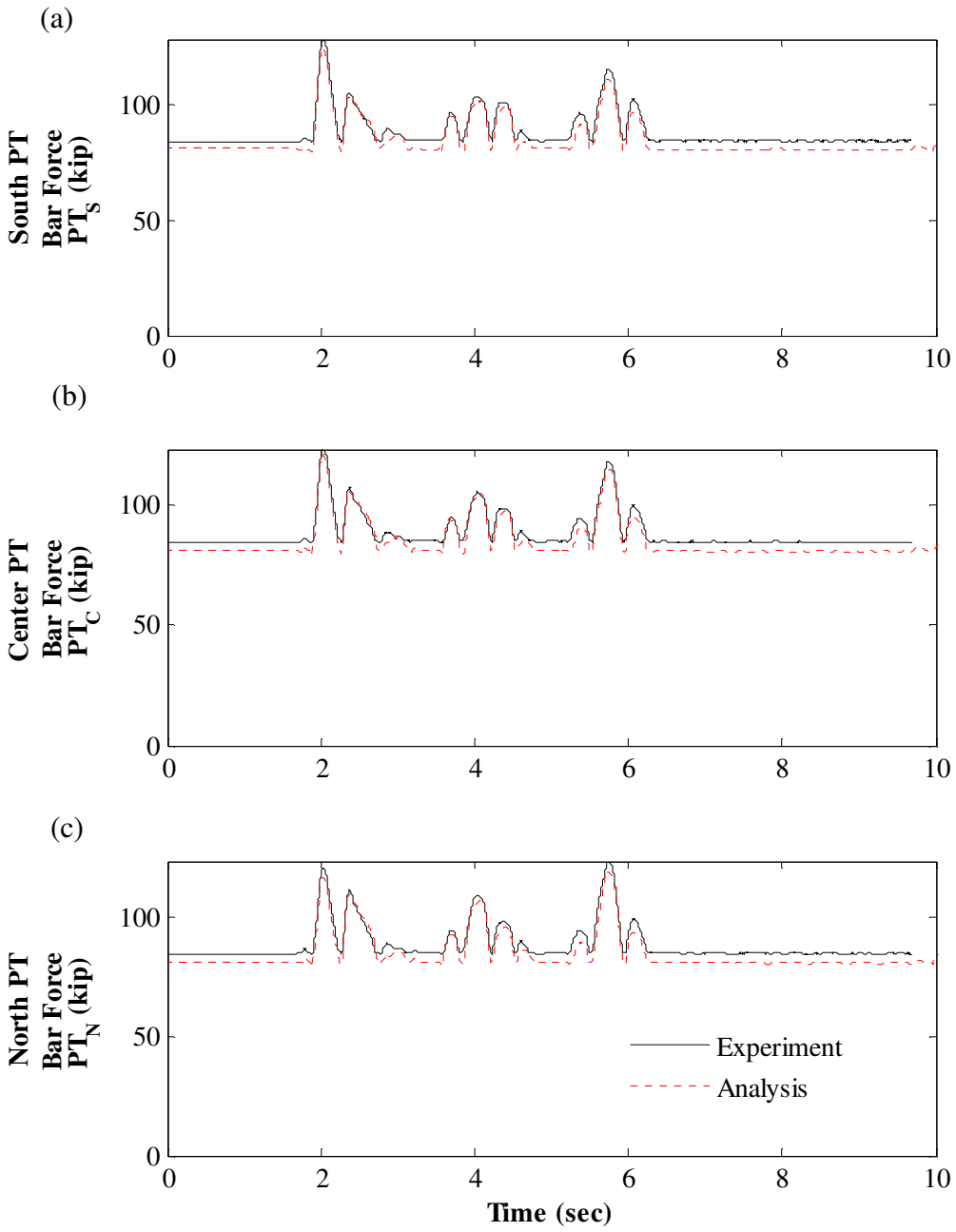

Figure 10.5 – Correlation of PT force response to DBE_cls000: (a) south PT bars; (b) center PT bars; (c) north PT bars

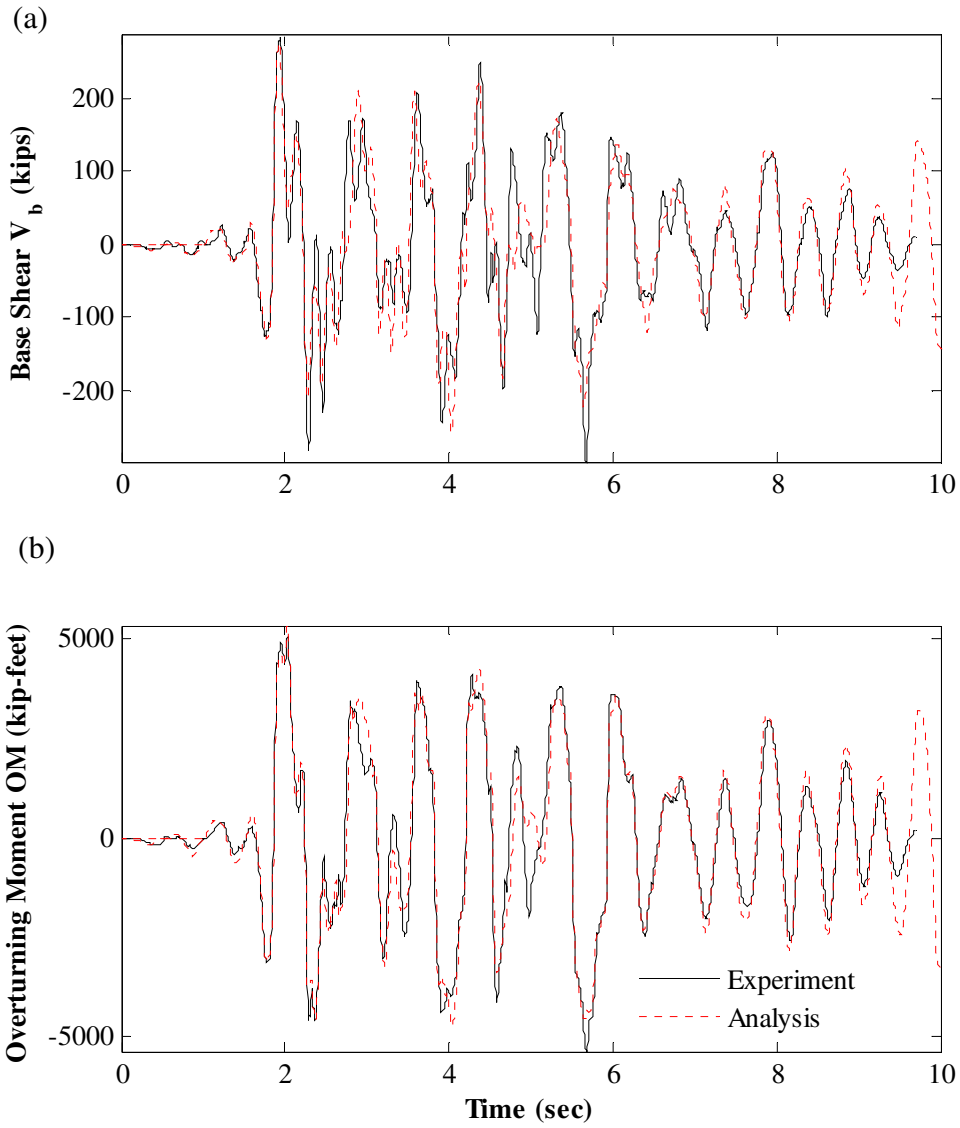

Figure 10.6 – DBE_cls000 response correlation: (a) base shear; (b) overturning moment

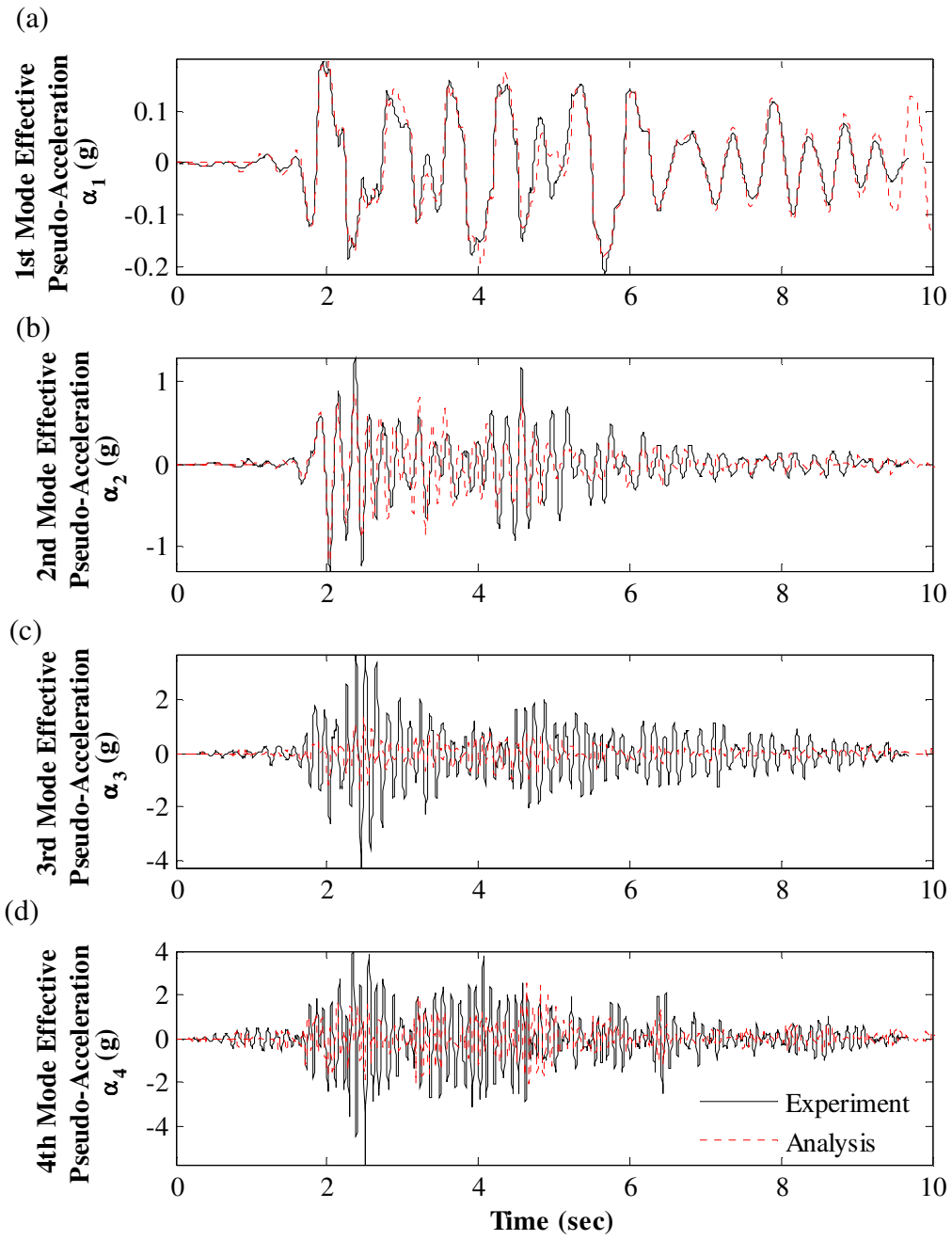

Figure 10.7 – Correlation of effective modal pseudo-acceleration response to DBE_cls000: (a) 1st mode; (b) 2nd mode; (c) 3rd mode; (d) 4th mode

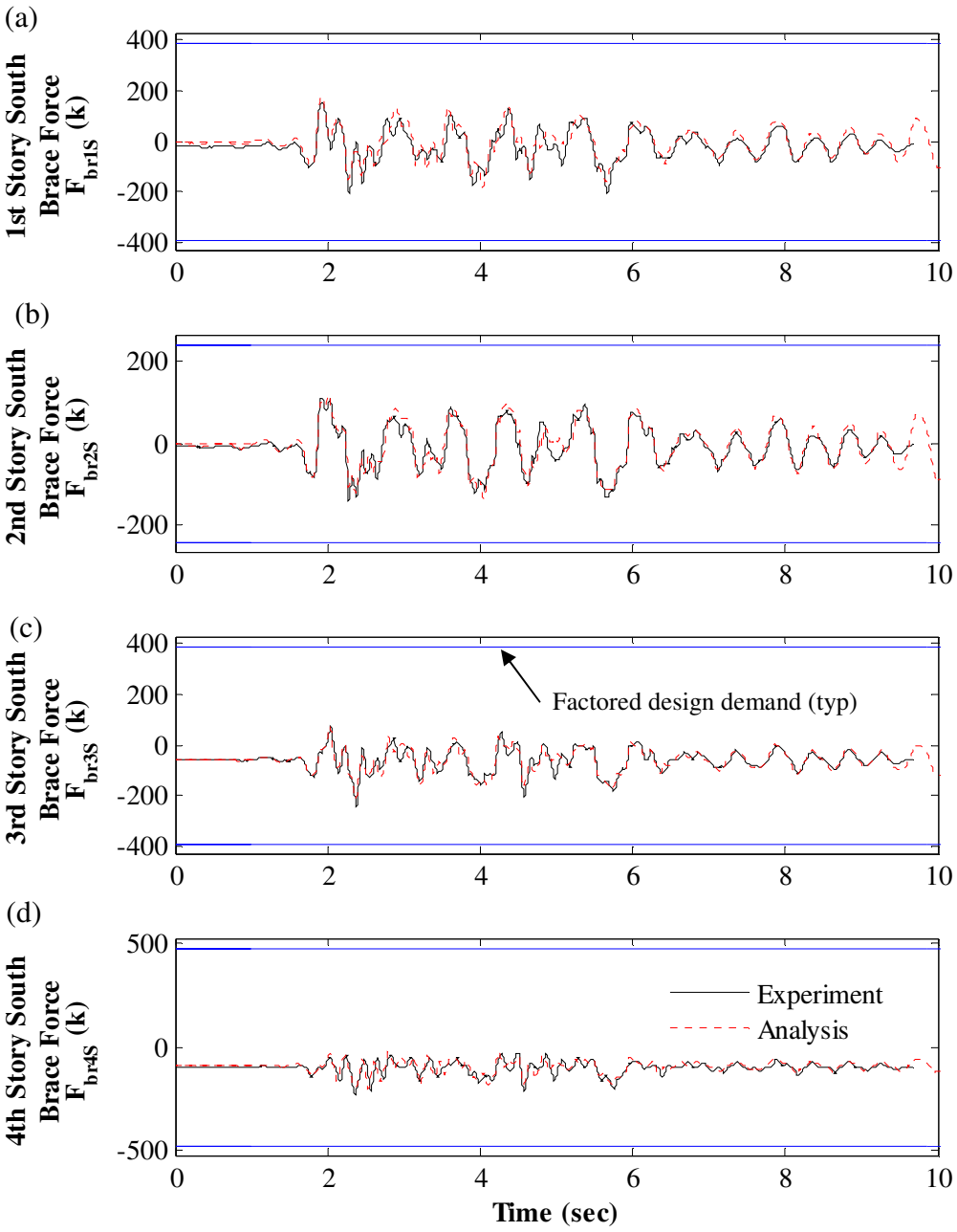

Figure 10.8 – Correlation of south brace axial force response to DBE_cls000: (a) 1st story; (b) 2nd story; (c) 3rd story; (d) 4th story

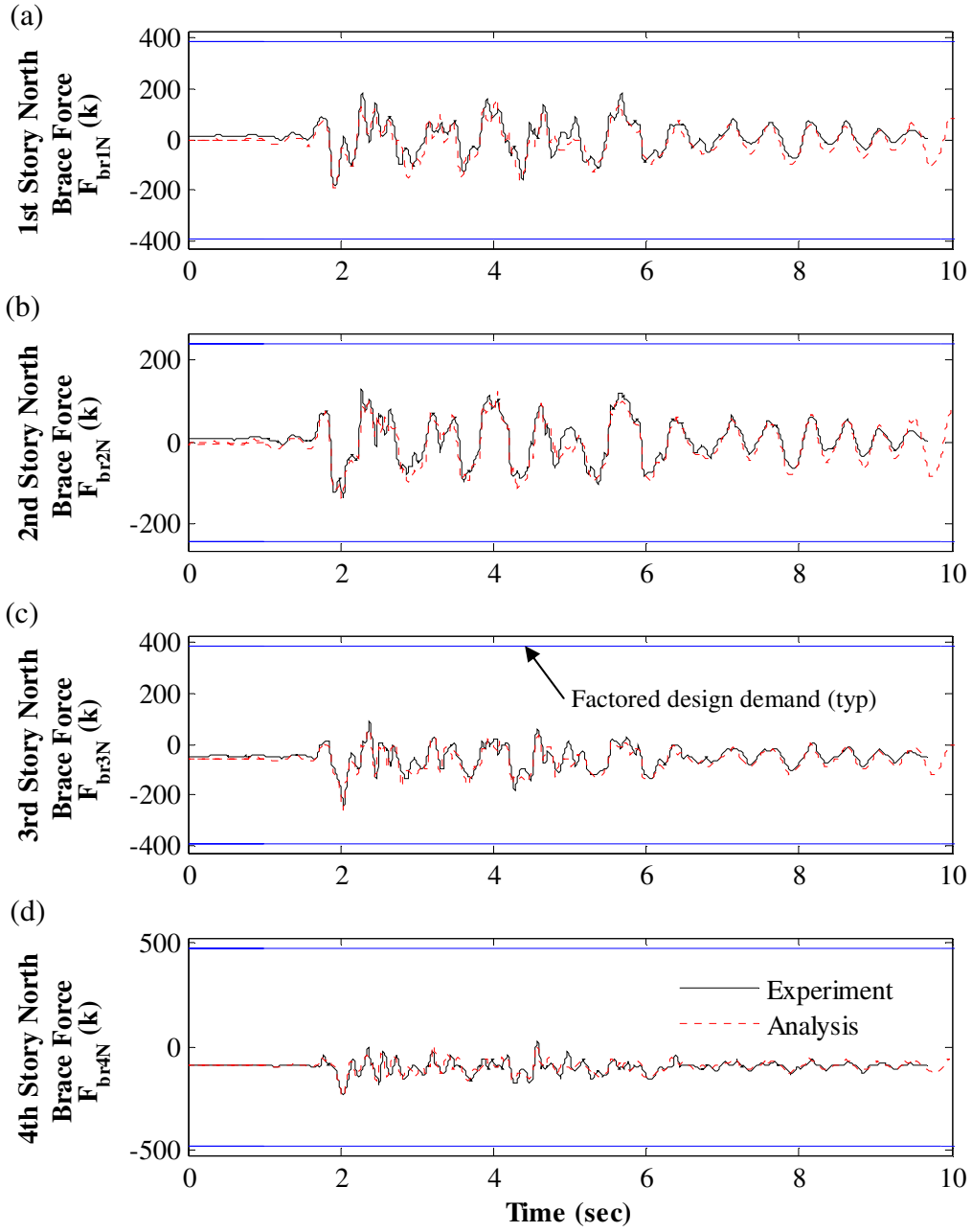

Figure 10.9 – Correlation of north brace axial force response to DBE_cls000: (a) 1st story; (b) 2nd story; (c) 3rd story; (d) 4th story

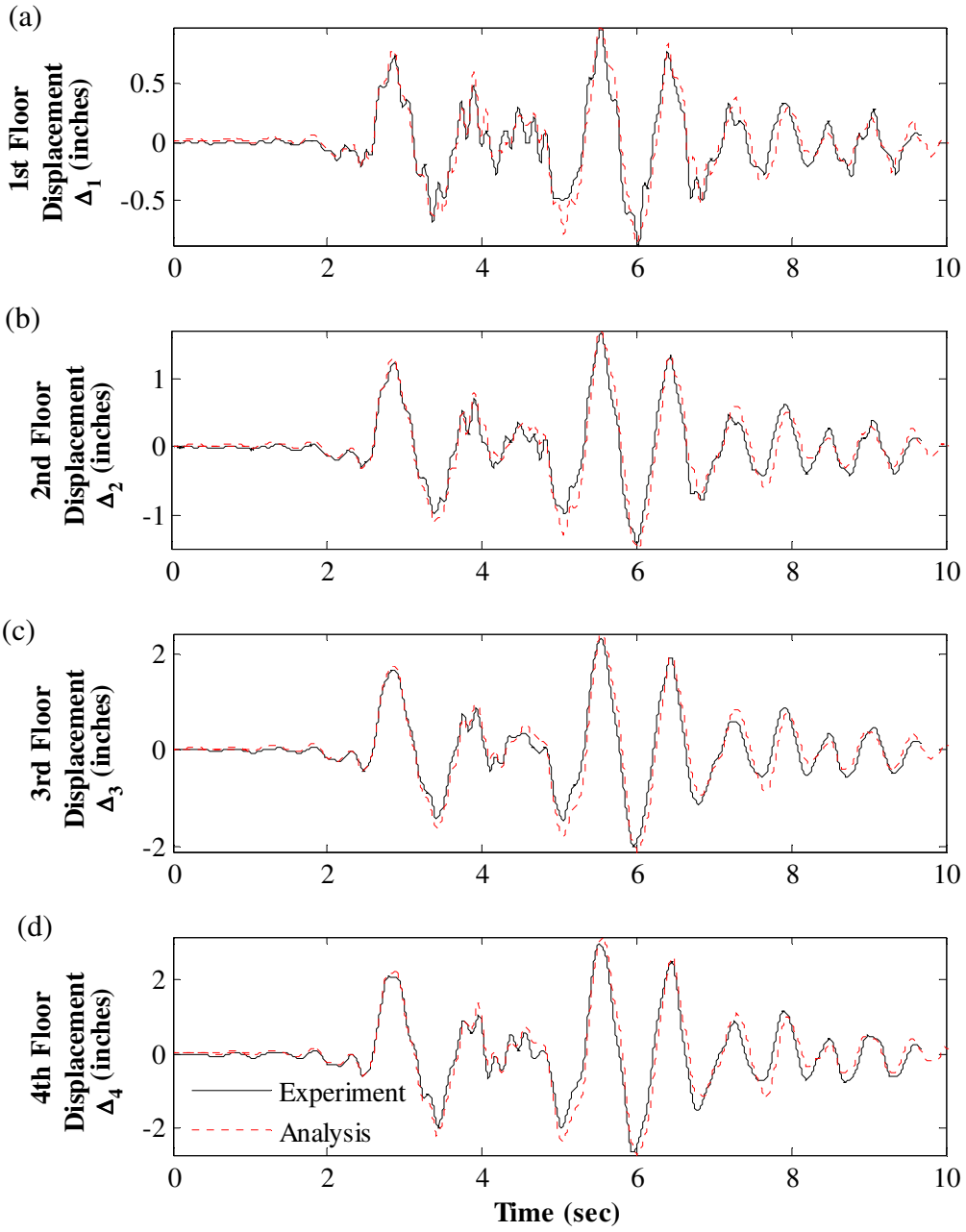

Figure 10.10 – Correlation of floor displacement response to DBE_5108-090: (a) 1st floor; (b) 2nd floor; (c) 3rd floor; (d) 4th floor

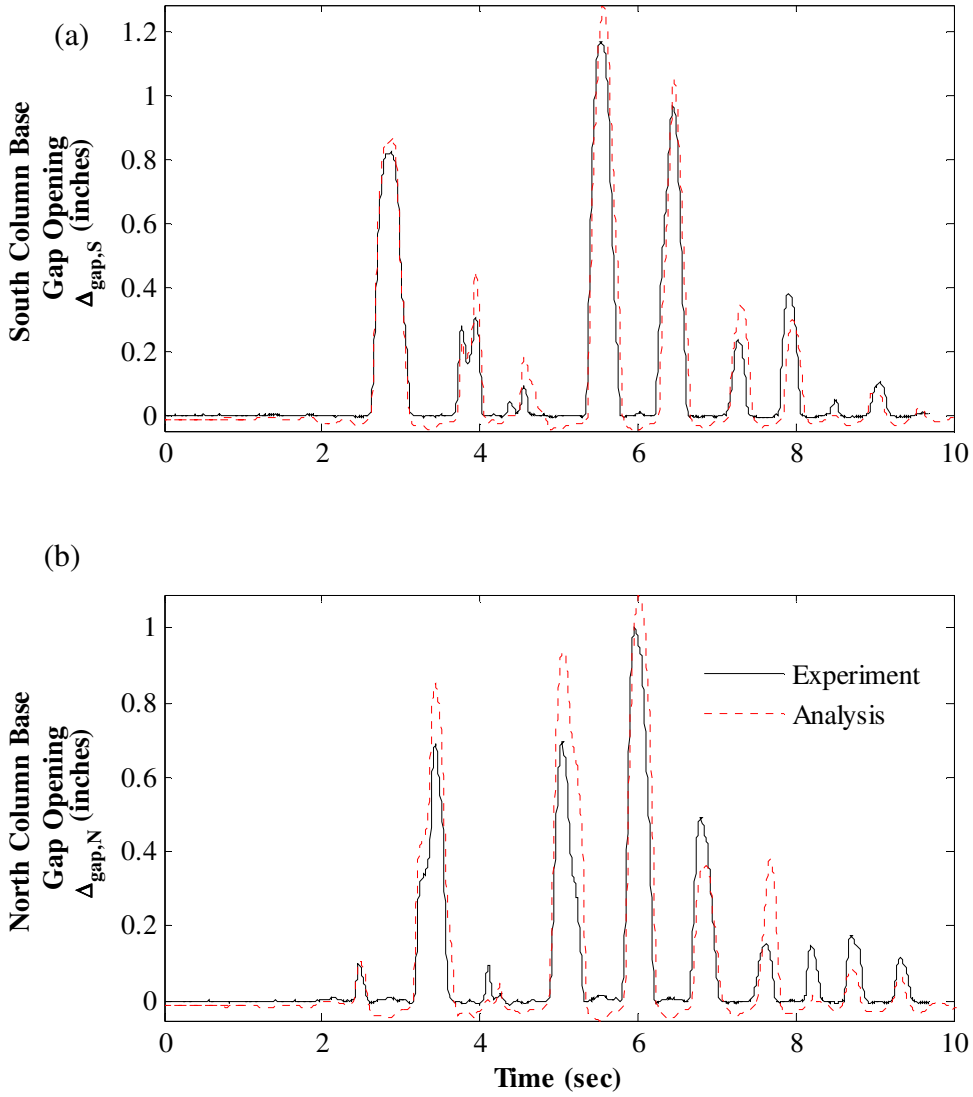

Figure 10.11 – Correlation of column base gap opening response to DBE_5108-090: (a) at south column base; (b) at north column base

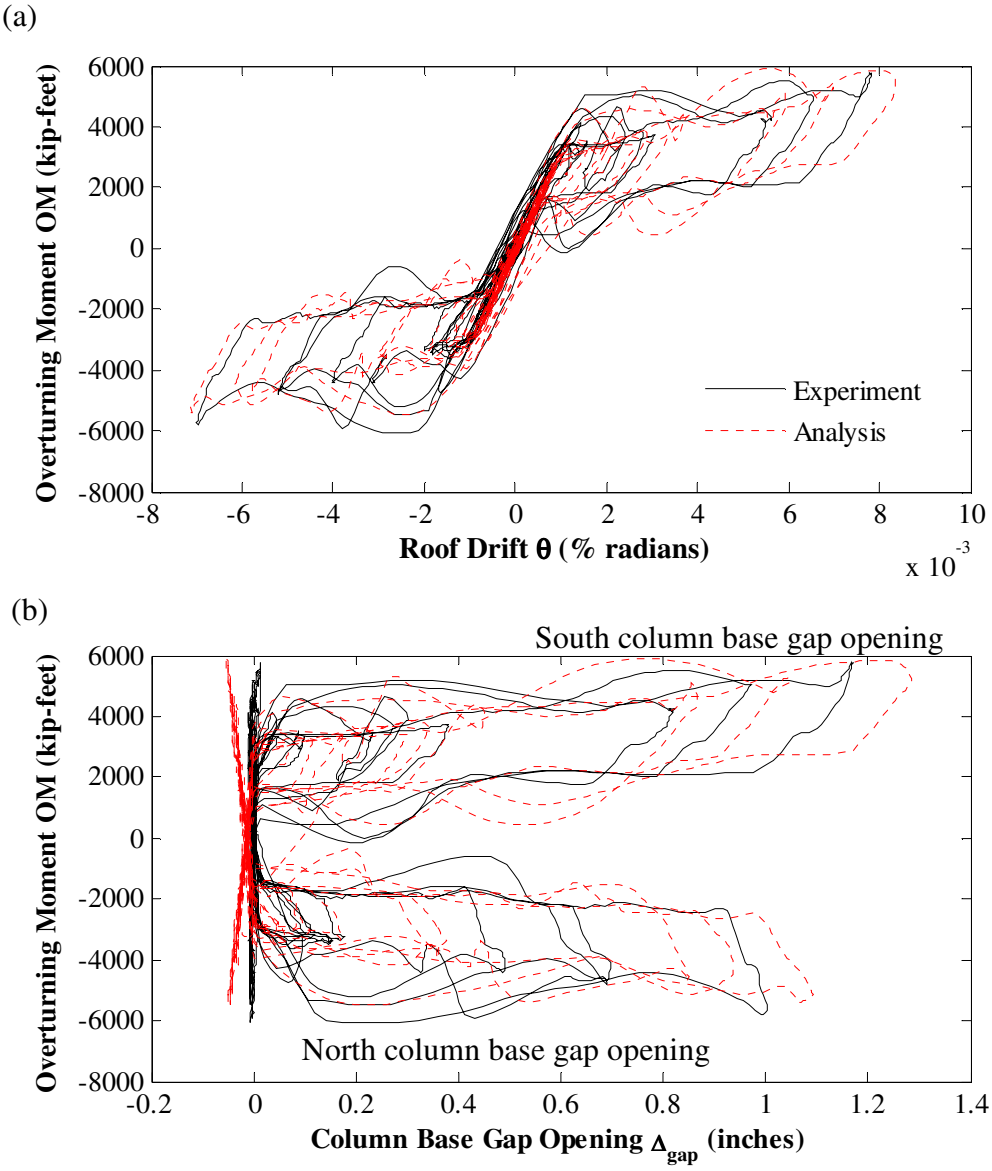

Figure 10.12 – Correlation of hysteretic response to DBE_5108-090: (a) overturning moment versus roof drift; (b) overturning moment versus column base gap opening

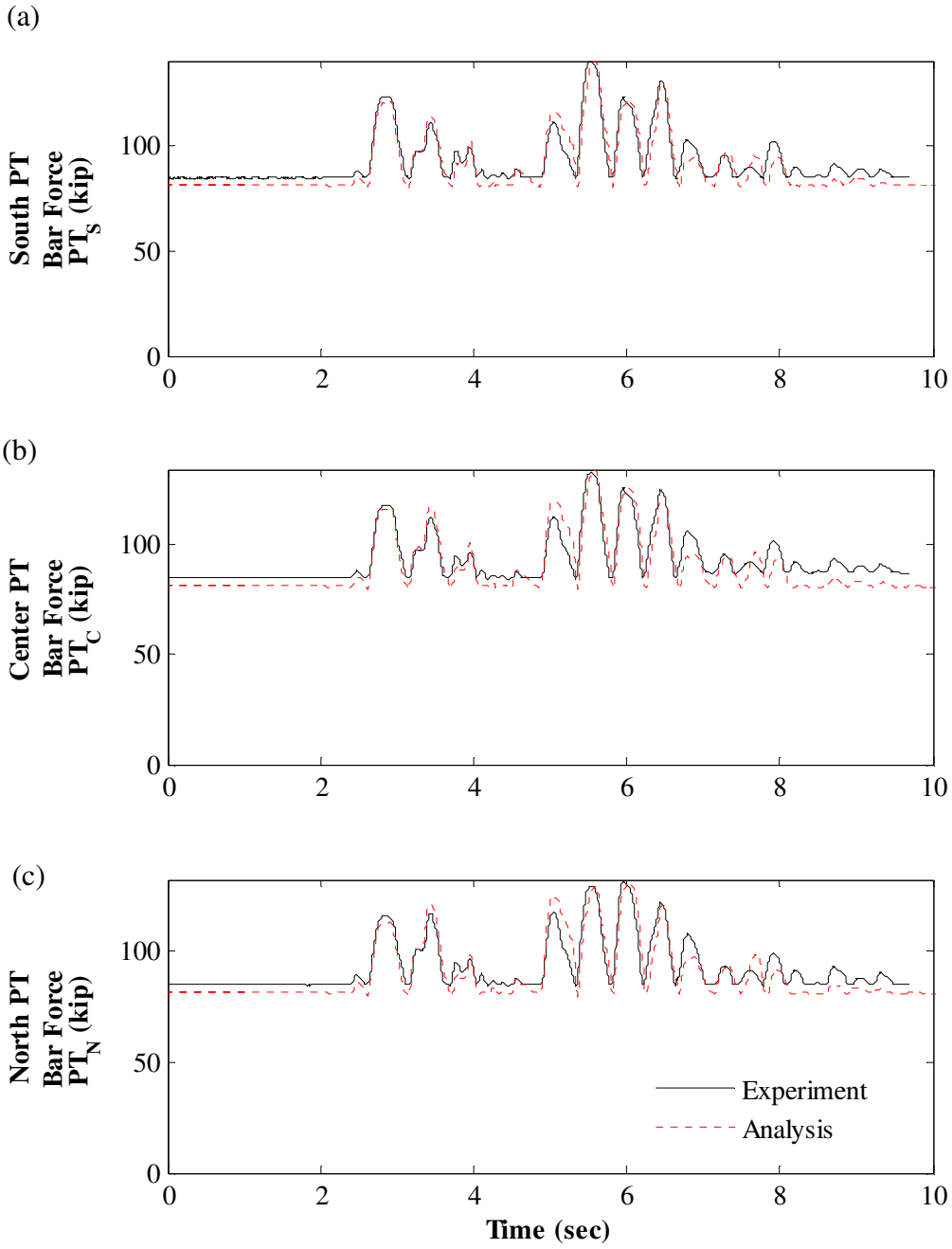

Figure 10.13 – Correlation of PT force response to DBE_5108-090: (a) south PT bars; (b) center PT bars; (c) north PT bars

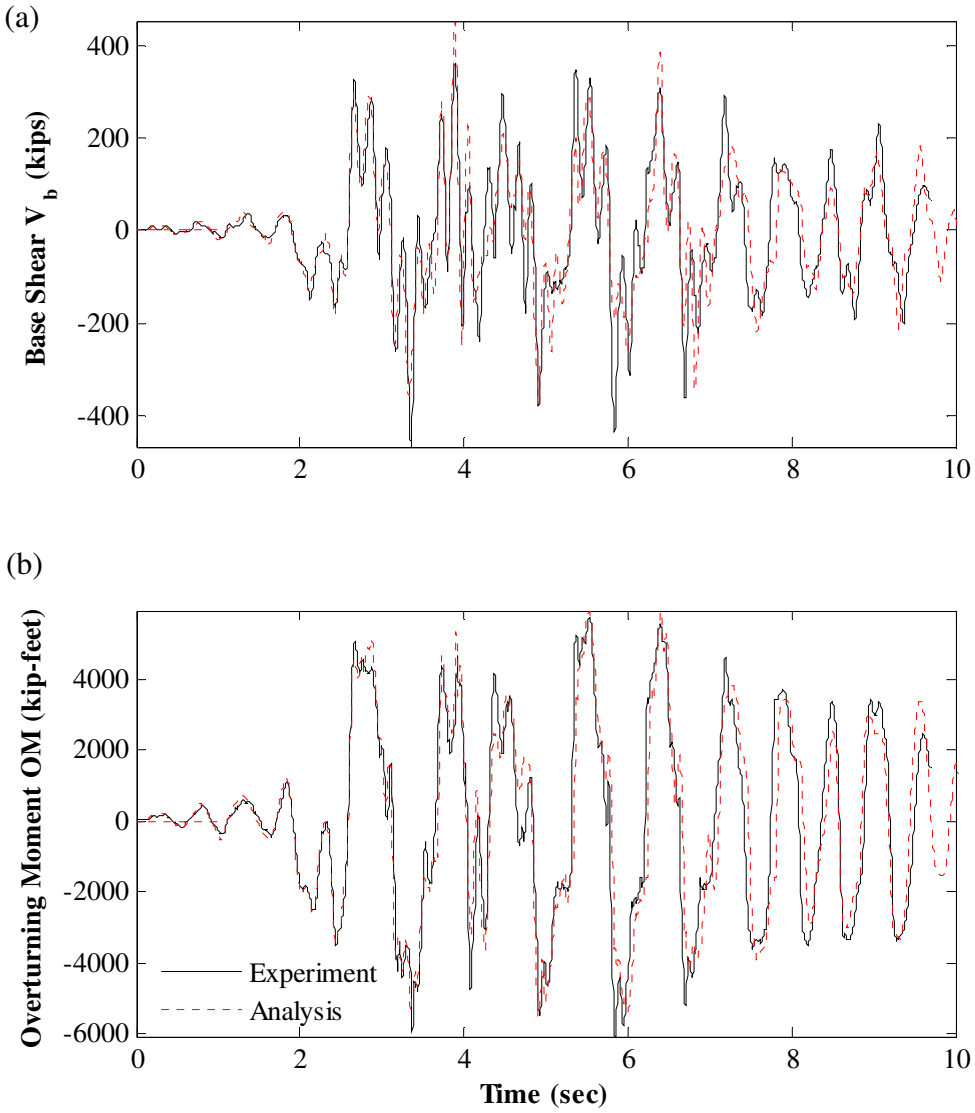

Figure 10.14 – DBE_5108-090 response correlation: (a) base shear; (b) overturning moment

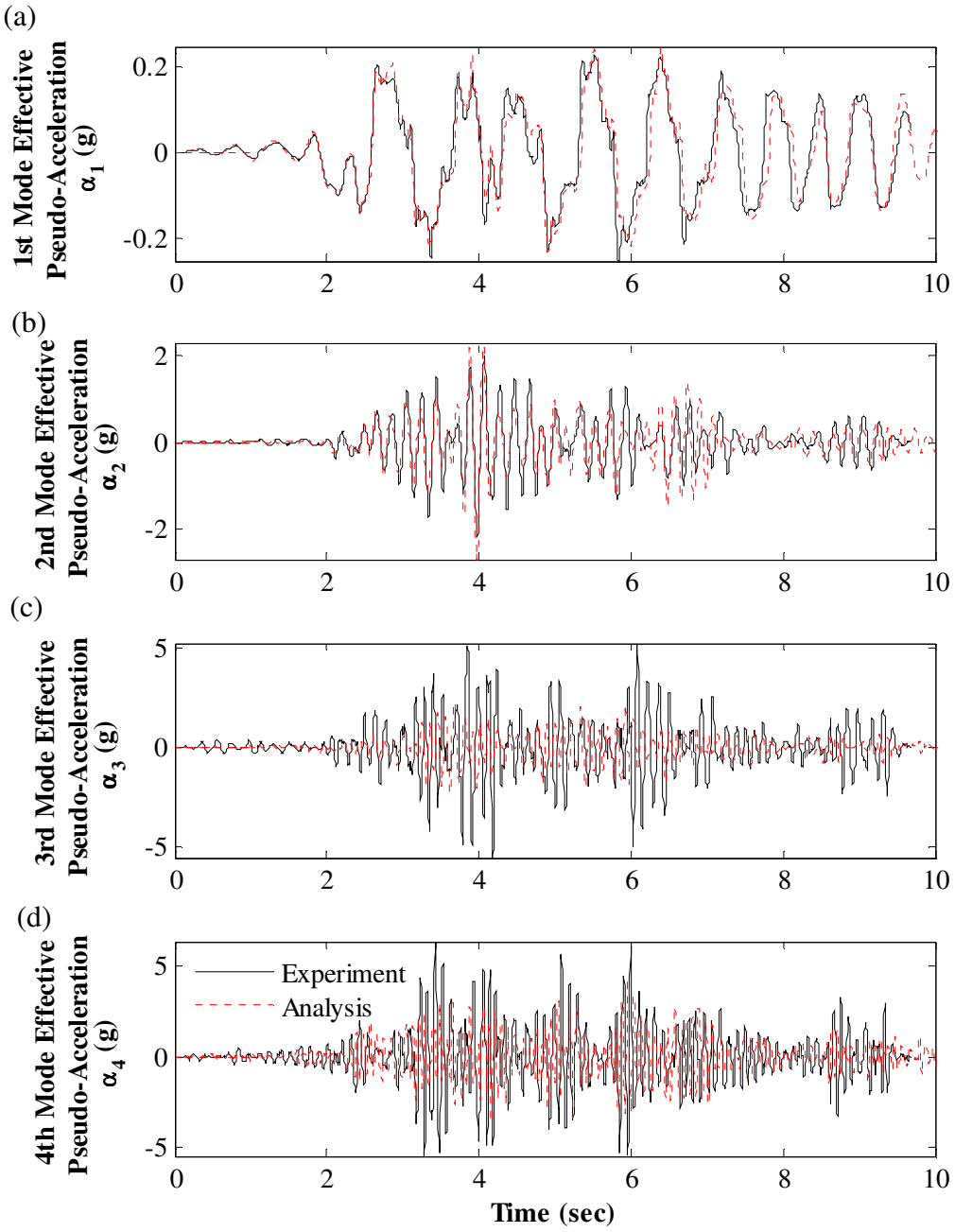

Figure 10.15 – Correlation of effective modal pseudo-acceleration response to DBE_5108-090: (a) 1st mode; (b) 2nd mode; (c) 3rd mode; (d) 4th mode

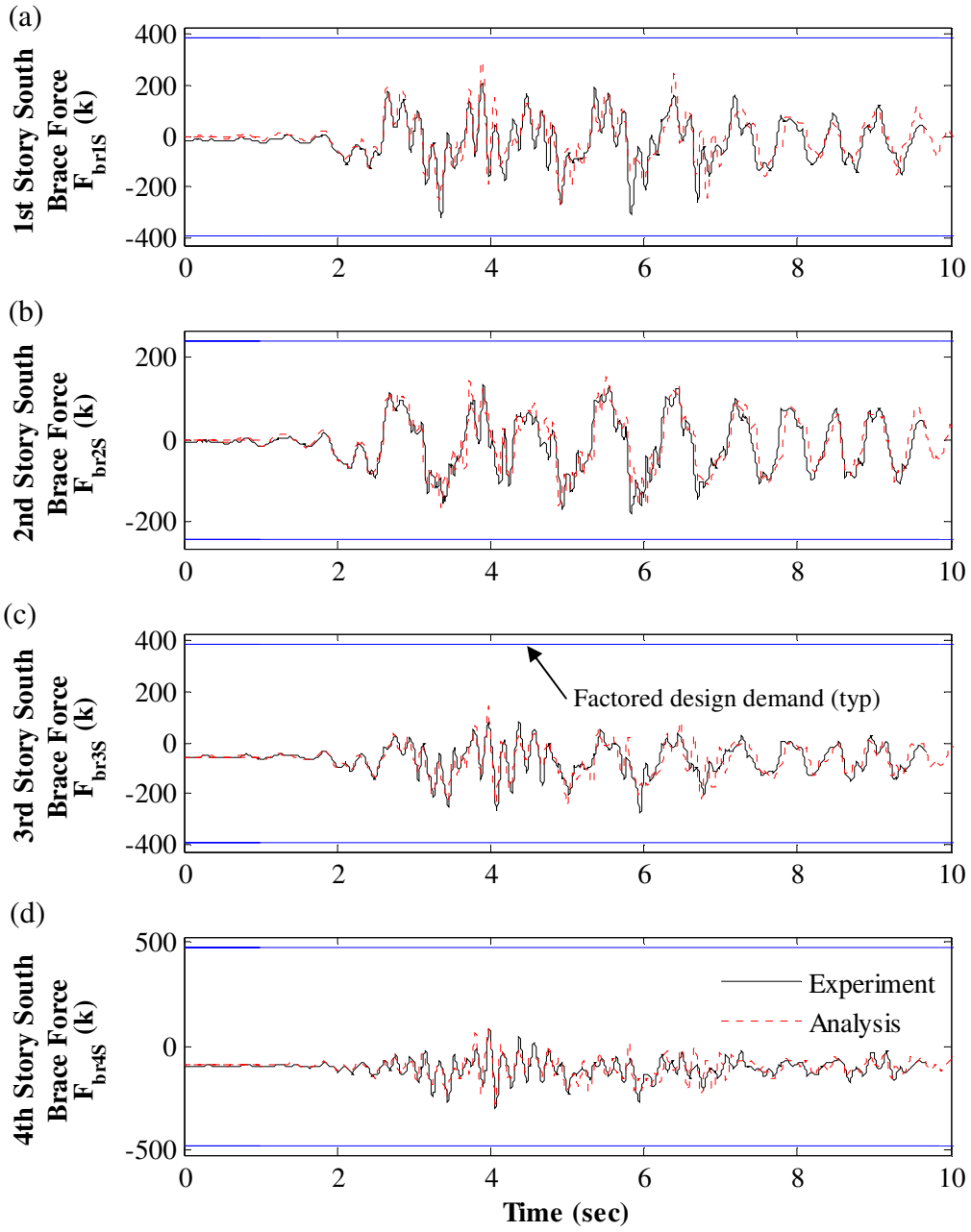

Figure 10.16 – Correlation of south brace axial force response to DBE_5108-090: (a) 1st story; (b) 2nd story; (c) 3rd story; (d) 4th story

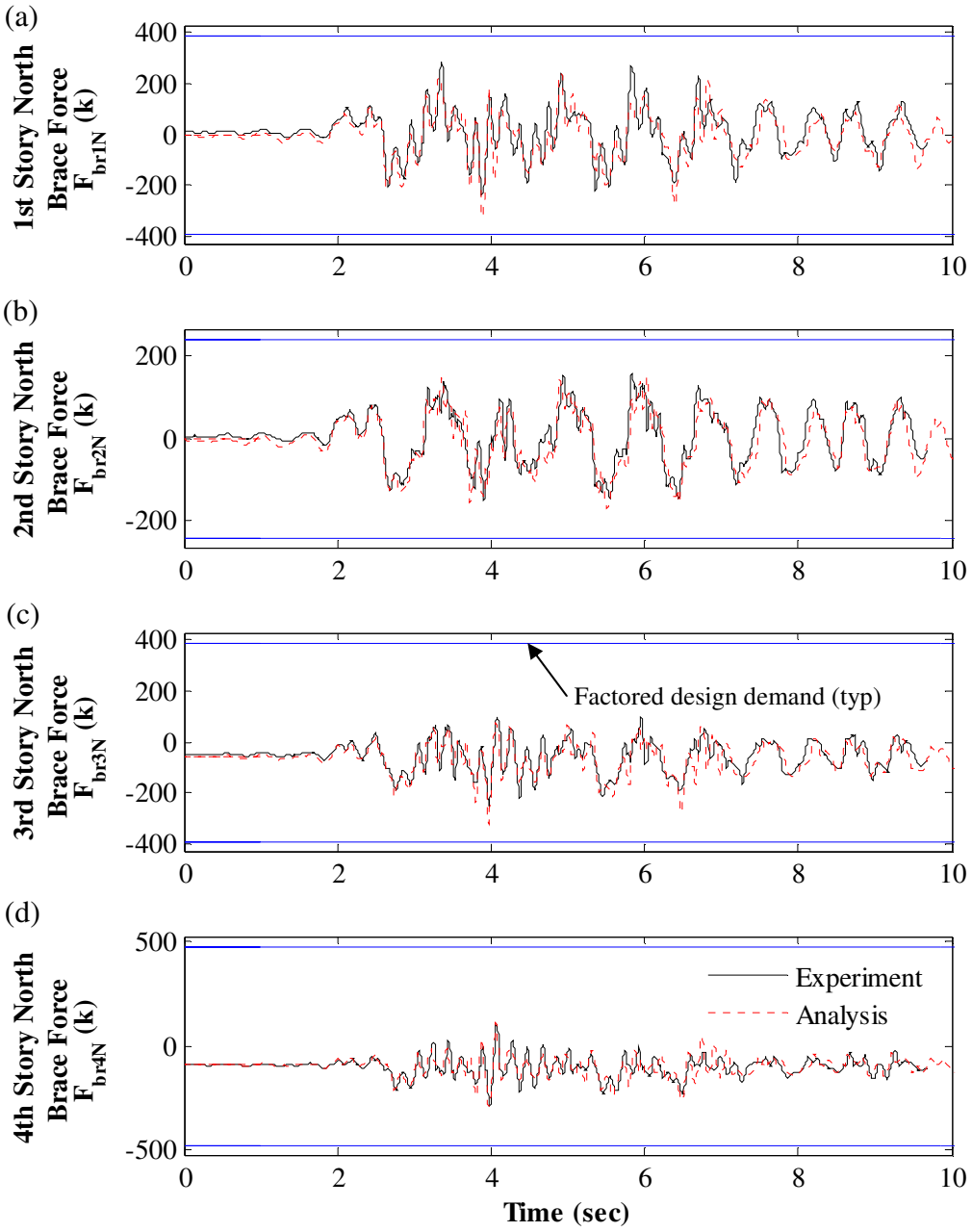

Figure 10.17 – Correlation of north brace axial force response to DBE_5108-090: (a) 1st story; (b) 2nd story; (c) 3rd story; (d) 4th story

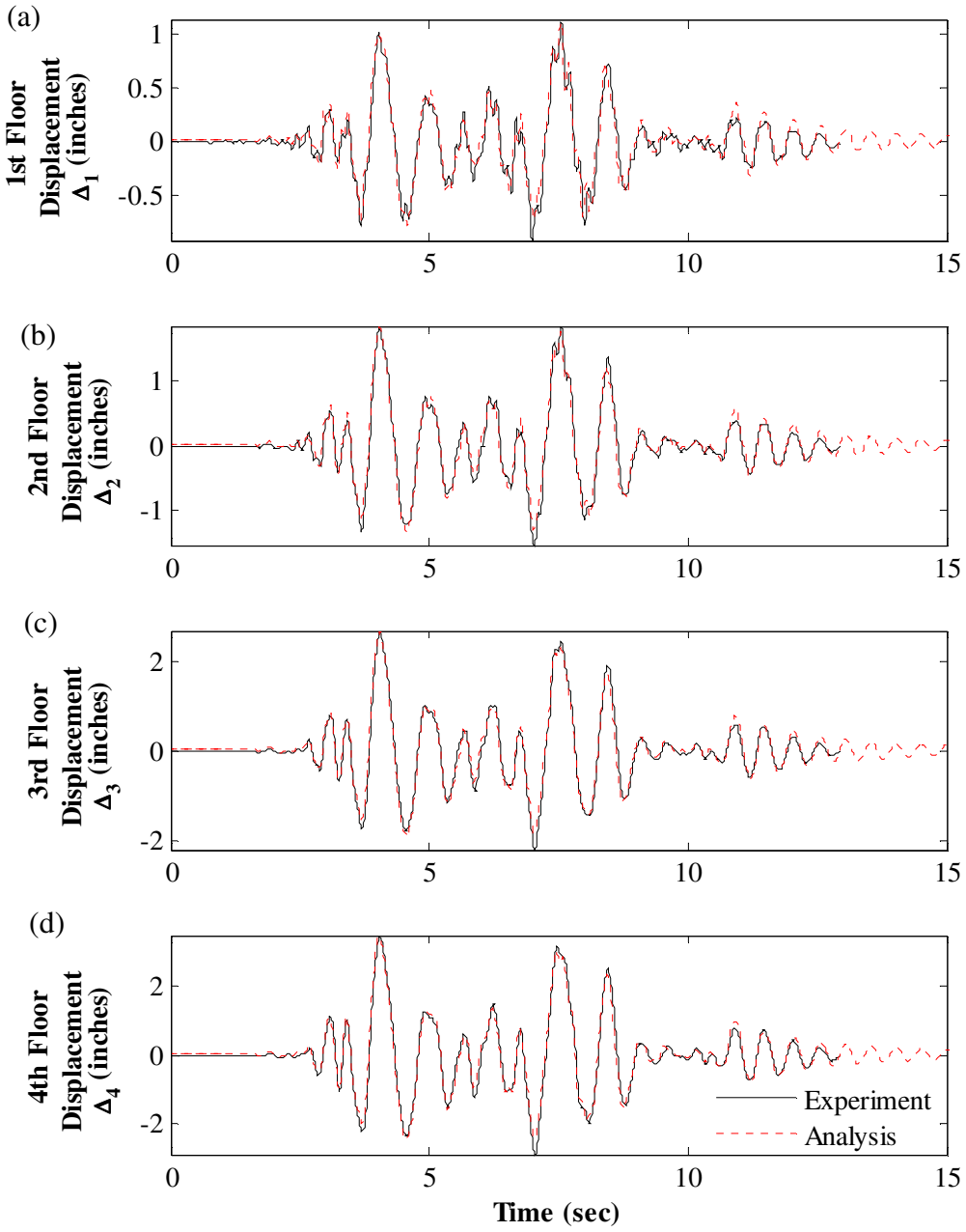

Figure 10.18 – Correlation of floor displacement response to DBE_h-shp270: (a) 1st floor; (b) 2nd floor; (c) 3rd floor; (d) 4th floor

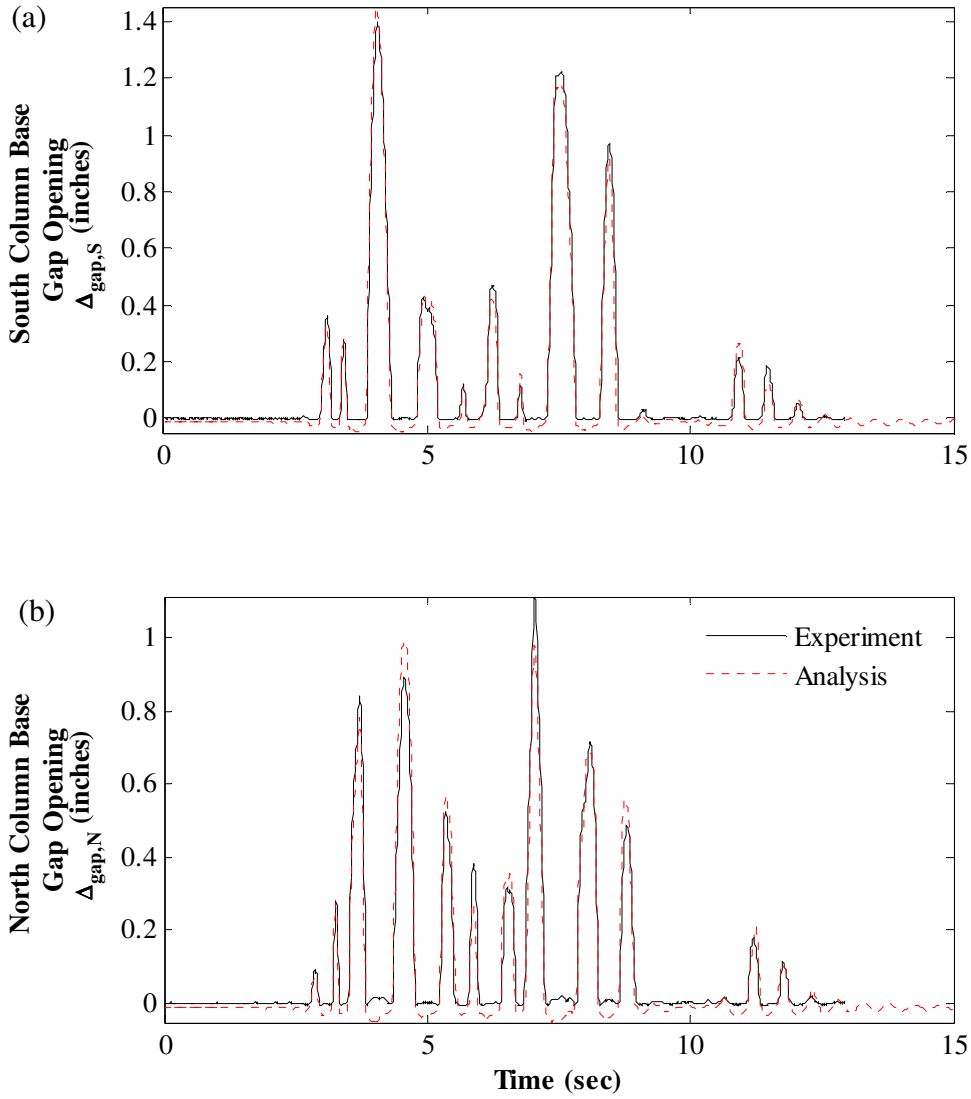

Figure 10.19 – Correlation of column base gap opening response to DBE_h-shp270: (a) at south column base; (b) at north column base

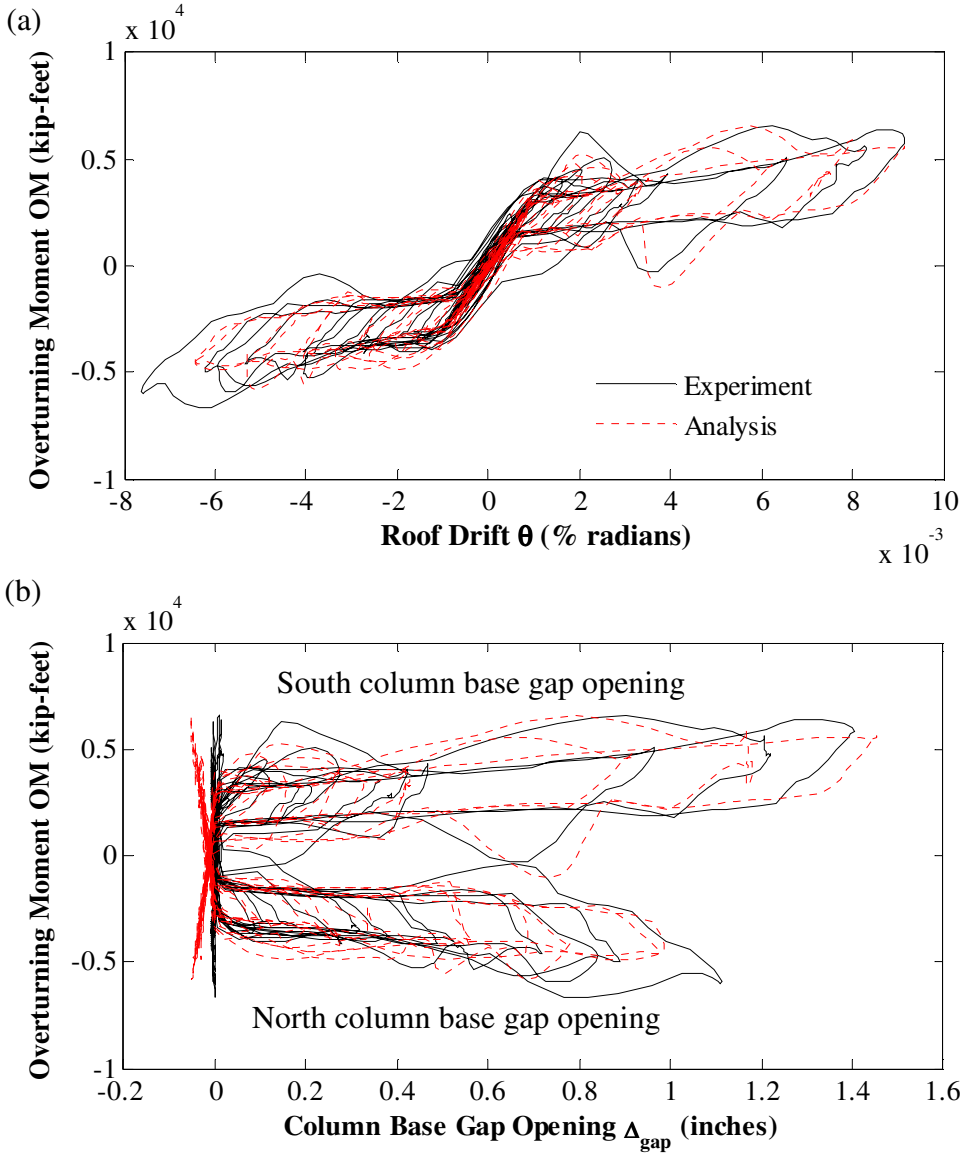

Figure 10.20 – Correlation of hysteretic response to DBE_h-shp270: (a) overturning moment versus roof drift; (b) overturning moment versus column base gap opening

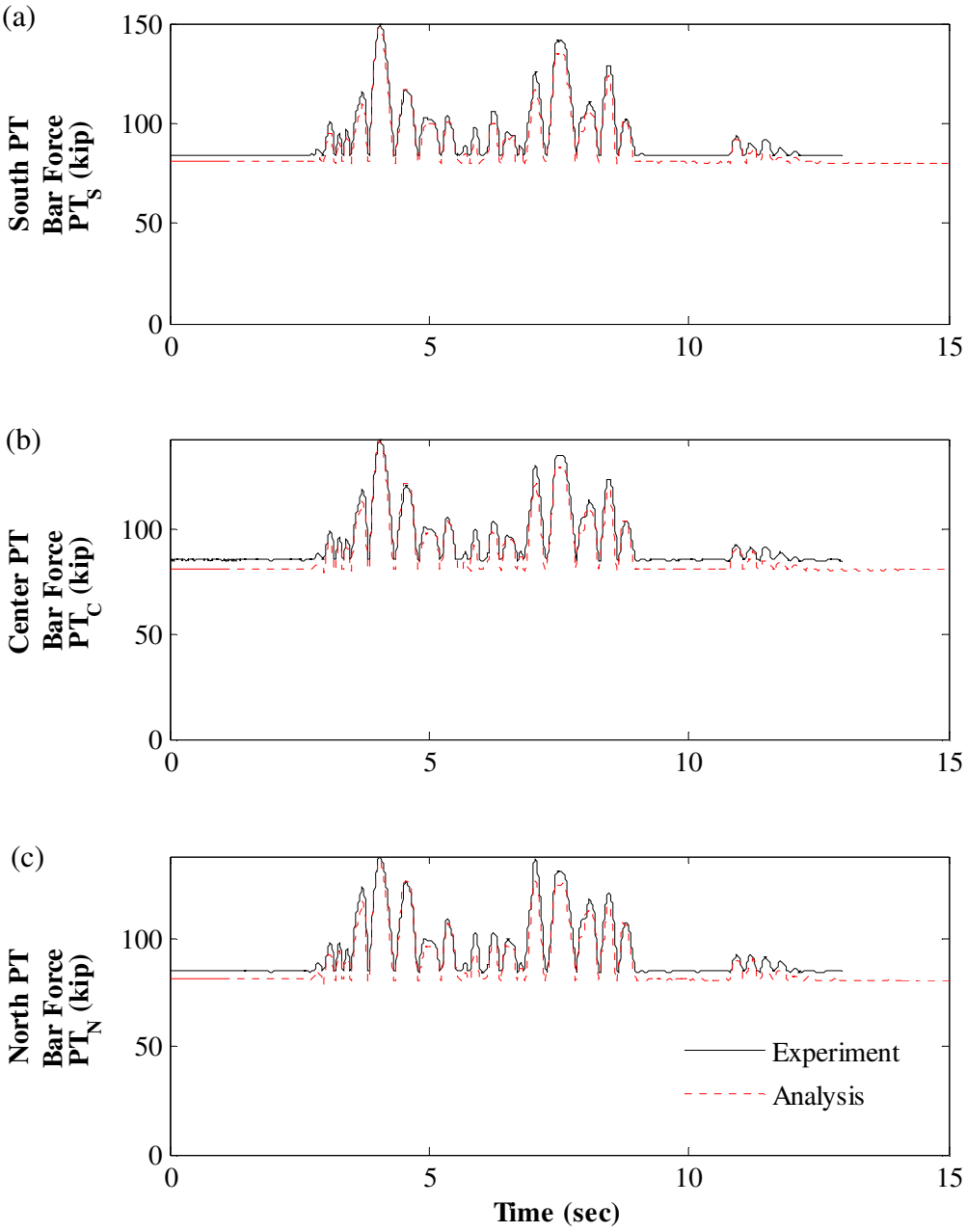

Figure 10.21 – Correlation of PT force response to DBE_h-shp270: (a) south PT bars; (b) center PT bars; (c) north PT bars

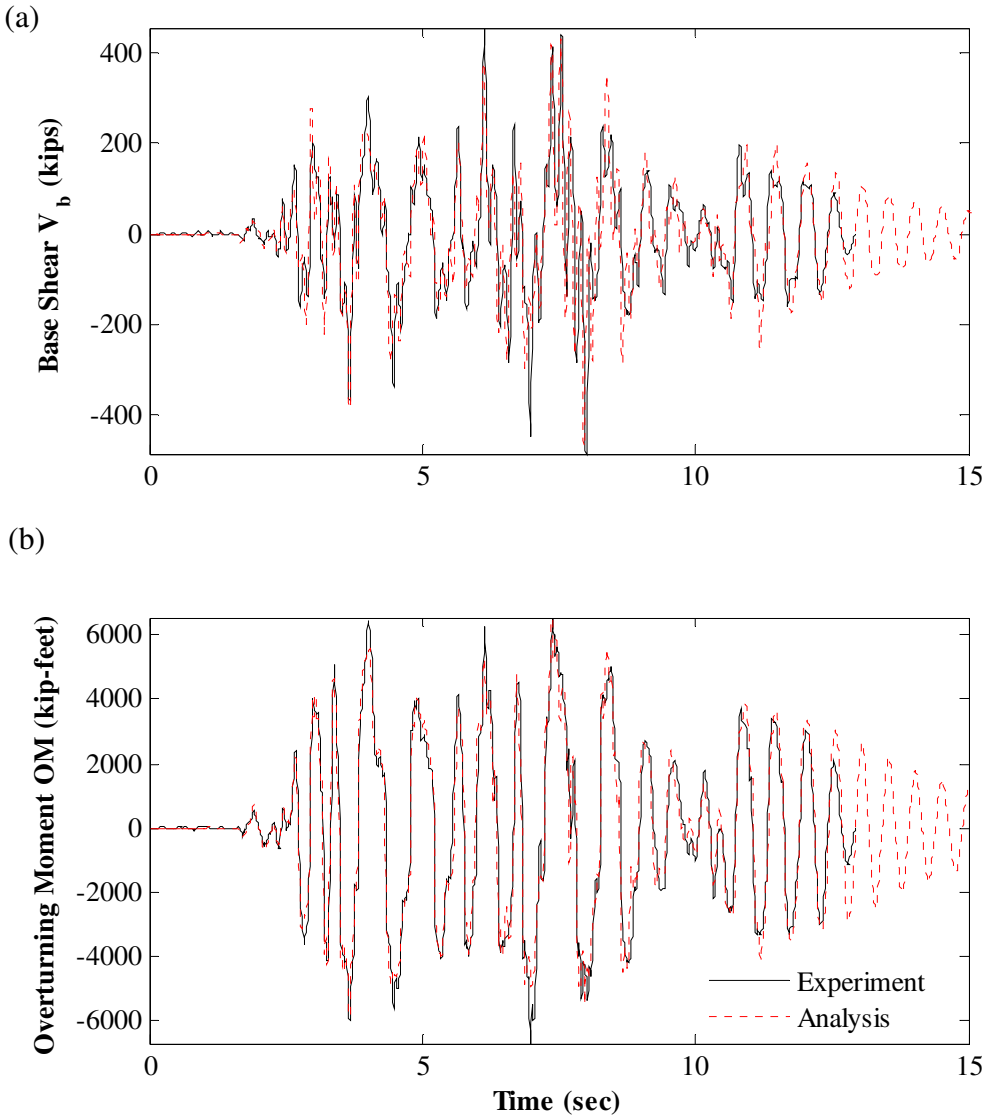

Figure 10.22 – DBE_h-shp270 response correlation: (a) base shear; (b) overturning moment

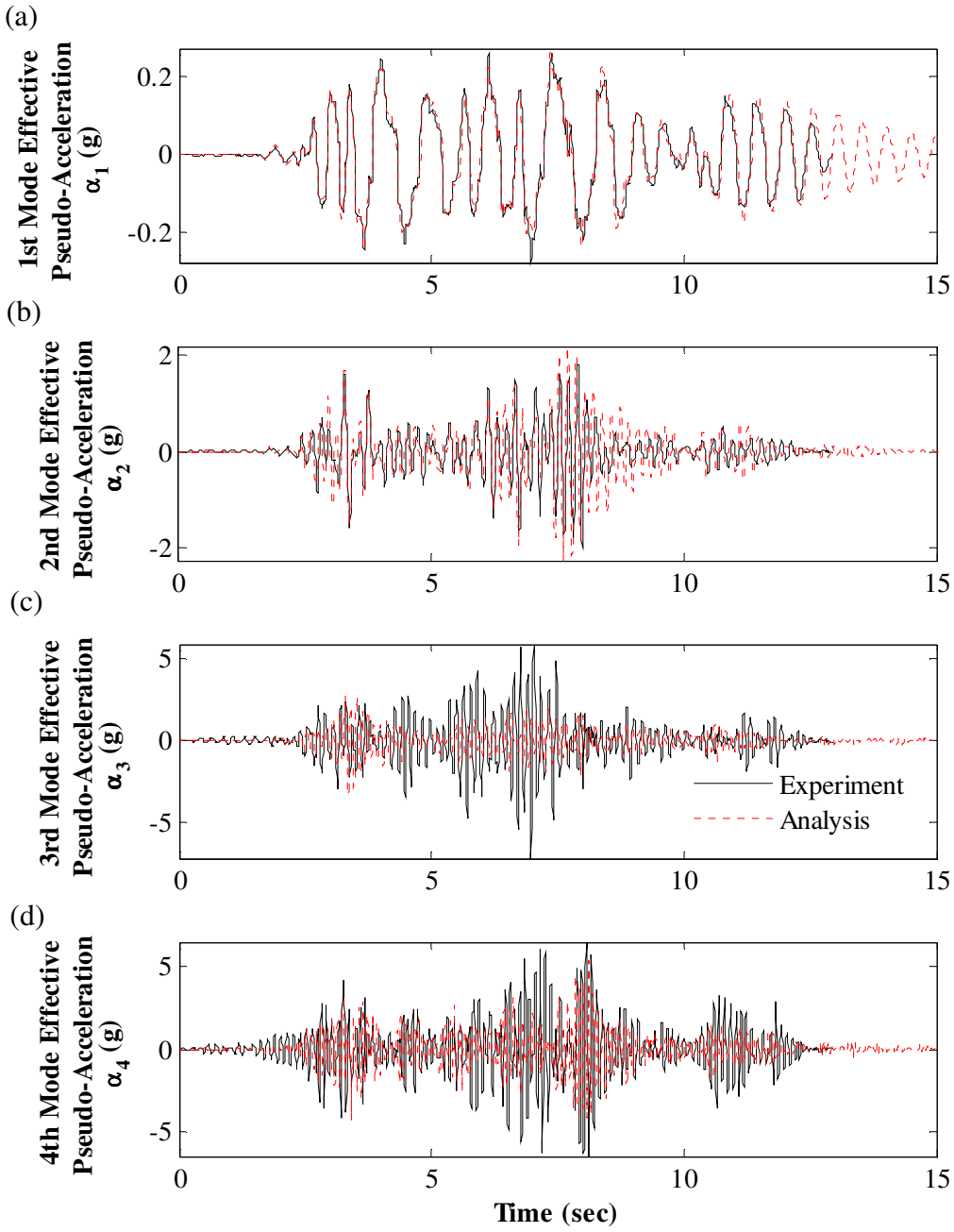

Figure 10.23 – Correlation of effective modal pseudo-acceleration response to DBE_h-shp270: (a) 1st mode; (b) 2nd mode; (c) 3rd mode; (d) 4th mode

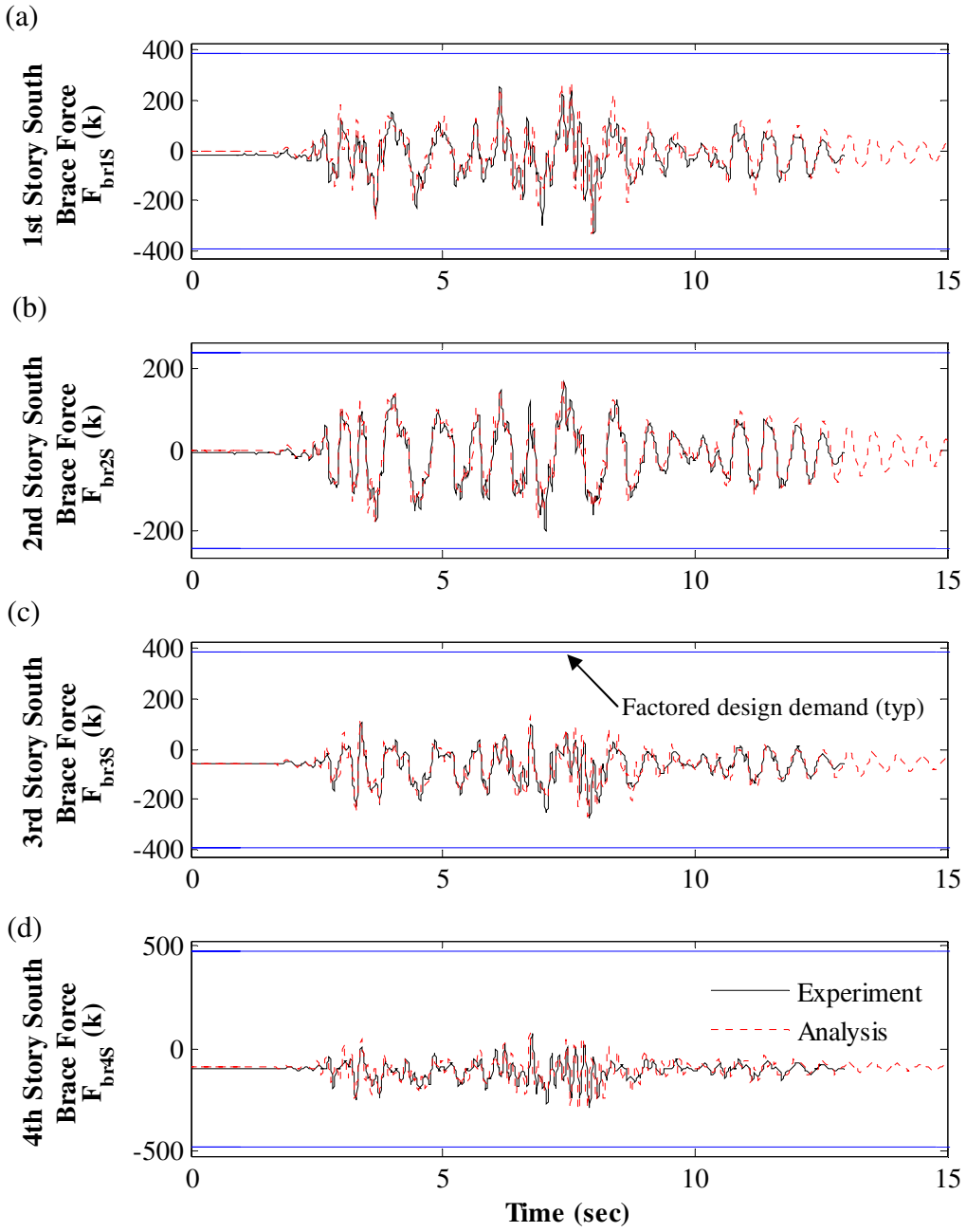

Figure 10.24 – Correlation of south brace axial force response to DBE_h-shp270: (a) 1st story; (b) 2nd story; (c) 3rd story; (d) 4th story

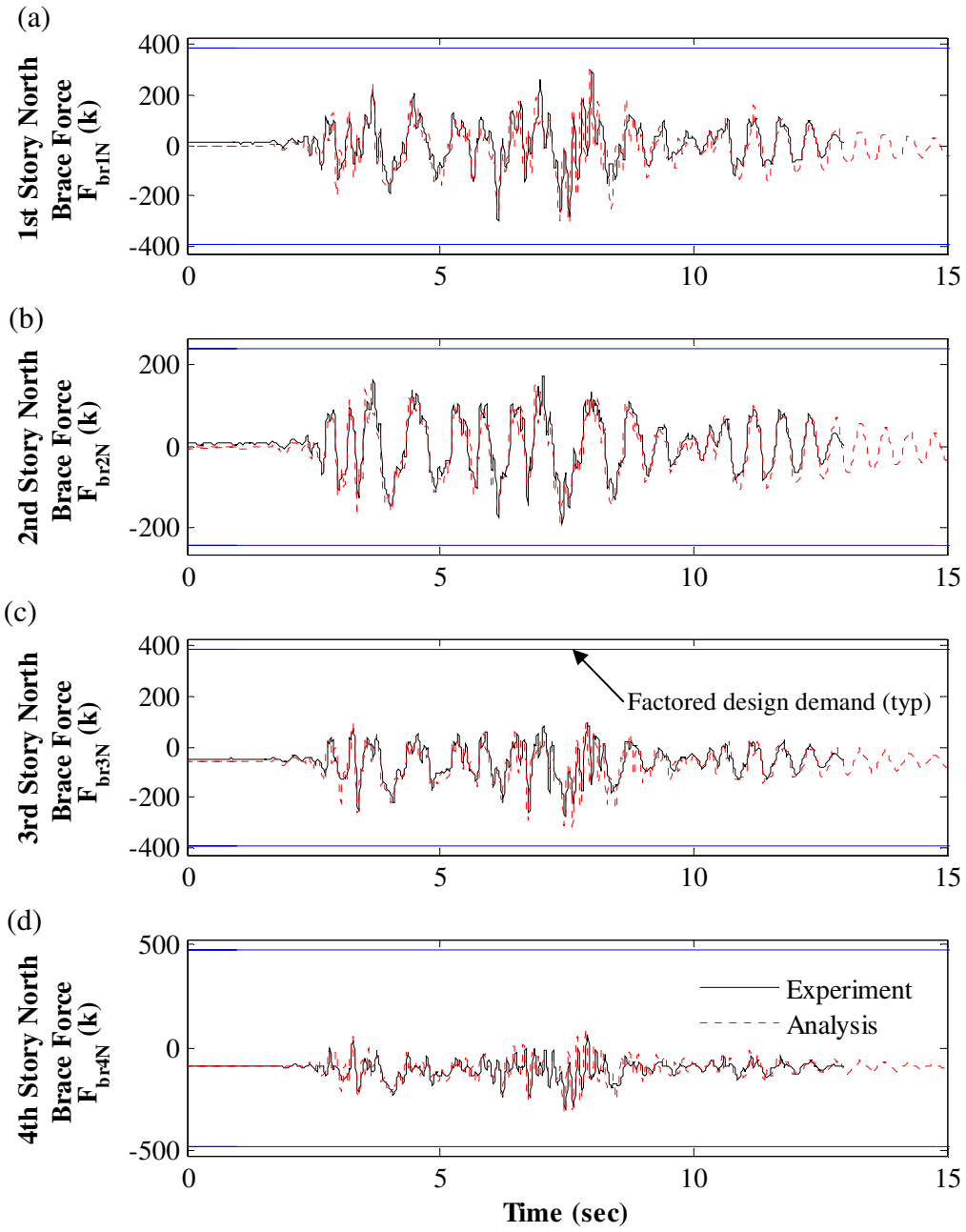

Figure 10.25 – Correlation of north brace axial force response to DBE_h-shp270: (a) 1st story; (b) 2nd story; (c) 3rd story; (d) 4th story

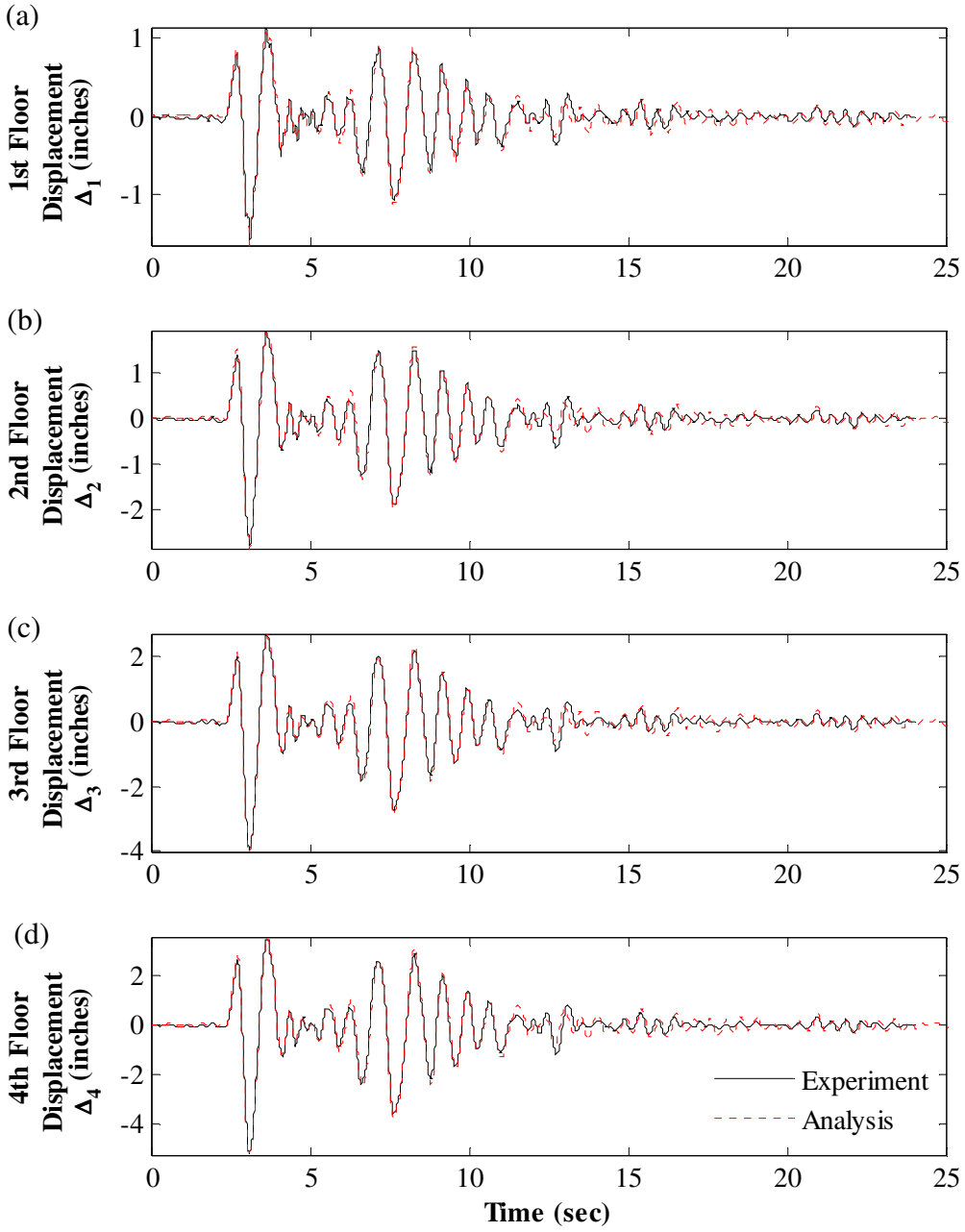

Figure 10.26 – Correlation of floor displacement response to DBE_arl090: (a) 1st floor; (b) 2nd floor; (c) 3rd floor; (d) 4th floor

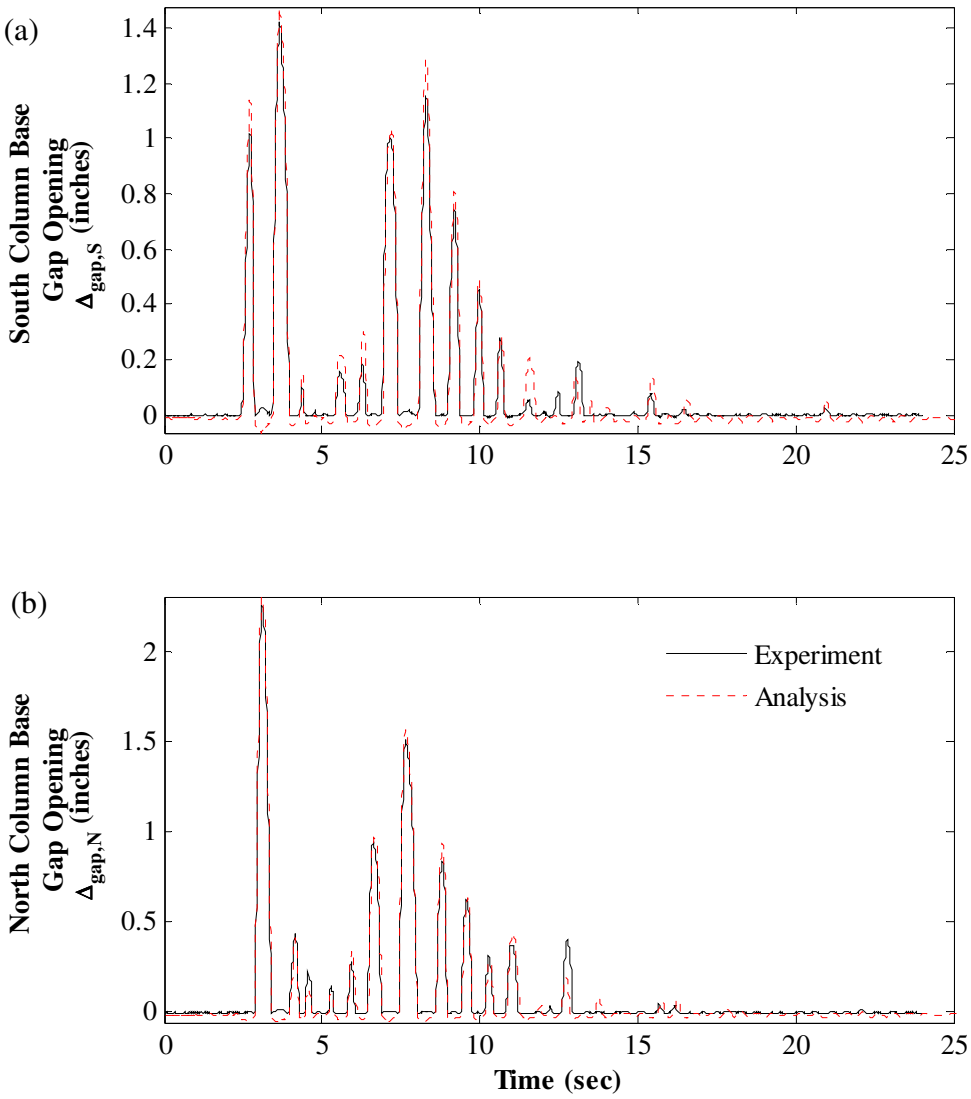

Figure 10.27 – Correlation of column base gap opening response to DBE_arl090: (a) at south column base; (b) at north column base

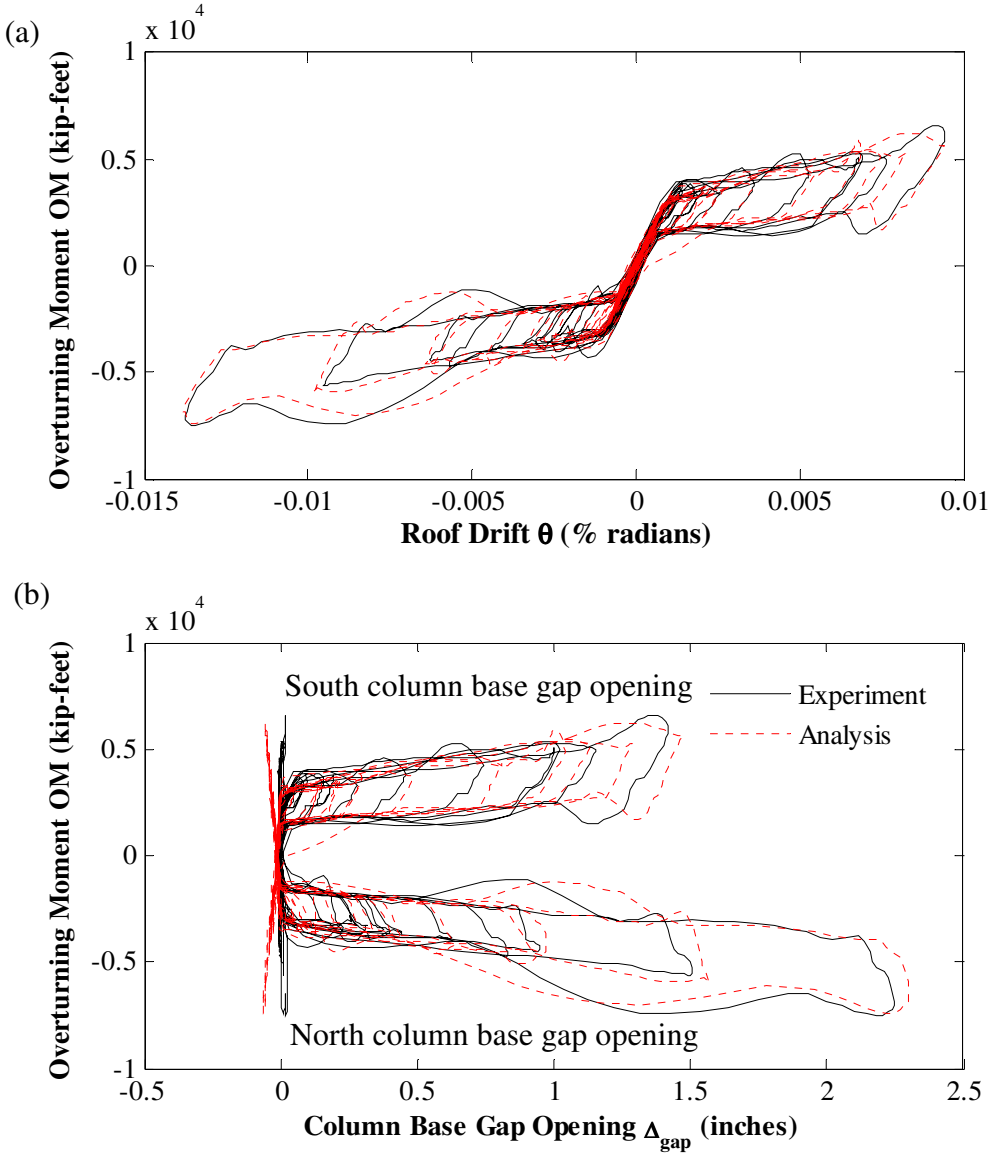

Figure 10.28 – Correlation of hysteretic response to DBE_arl090: (a) overturning moment versus roof drift; (b) overturning moment versus column base gap opening

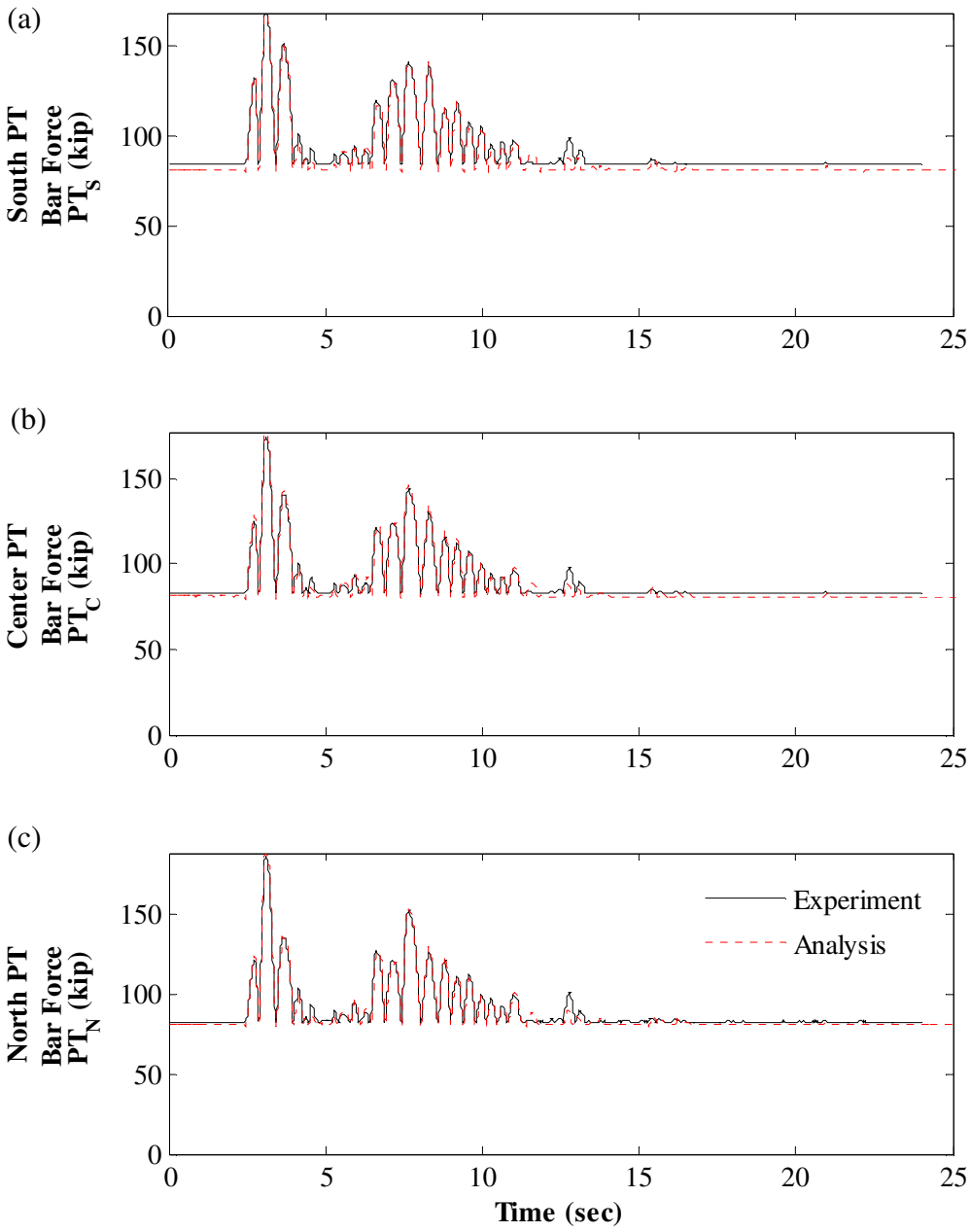

Figure 10.29 – Correlation of PT force response to DBE_arl090: (a) south PT bars; (b) center PT bars; (c) north PT bars

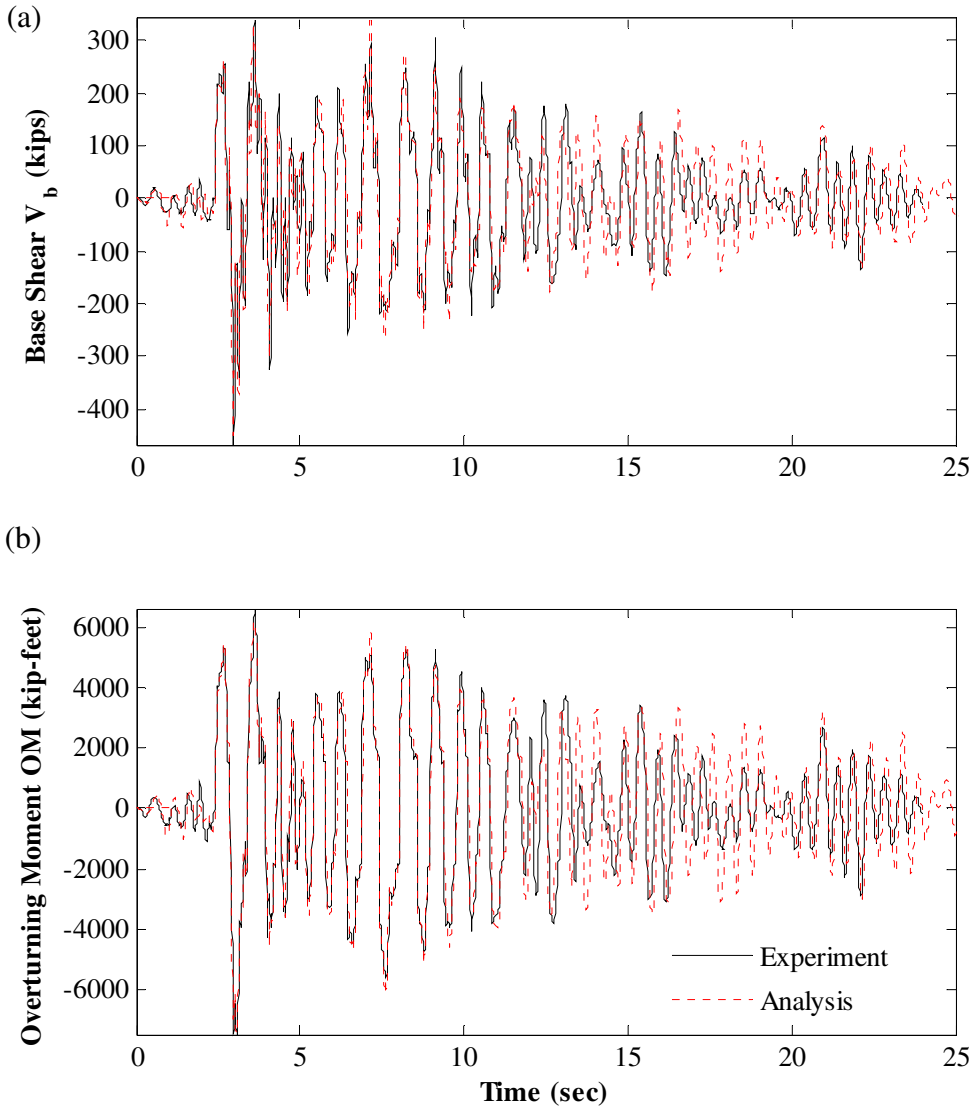

Figure 10.30 – DBE_arl090 response correlation: (a) base shear; (b) overturning moment

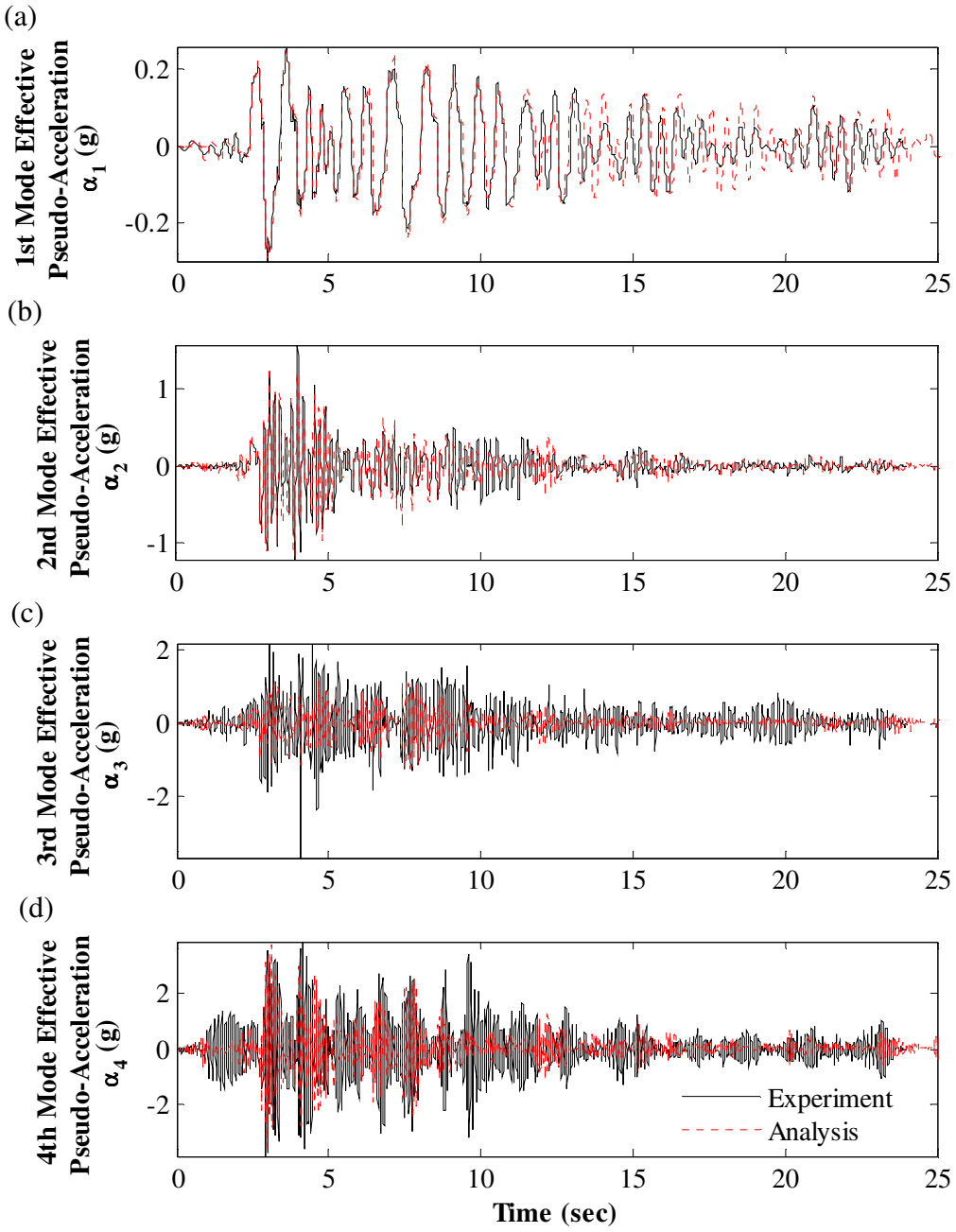

Figure 10.31 – Correlation of effective modal pseudo-acceleration response to DBE_arl090: (a) 1st mode; (b) 2nd mode; (c) 3rd mode; (d) 4th mode

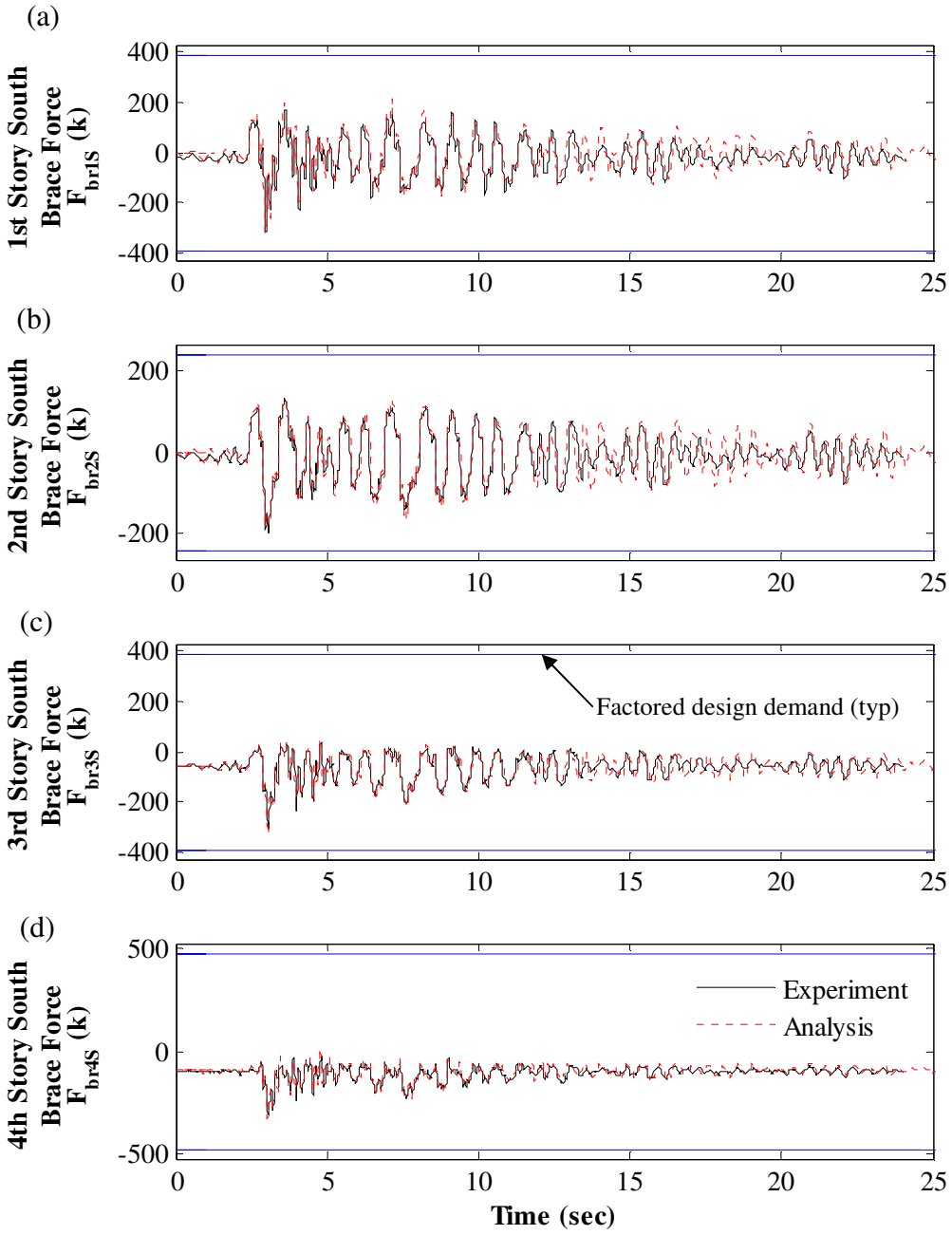

Figure 10.32 – Correlation of south brace axial force response to DBE_arl090: (a) 1st story; (b) 2nd story; (c) 3rd story; (d) 4th story

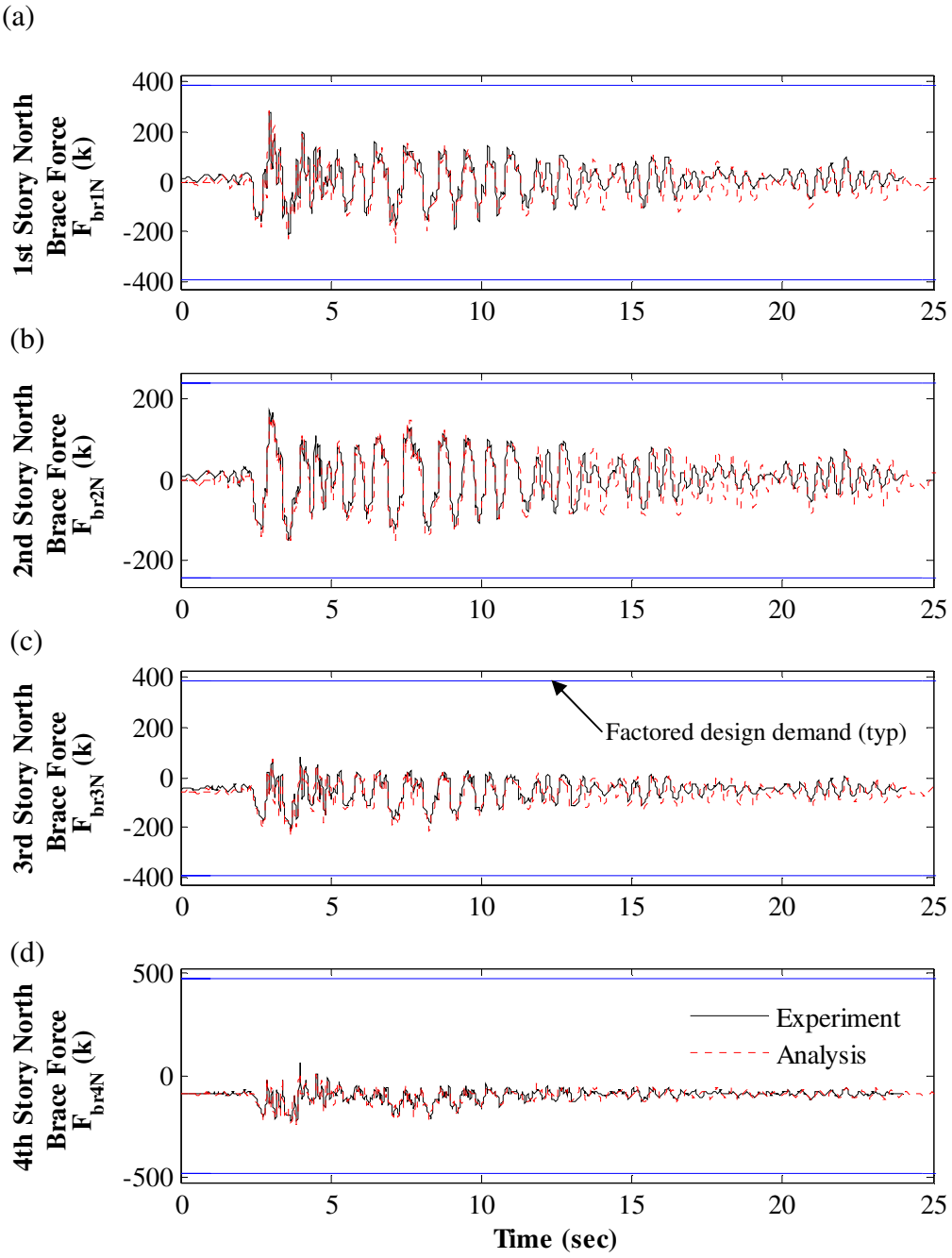

Figure 10.33 – Correlation of north brace axial force response to DBE_arl090: (a) 1st story; (b) 2nd story; (c) 3rd story; (d) 4th story

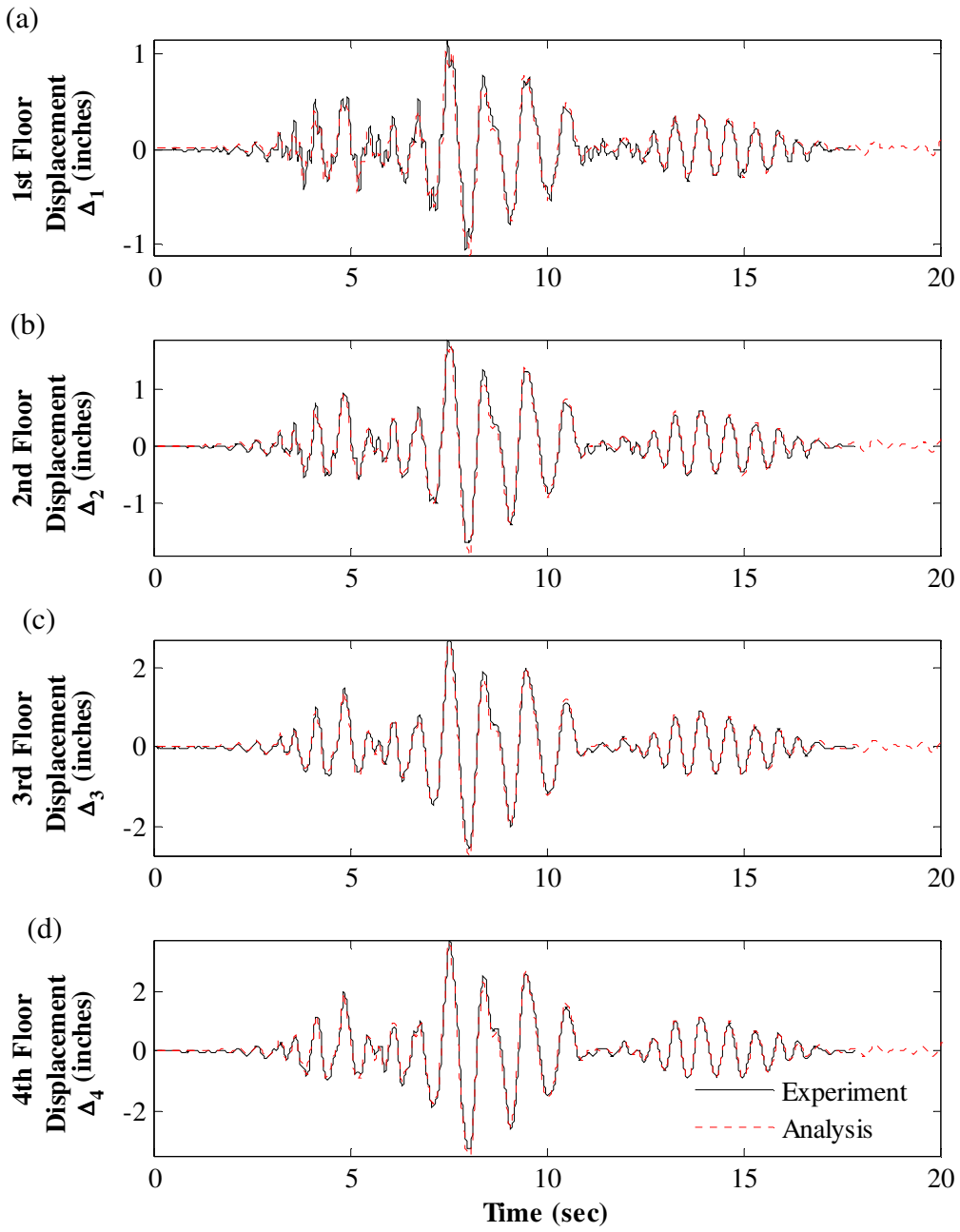

Figure 10.34 – Correlation of floor displacement response to DBE_nr-pel360: (a) 1st floor; (b) 2nd floor; (c) 3rd floor; (d) 4th floor

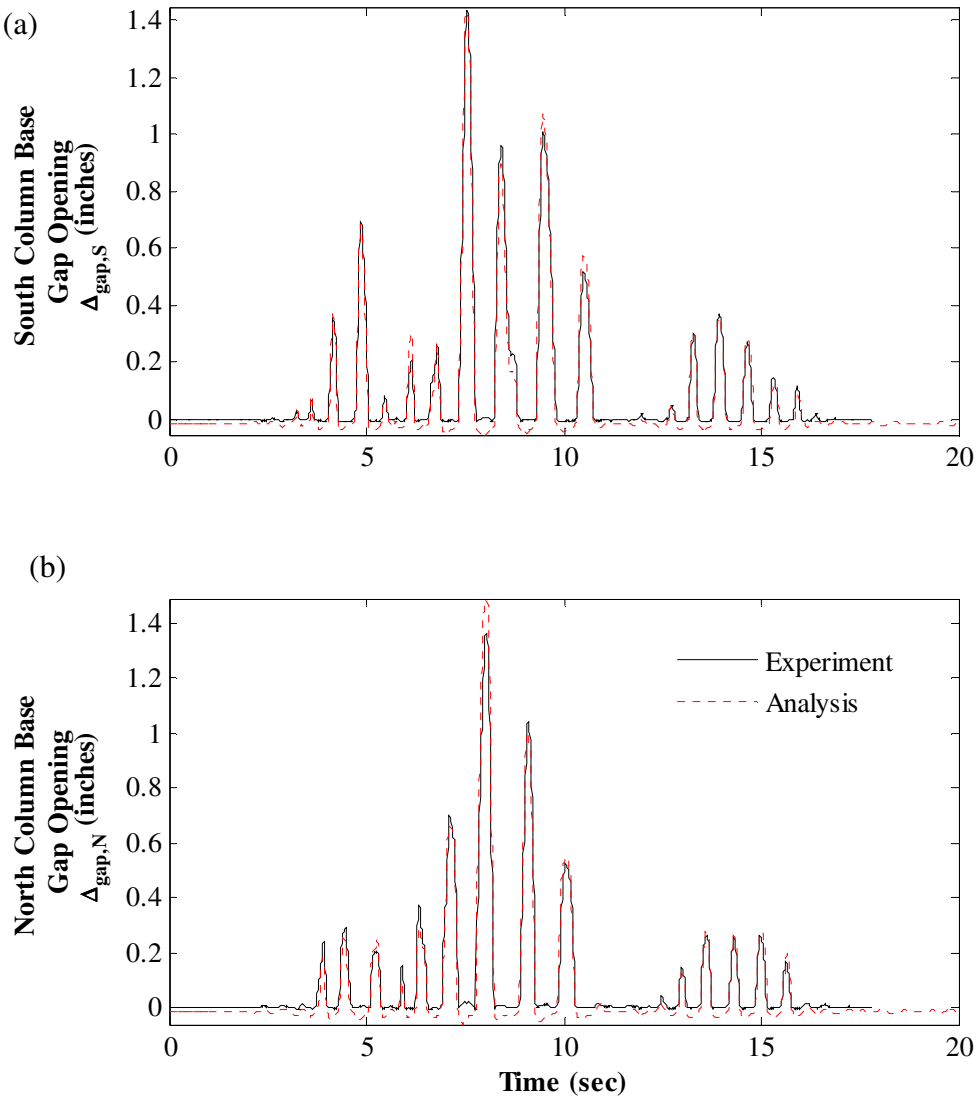

Figure 10.35 – Correlation of column base gap opening response to DBE_nr-pel360: (a) at south column base; (b) at north column base

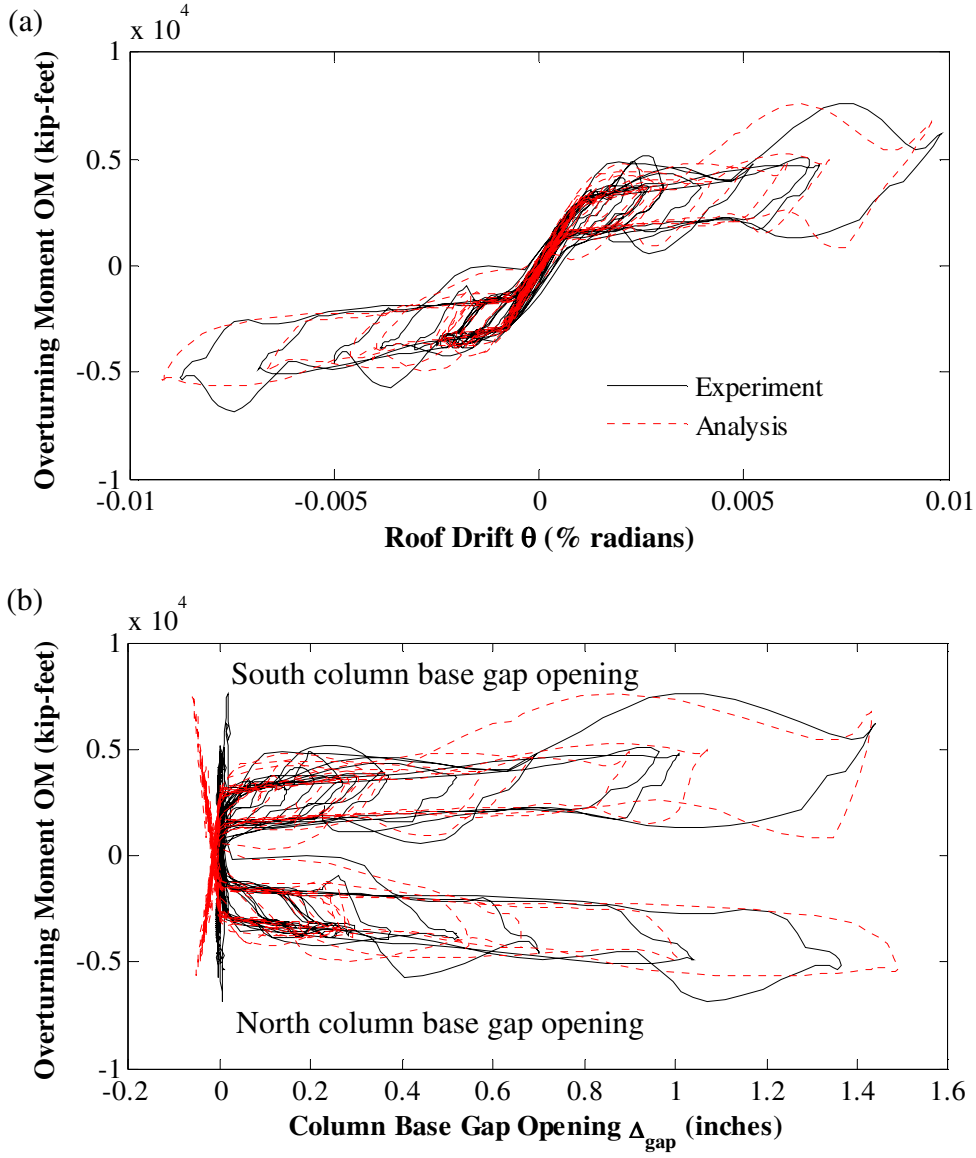

Figure 10.36 – Correlation of hysteretic response to DBE_nr-pel360: (a) overturning moment versus roof drift; (b) overturning moment versus column base gap opening

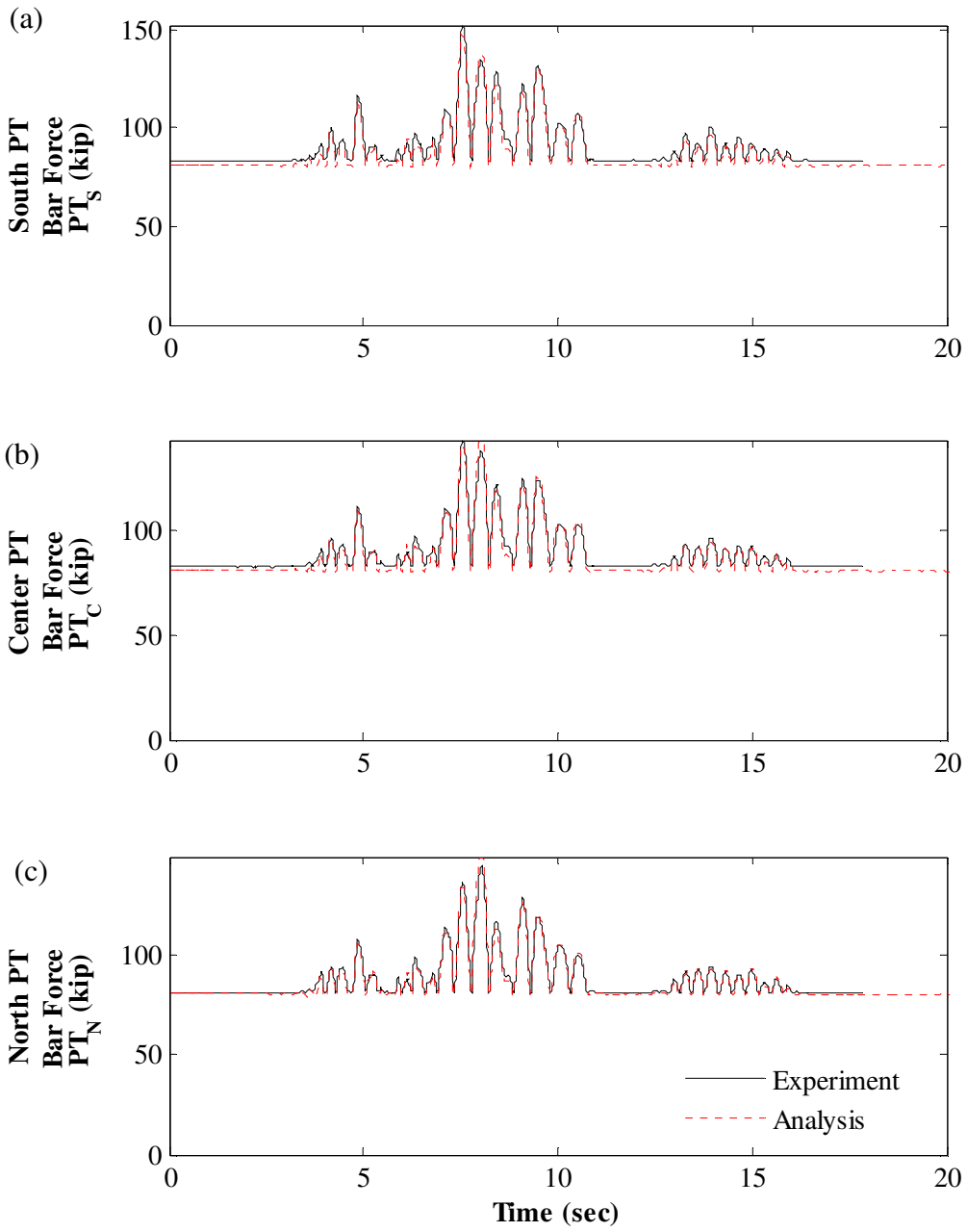

Figure 10.37 – Correlation of PT force response to DBE_nr-pel360: (a) south PT bars; (b) center PT bars; (c) north PT bars

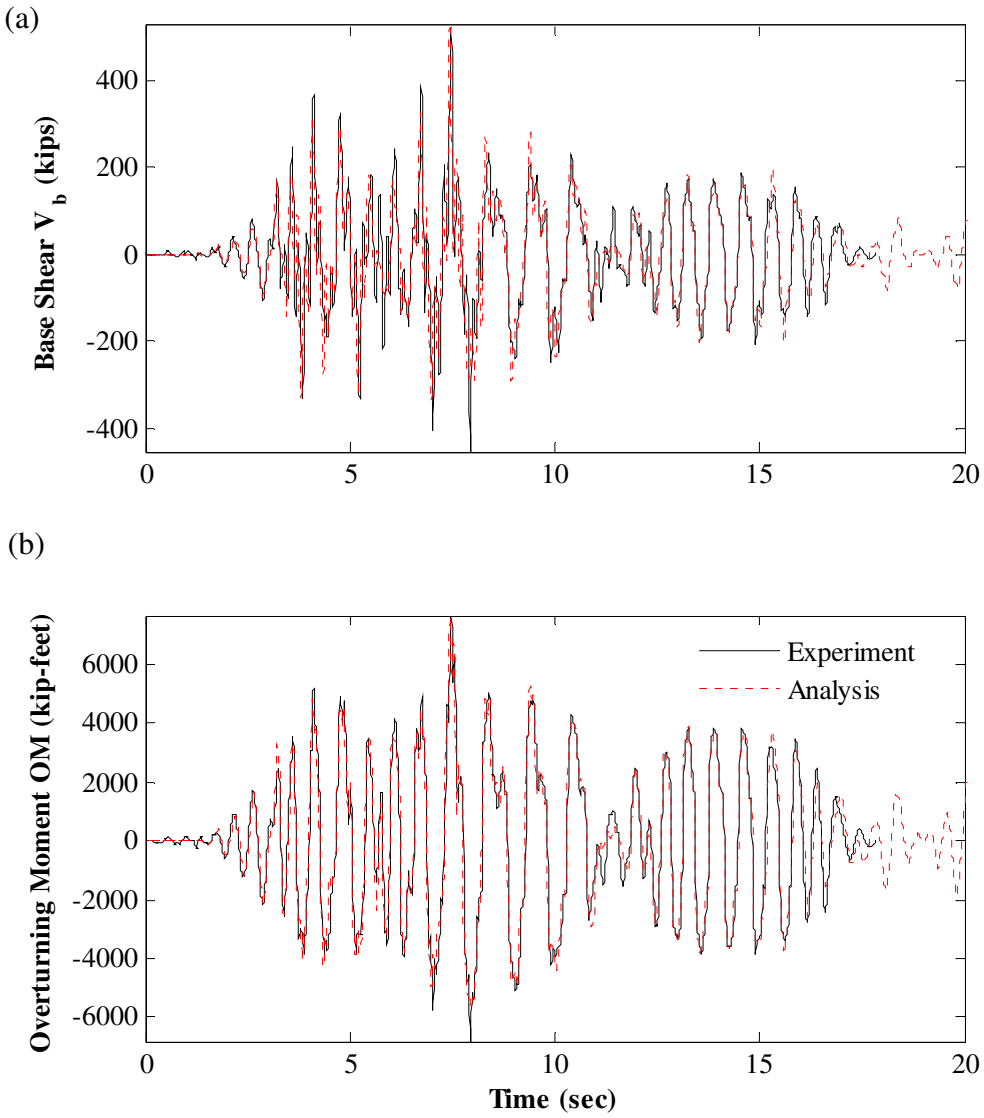

Figure 10.38 – DBE_nr-pel360 response correlation: (a) base shear; (b) overturning moment

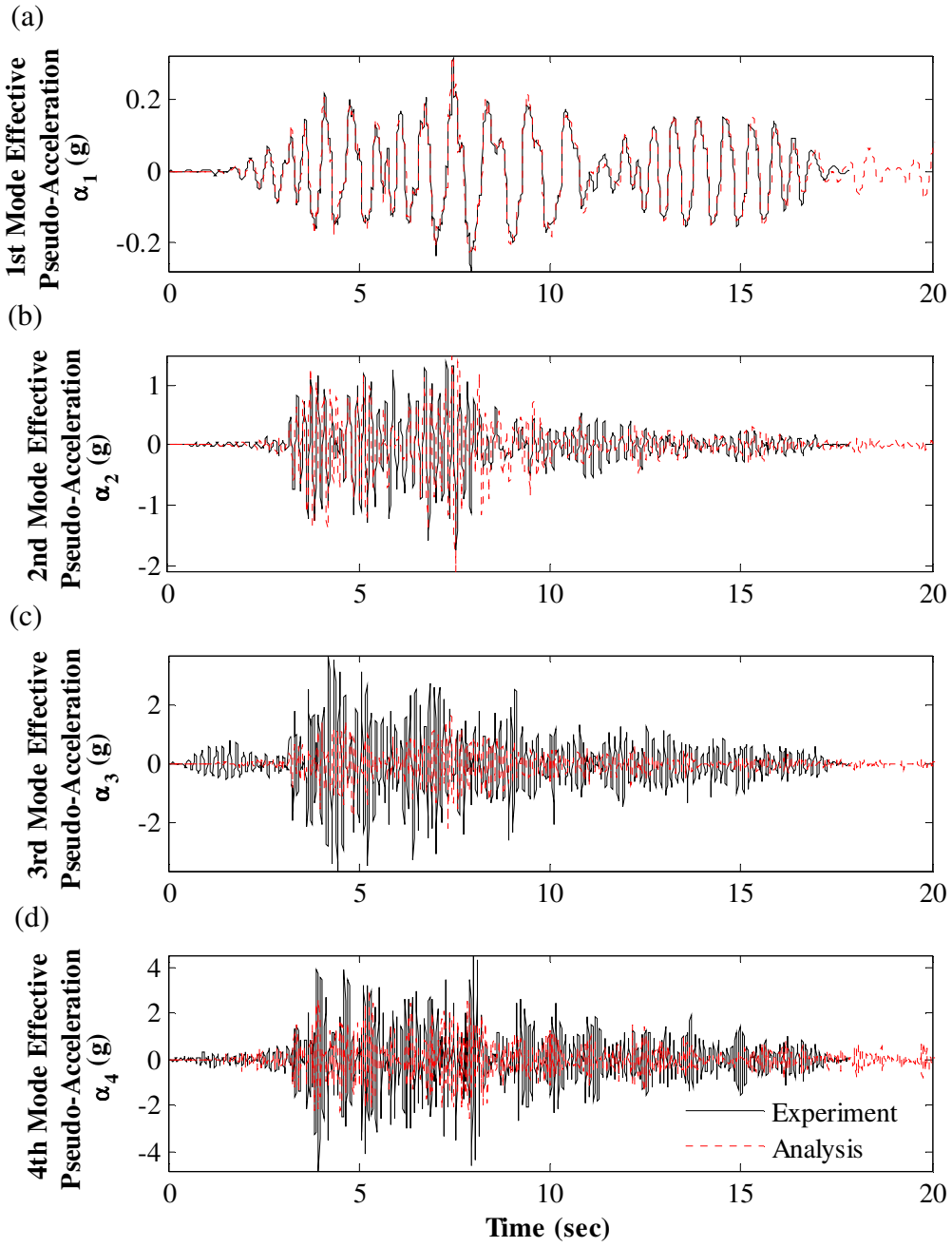

Figure 10.39 – Correlation of effective modal pseudo-acceleration response to DBE_nr-pel360: (a) 1st mode; (b) 2nd mode; (c) 3rd mode; (d) 4th mode

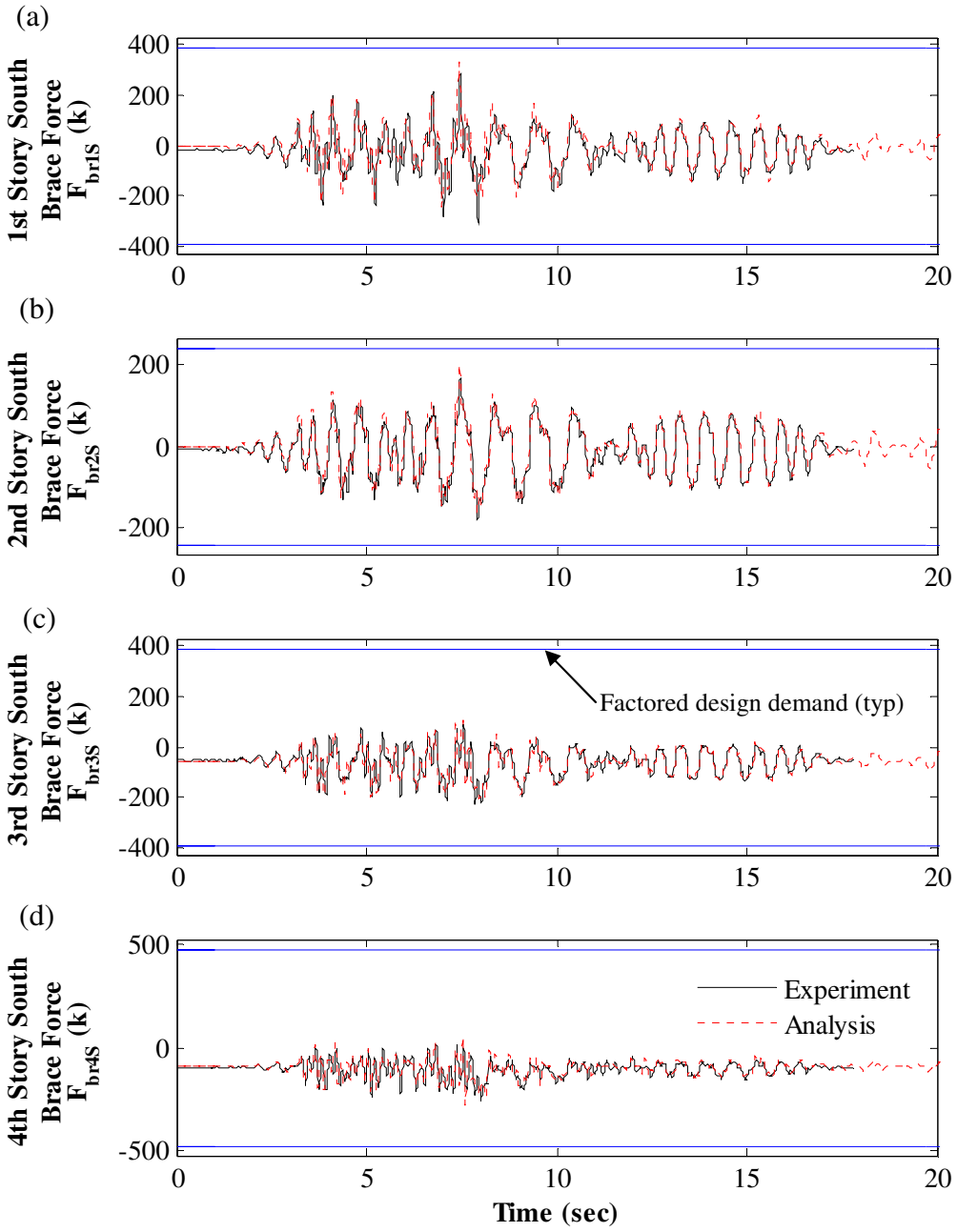

Figure 10.40 – Correlation of south brace axial force response to DBE_nr-pel360: (a) 1st story; (b) 2nd story; (c) 3rd story; (d) 4th story

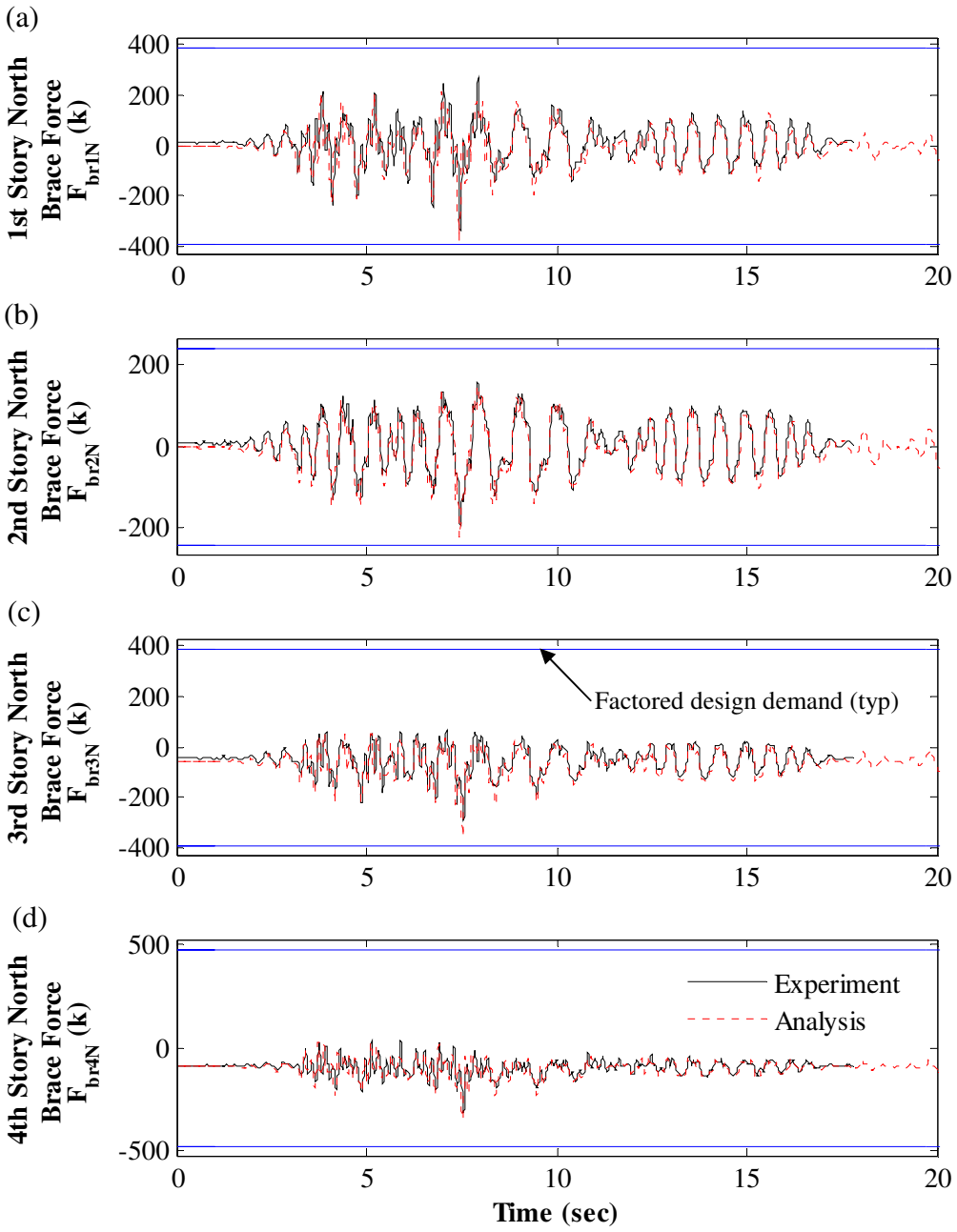

Figure 10.41 – Correlation of north brace axial force response to DBE_nr-pel360: (a) 1st story; (b) 2nd story; (c) 3rd story; (d) 4th story

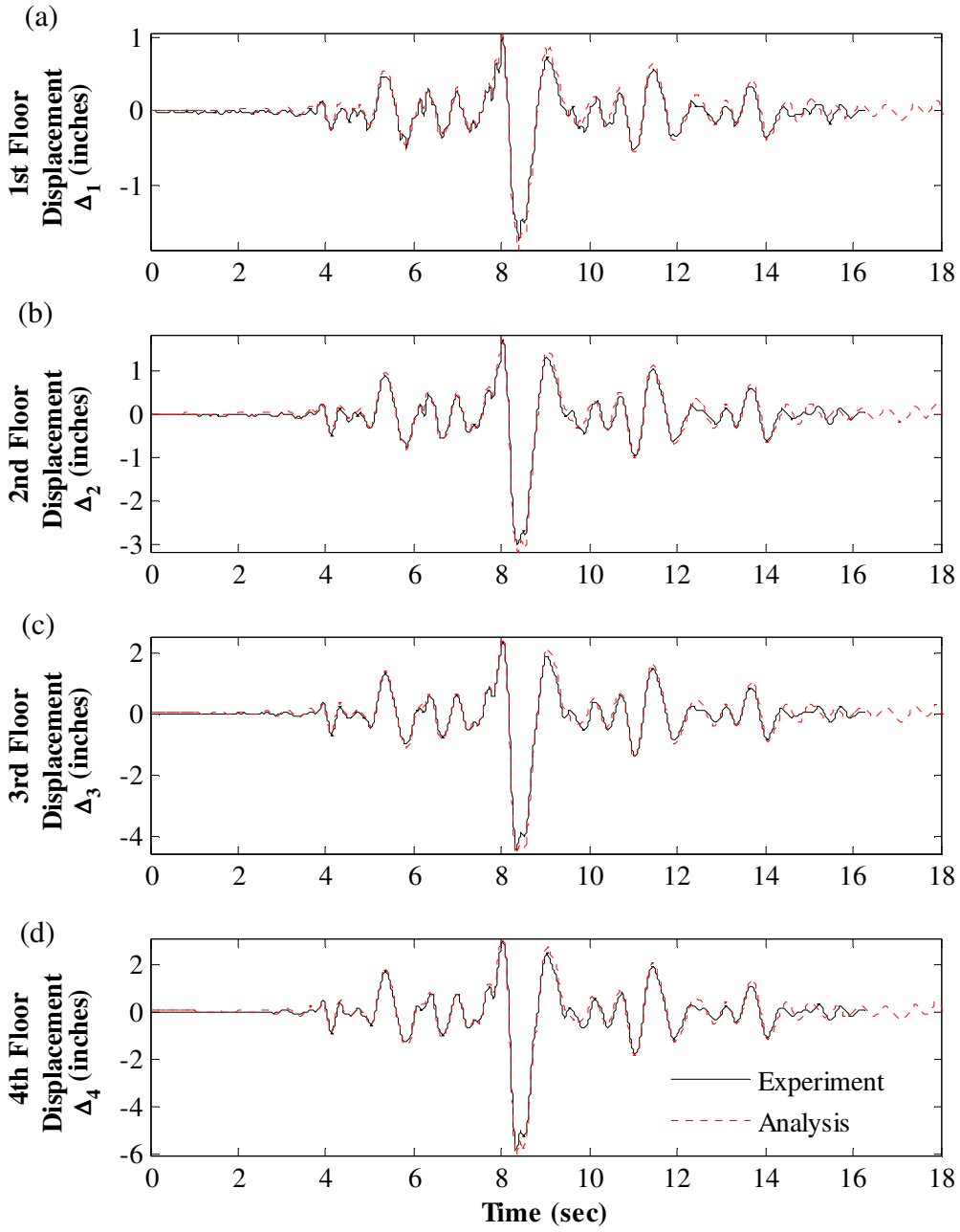

Figure 10.42 – Correlation of floor displacement response to MCE_stn110: (a) 1st floor; (b) 2nd floor; (c) 3rd floor; (d) 4th floor

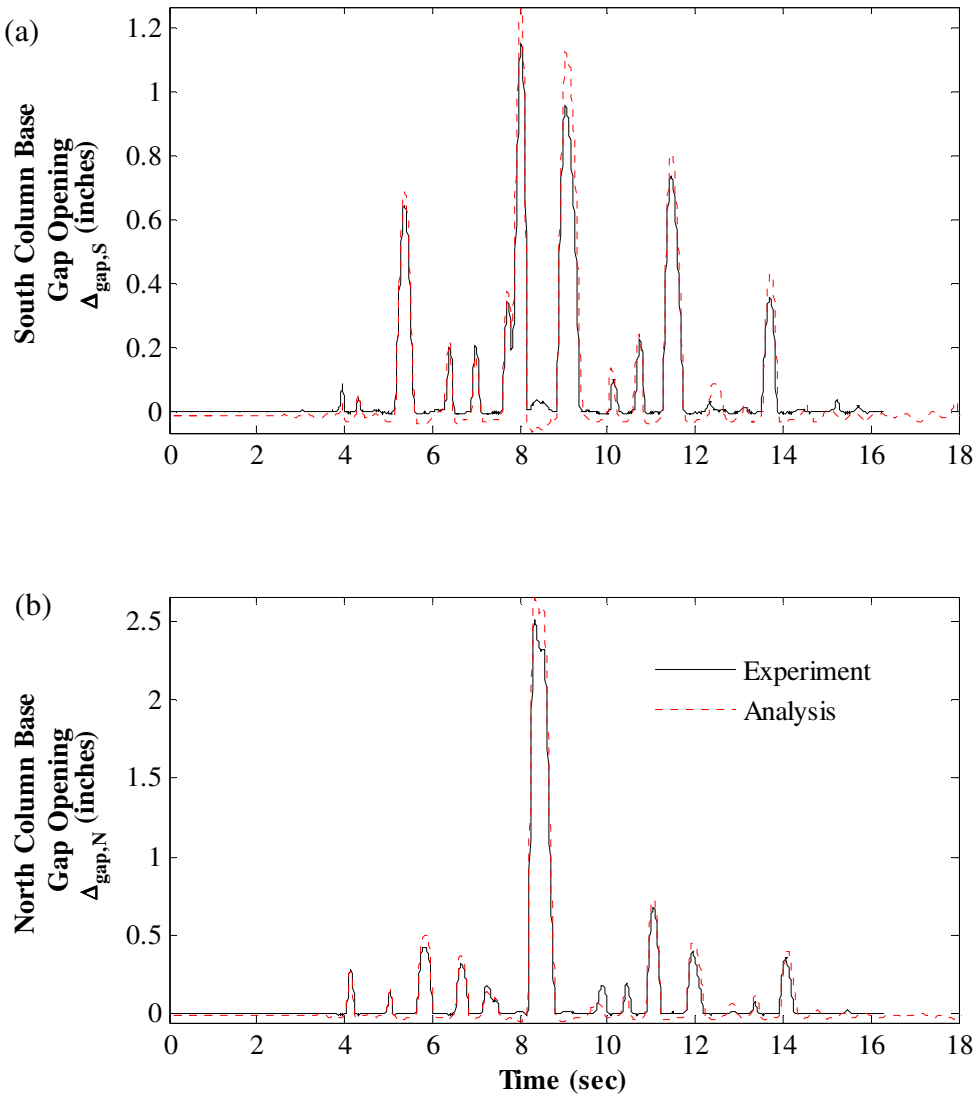

Figure 10.43 – Correlation of column base gap opening response to MCE_stn110: (a) at south column base; (b) at north column base

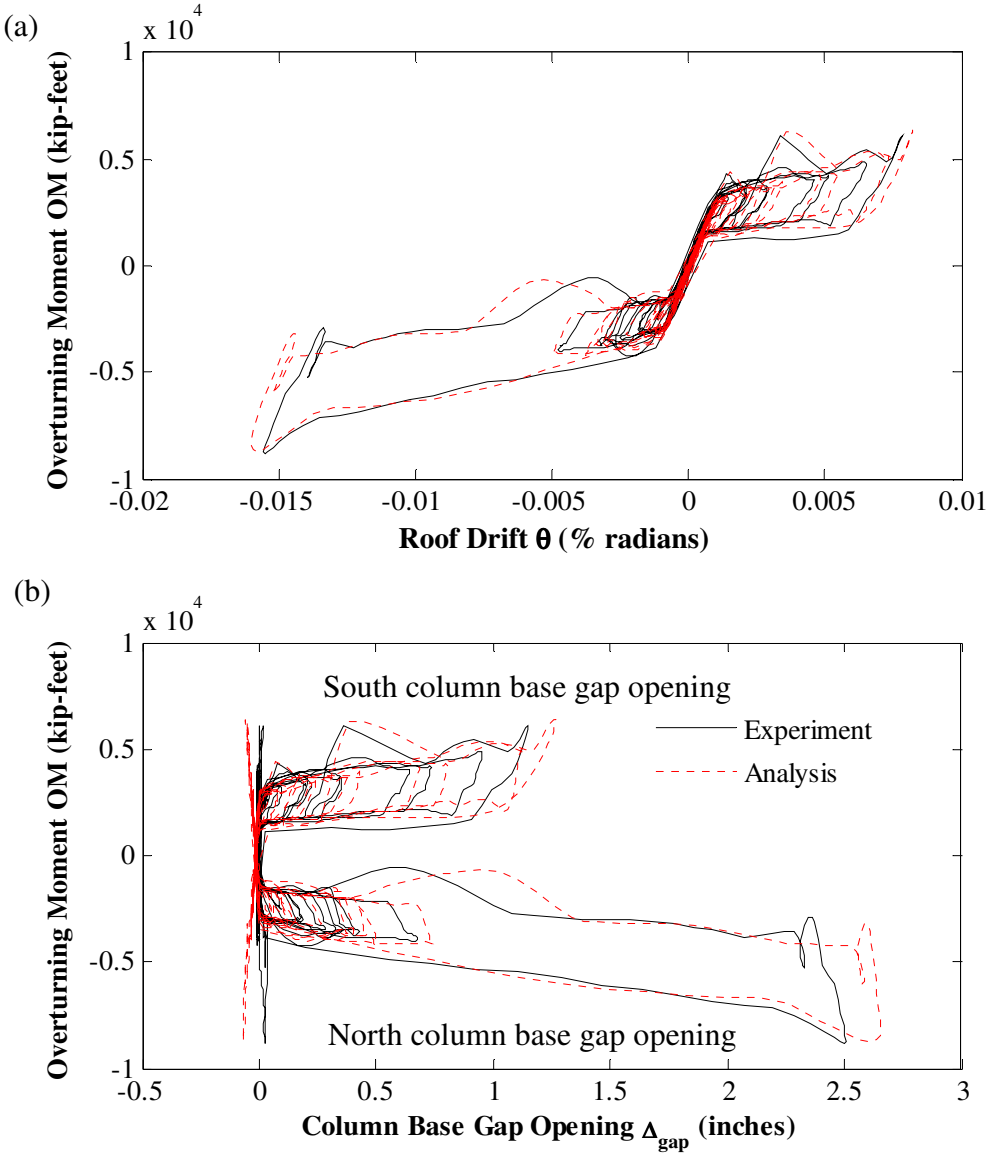

Figure 10.44 – Correlation of hysteretic response to MCE_stn110: (a) overturning moment versus roof drift; (b) overturning moment versus column base gap opening

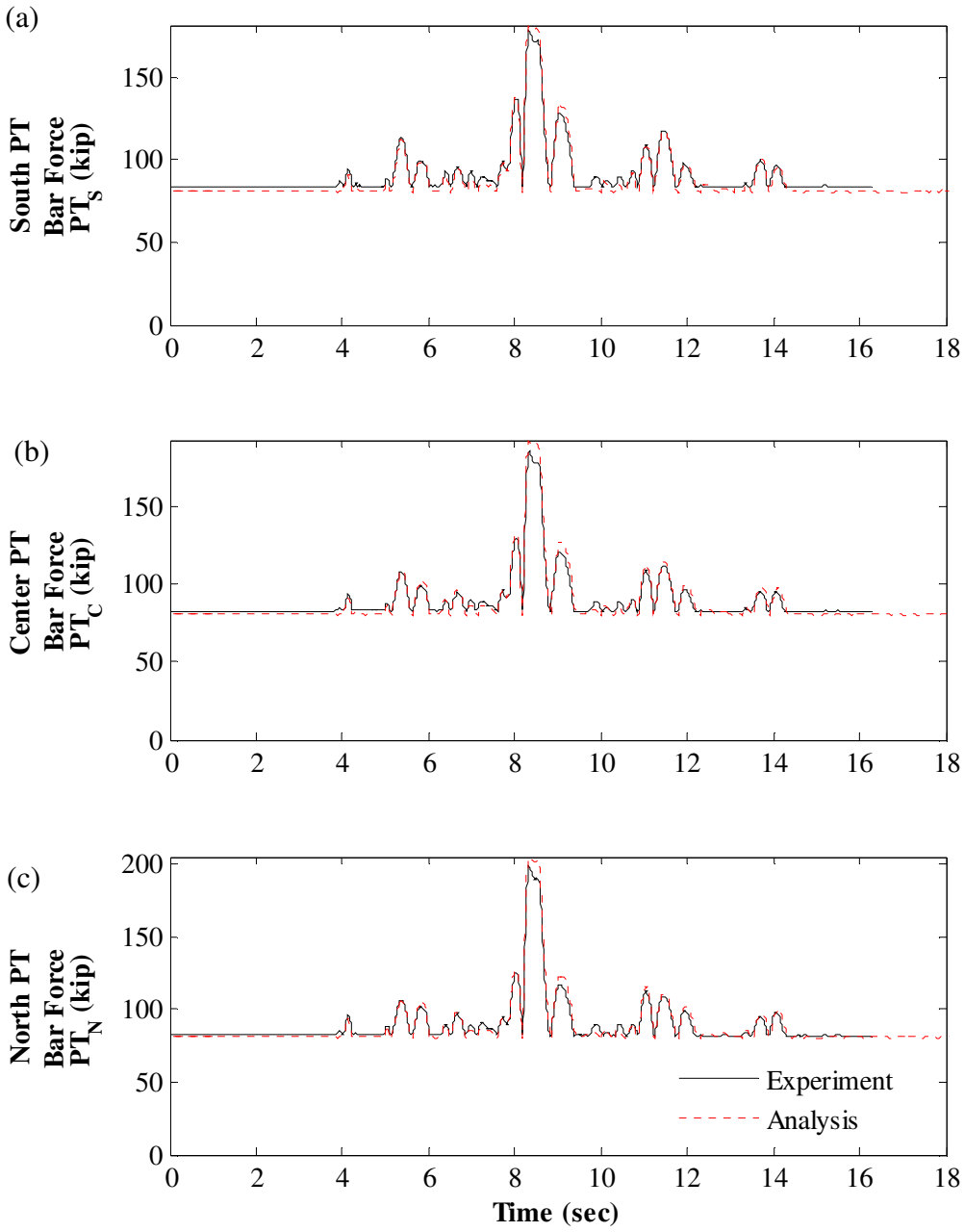

Figure 10.45 – Correlation of PT force response to MCE_stn110: (a) south PT bars; (b) center PT bars; (c) north PT bars

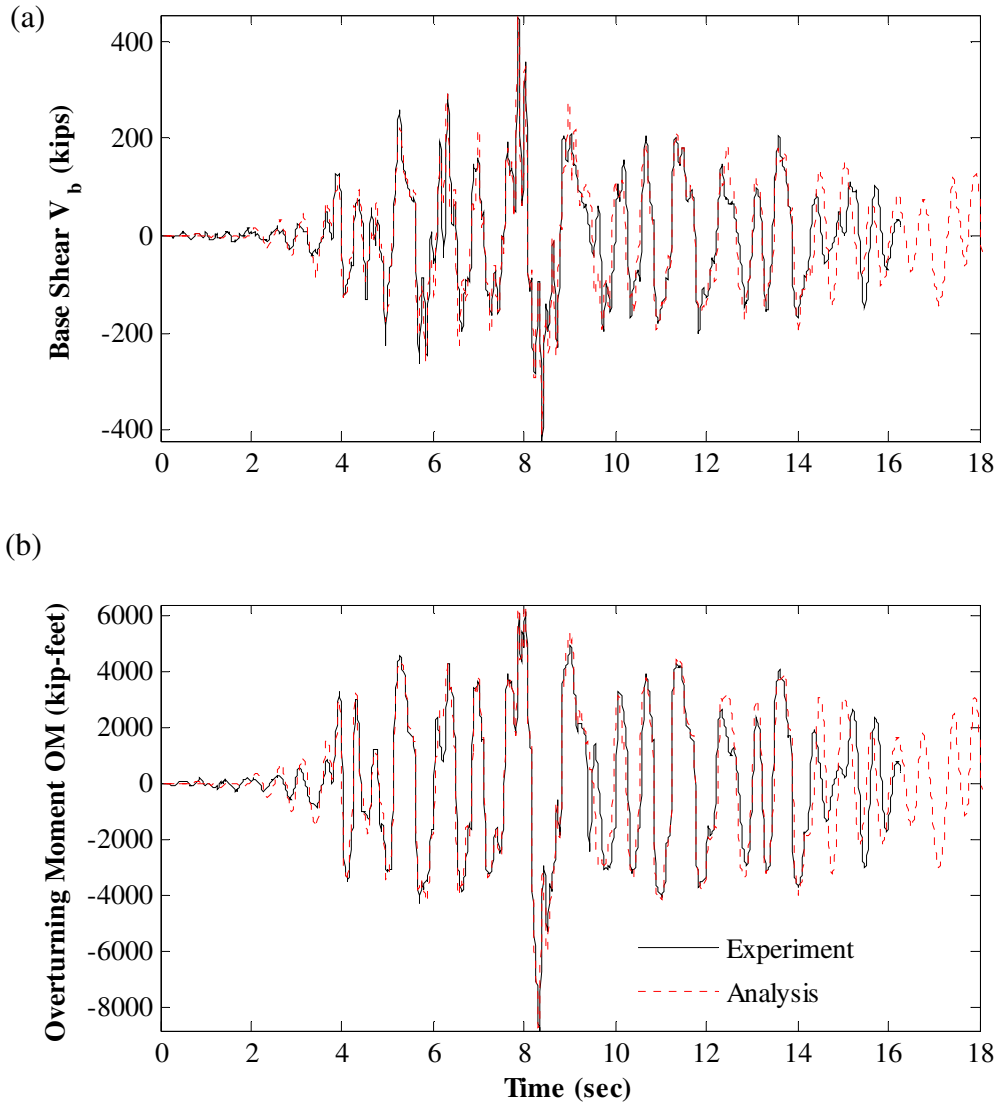

Figure 10.46 – MCE_stn110 response correlation: (a) base shear; (b) overturning moment

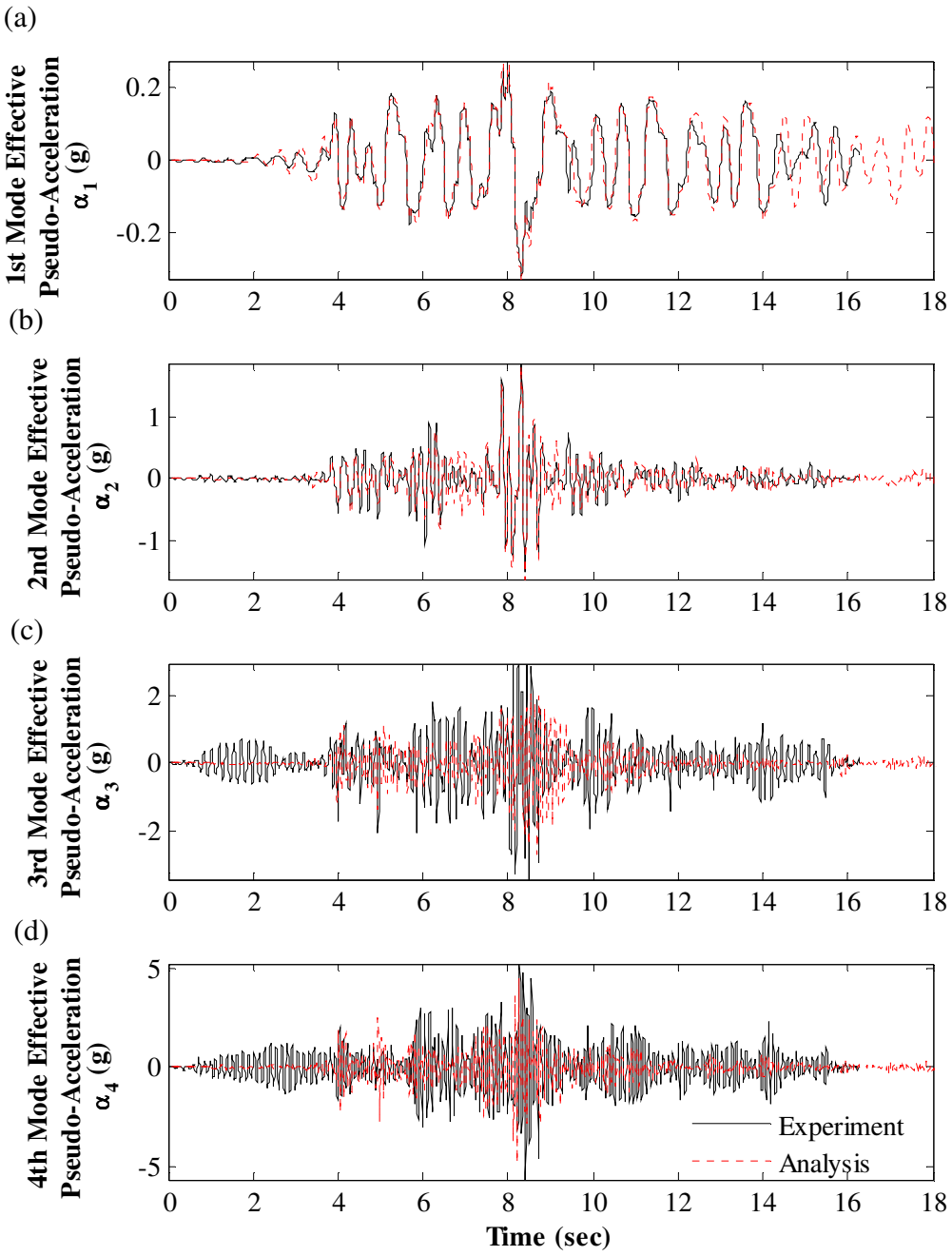

Figure 10.47 – Correlation of effective modal pseudo-acceleration response to MCE_stn110: (a) 1st mode; (b) 2nd mode; (c) 3rd mode; (d) 4th mode

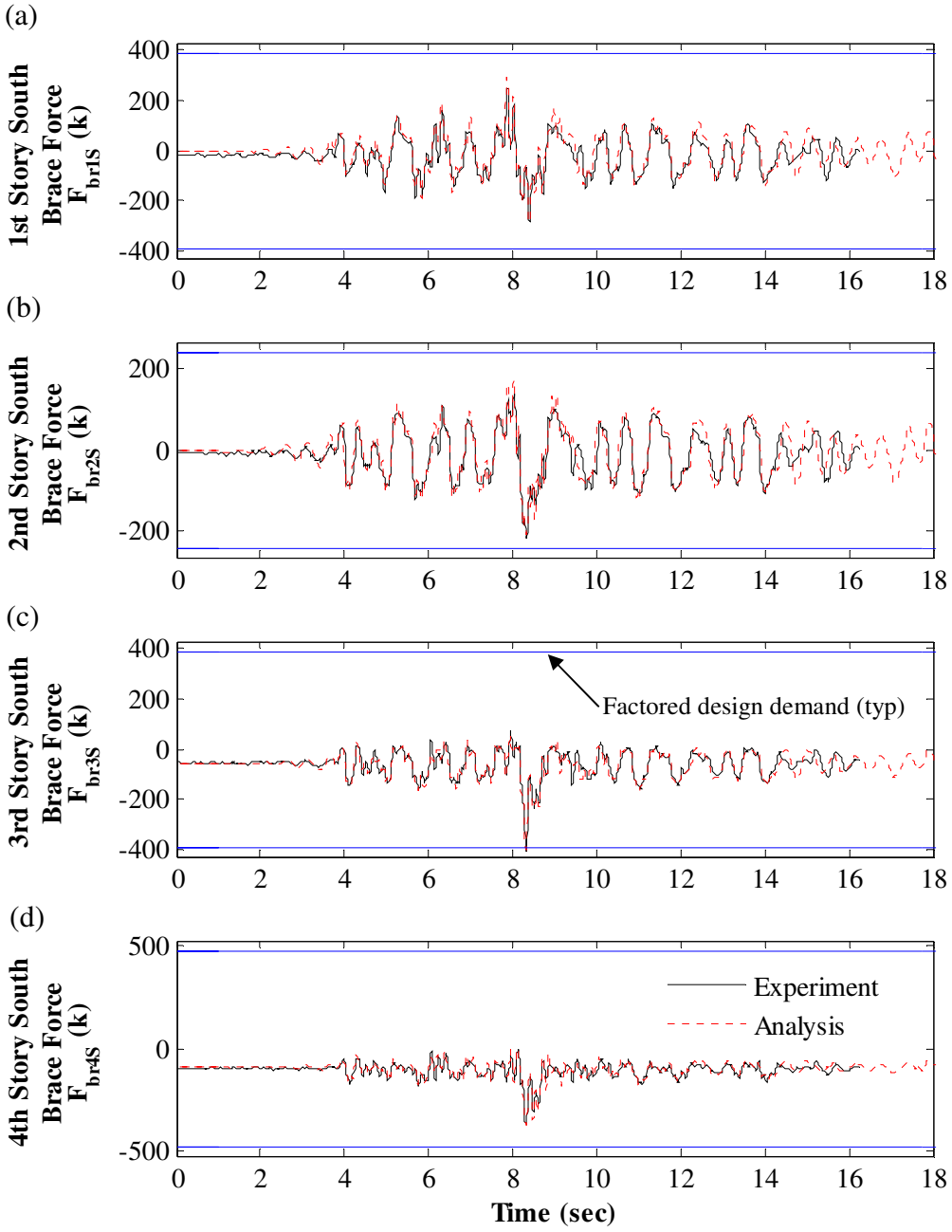

Figure 10.48 – Correlation of south brace axial force response to MCE_stn110: (a) 1st story; (b) 2nd story; (c) 3rd story; (d) 4th story

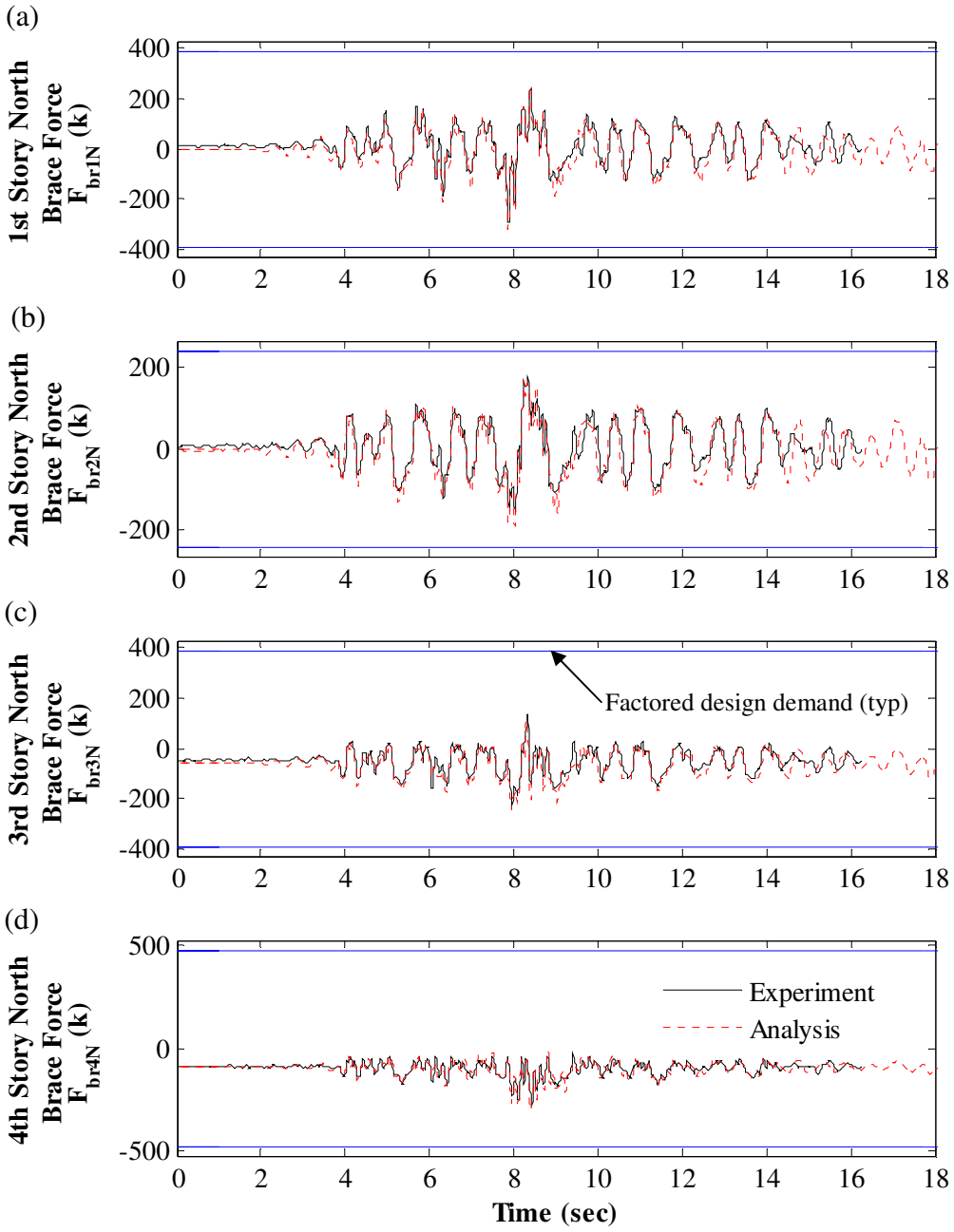

Figure 10.49 – Correlation of north brace axial force response to MCE_stn110: (a) 1st story; (b) 2nd story; (c) 3rd story; (d) 4th story

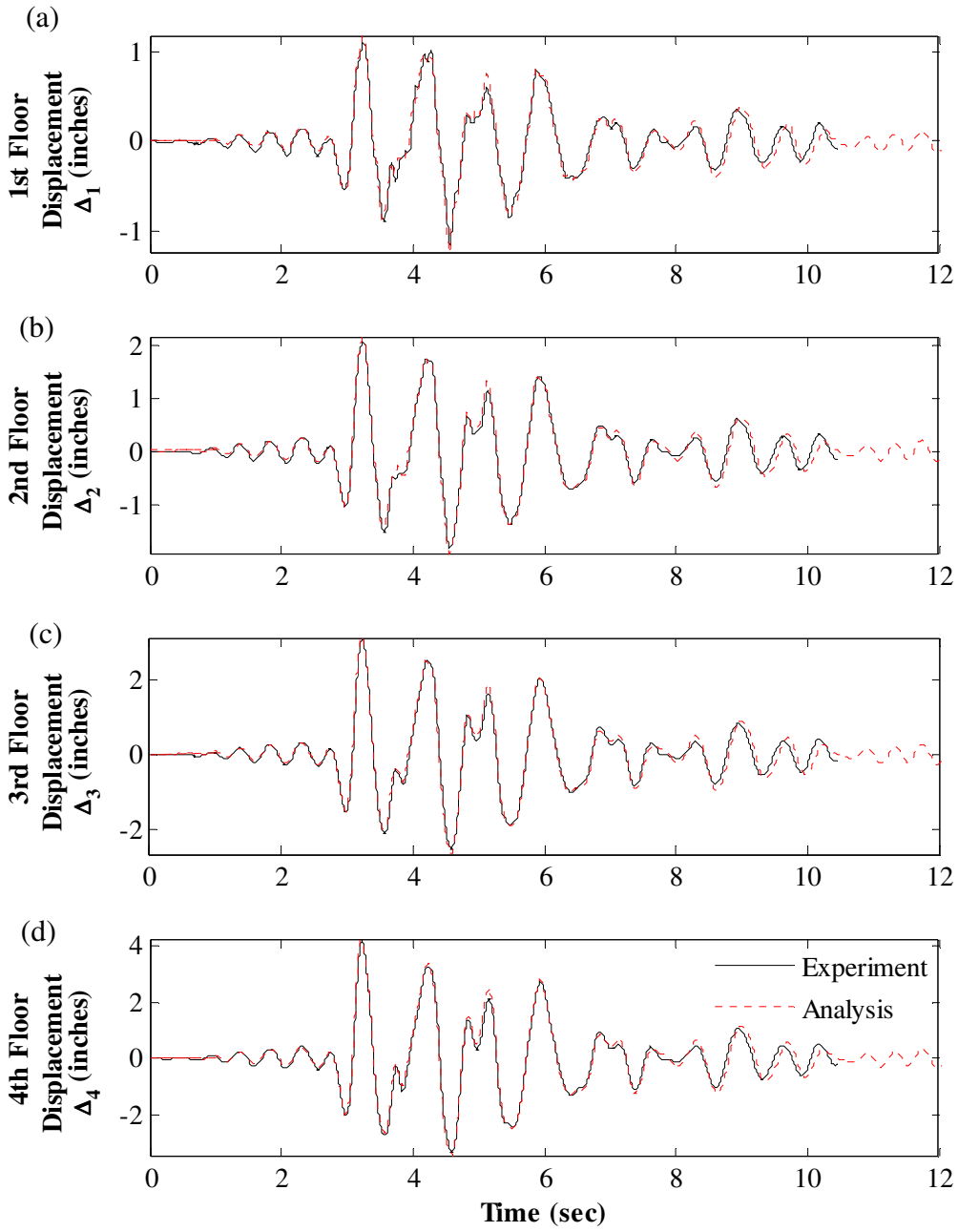

Figure 10.50 – Correlation of floor displacement response to MCE_a-tmz270: (a) 1st floor; (b) 2nd floor; (c) 3rd floor; (d) 4th floor

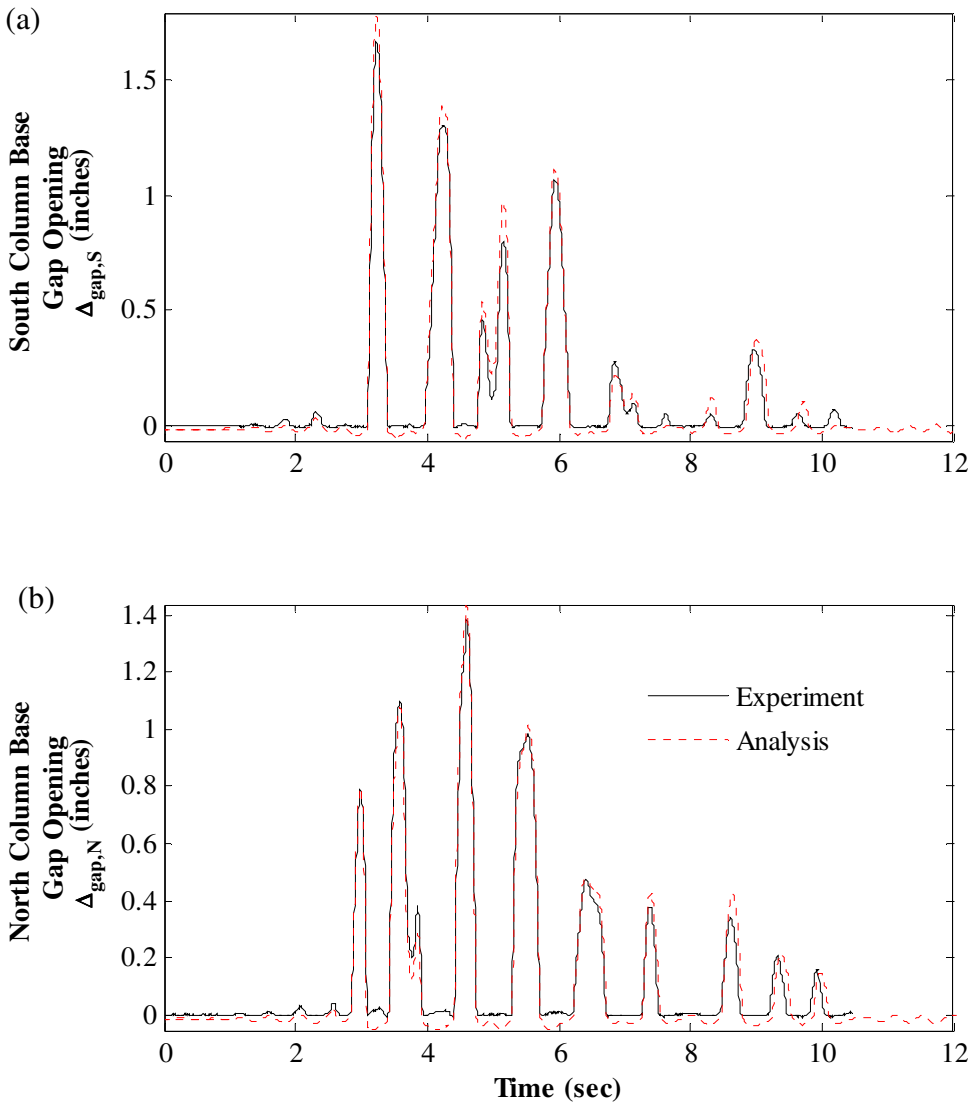

Figure 10.51 – Correlation of column base gap opening response to MCE_a-tmz270: (a) at south column base; (b) at north column base

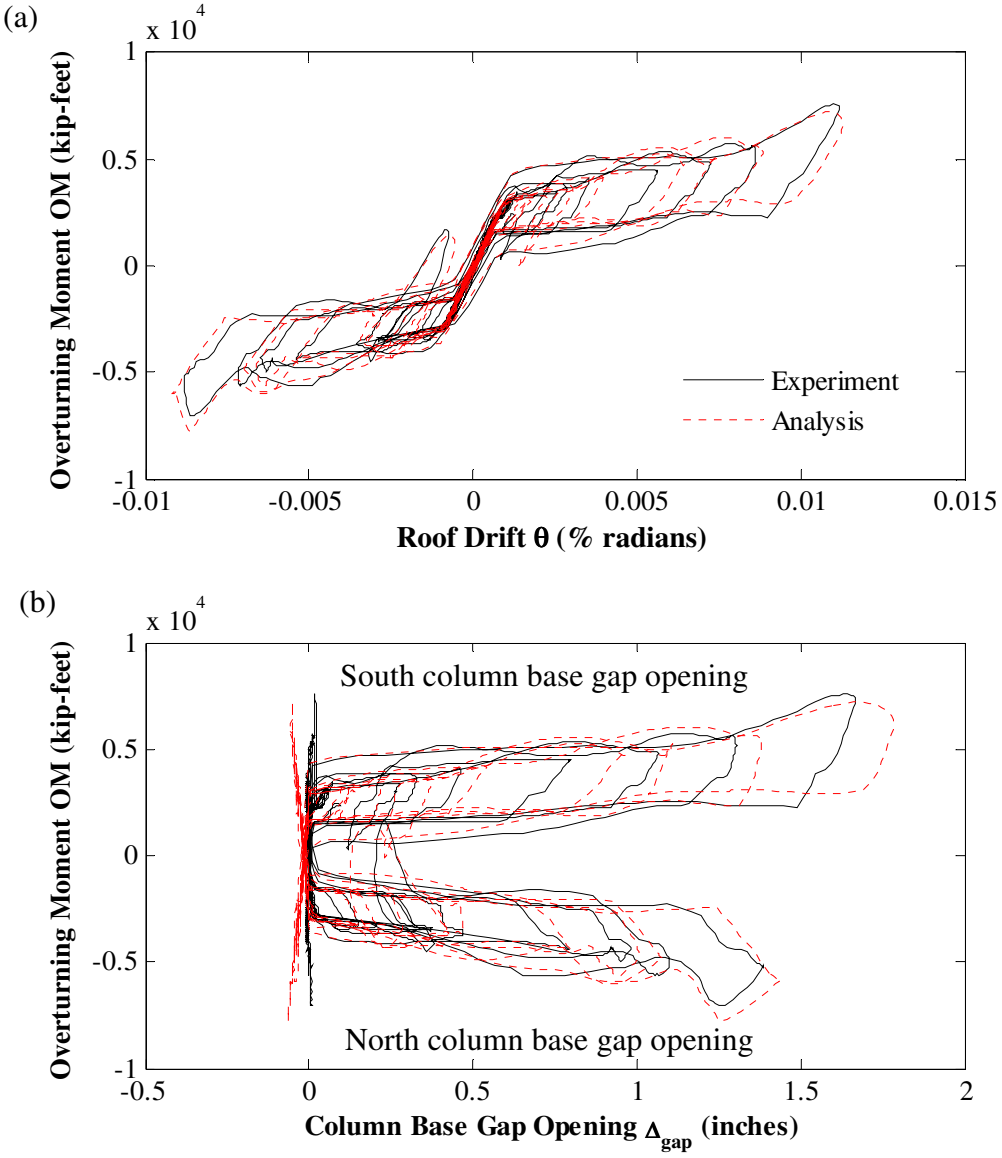

Figure 10.52 – Correlation of hysteretic response to MCE_a-tmz270: (a) overturning moment versus roof drift; (b) overturning moment versus column base gap opening

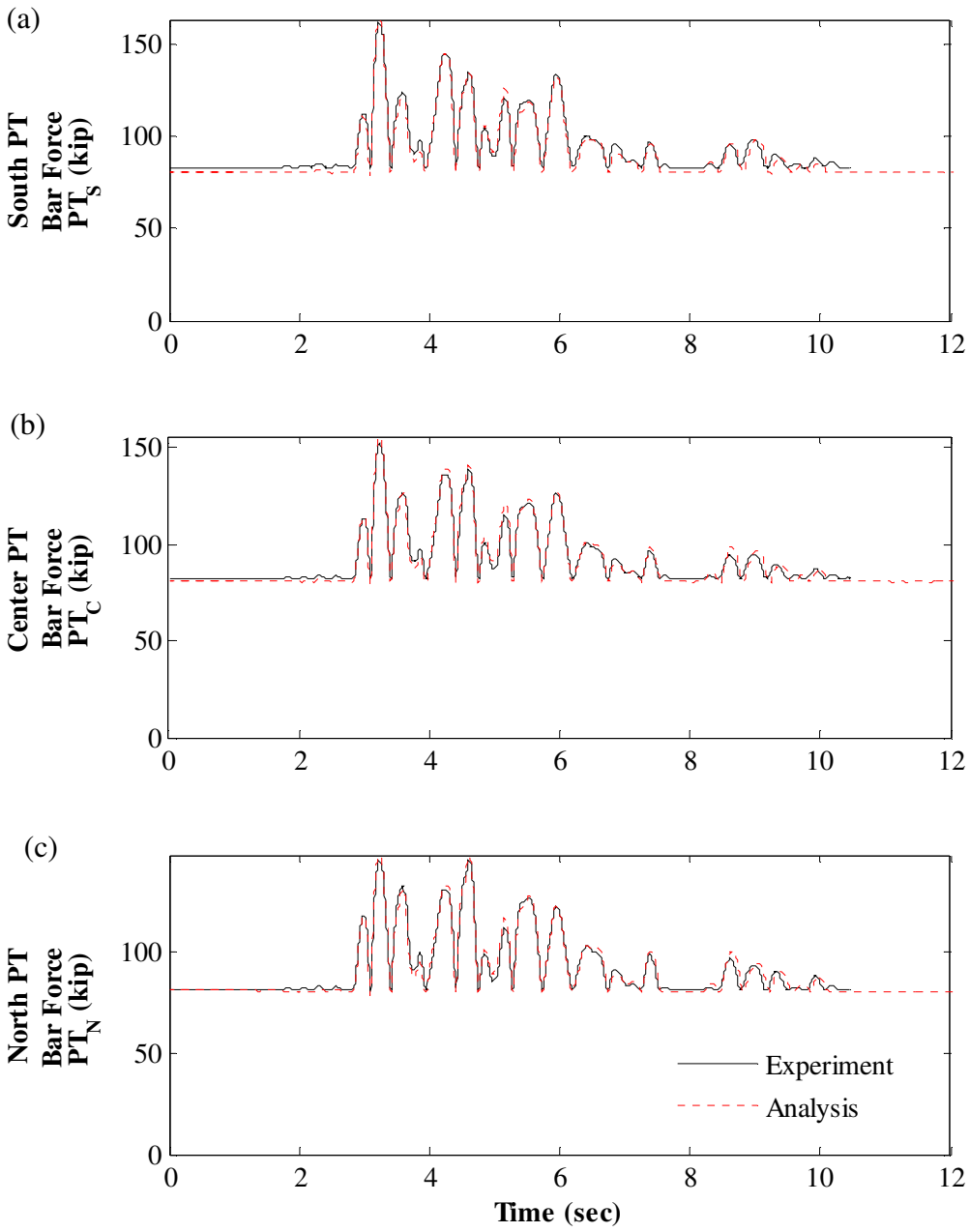

Figure 10.53 – Correlation of PT force response to MCE_a-tmz270: (a) south PT bars; (b) center PT bars; (c) north PT bars

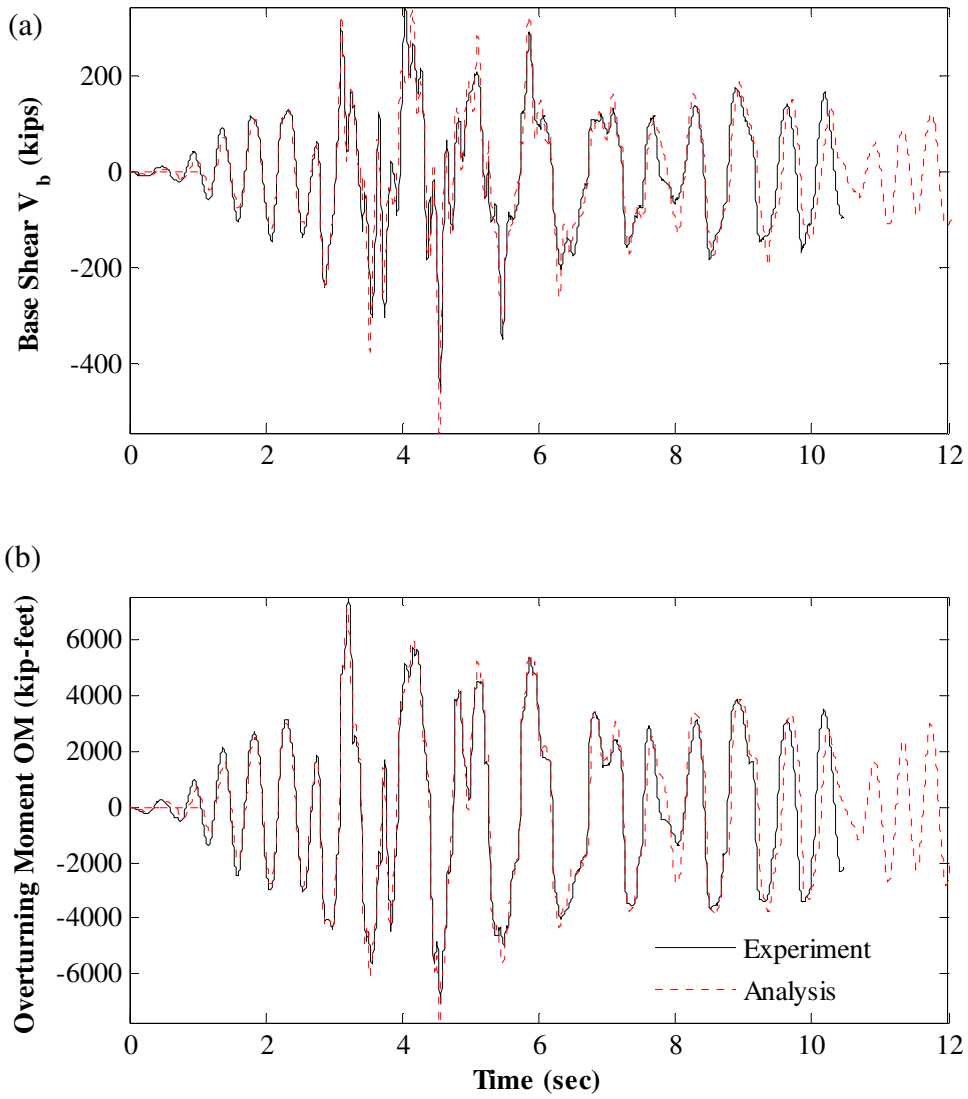

Figure 10.54 – MCE_a-tmz270 response correlation: (a) base shear; (b) overturning moment

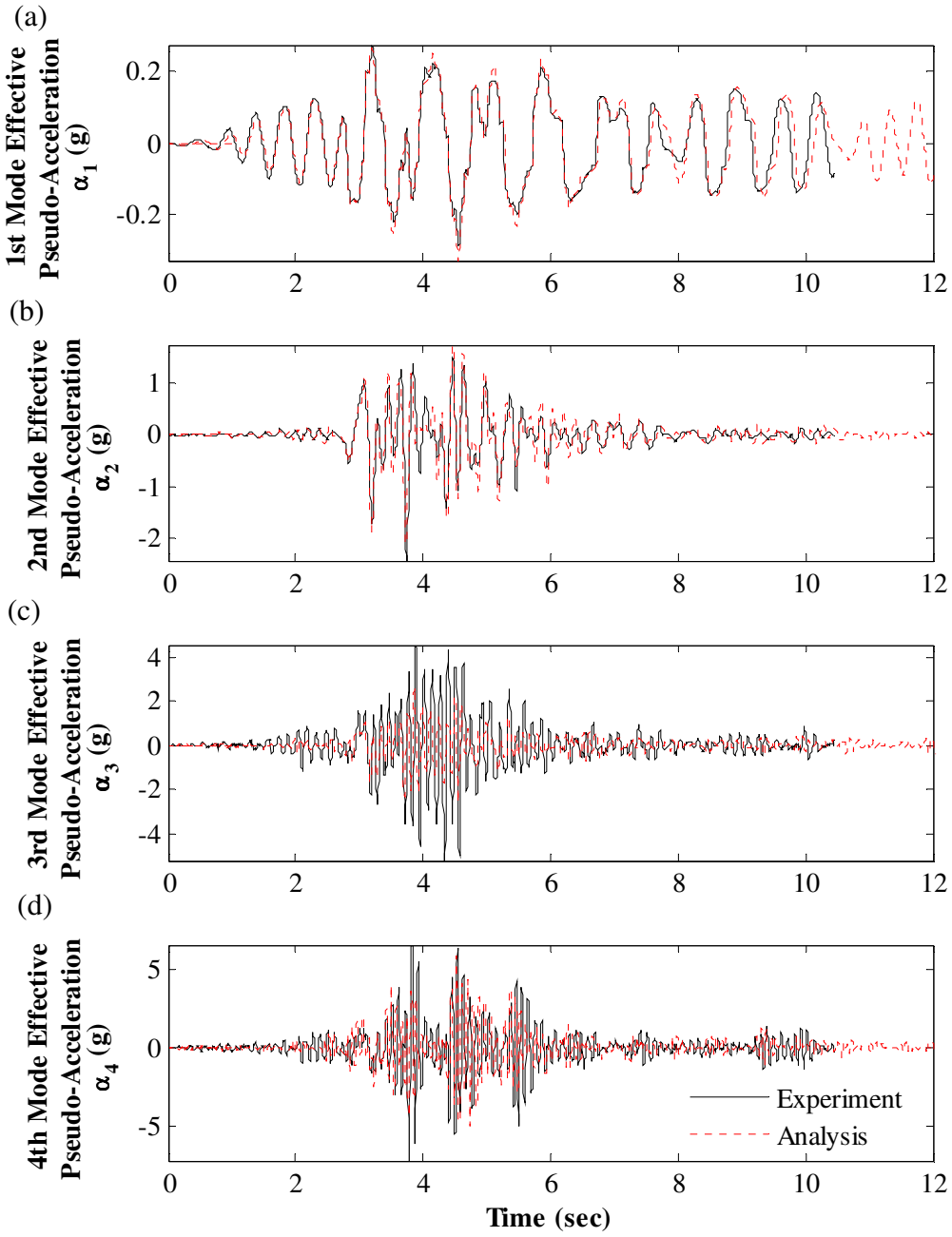

Figure 10.55 – Correlation of effective modal pseudo-acceleration response to MCE_a-tmz270: (a) 1st mode; (b) 2nd mode; (c) 3rd mode; (d) 4th mode

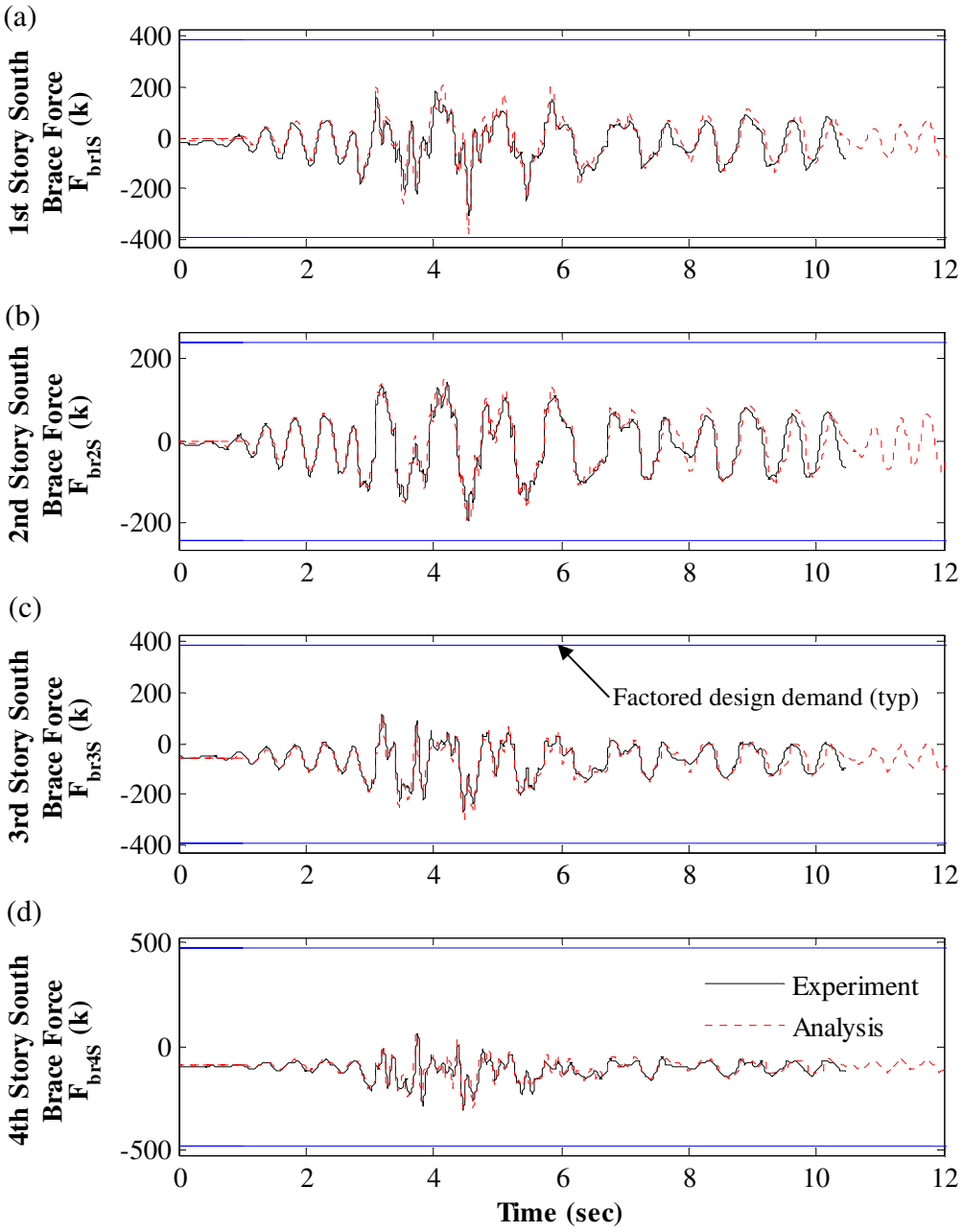

Figure 10.56 – Correlation of south brace axial force response to MCE_a-tmz270: (a) 1st story; (b) 2nd story; (c) 3rd story; (d) 4th story

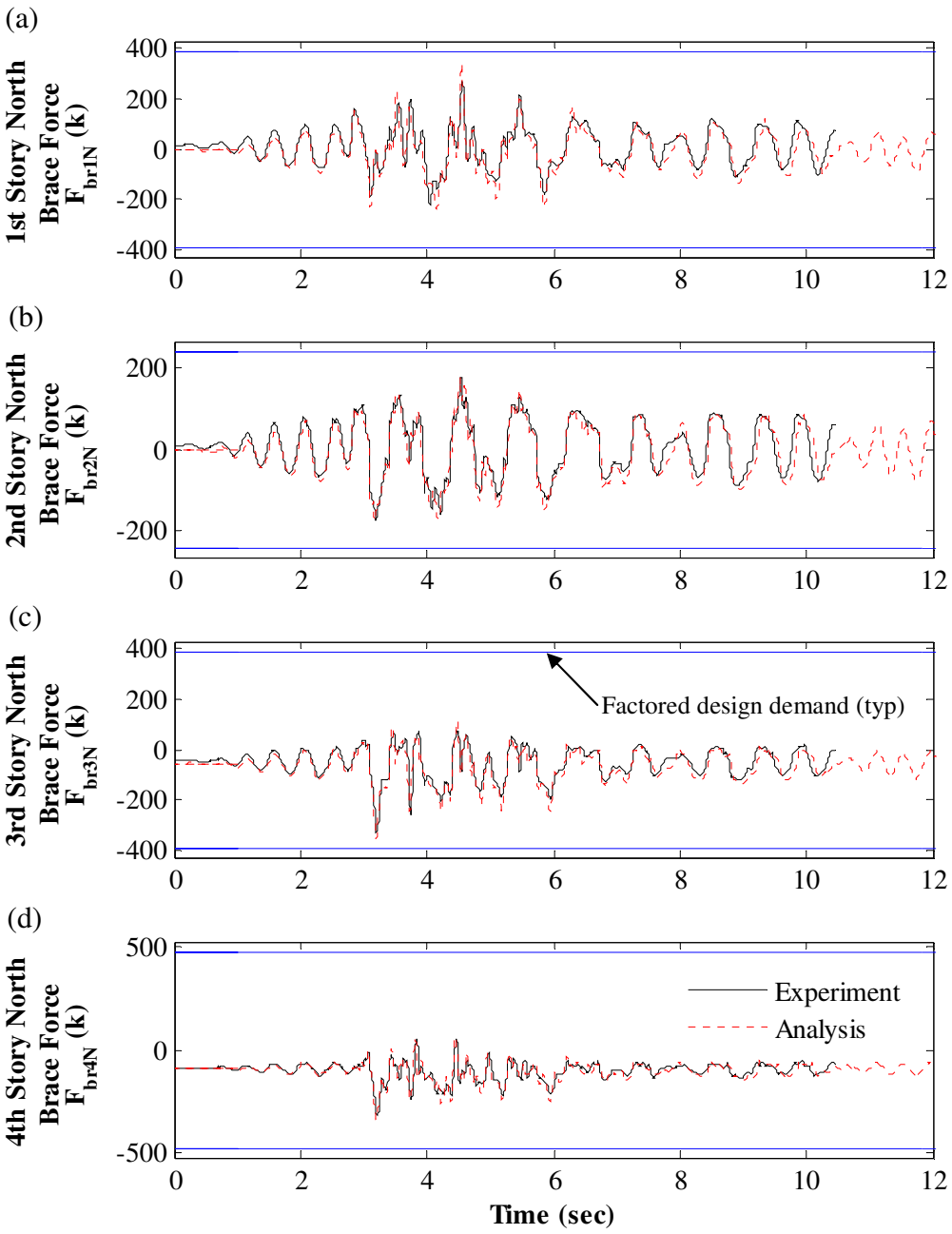

Figure 10.57 – Correlation of north brace axial force response to MCE_a-tmz270: (a) 1st story; (b) 2nd story; (c) 3rd story; (d) 4th story

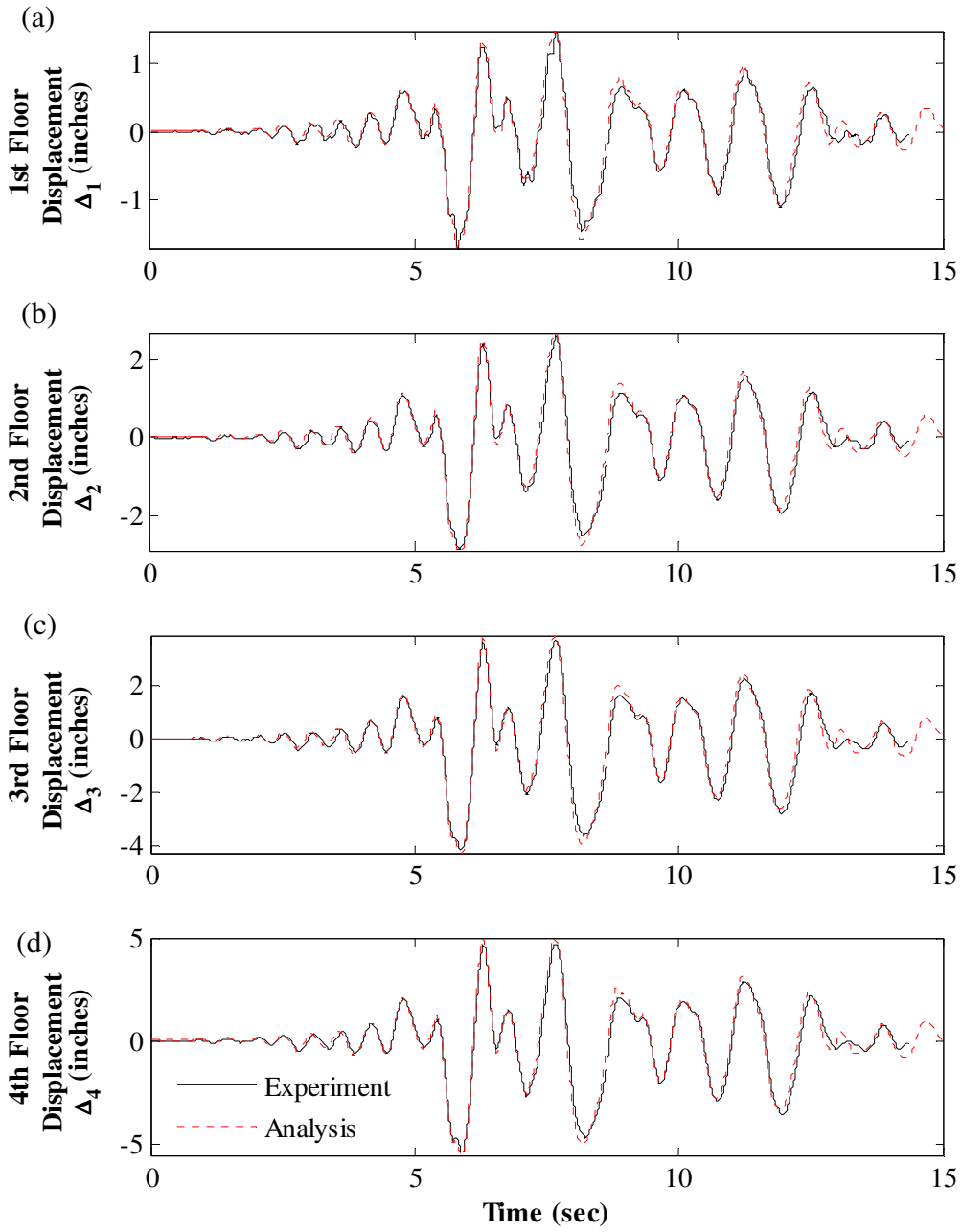

Figure 10.58 – Correlation of floor displacement response to MCE_lp-hda255: (a) 1st floor; (b) 2nd floor; (c) 3rd floor; (d) 4th floor

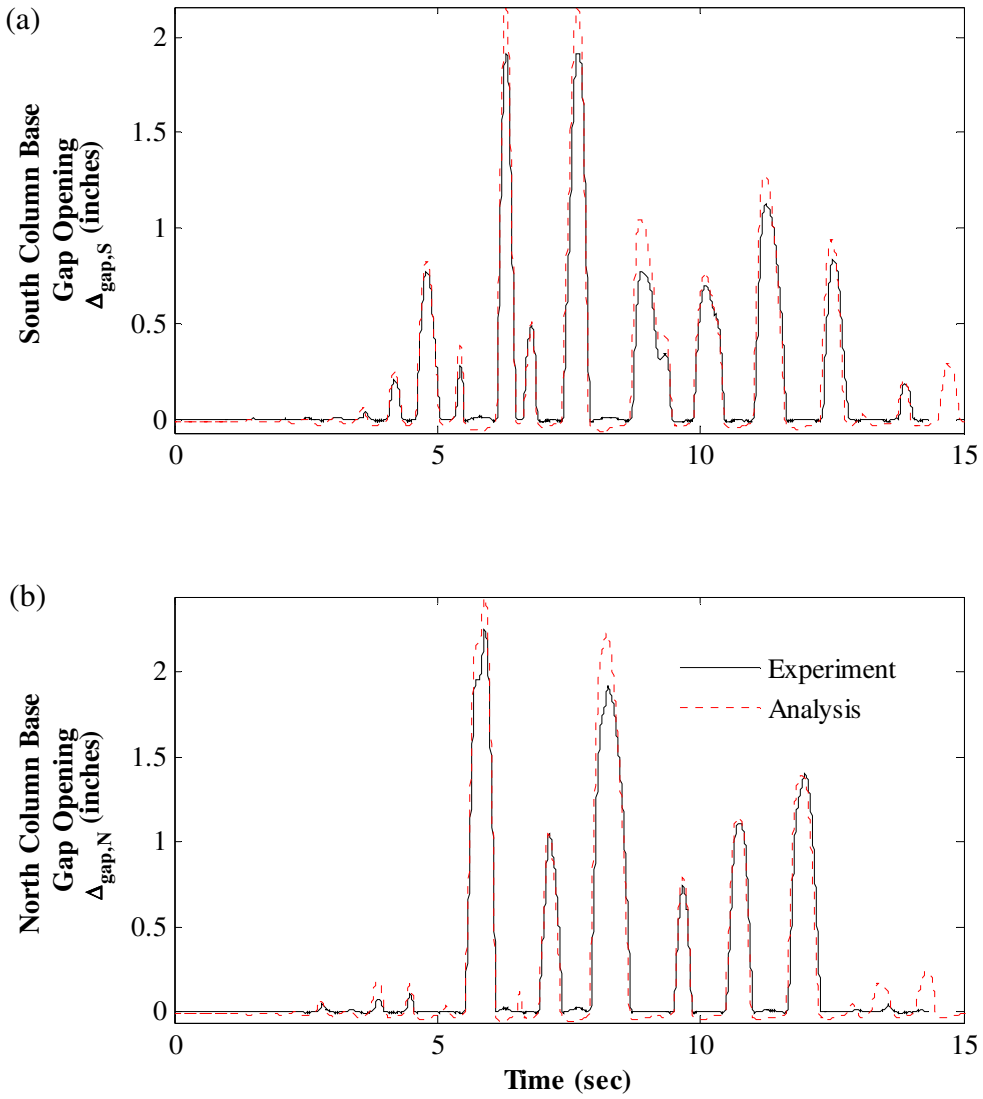

Figure 10.59 – Correlation of column base gap opening response to MCE_lp-hda255: (a) at south column base; (b) at north column base

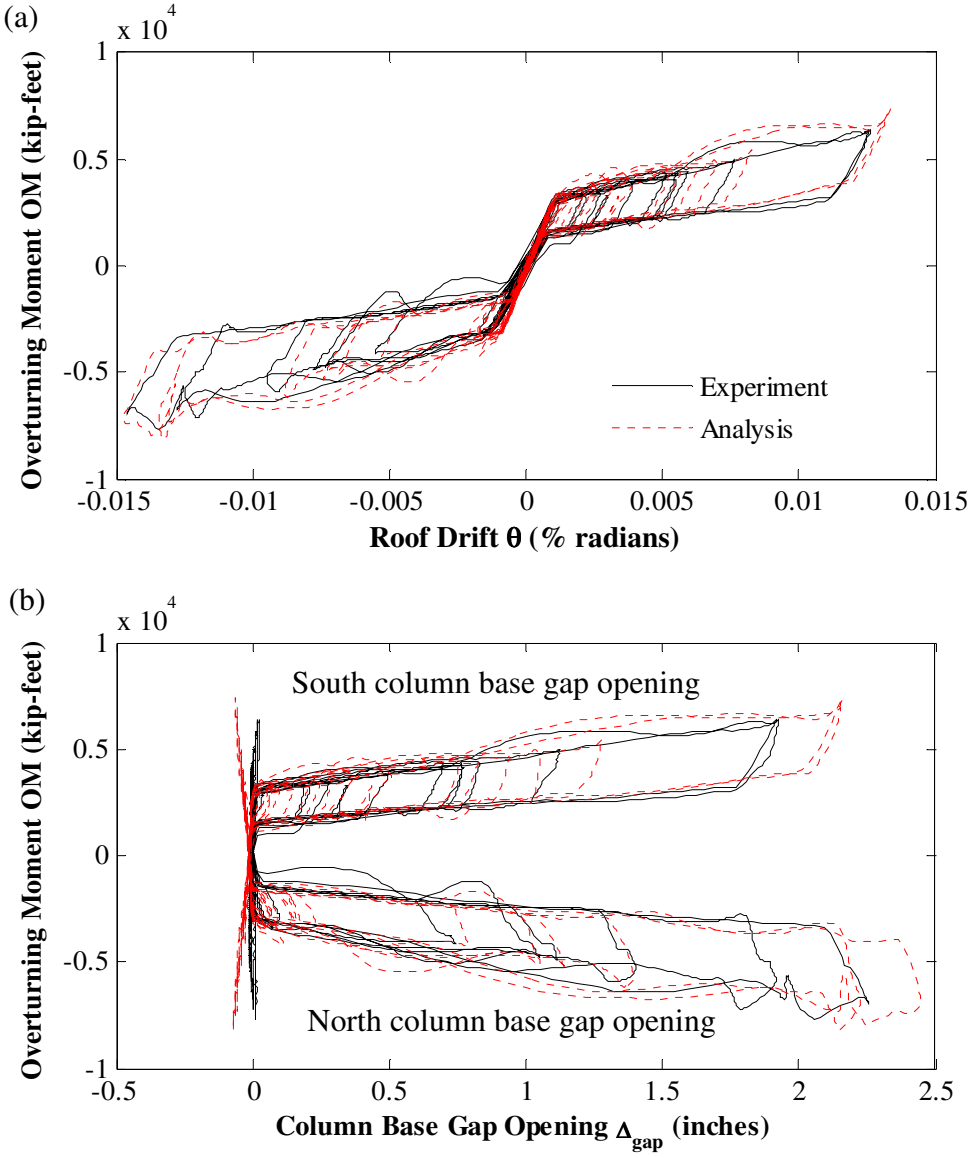

Figure 10.60 – Correlation of hysteretic response to MCE_lp-hda255: (a) overturning moment versus roof drift; (b) overturning moment versus column base gap opening

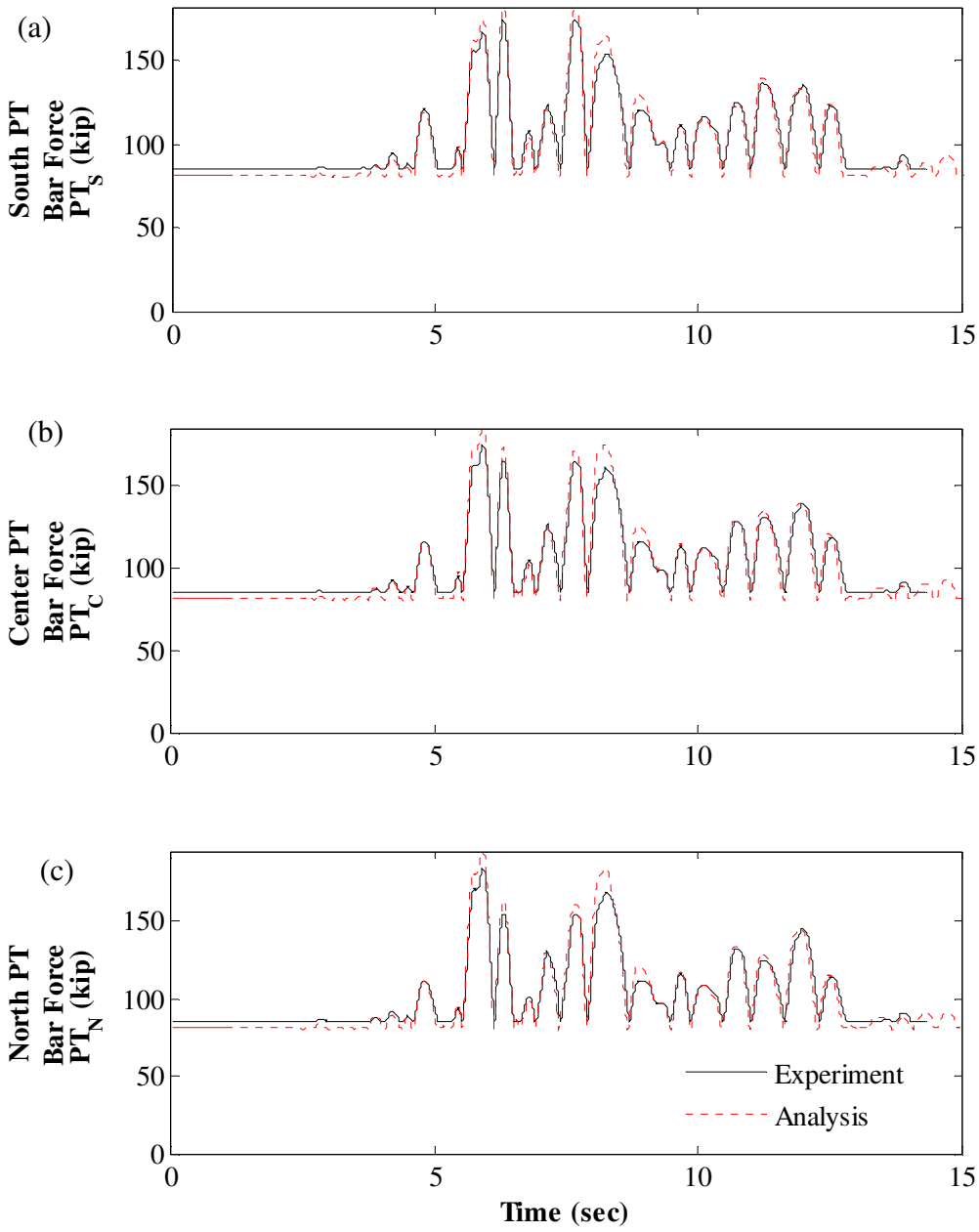

Figure 10.61 – Correlation of PT force response to MCE_lp-hda255: (a) south PT bars; (b) center PT bars; (c) north PT bars

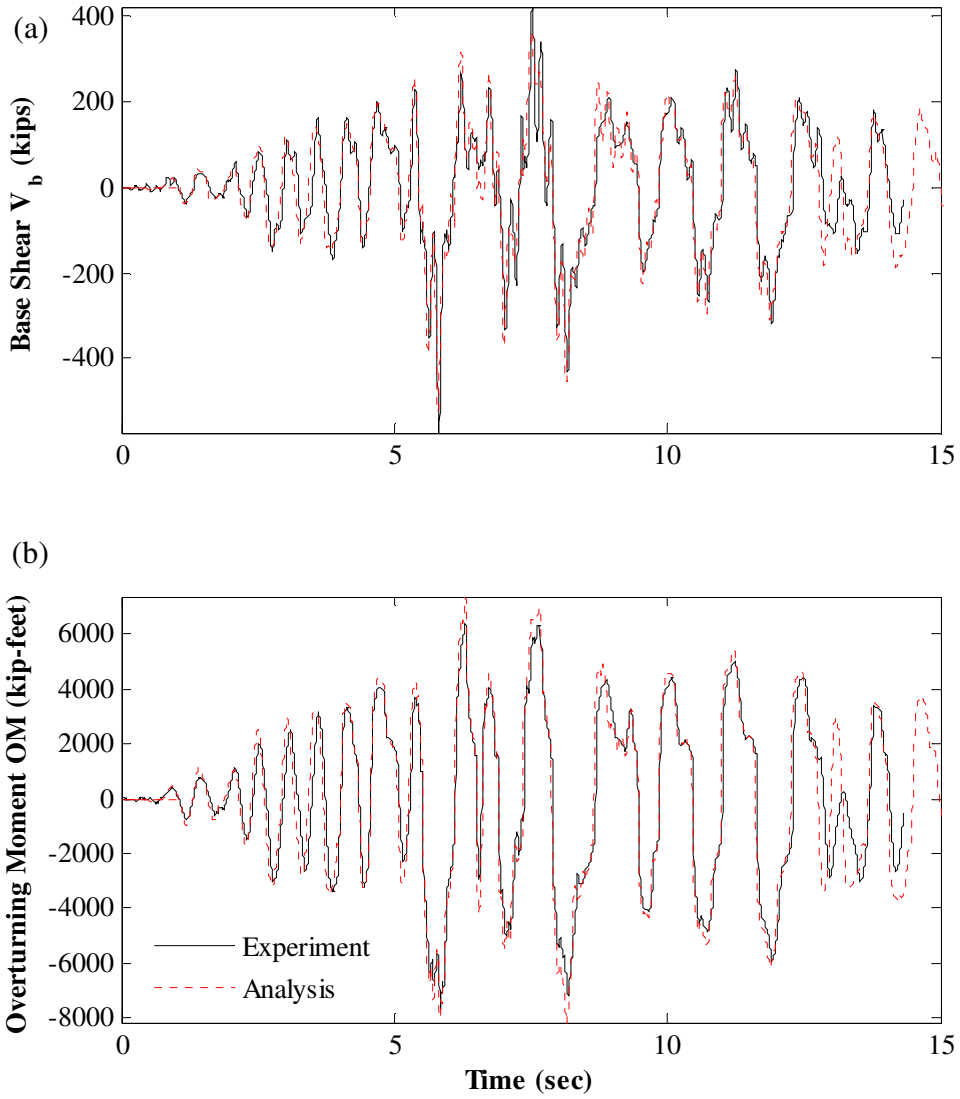

Figure 10.62 – MCE_lp-hda255 response correlation: (a) base shear; (b) overturning moment

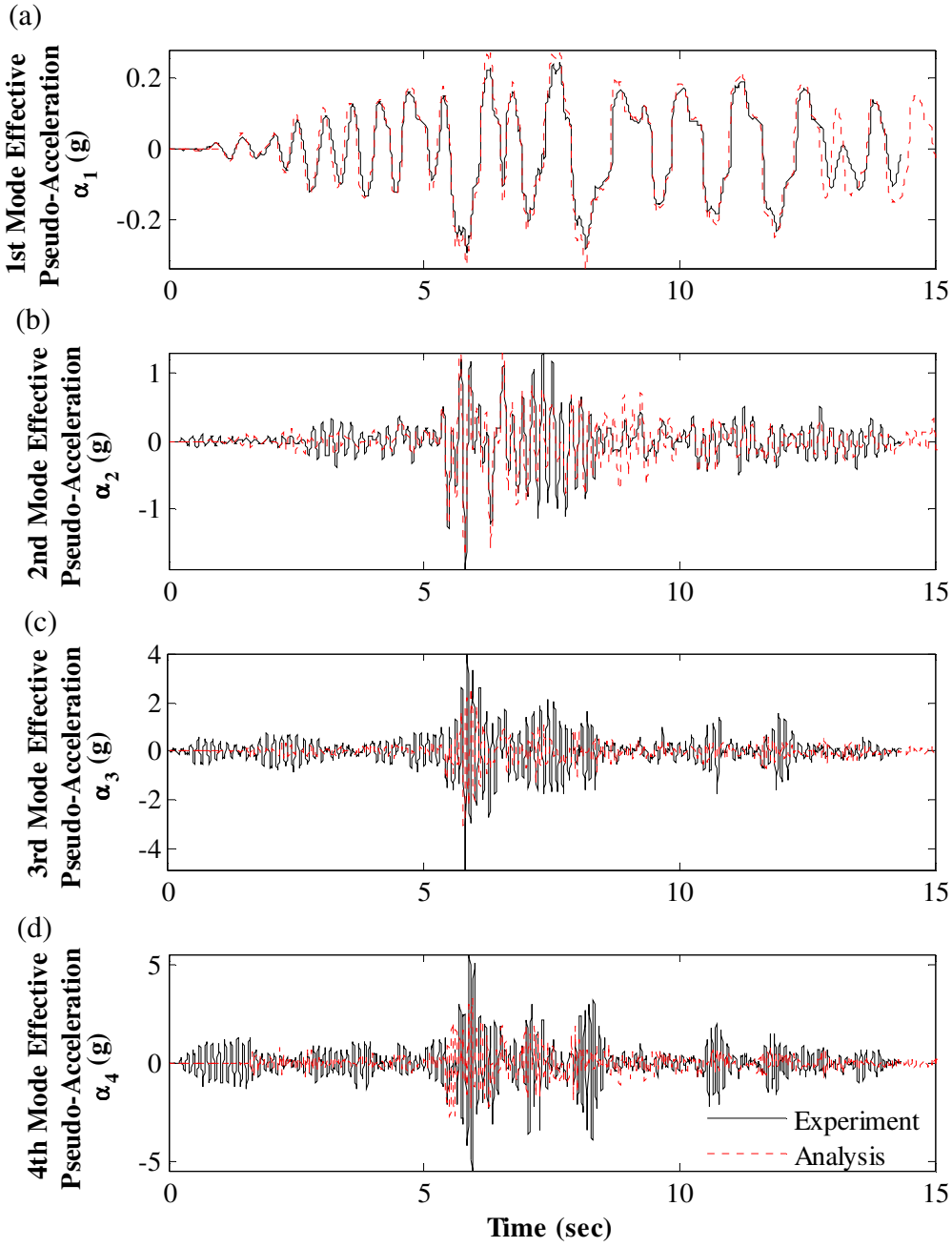

Figure 10.63 – Correlation of effective modal pseudo-acceleration response to MCE_lp-hda255: (a) 1st mode; (b) 2nd mode; (c) 3rd mode; (d) 4th mode

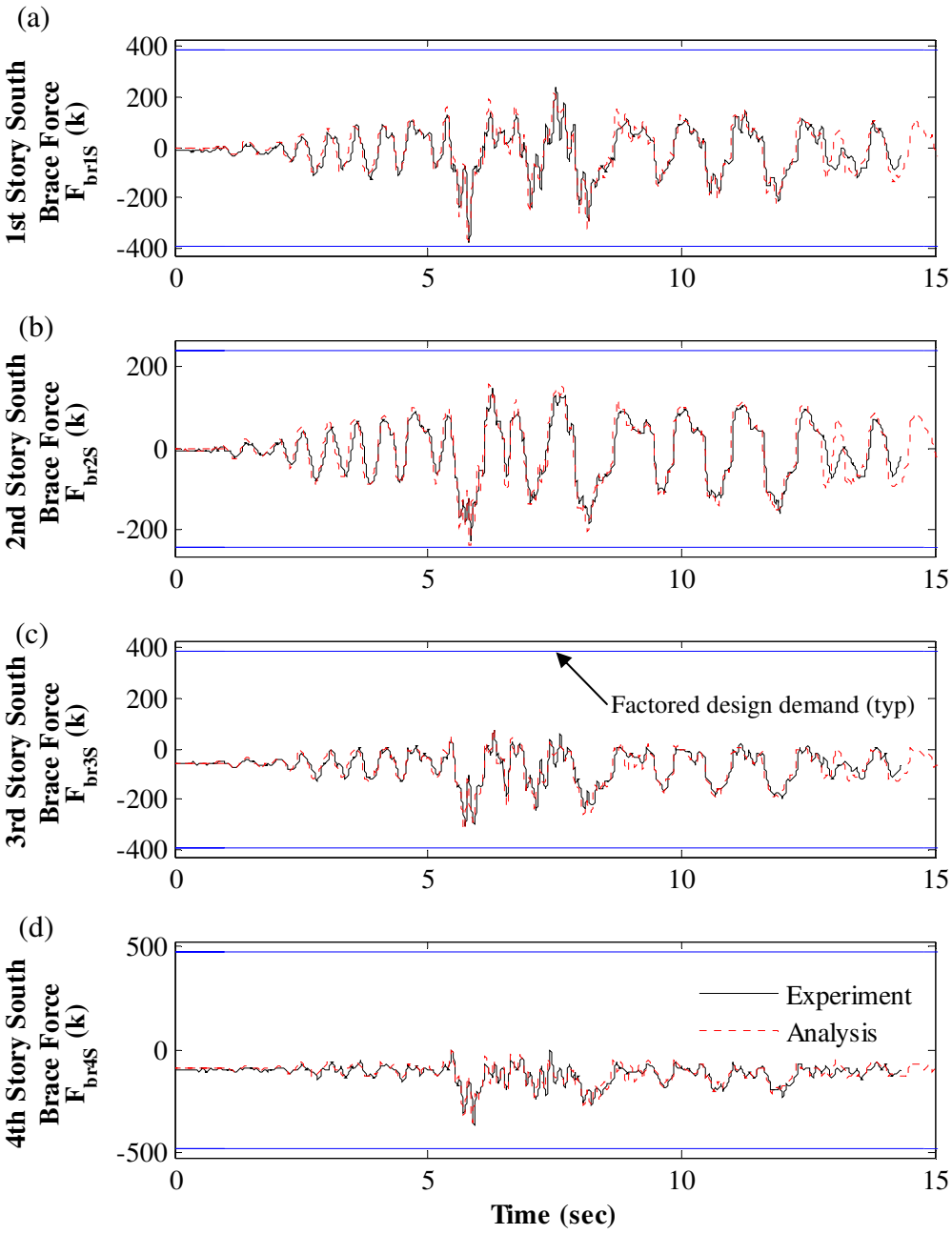

Figure 10.64 – Correlation of south brace axial force response to MCE_lp-hda255: (a) 1st story; (b) 2nd story; (c) 3rd story; (d) 4th story

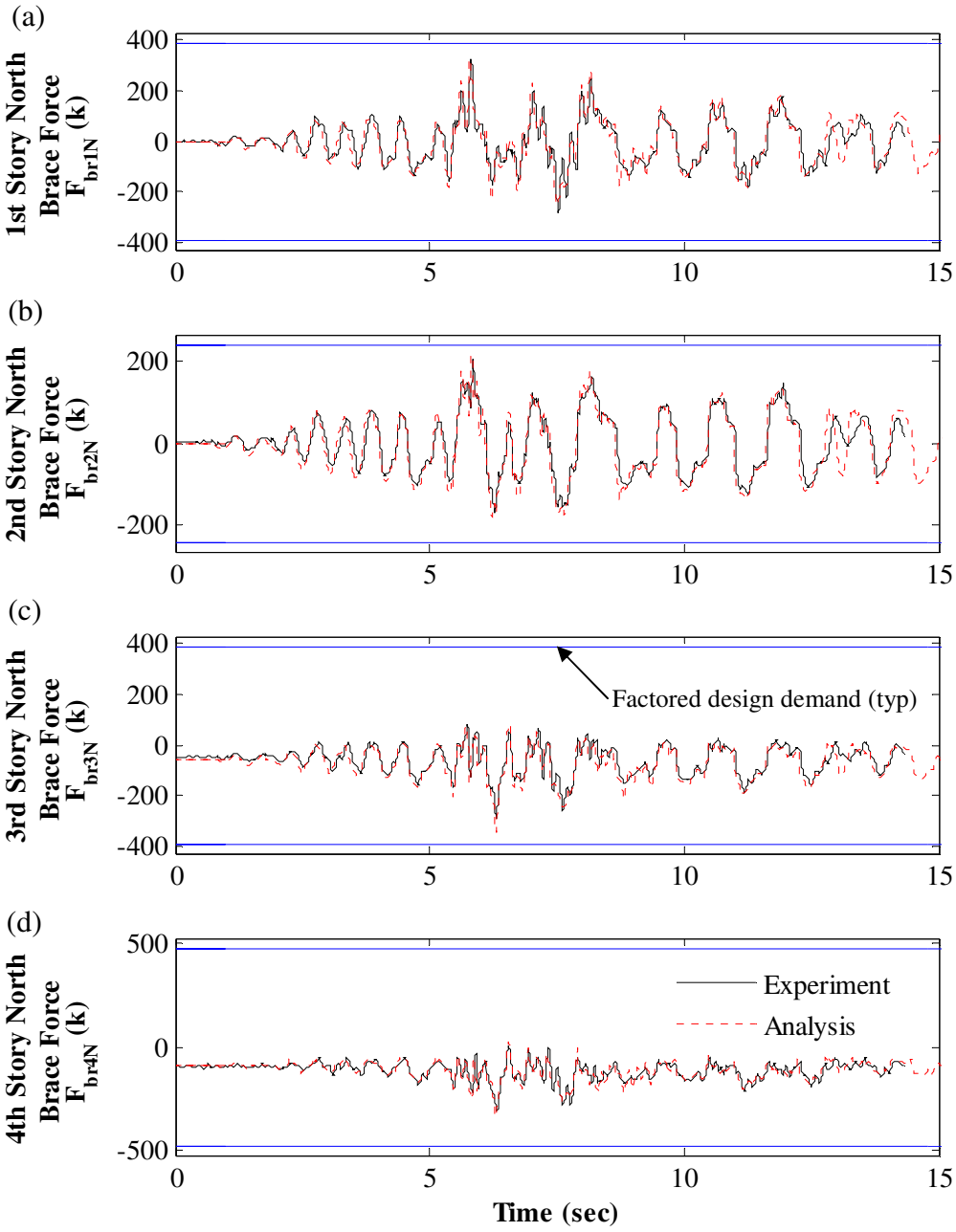

Figure 10.65 – Correlation of north brace axial force response to MCE_lp-hda255: (a) 1st story; (b) 2nd story; (c) 3rd story; (d) 4th story

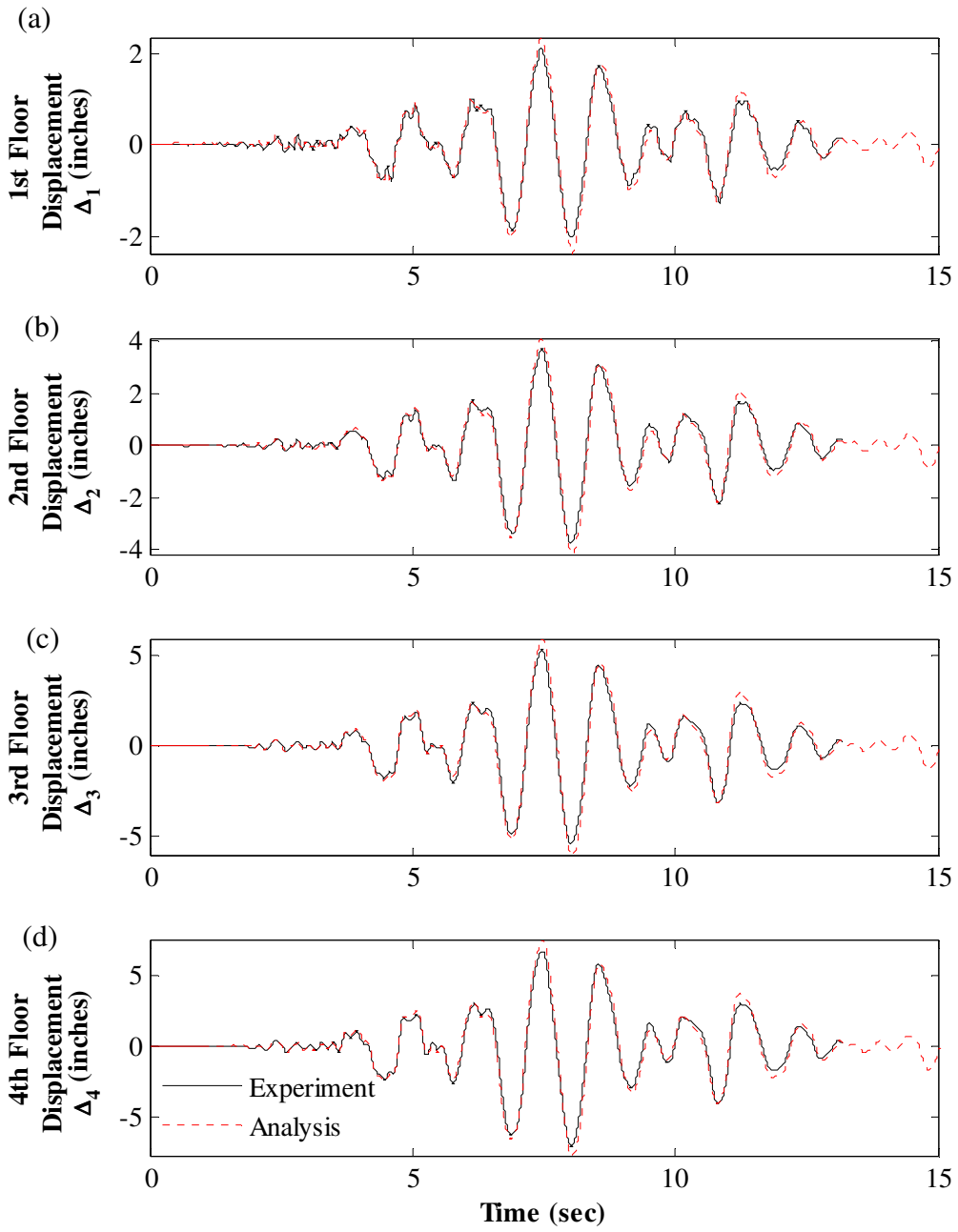

Figure 10.66 – Correlation of floor displacement response to MCE_cap000: (a) 1st floor; (b) 2nd floor; (c) 3rd floor; (d) 4th floor

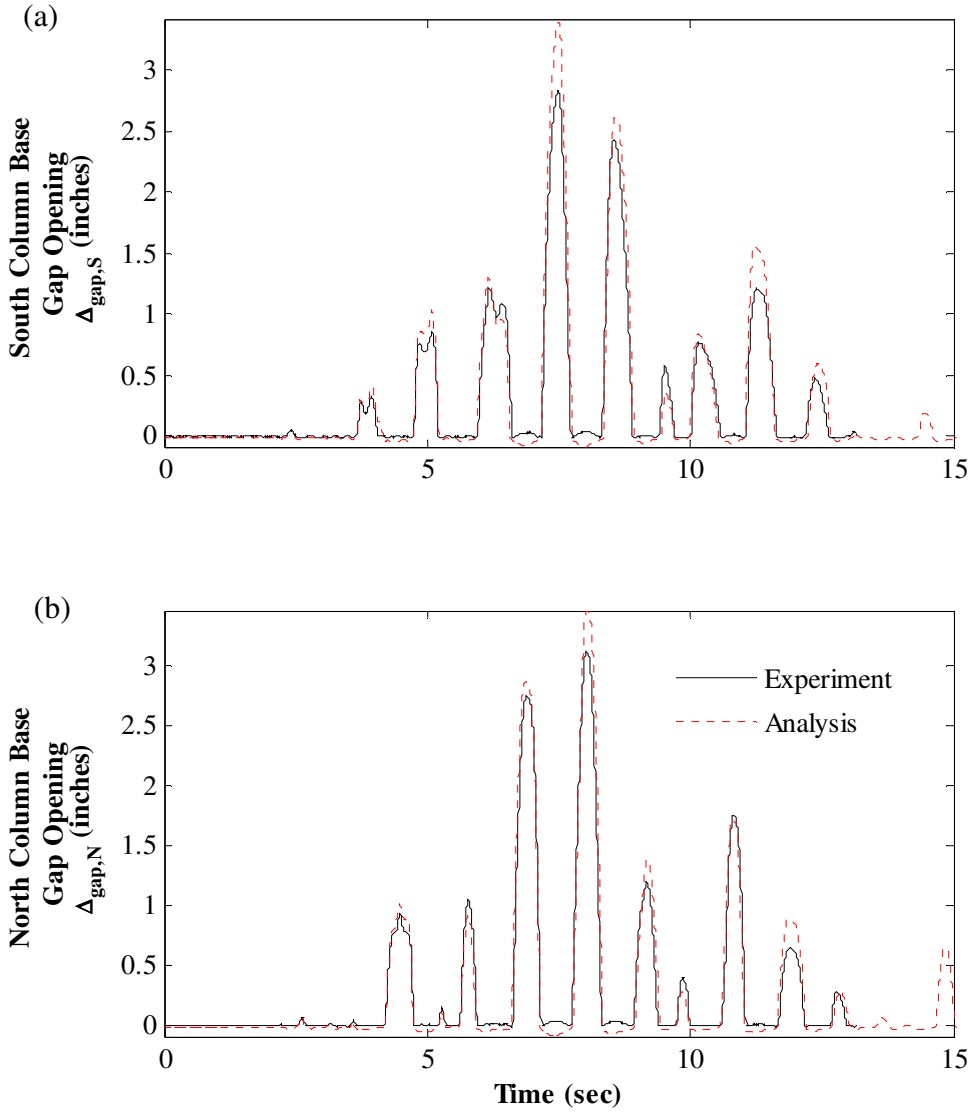

Figure 10.67 – Correlation of column base gap opening response to MCE_cap000: (a) at south column base; (b) at north column base

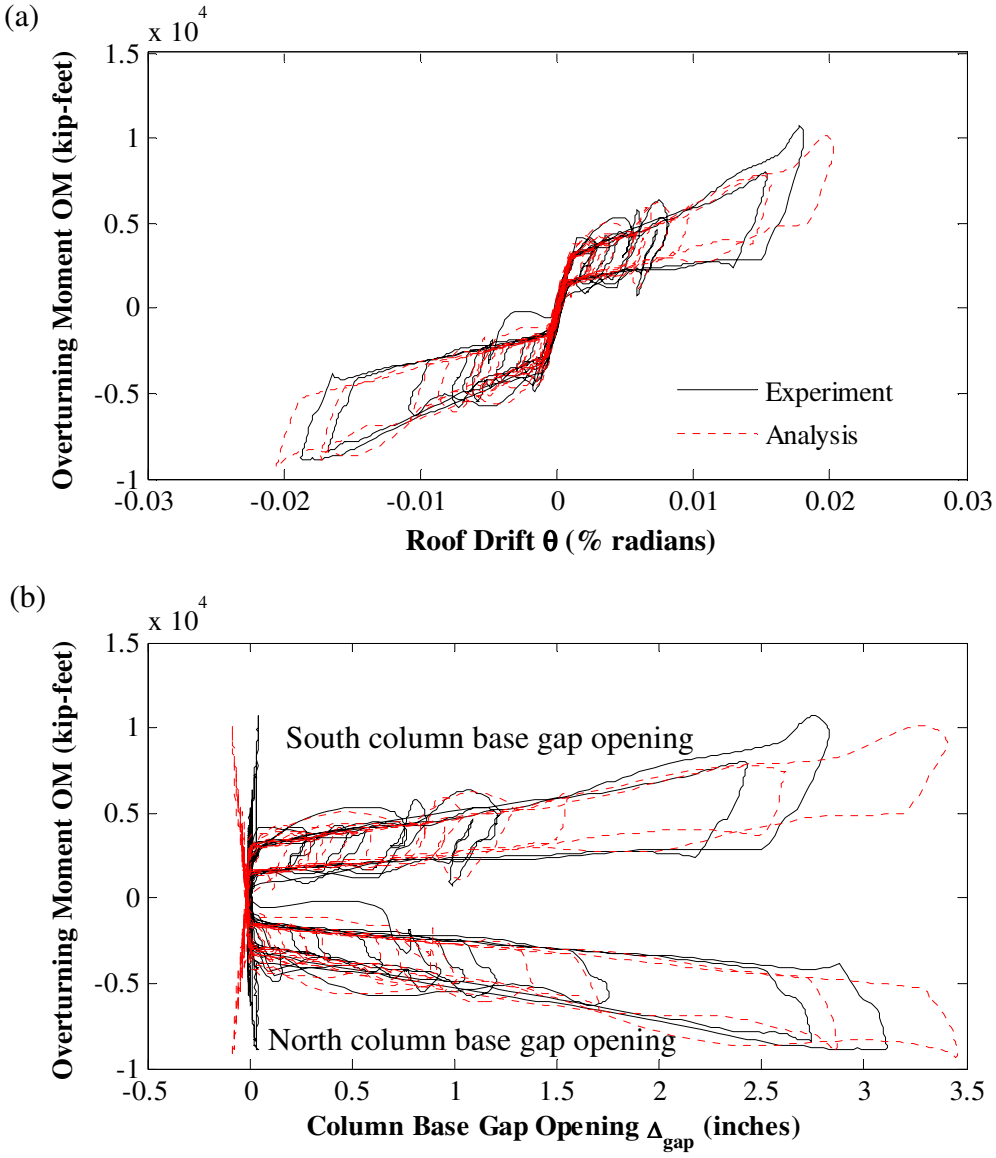

Figure 10.68 – Correlation of hysteretic response to MCE_cap000: (a) overturning moment versus roof drift; (b) overturning moment versus column base gap opening

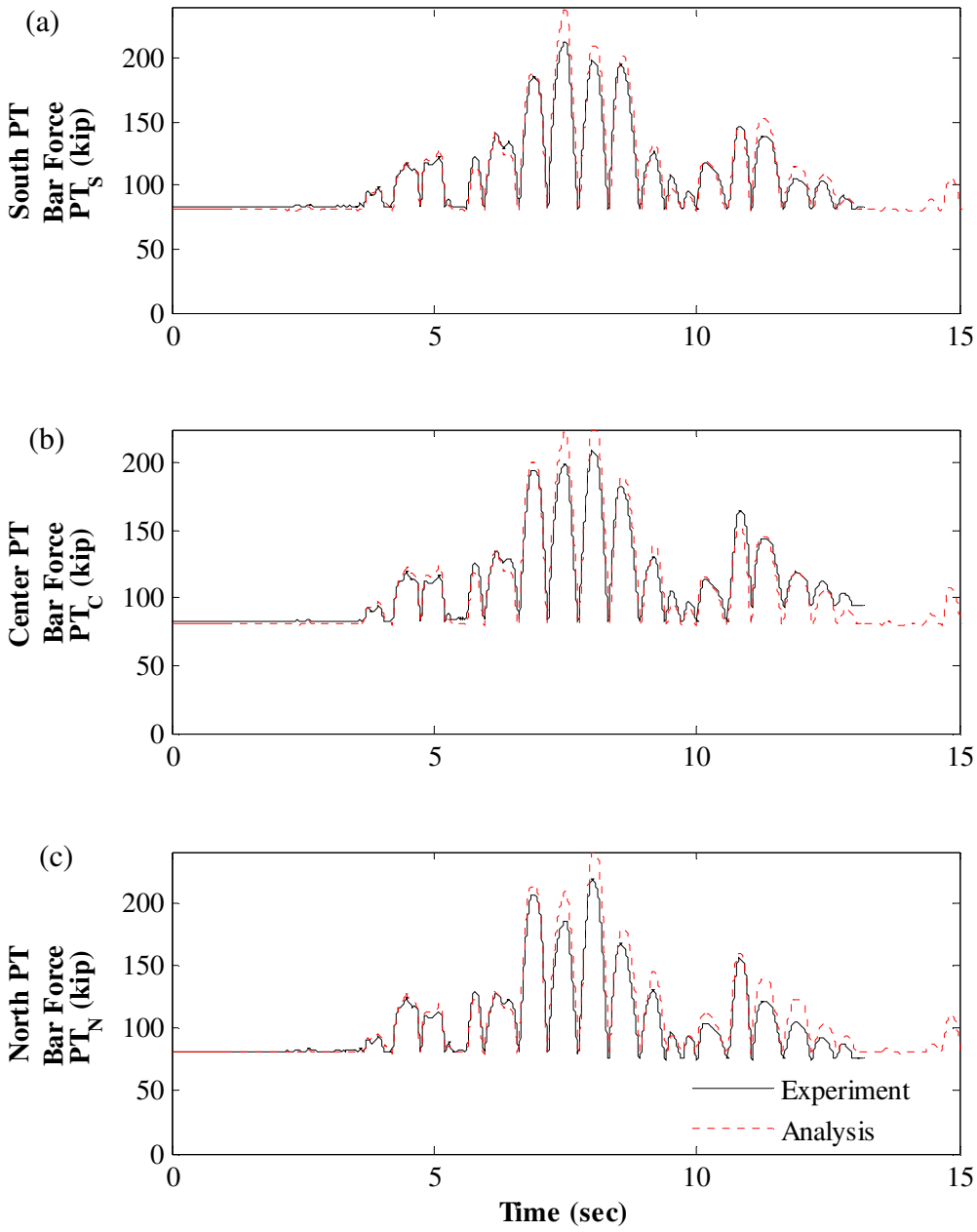

Figure 10.69 – Correlation of PT force response to MCE_cap000: (a) south PT bars; (b) center PT bars; (c) north PT bars

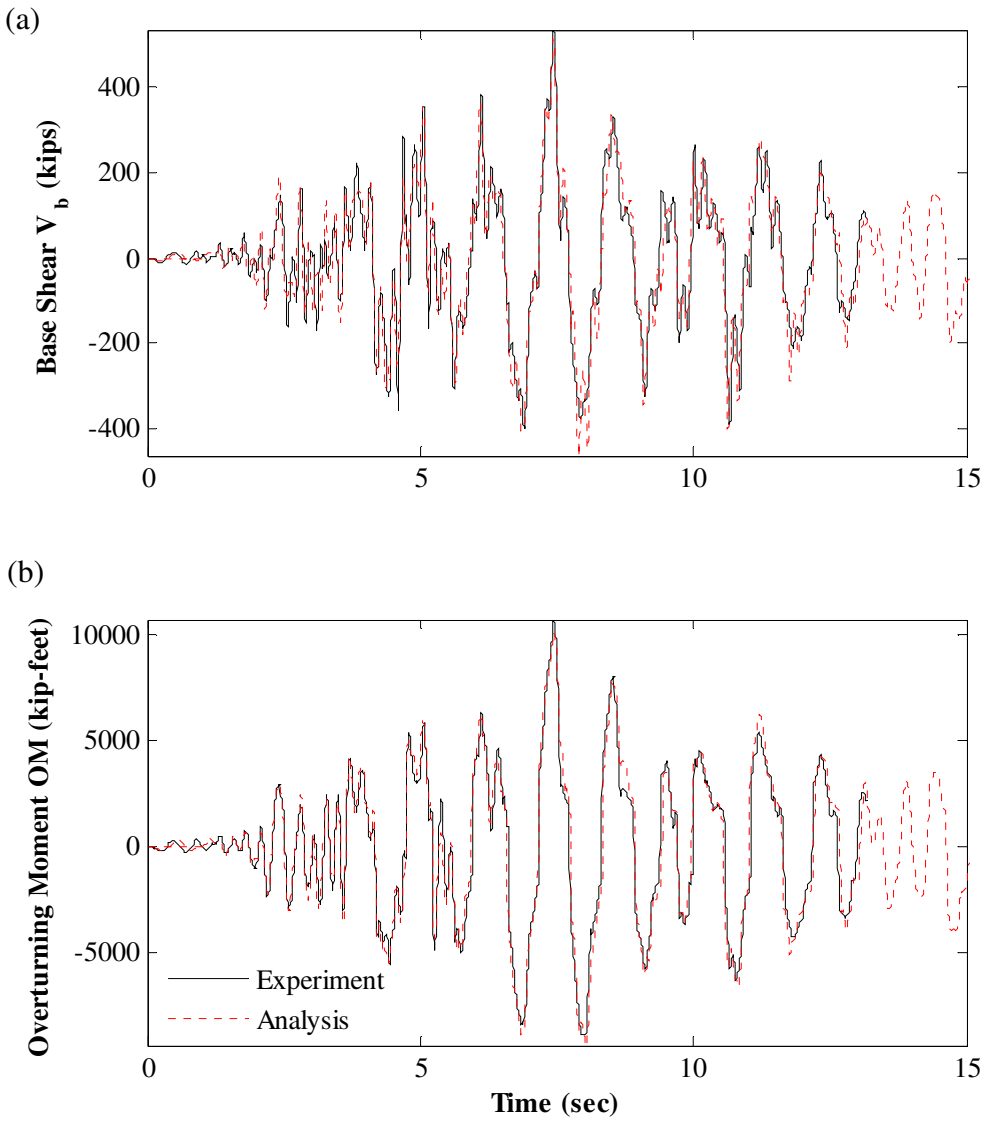

Figure 10.70 – MCE_cap000 response correlation: (a) base shear; (b) overturning moment

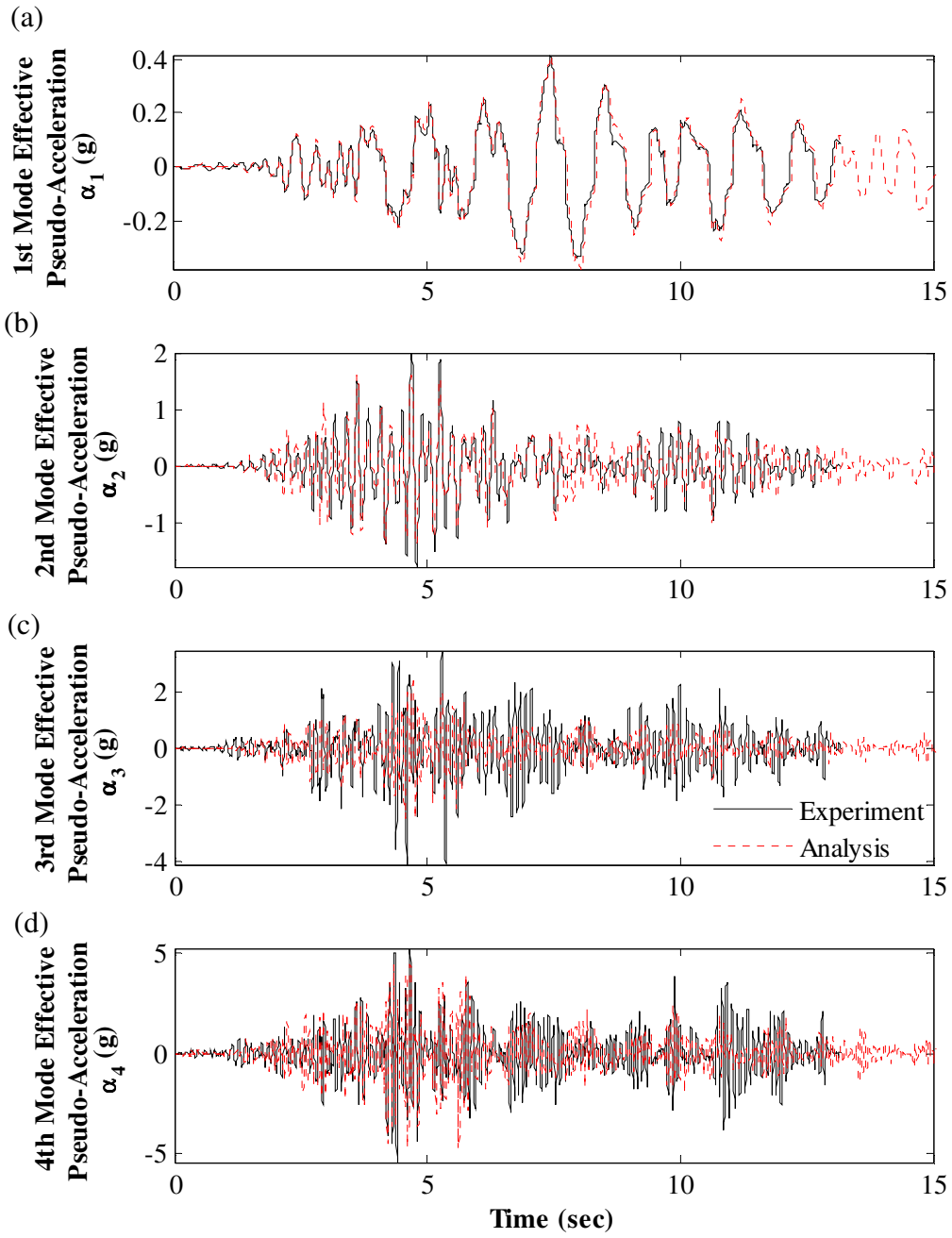

Figure 10.71 – Correlation of effective modal pseudo-acceleration response to MCE_cap000: (a) 1st mode; (b) 2nd mode; (c) 3rd mode; (d) 4th mode

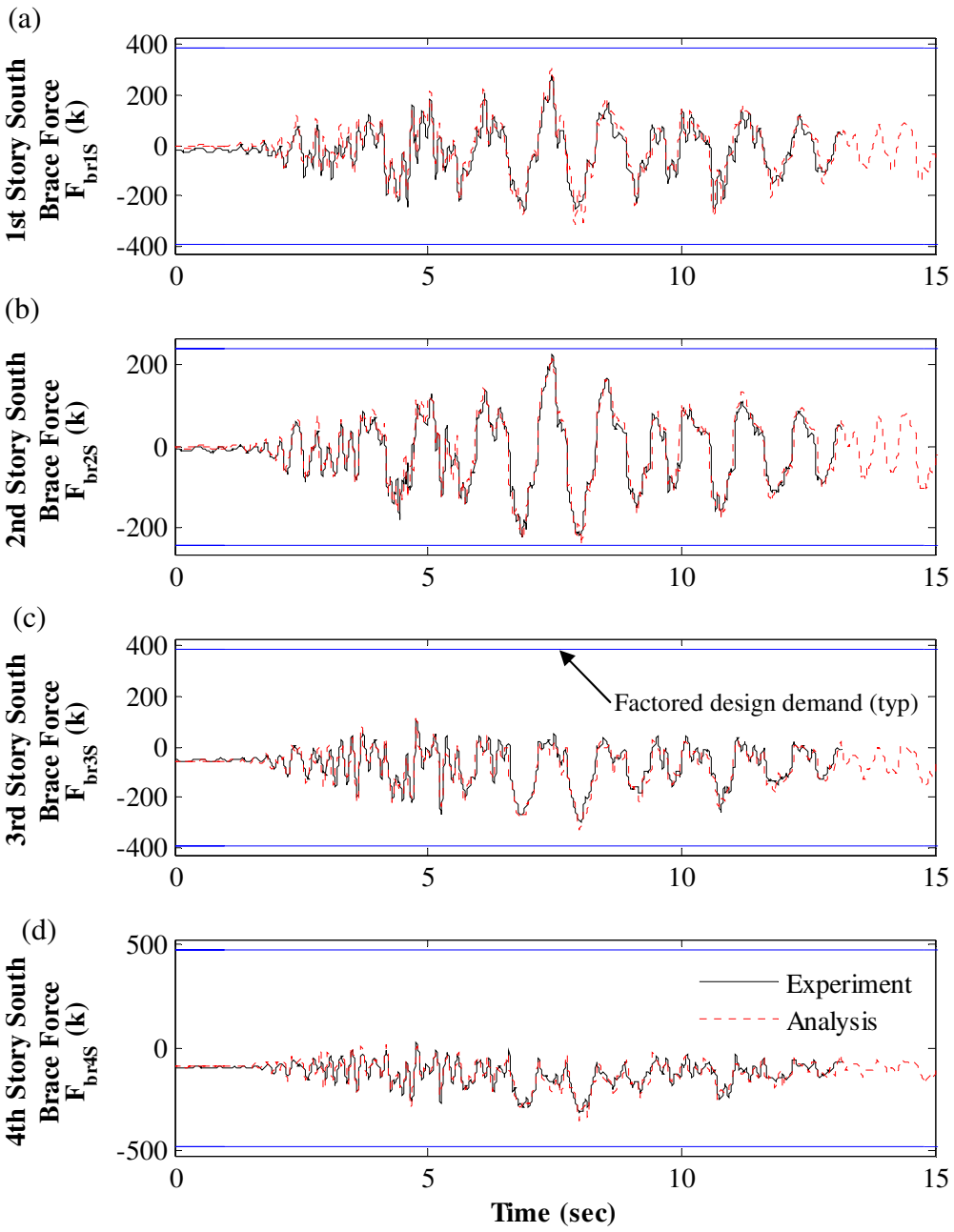

Figure 10.72 – Correlation of south brace axial force response to MCE_cap000: (a) 1st story; (b) 2nd story; (c) 3rd story; (d) 4th story

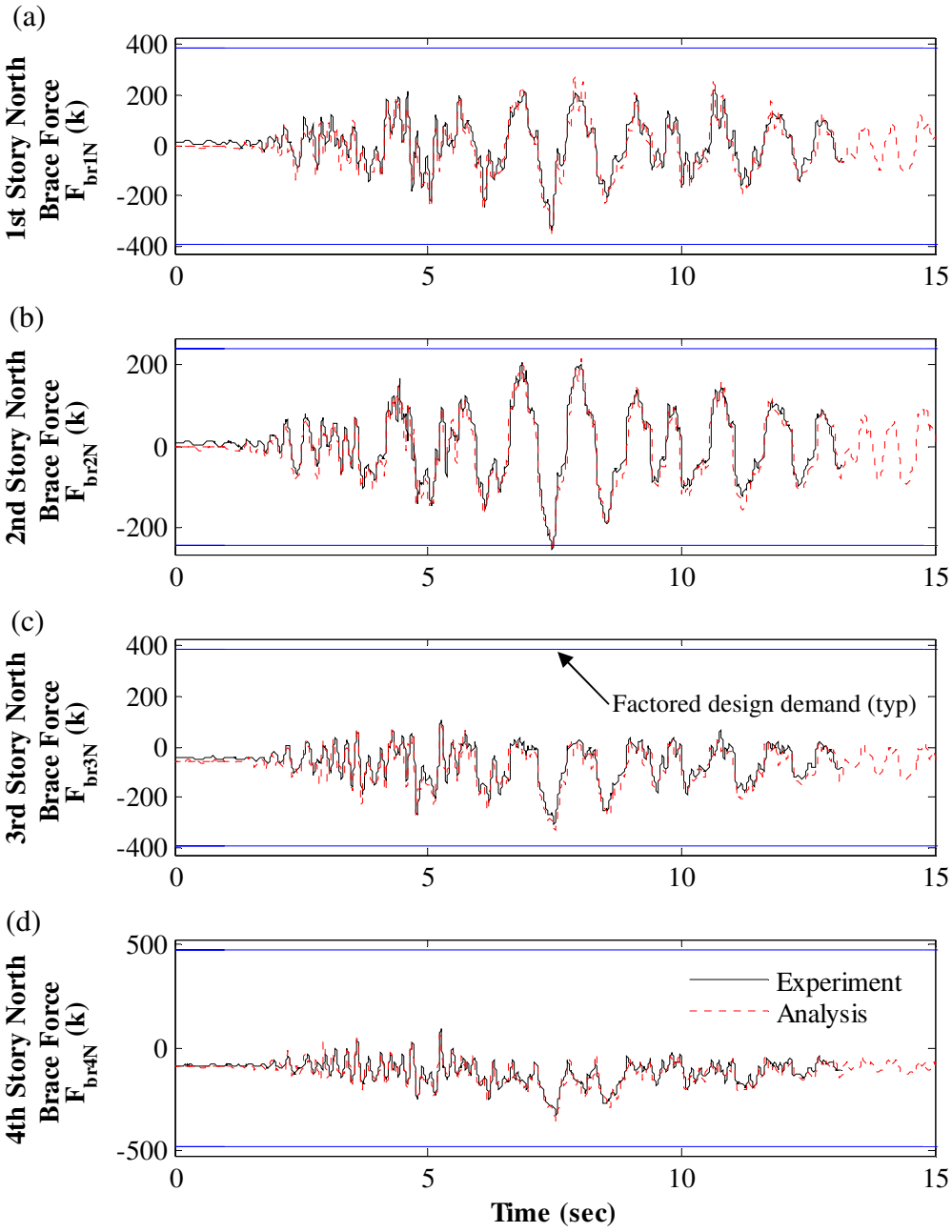

Figure 10.73 –Correlation of north brace axial force response to MCE_cap000: (a) 1st story; (b) 2nd story; (c) 3rd story; (d) 4th story

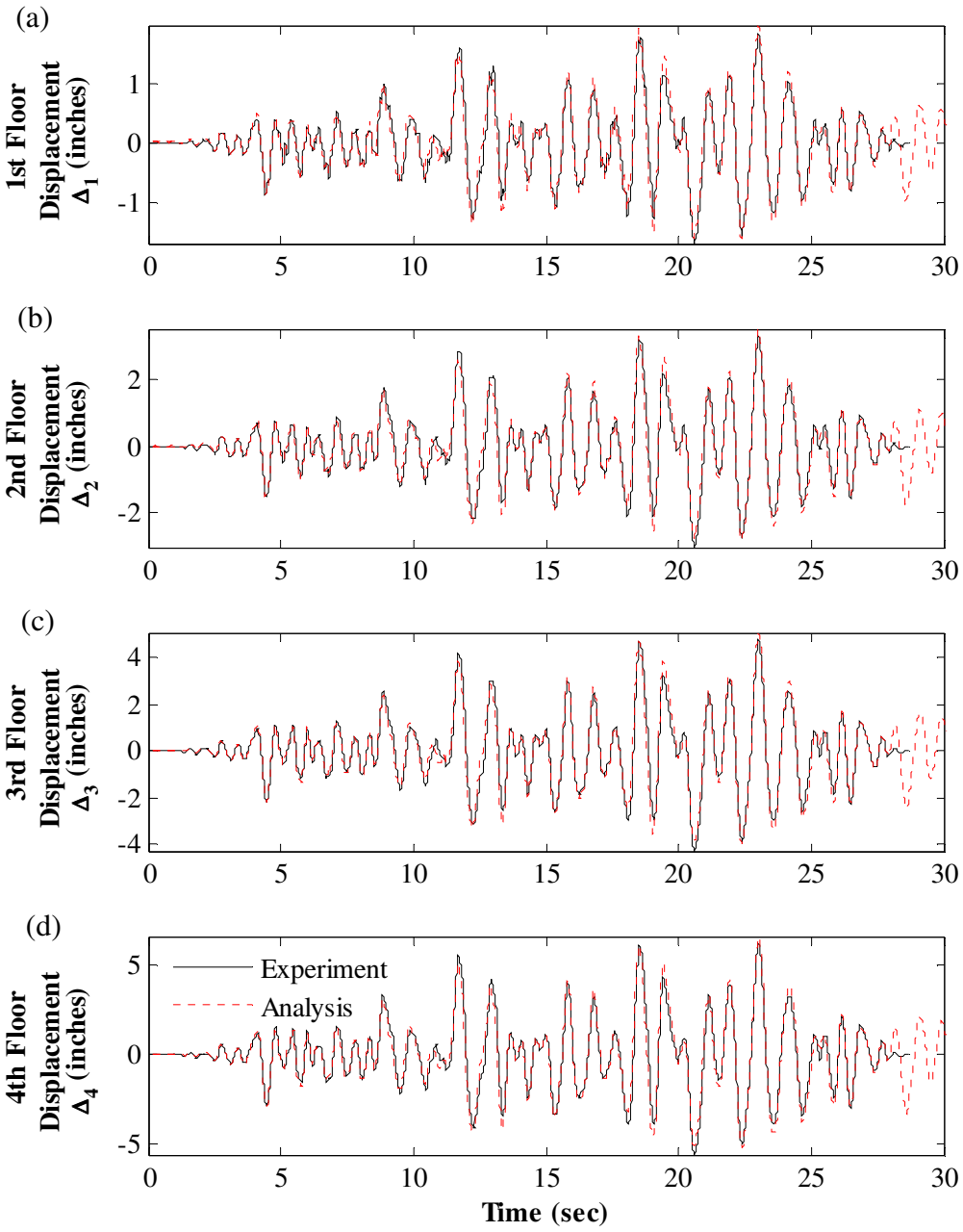

Figure 10.74 – Correlation of floor displacement response to MCE_h-cpe237: (a) 1st floor; (b) 2nd floor; (c) 3rd floor; (d) 4th floor

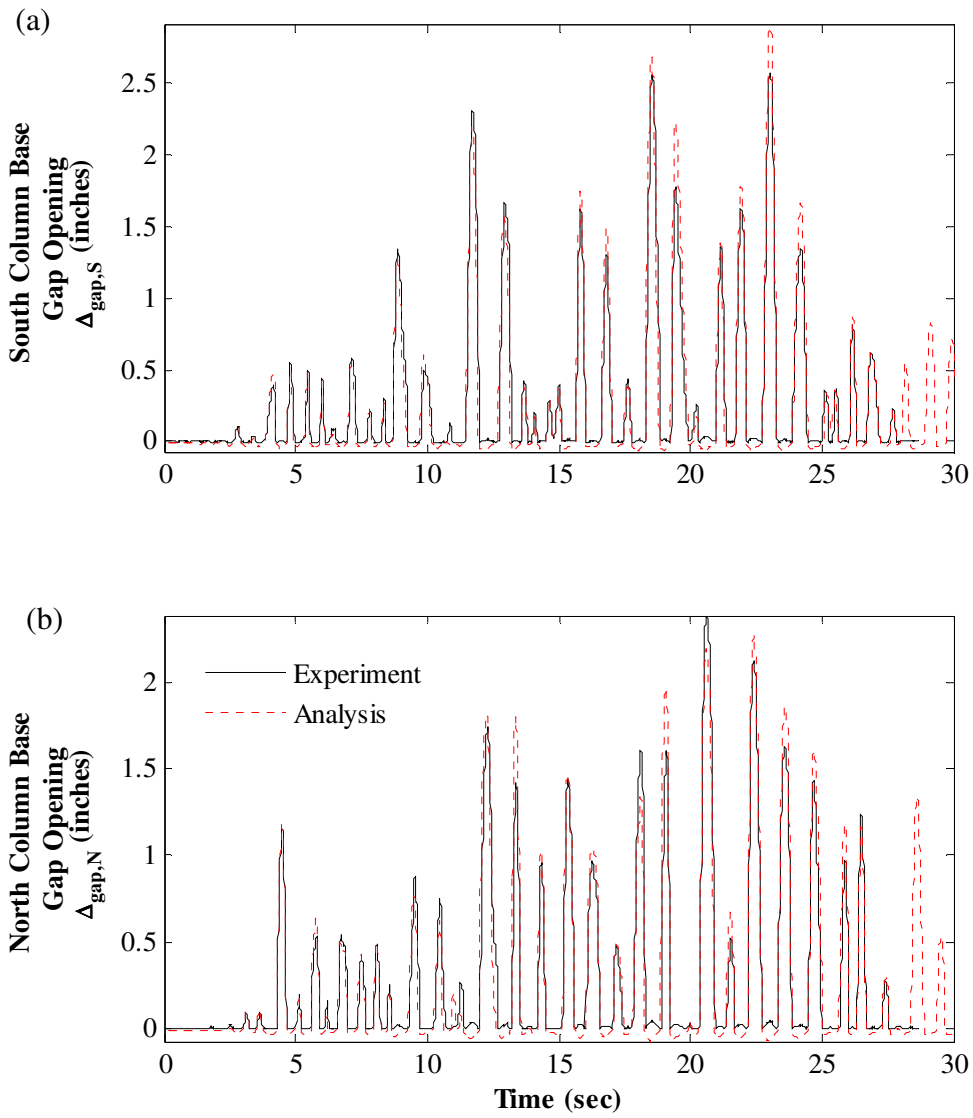

Figure 10.75 – Correlation of column base gap opening response to MCE_h-cpe237: (a) at south column base; (b) at north column base

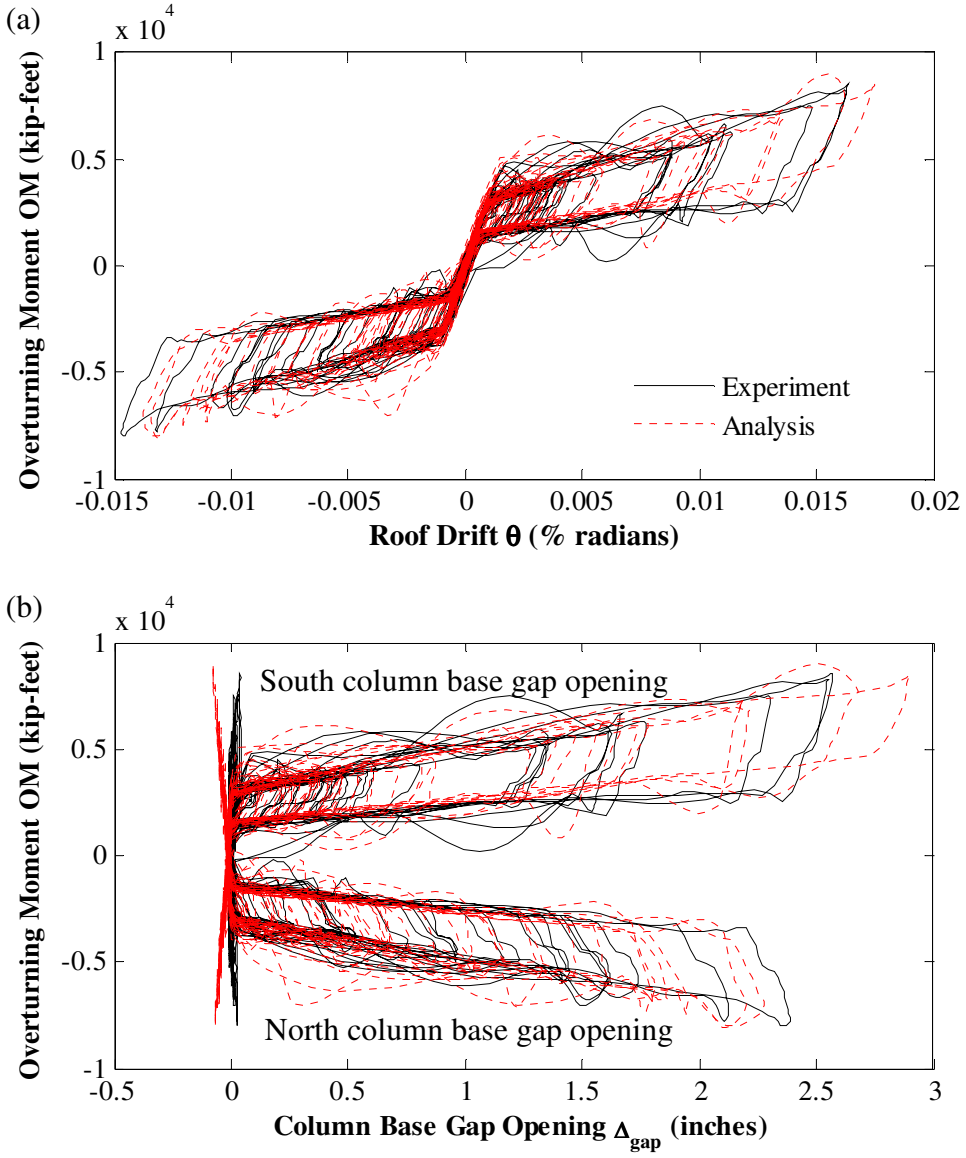

Figure 10.76 – Correlation of hysteretic response to MCE_h-cpe237: (a) overturning moment versus roof drift; (b) overturning moment versus column base gap opening

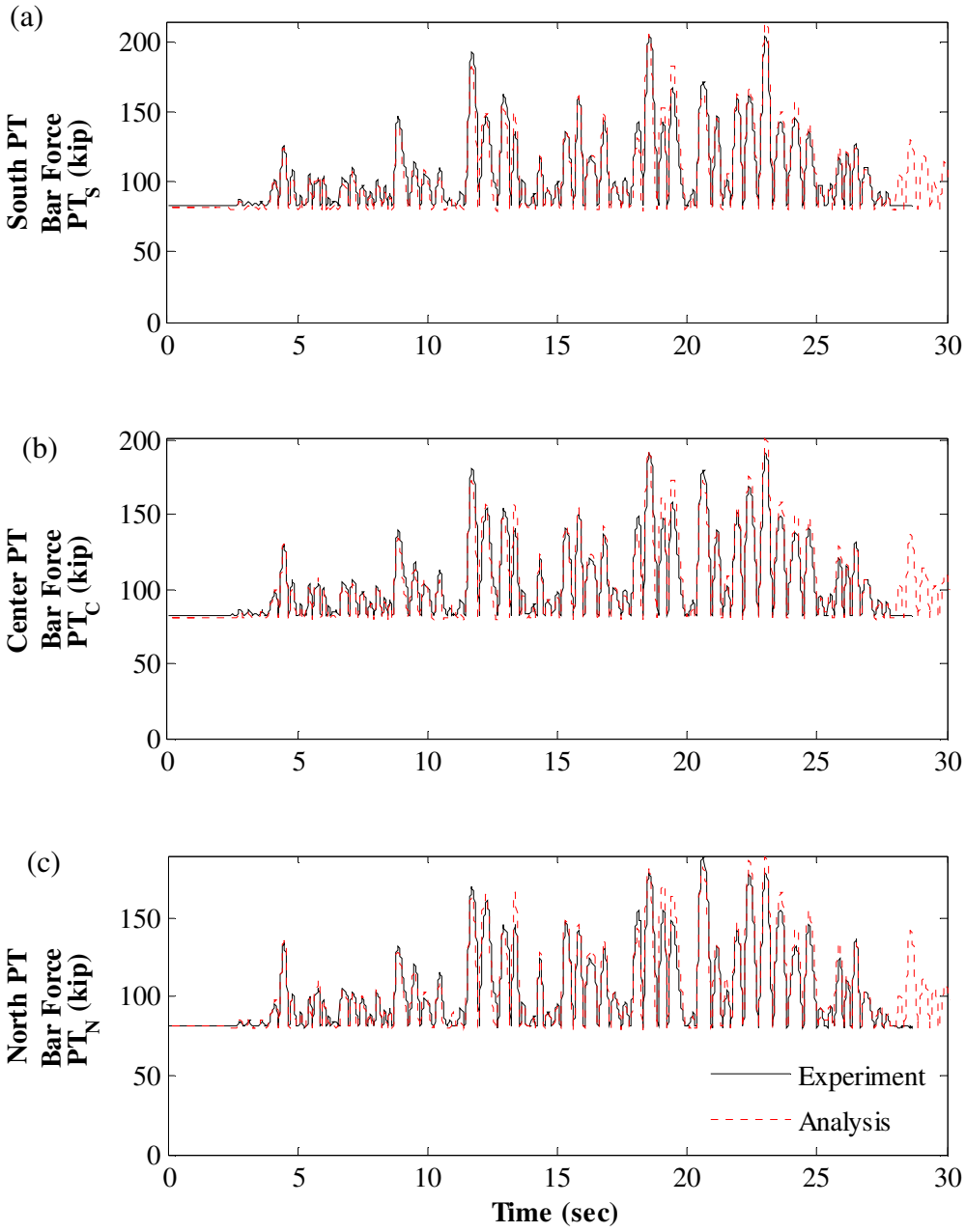

Figure 10.77 – Correlation of PT force response to |MCE_h-cpe237: (a) south PT bars; (b) center PT bars; (c) north PT bars

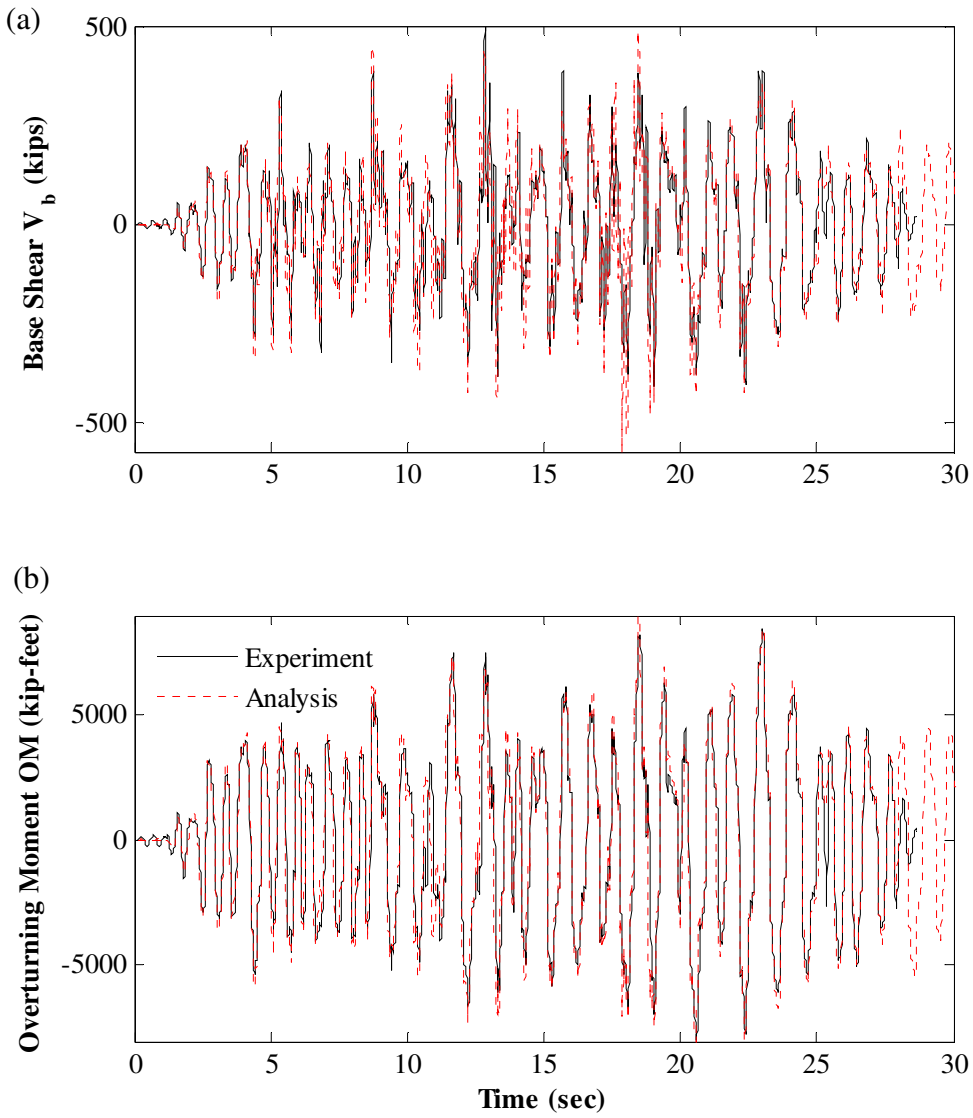

Figure 10.78 – MCE_h-cpe237 response correlation: (a) base shear; (b) overturning moment

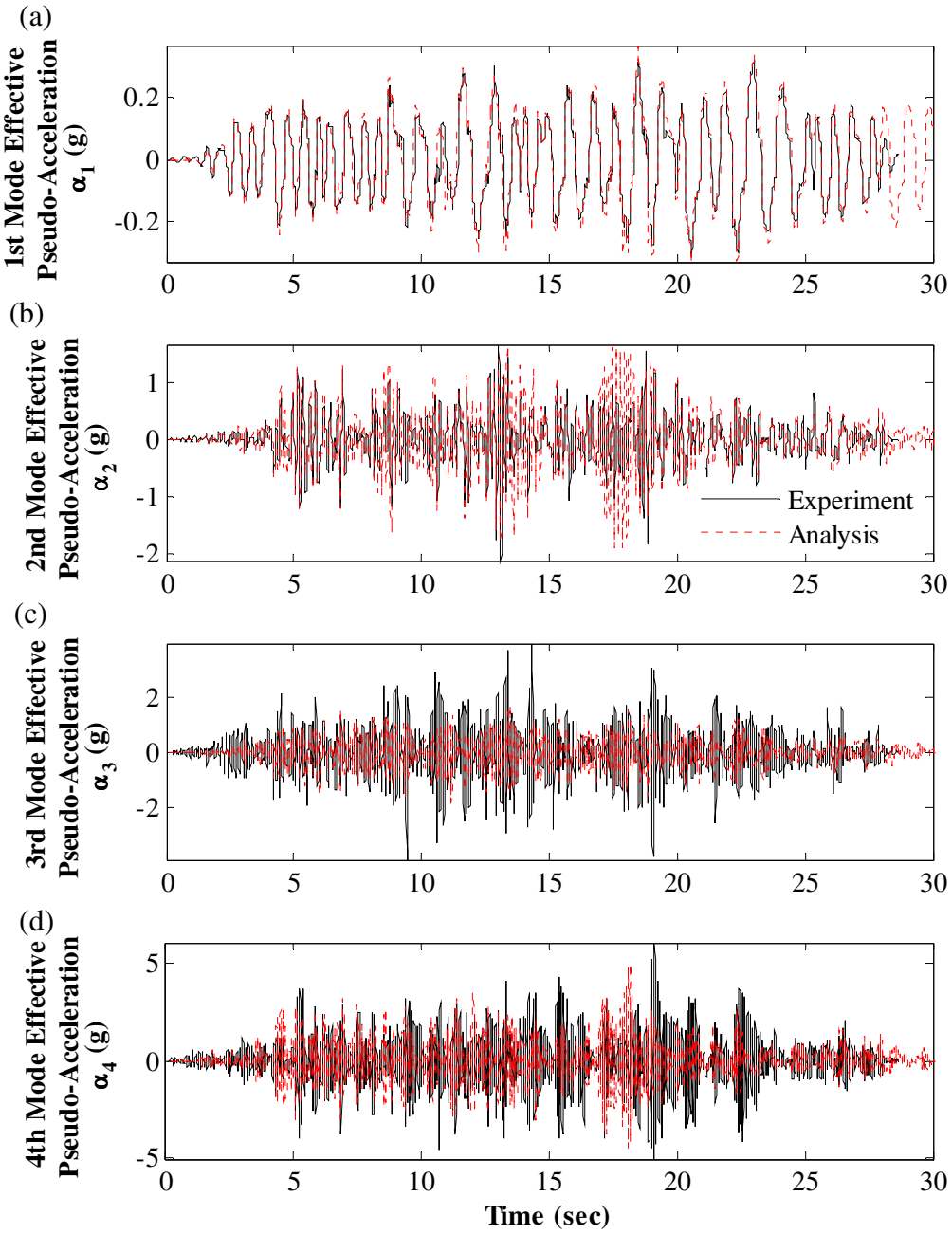

Figure 10.79 – Correlation of effective modal pseudo-acceleration response to MCE_h-cpe237: (a) 1st mode; (b) 2nd mode; (c) 3rd mode; (d) 4th mode

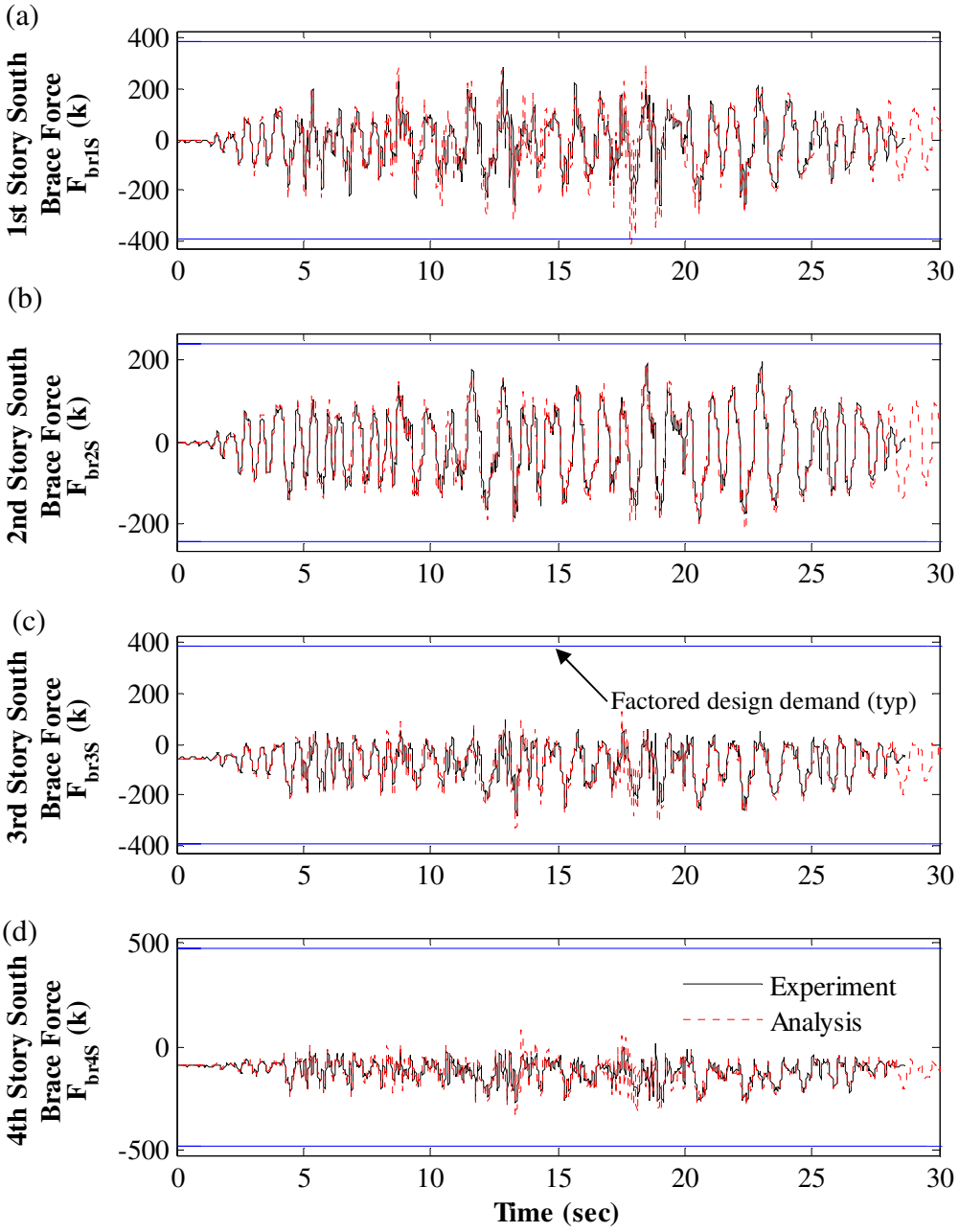

Figure 10.80 – Correlation of south brace axial force response to MCE_h-cpe237: (a) 1st story; (b) 2nd story; (c) 3rd story; (d) 4th story

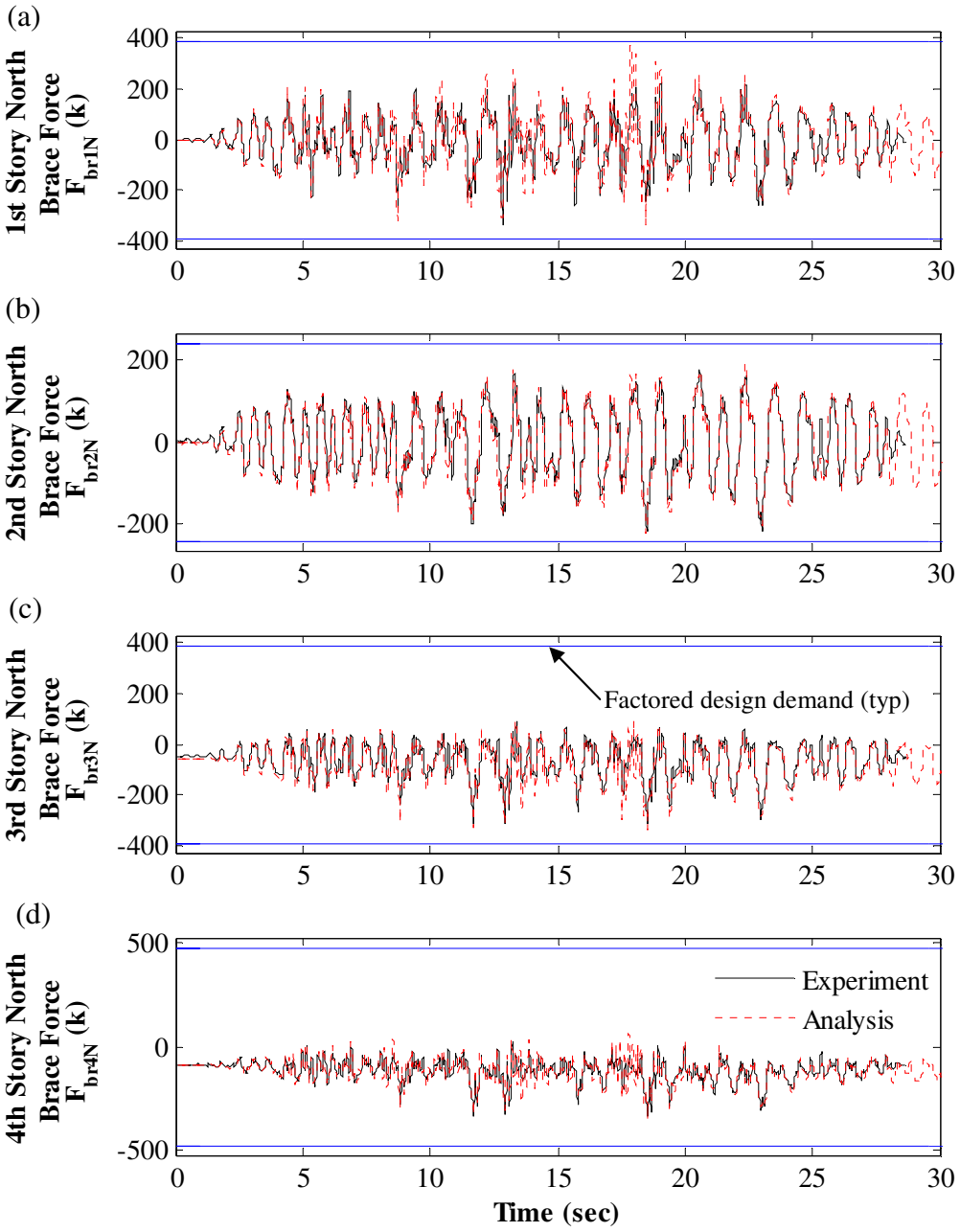

Figure 10.81 – Correlation of north brace axial force response to MCE_h-cpe237: (a) 1st story; (b) 2nd story; (c) 3rd story; (d) 4th story

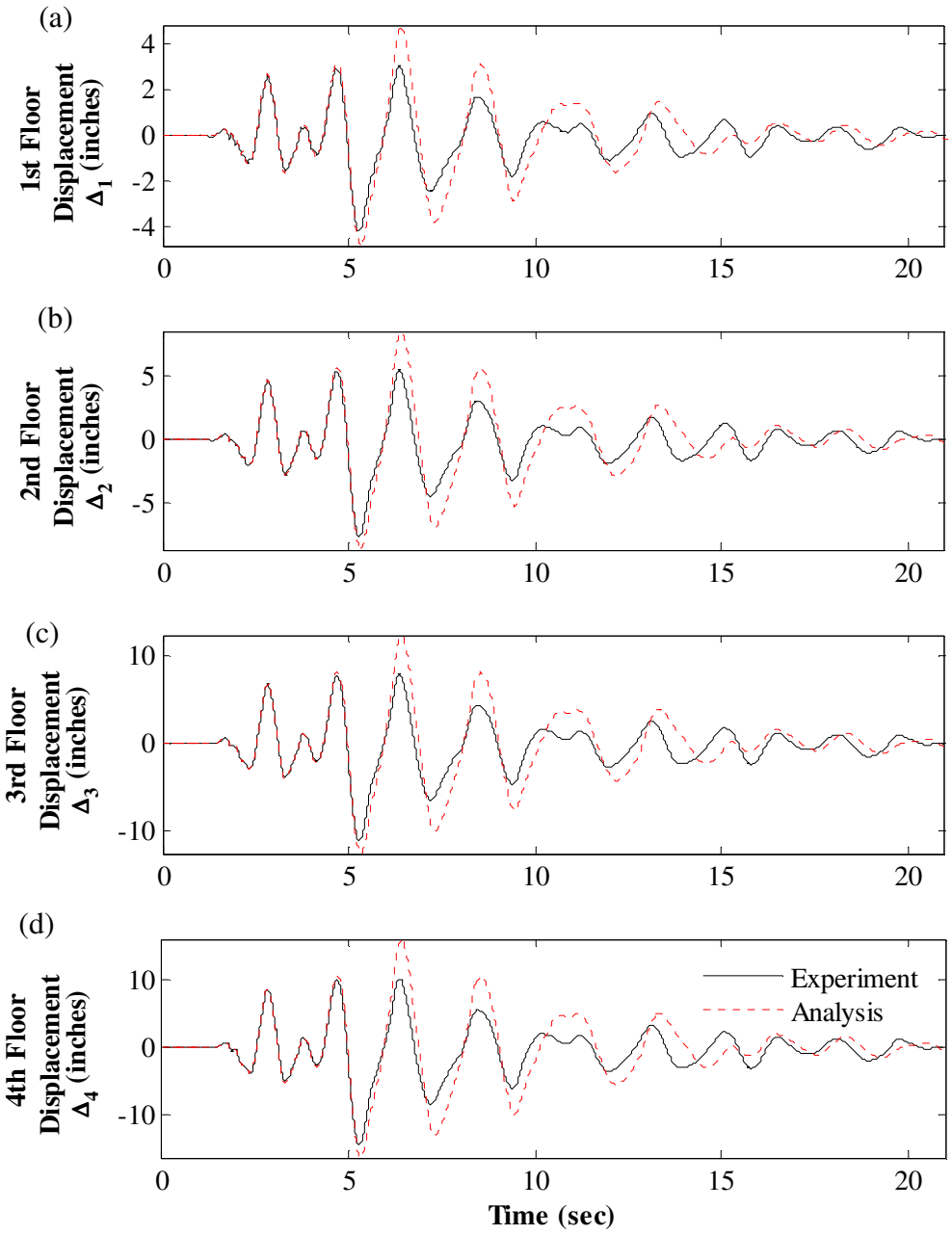

Figure 10.82 – Correlation of floor displacement response to xMCE_tak090: (a) 1st floor; (b) 2nd floor; (c) 3rd floor; (d) 4th floor

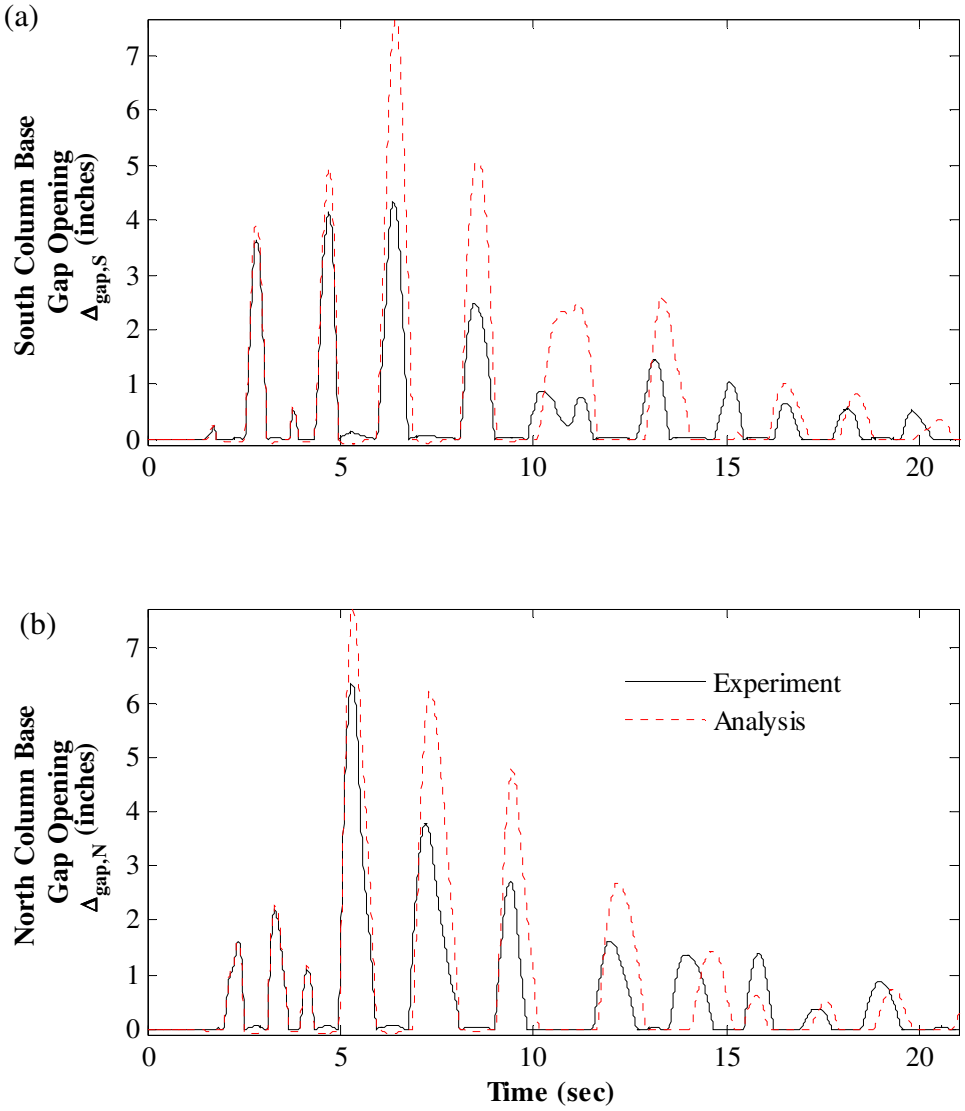

Figure 10.83 – Correlation of column base gap opening response to xMCE_tak090: (a) at south column base; (b) at north column base

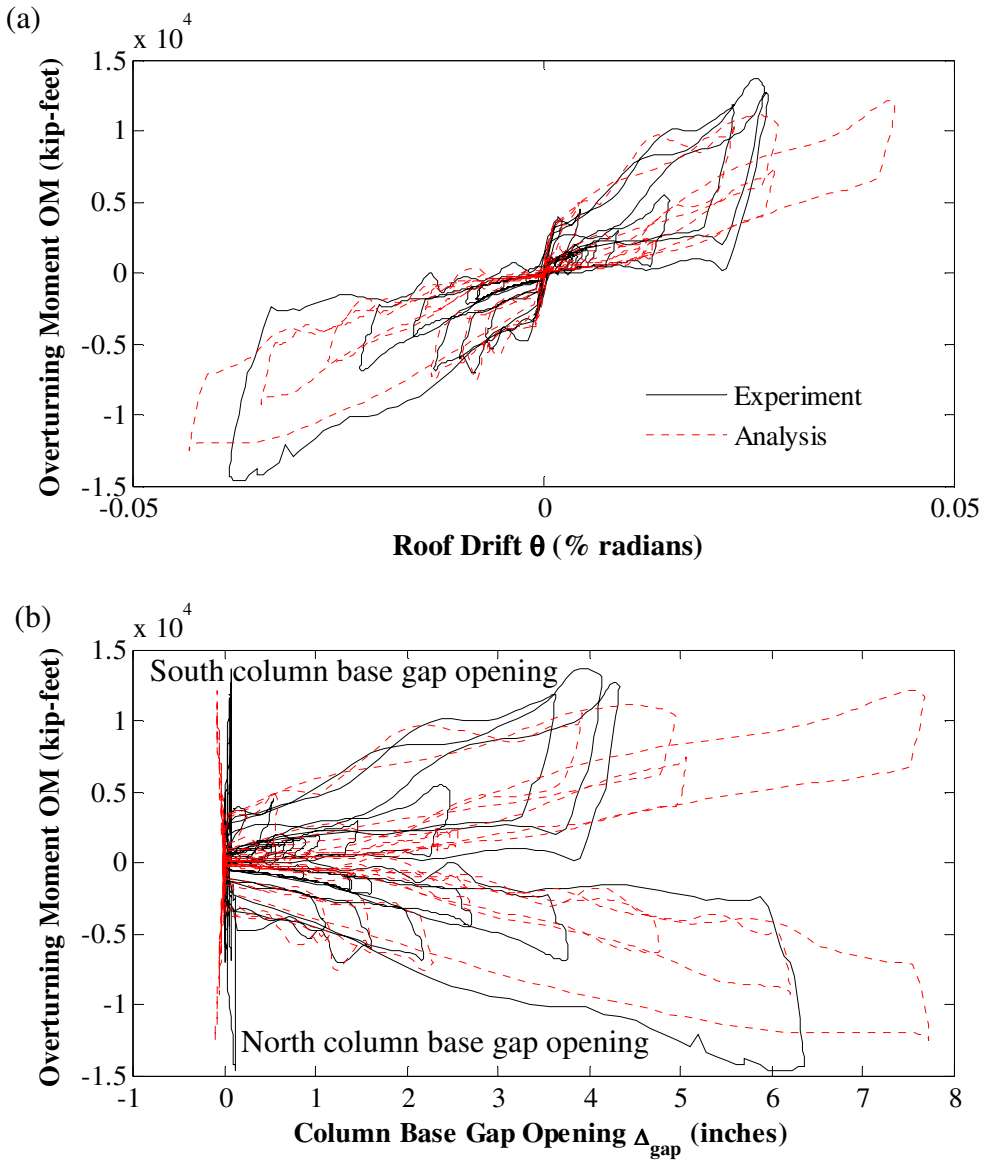

Figure 10.84 – Correlation of hysteretic response to xMCE_tak090: (a) overturning moment versus roof drift; (b) overturning moment versus column base gap opening

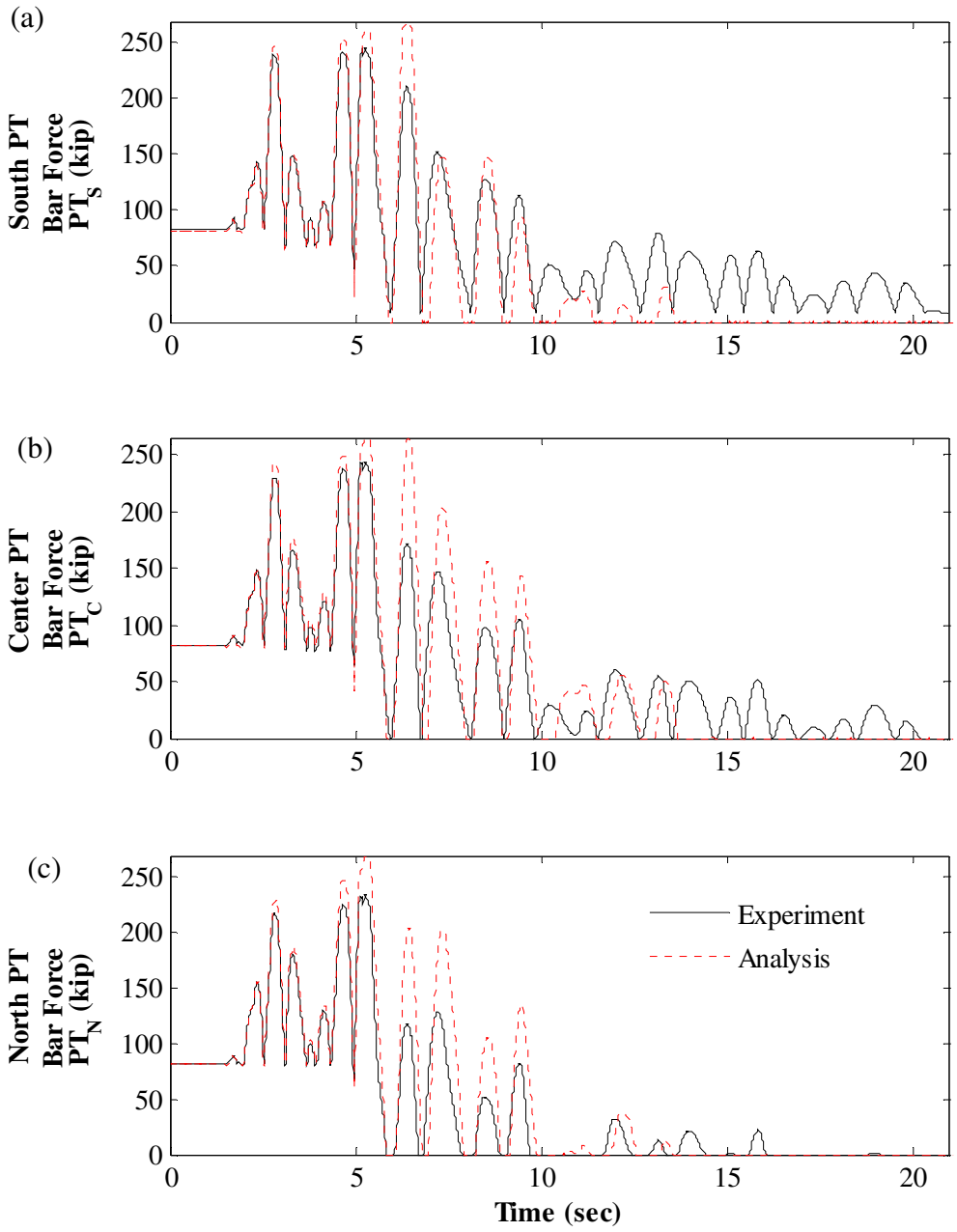

Figure 10.85 – Correlation of PT force response to xMCE_tak090: (a) south PT bars; (b) center PT bars; (c) north PT bars

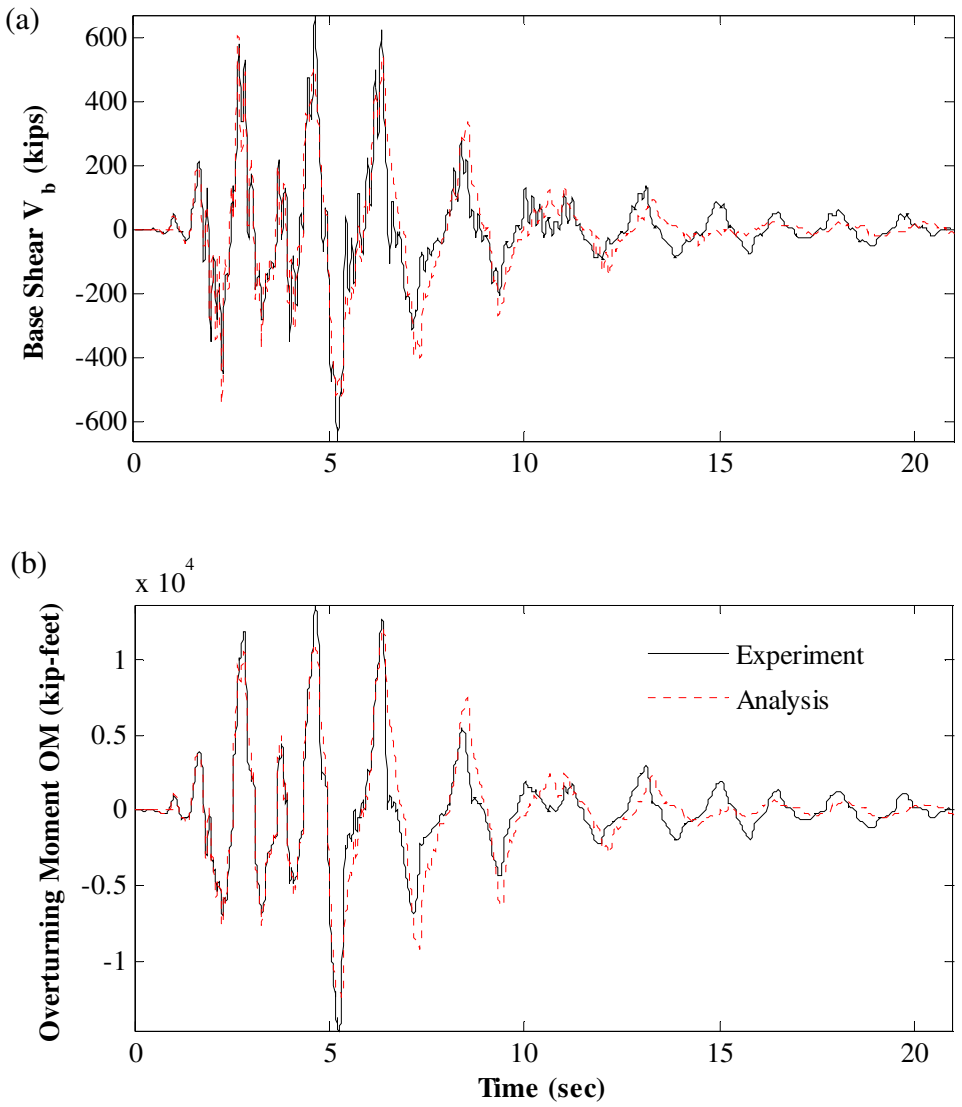

Figure 10.86 – xMCE_tak090 response correlation: (a) base shear; (b) overturning moment

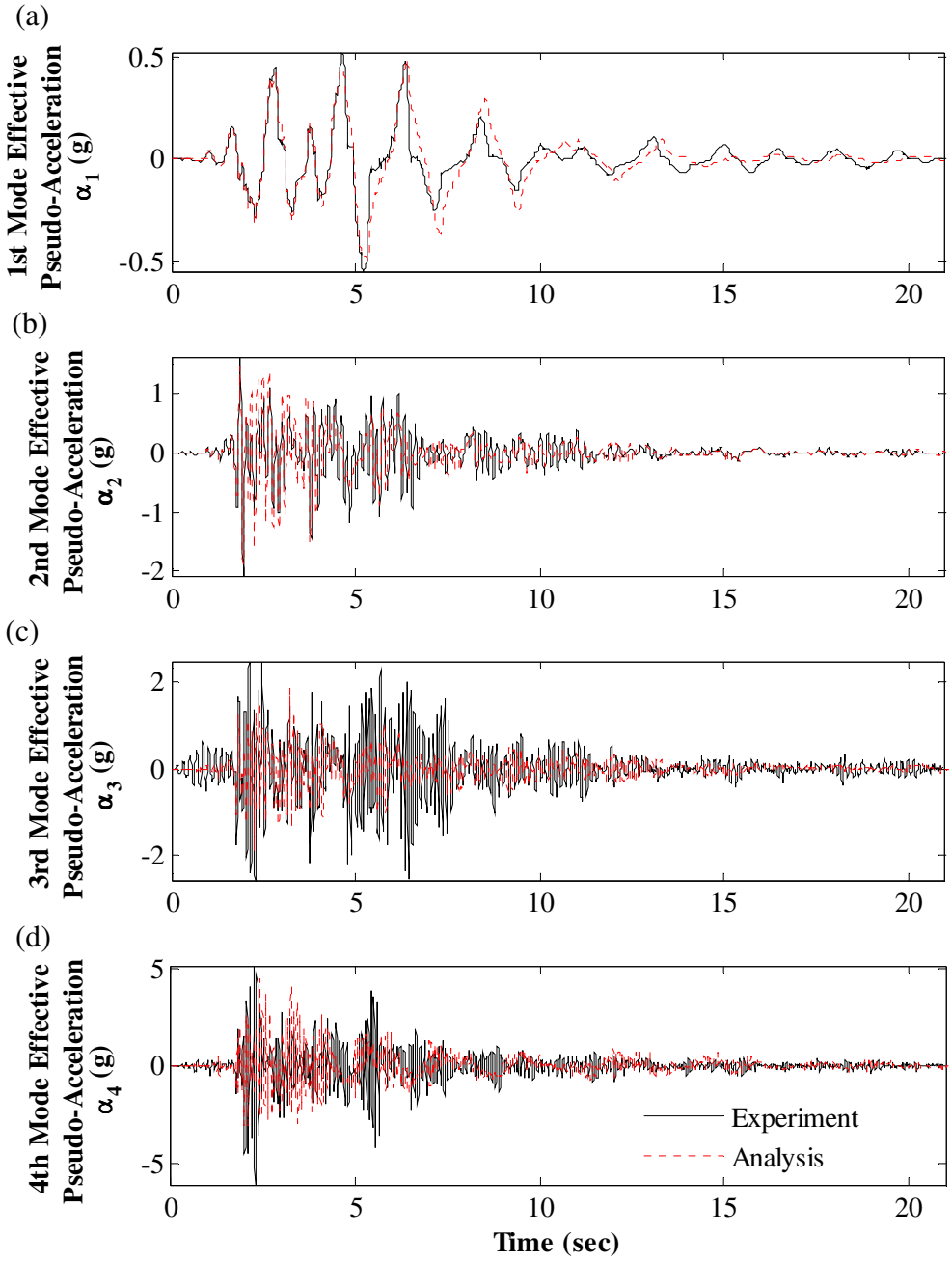

Figure 10.87 – Correlation of effective modal pseudo-acceleration response to xMCE_tak090: (a) 1st mode; (b) 2nd mode; (c) 3rd mode; (d) 4th mode

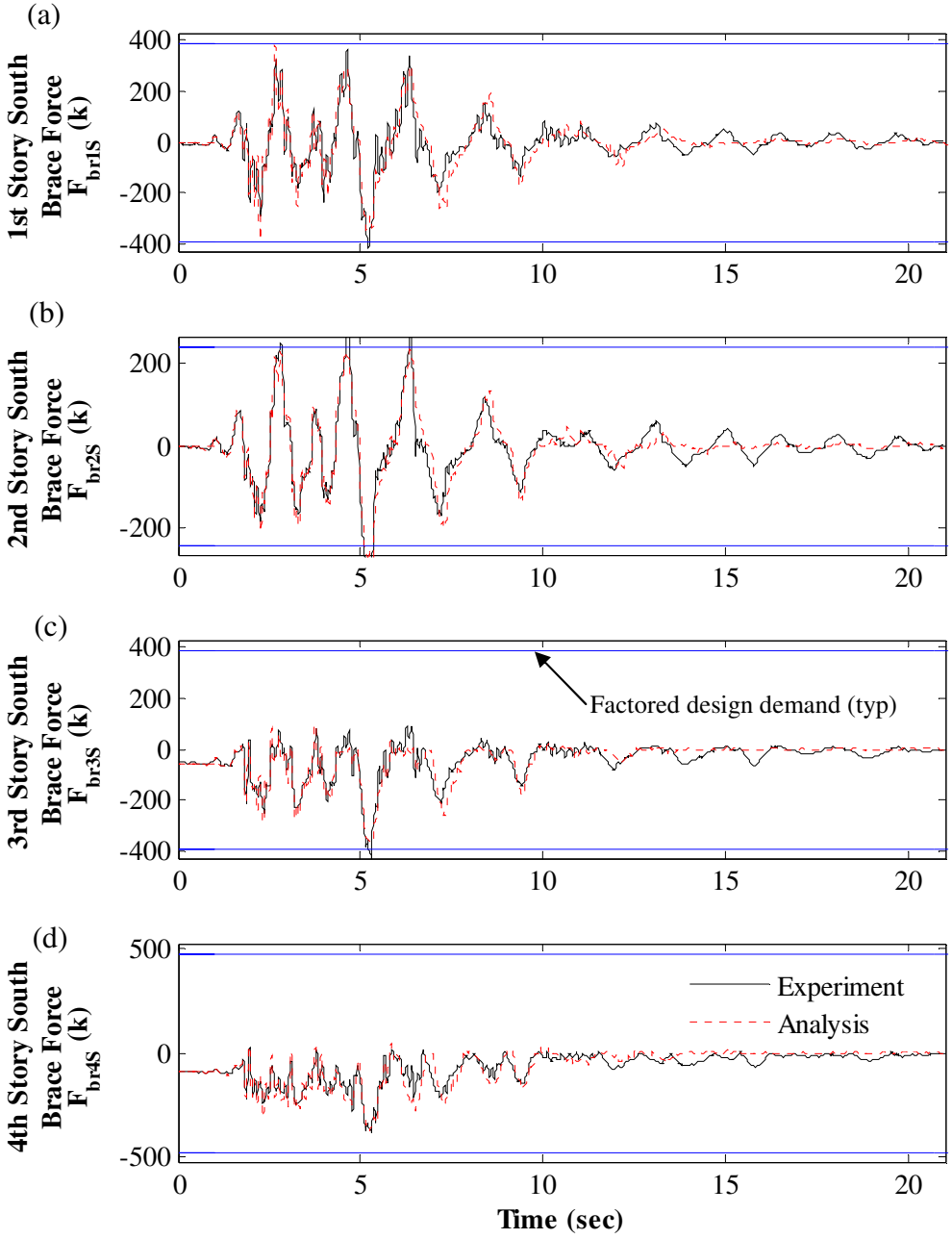

Figure 10.88 – Correlation of south brace axial force response to xMCE_tak090: (a) 1st story; (b) 2nd story; (c) 3rd story; (d) 4th story

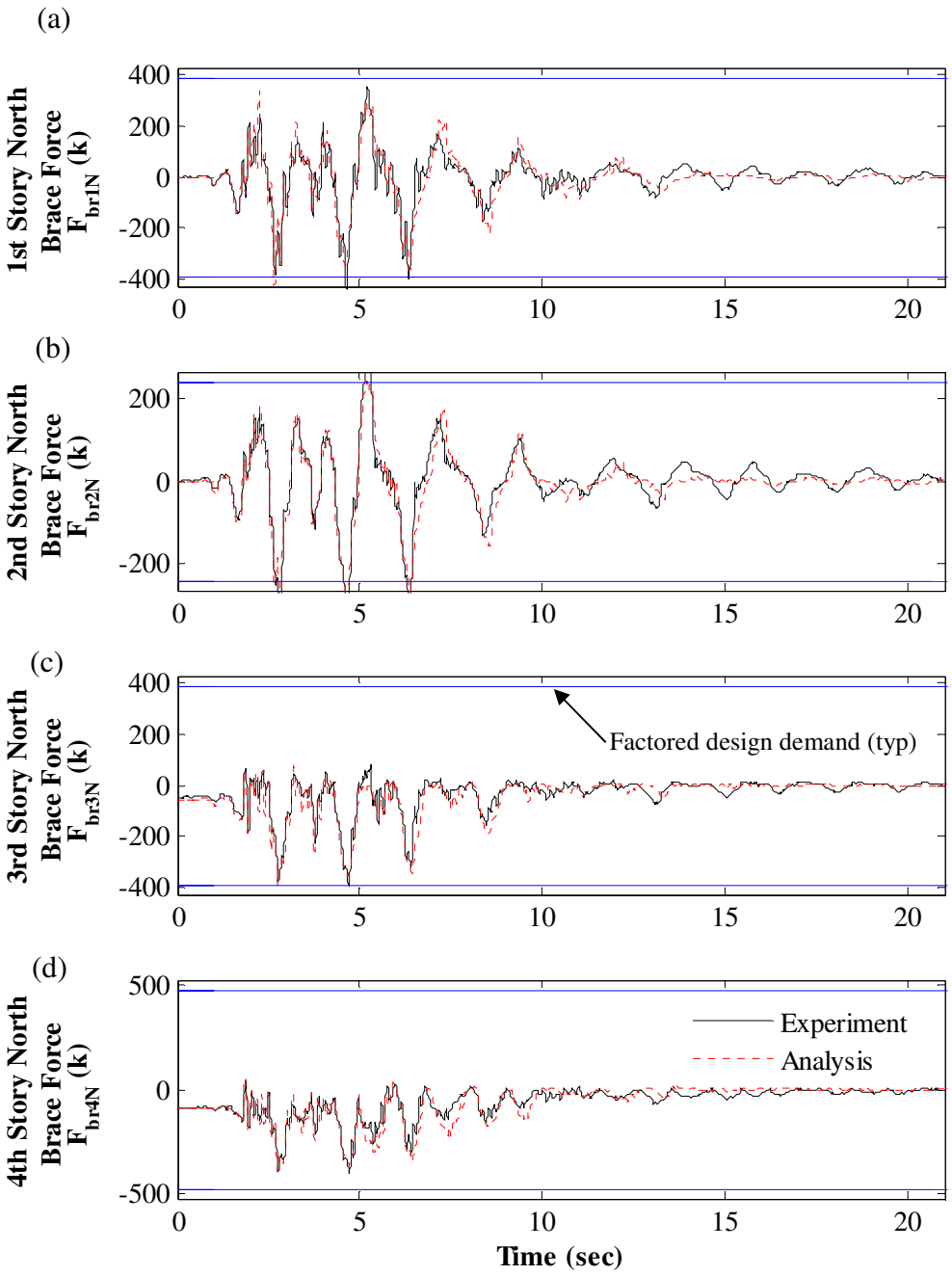

Figure 10.89 – Correlation of north brace axial force response to xMCE_tak090: (a) 1st story; (b) 2nd story; (c) 3rd story; (d) 4th story

CHAPTER 11

CORRELATION OF CALIBRATED NUMERICAL SIMULATION OF SC-CBF TEST STRUCTURE RESPONSE WITH EXPERIMENTAL RESULTS

This chapter discusses the results of the laboratory hybrid simulations and the correlation of these experimental results with numerical simulation results from calibrated analytical models. The calibrated analytical models were developed using OpenSEES (Mazzoni et al. 2009), as discussed in Chapter 8. The calibrated analytical models discussed in this chapter are modifications of the predictive analytical model discussed in Chapters 9 and 10. The "calibrations" are adjustments made to certain model parameters to more closely match the initial conditions of the SC-CBF test structure before each hybrid simulation.

11.1 Considerations for Calibrated Models

There are three primary parameters that were adjusted to calibrate the analytical models to the initial conditions of the SC-CBF test structure: the gaps at the lateral-load bearings, the initial forces in the PT bars, and the yield forces in the PT bars. These parameters are explained in this section.

11.1.1 Gaps at Lateral-Load Bearings

The distribution and magnitude of the gaps at the lateral-load bearings affects the effective height of the inertia force response of the structure. The effective height is

defined as the applied overturning moment divided by the applied base shear (Chopra 2007). The load path followed by the inertia forces in the SC-CBF test structure requires inertia forces to be transferred from the masses on the lean-on column to the north gravity column, as shown in Figure 8.2. In the hybrid simulations in the laboratory, this is achieved by making the degrees of freedom of the analytical substructure equal to the degrees of freedom of the experimental substructure. For the analytical model, this is achieved using stiff springs between the lean-on column and the north gravity column. From the north gravity column, the inertia forces are either transmitted through the north lateral-load bearings into the north SC-CBF column or through the loading beams to the south gravity column, then through the south lateral-load bearings into the south SC-CBF column, as shown in Figure 8.2. As the lateral gaps at the lateral-load bearings change between simulations, the vertical distribution of the lateral load transferred to the SC-CBF changes. This redistribution occurs due to the elastic stiffness of the lean-on column and the elastic stiffness of the adjacent north and south gravity columns; this elastic stiffness, combined with the variable gaps at the lateral-load bearings, permits some part of the inertia force from the mass at floor i to be transmitted into the lateral-load bearings at another floor level (i.e., floor i+1 or floor i-1).

To account for the change in the initial gap conditions of the SC-CBF test structure, the gaps at the bearings were measured between each simulation. Two measurements are taken at each bearing (i.e., one measurement at the east side of the bearing and one measurement at the west side). The north gap is determined as the average of the north-east and north-west measurements, and the south gap is determined as the average of the

south-east and south-west measurements. The total gap measurements (the north gap plus the south gap) for each simulation are summarized in Table 11.1.

11.1.2 Initial PT Force

The measured PT force at the beginning of each laboratory hybrid simulation was used in the calibrated analytical models. Due to the imprecise nature of stressing the PT bars in the laboratory, the actual forces (i.e., measured forces) were not equal to the value of PT_0 established during design. The actual initial PT forces summarized in Table 11.2 were used in the calibrated models.

11.1.3 PT Yield Force

As discussed in Section 9.1, the yield stress of the PT bars differed from the nominal yield stress; the average yield stress determined from tension tests was 143.6 ksi (Gonner et al. 2010), and the nominal yield stress is 120 ksi. The corresponding yield force for a pair of bars at each PT bar location based on the average yield stress of 143.6 ksi is 244.2 kip. However, there were differences among the apparent yield forces of the PT bars in hybrid simulations in the laboratory.

The PT yield forces used initially in the calibrated models were based on the force at which the bars first appeared to yield during the test program. The north PT bars appeared to yield initially at about 215 kip during hybrid simulation MCE_cap000_01-11-2010, as shown in Figure 11.1. The north PT bar yield force for the MCE_cap000_01-11-2010 numerical simulation and prior simulations is therefore set equal to 215 kip. The

south PT bars and central PT bars appeared to yield initially during hybrid simulation xMCE_tak090_01-13-2010 at 235.0 and 222.0 kip, respectively, as shown in Figure 11.2.

The forces at which the PT bars appeared to yield initially during hybrid simulations (235.0 kip, 222.0 kip, and 215.0 kip for the south, central, and north PT bar location, respectively) differ from the expected yield force from the average yield stress measured in tensile tests, 244.2 kip (Gonner et al. 2010). The apparent yield force from the hybrid simulations reflects the limit of proportionality of the stress-strain behavior of the PT bars; therefore, the apparent yield force is less than the yield force from tensile tests.

Due to the hardening behavior of the PT bars after yielding, the elastic range of the bars increases after the bar is loaded beyond its yield stress. Therefore, it is necessary to track the maximum force achieved at each PT location (south, center, and north), to determine the force at which the bars at that location will yield in subsequent simulations. Table 11.3 summarizes the maximum PT forces reached during each experimental simulation, and the PT yield force that was input into the analytical model. Forces that indicate a new yield force for the bars are shown in bold.

The peak force reached in the north PT bars during hybrid simulation MCE_cap000_01-11-2010 was 219.1 kip, which is reflected in the PT yield force for the calibrated models for subsequent simulations. The peak forces for the south PT bars and central PT bars during hybrid simulation xMCE_tak090_01-13-2010 are shown in Table 11.3 as the PT yield forces for MCE_lp-hda255.

11.2 Correlation of Experimental Response with Calibrated Numerical Analysis Results

The correlation of the experimental response with the results from the nonlinear dynamic analyses of the calibrated models will be discussed in this section. The response quantities that will be compared are: floor displacements at the north gravity column at each floor level i (Δ_i); the gap-opening displacement at the base of the SC-CBF columns due to rocking ($\Delta_{gap,S}$ for the south column gaps, $\Delta_{gap,N}$ for the north column gaps); the total PT force in each of the three PT bar locations (sum of the forces in the two bars at the south location, PT_S; center location, PT_C; and north location, PT_N); the base shear, V_b, determined by summing the actuator forces in the laboratory or by summing the forces in the stiff springs between the lean-on column and the north gravity column in the analytical model; the overturning moment, OM, calculated from the forces in the actuators in the laboratory or the forces in the springs between the lean-on column and the north gravity column in the analytical model; the effective modal pseudo-acceleration, α_n, for each mode; and the axial forces in the south and north braces in story i, F_{briS} and F_{briN}, respectively.

11.2.1 Correlation of DBE-Level Response

11.2.1.1 DBE_cls000_12-31-2009

The correlation of the numerical analysis of the response of the calibrated model to DBE_cls000 and the experimental results from hybrid simulation DBE_cls000_12-31-2009 is shown in Figures 11.3 through 11.10. Figure 11.3 shows the correlation of the

displacement response at each floor level. Figure 11.4 shows the correlation of the column base gap-opening displacements. The hysteretic response is shown in Figure 11.5; overturning moment is plotted against roof drift in Figure 11.5(a) and against column base gap opening in Figure 11.5(b). In Figure 11.5(b), positive values of *OM* correspond to $\Delta_{gap,S}$, and negative values of *OM* correspond to $\Delta_{gap,N}$. Figure 11.6 shows the correlation of the PT bar forces at each PT bar location. Figure 11.7 shows the correlation of the base shear (Figure 11.7(a)) and the overturning moment (Figure 11.7(b)). Correlation of α_n for each mode of vibration is shown in Figure 11.8. Figures 11.9 and 11.10 show the correlation of the south and north brace force response for each story.

11.2.1.2 DBE_5108-090_12-31-2009

The correlation of the response of the calibrated model to DBE_5108-090 and the experimental results from DBE_5108-090_12-31-2009 is shown in Figures 11.11 through 11.18. Figure 11.11 shows the correlation of the floor displacement response. Figure 11.12 shows the correlation of the column base gap-opening displacements. The hysteretic response is shown in Figure 11.13; overturning moment is plotted against roof drift in Figure 11.13(a) and against column base gap opening in Figure 11.13(b). In Figure 11.13(b), positive values of *OM* correspond to $\Delta_{gap,S}$, and negative values of *OM* correspond to $\Delta_{gap,N}$. Figure 11.14 shows the correlation of the PT bar forces. Figure 11.15 shows the correlation of the base shear (Figure 11.15(a)) and the overturning moment (Figure 11.15(b)). Correlation of α_n is shown in Figure 11.16. Figures 11.17 and 11.18 show the correlation of the south and north brace force response.

11.2.1.3 DBE_h-shp270_12-31-2009

The correlation of the response of the calibrated model to DBE_h-shp270 and the experimental results from DBE_h-shp270_12-31-2009 is shown in Figures 11.19 through 11.26. Figure 11.19 shows the correlation of the floor displacement response. Figure 11.20 shows the correlation of the column base gap-opening displacements. The hysteretic response is shown in Figure 11.21; overturning moment is plotted against roof drift in Figure 11.21(a) and against column base gap opening in Figure 11.21(b). In Figure 11.21(b), positive values of OM correspond to $\Delta_{gap,S}$, and negative values of OM correspond to $\Delta_{gap,N}$. Figure 11.22 shows the correlation of the PT bar forces. Figure 11.23 shows the correlation of the base shear (Figure 11.23(a)) and the overturning moment (Figure 11.23(b)). Correlation of α_n is shown in Figure 11.24. Figures 11.25 and 11.26 show the correlation of the south and north brace force response.

11.2.1.4 DBE_arl090_01-06-2010

The correlation of the response of the calibrated model to DBE_arl090 and the experimental results from DBE_arl090_01-06-2010 is shown in Figures 11.27 through 11.34. Figure 11.27 shows the correlation of the floor displacement response. Figure 11.28 shows the correlation of the column base gap-opening displacements. The hysteretic response is shown in Figure 11.29; overturning moment is plotted against roof drift in Figure 11.29(a) and against column base gap opening in Figure 11.29(b). In Figure 11.29(b), positive values of OM correspond to $\Delta_{gap,S}$, and negative values of OM correspond to $\Delta_{gap,N}$. Figure 11.30 shows the correlation of the PT bar forces. Figure

11.31 shows the correlation of the base shear (Figure 11.31(a)) and the overturning moment (Figure 11.31(b)). Correlation of α_n is shown in Figure 11.32. Figures 11.33 and 11.34 show the correlation of the south and north brace force response.

11.2.1.5 DBE_nr-pel360_01-08-2010

The correlation of the response of the calibrated model to DBE_nr-pel360 and the experimental results from DBE_nr-pel360_01-08-2010 is shown in Figures 11.35 through 11.42. Figure 11.35 shows the correlation of the floor displacement response. Figure 11.36 shows the correlation of the column base gap-opening displacements. The hysteretic response is shown in Figure 11.37; overturning moment is plotted against roof drift in Figure 11.37(a) and against column base gap opening in Figure 11.37(b). In Figure 11.37(b), positive values of OM correspond to $\Delta_{gap,S}$, and negative values of OM correspond to $\Delta_{gap,N}$. Figure 11.38 shows the correlation of the PT bar forces. Figure 11.39 shows the correlation of the base shear (Figure 11.39(a)) and the overturning moment (Figure 11.39(b)). Correlation of α_n is shown in Figure 11.40. Figures 11.41 and 11.42 show the correlation of the south and north brace force response.

11.2.2 Correlation of MCE-Level Response

11.2.2.1 MCE_stn110_01-07-2010

The correlation of the response of the calibrated model to MCE_stn110 and the experimental results from MCE_stn110_01-07-2010 is shown in Figures 11.43 through 11.50. Figure 11.43 shows the correlation of the floor displacement response. Figure 11.44 shows the correlation of the column base gap-opening displacements. The

hysteretic response is shown in Figure 11.45; overturning moment is plotted against roof drift in Figure 11.45(a) and against column base gap opening in Figure 11.45(b). In Figure 11.45(b), positive values of *OM* correspond to $\Delta_{gap,S}$, and negative values of *OM* correspond to $\Delta_{gap,N}$. Figure 11.46 shows the correlation of the PT bar forces. Figure 11.47 shows the correlation of the base shear (Figure 11.47(a)) and the overturning moment (Figure 11.47(b)). Correlation of α_n is shown in Figure 11.48. Figures 11.49 and 11.50 show the correlation of the south and north brace force response.

11.2.2.2 MCE_a-tmz270_01-07-2010

The correlation of the response of the calibrated model to MCE_a-tmz270 and the experimental results from MCE_a-tmz270_01-07-2010 is shown in Figures 11.51 through 11.58. Figure 11.51 shows the correlation of the floor displacement response. Figure 11.52 shows the correlation of the column base gap-opening displacements. The hysteretic response is shown in Figure 11.53; overturning moment is plotted against roof drift in Figure 11.53(a) and against column base gap opening in Figure 11.53(b). In Figure 11.53(b), positive values of *OM* correspond to $\Delta_{gap,S}$, and negative values of *OM* correspond to $\Delta_{gap,N}$. Figure 11.54 shows the correlation of the PT bar forces. Figure 11.55 shows the correlation of the base shear (Figure 11.55(a)) and the overturning moment (Figure 11.55(b)). Correlation of α_n is shown in Figure 11.56. Figures 11.57 and 11.58 show the correlation of the south and north brace force response.

11.2.2.3 MCE_lp-hda255_02-02-2010

The correlation of the response of the calibrated model to MCE_lp-hda255 and the experimental results from MCE_lp-hda255_02-02-2010 is shown in Figures 11.59 through 11.66. Figure 11.59 shows the correlation of the floor displacement response. Figure 11.60 shows the correlation of the column base gap-opening displacements. The hysteretic response is shown in Figure 11.61; overturning moment is plotted against roof drift in Figure 11.61(a) and against column base gap opening in Figure 11.61(b). In Figure 11.61(b), positive values of OM correspond to $\Delta_{gap,S}$, and negative values of OM correspond to $\Delta_{gap,N}$. Figure 11.62 shows the correlation of the PT bar forces. Figure 11.63 shows the correlation of the base shear (Figure 11.63(a)) and the overturning moment (Figure 11.63(b)). Correlation of α_n is shown in Figure 11.64. Figures 11.65 and 11.66 show the correlation of the south and north brace force response.

11.2.2.4 MCE_cap000_01-11-2010

The correlation of the response of the calibrated model to MCE_cap000 and the experimental results from MCE_cap000_01-11-2010 is shown in Figures 11.67 through 11.74. Figure 11.67 shows the correlation of the floor displacement response. Figure 11.68 shows the correlation of the column base gap-opening displacements. The hysteretic response is shown in Figure 11.69; overturning moment is plotted against roof drift in Figure 11.69(a) and against column base gap opening in Figure 11.69(b). In Figure 11.69(b), positive values of OM correspond to $\Delta_{gap,S}$, and negative values of OM correspond to $\Delta_{gap,N}$. Figure 11.70 shows the correlation of the PT bar forces. Figure

11.71 shows the correlation of the base shear (Figure 11.71(a)) and the overturning moment (Figure 11.71(b)). Correlation of α_n is shown in Figure 11.72. Figures 11.73 and 11.74 show the correlation of the south and north brace force response.

11.2.2.5 MCE_h-cpe237_01-13-2010

The correlation of the response of the calibrated model to MCE_h-cpe237 and the experimental results from MCE_h-cpe237_01-13-2010 is shown in Figures 11.75 through 11.82. Figure 11.75 shows the correlation of the floor displacement response. Figure 11.76 shows the correlation of the column base gap-opening displacements. The hysteretic response is shown in Figure 11.77; overturning moment is plotted against roof drift in Figure 11.77(a) and against column base gap opening in Figure 11.77(b). In Figure 11.77(b), positive values of *OM* correspond to $\Delta_{gap,S}$, and negative values of *OM* correspond to $\Delta_{gap,N}$. Figure 11.78 shows the correlation of the PT bar forces. Figure 11.79 shows the correlation of the base shear (Figure 11.79(a)) and the overturning moment (Figure 11.79(b)). Correlation of α_n is shown in Figure 11.80. Figures 11.81 and 11.82 show the correlation of the south and north brace force response.

11.2.3 Correlation of Extreme MCE-Level Response: xMCE_tak090_02-05-2010

As discussed in Section 8.4.7, the coefficient of friction used in the gap-friction elements that model the lateral-load bearings is 0.45. However, as shown in Section 10.3.4, damage to the lateral-load bearings (i.e., the brass friction plates) increases the effective coefficient of friction. Therefore, two numerical simulations of the response of the SC-CBF test structure to xMCE_tak090 were performed, considering two different values of

μ: (1) μ equal to 0.45, the same value used for the numerical simulations of the other ground motions; and (2) μ equal to 0.55, to reflect the increase in the effective coefficient of friction due to the damage to the friction plates. The results of these numerical simulations are presented in this section.

11.2.3.1 Correlation with $\mu = 0.45$

The correlation of the response of the calibrated model, with μ equal to 0.45, to xMCE_tak090 and the experimental results from xMCE_tak090_02-05-2010 is shown in Figures 11.83 through 11.90. Figure 11.83 shows the correlation of the floor displacement response. Figure 11.84 shows the correlation of the column base gap-opening displacements. The hysteretic response is shown in Figure 11.85; overturning moment is plotted against roof drift in Figure 11.85(a) and against column base gap opening in Figure 11.85(b). In Figure 11.85(b), positive values of *OM* correspond to $\Delta_{gap,S}$, and negative values of *OM* correspond to $\Delta_{gap,N}$. Figure 11.86 shows the correlation of the PT bar forces. Figure 11.87 shows the correlation of the base shear (Figure 11.87(a)) and the overturning moment (Figure 11.87(b)). Correlation of α_n is shown in Figure 11.88. Figures 11.89 and 11.90 show the correlation of the south and north brace force response.

Over the first five seconds of response, the results of the numerical analysis of the calibrated model closely match the response of the hybrid simulation. However, at the negative peak response just after t = 5 s, the numerical analysis response diverges from the hybrid simulation response. From this point on, the numerical analysis response does

not agree with the response of the test structure. After the laboratory hybrid simulation was performed, the lateral-load bearings were inspected and damage to the brass friction plates was discovered. This damage is shown in Figure 11.91, which shows a view from underneath the north lateral-load bearing at the fourth floor. The damage shown is typical damage to the brass friction plates at the upper floors after xMCE_tak090_02-05-2010. The brass friction plates, as shown in Figure 11.91, are located on the SC-CBF columns, and the steel bearings are located on the gravity columns. The gouging indicated in the Figure 11.91 is from the large lateral forces on the SC-CBF at the fourth floor near the time of the peak displacement; the combination of the large displacement and the large contact force in the lateral-load bearing caused this damage to the brass friction plate.

11.2.3.2 Correlation with $\mu = 0.55$

As previously mentioned, the damage to the bearing plates shown in Figure 11.91 increased the effective coefficient of friction at the lateral-load bearings. To model this effect, the coefficient of friction in the calibrated model was increased from 0.45 to 0.55 and a second numerical analysis of the response to the xMCE_tak090 ground motion was conducted.

The correlation of the response of the calibrated model, with μ equal to 0.55, to xMCE_tak090 and the experimental results from xMCE_tak090_02-05-2010 is shown in Figures 11.92 through 11.99. Figure 11.92 shows the correlation of the floor displacement response. Figure 11.93 shows the correlation of the column base gap-opening displacements. The hysteretic response is shown in Figure 11.94; overturning

moment is plotted against roof drift in Figure 11.94(a) and against column base gap opening in Figure 11.94(b). In Figure 11.94(b), positive values of *OM* correspond to $\Delta_{gap,S}$, and negative values of *OM* correspond to $\Delta_{gap,N}$. Figure 11.95 shows the correlation of the PT bar forces. Figure 11.96 shows the correlation of the base shear (Figure 11.96(a)) and the overturning moment (Figure 11.96(b)). Correlation of α_n is shown in Figure 11.97. Figures 11.98 and 11.99 show the correlation of the south and north brace force response.

Comparing Figure 11.83 with Figure 11.92, the floor displacements after t = 5 s are predicted better by the model with a higher coefficient of friction (μ equal to 0.55) at the lateral-load bearings. For the model with the original coefficient of friction (μ equal to 0.45), the response from the numerical analysis was greater than the experimental response.

11.3 Summary

The correlation of the results from nonlinear analysis and the results from the laboratory hybrid simulations is strong. Calibrating the gaps at the lateral-load bearings, the initial PT forces, and the PT yield forces of the SC-CBF to the initial conditions of the test structure in the laboratory improved the correlation between the numerical analysis results and the laboratory hybrid simulation results. The results show that the analytical model accurately reflects the behavior of the SC-CBF system, validating the nonlinear analyses presented in Chapter 5 for the SC-CBF configuration study and in Chapter 9 for

the predictions of the dynamic response of the SC-CBF for the DBE-level, MCE-level, and extreme MCE-level ground motions.

Table 11.1 – Summary of lateral-load bearing gap measurements for each hybrid simulation

Hybrid Simulation	Total Gap			
	First Floor (in)	Second Floor (in)	Third Floor (in)	Fourth Floor (in)
DBE_cls000_12-31-2009	0.0265	0.0225	0.0225	0.0420
DBE_5108-090_12-31-2009	0.0265	0.0225	0.0225	0.0420
DBE_h-shp270_12-31-2009	0.0265	0.0225	0.0225	0.0420
DBE_arl090_01-06-2010	0.0275	0.0125	0.0000	0.0000
MCE_stn110_01-07-2010	0.0255	0.0200	0.0000	0.0025
MCE_a-tmz270_01-07-2010	0.0315	0.0205	0.0000	0.0020
DBE_nr-pel360_01-08-2010	0.0375	0.0250	0.0000	0.0010
MCE_cap000_01-11-2010	0.0370	0.0275	0.0065	0.0060
MCE_h-cpe237_01-13-2010	0.0320	0.0165	0.0000	0.0000
MCE_lp-hda255_02-02-2010	0.0140	0.0180	0.0015	0.0045
xMCE_tak090_02-05-2010	0.0245	0.0150	0.0000	0.0045

Table 11.2 – Summary of initial PT force for each hybrid simulation

Hybrid Simulation	Initial PT Force		
	South PT Bars (kip)	Center PT Bars (kip)	North PT Bars (kip)
DBE_cls000_12-31-2009	84.3	84.4	84.5
DBE_5108-090_12-31-2009	84.3	84.5	84.5
DBE_h-shp270_12-31-2009	84.4	85.3	84.6
DBE_arl090_01-06-2010	83.7	82.8	82.4
MCE_stn110_01-07-2010	83.8	83.1	82.4
MCE_a-tmz270_01-07-2010	83.2	82.1	81.4
DBE_nr-pel360_01-08-2010	83.2	82.7	81.4
MCE_cap000_01-11-2010	82.9	82.2	81.1
MCE_h-cpe237_01-13-2010	83.0	82.4	81.1
MCE_lp-hda255_02-02-2010	85.2	84.4	85.2
xMCE_tak090_02-05-2010	82.8	82.2	80.9

Table 11.3 – Summary of PT force maxima and yield forces

Hybrid Simulation	South PT Bars		Center PT Bars		North PT Bars	
	Max Force (kip)	Input Yield Force (kip)	Max Force (kip)	Input Yield Force (kip)	Max Force (kip)	Input Yield Force (kip)
DBE_cls000_12-31-2009	128.8	235.0	123.1	222.0	123.3	215.0
DBE_5108-090_12-31-2009	139.4	235.0	132.5	222.0	131.9	215.0
DBE_h-shp270_12-31-2009	150.7	235.0	143.1	222.0	137.9	215.0
DBE_arl090_01-06-2010	168.1	235.0	174.3	222.0	186.3	215.0
DBE_nr-pel360_01-08-2010	152.3	235.0	143.4	222.0	145.0	215.0
MCE_stn110_01-07-2010	178.6	235.0	185.4	222.0	198.5	215.0
MCE_a-tmz270_01-07-2010	162.3	235.0	151.8	222.0	145.9	215.0
MCE_cap000_01-11-2010	213.4	235.0	209.3	222.0	**219.1**	215.0
MCE_h-cpe237_01-13-2010	204.6	235.0	191.5	222.0	189.5	**219.1**
xMCE_tak090_01-13-2010†	**245.1**	235.0	**243.7**	222.0	**233.9**	219.1
MCE_lp-hda255_02-02-2010	174.8	**245.1**	173.6	**243.7**	183.7	**233.9**
xMCE_tak090_02-03-2010*†	244.3	245.1	**243.7**	243.7	**235.8**	233.9
xMCE_tak090_02-05-2010	**250.0**	245.1	**275.4**	243.7	**242.8**	**235.8**

* – Simulation was not run to its full duration
† – Simulation is not presented in this dissertation

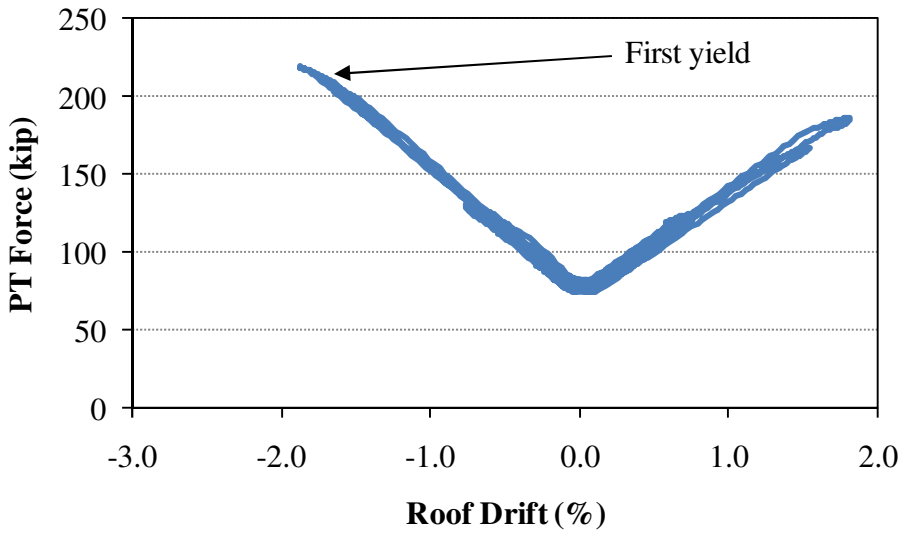

Figure 11.1 – North PT force plotted against roof drift response for hybrid simulation MCE_cap000_01-11-2010

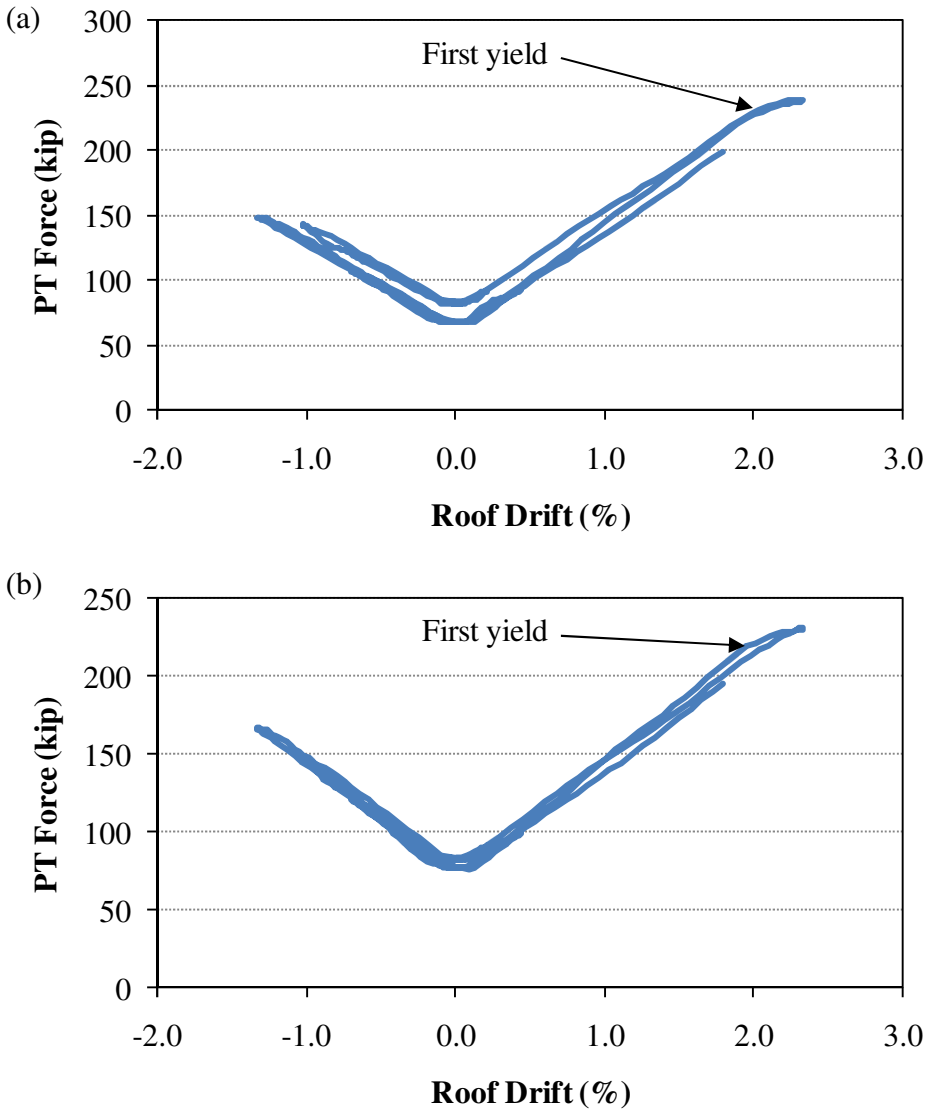

Figure 11.2 – PT force plotted against roof drift response for hybrid simulation xMCE_tak090_01-13-2010: (a) south PT force; (b) center PT force

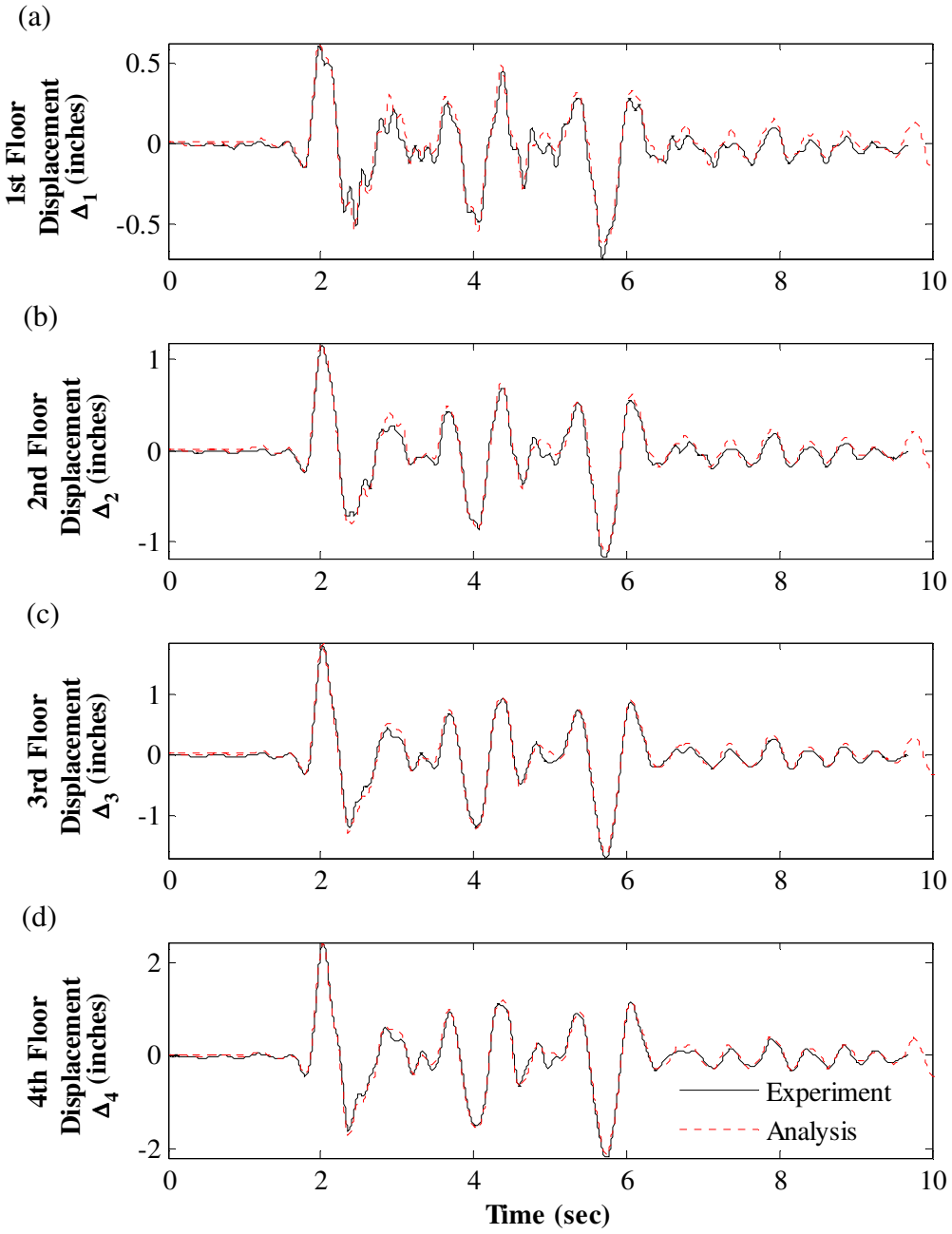

Figure 11.3 – Correlation of floor displacement response to DBE_cls000: (a) 1st floor; (b) 2nd floor; (c) 3rd floor; (d) 4th floor

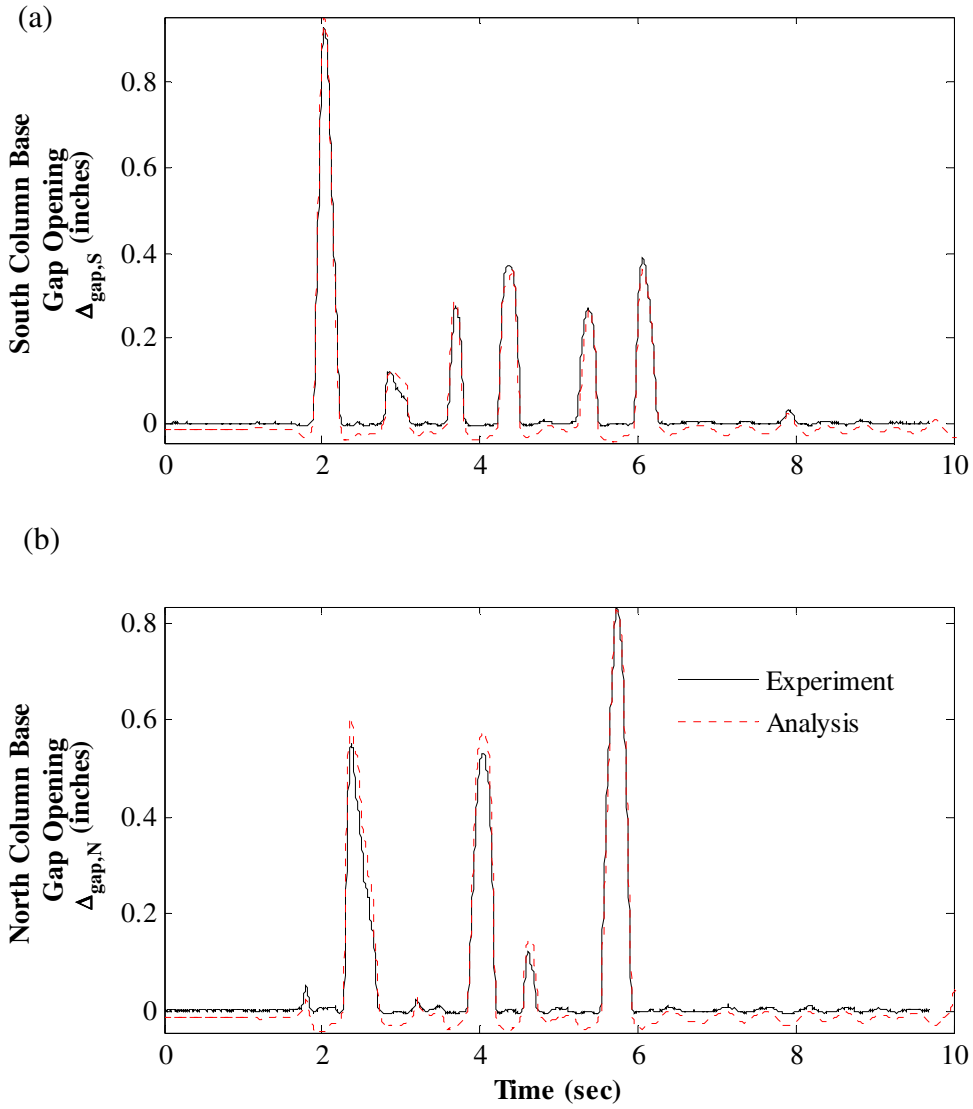

Figure 11.4 – Correlation of column base gap opening response to DBE_cls000: (a) at south column base; (b) at north column base

(a)

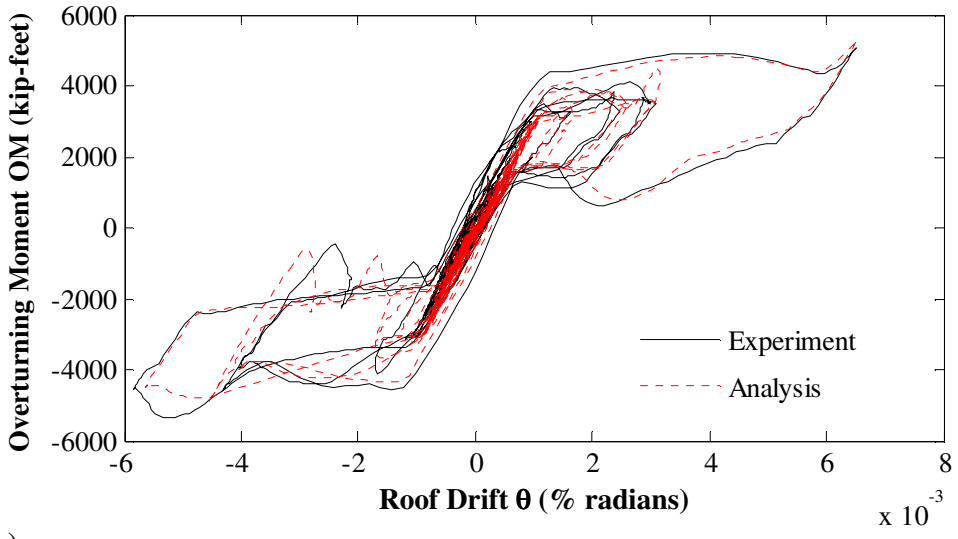

(b)

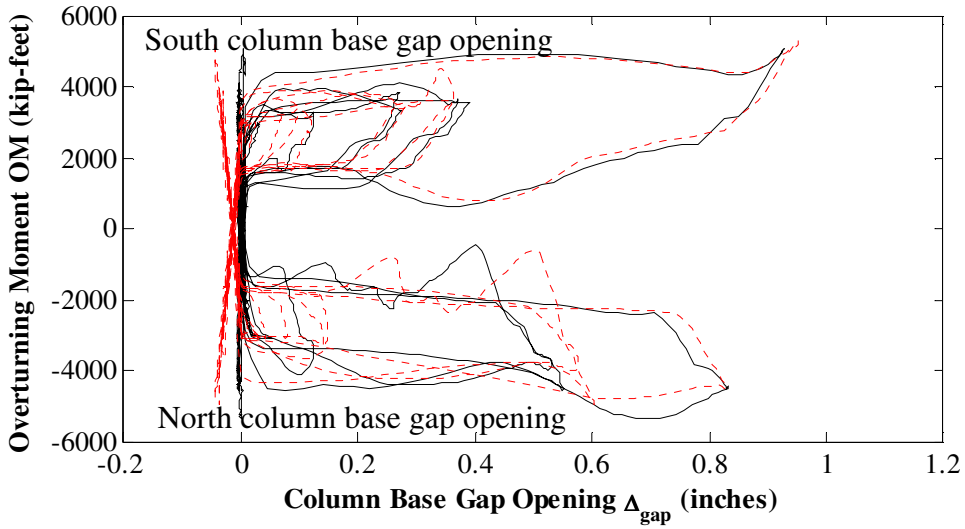

Figure 11.5 – Correlation of hysteretic response to DBE_cls000: (a) overturning moment versus roof drift; (b) overturning moment versus column base gap opening

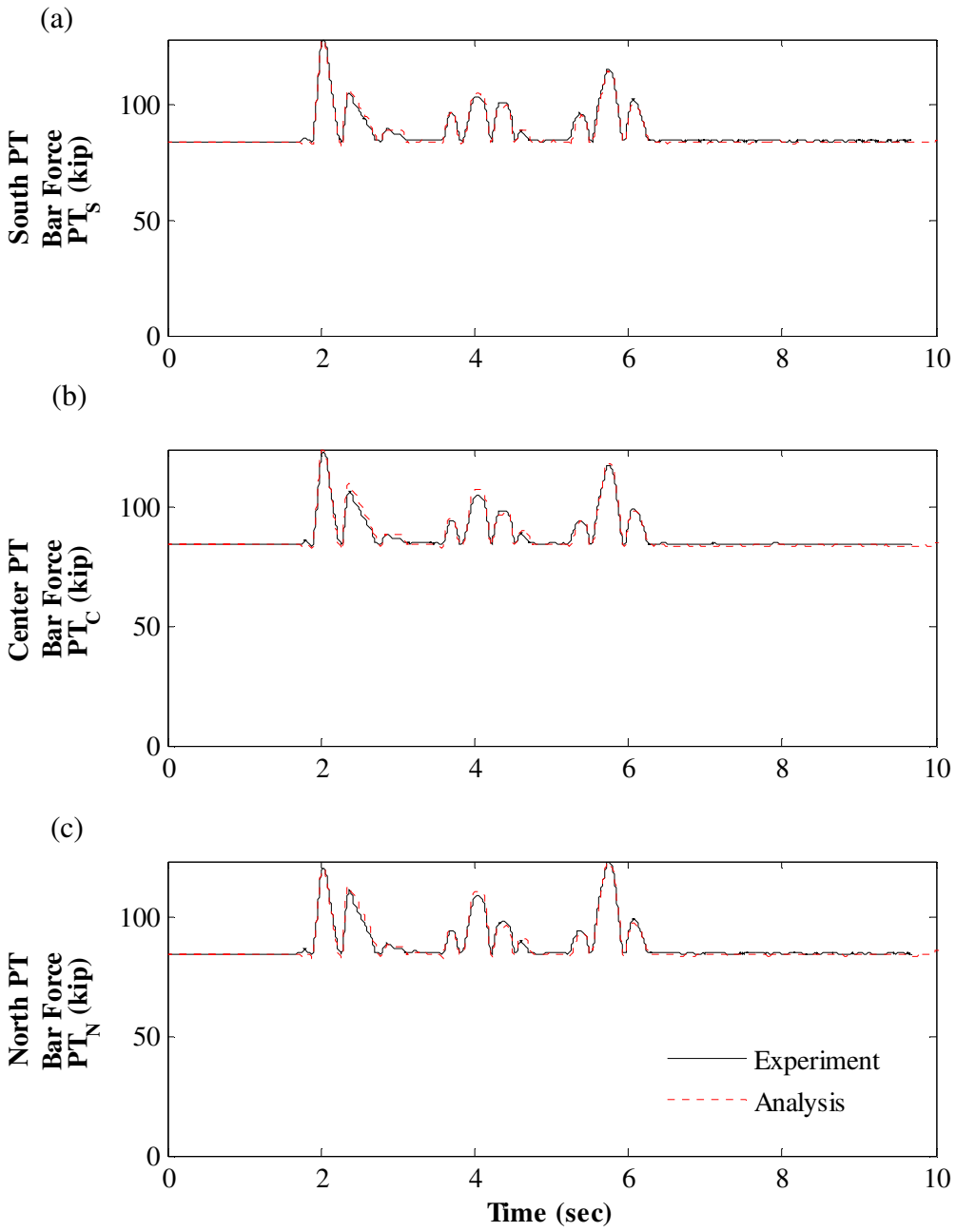

Figure 11.6 – Correlation of PT force response to DBE_cls000: (a) south PT bars; (b) center PT bars; (c) north PT bars

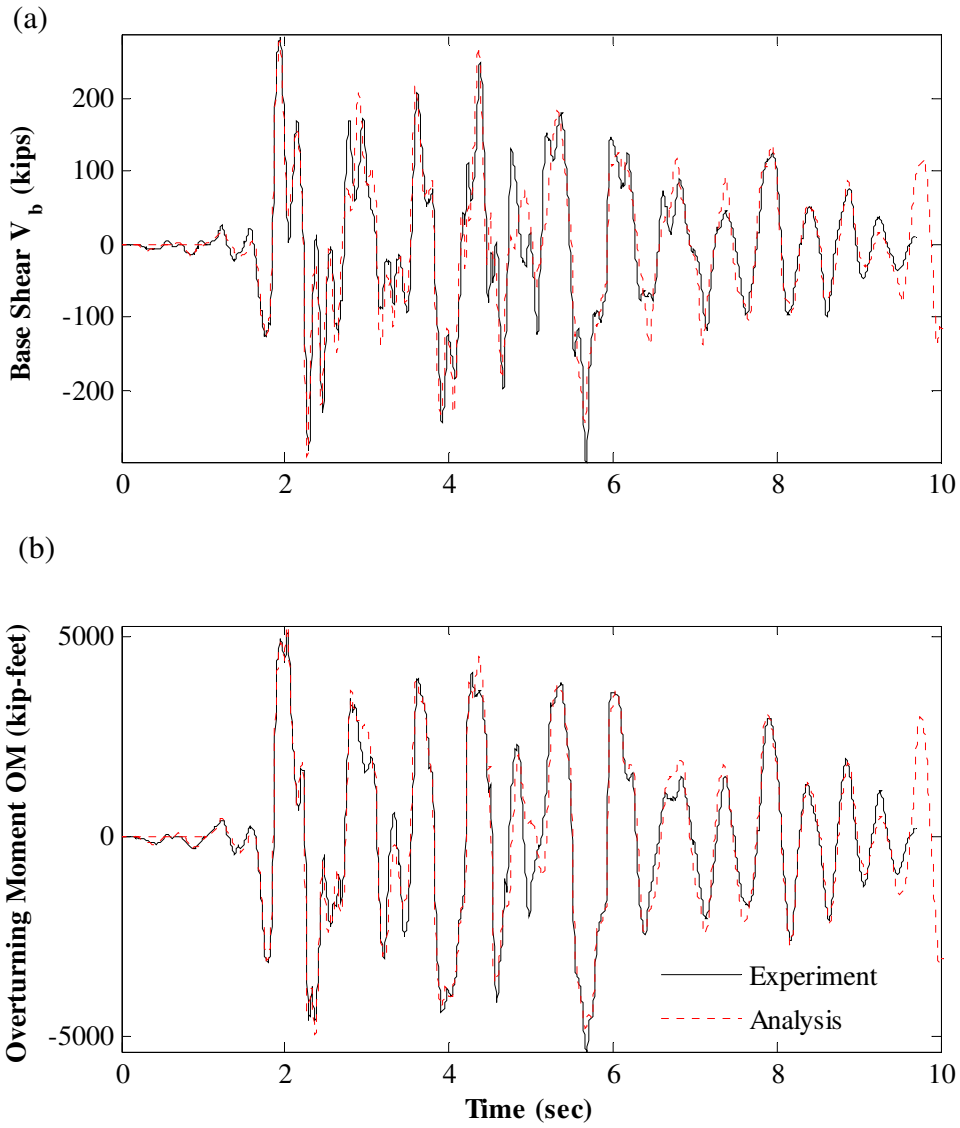

Figure 11.7 – DBE_cls000 response correlation: (a) base shear; (b) overturning moment

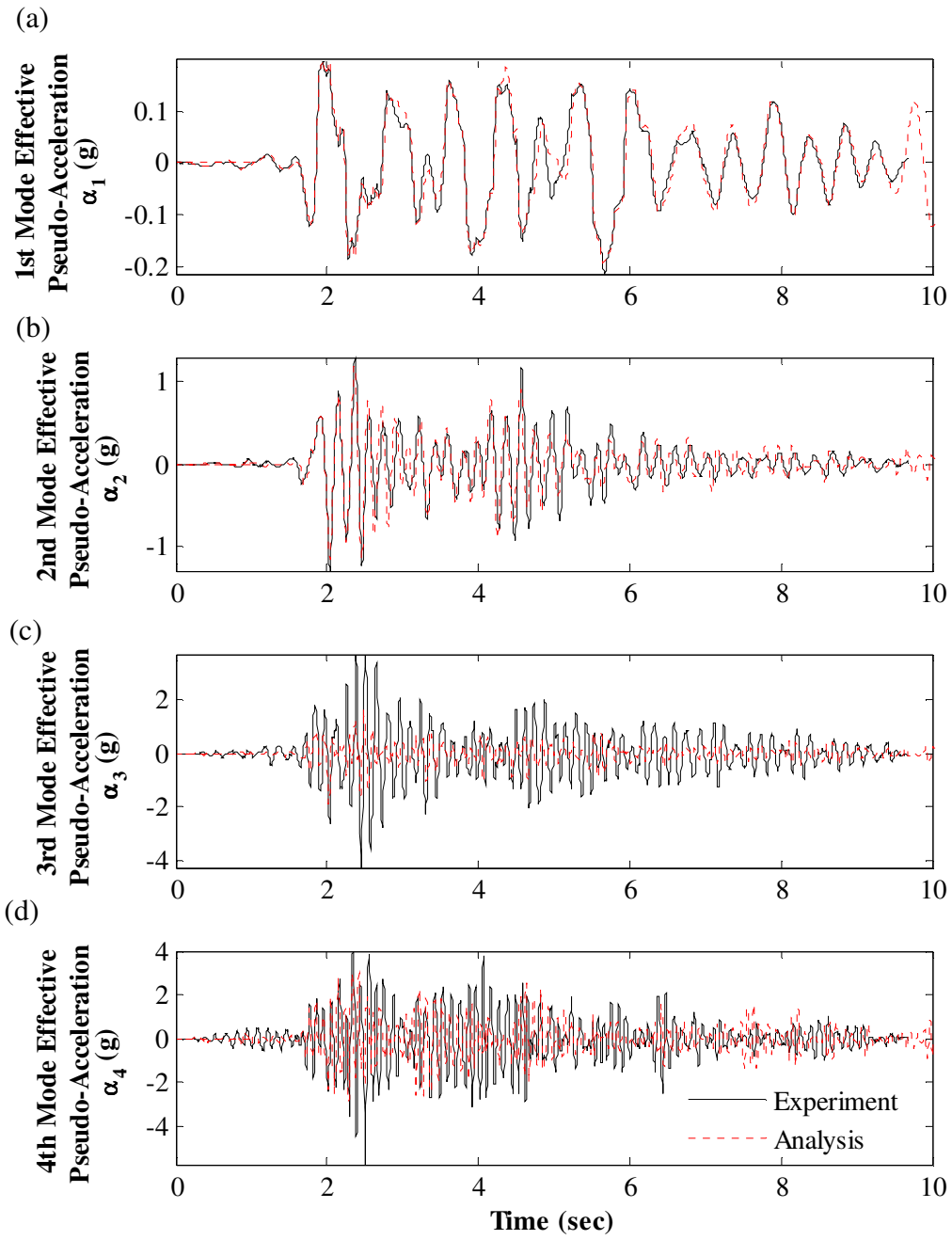

Figure 11.8 – Correlation of effective modal pseudo-acceleration response to DBE_cls000: (a) 1st mode; (b) 2nd mode; (c) 3rd mode; (d) 4th mode

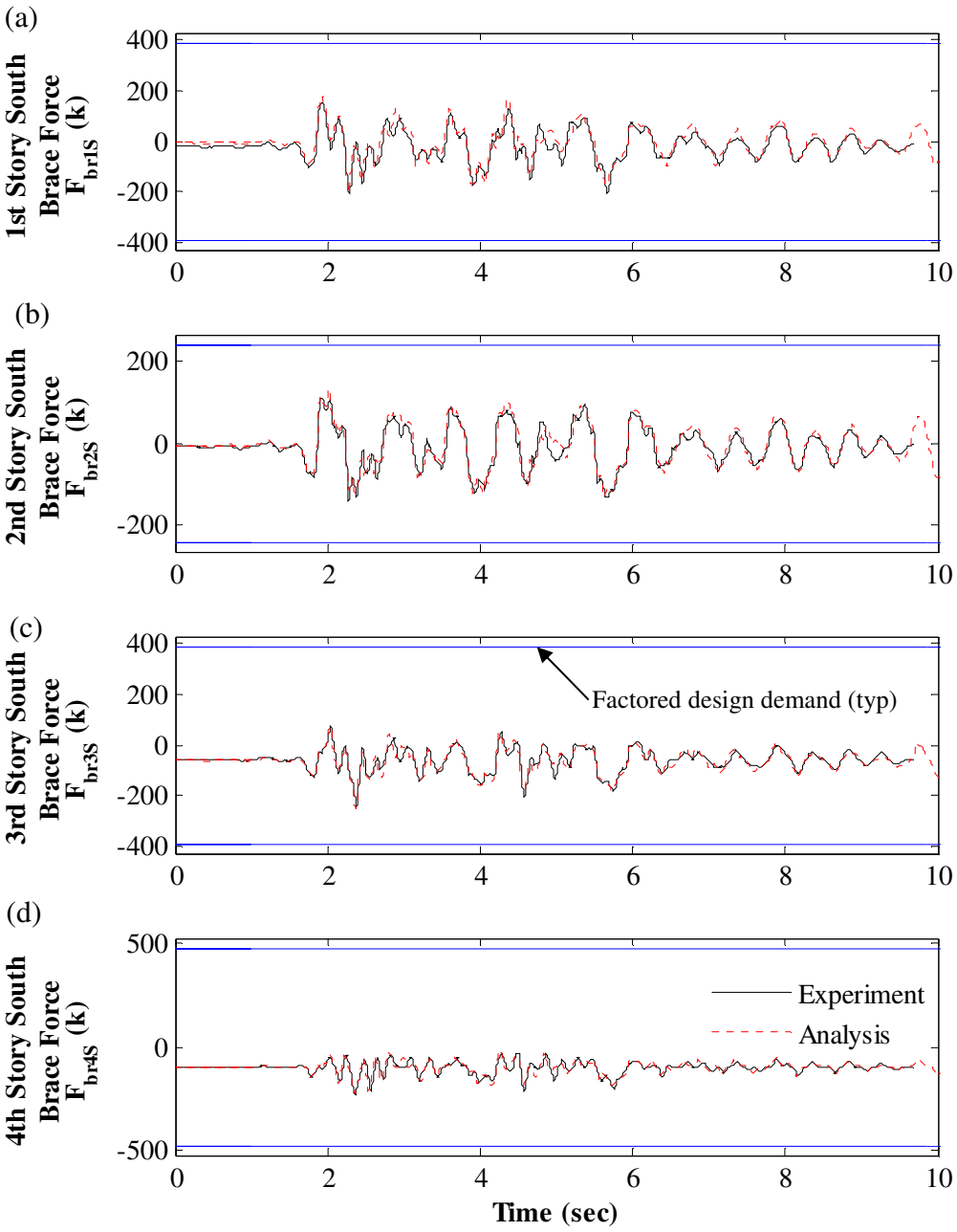

Figure 11.9 – Correlation of south brace axial force response to DBE_cls000: (a) 1st story; (b) 2nd story; (c) 3rd story; (d) 4th story

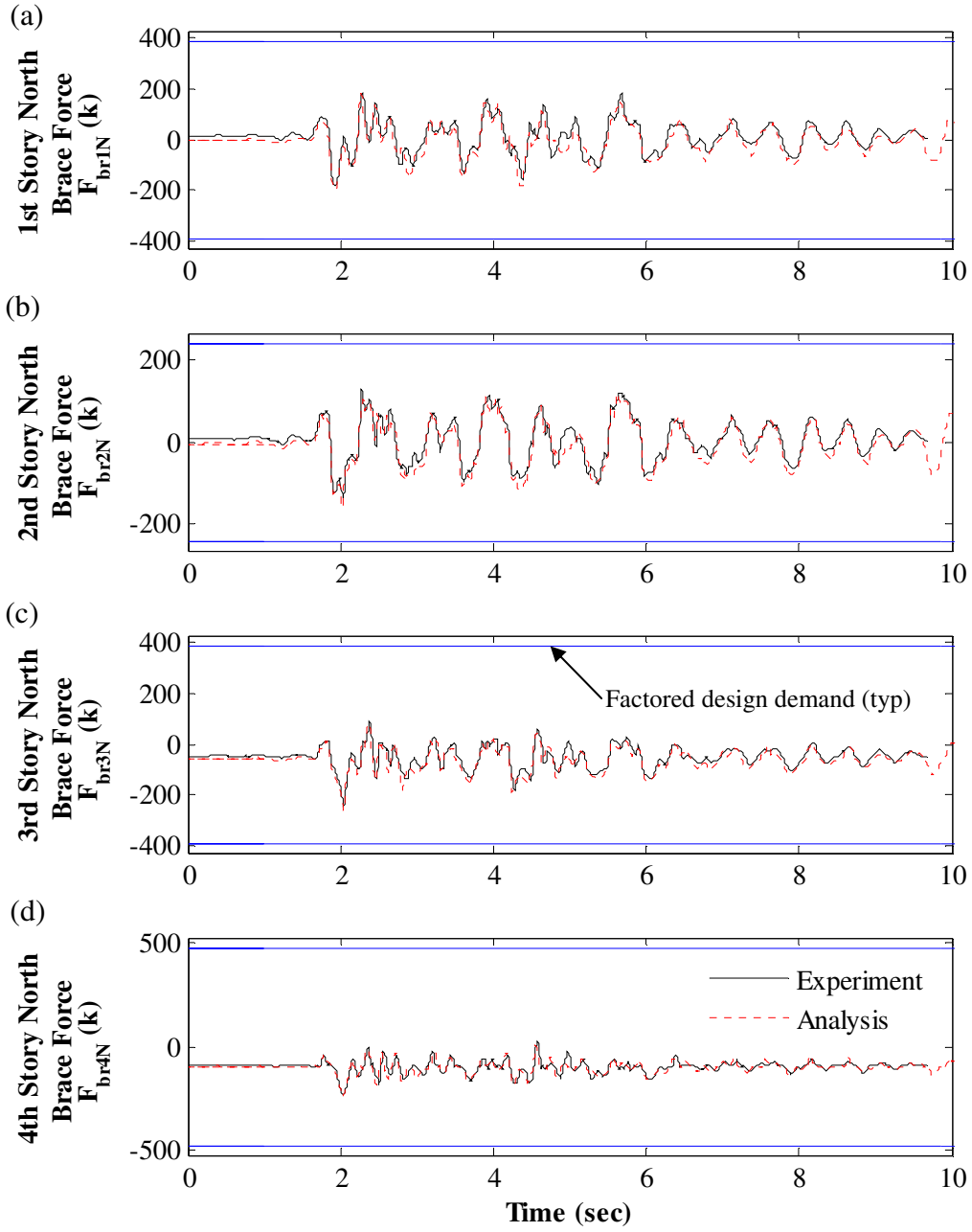

Figure 11.10 – Correlation of north brace axial force response to DBE_cls000: (a) 1st story; (b) 2nd story; (c) 3rd story; (d) 4th story

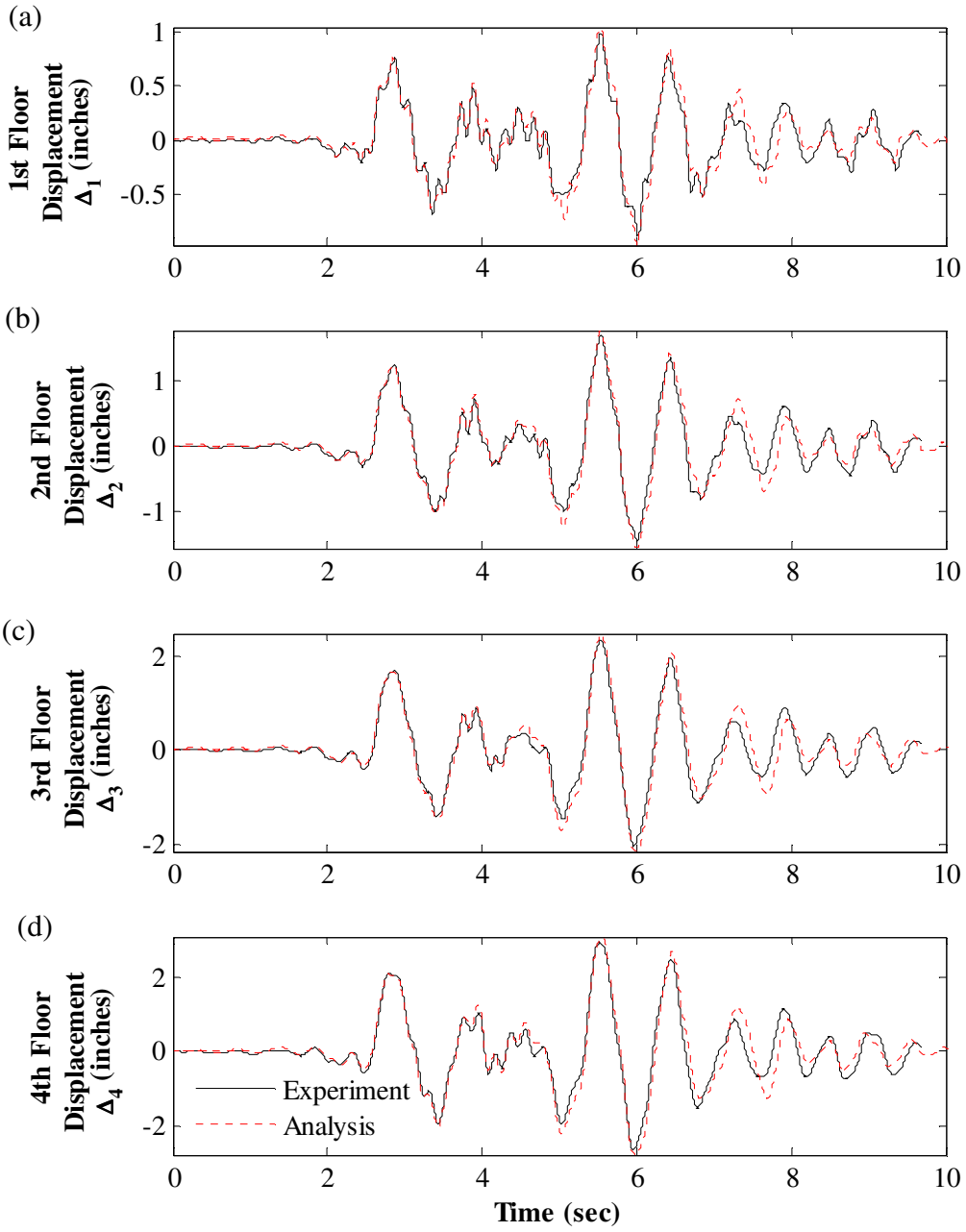

Figure 11.11 – Correlation of floor displacement response to DBE_5108-090: (a) 1st floor; (b) 2nd floor; (c) 3rd floor; (d) 4th floor

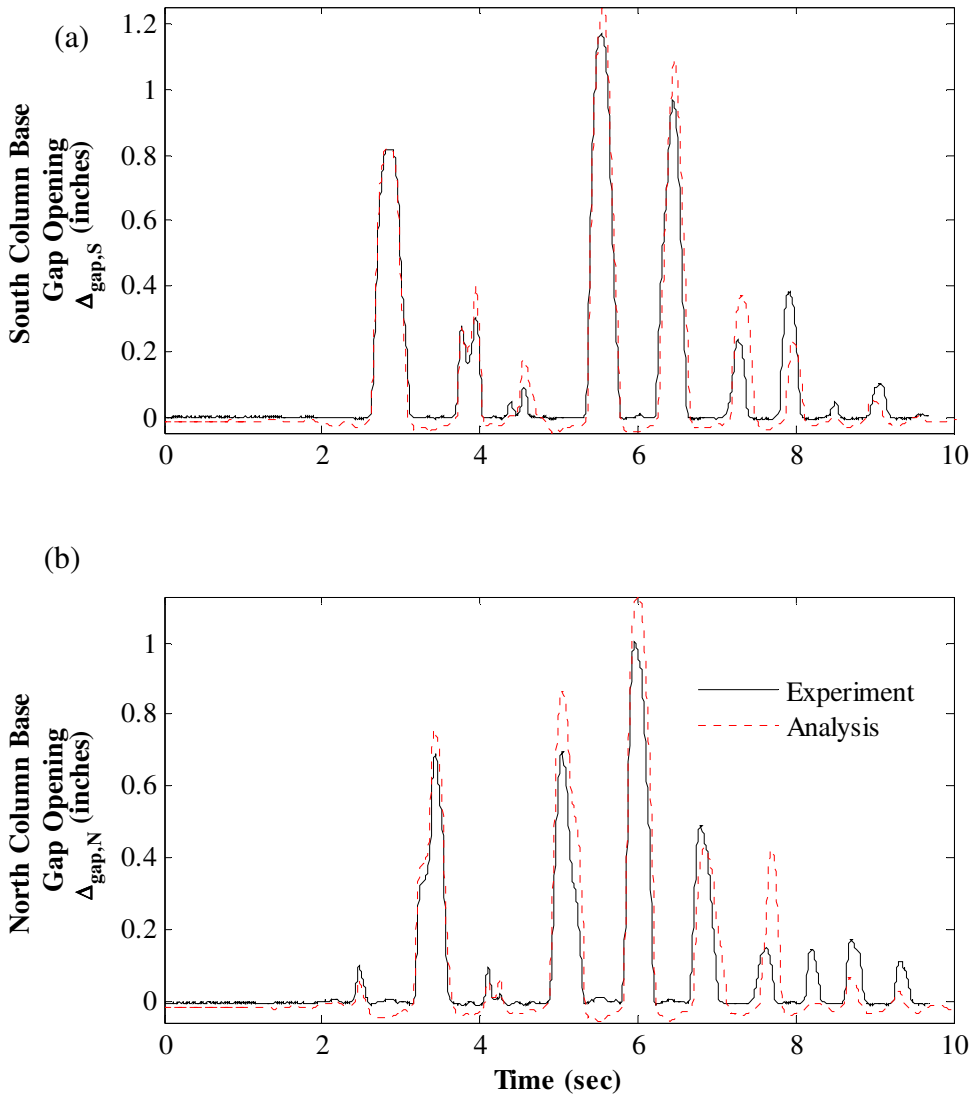

Figure 11.12 – Correlation of column base gap opening response to DBE_5108-090: (a) at south column base; (b) at north column base

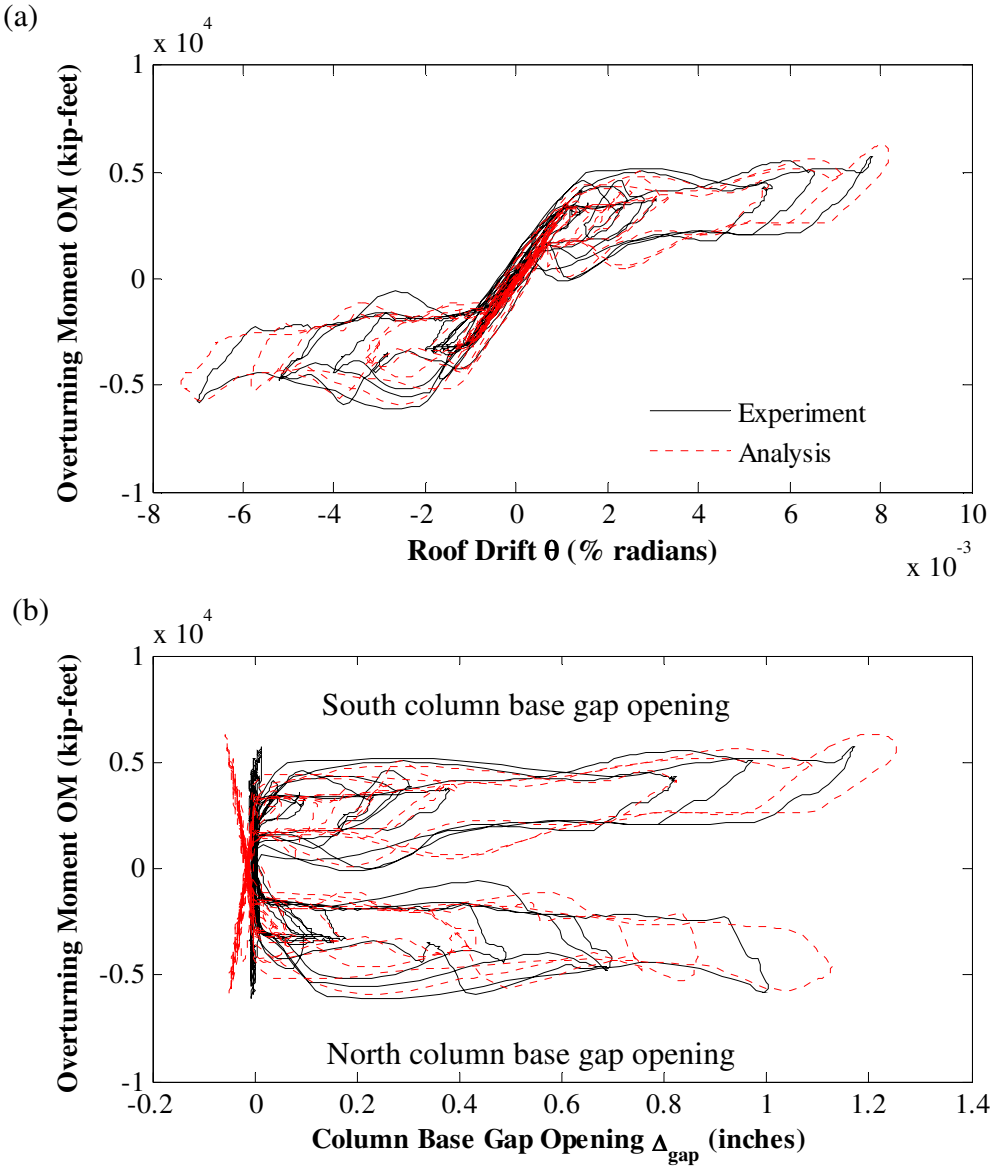

Figure 11.13 – Correlation of hysteretic response to DBE_5108-090: (a) overturning moment versus roof drift; (b) overturning moment versus column base gap opening

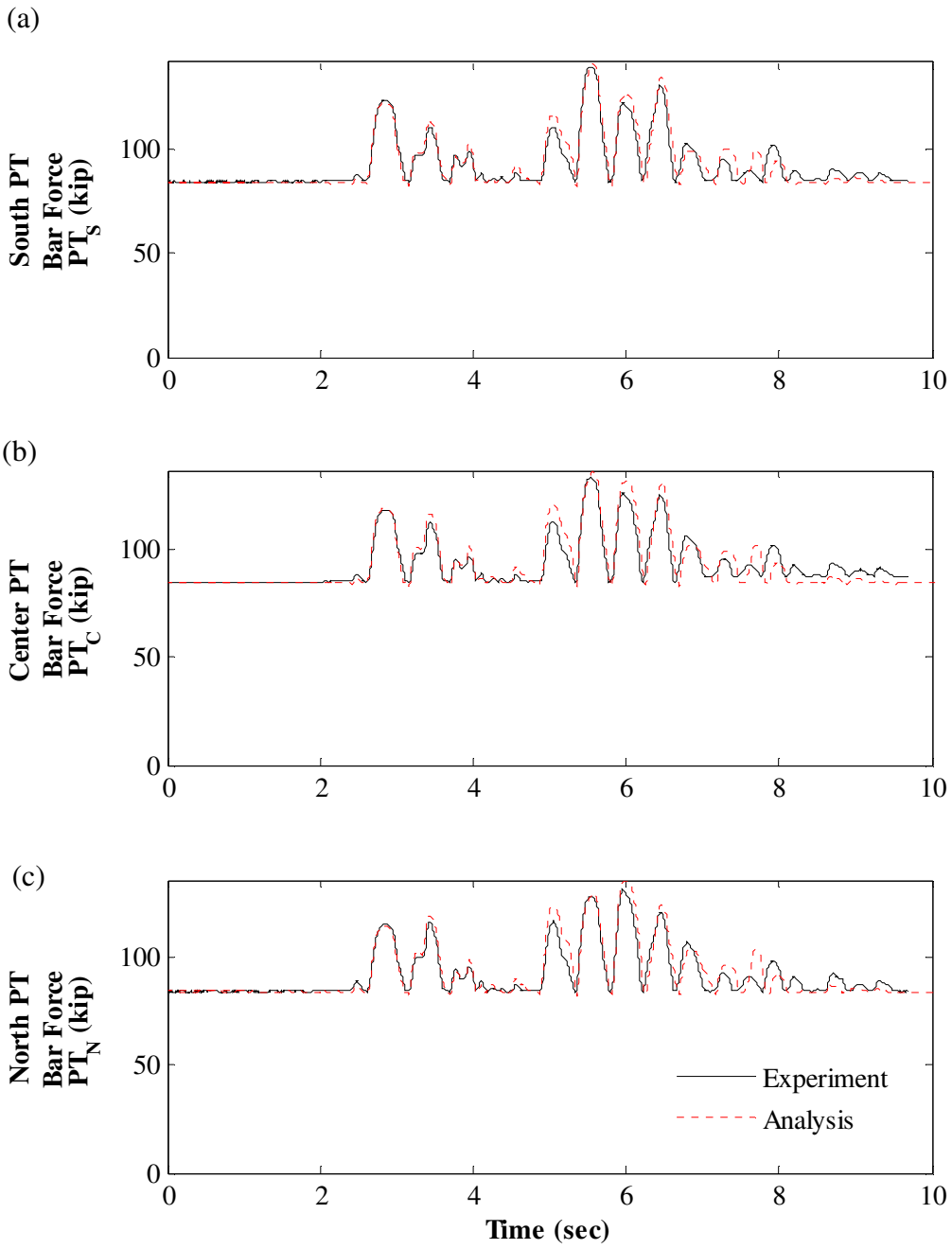

Figure 11.14 – Correlation of PT force response to DBE_5108-090: (a) south PT bars; (b) center PT bars; (c) north PT bars

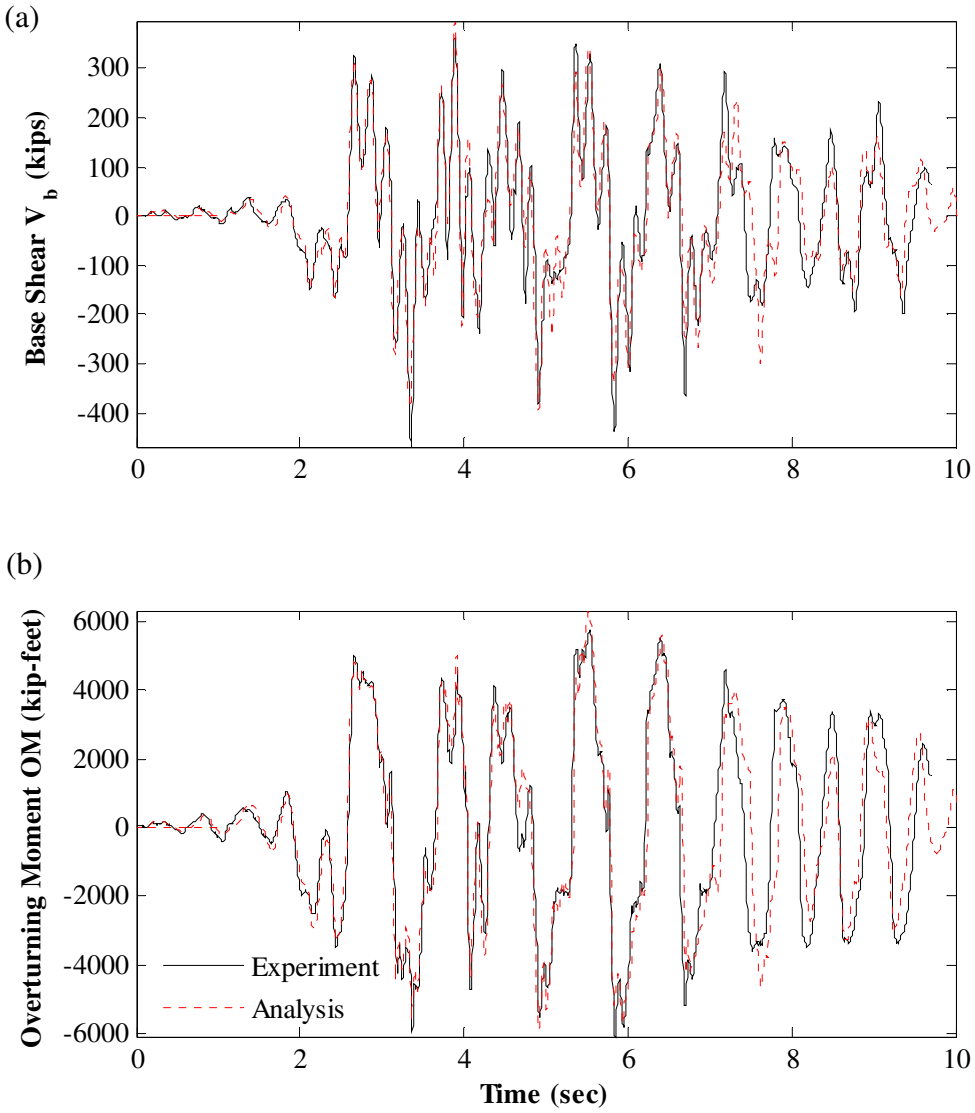

Figure 11.15 – DBE_5108-090 response correlation: (a) base shear; (b) overturning moment

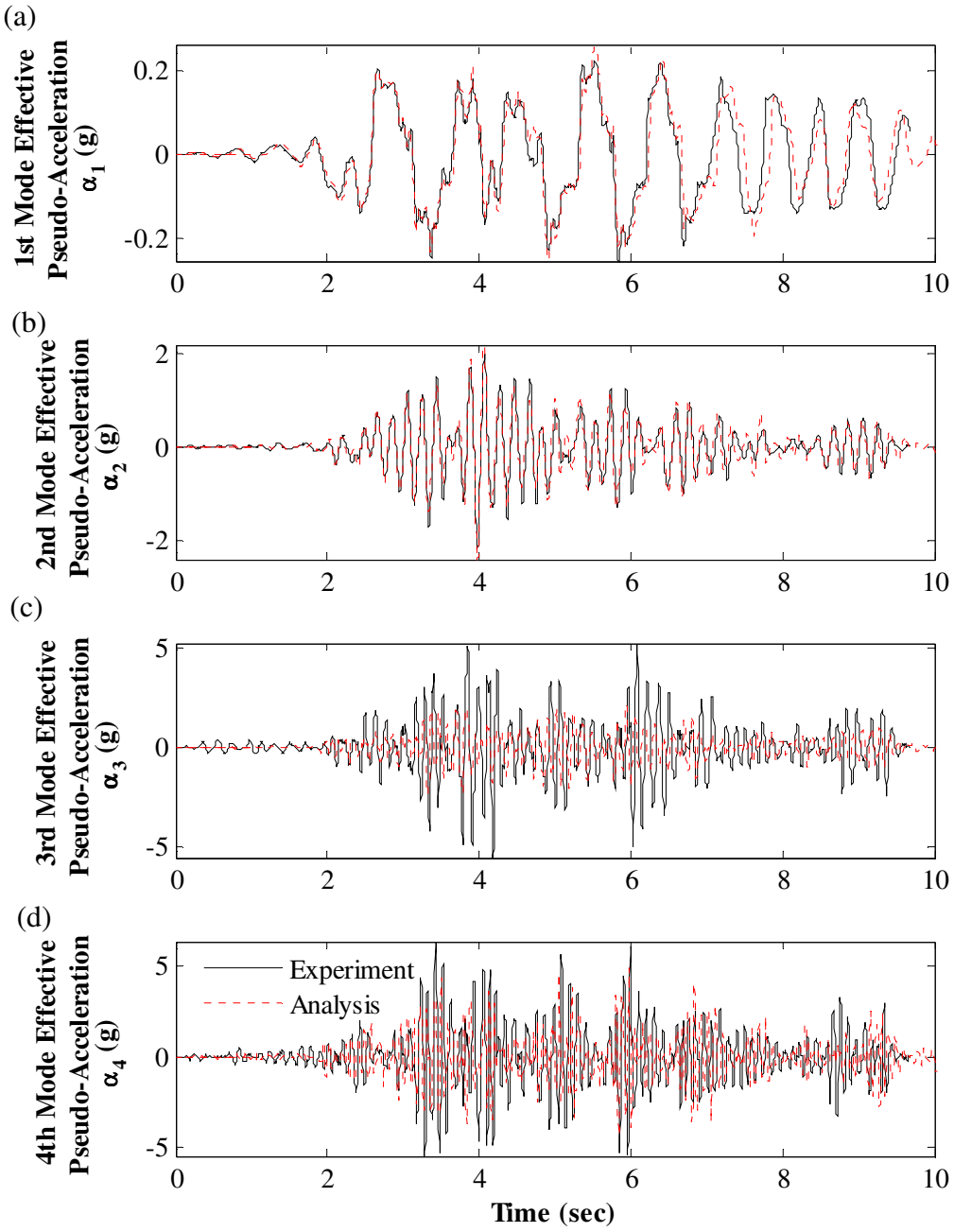

Figure 11.16 – Correlation of effective modal pseudo-acceleration response to DBE_5108-090: (a) 1st mode; (b) 2nd mode; (c) 3rd mode; (d) 4th mode

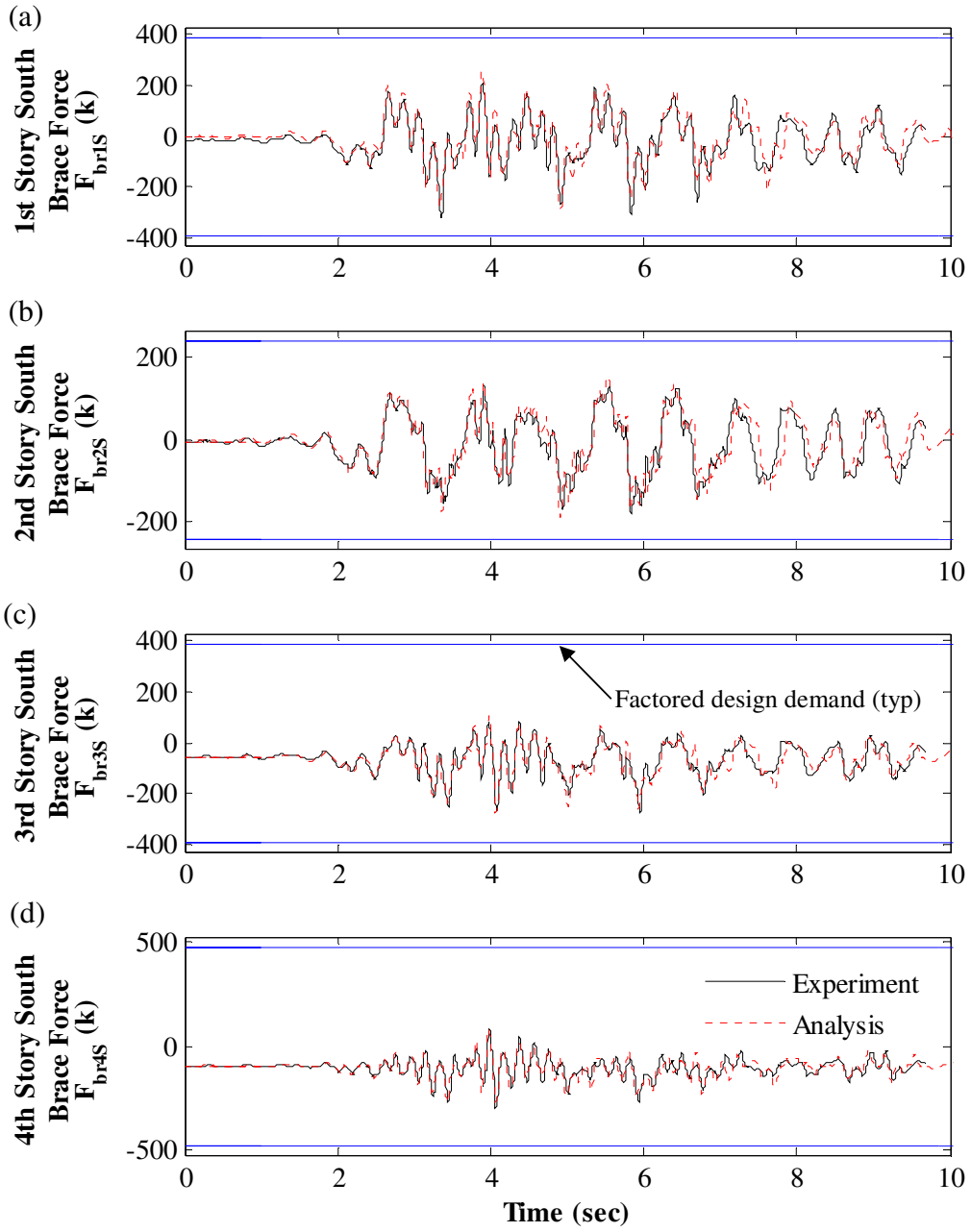

Figure 11.17 – Correlation of south brace axial force response to DBE_5108-090: (a) 1st story; (b) 2nd story; (c) 3rd story; (d) 4th story

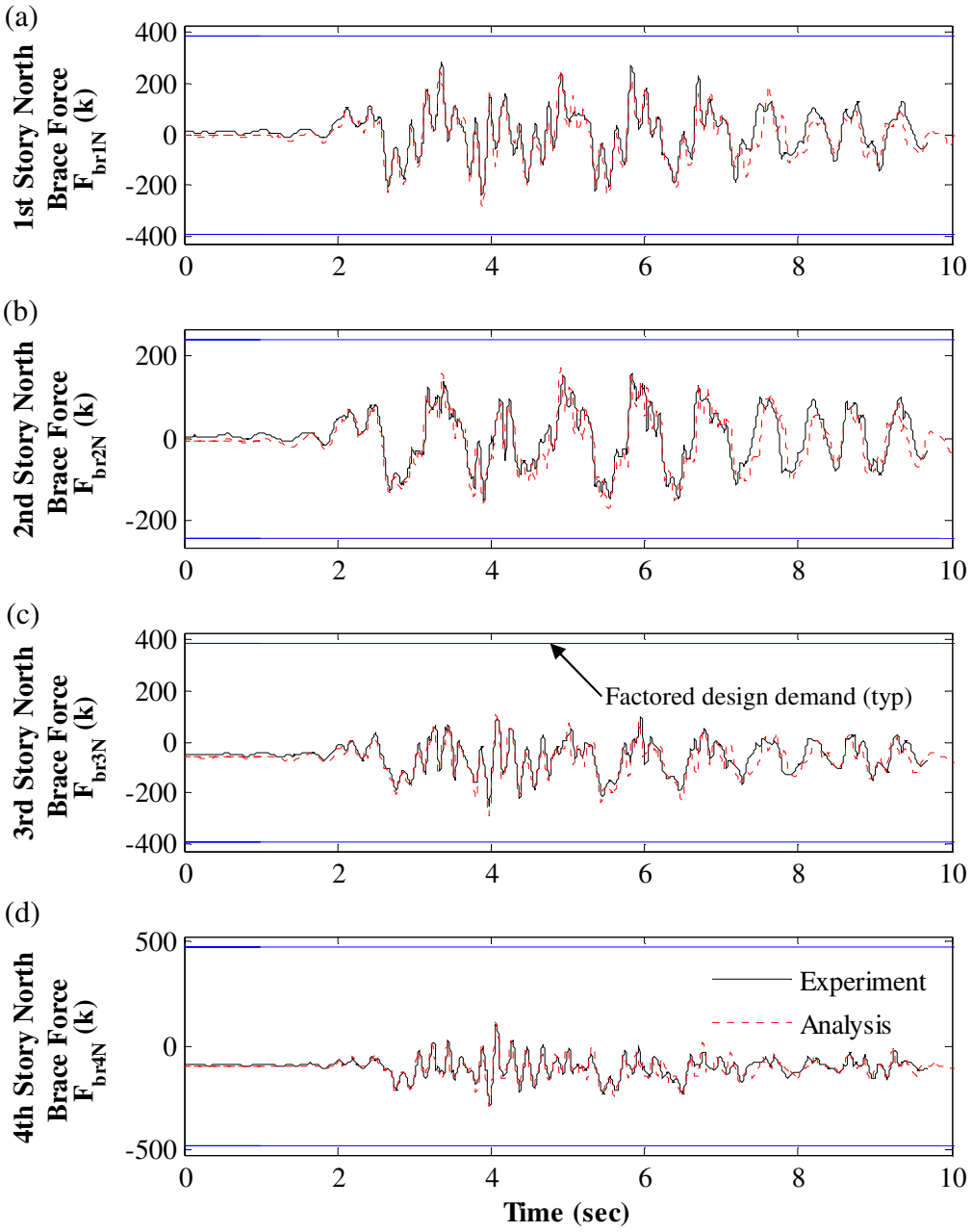

Figure 11.18 – Correlation of north brace axial force response to DBE_5108-090: (a) 1st story; (b) 2nd story; (c) 3rd story; (d) 4th story

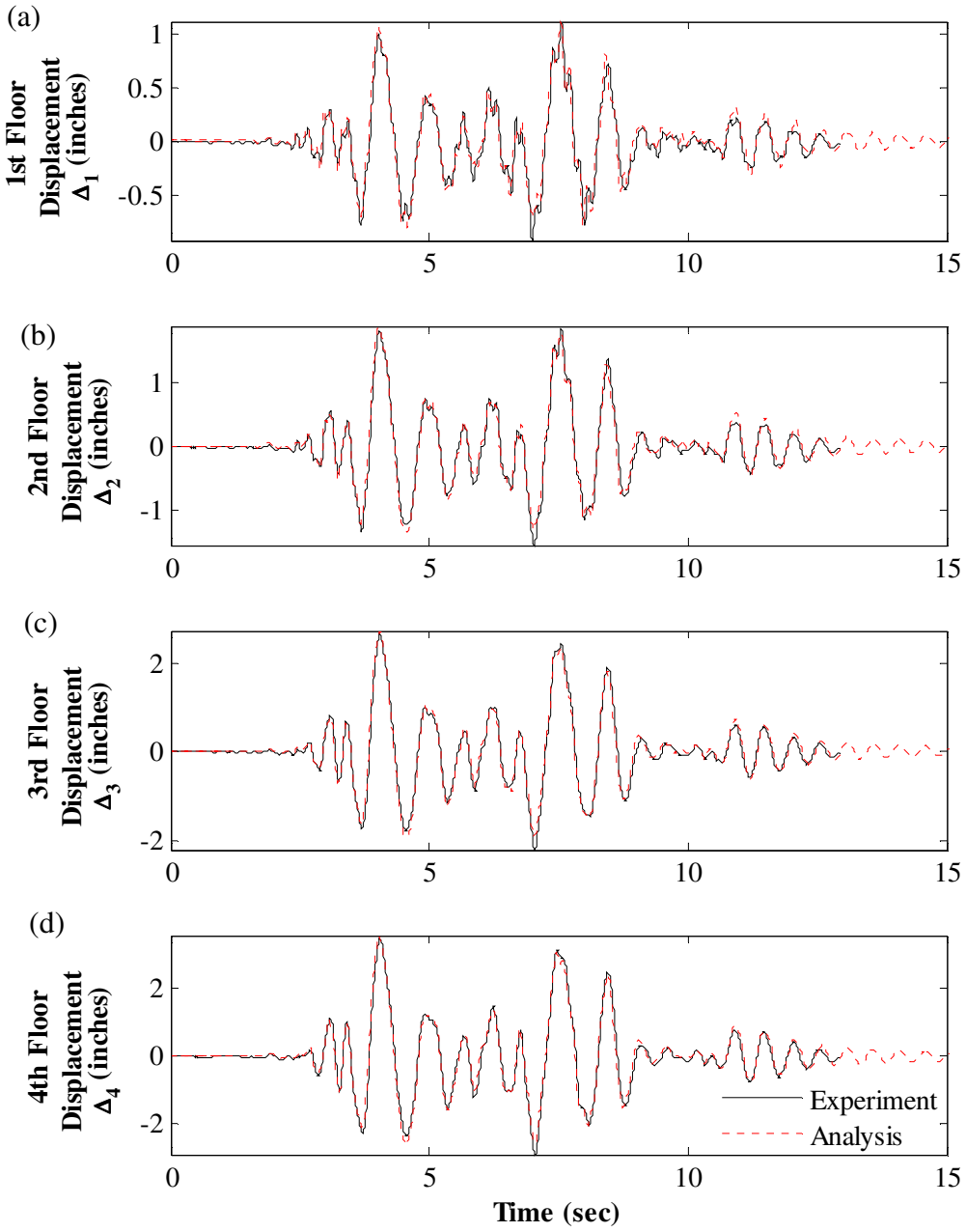

Figure 11.19 – Correlation of floor displacement response to DBE_h-shp270: (a) 1st floor; (b) 2nd floor; (c) 3rd floor; (d) 4th floor

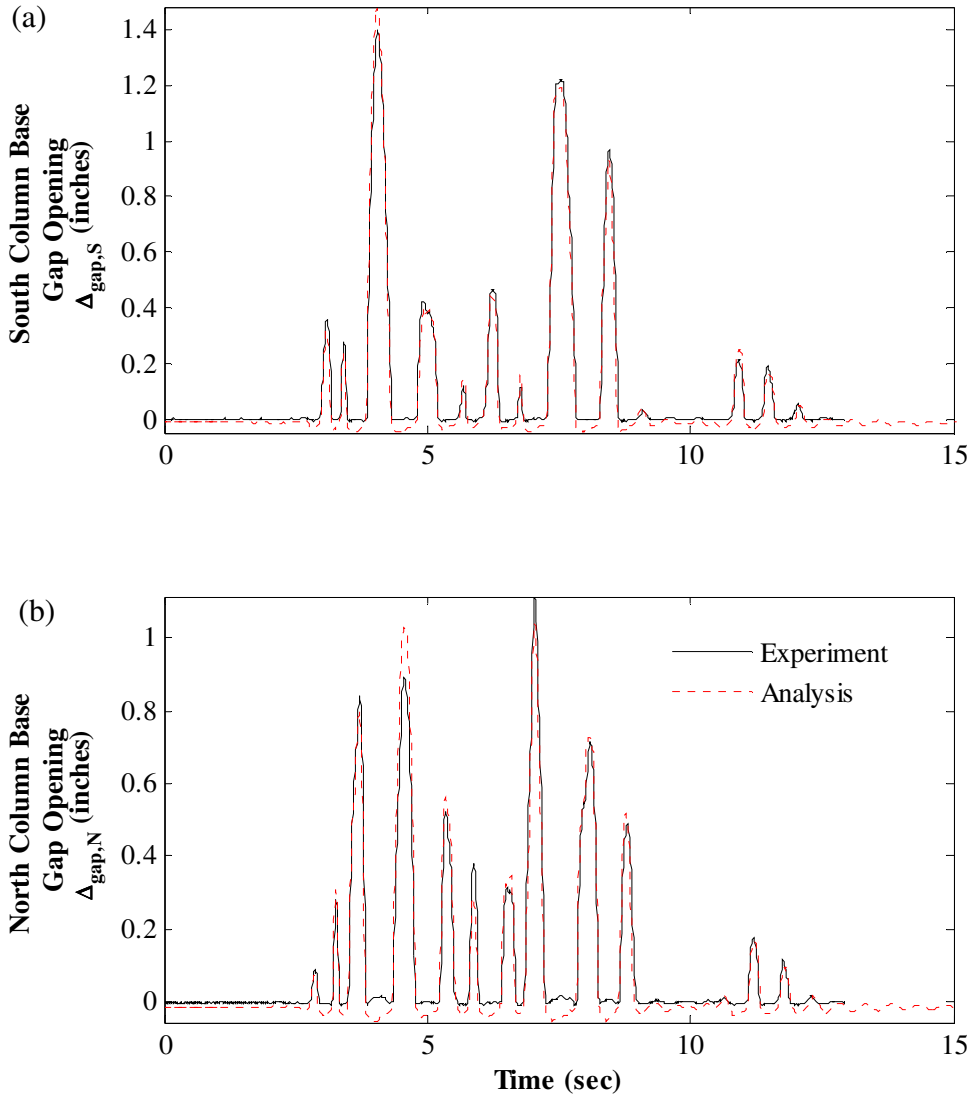

Figure 11.20 – Correlation of column base gap opening response to DBE_h-shp270: (a) at south column base; (b) at north column base

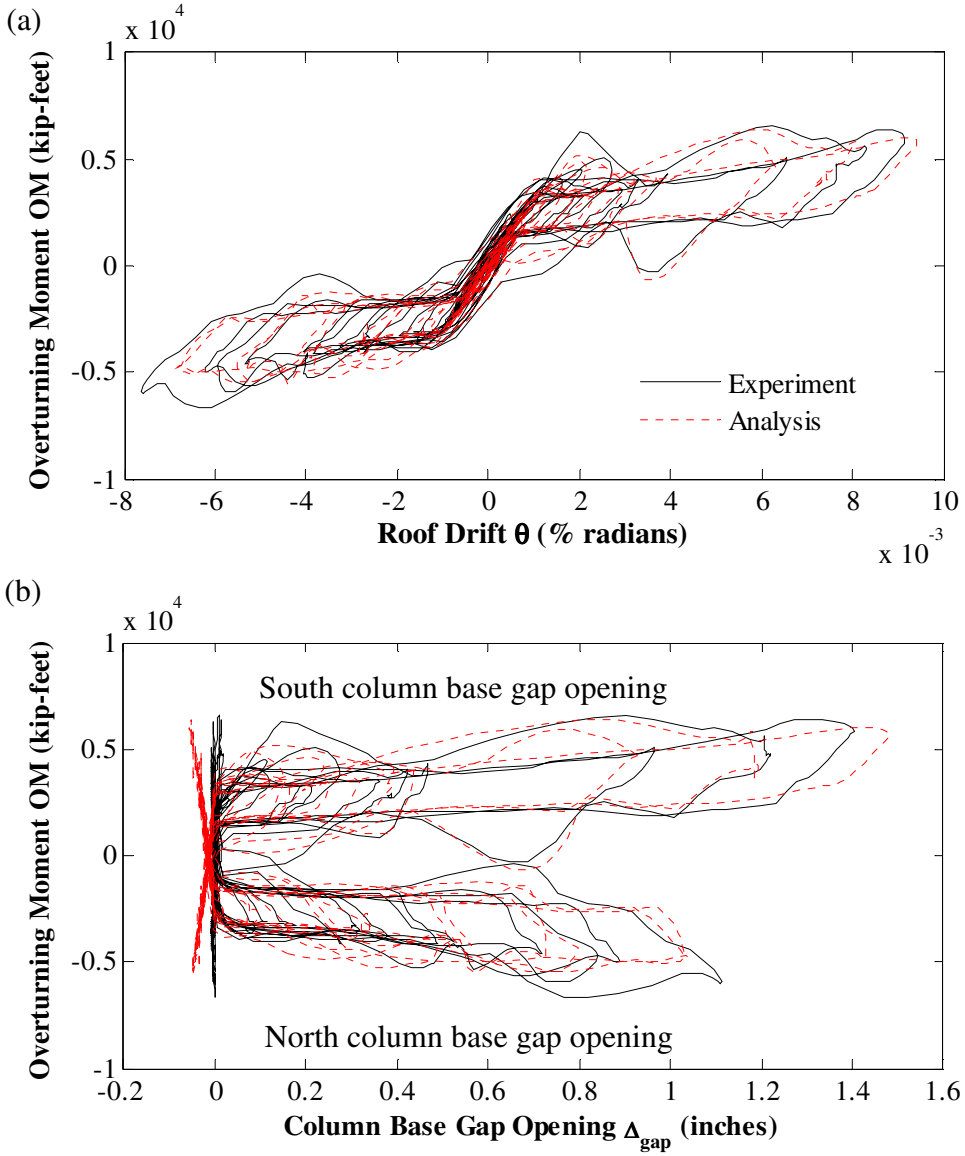

Figure 11.21 – Correlation of hysteretic response to DBE_h-shp270: (a) overturning moment versus roof drift; (b) overturning moment versus column base gap opening

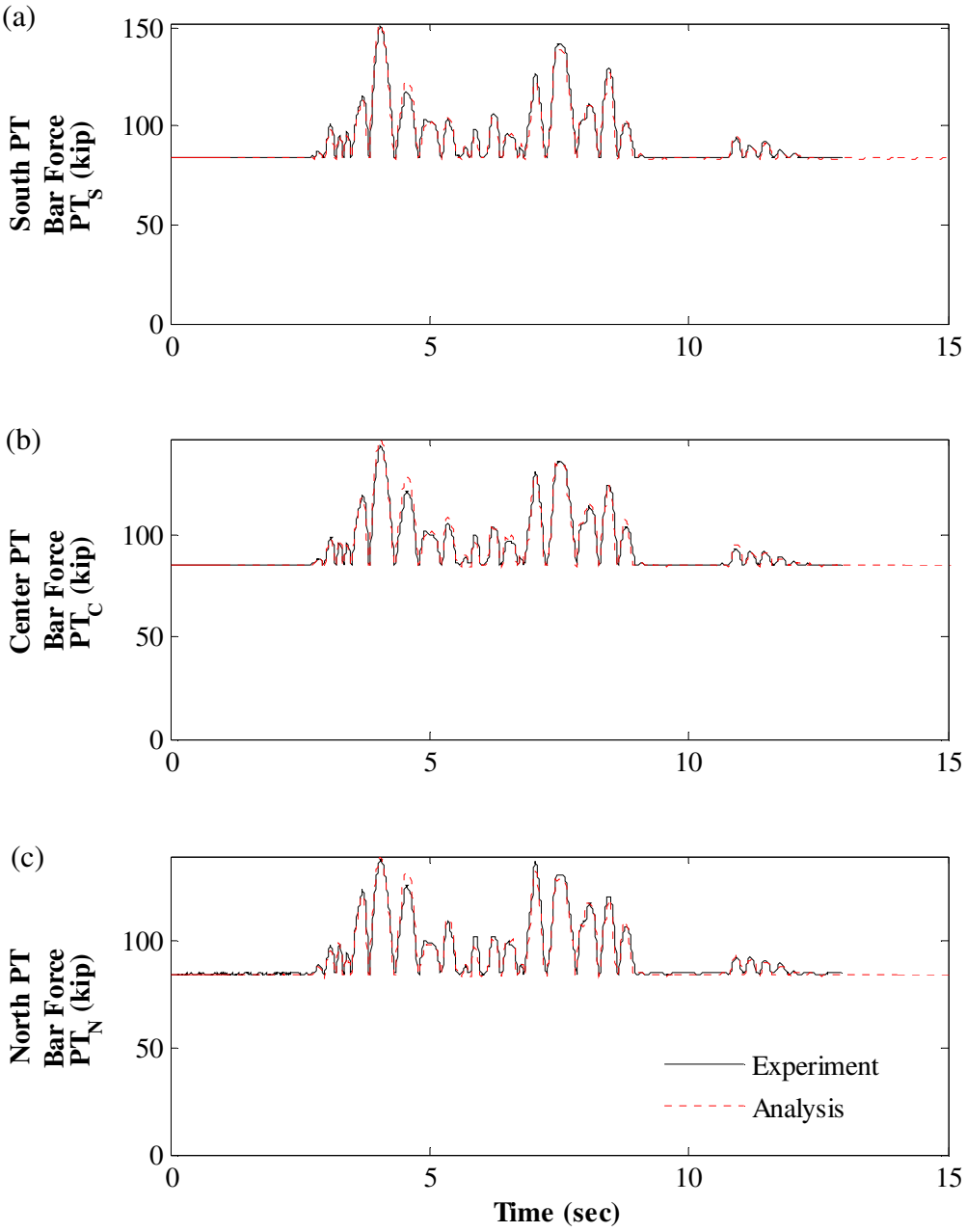

Figure 11.22 – Correlation of PT force response to DBE_h-shp270: (a) south PT bars; (b) center PT bars; (c) north PT bars

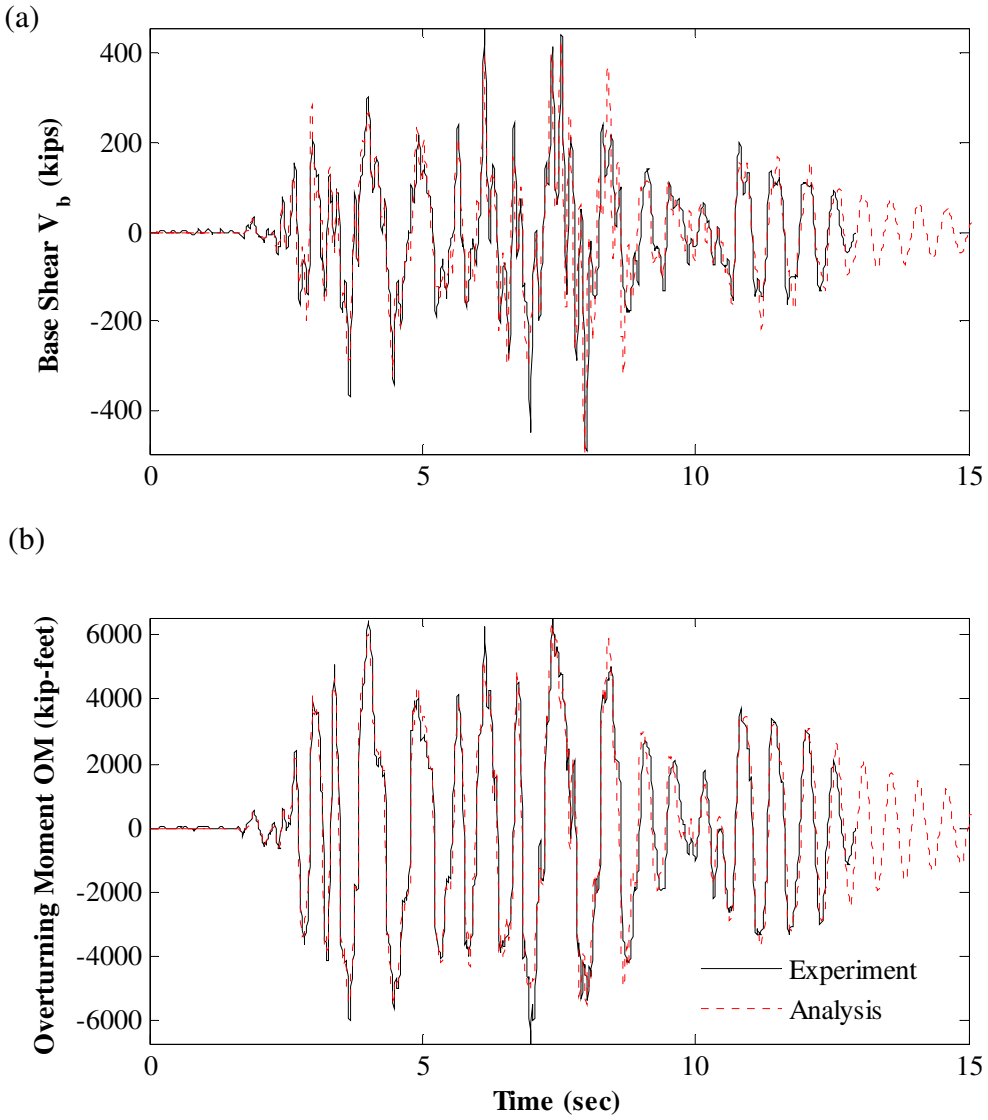

Figure 11.23 – DBE_h-shp270 response correlation: (a) base shear; (b) overturning moment

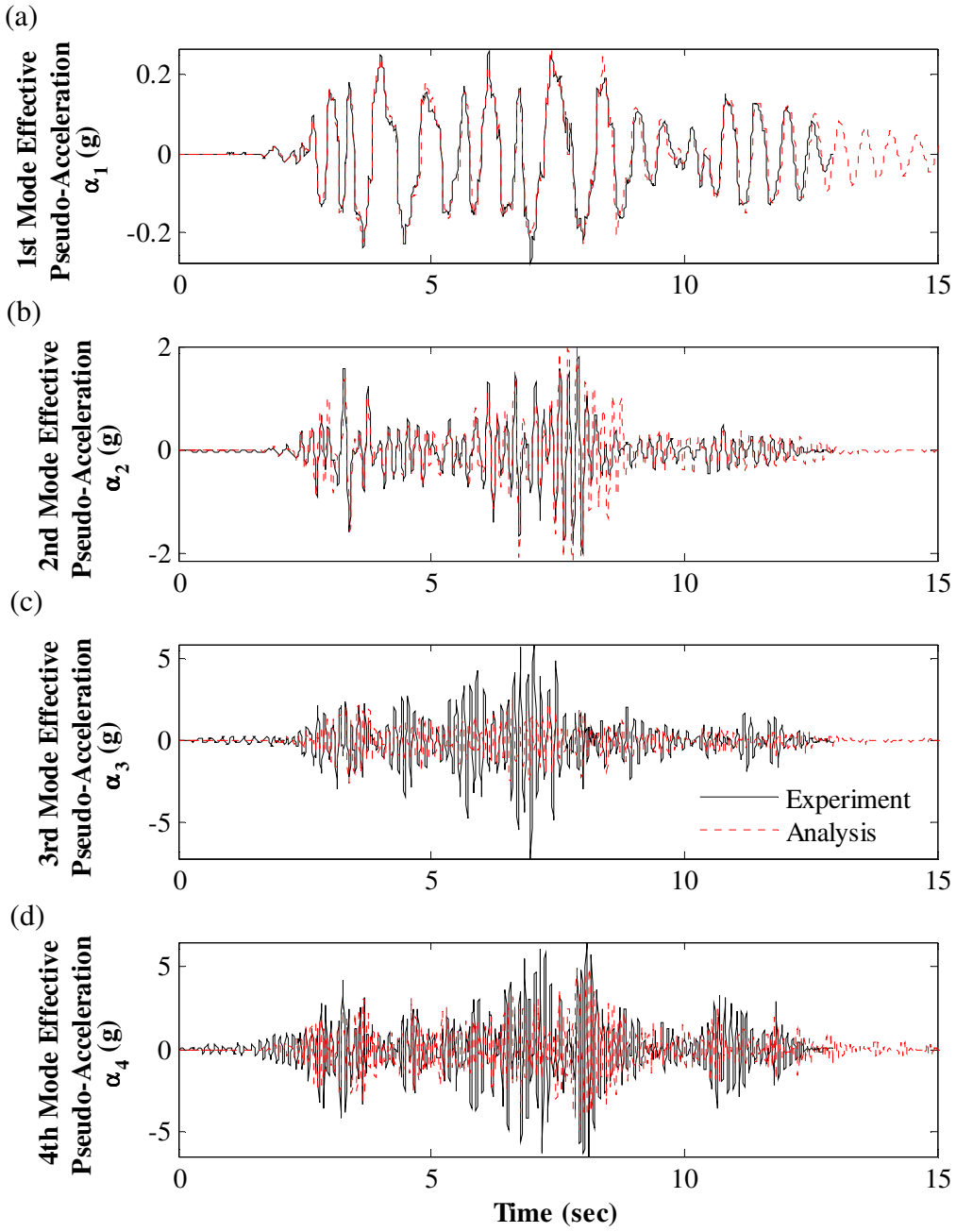

Figure 11.24 – Correlation of effective modal pseudo-acceleration response to DBE_h-shp270: (a) 1st mode; (b) 2nd mode; (c) 3rd mode; (d) 4th mode

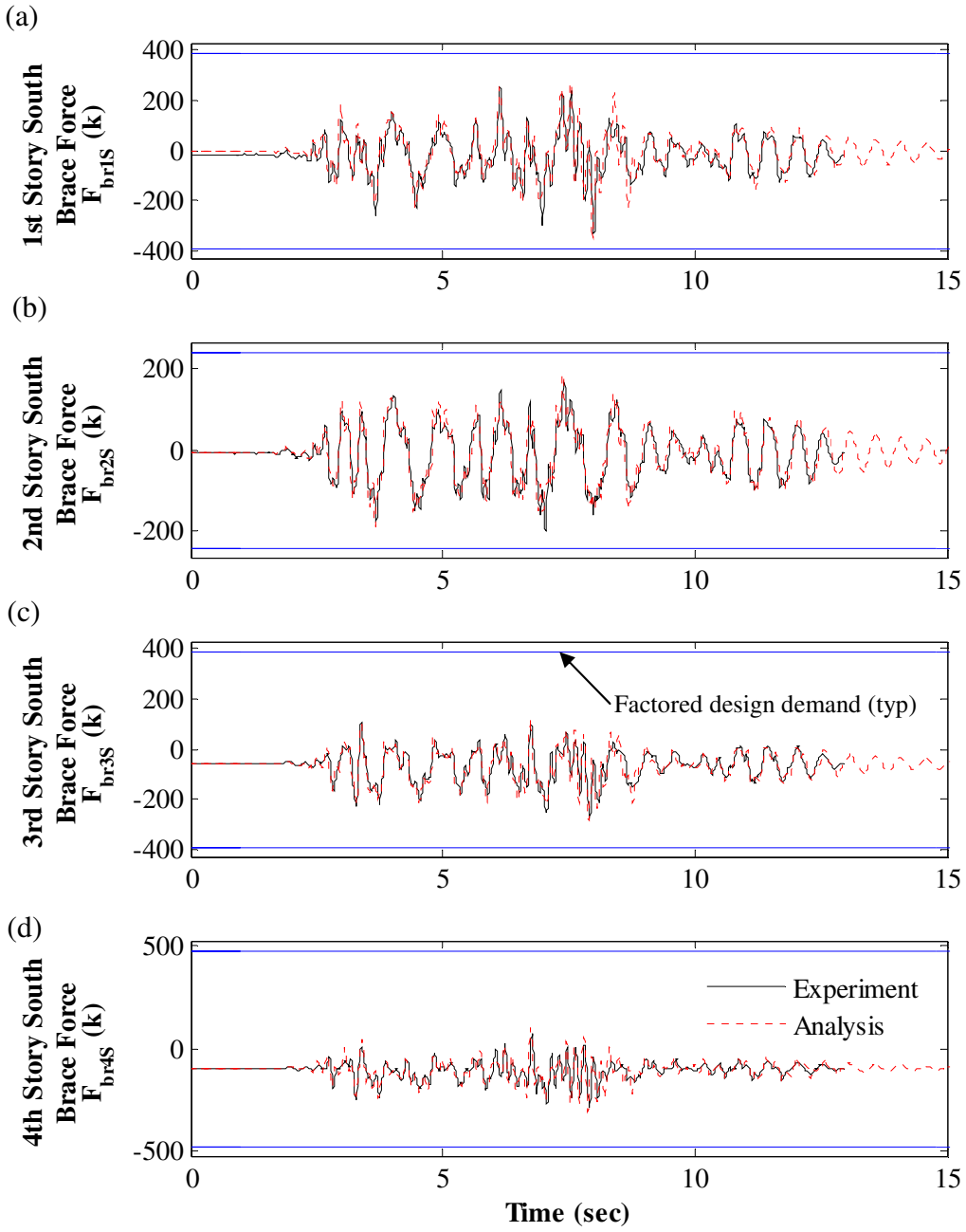

Figure 11.25 – Correlation of south brace axial force response to DBE_h-shp270: (a) 1st story; (b) 2nd story; (c) 3rd story; (d) 4th story

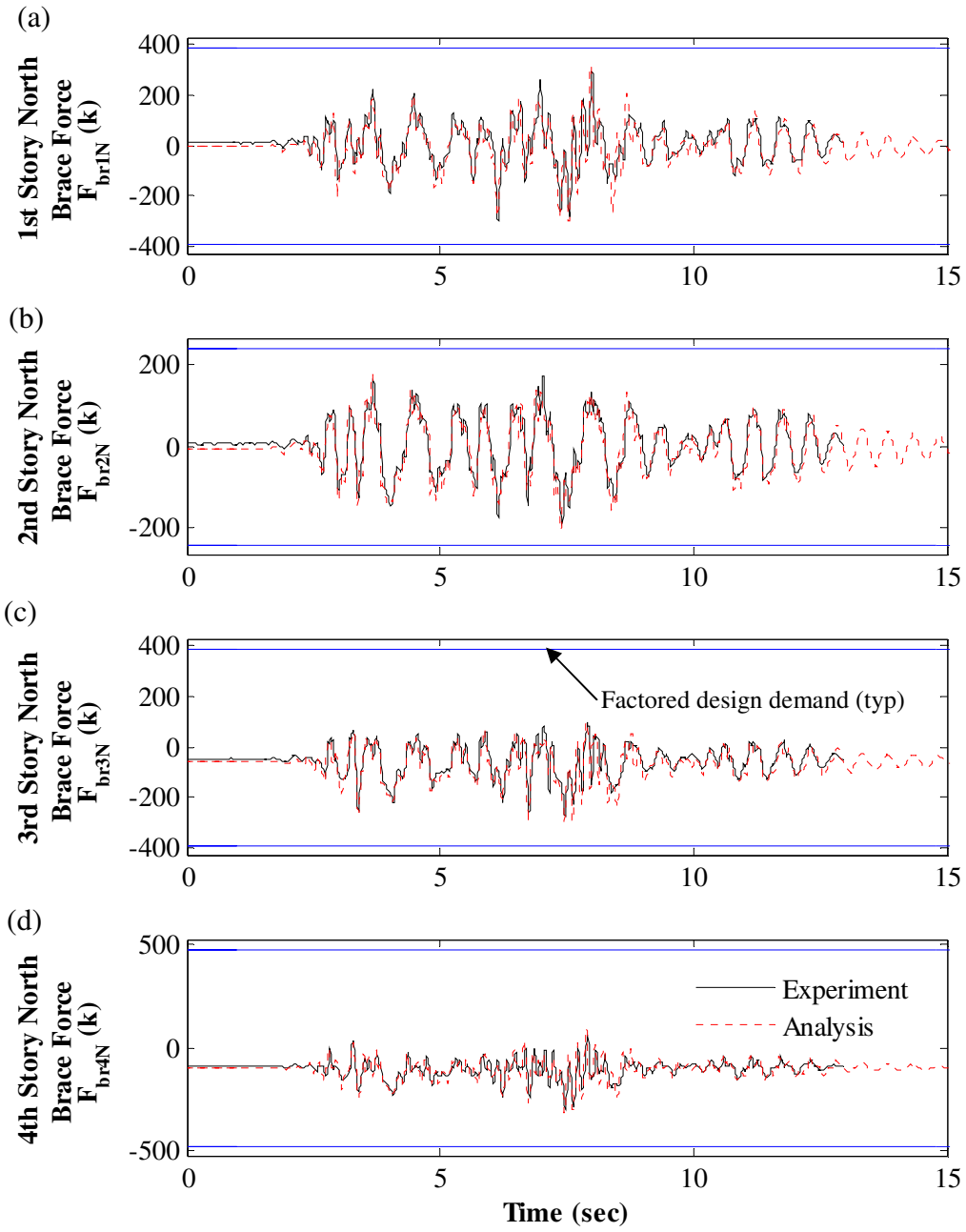

Figure 11.26 – Correlation of north brace axial force response to DBE_h-shp270: (a) 1st story; (b) 2nd story; (c) 3rd story; (d) 4th story

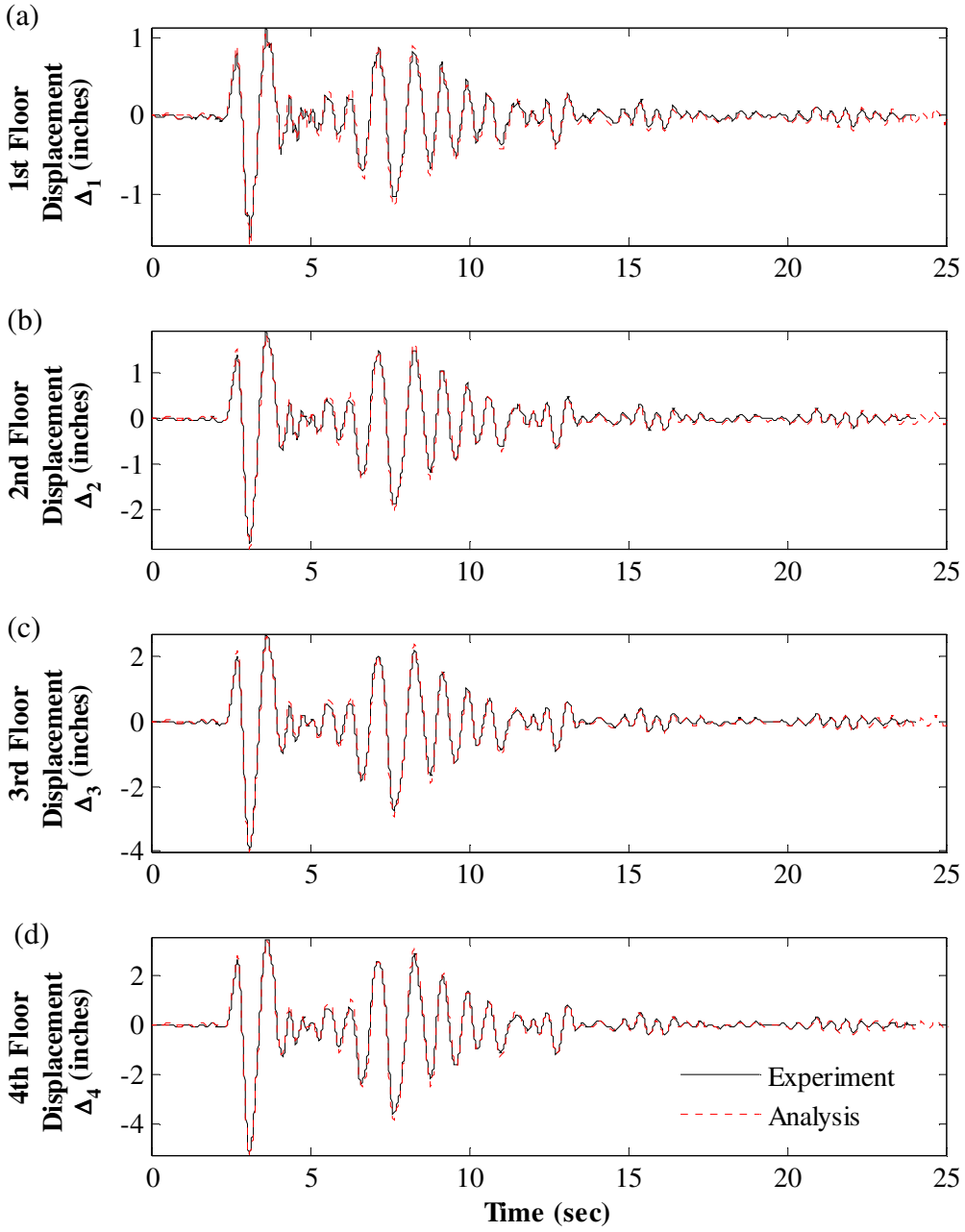

Figure 11.27 – Correlation of floor displacement response to DBE_arl090: (a) 1st floor; (b) 2nd floor; (c) 3rd floor; (d) 4th floor

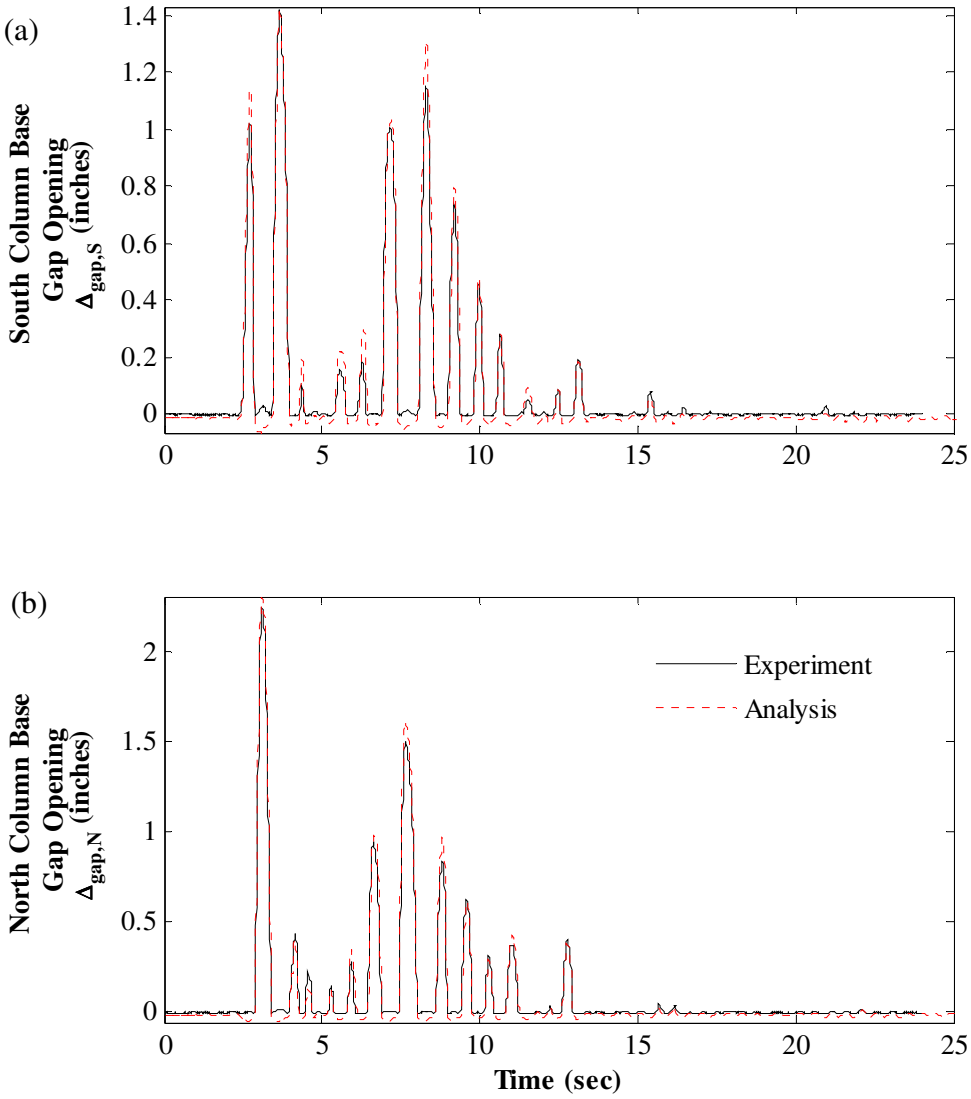

Figure 11.28 – Correlation of column base gap opening response to DBE_arl090: (a) at south column base; (b) at north column base

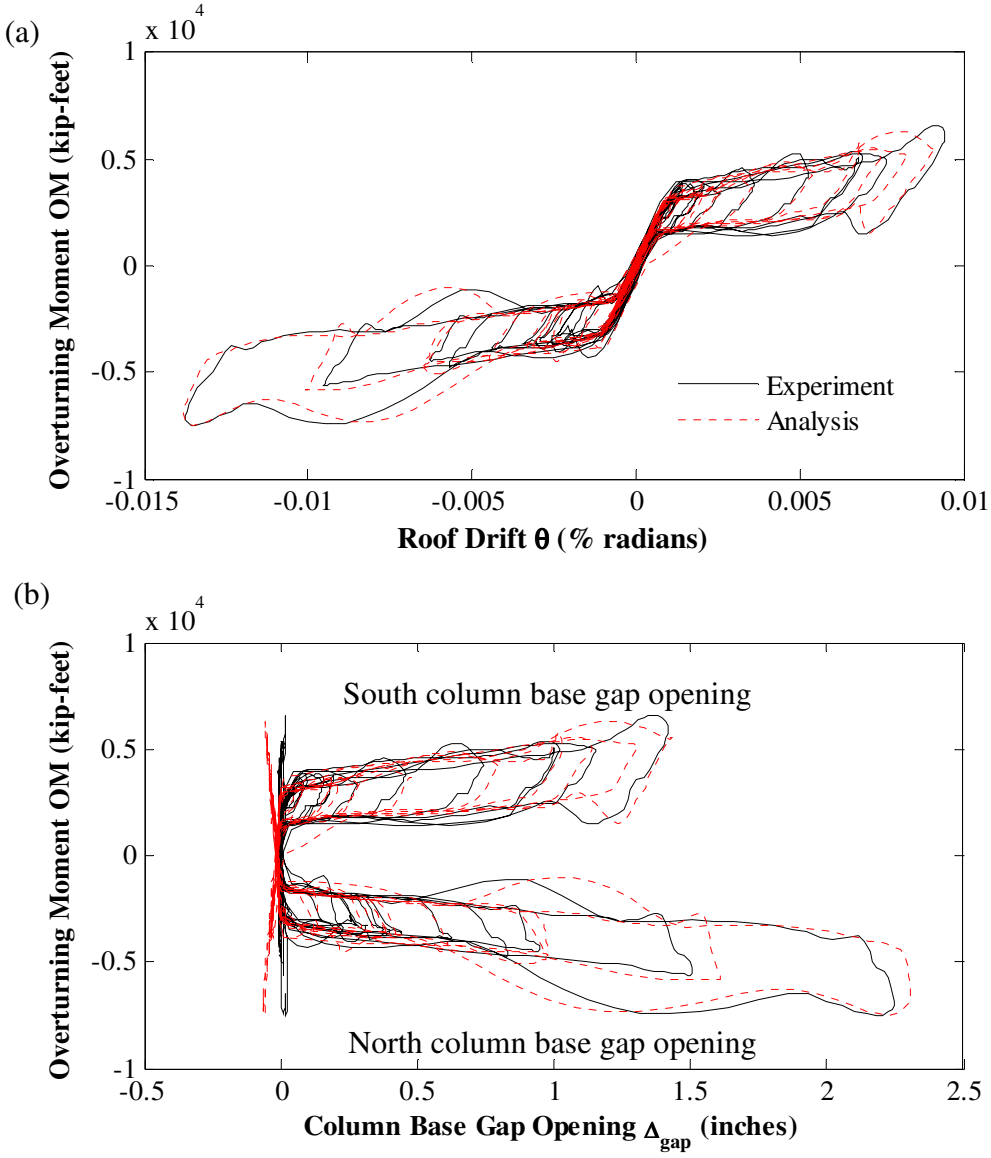

Figure 11.29 – Correlation of hysteretic response to DBE_arl090: (a) overturning moment versus roof drift; (b) overturning moment versus column base gap opening

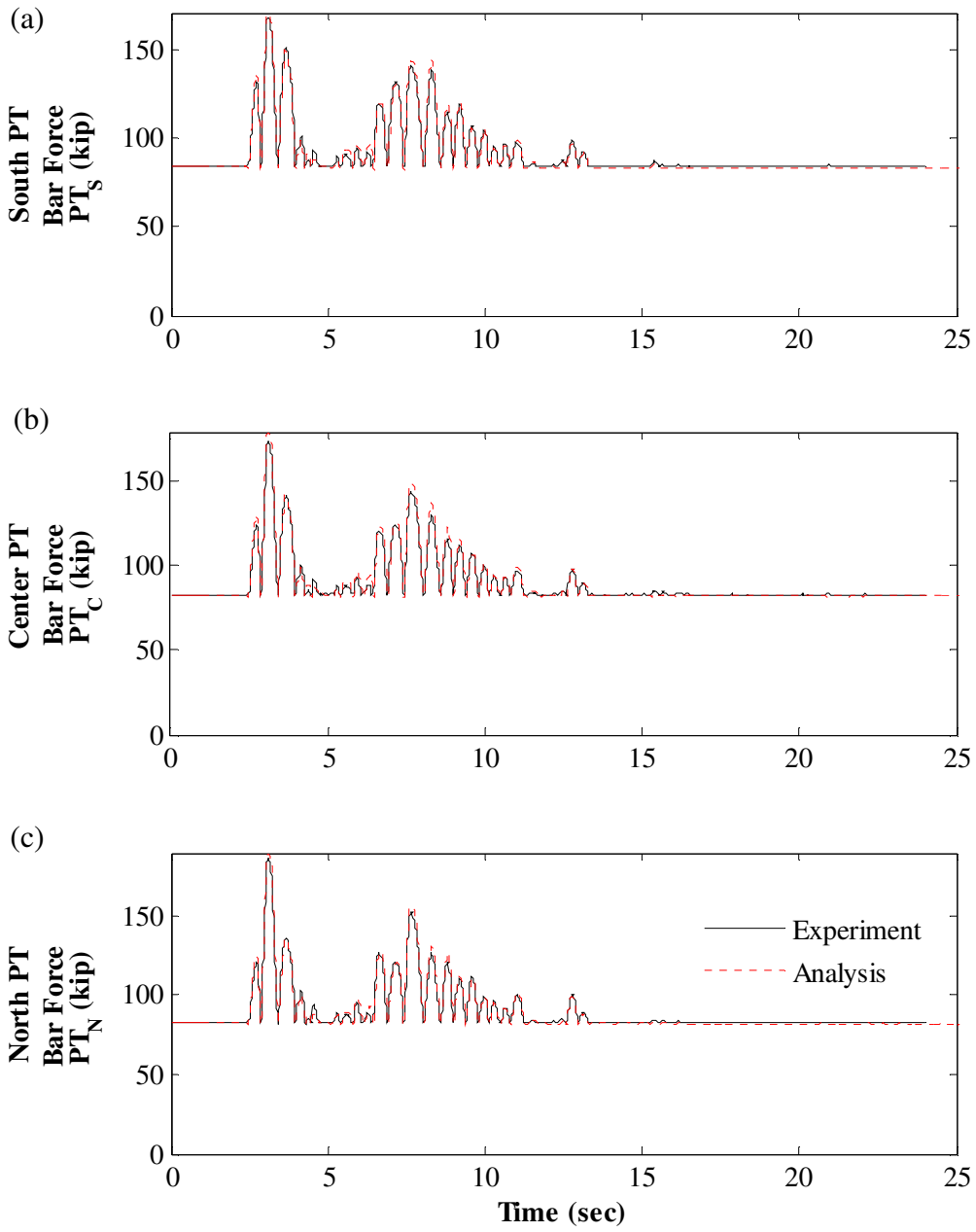

Figure 11.30 – Correlation of PT force response to DBE_arl090: (a) south PT bars; (b) center PT bars; (c) north PT bars

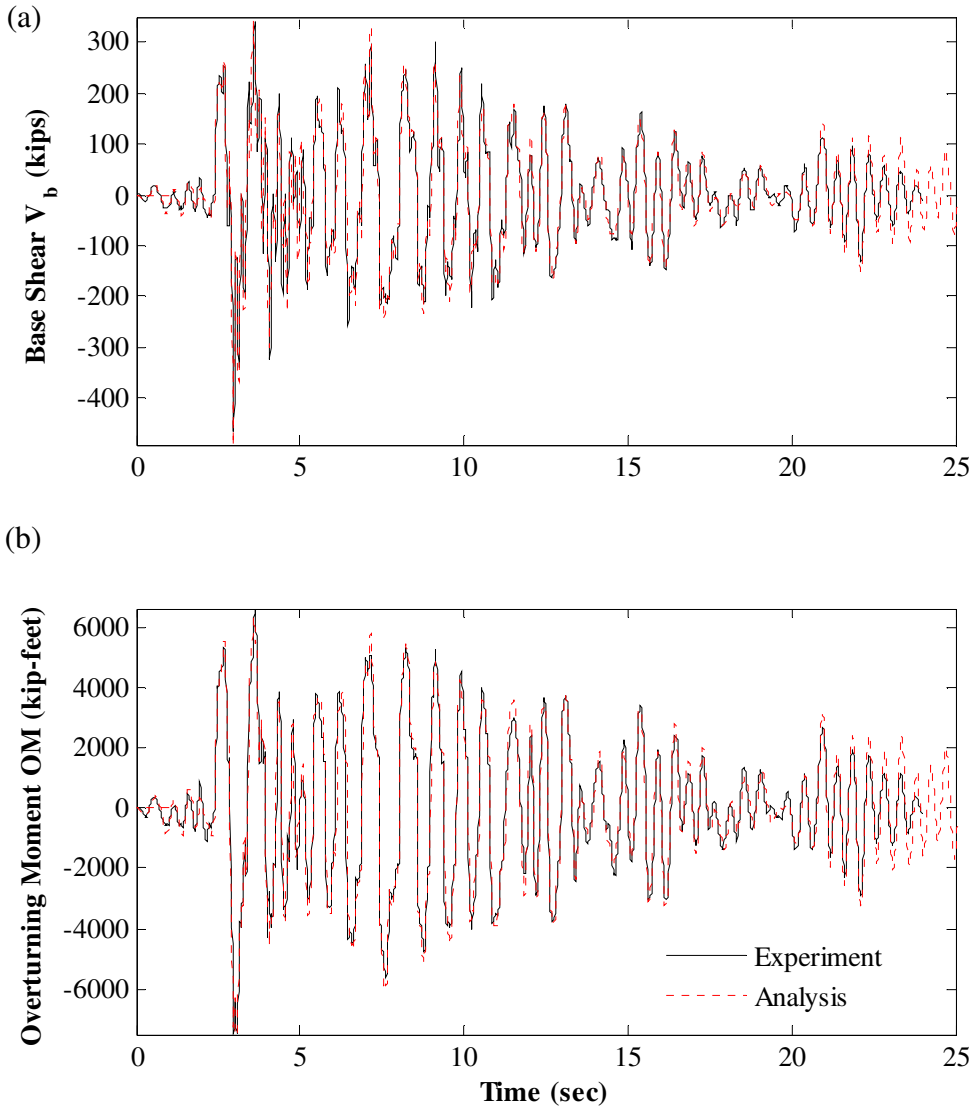

Figure 11.31 – DBE_arl090 response correlation: (a) base shear; (b) overturning moment

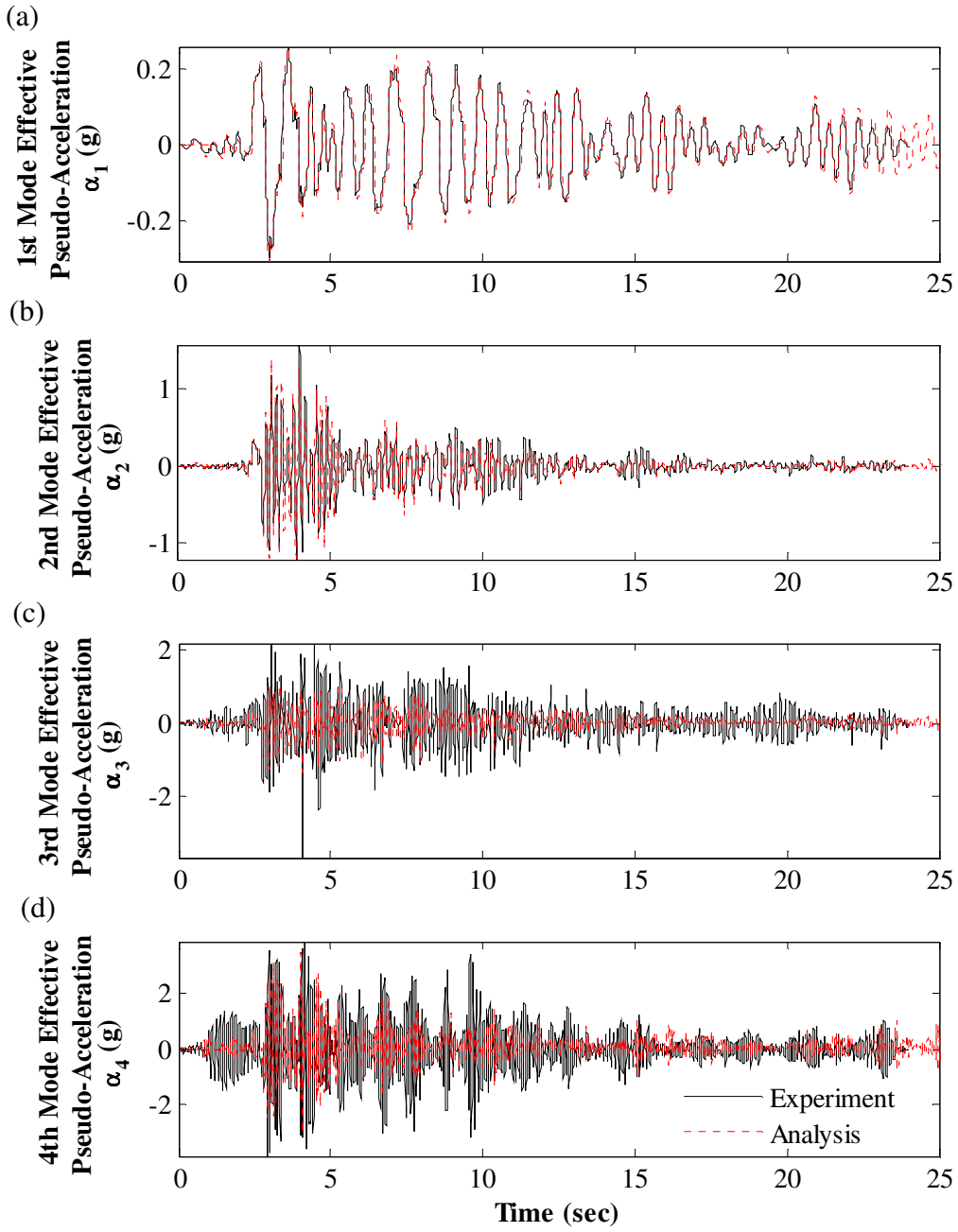

Figure 11.32 – Correlation of effective modal pseudo-acceleration response to DBE_arl090: (a) 1st mode; (b) 2nd mode; (c) 3rd mode; (d) 4th mode

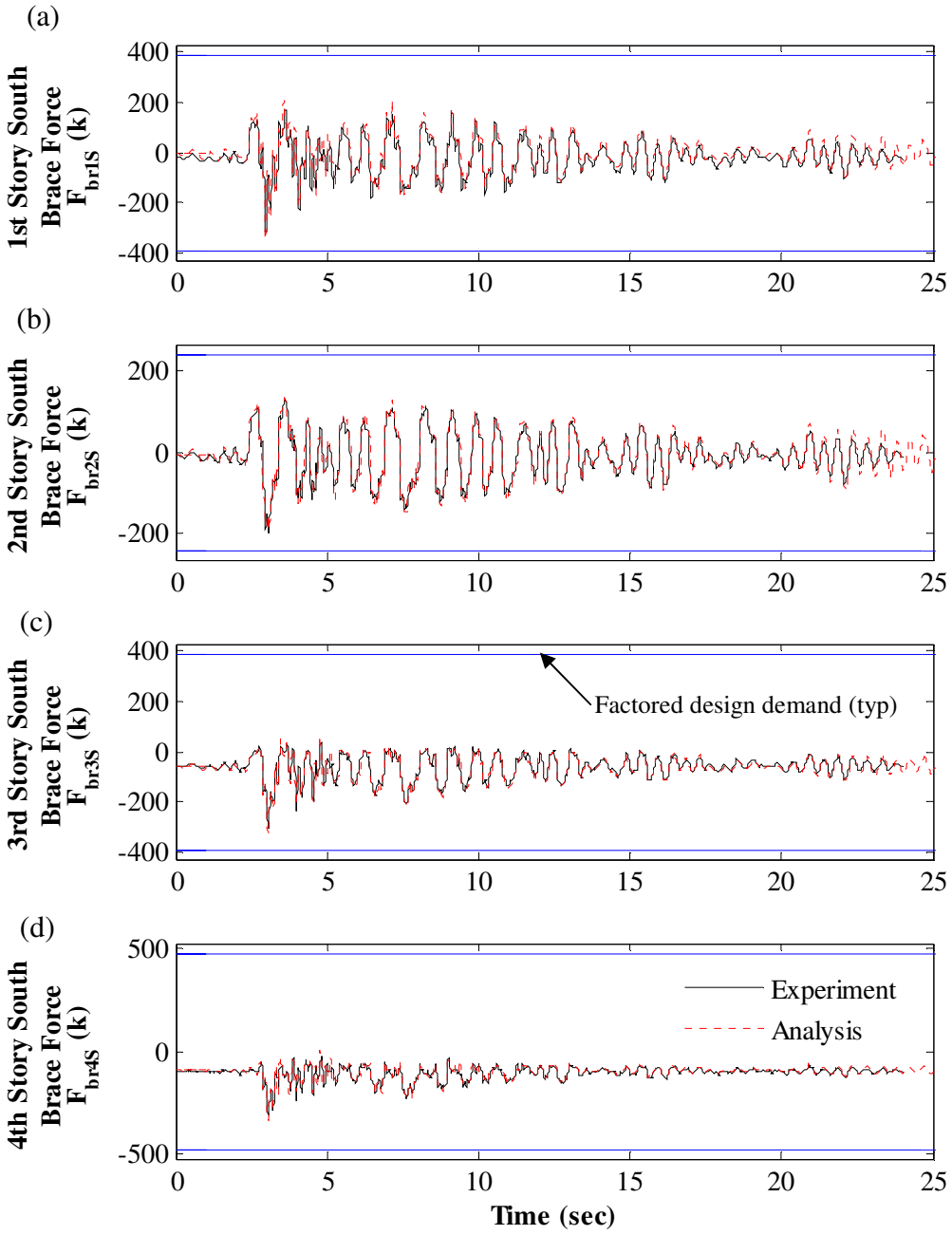

Figure 11.33 – Correlation of south brace axial force response to DBE_arl090: (a) 1st story; (b) 2nd story; (c) 3rd story; (d) 4th story

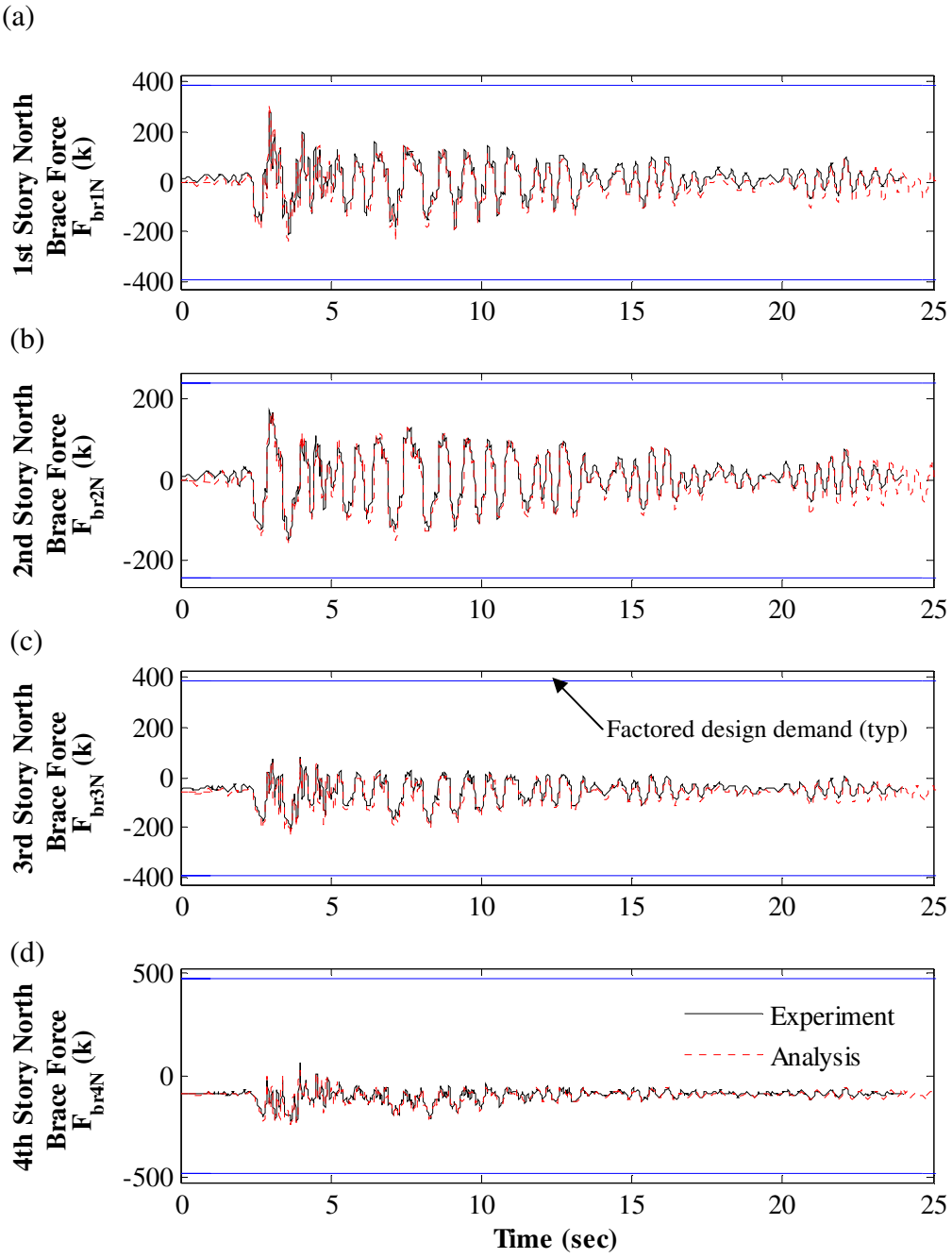

Figure 11.34 – Correlation of north brace axial force response to DBE_arl090: (a) 1st story; (b) 2nd story; (c) 3rd story; (d) 4th story

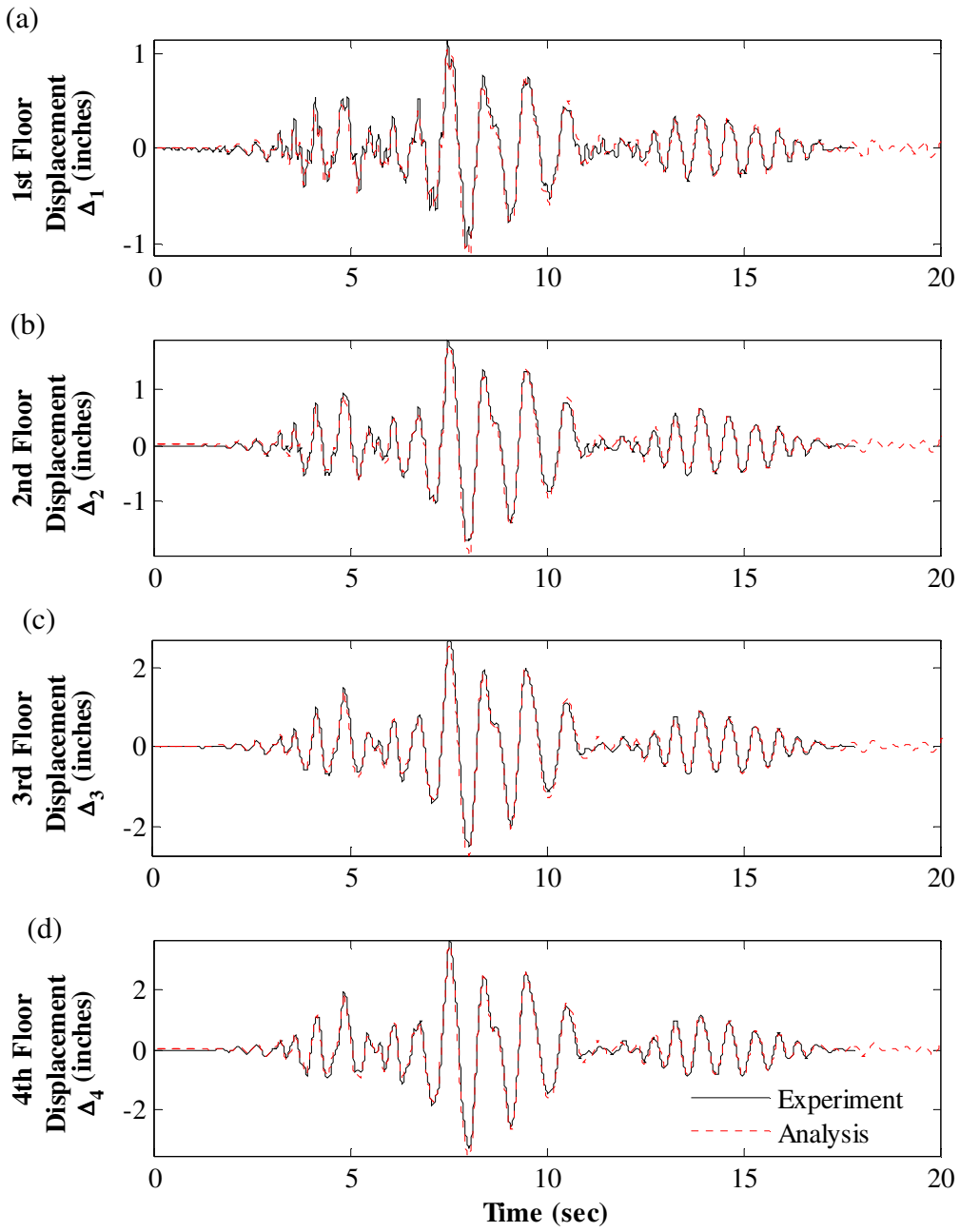

Figure 11.35 – Correlation of floor displacement response to DBE_nr-pel360: (a) 1st floor; (b) 2nd floor; (c) 3rd floor; (d) 4th floor

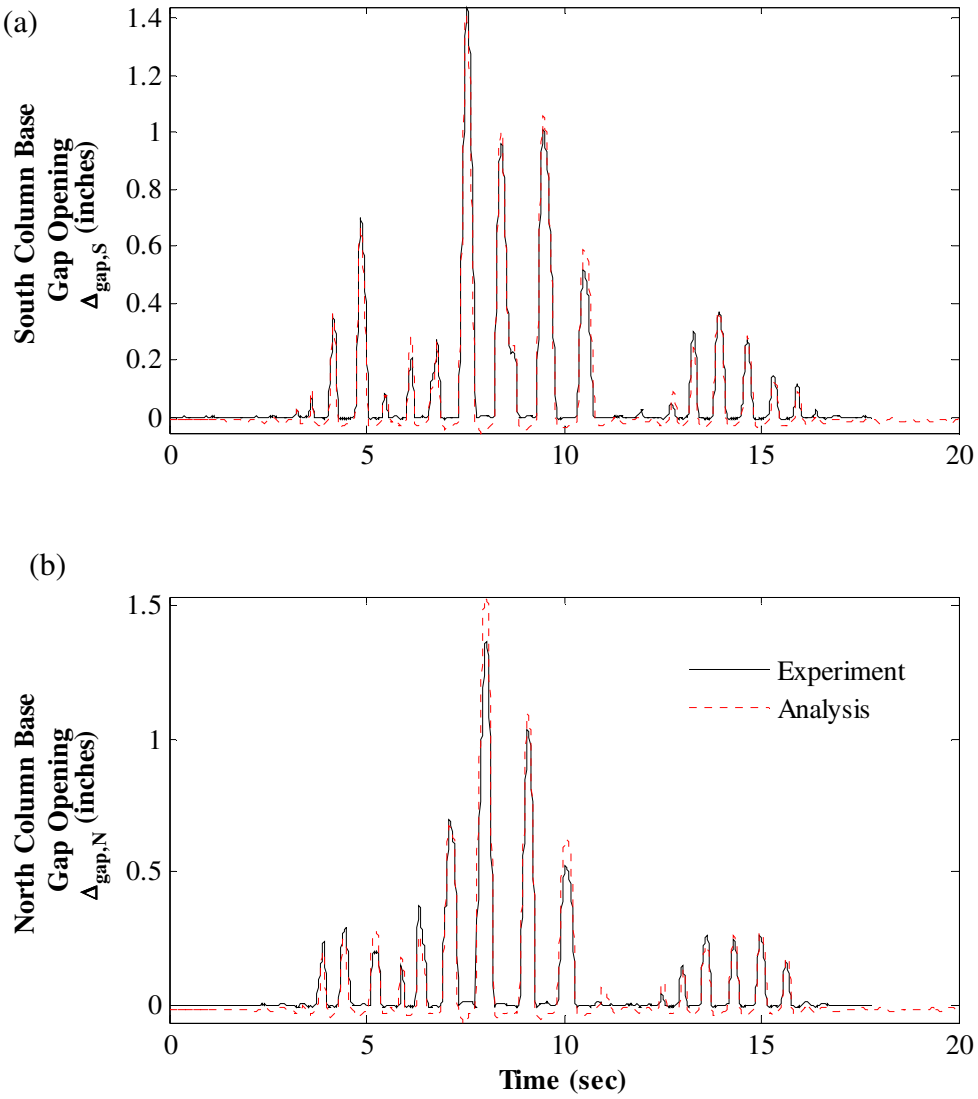

Figure 11.36 – Correlation of column base gap opening response to DBE_nr-pel360: (a) at south column base; (b) at north column base

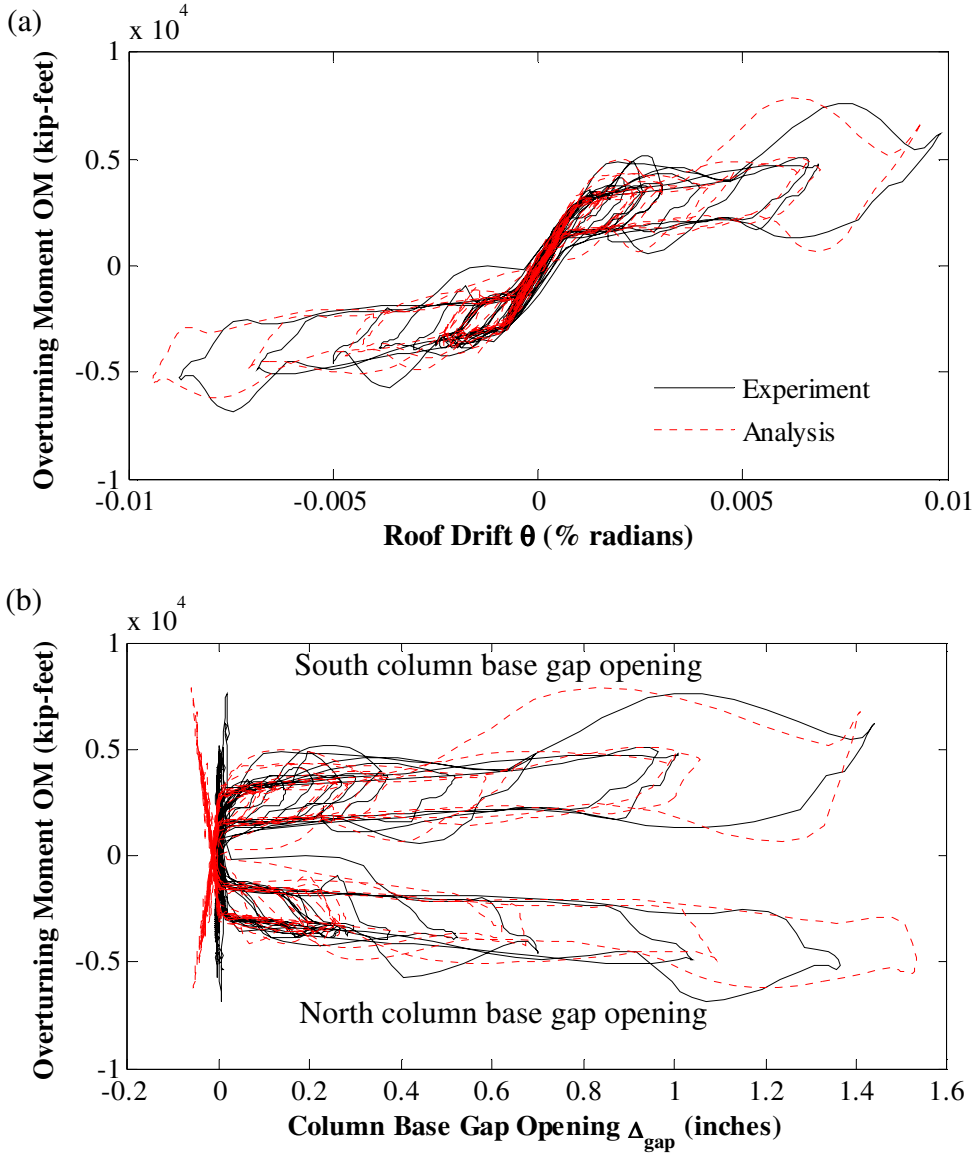

Figure 11.37 – Correlation of hysteretic response to DBE_nr-pel360: (a) overturning moment versus roof drift; (b) overturning moment versus column base gap opening

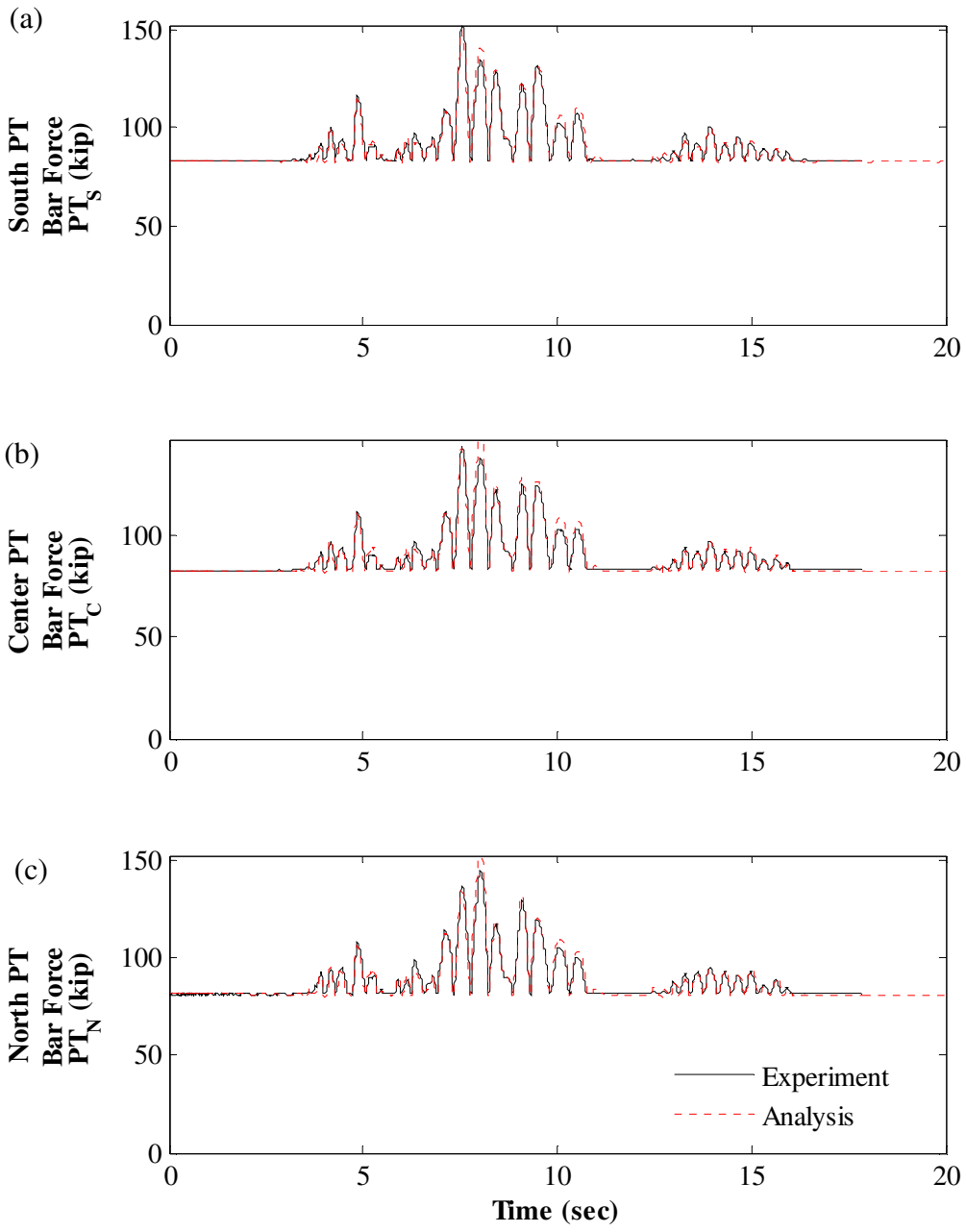

Figure 11.38 – Correlation of PT force response to DBE_nr-pel360: (a) south PT bars; (b) center PT bars; (c) north PT bars

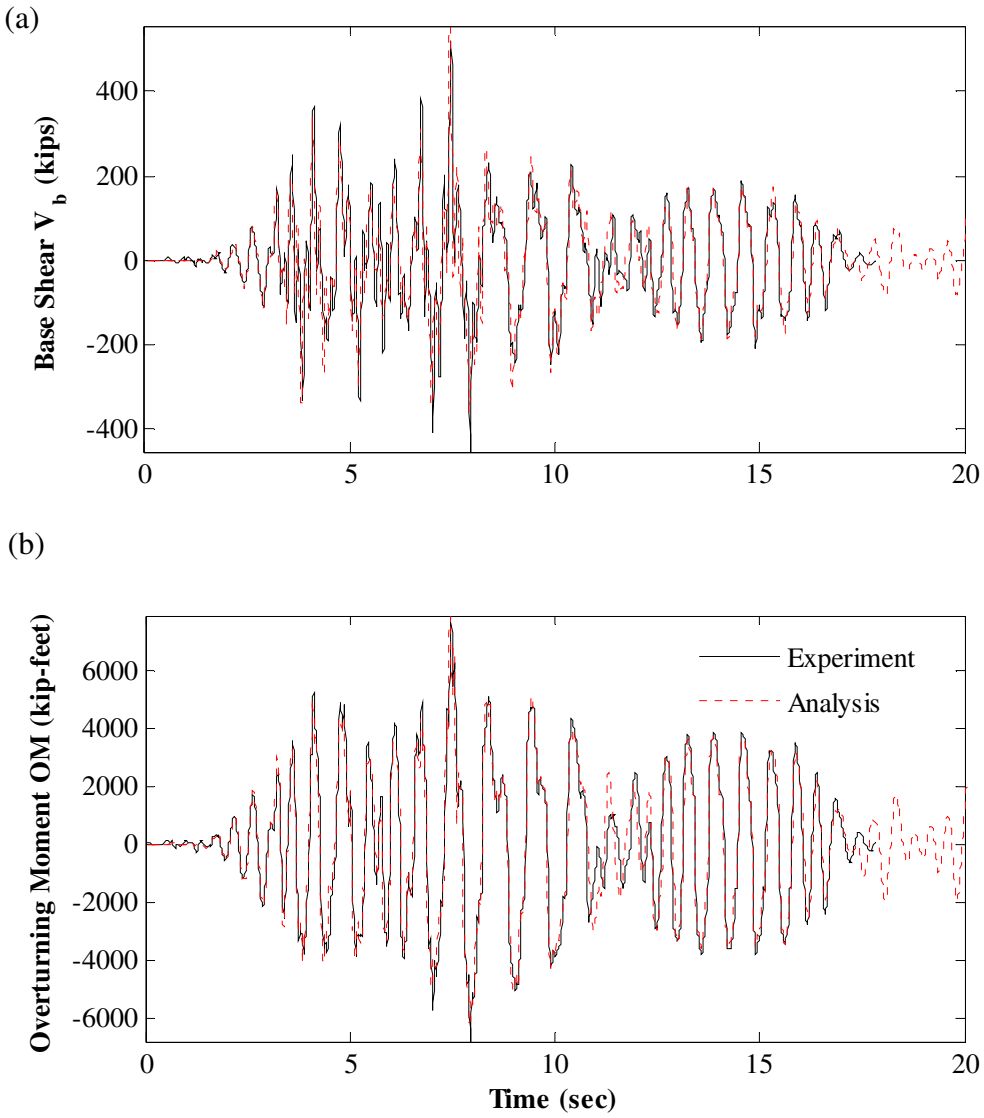

Figure 11.39 – DBE_nr-pel360 response correlation: (a) base shear; (b) overturning moment

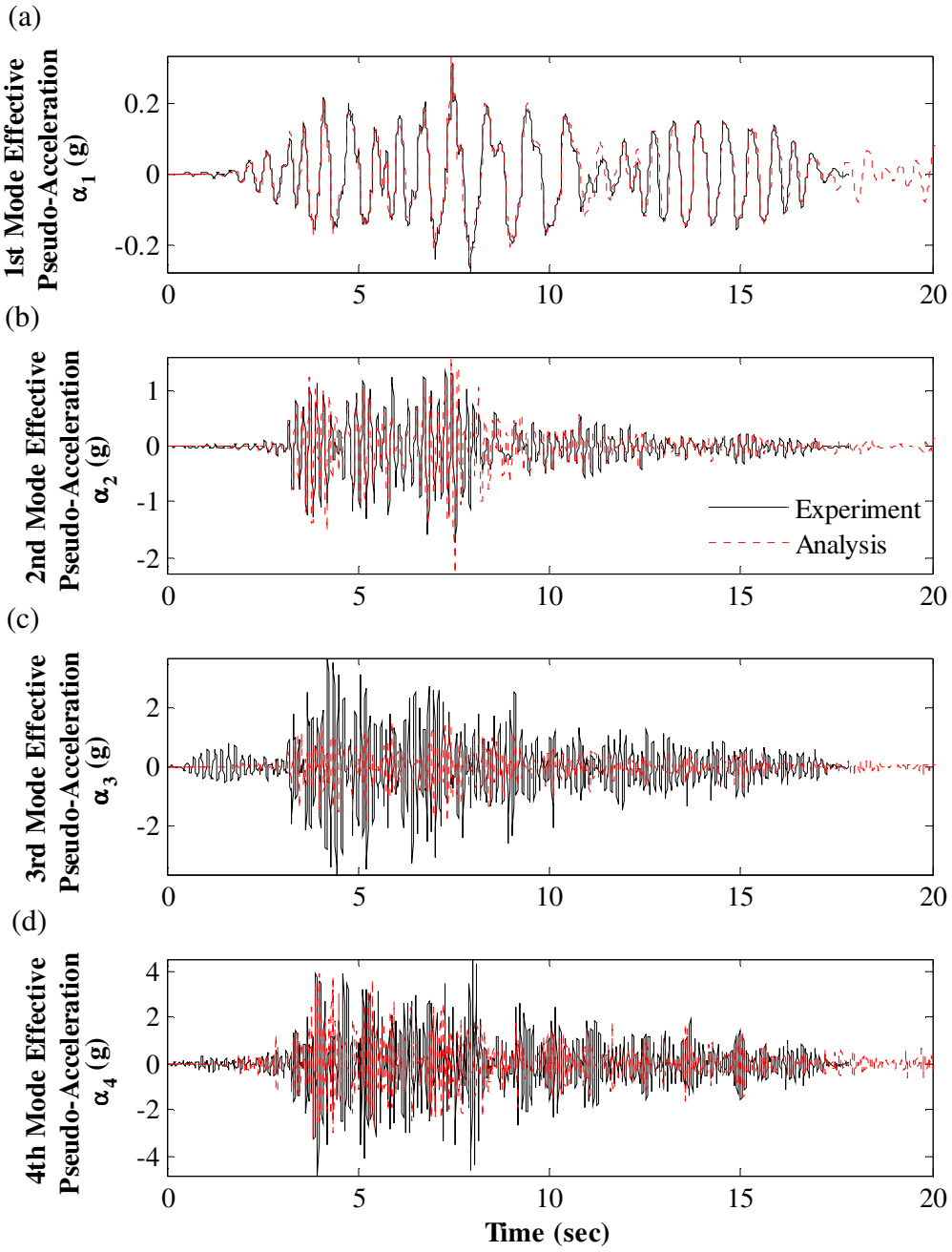

Figure 11.40 – Correlation of effective modal pseudo-acceleration response to DBE_nr-pel360: (a) 1st mode; (b) 2nd mode; (c) 3rd mode; (d) 4th mode

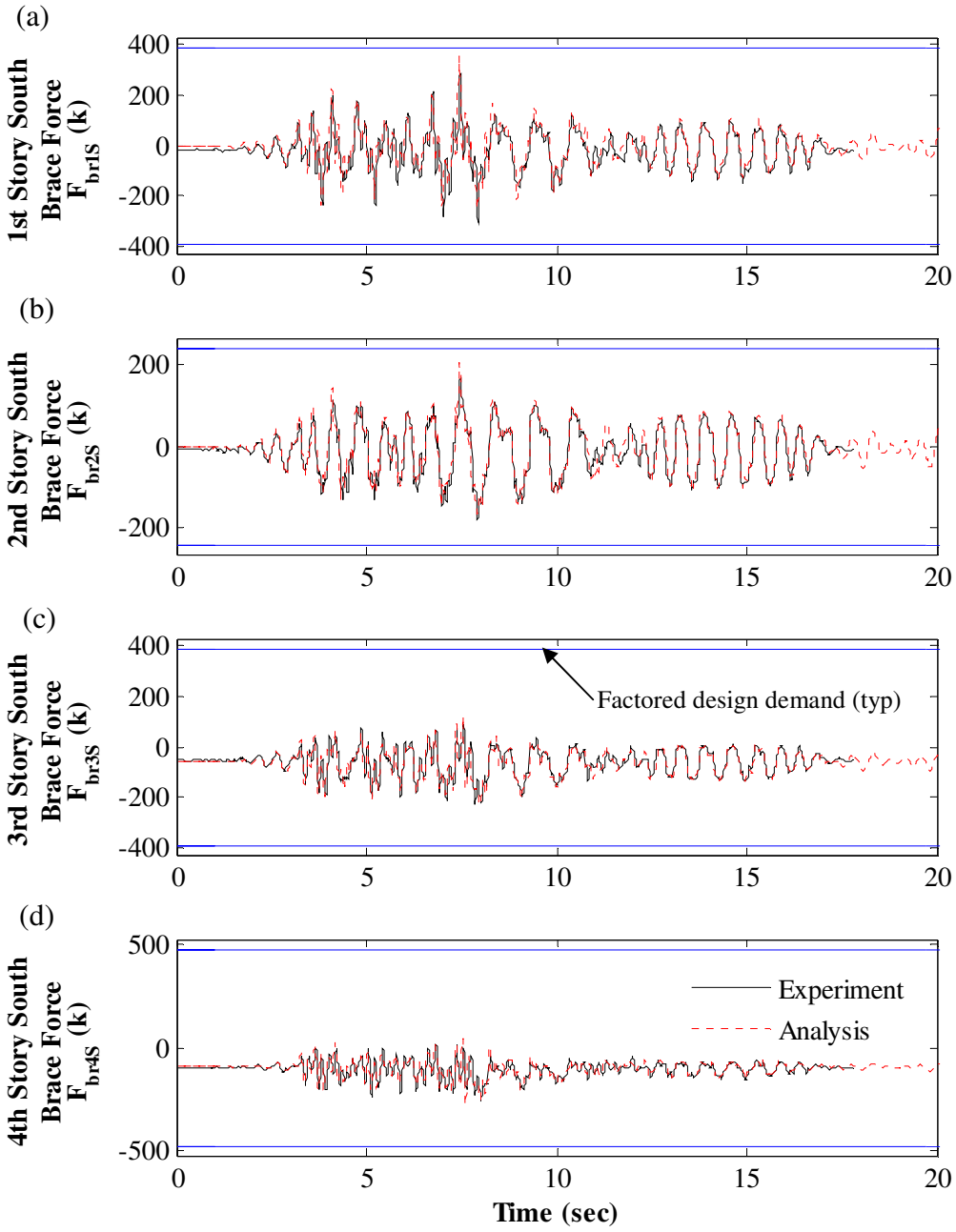

Figure 11.41 – Correlation of south brace axial force response to DBE_nr-pel360: (a) 1st story; (b) 2nd story; (c) 3rd story; (d) 4th story

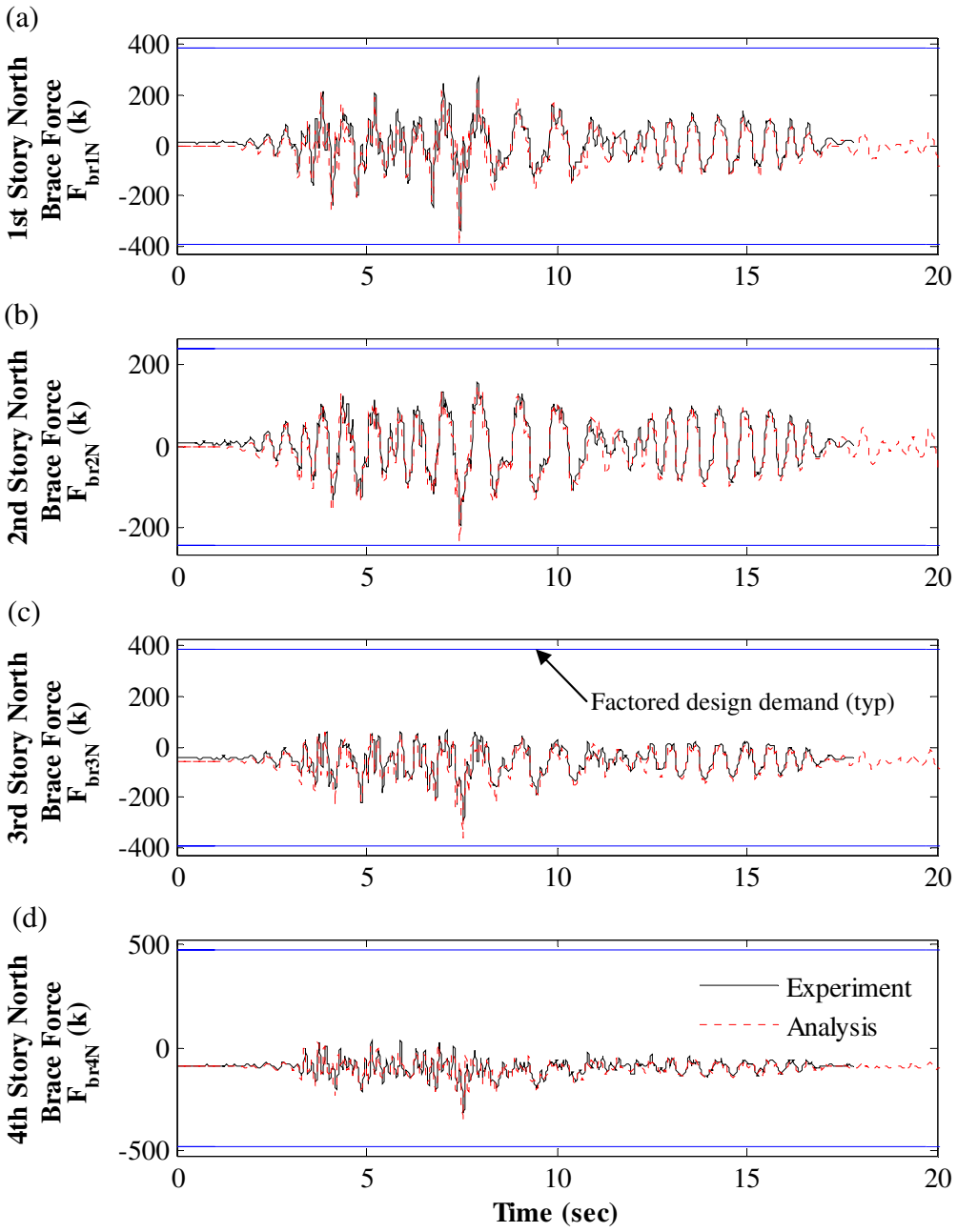

Figure 11.42 – Correlation of north brace axial force response to DBE_nr-pel360: (a) 1st story; (b) 2nd story; (c) 3rd story; (d) 4th story

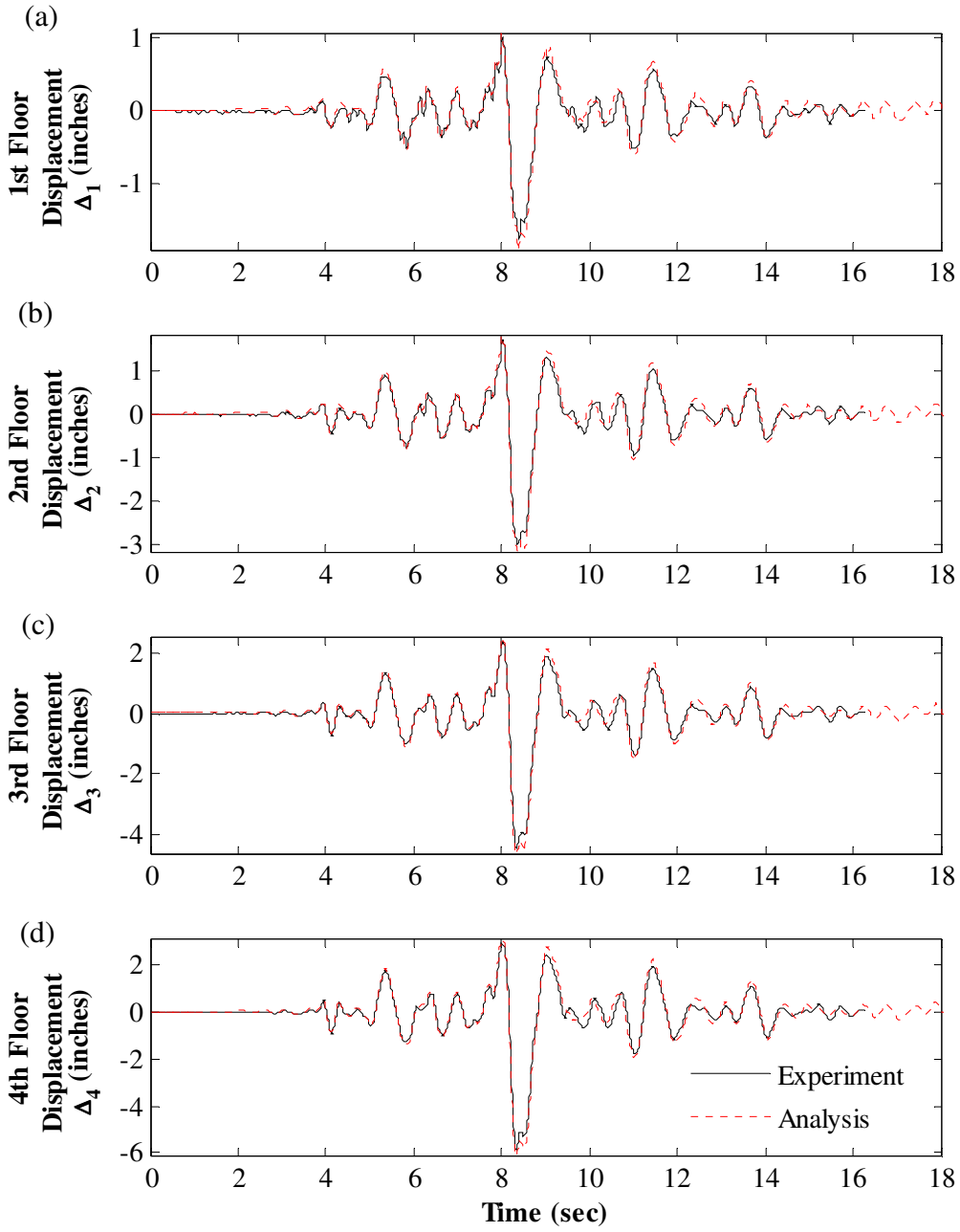

Figure 11.43 – Correlation of floor displacement response to MCE_stn110: (a) 1st floor; (b) 2nd floor; (c) 3rd floor; (d) 4th floor

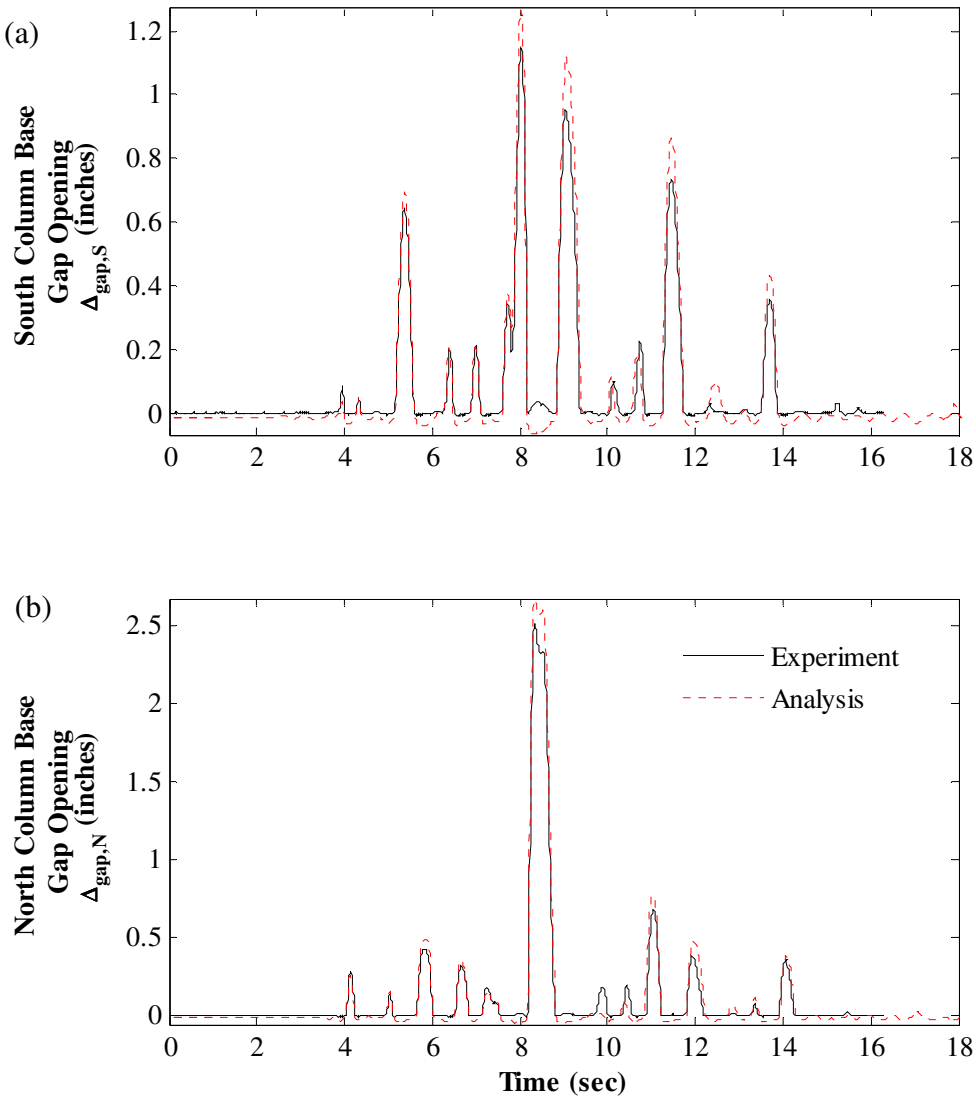

Figure 11.44 – Correlation of column base gap opening response to MCE_stn110: (a) at south column base; (b) at north column base

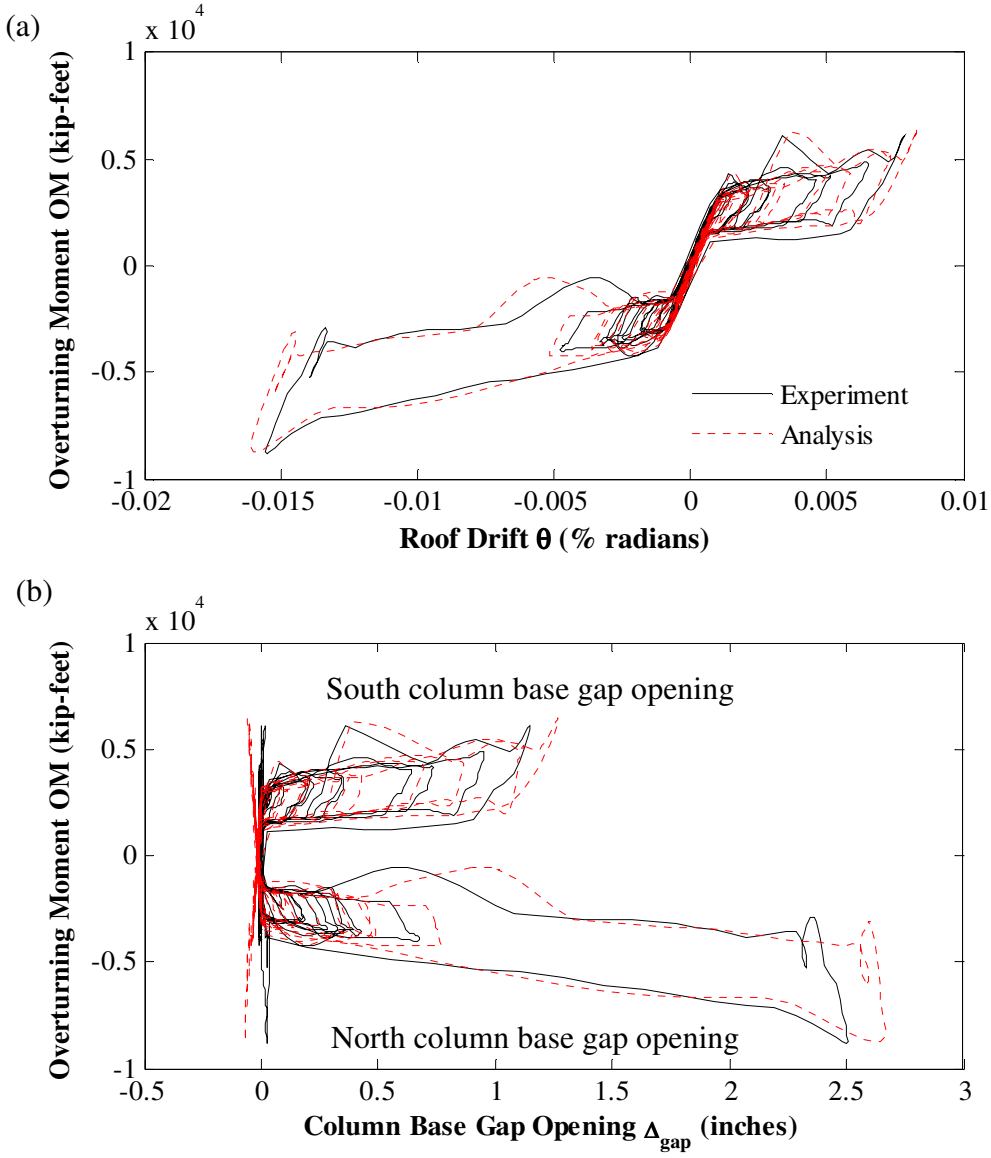

Figure 11.45 – Correlation of hysteretic response to MCE_stn110: (a) overturning moment versus roof drift; (b) overturning moment versus column base gap opening

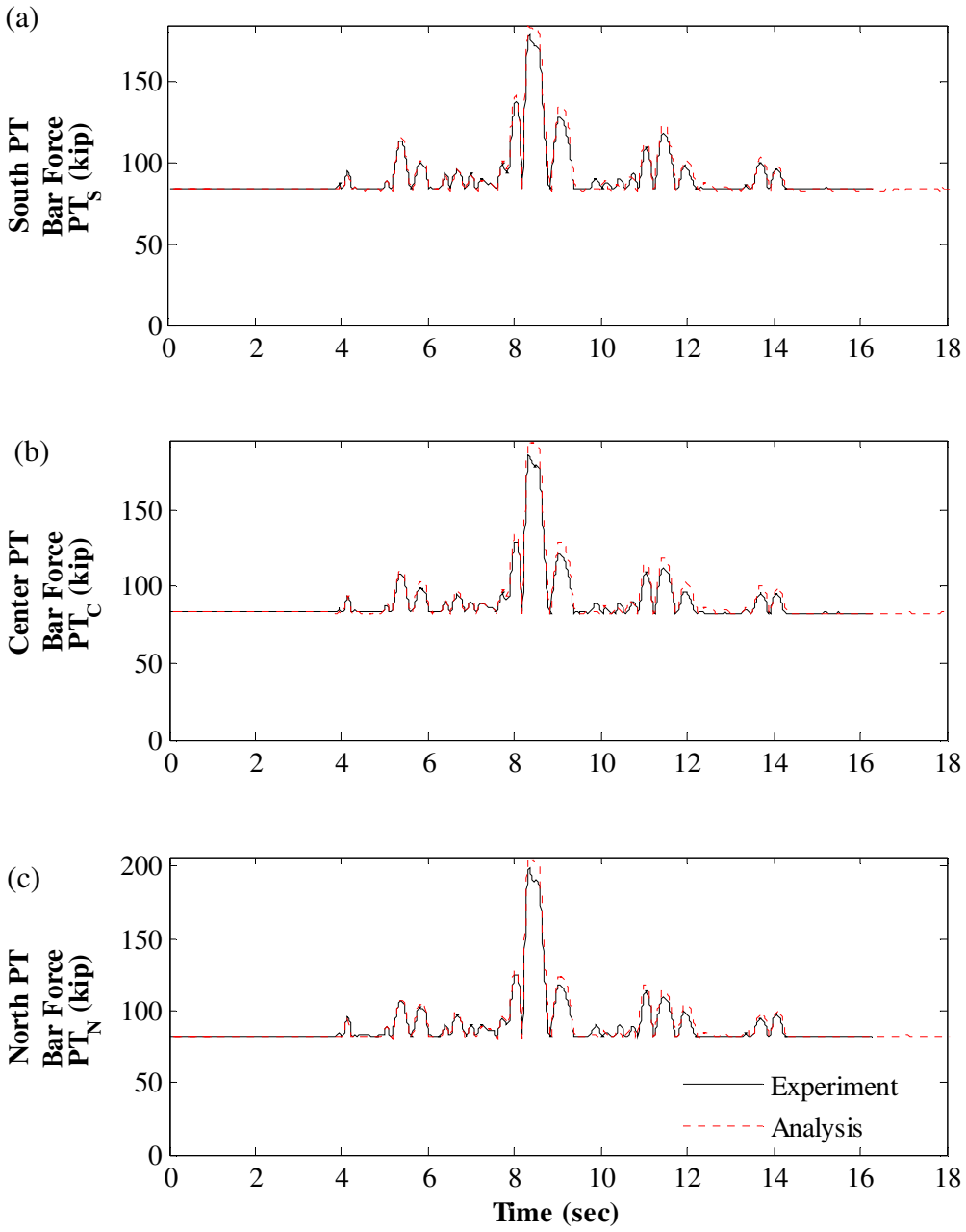

Figure 11.46 – Correlation of PT force response to MCE_stn110: (a) south PT bars; (b) center PT bars; (c) north PT bars

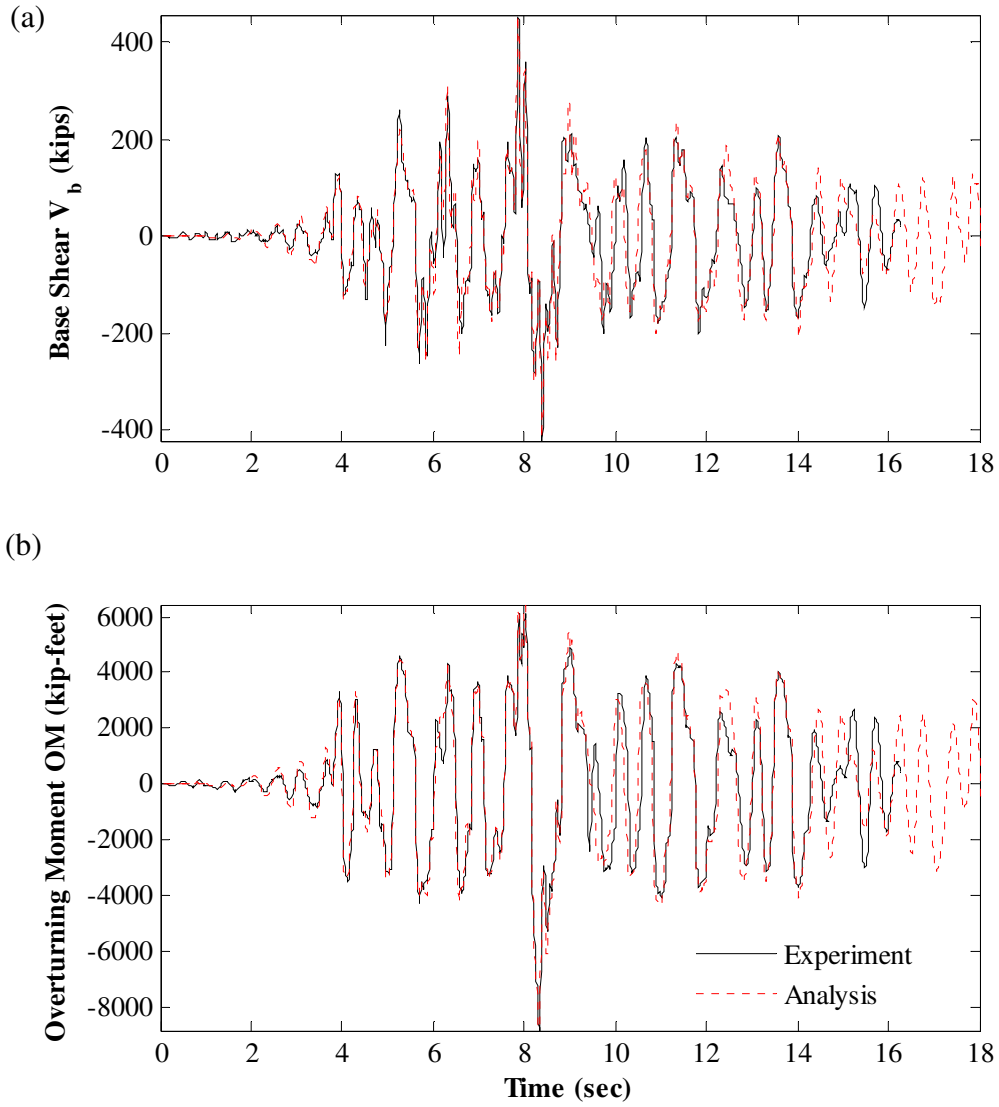

Figure 11.47 – MCE_stn110 response correlation: (a) base shear; (b) overturning moment

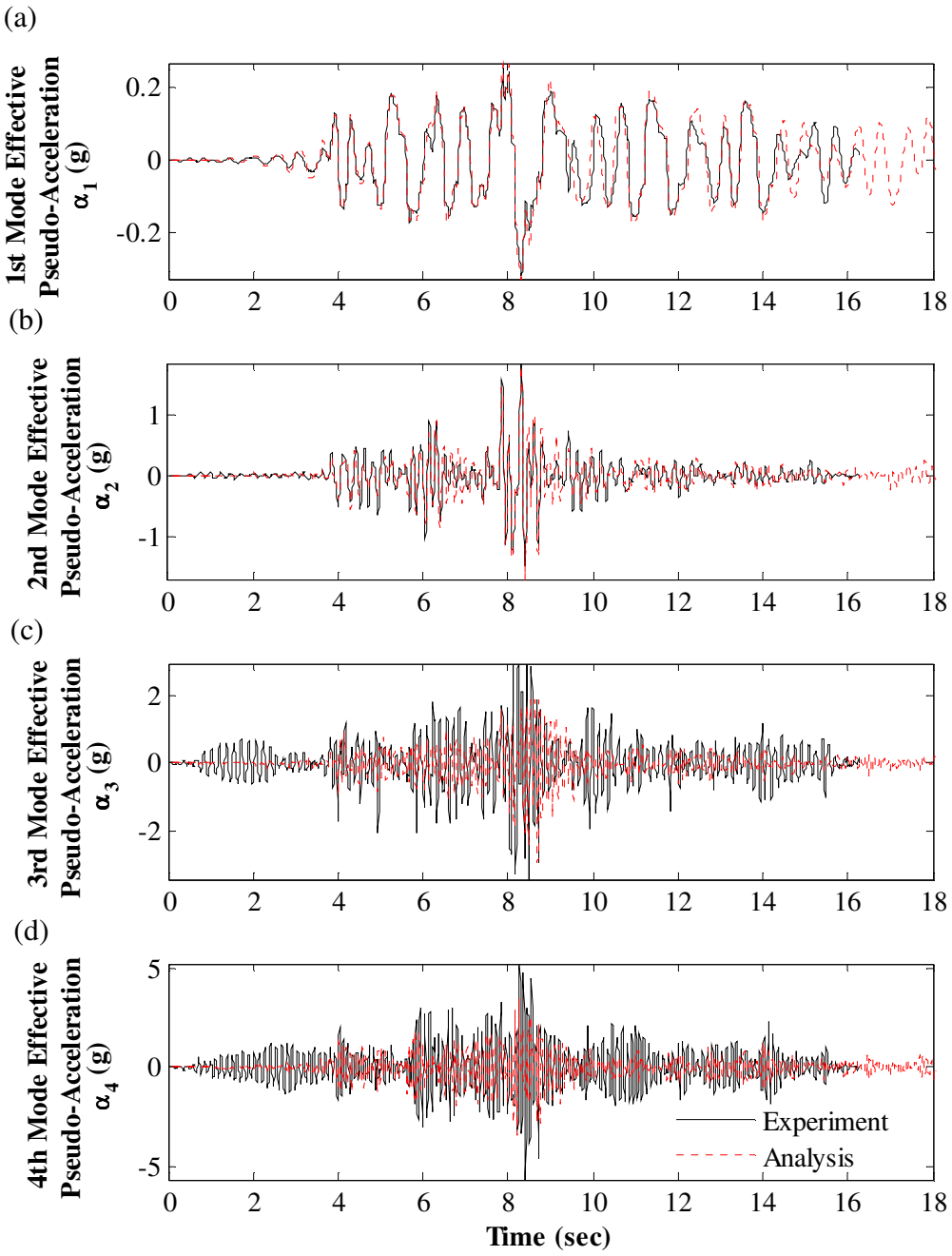

Figure 11.48 – Correlation of effective modal pseudo-acceleration response to MCE_stn110: (a) 1st mode; (b) 2nd mode; (c) 3rd mode; (d) 4th mode

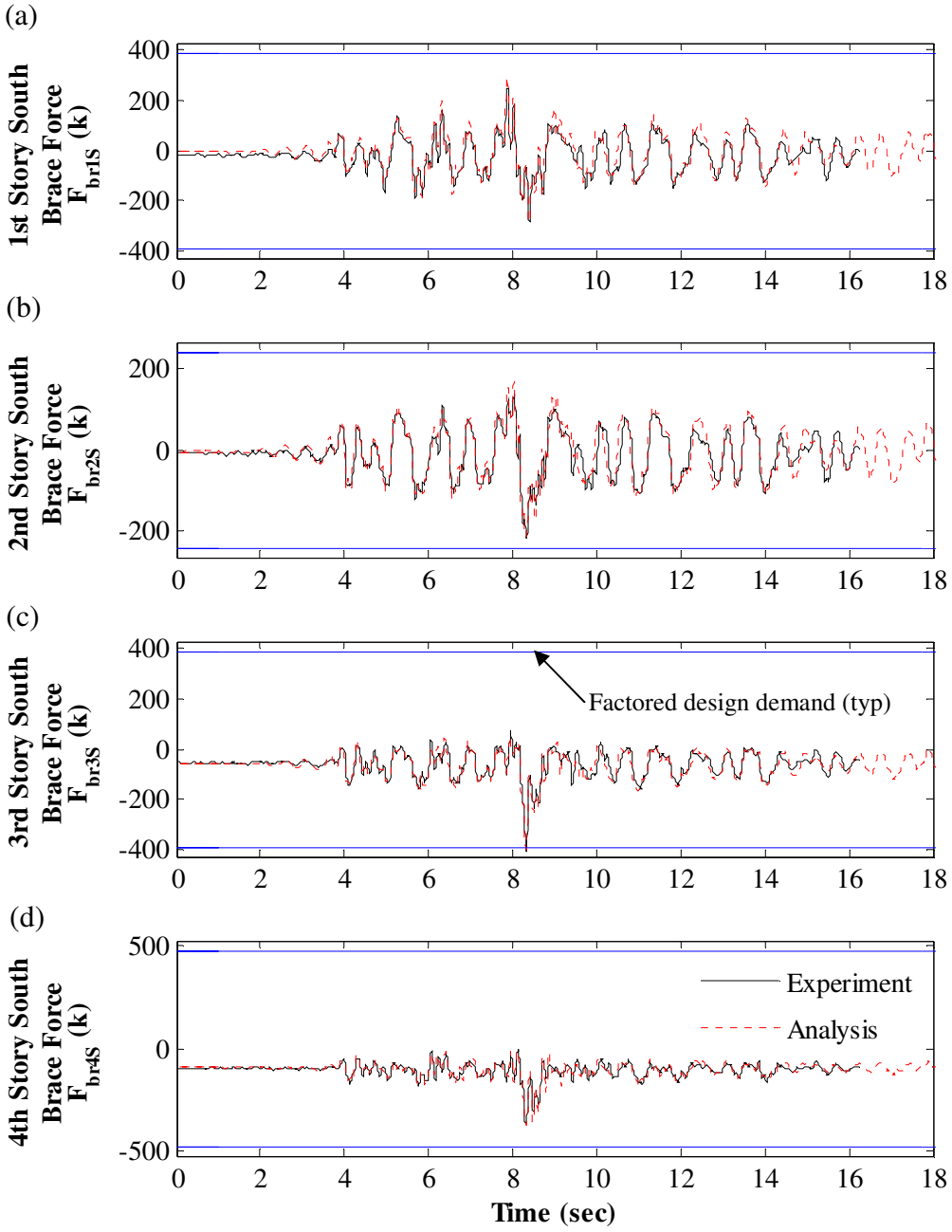

Figure 11.49 – Correlation of south brace axial force response to MCE_stn110: (a) 1st story; (b) 2nd story; (c) 3rd story; (d) 4th story

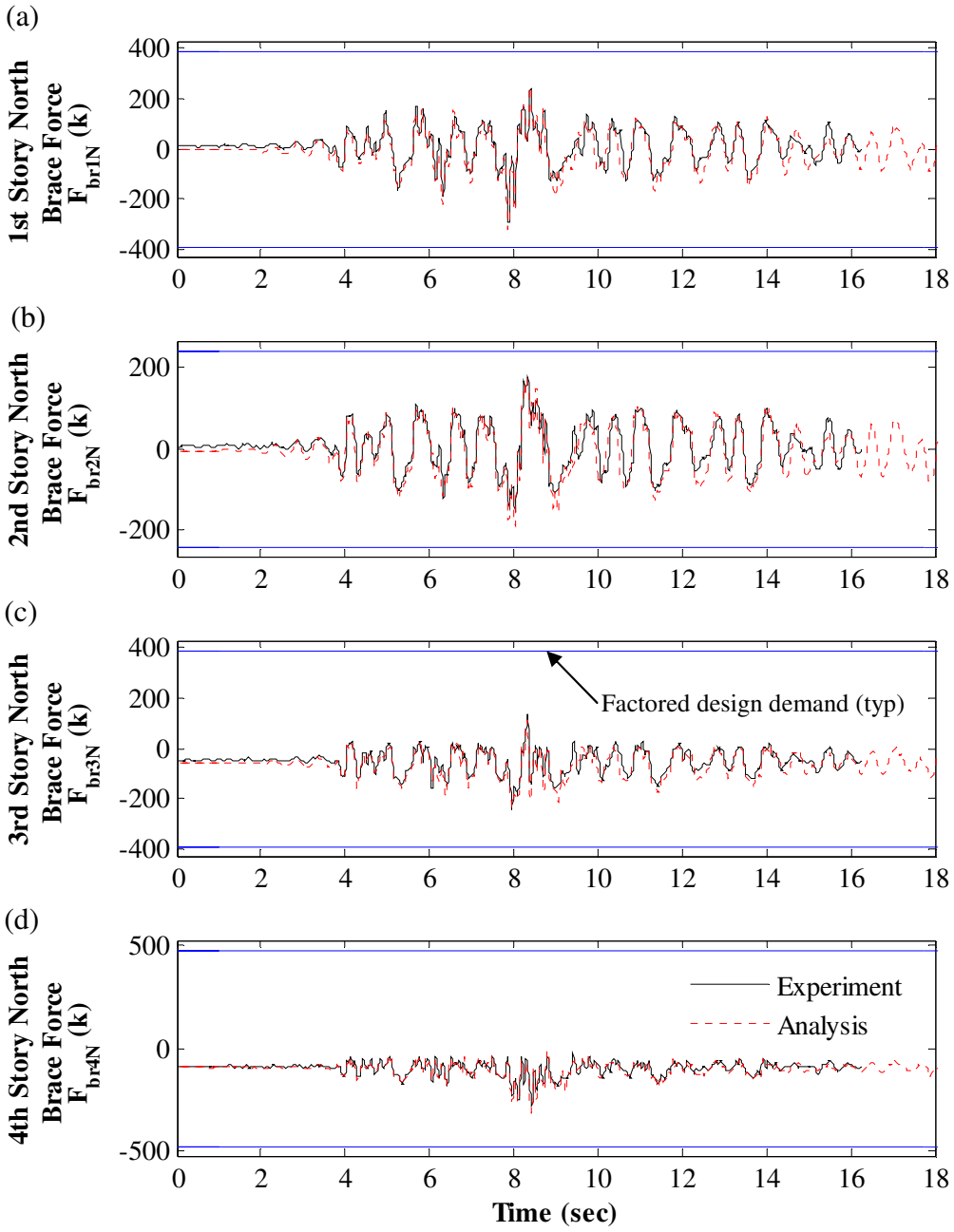

Figure 11.50 – Correlation of north brace axial force response to MCE_stn110: (a) 1st story; (b) 2nd story; (c) 3rd story; (d) 4th story

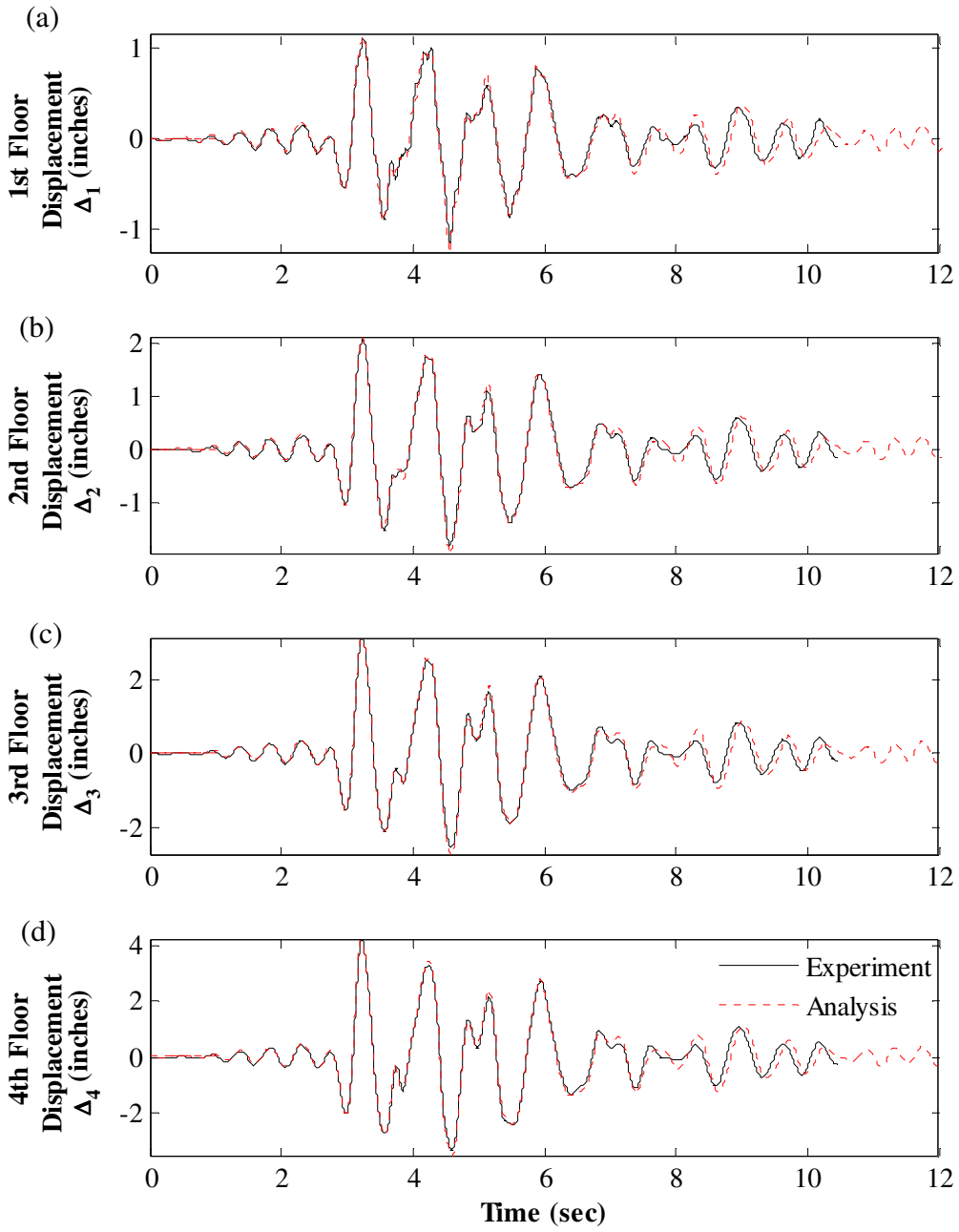

Figure 11.51 – Correlation of floor displacement response to MCE_a-tmz270: (a) 1st floor; (b) 2nd floor; (c) 3rd floor; (d) 4th floor

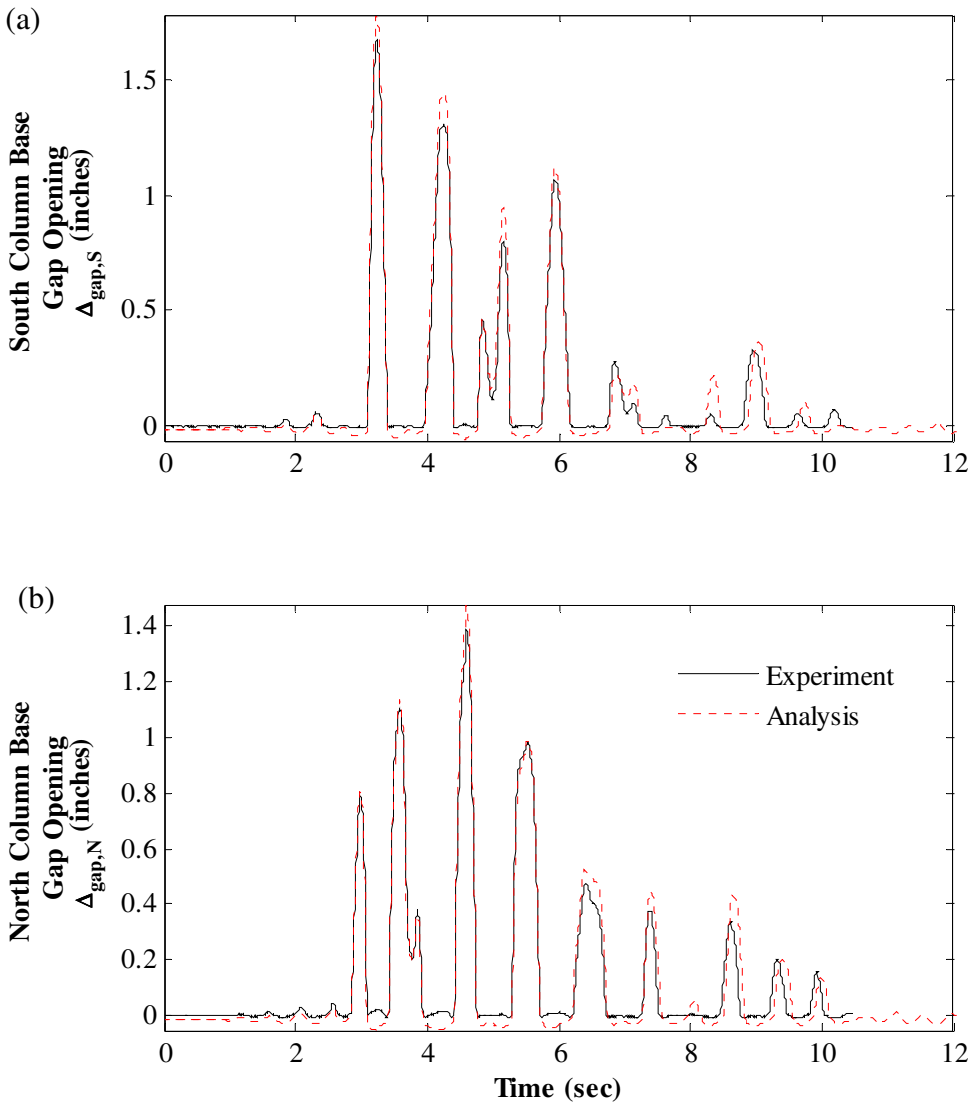

Figure 11.52 – Correlation of column base gap opening response to MCE_a-tmz270: (a) at south column base; (b) at north column base

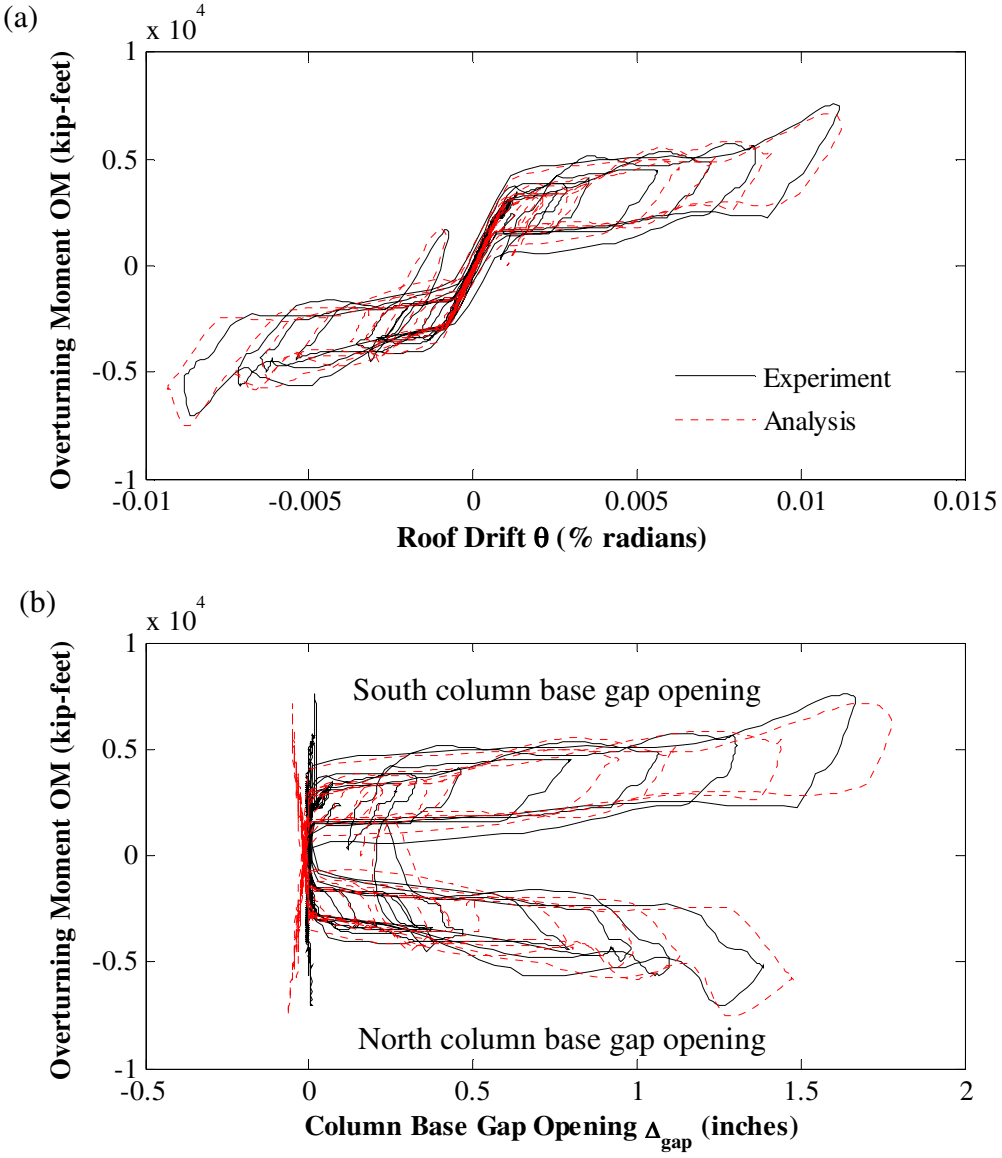

Figure 11.53 – Correlation of hysteretic response to MCE_a-tmz270: (a) overturning moment versus roof drift; (b) overturning moment versus column base gap opening

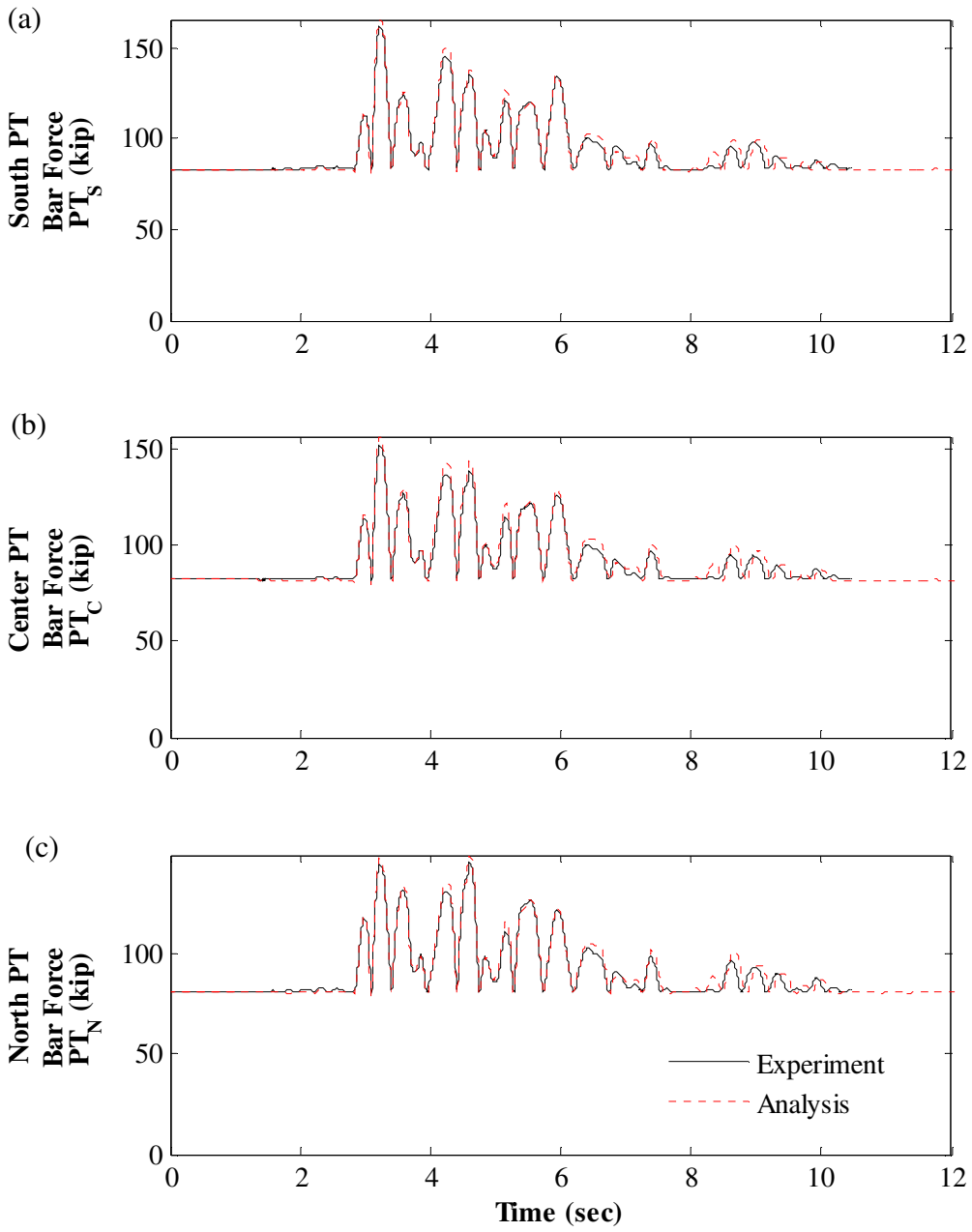

Figure 11.54 – Correlation of PT force response to MCE_a-tmz270: (a) south PT bars; (b) center PT bars; (c) north PT bars

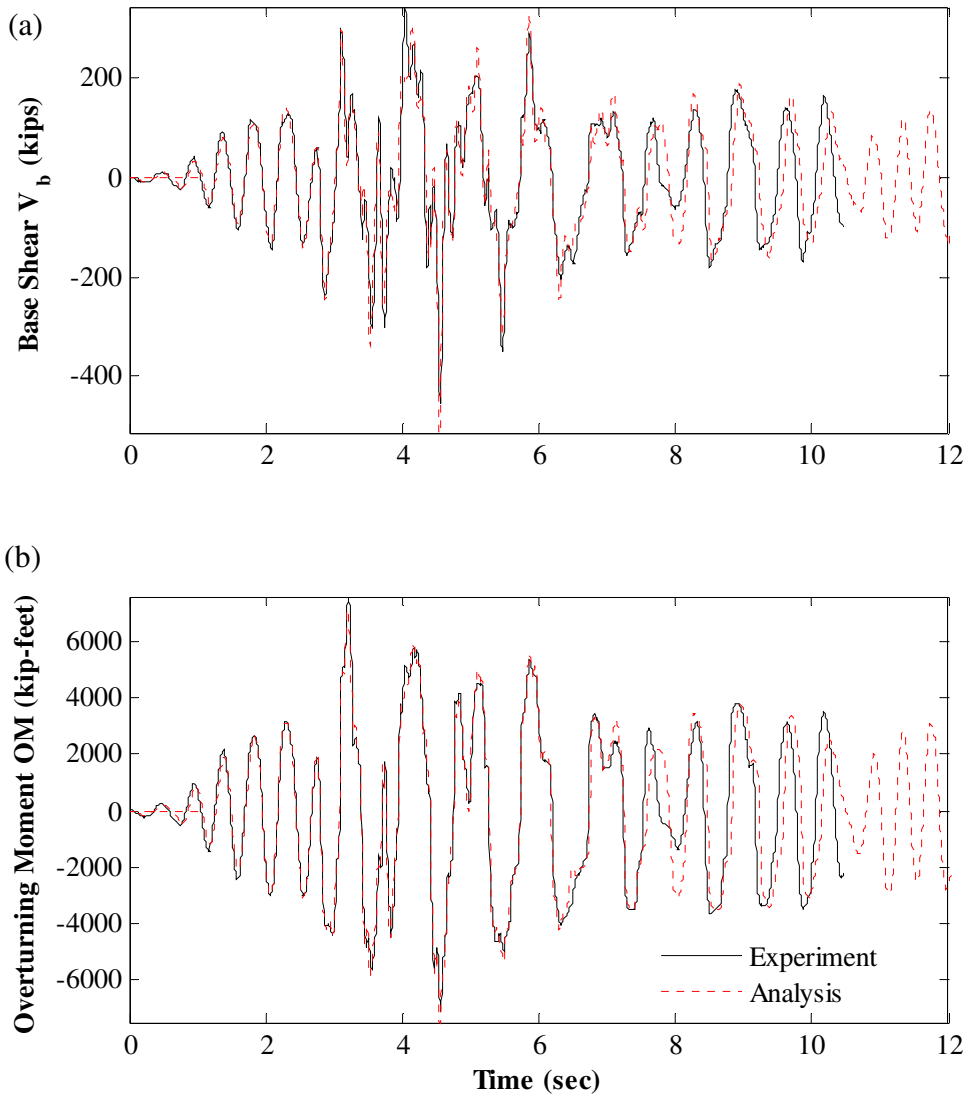

Figure 11.55 – MCE_a-tmz270 response correlation: (a) base shear; (b) overturning moment

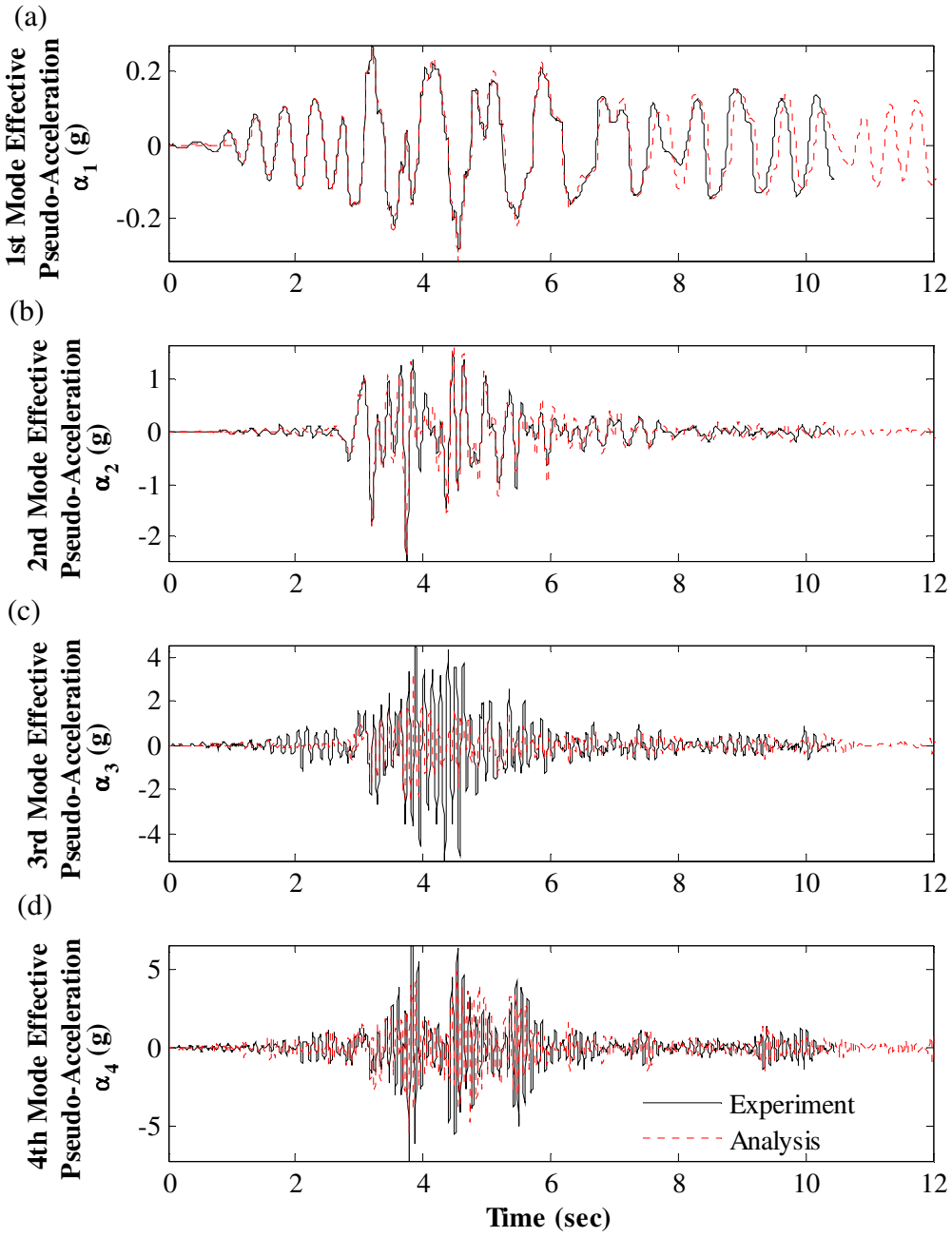

Figure 11.56 – Correlation of effective modal pseudo-acceleration response to MCE_a-tmz270: (a) 1st mode; (b) 2nd mode; (c) 3rd mode; (d) 4th mode

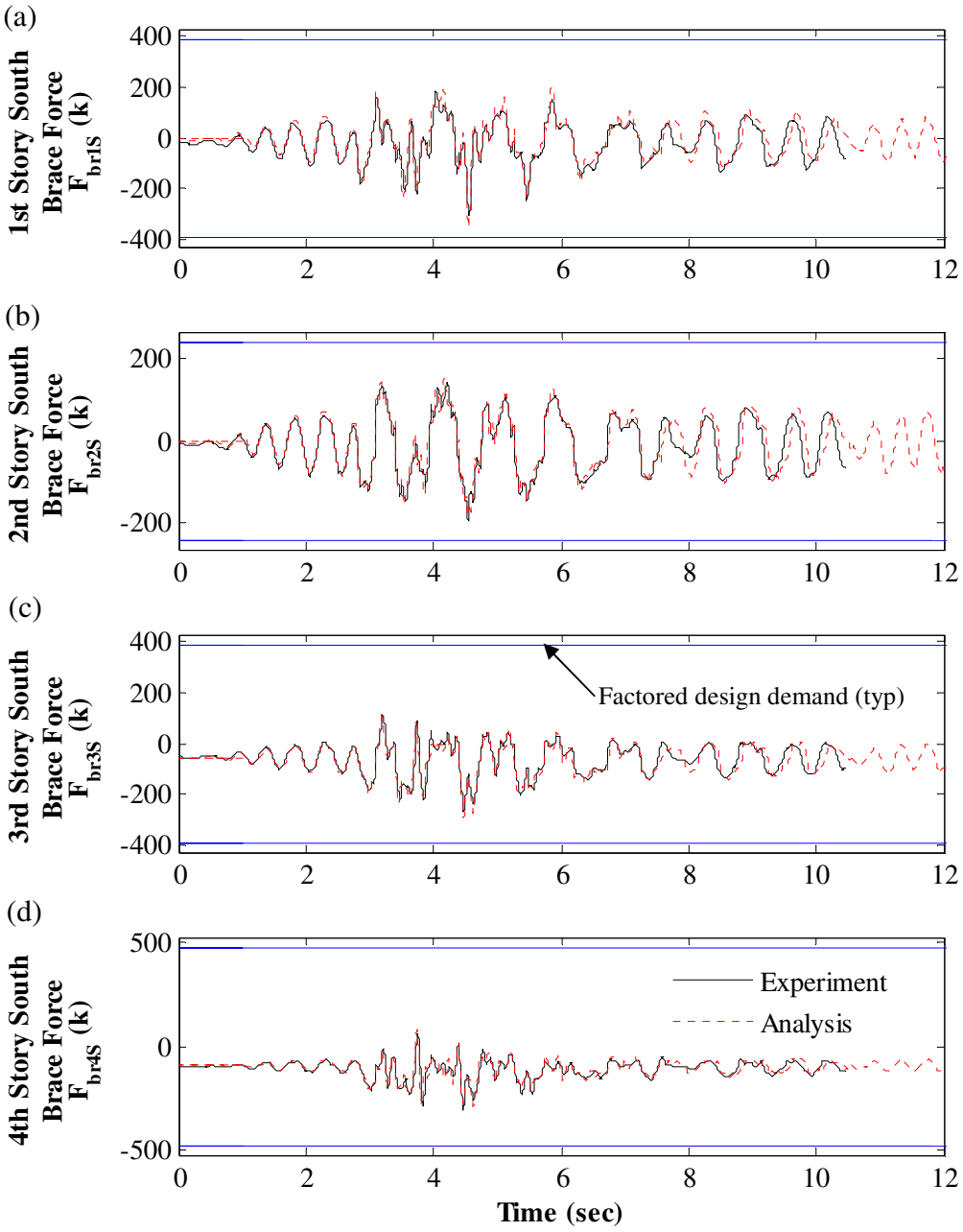

Figure 11.57 – Correlation of south brace axial force response to MCE_a-tmz270: (a) 1st story; (b) 2nd story; (c) 3rd story; (d) 4th story

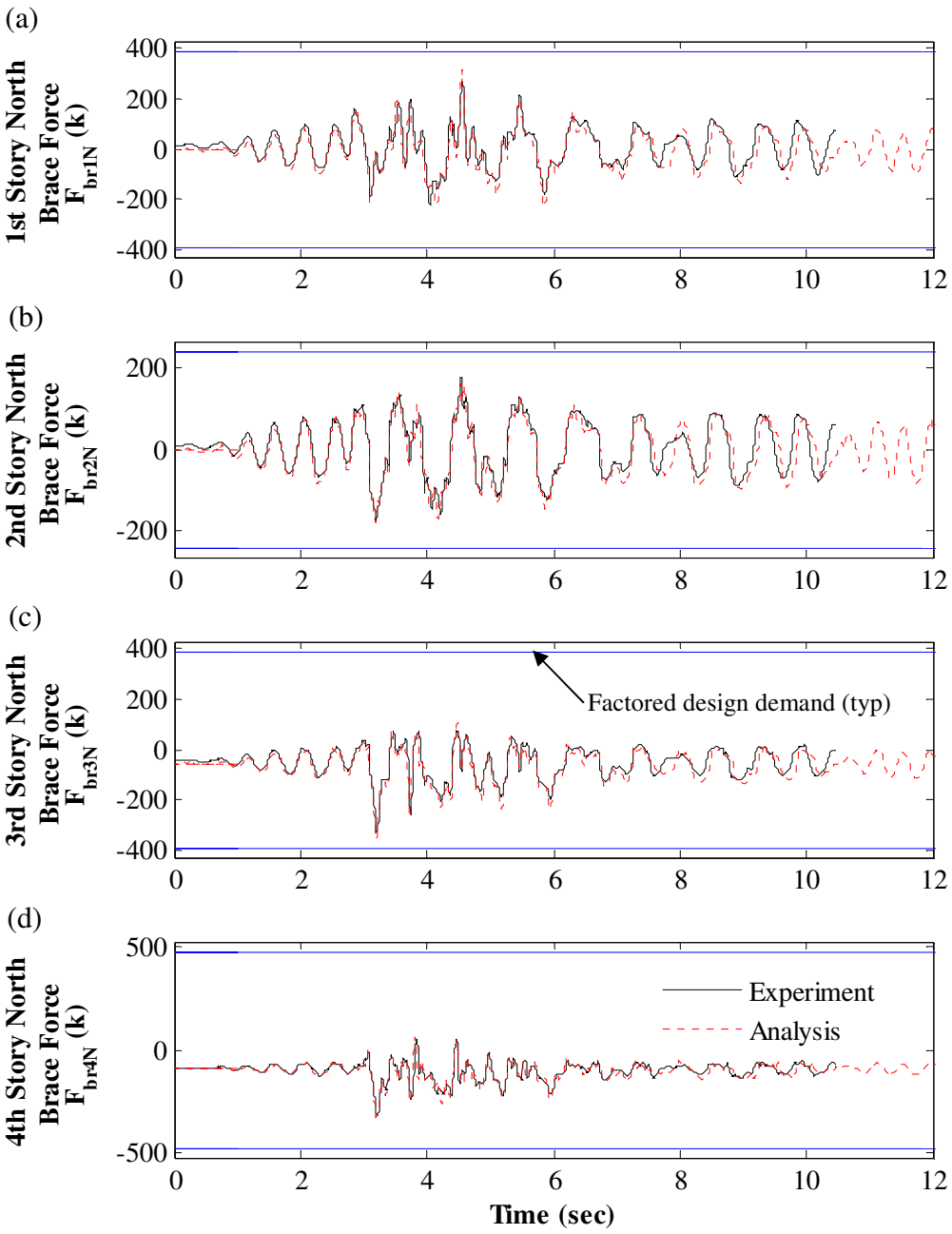

Figure 11.58 – Correlation of north brace axial force response to MCE_a-tmz270: (a) 1st story; (b) 2nd story; (c) 3rd story; (d) 4th story

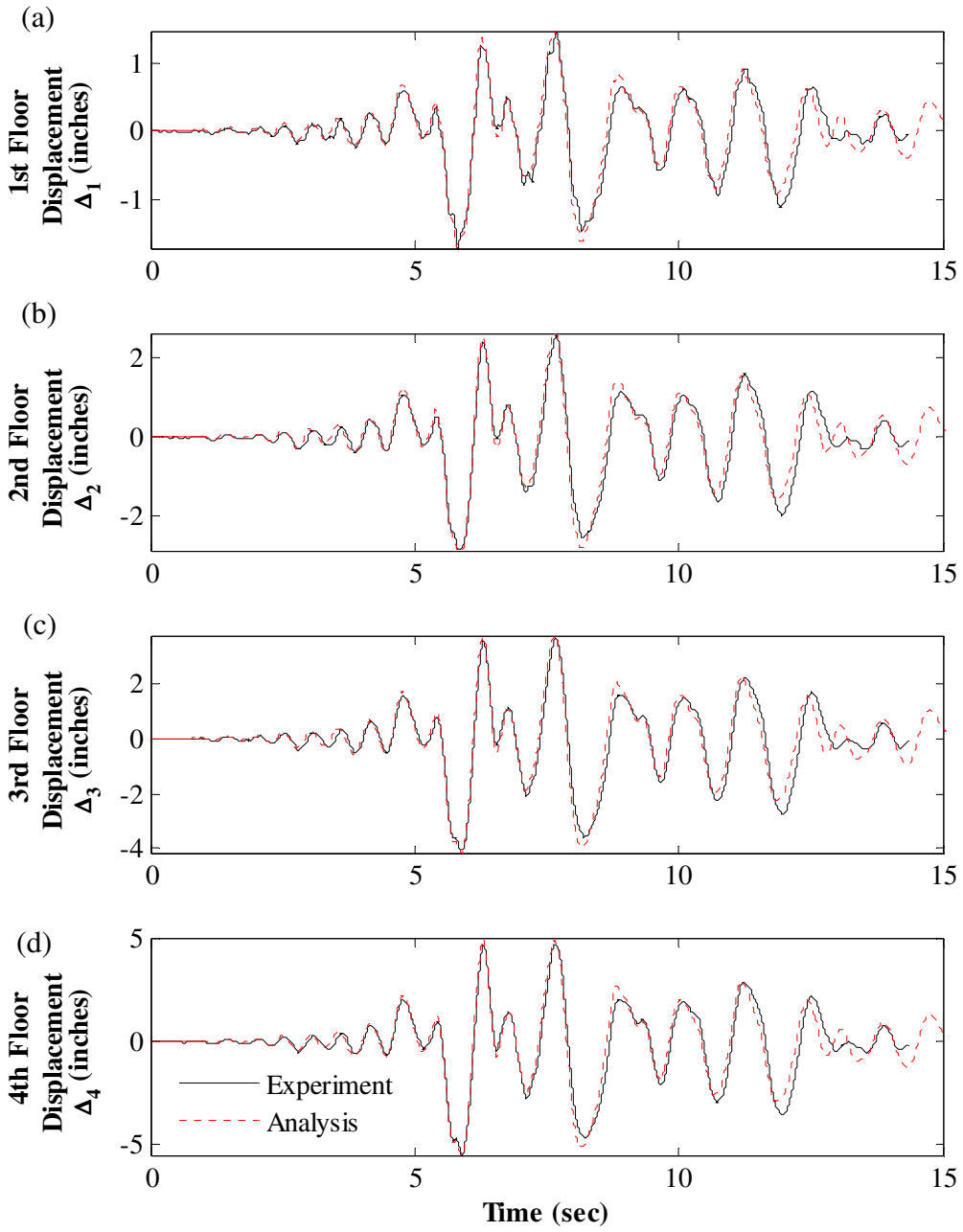

Figure 11.59 – Correlation of floor displacement response to MCE_lp-hda255: (a) 1st floor; (b) 2nd floor; (c) 3rd floor; (d) 4th floor

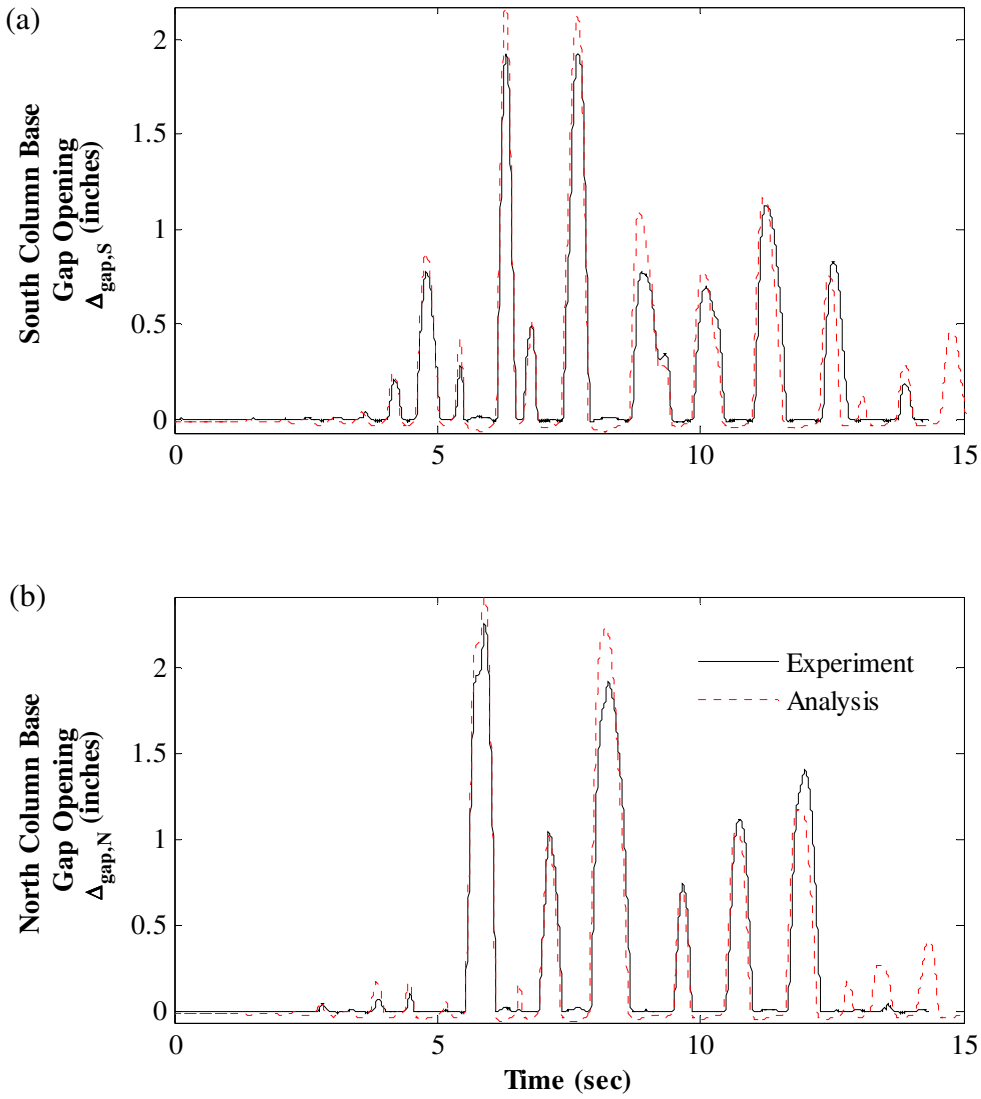

Figure 11.60 – Correlation of column base gap opening response to MCE_lp-hda255: (a) at south column base; (b) at north column base

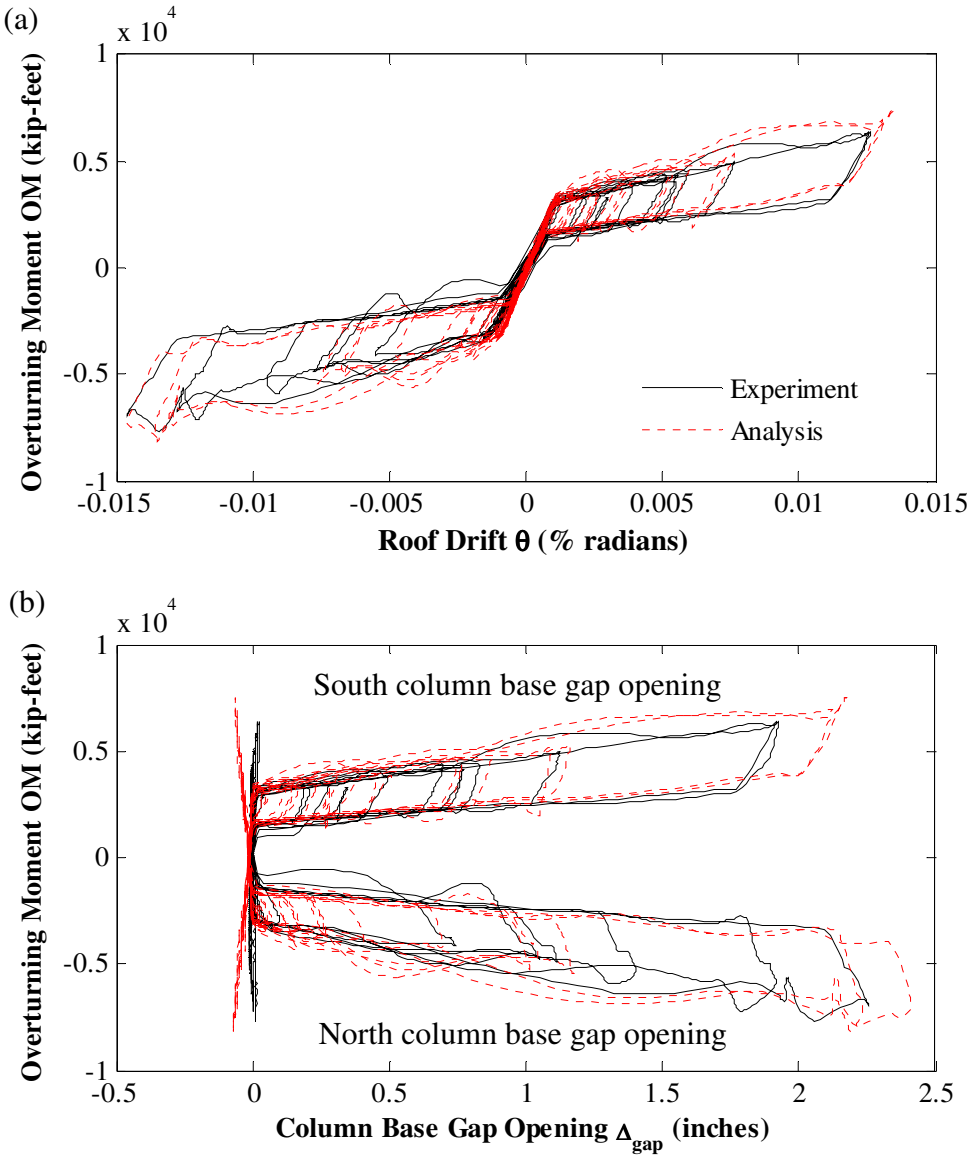

Figure 11.61 – Correlation of hysteretic response to MCE_lp-hda255: (a) overturning moment versus roof drift; (b) overturning moment versus column base gap opening

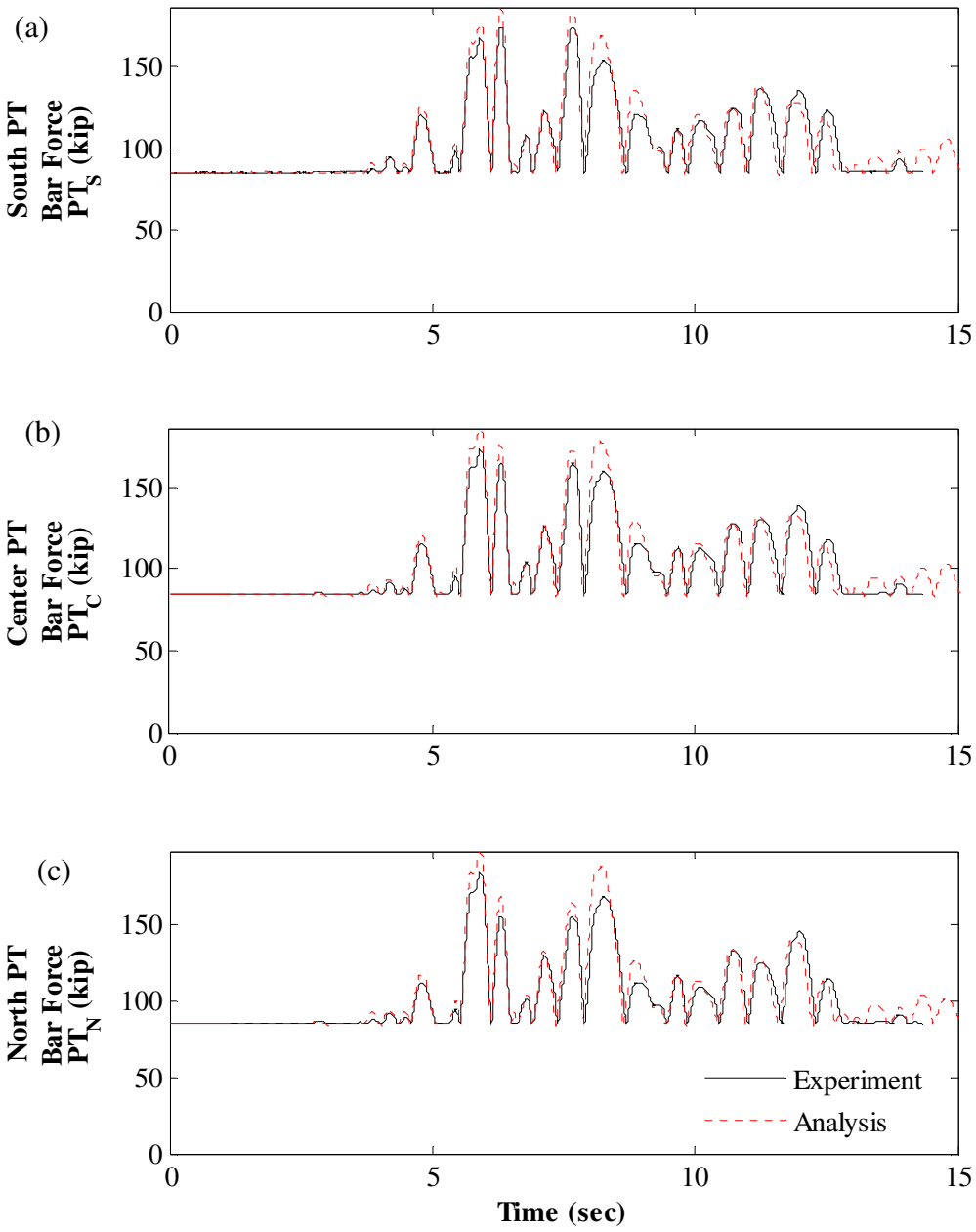

Figure 11.62 – Correlation of PT force response to MCE_lp-hda255: (a) south PT bars; (b) center PT bars; (c) north PT bars

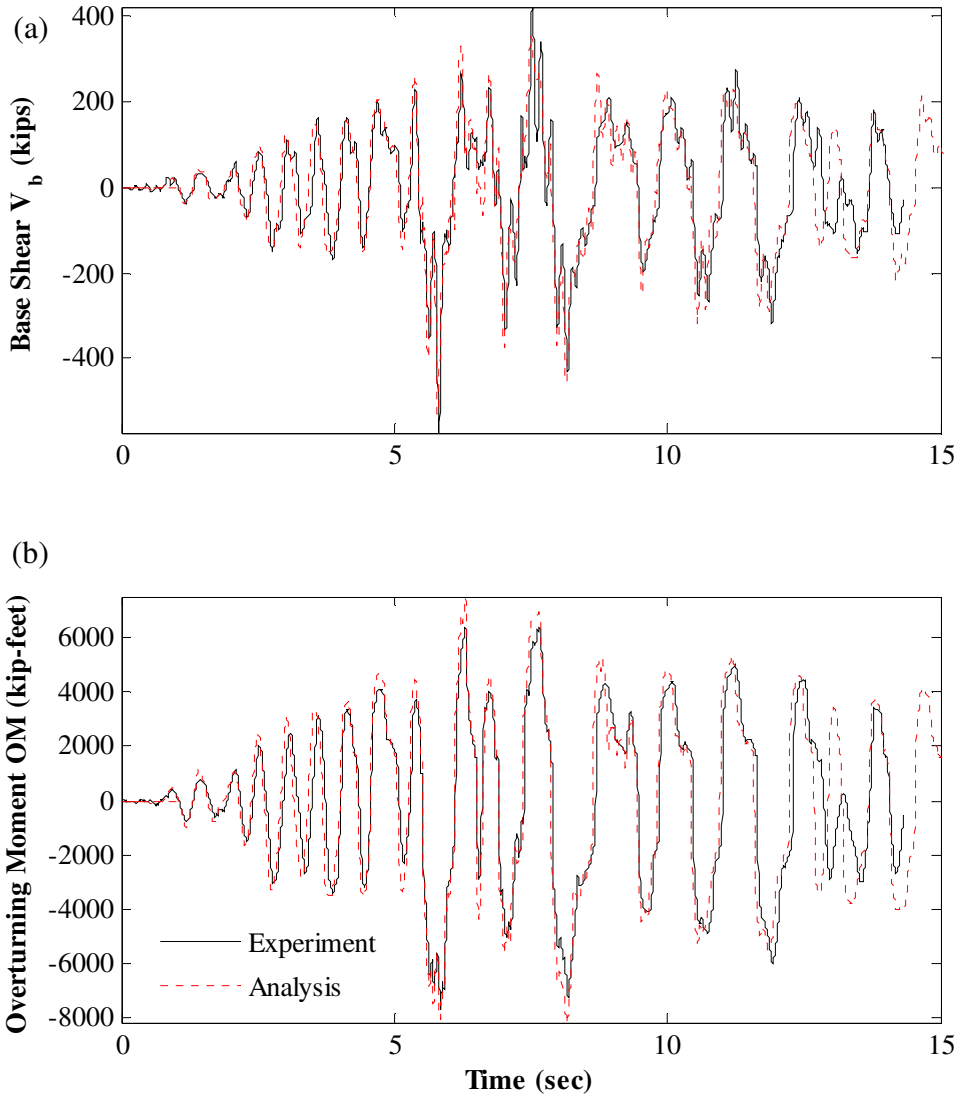

Figure 11.63 – MCE_lp-hda255 response correlation: (a) base shear; (b) overturning moment

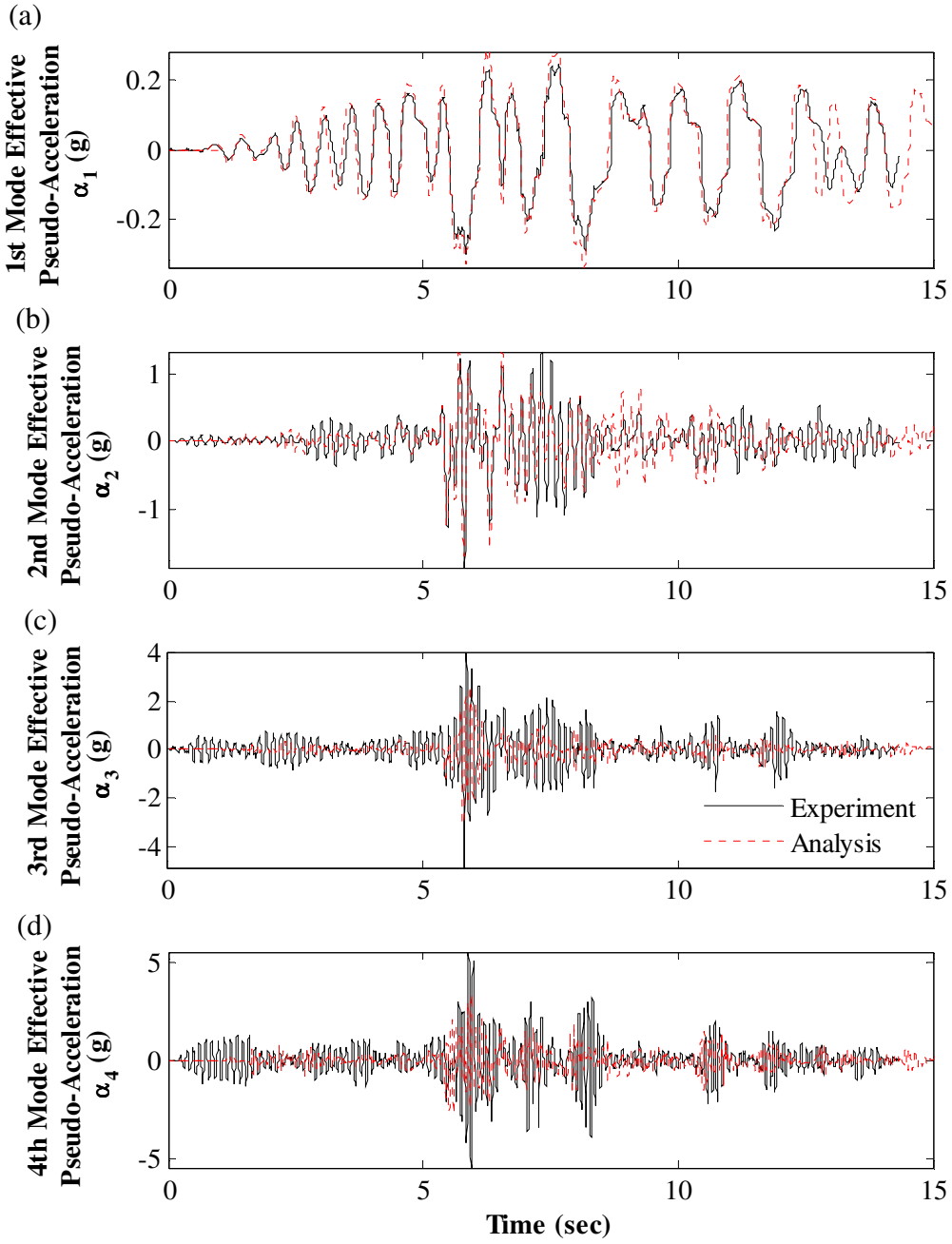

Figure 11.64 – Correlation of effective modal pseudo-acceleration response to MCE_lp-hda255: (a) 1st mode; (b) 2nd mode; (c) 3rd mode; (d) 4th mode

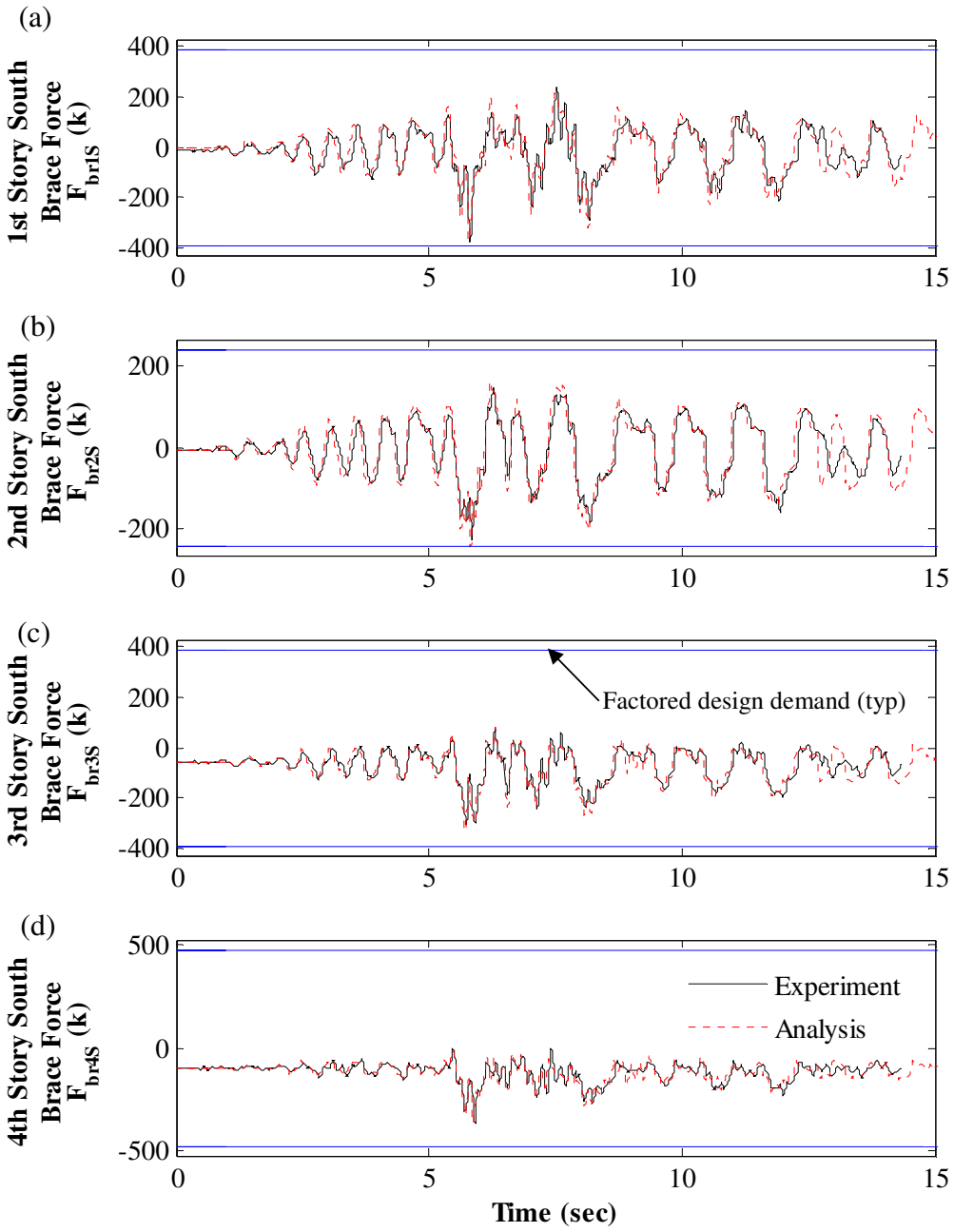

Figure 11.65 – Correlation of south brace axial force response to MCE_lp-hda255: (a) 1st story; (b) 2nd story; (c) 3rd story; (d) 4th story

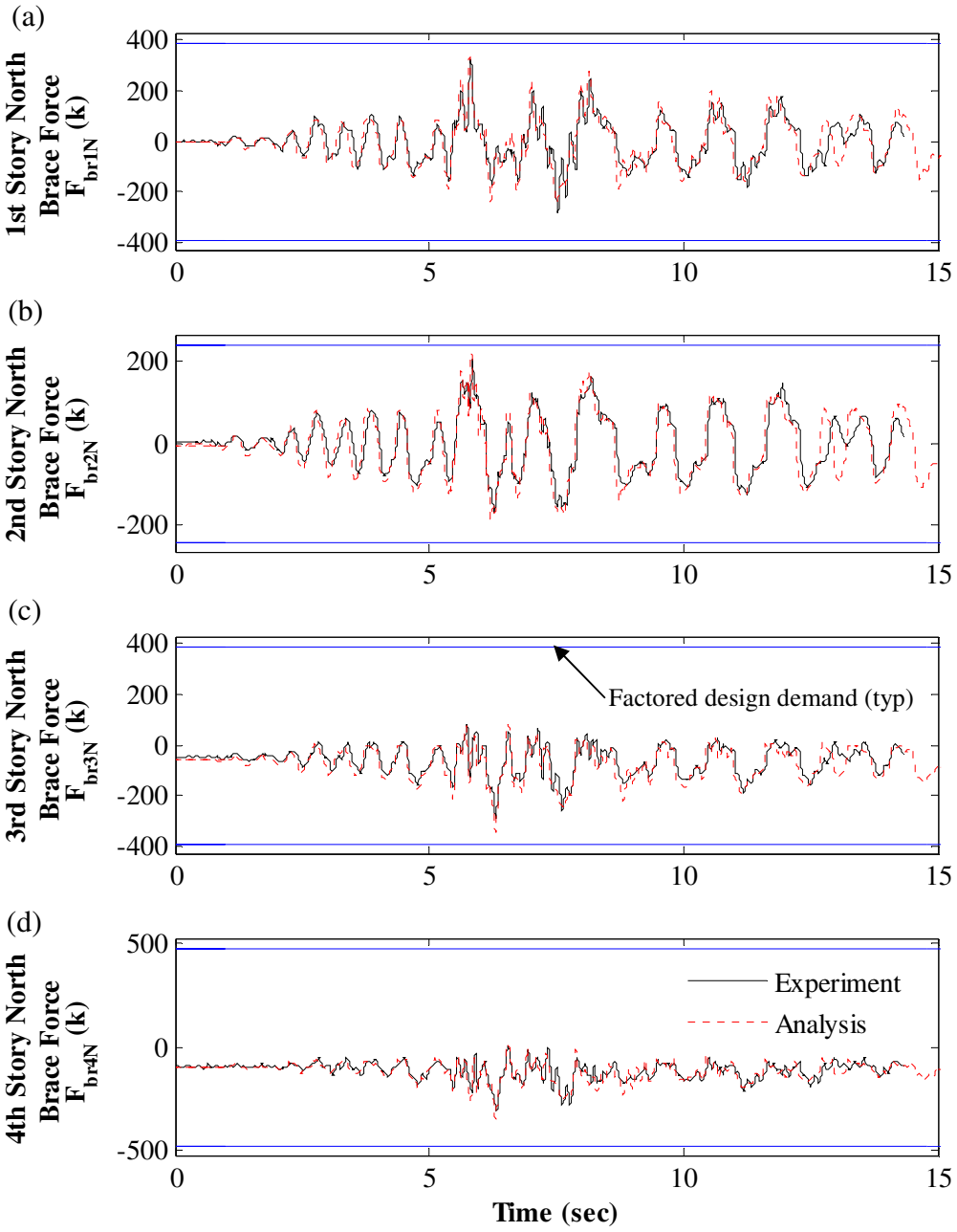

Figure 11.66 – Correlation of north brace axial force response to MCE_lp-hda255: (a) 1st story; (b) 2nd story; (c) 3rd story; (d) 4th story

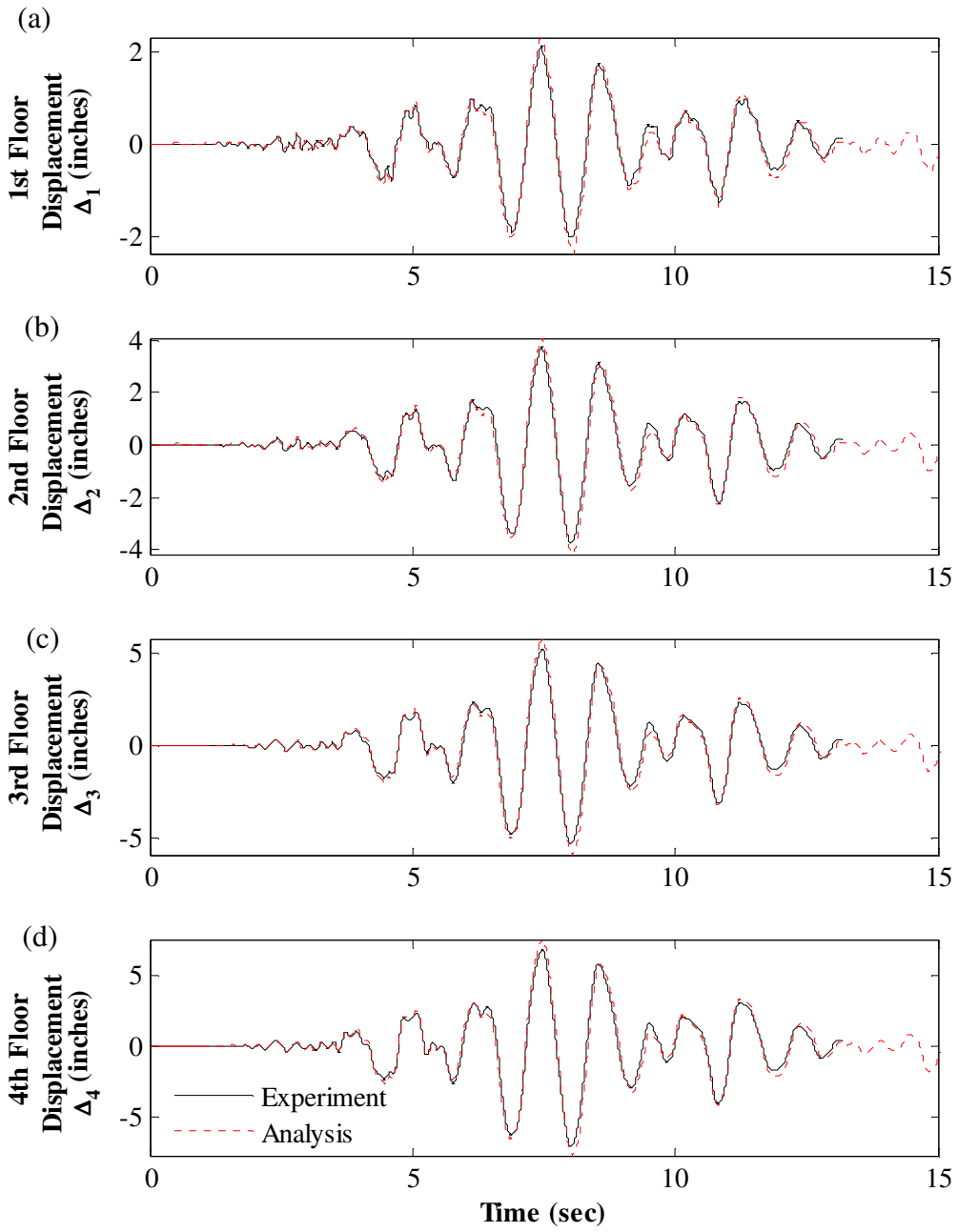

Figure 11.67 – Correlation of floor displacement response to MCE_cap000: (a) 1st floor; (b) 2nd floor; (c) 3rd floor; (d) 4th floor

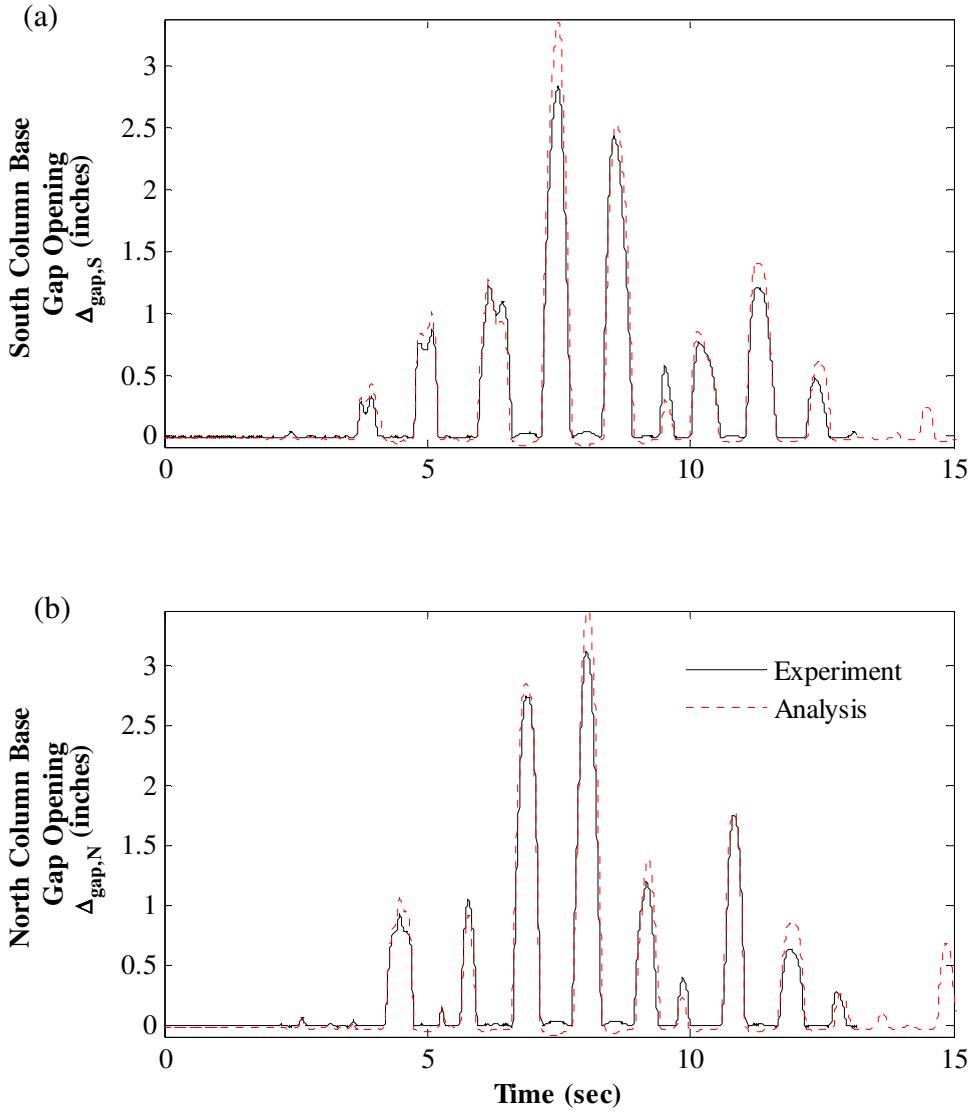

Figure 11.68 – Correlation of column base gap opening response to MCE_cap000: (a) at south column base; (b) at north column base

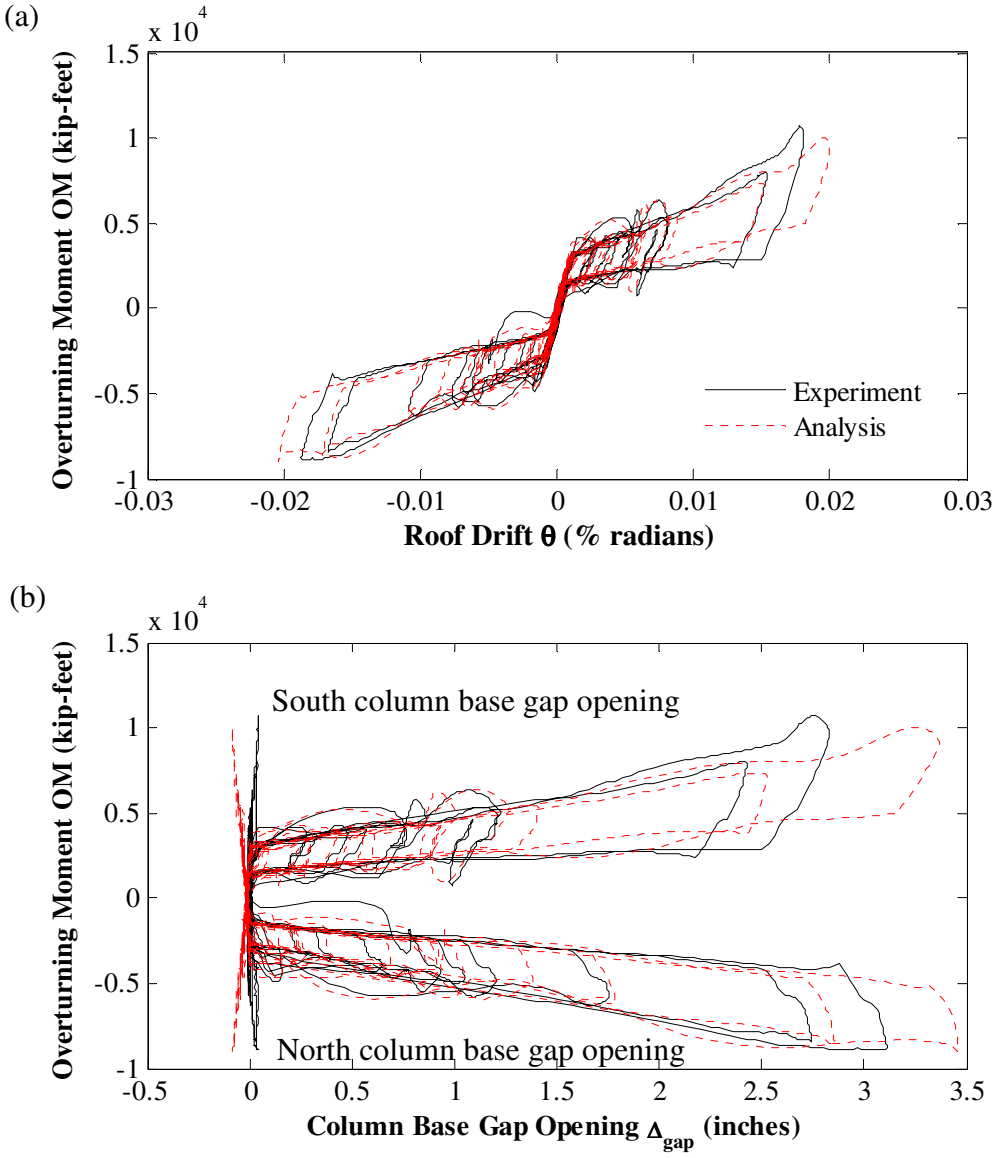

Figure 11.69 – Correlation of hysteretic response to MCE_cap000: (a) overturning moment versus roof drift; (b) overturning moment versus column base gap opening

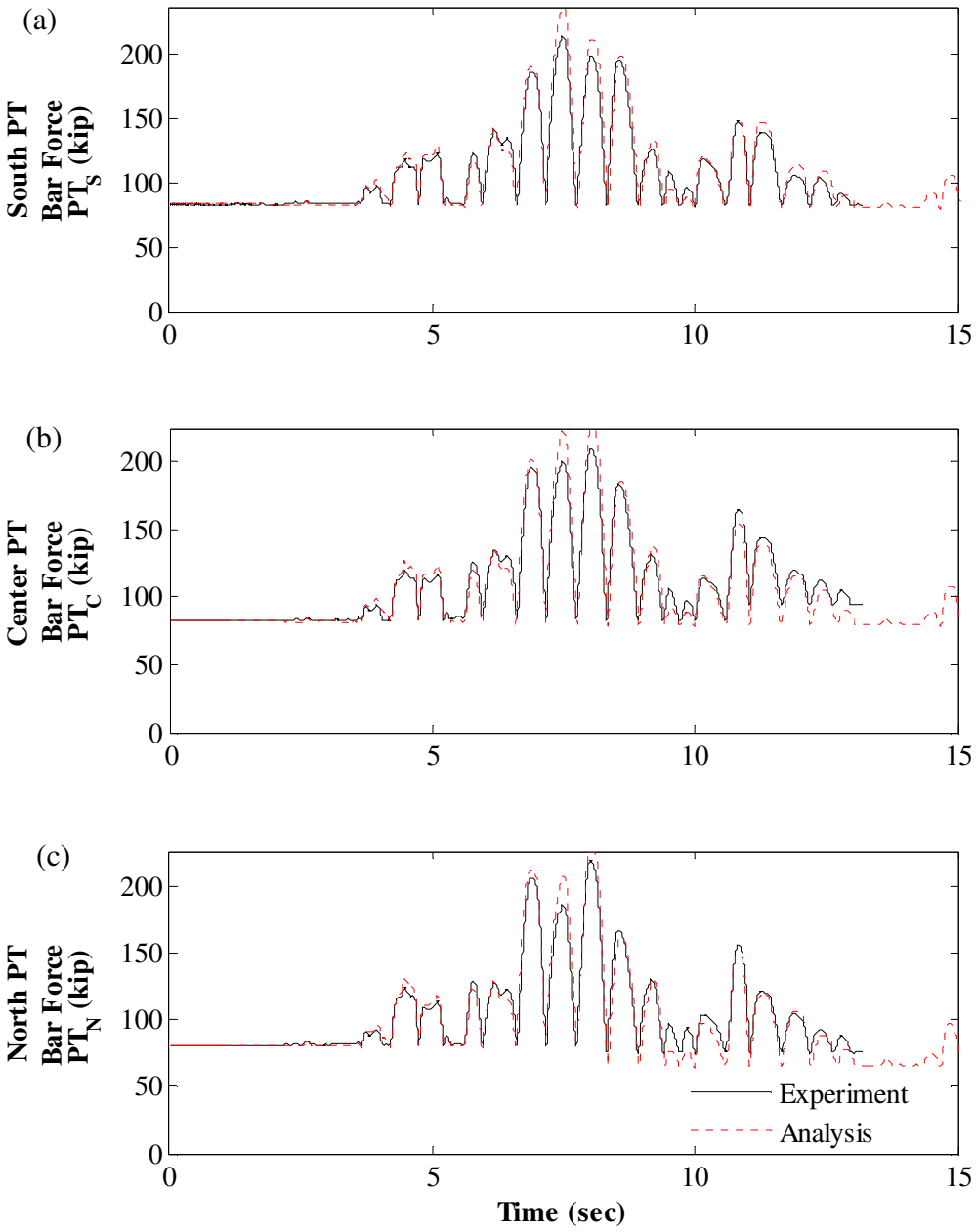

Figure 11.70 – Correlation of PT force response to MCE_cap000: (a) south PT bars; (b) center PT bars; (c) north PT bars

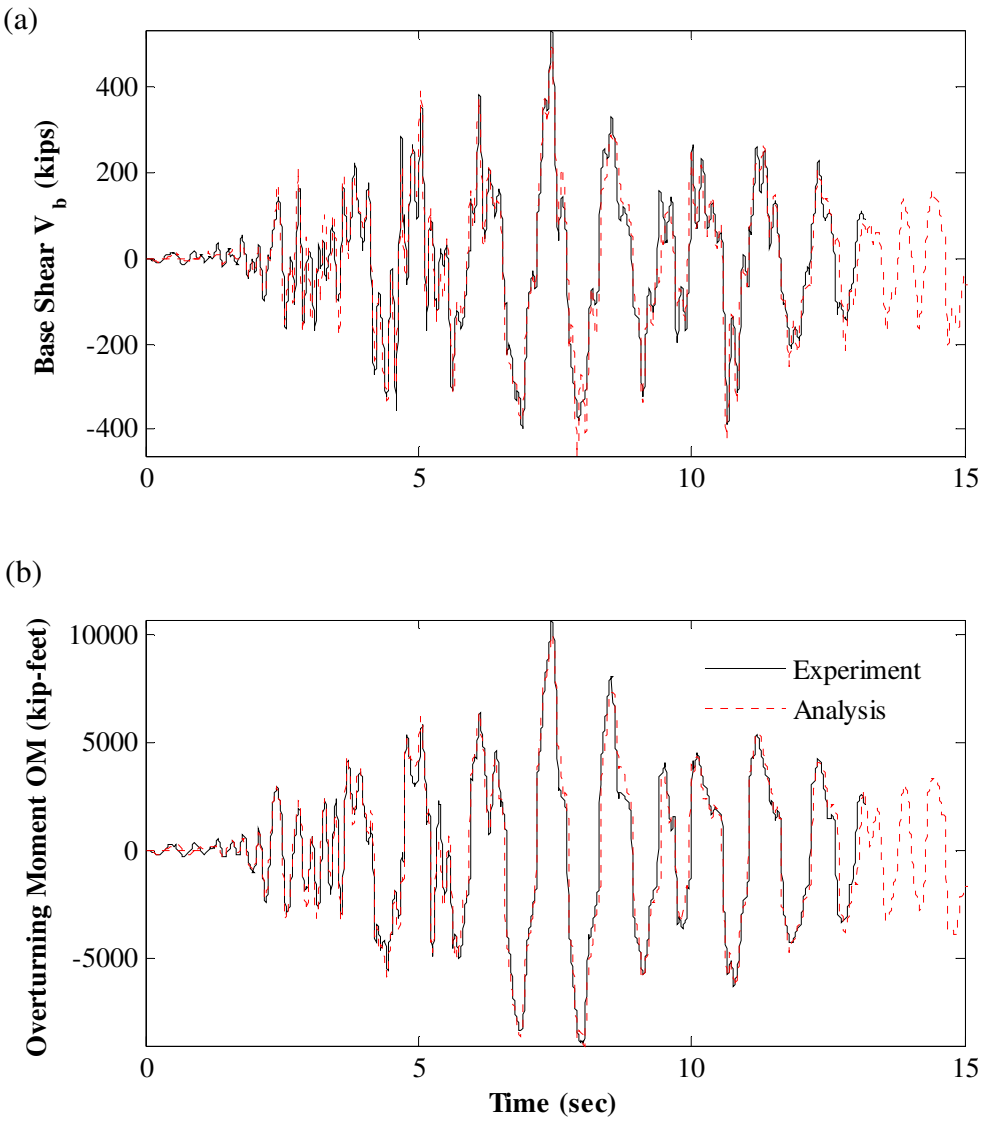

Figure 11.71 – MCE_cap000 response correlation: (a) base shear; (b) overturning moment

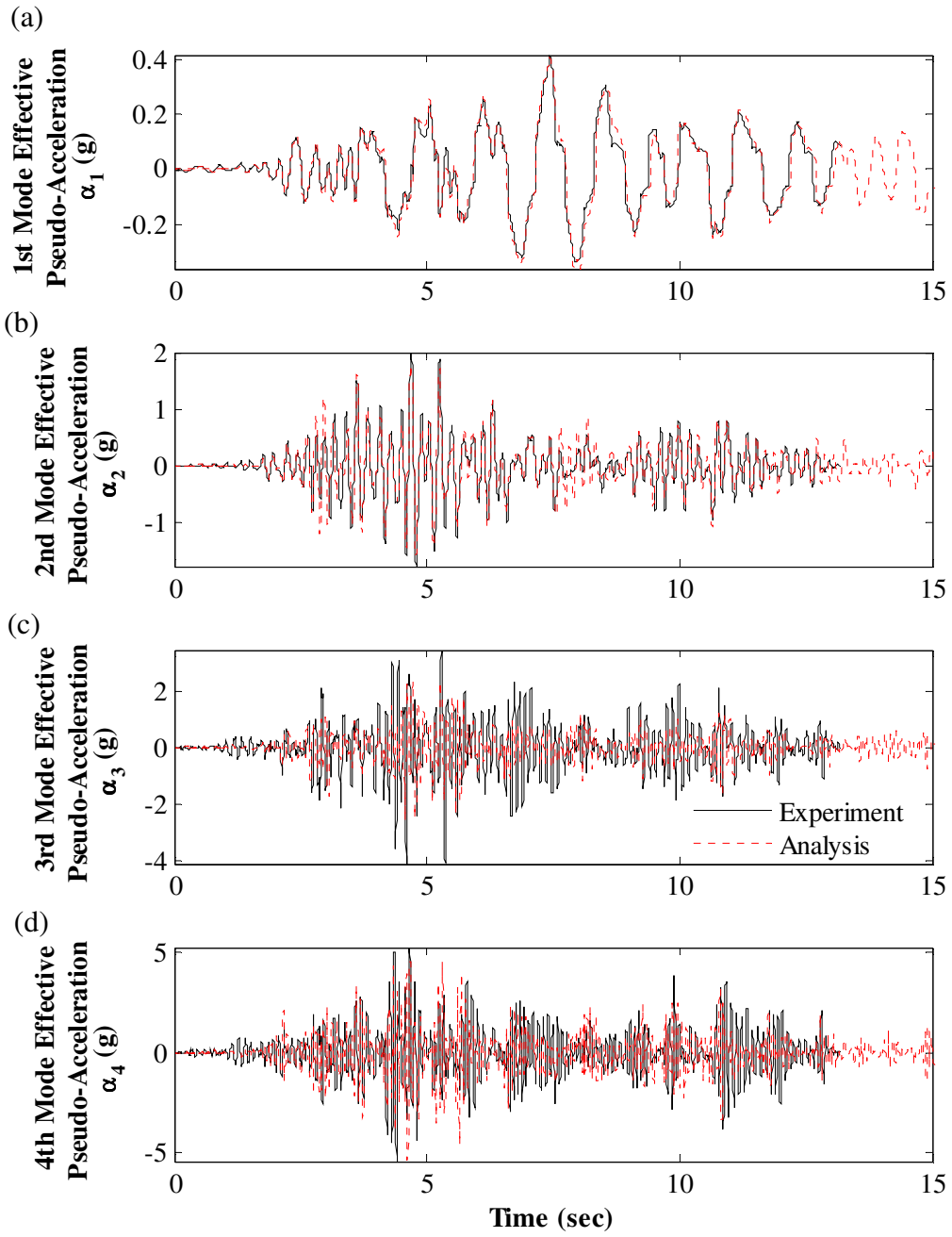

Figure 11.72 – Correlation of effective modal pseudo-acceleration response to MCE_cap000: (a) 1st mode; (b) 2nd mode; (c) 3rd mode; (d) 4th mode

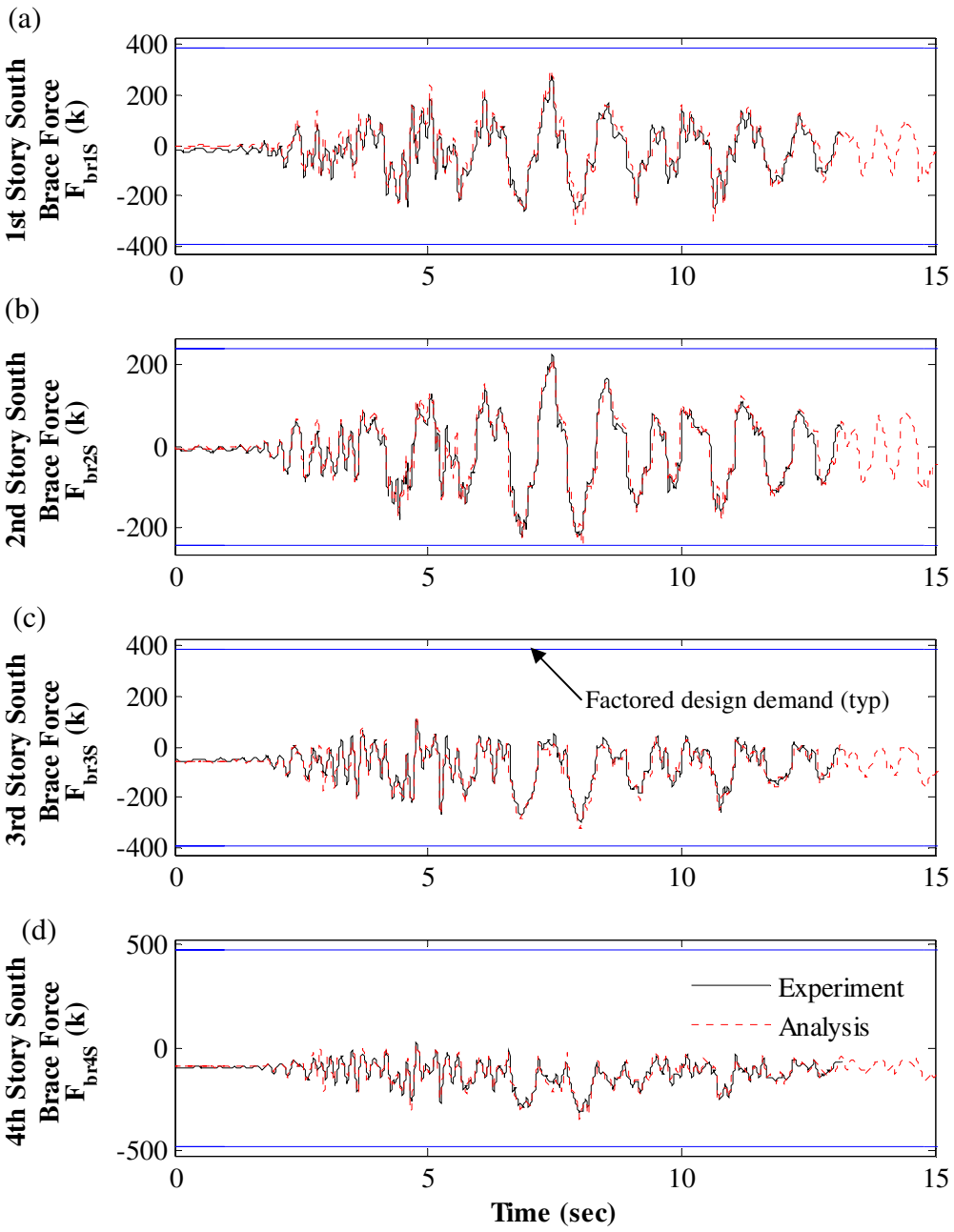

Figure 11.73 – Correlation of south brace axial force response to MCE_cap000: (a) 1st story; (b) 2nd story; (c) 3rd story; (d) 4th story

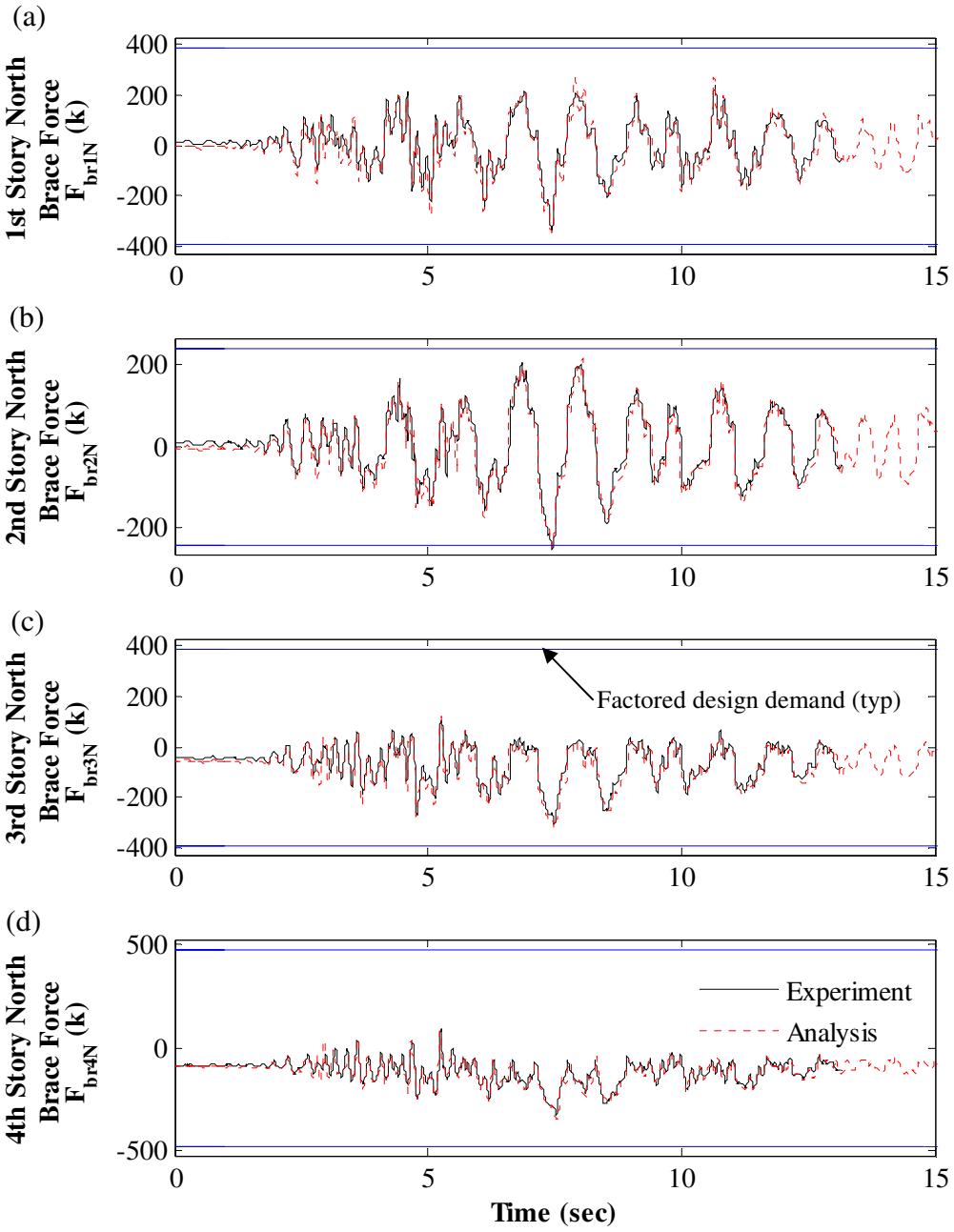

Figure 11.74 –Correlation of north brace axial force response to MCE_cap000: (a) 1st story; (b) 2nd story; (c) 3rd story; (d) 4th story

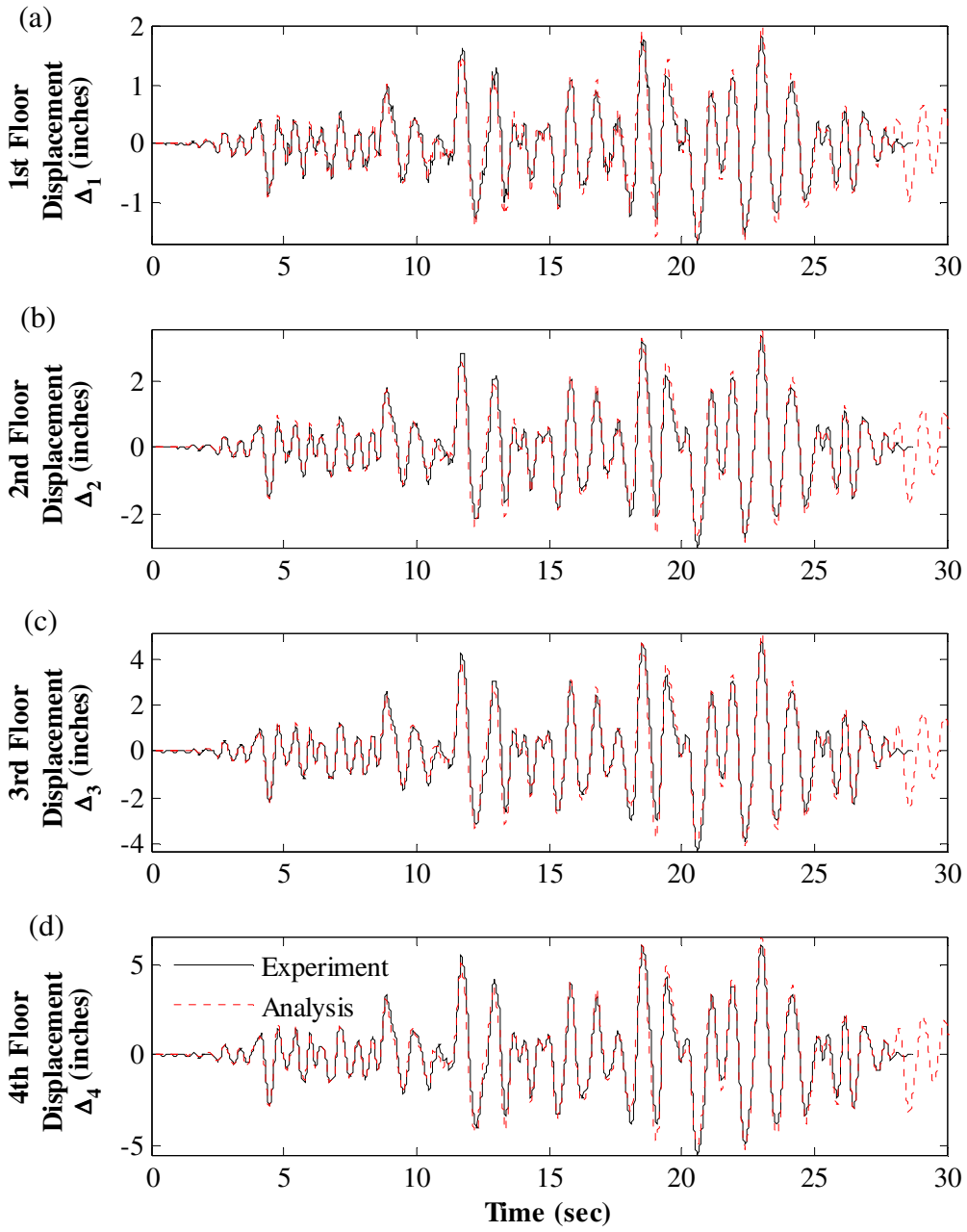

Figure 11.75 – Correlation of floor displacement response to MCE_h-cpe237: (a) 1st floor; (b) 2nd floor; (c) 3rd floor; (d) 4th floor

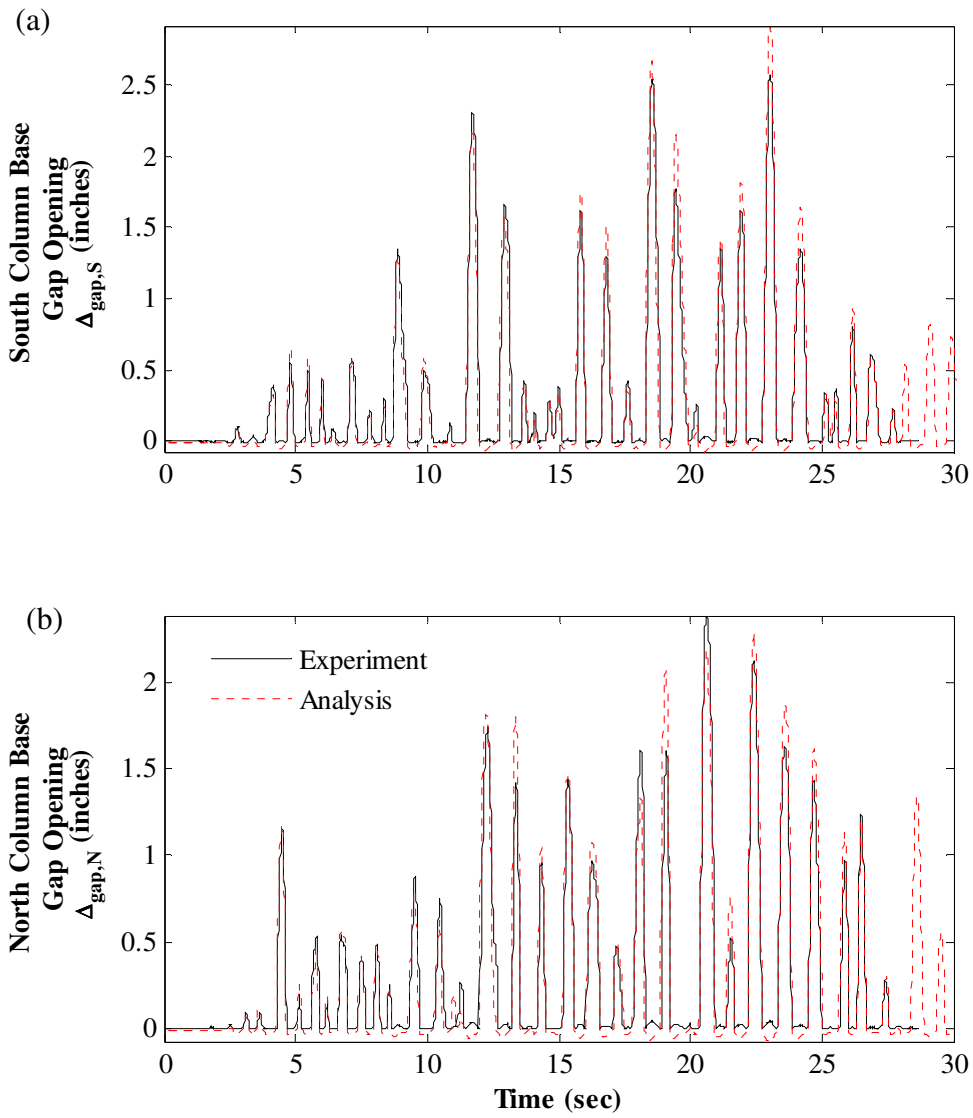

Figure 11.76 – Correlation of column base gap opening response to MCE_h-cpe237: (a) at south column base; (b) at north column base

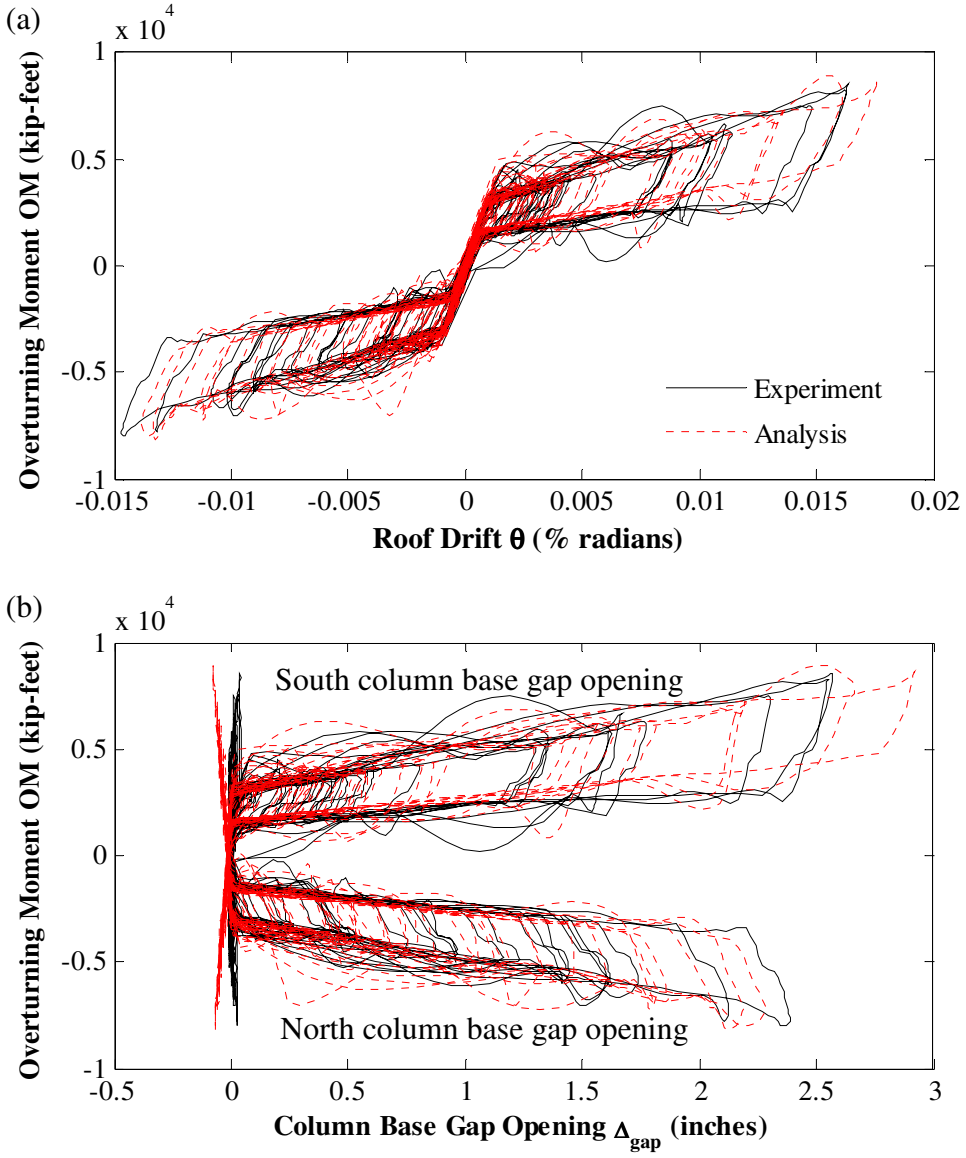

Figure 11.77 – Correlation of hysteretic response to MCE_h-cpe237: (a) overturning moment versus roof drift; (b) overturning moment versus column base gap opening

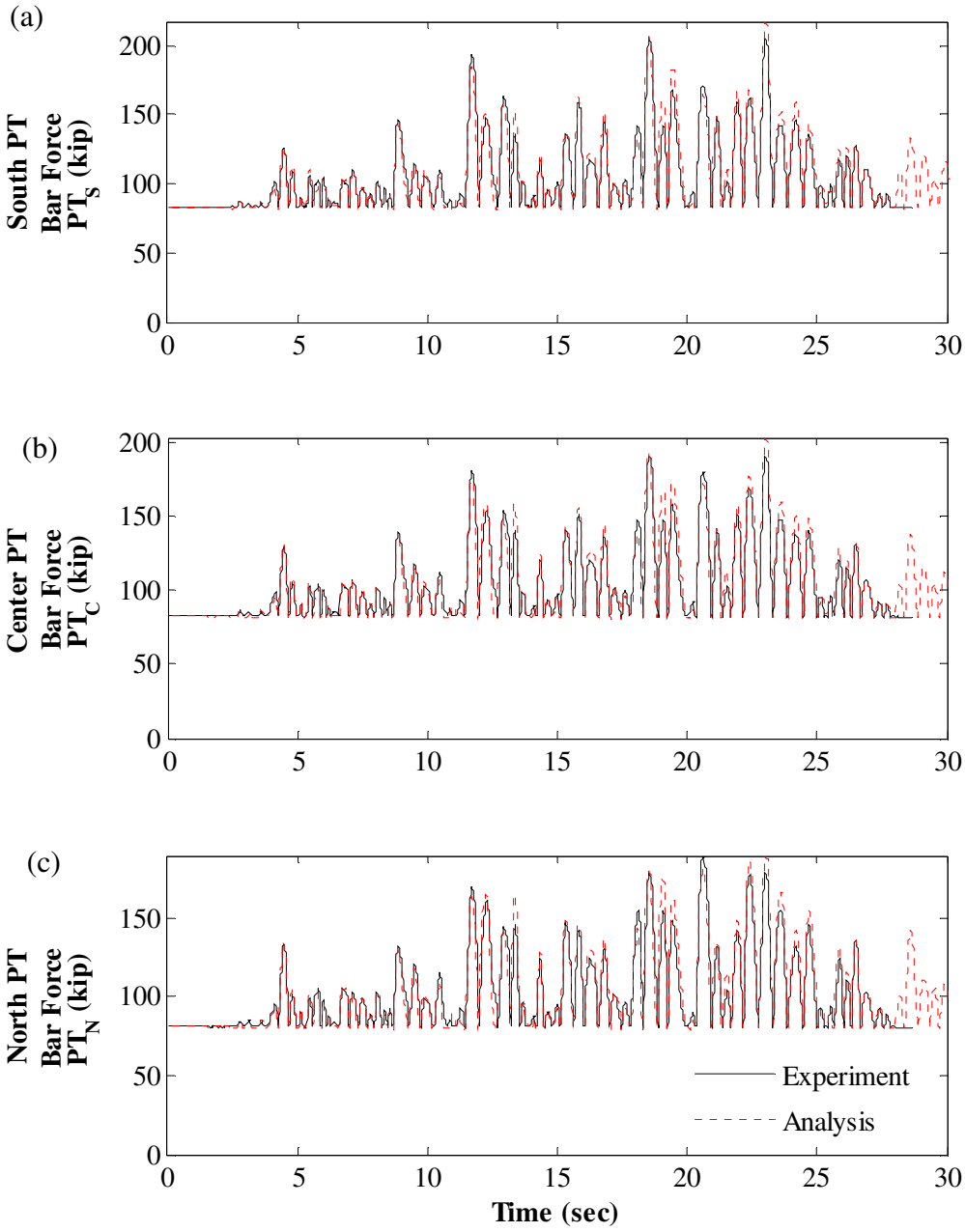

Figure 11.78 – Correlation of PT force response to |MCE_h-cpe237: (a) south PT bars; (b) center PT bars; (c) north PT bars

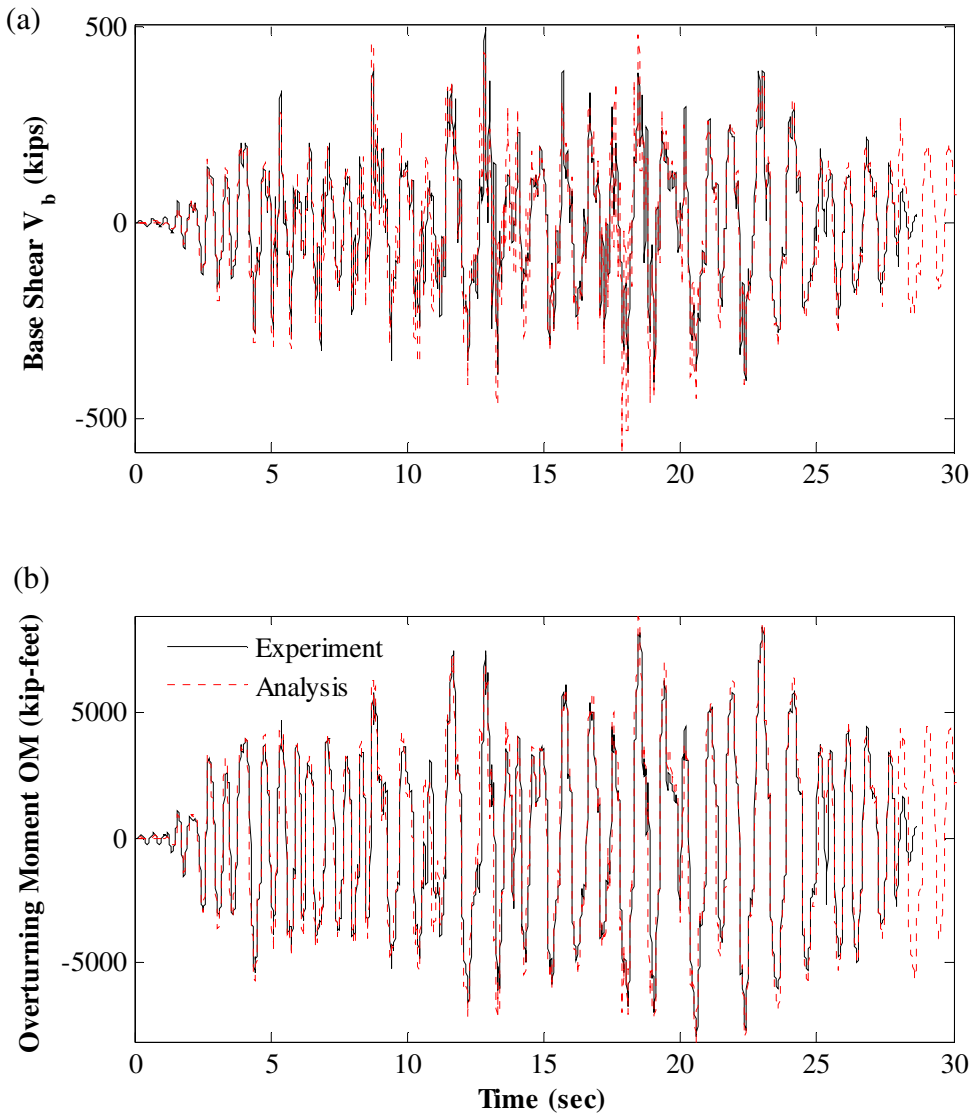

Figure 11.79 – MCE_h-cpe237 response correlation: (a) base shear; (b) overturning moment

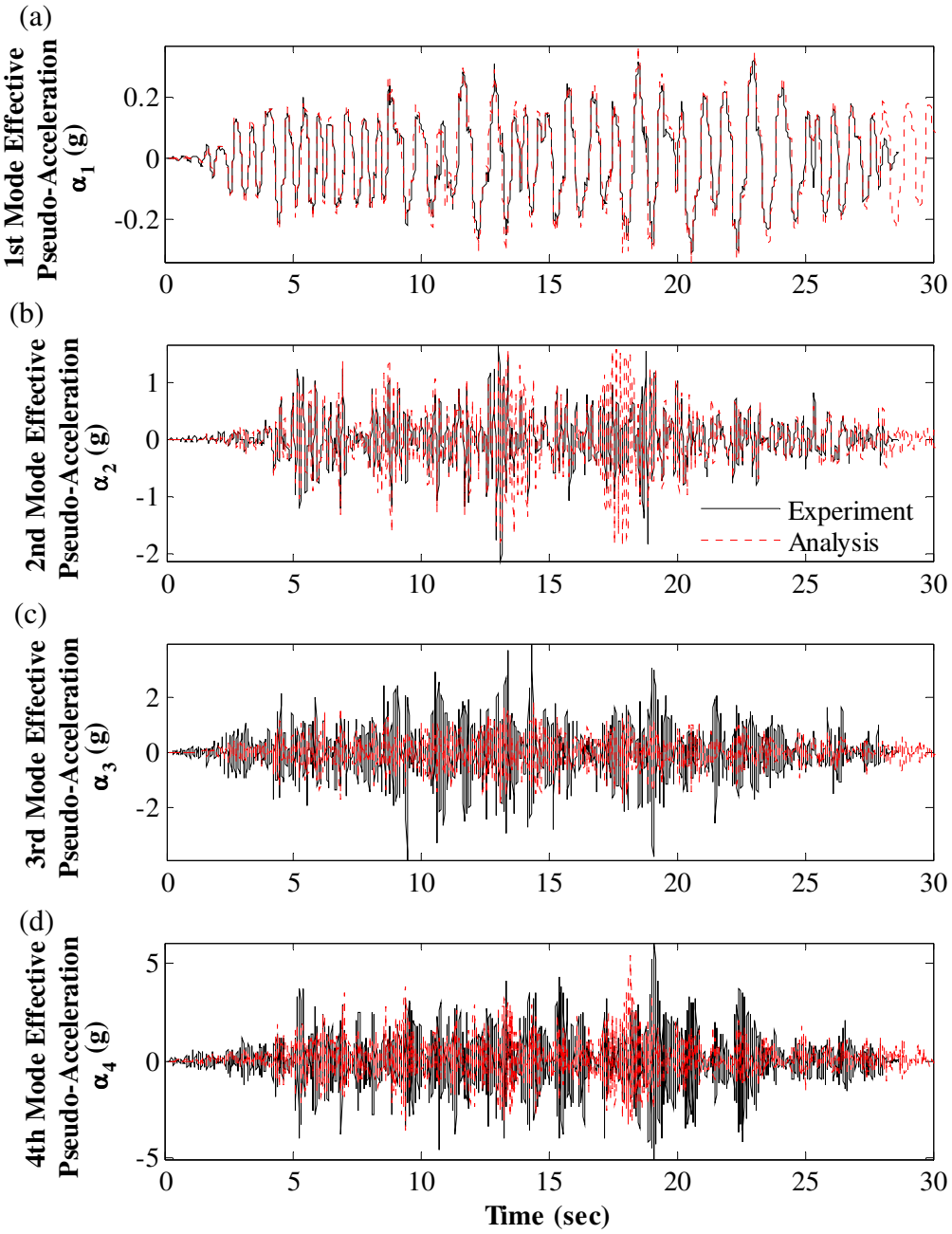

Figure 11.80 – Correlation of effective modal pseudo-acceleration response to MCE_h-cpe237: (a) 1st mode; (b) 2nd mode; (c) 3rd mode; (d) 4th mode

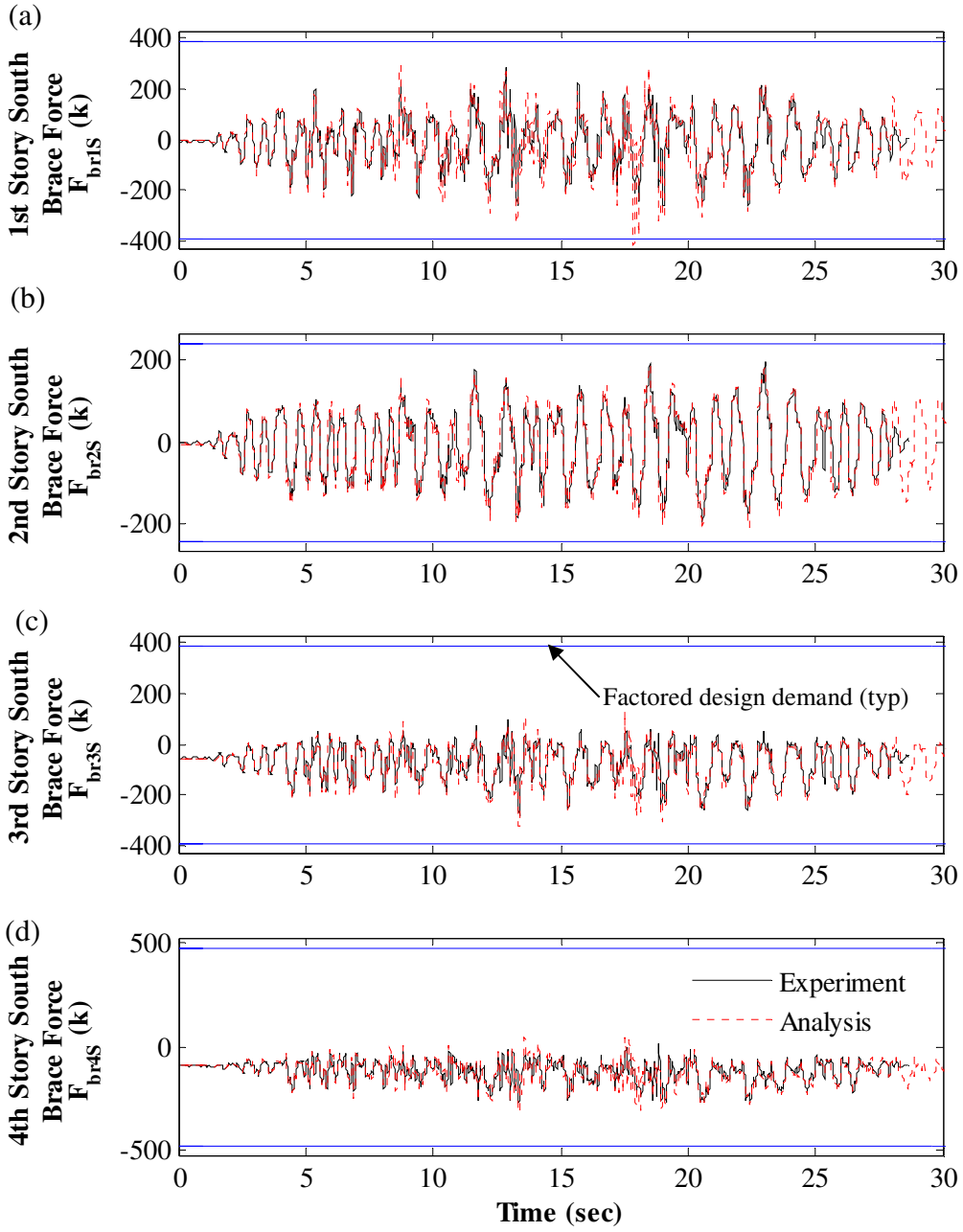

Figure 11.81 – Correlation of south brace axial force response to MCE_h-cpe237: (a) 1st story; (b) 2nd story; (c) 3rd story; (d) 4th story

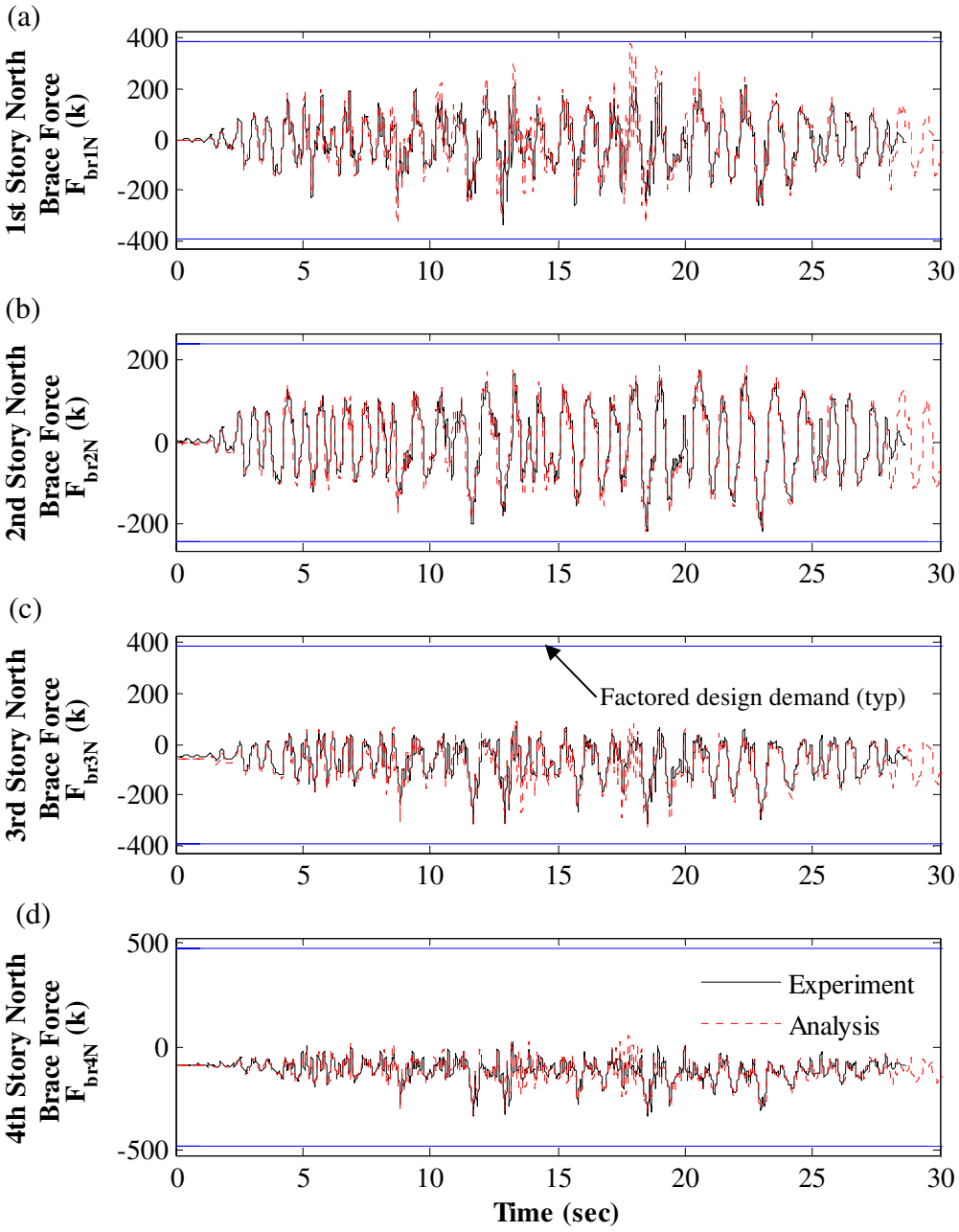

Figure 11.82 – Correlation of north brace axial force response to MCE_h-cpe237: (a) 1st story; (b) 2nd story; (c) 3rd story; (d) 4th story

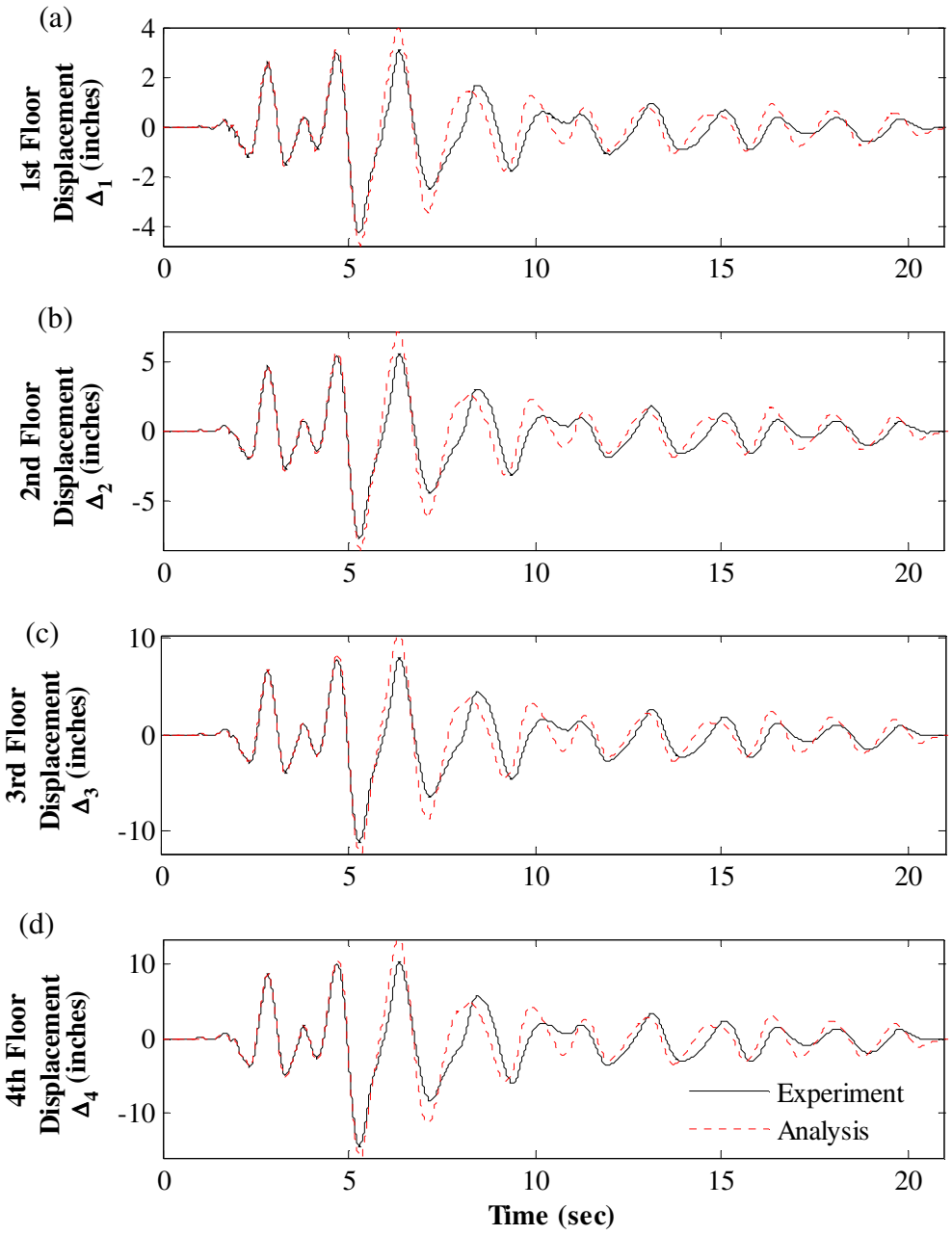

Figure 11.83 – Correlation of floor displacement response to xMCE_tak090 with μ = 0.45: (a) 1st floor; (b) 2nd floor; (c) 3rd floor; (d) 4th floor

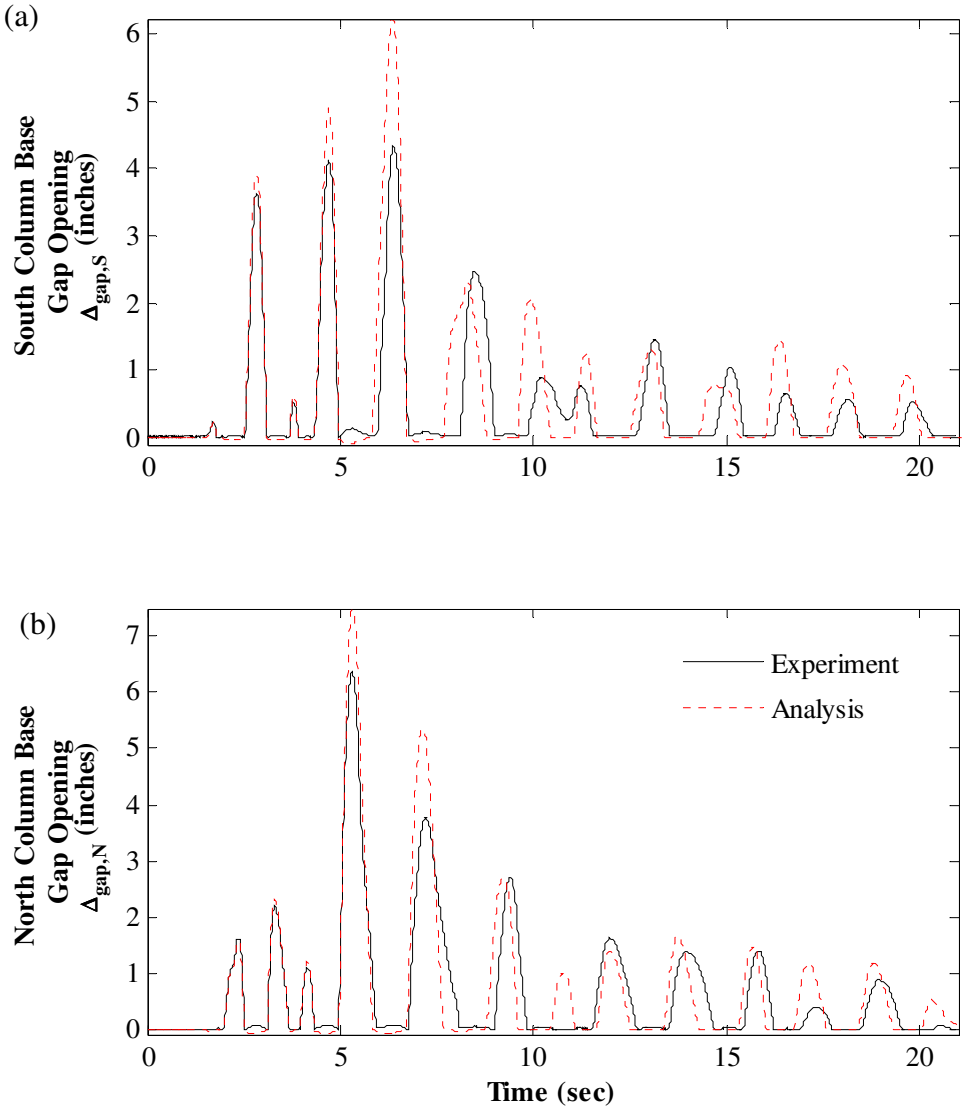

Figure 11.84 – Correlation of column base gap opening response to xMCE_tak090 with μ = 0.45: (a) at south column base; (b) at north column base

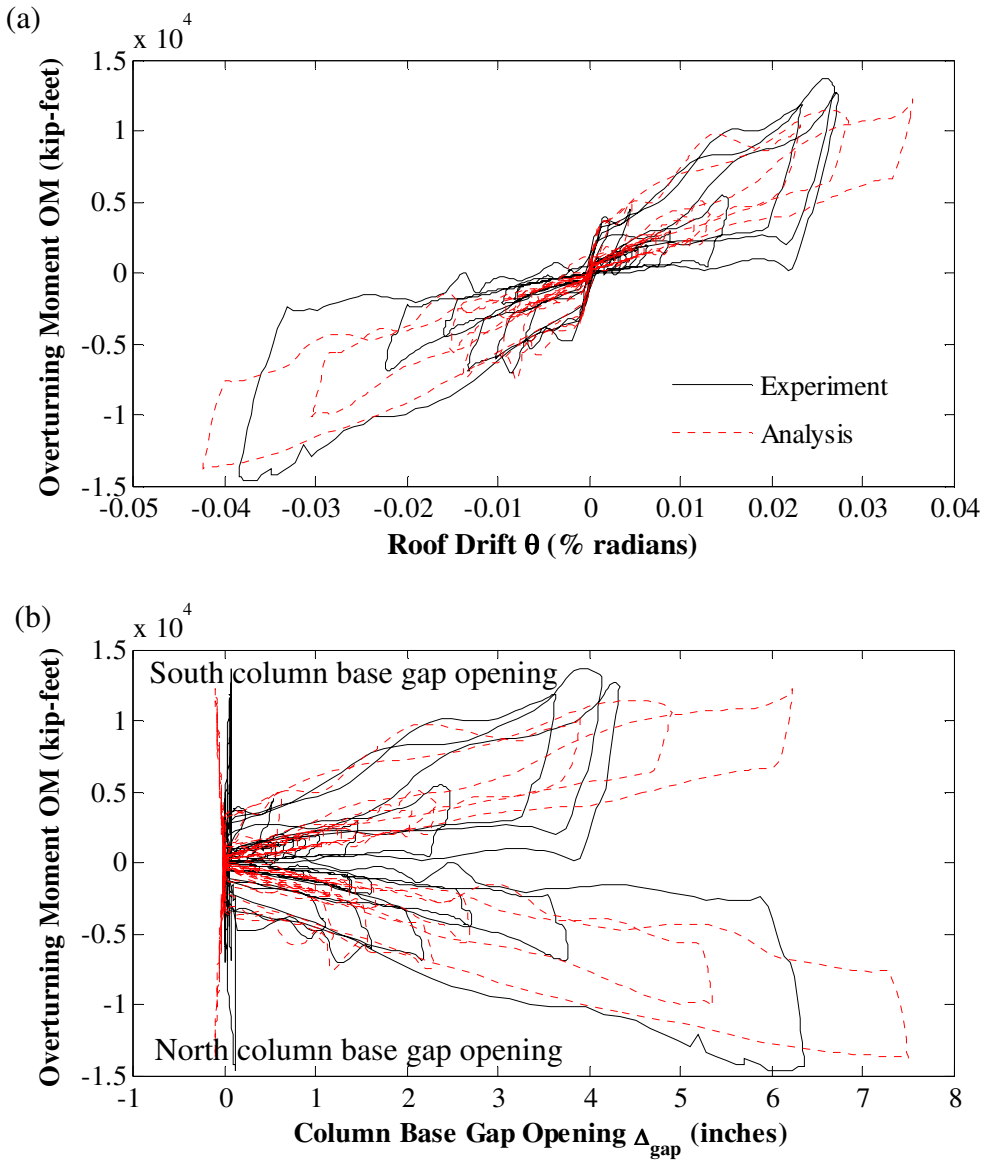

Figure 11.85 – Correlation of hysteretic response to xMCE_tak090 with $\mu = 0.45$: (a) overturning moment versus roof drift; (b) overturning moment versus column base gap opening

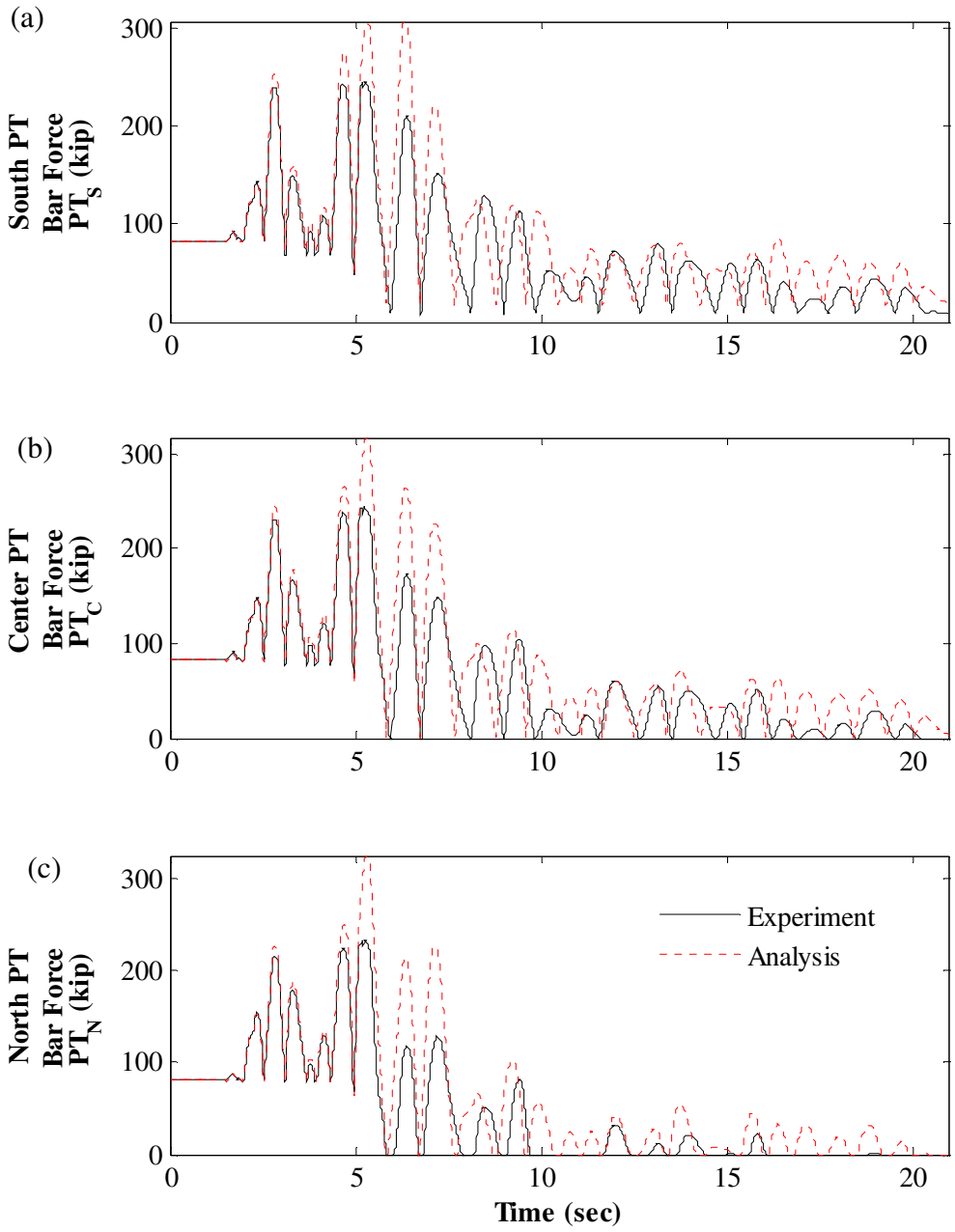

Figure 11.86 – Correlation of PT force response to xMCE_tak090 with $\mu = 0.45$: (a) south PT bars; (b) center PT bars; (c) north PT bars

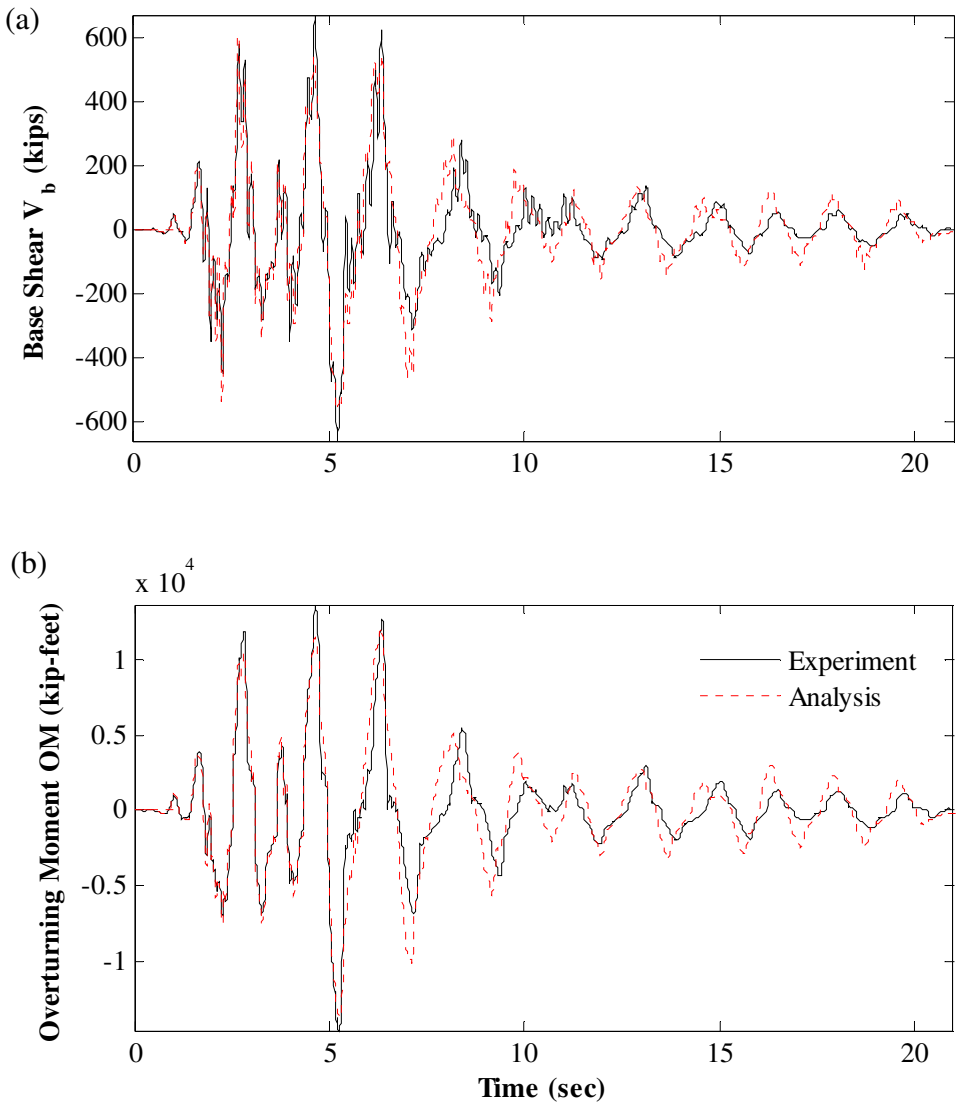

Figure 11.87 – xMCE_tak090 response correlation with $\mu = 0.45$: (a) base shear; (b) overturning moment

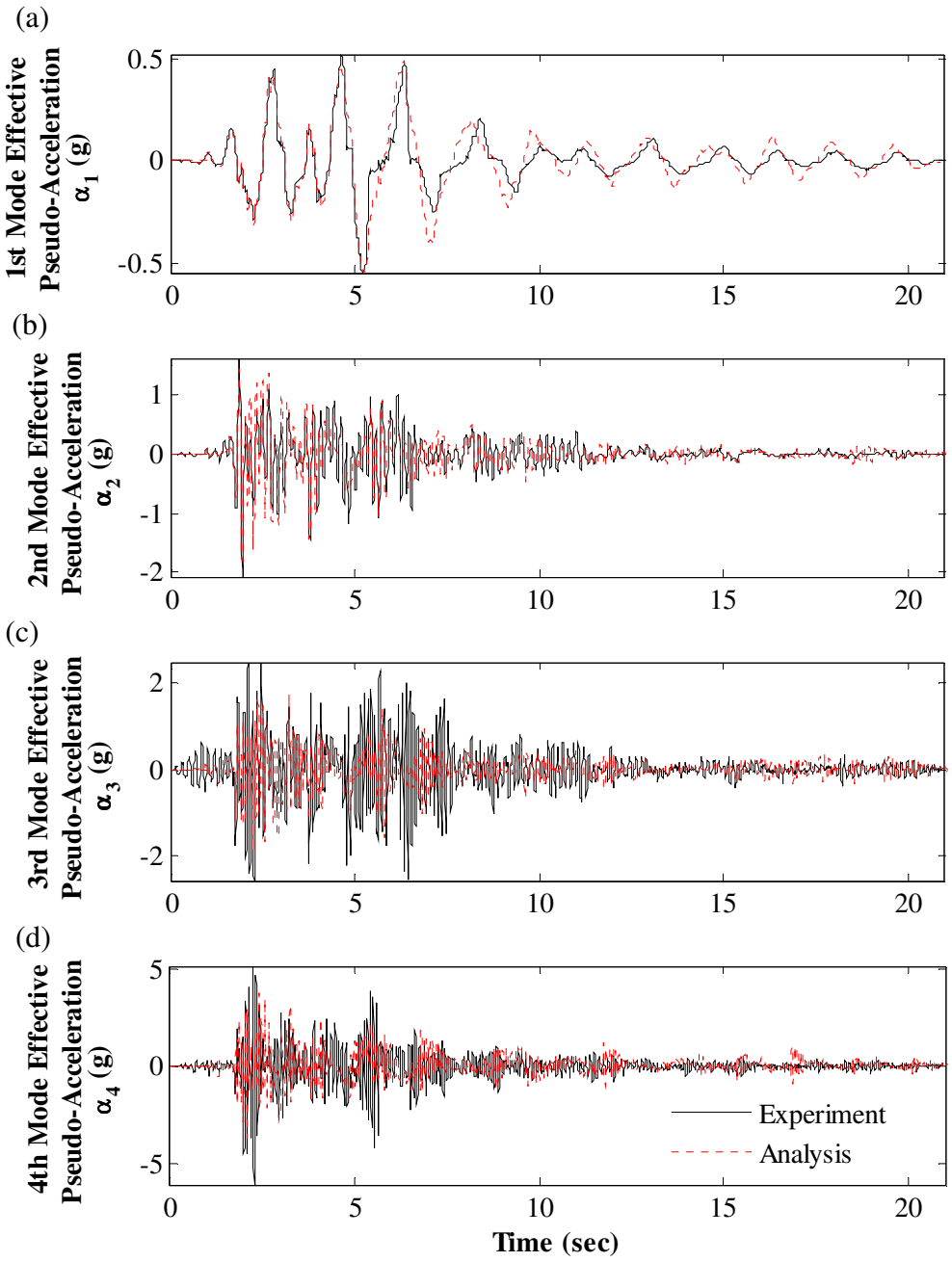

Figure 11.88 – Correlation of effective modal pseudo-acceleration response to xMCE_tak090 with $\mu = 0.45$: (a) 1st mode; (b) 2nd mode; (c) 3rd mode; (d) 4th mode

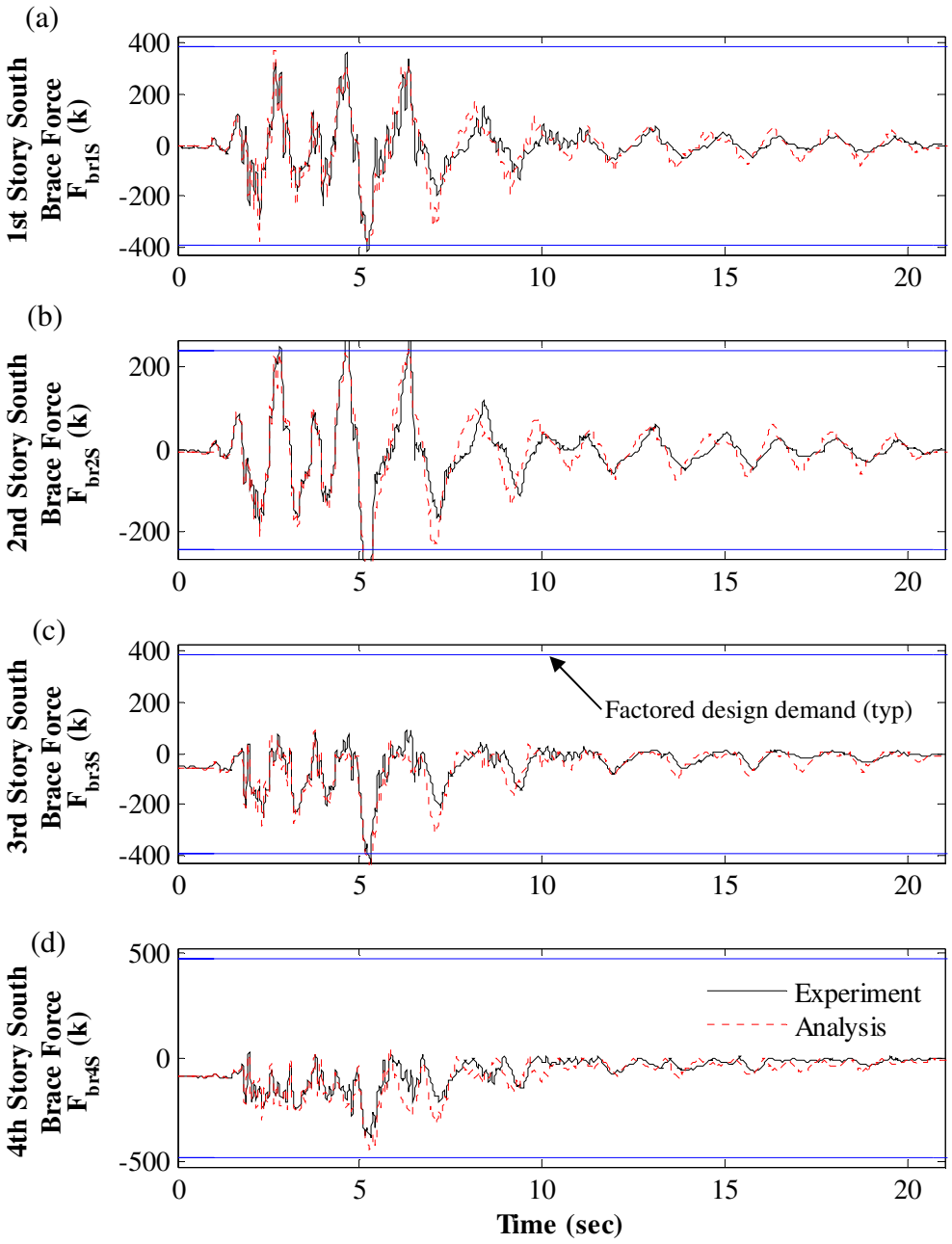

Figure 11.89 – Correlation of south brace axial force response to xMCE_tak090 with μ = 0.45: (a) 1st story; (b) 2nd story; (c) 3rd story; (d) 4th story

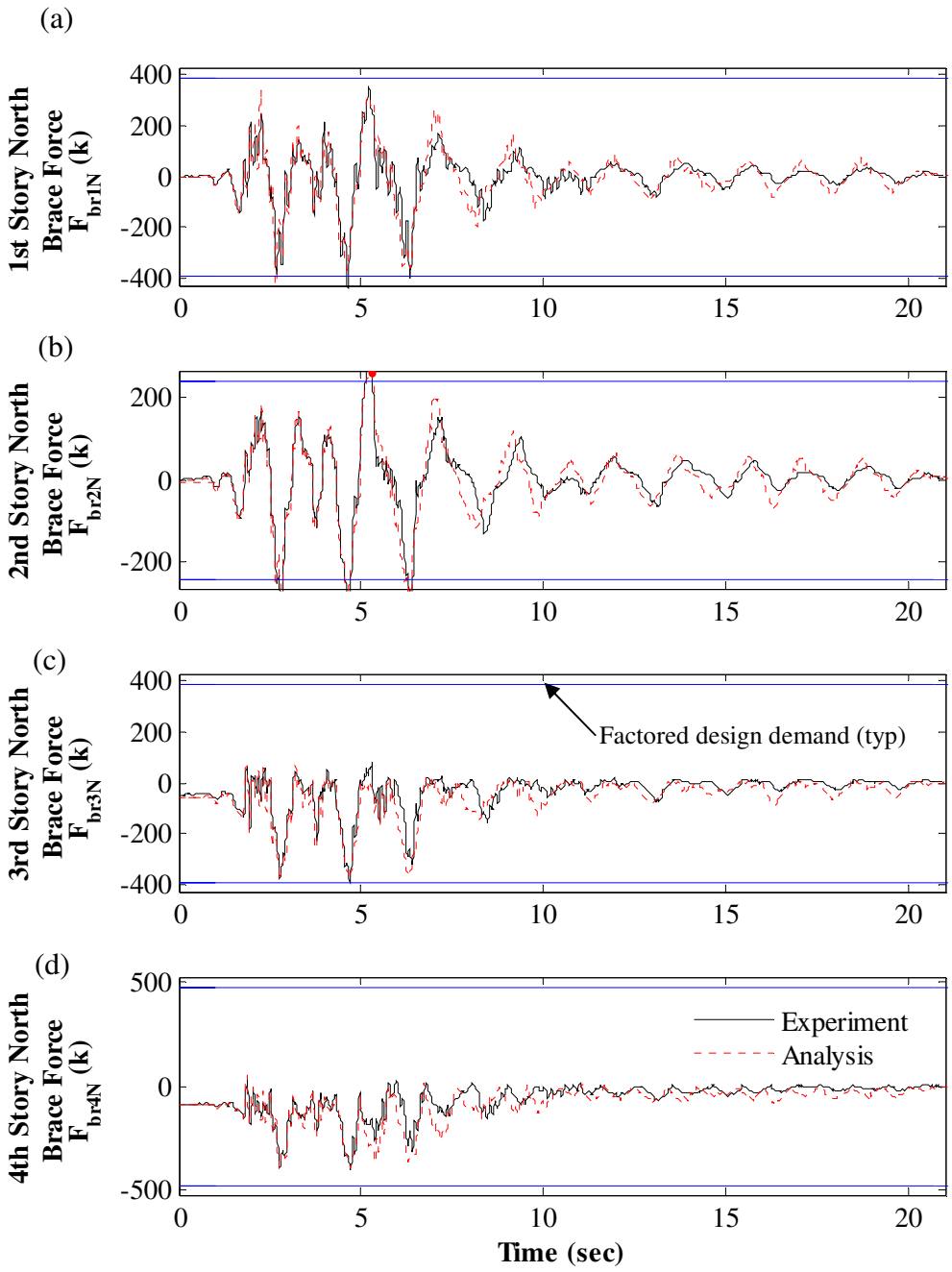

Figure 11.90 – Correlation of north brace axial force response to xMCE_tak090 with μ = 0.45: (a) 1st story; (b) 2nd story; (c) 3rd story; (d) 4th story

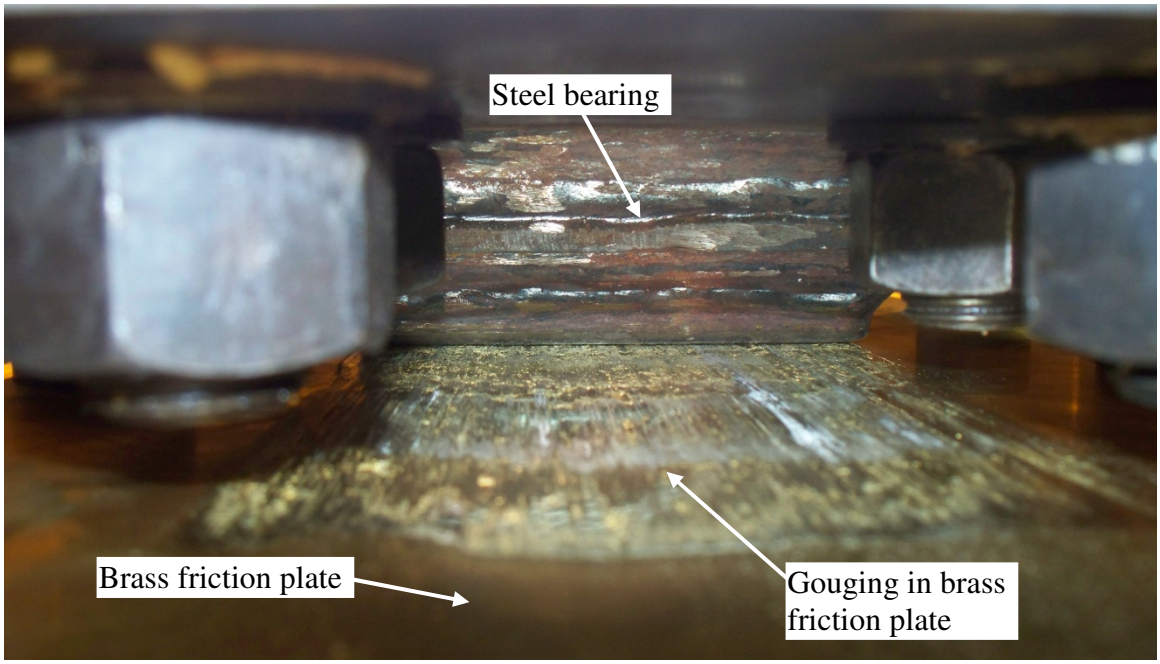

Figure 11.91 – Lateral-load bearing friction plate damaged after xMCE_tak090_02-05-2010

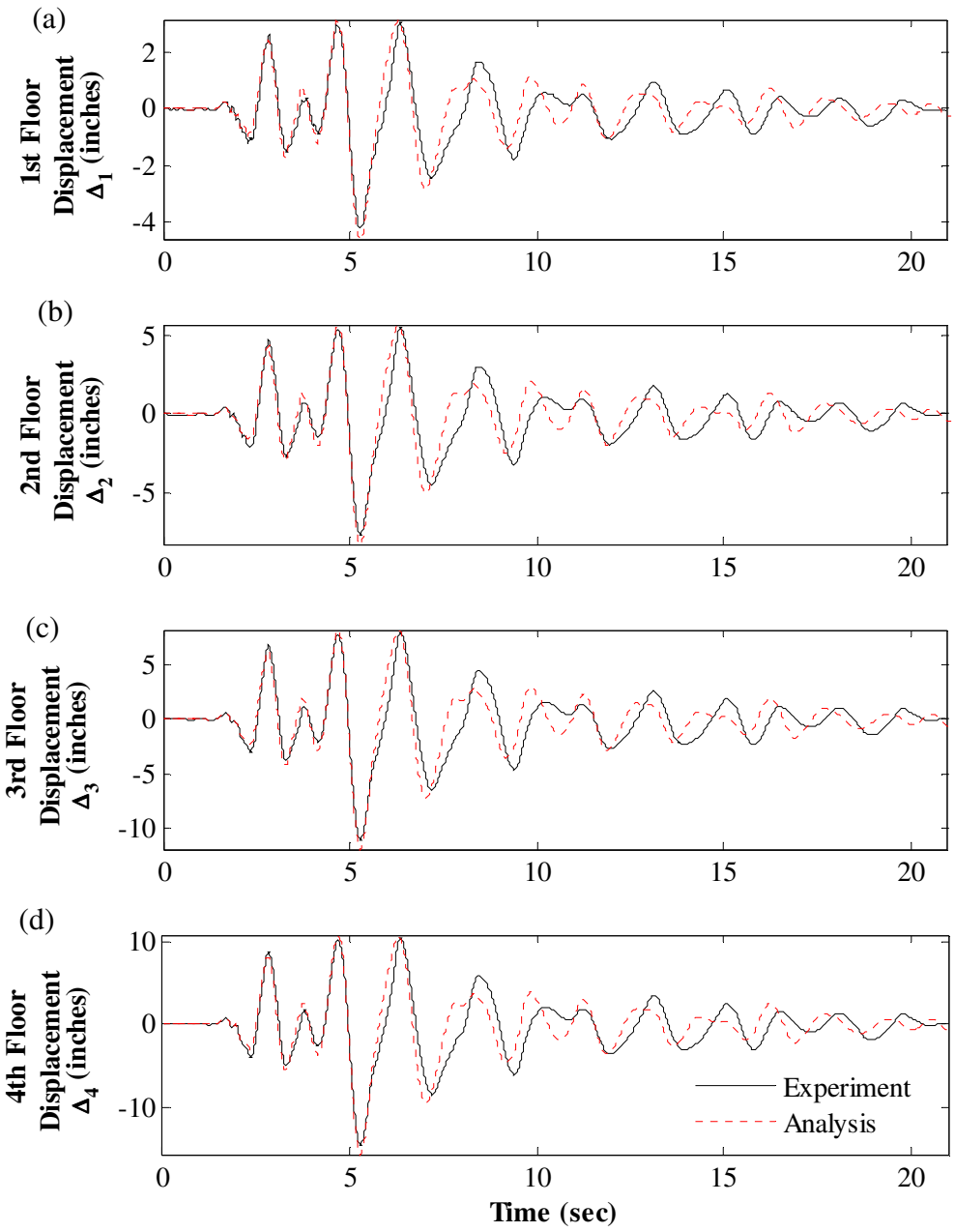

Figure 11.92 – Correlation of floor displacement response to xMCE_tak090 with μ = 0.55: (a) 1st floor; (b) 2nd floor; (c) 3rd floor; (d) 4th floor

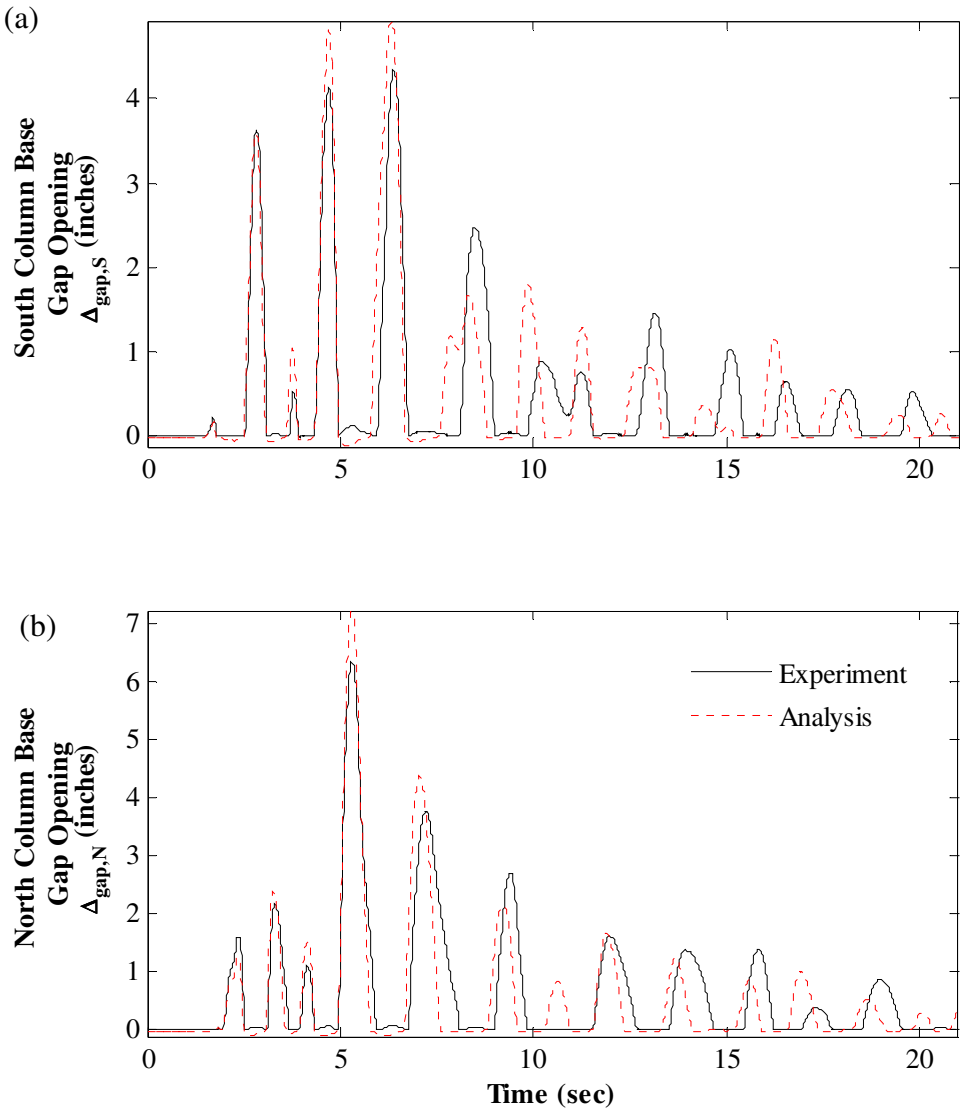

Figure 11.93 – Correlation of column base gap opening response to xMCE_tak090 with μ = 0.55: (a) at south column base; (b) at north column base

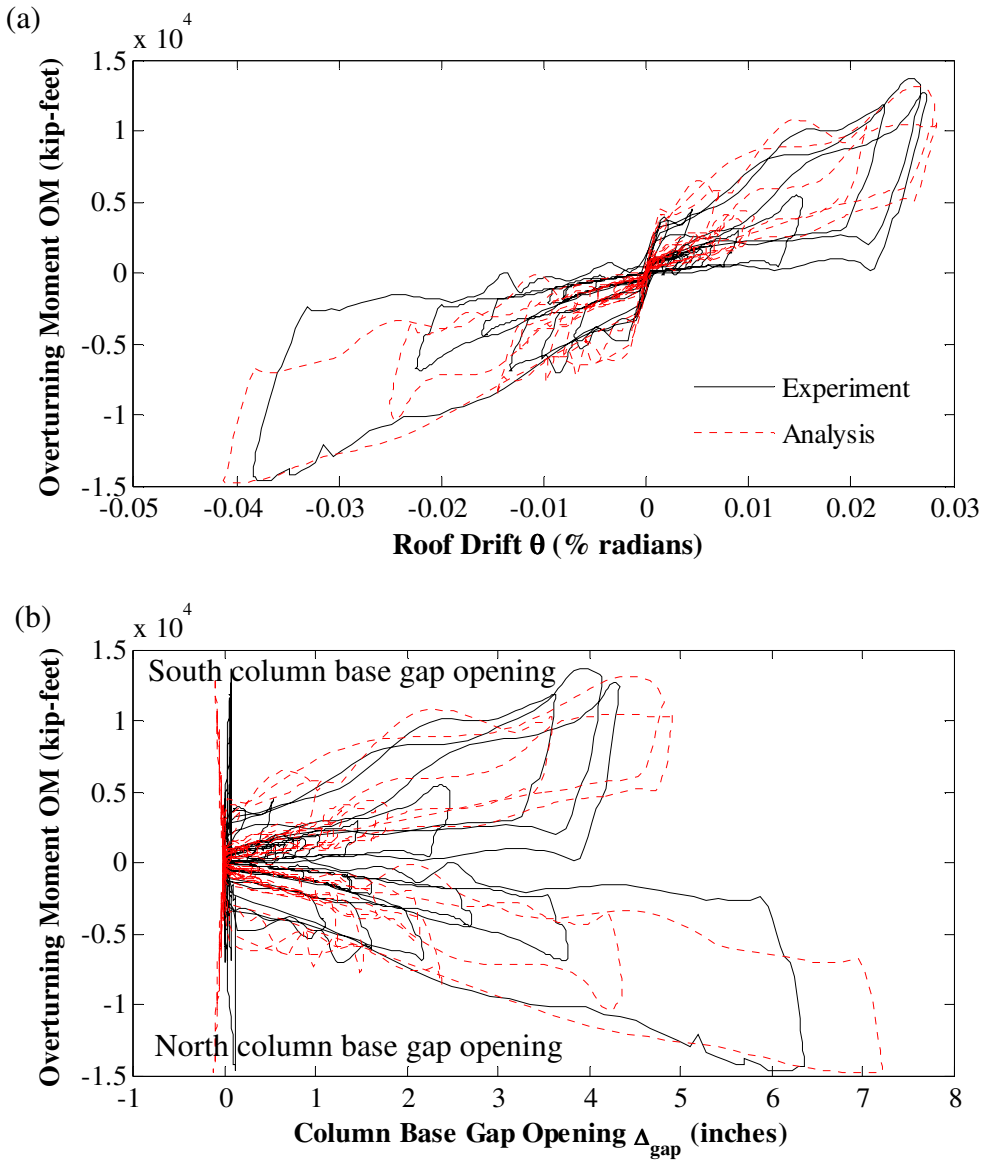

Figure 11.94 – Correlation of hysteretic response to xMCE_tak090 with $\mu = 0.55$: (a) overturning moment versus roof drift; (b) overturning moment versus column base gap opening

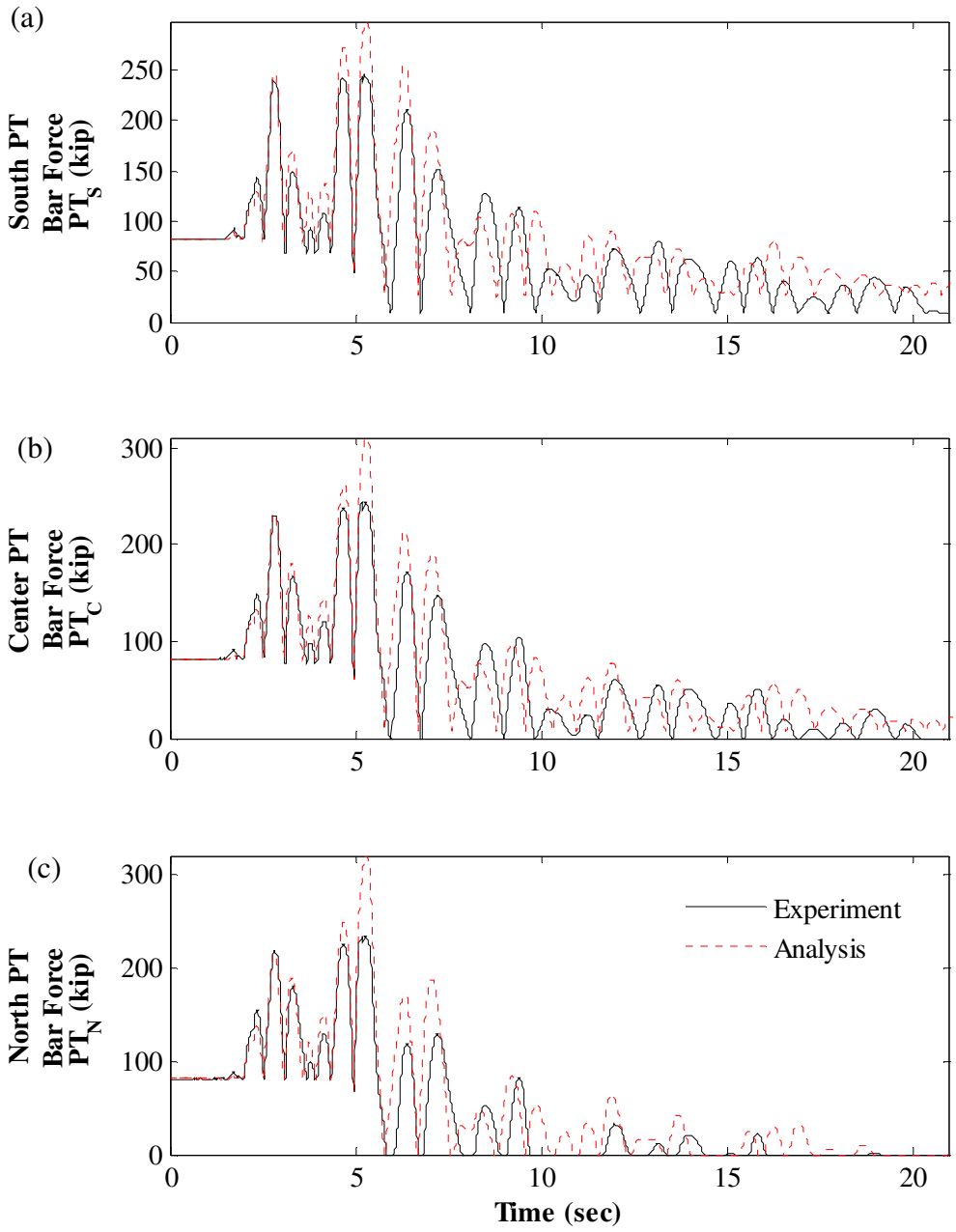

Figure 11.95 – Correlation of PT force response to xMCE_tak090 with $\mu = 0.55$: (a) south PT bars; (b) center PT bars; (c) north PT bars

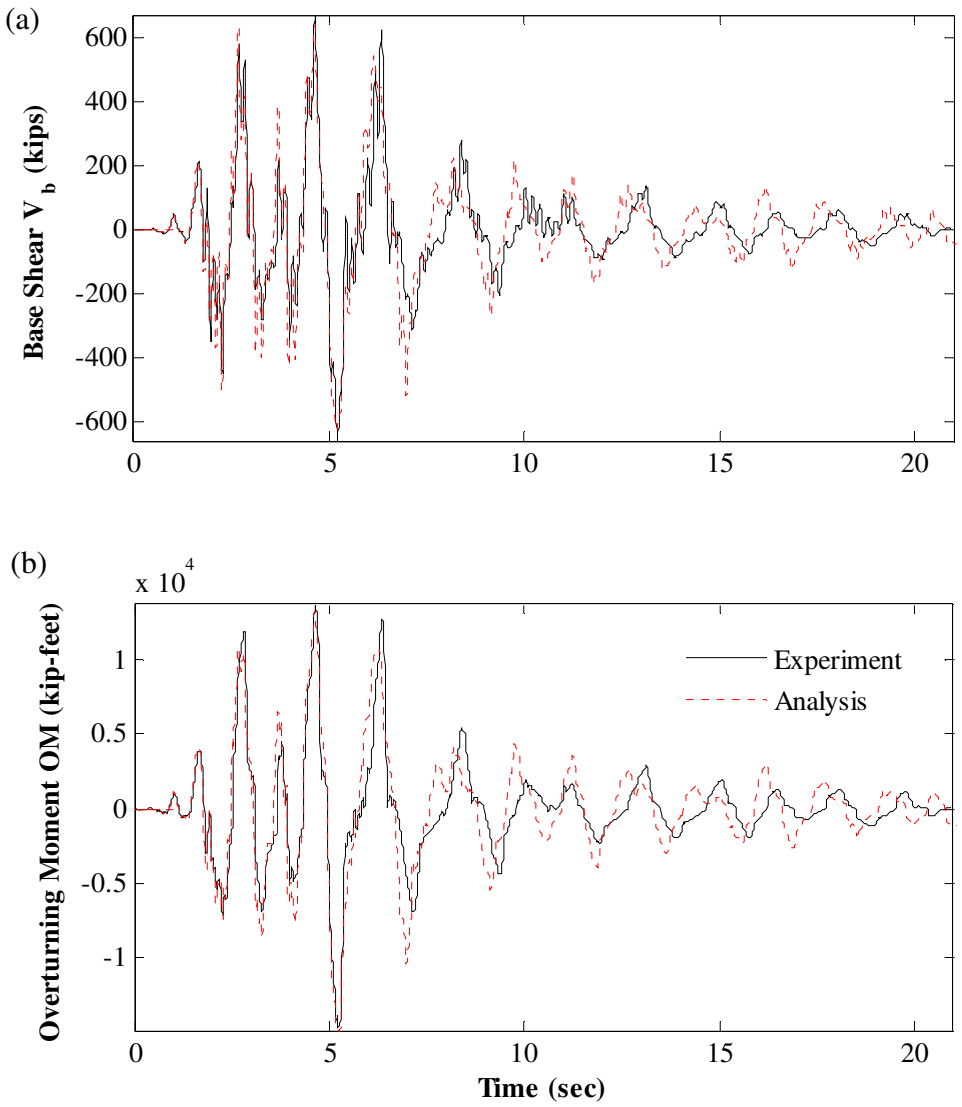

Figure 11.96 – xMCE_tak090 response correlation with $\mu = 0.55$: (a) base shear; (b) overturning moment

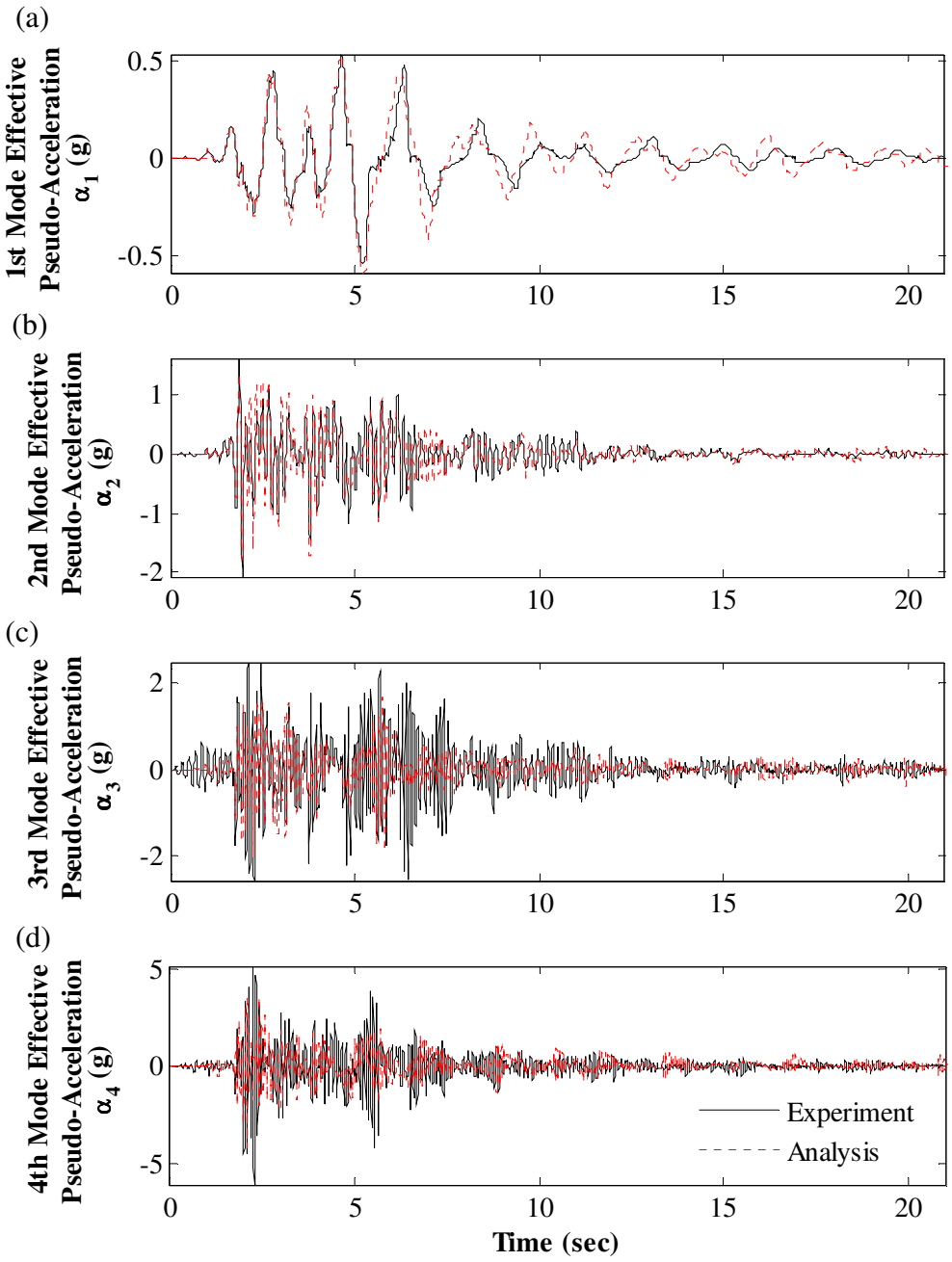

Figure 11.97 – Correlation of effective modal pseudo-acceleration response to xMCE_tak090 with $\mu = 0.55$: (a) 1st mode; (b) 2nd mode; (c) 3rd mode; (d) 4th mode

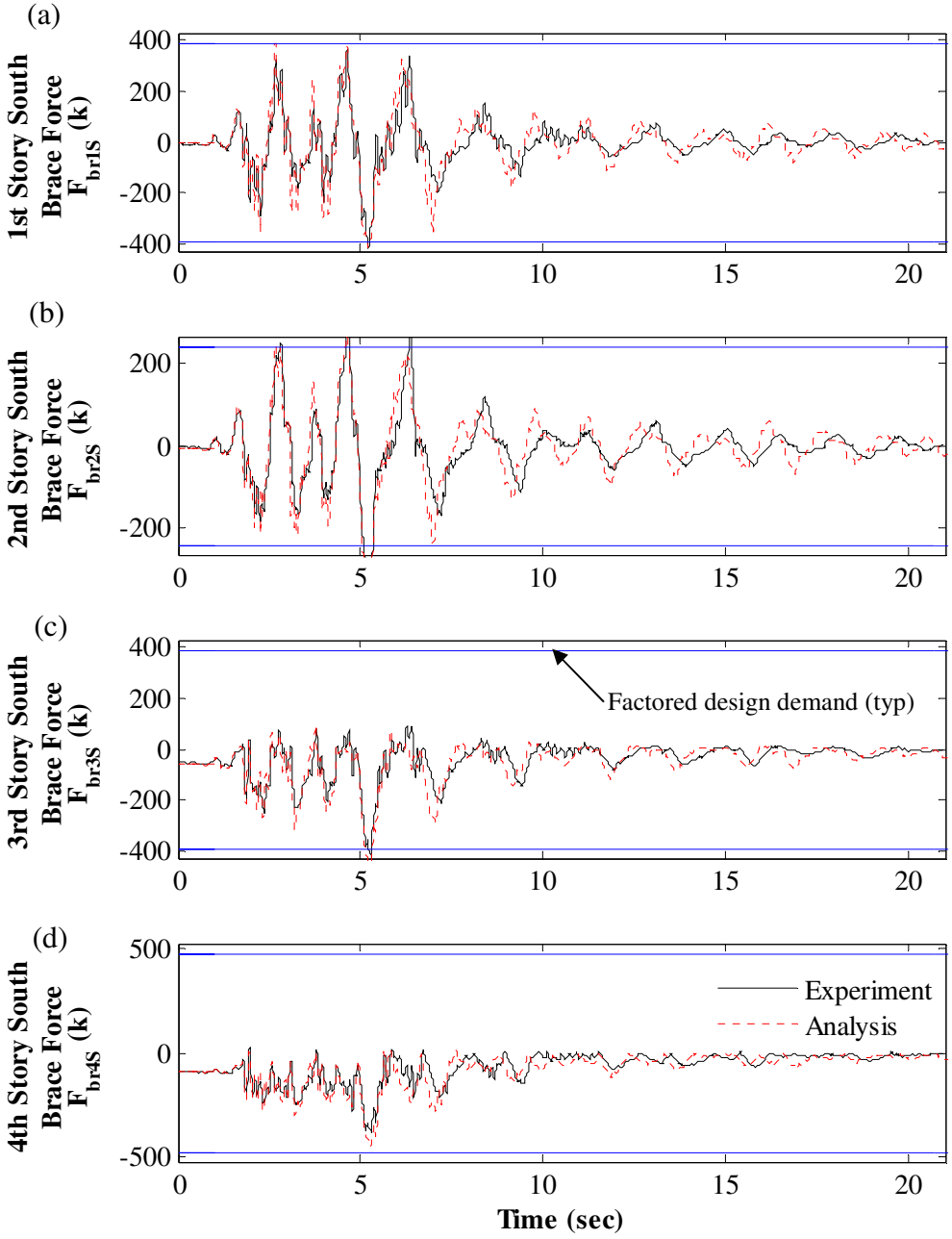

Figure 11.98 – Correlation of south brace axial force response to xMCE_tak090 with μ = 0.55: (a) 1st story; (b) 2nd story; (c) 3rd story; (d) 4th story

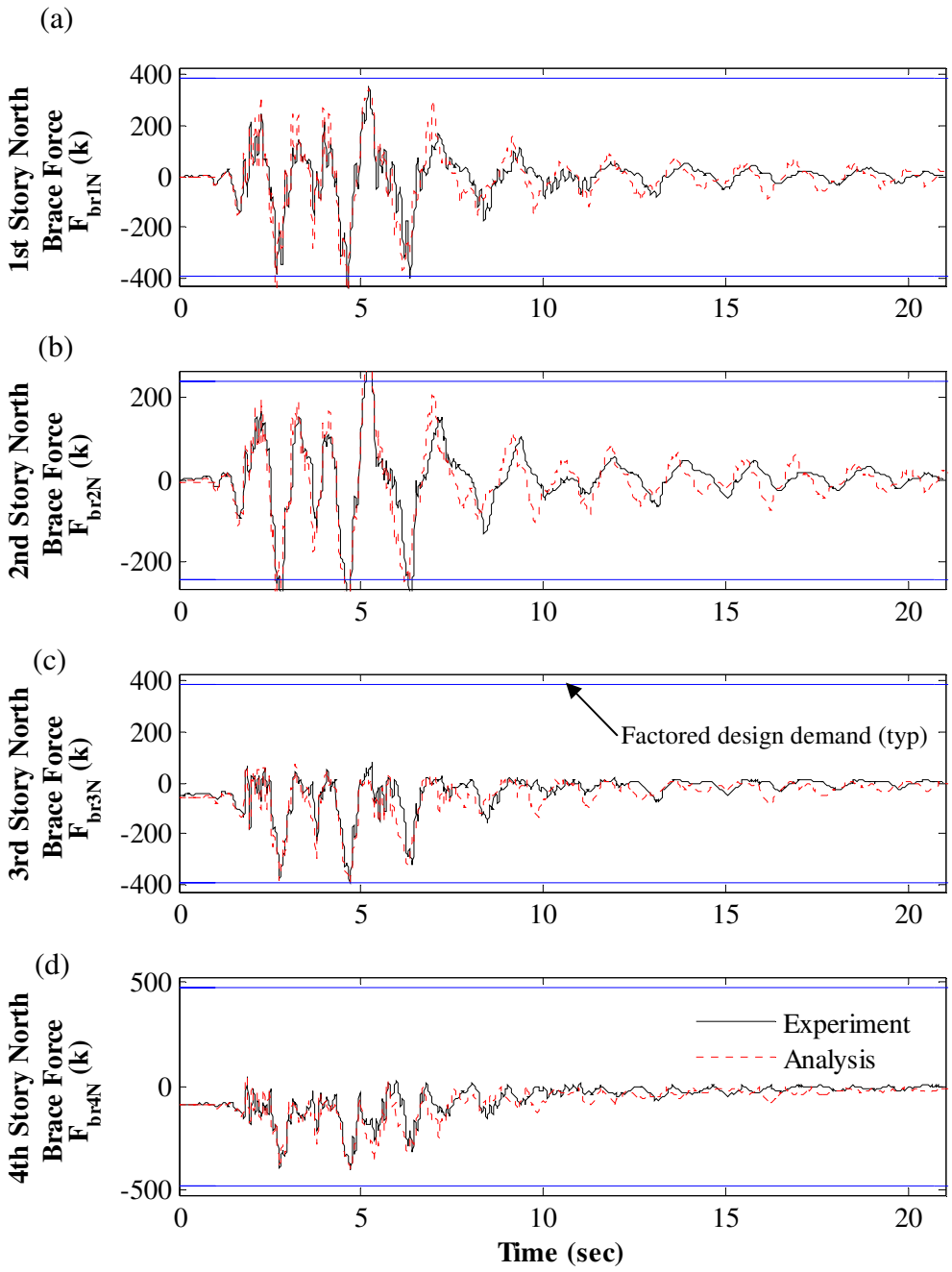

Figure 11.99 – Correlation of north brace axial force response to xMCE_tak090 with μ = 0.55: (a) 1st story; (b) 2nd story; (c) 3rd story; (d) 4th story

CHAPTER 12

EVALUATION OF SC-CBF PERFORMANCE

The response of the SC-CBF test structure, as determined from the numerical analysis results presented in Chapter 9, is evaluated in this chapter with respect to the performance-based design (PBD) approach and criteria presented in Chapters 4, 6, and 7. The numerical analysis results are used rather than the experimental results because the numerical results provide a larger data set, and the correlation study presented in Chapter 10 shows that the model used for the numerical analyses is sufficiently accurate to represent the response of the SC-CBF test structure.

In this chapter, the performance objectives from Chapter 4 and PBD criteria from Chapters 6 and 7 will be reviewed first. Then the response of the SC-CBF test structure to the DBE-level, MCE-level, and extreme MCE-level ground motions will be compared with the PBD criteria to determine whether the response of the SC-CBF satisfies the proposed performance objectives.

12.1 Review of Performance-Based Design Objectives and Criteria

The performance-based design (PBD) objectives established in Chapter 4 are reviewed in this section. The structural limit states for the SC-CBF system are decompression, PT bar yielding, member yielding, and member failure. The performance levels considered for

the SC-CBF system are immediate occupancy (IO) and collapse prevention (CP). The seismic input levels addressed in the PBD criteria are the design basis earthquake (DBE) and the maximum considered earthquake (MCE).

The performance objectives of the SC-CBF are IO performance under the DBE and CP performance under the MCE. Column decompression and minor PT bar yielding are considered to be acceptable for IO performance and are permitted under the DBE. Significant PT bar yielding and member yielding are not permitted under the DBE. Column decompression, PT bar yielding, and member yielding are considered to be acceptable for CP performance and are permitted under the MCE. Member failure is not permitted under the DBE or the MCE.

As presented in Chapters 6 and 7, design criteria were developed from these PBD objectives. The limit state of column decompression is permitted for the performance levels considered (IO, CP) and under the seismic input levels considered (DBE, MCE); therefore, there is no need to review column decompression to evaluate the SC-CBF performance. The probability of reaching (or exceeding) the PT bar yielding limit state under the DBE should be around 50%. The probability of reaching (or exceeding) the member yielding limit state under the DBE should be around 5%. The limit states of PT bar yielding and member yielding should have greater probabilities of exceedance under the MCE (e.g., greater than 50% for PT bar yielding, and greater than 5% for member yielding); however, these probabilities of exceedance were not established in developing the PBD criteria.

12.2 Evaluation of Structural Response

This section evaluates the response of the SC-CBF test structure to four levels (or types) of seismic input: (1) DBE-level ground motions; (2) MCE-level ground motions, (3) extreme MCE-level ground motions, and (4) a post-MCE DBE-level ground motion. The evaluation focuses on the limit states of PT bar yielding and member yielding. For the DBE-level and MCE-level ground motions, sufficient data exist to estimate the probability of exceedance for these limit states.

The probability of exceedance is calculated assuming that the responses (i.e., the demands) follow a lognormal distribution, as discussed in Chapter 6. The probability of a lognormally distributed random variable x exceeding a value X is calculated as:

$$P(x > X) = 1 - \Phi\left(\frac{ln(X) - ln(x_m)}{\zeta_x}\right) \tag{12.1}$$

where,

Φ = cumulative distribution function of the standard normal variate (Ang and Tang 2007)

x_m = median value of x

$$\zeta_x = \sqrt{\ln(1 + \delta_x^2)} \tag{12.2}$$

δ_x = coefficient of variation of x

12.2.1 DBE-Level Ground Motions

Table 12.1 summarizes the maximum roof drift and brace force responses of the SC-CBF test structure for the DBE-level ground motions. The response quantities in Table 12.1 are the maximum roof drift response for each ground motion (θ_{DBE}) and the maximum brace force in each story for each ground motion (F_{bri}). Response values that exceed the factored design demands ($\theta_{DBE,fdd}$ and $F_{bri,fdd}$, respectively) are in bold text in the table.

12.2.1.1 Evaluation of PT Bar Yielding

Table 12.2 summarizes the probability of θ_{DBE} exceeding selected design quantities related to the PBD criteria for PT bar yielding. The data in the second column of Table 12.2 are the values of the variables listed in the first column, and the data in the third column are the probabilities of θ_{DBE} exceeding the tabulated values in the second column. The tabulated values are the mean roof drift response (μ_θ), the median roof drift response ($\theta_{DBE,m}$), the DBE-level roof drift design demand ($\theta_{DBE,dd}$), the DBE-level factored roof drift design demand ($\theta_{DBE,fdd}$, determined using γ_θ equal to 1.0), the nominal roof drift capacity at PT bar yield estimated as described in Section 7.3.2.2 ($\theta_{Y,n}$), the roof drift capacity at PT bar yield from a nonlinear pushover analysis ($\theta_{Y,FA}$), the DBE-level roof drift design demand calculated by Gonner (2009) ($\theta_{dd,G}$), and the nominal roof drift capacity at PT bar yield calculated by Gonner (2009) ($\theta_{Y,G}$). $\theta_{Y,FA}$ was determined by applying lateral forces to the predictive analytical model discussed in Chapter 9 that are proportional to the first mode lateral forces and increasing these forces until the PT bars located at midbay yielded.

The definition of the factored roof drift design demand for the limit state of PT bar yielding presented in Chapter 6 permits a 50% probability that θ_{DBE} exceeds $\theta_{DBE,fdd}$. The analytical results, however, show the probability of θ_{DBE} exceeding $\theta_{DBE,fdd}$ is only 15.7%. It was assumed that $\theta_{DBE,dd}$ is an estimate of the median response $\theta_{DBE,m}$, and, with γ_θ equal to 1.0, $\theta_{DBE,fdd}$ should also be approximately equal to $\theta_{DBE,m}$, resulting in a 50% probability of exceedance. However, as shown in Table 12.2, $\theta_{DBE,m}$ is only 72% of $\theta_{DBE,dd}$. This reflects conservatism in the μ-R-T relationship discussed in Chapter 6 that was used to estimate the roof drift response of the SC-CBF system (i.e., used to estimate $\theta_{DBE,dd}$).

As discussed in Chapter 7, the PBD criterion for the limit state of PT bar yielding permits up to a 50% probability that θ_{DBE} exceeds $\theta_{Y,n}$. Due to the conservatism in the design demand discussed above and assuming that $\theta_{Y,n}$ equals (or is only slightly larger than) $\theta_{DBE,fdd}$, the probability of θ_{DBE} exceeding $\theta_{Y,n}$ is expected to be slightly less than 15.7% (which is the probability of θ_{DBE} exceeding $\theta_{DBE,fdd}$). The actual probability that θ_{DBE} exceeds $\theta_{Y,n}$ is only 5.0%. $P(\theta_{DBE} > \theta_{Y,n})$ is less than $P(\theta_{DBE} > \theta_{DBE,fdd})$ because $\theta_{Y,n}$ is substantially greater than $\theta_{DBE,fdd}$ for two primary reasons: (1) the margin between $\theta_{DBE,ddG}$ and $\theta_{Y,G}$ due to the availability of discrete PT bar sizes; and (2) the margin between $\theta_{DBE,ddG}$ (from Gonner (2009)) and $\theta_{DBE,fdd}$ (from the procedure in Chapter 6) due to the different design procedure and frame configuration used by Gonner (2009), who designed the PT bars for the SC-CBF test structure. The margin between $\theta_{Y,n}$ and $\theta_{DBE,fdd}$ is discussed further below.

The margin between $\theta_{DBE,ddG}$ and $\theta_{Y,G}$ is only 2%, and, as mentioned in Chapter 8, $\theta_{Y,n}$ is close to $\theta_{Y,G}$. $\theta_{DBE,ddG}$ equals 1.40% radians (Gonner 2009), $\theta_{Y,G}$ was estimated as 1.43% radians (1.43% radians), and $\theta_{Y,n}$ is estimated as 1.42% radians (from the procedure in Chapter 6), which is nearly equal to $\theta_{Y,G}$. The margin between $\theta_{DBE,ddG}$ and $\theta_{Y,G}$ due to the availability of discrete PT bar sizes, therefore, does not significantly affect the difference between $P(\theta_{DBE} > \theta_{Y,n})$ and $P(\theta_{DBE} > \theta_{DBE,fdd})$ for the SC-CBF test structure.

The margin between $\theta_{DBE,ddG}$ and $\theta_{DBE,fdd}$ is 17.1%, and $P(\theta_{DBE} > \theta_{DBE,ddG})$ is much smaller than $P(\theta_{DBE} > \theta_{DBE,fdd})$. Gonner (2009) designed the PT bars for $\theta_{DBE,ddG}$ equal to 1.40% radians, but the procedure presented in Chapter 6 resulted in $\theta_{DBE,fdd}$ equal to 1.16% radians. The procedure used by Gonner (2009) used the entire tributary mass in calculating $\theta_{DBE,ddG}$ while the procedure presented in Chapter 6 used the first mode effective tributary mass in calculating $\theta_{DBE,fdd}$. In addition, there were differences in the hysteretic energy dissipation ratio β_E and the ratio of post-decompression stiffness to elastic stiffness α_k, used in these calculations, as discussed in Chapter 8. The margin between $\theta_{DBE,ddG}$ and $\theta_{DBE,fdd}$ accounts for most of the significant difference between $P(\theta_{DBE} > \theta_{Y,n})$ and $P(\theta_{DBE} > \theta_{DBE,fdd})$.

In addition to the differences between $\theta_{DBE,ddG}$ and $\theta_{DBE,fdd}$, the roof drift capacity at yield from the pushover analyses (and for the SC-CBF test structure in the laboratory) was much larger than expected (i.e., $\theta_{Y,FA} > \theta_{Y,n}$), leading to further conservatism in the probability of yielding the PT bars. It was determined that $\theta_{Y,n}$ is a conservative estimate of the roof drift capacity of the SC-CBF test structure due to two factors: (1) the

overstrength of the PT bars, and (2) the flexibility of the basement substructure of the SC-CBF test structure.

To demonstrate the effect of these factors, a parametric study was performed considering two variables, the PT bar yield stress and the flexibility of the basement substructure of the SC-CBF test structure. Two conditions are considered for each parameter. For the PT bar yield stress, the two values considered are: (1) the nominal yield stress, equal to 120 ksi, and (2) the mean effective yield stress (i.e., actual yield stress) determined from tensile tests presented by Gonner et al. (2010), equal to 143.6 ksi. For the basement substructure of the SC-CBF test structure, the two conditions considered are: (1) the basement substructure of the SC-CBF test structure modeled as discussed in Chapter 8 and (2) a rigid basement substructure (similar to that used in the analytical models used to determine the design demands in the procedure presented in Chapter 6). The parametric study was performed by applying lateral forces proportional to the first mode lateral forces to each analytical model. The forces were increased until the PT bars located at midbay yielded. The roof drift at PT bar yield for each model is summarized in Table 12.3.

The model denoted "RN" in Table 12.3 has a rigid basement substructure and uses the nominal yield stress of the PT bars; this model reflects the assumptions made for the analytical model used in calculating $\theta_{Y,n}$. As shown in Table 12.3, $\theta_{Y,RN}$ equals 1.41 % radians, which is almost identical to $\theta_{Y,n}$ (1.42 % radians). Therefore, $\theta_{Y,n}$ calculated using the simple analytical approach described in Chapter 6 is an accurate estimate of $\theta_{Y,RN}$

from a rigorous analytical model when the analytical models are based on similar assumptions.

The model denoted "FN" in Table 12.3 includes the flexibility of the basement substructure of the SC-CBF test structure. Table 12.3 shows the basement substructure flexibility causes a 15% increase from $\theta_{Y,RN}$ to $\theta_{Y,FN}$, when the model uses the nominal yield stress of the PT bars. The models denoted "RA" and "FA" use the actual yield stress of the PT bars. When the actual yield stress is used, the basement substructure flexibility causes a 24% increase from $\theta_{Y,RA}$ to $\theta_{Y,FA}$.

The effect of the difference between the actual yield stress and the nominal yield stress of the PT bars (overstrength of the PT bars) is illustrated by comparing the values of $\theta_{Y,RN}$ with $\theta_{Y,RA}$. The overstrength of the PT bars causes a 31% increase from $\theta_{Y,RN}$ to $\theta_{Y,RA}$, for the models with a rigid basement substructure, and the overstrength of the PT bars causes a 42% increase from $\theta_{Y,FN}$ to $\theta_{Y,FA}$ for the models with a flexible basement substructure.

$\theta_{Y,FA}$ is more representative of the actual roof drift at PT yield for the SC-CBF test structure than $\theta_{Y,n}$ because the flexibility of the basement substructure and the overstrength of the PT bars are included in the model, whereas $\theta_{Y,n}$ does not account for these factors. Table 12.2 shows that $\theta_{Y,FA}$ is much larger than $\theta_{Y,n}$, and, therefore, the probability that θ_{DBE} exceeds $\theta_{Y,FA}$, shown in Table 12.2, is very small.

In summary, the probability of PT bar yielding under the DBE is very small, in part because the design demand used to design the PT bars, $\theta_{DBE,ddG}$, is much larger than the

median DBE response, $\theta_{DBE,m}$, and in part because the actual capacity, $\theta_{Y,FA}$, is much larger than the nominal design capacity, $\theta_{Y,n}$.

12.2.1.2 Evaluation of Member Yielding

The evaluation of the member yielding performance of the SC-CBF test structure begins with an evaluation of the spectral accelerations used to estimate the member force design demands, $F_{x,fdd}$. Table 12.4 summarizes the probability of the effective pseudo-acceleration, α_n, from the numerical analysis results for the DBE-level ground motions exceeding certain spectral acceleration values represented by the variables in the first column of the table. The second, fourth, sixth, and eighth columns of Table 12.4 give the values of these variables for the first, second, third, and fourth modes, respectively. The third, fifth, seventh, and ninth columns give the probabilities of α_n exceeding these tabulated values. The variables are: the mean value of α_n (μ_α) and the median value of α_n ($\alpha_{n,m}$) from the dynamic analysis results; the design spectral acceleration ($\alpha_{Y,1}$ for the first mode and the spectral acceleration from the DBE design spectrum for the higher modes) determined from analytical models used in design (i.e., design models, DM), denoted $SA_{n,DM}$, as well as the factored design spectral acceleration ($\gamma_n \cdot SA_{n,DM}$); the design spectral acceleration ($\alpha_{Y,1}$ for the first mode and the spectral acceleration from the DBE design spectrum for the higher modes) determined from the properties of the predictive analytical model (PM), denoted $SA_{n,PM}$, as well as the factored design spectral acceleration ($\gamma_n \cdot SA_{n,PM}$). The differences between the DM and PM results are as follows. DM results for $\alpha_{Y,1}$ are based on the nominal PT bar yield stress, while PM results for $\alpha_{Y,1}$

are based on the actual PT bar yield stress. For the higher modes, the periods from the DM and the PM differ, resulting in different SA_n values from the DBE design spectrum.

In Chapter 6, the values for γ_n were selected such that the probability of α_n exceeding $\gamma_n \cdot SA_{n,DM}$ was small (e.g., approximately 5%). Table 12.4 shows that the probability of α_n exceeding $\gamma_n \cdot SA_{n,DM}$ for the SC-CBF test structure is too high (e.g., $P(\alpha_1 > \gamma_1 \cdot SA_{1,DM})$ equals 19.7%). There are two factors that contribute to the high probability of α_n exceeding $\gamma_n \cdot SA_{n,DM}$: (1) the properties (i.e., the PT bar yield stress and the higher mode periods) of the SC-CBF test structure are different from those assumed in the analyses used to estimate the design demands; and (2) the DBE-level ground motions (presented in Chapter 5) used to determine the values of γ_n are different from the DBE-level ground motions (presented in Chapter 9) used to estimate the DBE-level response of the SC-CBF test structure.

Table 12.4 compares the values of $\gamma_n \cdot SA_{n,DM}$ and $P(\alpha_n > \gamma_n \cdot SA_{n,DM})$ with the values of $\gamma_n \cdot SA_{n,PM}$ and $P(\alpha_n > \gamma_n \cdot SA_{n,PM})$. The first mode results are sensitive to the PT bar yield stress. Since the actual PT bar yield stress (143.6 ksi) is greater than the nominal yield stress (120 ksi), both the factored design value (i.e., $\gamma_n \cdot SA_n$, where SA_n equals $\alpha_{Y,1}$ for the first mode) and the effective pseudo-acceleration response, α_1, from the nonlinear dynamic analyses increase accordingly. When the actual PT bar yield stress is used in both the design calculation and the nonlinear dynamic analysis model, the probability of α_1 exceeding $\gamma_1 \cdot \alpha_{Y,1}$ is about 5% (i.e., $P(\alpha_1 > \gamma_1 \cdot SA_{1,PM})$ equals 5.3%), indicating that the value of γ_1 estimated in Chapter 6 is appropriate when actual properties are used to

determine the value of $\alpha_{Y,1}$ for design. For the higher modes, the periods calculated from the design analytical model (DM) and the predictive analytical model (PM) are different, resulting in different values of SA_3 and SA_4 from the DBE design spectrum. The effective modal masses for these modes are small, and these differences will not significantly affect $F_{x,fdd}$.

To study the effect of the different sets of DBE-level ground motions used in this research, the spectral accelerations of the ground motions used in the analysis of Frame D_{DIST}v2 (presented in Chapter 5) and the spectral accelerations of the ground motions used in the analysis of the SC-CBF test structure (presented in Chapter 9) are compared. The periods and spectral accelerations for the SC-CBF test structure from the design model (DM), and the predictive analytical model (PM) are shown in Table 12.5. The tabulated data are: the period, T_n, based on design model (DM) or predictive model (PM) properties; the design spectral acceleration ($\alpha_{Y,1}$ for the first mode and SA_n from the DBE design spectrum for the higher modes) based on design model (DM) or predictive model (PM) properties, denoted $SA_{n,x}$, where x is either DM or PM, and the corresponding factored spectral acceleration from the design spectrum, $\gamma_n \cdot SA_{n,x}$; the median spectral acceleration for the set of DBE-level ground motions (presented in Chapter 9), based on the design model (DM) period or the predictive model (PM) period, $SA_{m,x,n}$, where x is either DM or PM, and the corresponding ratio $SA_{m,n,x}$ / $SA_{n,x}$. Table 12.6 shows similar data for Frame D_{DIST}v2, where the periods are from an analytical model similar to the DM, and the median spectral acceleration is for the suite of DBE ground motions presented in Chapter 5 (see Section 6.5).

For the first mode, the ratio $SA_{m,x,n}$ / $SA_{n,x}$ in Tables 12.5 and 12.6 is given for consistency, but is not applicable for the following discussion since the design spectral acceleration, $\alpha_{Y,1}$, is not determined from a linear elastic response spectrum. For the second mode, the values of $SA_{m,x,n}$ / $SA_{n,x}$ for the SC-CBF test structure and corresponding ground motions, as well as for Frame D_{DIST}v2 and the corresponding ground motions, are approximately 1.2, so the different sets of ground motions used in these analyses do not produce significantly different second mode responses. For the third and fourth modes, the ratio $SA_{m,x,n}$ / $SA_{n,x}$ for the SC-CBF test structure and corresponding ground motions set is close to 1.0, while for Frame D_{DIST}v2 and the corresponding ground motions, $SA_{m,x,n}$ / $SA_{n,x}$ is about 0.75. This result can also be seen in plots of the spectral accelerations in Figure 12.1. Figure 12.1(a) shows the response spectra for the ground motions used for the SC-CBF test structure, discussed in Chapter 9, and Figure 12(b) shows the response spectra for the ground motions used for Frame D_{DIST}v2, discussed in Chapter 5. The increased values of the ratio $SA_{m,n,x}$ / $SA_{n,x}$ for the test structure and associated ground motions (i.e., 1.0 versus 0.75) indicate that the third and fourth mode response of the SC-CBF test structure are expected to be greater than was observed for Frame D_{DIST}v2, which helps to explain why $P(\alpha_n > \gamma_n \cdot SA_{n,DM})$ and $P(\alpha_n > \gamma_n \cdot SA_{n,PM})$ are much larger than the target value of 5%.

Table 12.7 summarizes the probability of the brace axial force response in story i (F_{bri}) exceeding certain design quantities related to member yielding. The data in the second, fourth, sixth, and eighth columns of Table 12.7 are the values of the variables listed in the first column, for stories i equal 1 through 4, respectively, and the data in the third, fifth,

seventh, and ninth columns are the probabilities of F_{bri} exceeding the tabulated values. The tabulated values for each story i are: the mean response, μ_{Fbri} and the median response, $F_{bri,m}$, from the dynamic analysis results for the DBE-level ground motions; the factored design demand, $F_{bri,fdd}$; the nominal capacity (determined using the AISC-LRFD criteria (AISC 2005b)), $F_{bri,n}$; $F_{bri,fdd}$ calculated using a value of $\alpha_{Y,1}$ based on the actual PT bar yield stress; and the factored design demand presented by Gonner (2009), $F_{bri,fdd,G}$.

The probabilities of F_{bri} exceeding $F_{bri,fdd}$ (e.g., P($F_{br1} > F_{br1,fdd}$) equals 12.6%) are less than the probabilities of α_n exceeding $\gamma_n \cdot SA_{n,x}$ given in Table 12.4 (e.g., P($\alpha_1 > \gamma_1 \cdot SA_{1,DM}$) equals 19.7%). This result suggests the values of the correlation matrix [ρ] used in the modal combination are conservative for the SC-CBF test structure. When the actual PT bar yield stress is considered in determining the value of $\alpha_{Y,1}$, and the corresponding values of $F_{bri,fdd}$, the probability of F_{bri} exceeding $F_{bri,fdd}$ is 3.6% (for the first story braces) or less, which satisfies the PBD criteria. Although for the third and fourth modes, the ratio $SA_{m,x,n}$ / $SA_{n,x}$ for the test structure and associated ground motions was larger than for the structure and ground motions used to determine γ_n (i.e., 1.0 versus 0.75), suggesting that an increase in γ_n may be needed, the effective modal masses for these modes are small, resulting in no significant effect on $F_{x,fdd}$.

There is a significant margin between $F_{bri,fdd}$ and $F_{bri,n}$, as indicated in Table 12.8. As discussed in Chapter 8, there are a number of reasons for this margin: (1) the need to select from discrete sizes of structural shapes, (2) the use of interaction equations (AISC 2005b) to select the members rather than designing for axial forces alone, (3) the resistance factor ϕ in the capacity calculations (AISC 2005b), and (4) the second story

brace sizes were increased to make the brace members more uniform. Although the brace force response, F_{bri}, for some DBE-level ground motions (i.e., DBE_abbar--l, DBE_abbar--t, DBE_nr-pel360, DBE_ucl360, and DBE_wah090) exceeds $F_{bri,fdd}$, actual member yielding (i.e., F_{bri} exceeding $F_{bri,n}$) does not occur due to the margin between $F_{bri,fdd}$ and $F_{bri,n}$.

12.2.2 MCE-Level Ground Motions

Table 12.9 summarizes the maximum roof drift and brace force responses of the SC-CBF test structure for the MCE-level ground motions. The response quantities in Table 12.8 are the maximum roof drift response for each ground motion (θ_{MCE}) and the maximum brace force in each story for each ground motion (F_{bri}). Response values that exceed the factored design demands ($\theta_{DBE,fdd}$ and $F_{bri,fdd}$, respectively) are in bold text in the table.

12.2.2.1 Evaluation of PT Bar Yielding

Table 12.10 summarizes the probability of θ_{MCE} exceeding selected design quantities related to the PBD criteria for PT bar yielding. The data in the second column of Table 12.10 are the values of the variables listed in the first column, and the data in the third column are the probabilities of θ_{MCE} exceeding the tabulated values in the second column. The tabulated values are the mean roof drift response (μ_θ), the median roof drift response ($\theta_{MCE,m}$), $\theta_{DBE,dd}$, $\theta_{DBE,fdd}$ (determined using γ_θ equal to 1.0), $\theta_{Y,n}$, $\theta_{Y,FA}$, $\theta_{dd,G}$, and $\theta_{Y,G}$. These quantities are defined in Section 12.2.1.1.

The definition of the roof drift design demand for the limit state of PT bar yielding presented in Chapter 6 permits a 50% probability that θ_{DBE} exceeds $\theta_{DBE,fdd}$. The

probability that θ_{MCE} exceeds $\theta_{DBE,fdd}$ is expected to be greater than 50%. The numerical analysis results show a probability of θ_{MCE} exceeding $\theta_{DBE,fdd}$ of 70.7%, which is acceptable for response to MCE-level seismic input. The probability of θ_{MCE} exceeding $\theta_{Y,FA}$ is 6.9%, which indicates that the performance of the SC-CBF test structure is significantly better than that required by the PBD objectives. The reasons for the low probability of θ_{MCE} exceeding $\theta_{Y,FA}$ are discussed in Section 12.2.1.1.

12.2.2.2 Evaluation of Member Yielding Factored Design Demands

The evaluation of the member yielding performance of the SC-CBF test structure begins with an evaluation of the spectral accelerations. Table 12.11 summarizes the probability of α_n from the numerical analysis results for the MCE-level ground motions exceeding certain spectral acceleration values represented by the variables in the first column of the table. The second, fourth, sixth, and eighth columns of Table 12.11 give the values of these variables for the first, second, third, and fourth modes, respectively. The third, fifth, seventh, and ninth columns give the probabilities of α_n exceeding these tabulated values. The variables are: μ_α, $\alpha_{n,m}$, $SA_{n,DM}$, $\gamma_n \cdot SA_{n,DM}$, $SA_{n,PM}$, and $\gamma_n \cdot SA_{n,PM}$. These quantities are defined in Section 12.2.1.2.

In Chapter 6, the values for γ_n were selected such that the probability of α_n exceeding $\gamma_n \cdot SA_{n,DM}$ was small (e.g., approximately 5%) under DBE-level earthquake input. Table 12.10 shows that the probability of α_n exceeding $\gamma_n \cdot SA_{n,DM}$ under MCE-level seismic input is high (e.g., about 60% for the first and third modes and 33% for the second mode). When the actual PT bar yield stress is used in both the design calculation and the

nonlinear dynamic analysis model, however, the probability of α_1 exceeding $\gamma_1 \cdot \alpha_{Y,1}$ is only about 29%.

Table 12.12 summarizes the probability of the brace axial force response in story i (F_{bri}) exceeding certain design quantities related to member yielding. The data in the second, fourth, sixth, and eighth columns of Table 12.12 are the values of the variables listed in the first column, for stories i equal 1 through 4, respectively, and the data in the third, fifth, seventh, and ninth columns are the probabilities of F_{bri} exceeding the tabulated values. The tabulated values for each story i are: μ_{Fbri} and $F_{bri,m}$ from the dynamic analysis results for the MCE-level ground motions; $F_{bri,fdd}$ and $F_{bri,n}$; $F_{bri,fdd}$, and $F_{bri,fdd,G}$. These quantities are defined in Section 12.2.1.2.

The probabilities of F_{bri} exceeding $F_{bri,fdd}$ are less than the probability of α_n exceeding $\gamma_n \cdot SA_{n,x}$ given in Table 12.11. This result suggests the values of the correlation matrix [ρ] used in the modal combination are conservative for the SC-CBF test structure. When the actual PT bar yield stress is considered in determining the value of $\alpha_{Y,1}$ and the corresponding values of $F_{bri,fdd}$, the probability of F_{bri} exceeding $F_{bri,fdd}$ is only 10.2% under the MCE, which is close to the PBD criterion for member yielding under the DBE. The probability of F_{bri} exceeding $F_{bri,fdd}$ under the MCE is not significantly greater than the probability of F_{bri} exceeding $F_{bri,fdd}$ under the DBE. This suggests that detailing the structural members and connections for ductility based on the seismic design criteria (AISC 2005a) may not be necessary, as the design criteria for yielding under the DBE provide a low probability of member yielding under MCE-level response. As a result, the probability of member failure and subsequent structural collapse is very small.

As discussed in Section 12.2.1, there is a significant margin between $F_{bri,fdd}$ and $F_{bri,n}$, as indicated in Table 12.8. This margin causes the probability of F_{bri} exceeding $F_{bri,n}$ to be significantly less than the probability of F_{bri} exceeding $F_{bri,fdd}$. However, the values of F_{br1} for ground motions 5082-235 and dzc270 shown in Table 12.9, are greater than the capacity $F_{br1,n}$ shown in Table 12.8. As discussed in Chapter 8, the structural members are modeled as linear-elastic beam-column elements. The analytical model is not intended to evaluate whether or not the SC-CBF members have the ductility to withstand nonlinear deformation demands from these ground motions without failure.

12.2.3 Extreme MCE-Level Ground Motions

Table 12.13 summarizes the maximum roof drift and brace force responses of the SC-CBF test structure for the extreme MCE-level ground motions. The response quantities in Table 12.13 are the maximum roof drift response for each ground motion (θ_{xMCE}) and the maximum brace force in each story for each ground motion (F_{bri}). Response values that exceed the design demands ($\theta_{DBE,fdd}$ and $F_{bri,fdd}$, respectively) are in bold text in the table.

Table 12.14 expresses the maxima shown in Table 12.13 as a number of standard deviations above or below the mean MCE-level response. θ_{xMCE} for the ground motions recorded at the Takatori station are particularly high; the values of θ_{xMCE} for the unscaled ground motions are 6.75 and 7.54 standard deviations above the mean MCE-level response, indicating that the probability of θ_{MCE} exceeding these values is extremely low. Note that the PT bars have yielded for these ground motions and the values of F_{bri} (as shown in Table 12.13) are greater than $F_{bri,fdd}$. However, the values of F_{bri} do not exceed

the member capacities $F_{bri,n}$, shown in Table 12.8. Under extreme roof drift demand (7.5 standard deviations above the mean MCE-level response), the structural members do not yield (and, of course, do not fail).

12.2.4 Post-MCE Aftershock

To assess the performance of the SC-CBF test structure after damage has occurred, a post-MCE aftershock hybrid simulation was performed in the laboratory. Before this simulation, the PT bars were yielded from previous laboratory tests to the point that slack developed in some of the bars. As a result, column uplift and rocking occur before forces develop in the PT bars. The ground motion used for the aftershock simulation was DBE_5108-090, and the simulation is designated DBE_5108-090a_02-09-2010.

Figure 12.2 shows the roof drift response from post-MCE aftershock hybrid simulation DBE_5108-090a_02-09-2010 and the roof drift response from DBE-level hybrid simulation DBE_5108-090_12-31-2009. From this figure, it is clear that the initial low-level dynamic response (i.e., the first two seconds of response) is identical and not sensitive to the initial PT force. The lack of initial force in the PT bars, however, reduces the overturning moment resistance of the test structure. Recalling Equation 7.16, which expresses the overturning moment resistance at decompression for Frame D_{DF}:

$$OM_D = \left(PT_0 + W_{SC-CBF}\right)\frac{b_{SC-CBF}}{2} + OM_{ED,D} \tag{12.3}$$

The overturning moment resistance of Frame D_{DF} with zero initial PT force, $OM_{D,0}$, can be expressed as:

$$OM_{D,0} = (W_{SC-CBF})\frac{b_{SC-CBF}}{2} + OM_{ED,D,0} \tag{12.4}$$

where,

$$OM_{ED,D,0} = \eta \cdot OM_{D,0} \tag{12.5}$$

When the overturning moment demand is large enough to overcome $OM_{D,0}$ during the post-MCE aftershock simulation (DBE_5108-090a_02-09-2010), the SC-CBF column base uplifts and the SC-CBF rocks. This response deviates from the DBE-level simulation (DBE_5108-090_12-31-2009), where column decompression has not yet occurred.

Figure 12.2 shows that the peak roof drift response is larger for the post-MCE aftershock simulation (DBE_5108-090a_02-09-2010) than for the DBE-level simulation (DBE_5108-090_12-31-2009). This difference is due to the reduced stiffness of the system, seen in Figure 12.3, which shows the overturning moment versus roof drift hysteresis behavior of the SC-CBF system in each simulation. Figure 12.3(a) shows the hysteretic behavior from the DBE-level simulation (DBE_5108-090_12-31-2009) with initial force in the PT bars (PT_0), which exhibits the flag-shaped hysteresis loops that are characteristic of SC systems. Figure 12.3(b) shows the hysteretic behavior from the post-MCE aftershock simulation (DBE_5108-090a_02-09-2010) with zero initial force in the PT bars. This response does not have a true "elastic" range separating the two quadrants of hysteretic response; however, the overall energy dissipated in the system (i.e., the area within the hysteresis loops) is similar.

The performance of the SC-CBF test structure under the post-MCE aftershock was excellent. Even without initial force in the PT bars, the SC-CBF self-centered and no damage occurred to the structural members, suggesting that the SC-CBF system can achieve the performance objective of CP performance under a post-MCE aftershock.

12.3 Nonstructural Considerations

Chapter 4 introduced nonstructural performance considerations as well as the structural limit states. This section addresses the performance of the SC-CBF test structure with respect to the nonstructural considerations of story drift, floor accelerations, and system overstrength.

12.3.1 Story Drift

Tables 12.15 and 12.16 show the maximum story drift (θ_s) from the DBE-level ground motions and the MCE-level ground motions, respectively. Table 12.17 gives the mean (μ_x) and median (x_m) values of θ_s. The mean and median values of θ_s for DBE-level response are 0.98% radians and 0.93% radians, respectively. The mean and median values of θ_s for MCE-level response are 1.59% radians and 1.51% radians, respectively. Table 12.17 also summarizes the probability of θ_s at each earthquake input level exceeding the code-based drift limit of 2% under the DBE (ASCE 2005), which is treated as an index value (i.e., benchmark) for comparison. For DBE-level earthquake input, the probability of θ_s exceeding 2% radians is only 0.9%. For MCE-level earthquake input, the probability of θ_s exceeding 2% radians is 18.9%, which clearly satisfies CP

performance but not necessarily IO performance. Both results are consistent with the PBD criteria for the SC-CBF system.

12.3.2 Floor Accelerations

Tables 12.15 and 12.16 show the maximum floor accelerations ($a_{i,max}$) from the DBE-level ground motions and the MCE-level ground motions, respectively. Table 12.17 gives the mean (μ_x) and median (x_m) values of a_{max}, which is the peak floor acceleration (the maximum over all floors). The mean and median values of a_{max} for DBE-level response are 0.88 g and 0.82 g, respectively. The mean and median values of a_{max} for MCE-level response are 1.04 g and 0.98 g, respectively. Table 12.17 also summarizes the probability of a_{max} at each seismic input level exceeding the index value 1.0g. There is a high probability of a_{max} exceeding 1.0g. It is important to design the nonstructural elements to accommodate these accelerations.

12.3.3 Overstrength

Tables 12.15 and 12.16 show the maximum base shear ($V_{b,max}$) from the DBE-level ground motions and the MCE-level ground motions, respectively. These values are then normalized by the design base shear (i.e., the base shear from the ELF procedure (ASCE 2005)) to determine the system overstrength Ω_0. For a conventional CBF system, the overstrength specified by the code ($\Omega_{0,CBF}$) is 2.0, which is treated as an index value for comparison. Table 12.17 gives the mean (μ_x) and median (x_m) values of Ω_0. The mean and median values of Ω_0 for DBE-level response are 2.7 and 2.6, respectively. The mean and median values of Ω_0 for MCE-level response are 3.3 and 3.2, respectively. Table

12.17 also summarizes the probability of Ω_0 for each seismic input level exceeding $\Omega_{0,CBF}$. For the DBE-level ground motions, the mean overstrength of 2.7 is not significantly greater than the overstrength for a conventional CBF system, indicating that the improved behavior of the SC-CBF system is not merely due to excessive system strength, but is a function of the column decompression and rocking behavior of the SC-CBF.

For the MCE-level ground motions, the mean overstrength is 3.3. The continued increase in overstrength indicates that the SC-CBF system has considerable strength beyond the DBE-level response, and that there is a significant margin between mean MCE-level response and collapse.

12.4 Summary

Nonlinear dynamic analysis of the four-story SC-CBF test structure has shown that the system performance is consistent with the performance based design (PBD) objectives set forth for the DBE and the MCE. For the limit state of PT bar yielding, the analysis procedures for estimating the design demand and capacity are conservative, and there was only a 15.7% probability of exceeding the roof drift design demand under the DBE, although the PBD criteria target a 50% probability of exceedance. The conservatism in the procedure for estimating the design demand could be addressed with further study of the ductility demands on SC-CBF systems. The conservatism in the procedure for estimating the capacity could be addressed by considering possible foundation flexibility and possible overstrength of the PT bars.

For the limit state of member yielding, the PBD criteria were essentially satisfied. Under the DBE, the PBD criteria target a 5% probability of the member force response exceeding the nominal member force capacity (which is assumed to be close to the factored member force design demand $F_{x,fdd}$). The numerical analysis results show a 12.6% probability of the first story brace force response, F_{br1}, exceeding the factored design demand, $F_{br1,fdd}$, with smaller probabilities of exceedance in the other stories. If the actual PT yield stress rather than the nominal yield stress had been considered in estimating the brace force design demands, the probability of F_{br1} exceeding $F_{br1,fdd}$ is only 3.6% under the DBE. For the MCE input level, collapse prevention (CP) performance is the objective. Under the MCE, however, the numerical analysis results show only a 29.8% probability of F_{br1} exceeding $F_{br1,fdd}$, with smaller probabilities of exceedance for the other stories. This low probability of member yielding, combined with the ductility of the braces required by the seismic design criteria (AISC 2005a), creates a large margin against collapse under the MCE.

The seismic performance of the SC-CBF test structure after loss of prestress due to PT bar yielding was excellent. The laboratory hybrid simulation results indicate that the peak roof drift demand is greater for an SC-CBF with no initial force in the PT bars (i.e., after the prestress has been lost due to PT bar yielding) than for the SC-CBF with initial force in the PT bars (i.e., as designed); however, the SC-CBF self-centered under the aftershock and the PBD criteria of collapse prevention (assuming that the PT bars yielded under MCE-level seismic input) are satisfied.

Nonstructural considerations also show the SC-CBF system is a viable earthquake-resistant system. Under the DBE, the maximum story drifts are all below the typical building code limit of 2% (e.g., ASCE 2005), and the mean maximum story drifts for the MCE are also below this limit. Floor accelerations for the SC-CBF test structure must be considered in the design of nonstructural elements. The SC-CBF system provides a large drift capacity prior to initiation of damage of the main structural members, relative to a conventional CBF system, without increasing the force levels. The system overstrength, Ω_0, averages to 2.7 for the DBE and 3.3 for the MCE, compared to the estimated value of 2.0 for a conventional CBF system (ASCE 2005).

Table 12.1 – Summary of maximum roof drift and brace axial force response for the DBE-level ground motions from analysis of the predictive model

Ground Motion	θ_{DBE} (% rad)	F_{br1} (kip)	F_{br2} (kip)	F_{br3} (kip)	F_{br4} (kip)
DBE_5108-090	0.84	324.7	171.5	323.6	286.9
DBE_5108-360	0.66	324.4	195.3	296.0	311.4
DBE_a-tmz000	0.53	236.6	157.8	225.8	236.1
DBE_a-tmz270	0.76	200.5	146.0	258.3	248.6
DBE_abbar--l	0.79	**411.3**	222.6	281.6	311.7
DBE_abbar--t	**1.48**	**440.1**	228.7	**388.9**	370.6
DBE_arl090	**1.38**	320.9	183.0	311.3	325.4
DBE_arl360	0.75	292.7	163.3	253.0	249.1
DBE_cap000	**1.18**	255.9	180.4	229.5	252.9
DBE_cap090	0.51	171.0	118.9	183.9	174.1
DBE_cls000	0.65	197.8	138.9	259.6	239.6
DBE_cls090	0.76	181.4	134.6	199.5	205.0
DBE_cpe045	**1.25**	311.9	207.2	295.7	308.3
DBE_cpe315	0.55	219.3	128.3	213.2	215.2
DBE_h-shp000	0.56	327.8	159.9	249.7	263.8
DBE_h-shp270	0.92	332.3	196.1	310.6	312.2
DBE_hwa059-e	0.76	163.9	128.0	188.1	195.9
DBE_hwa059-n	0.61	188.0	130.8	173.5	185.4
DBE_nr-pel090	0.81	235.8	152.8	191.1	208.8
DBE_nr-pel360	0.95	**388.3**	217.6	352.6	349.0
DBE_ro3000	0.63	231.2	143.6	206.6	206.2
DBE_ro3090	**1.52**	322.9	221.4	295.1	315.1
DBE_shi000	**1.18**	187.0	167.4	231.5	243.1
DBE_shi090	0.82	196.9	142.1	193.0	201.9
DBE_sjte225	0.56	313.5	155.3	244.0	236.9
DBE_sjte315	0.79	292.5	152.1	237.4	231.5
DBE_ucl090	0.97	390.5	203.6	350.0	330.3
DBE_ucl360	**1.25**	**455.1**	**273.6**	374.2	360.3
DBE_wah000	0.80	286.9	172.6	305.7	270.8
DBE_wah090	**1.18**	**452.0**	230.5	355.3	334.7

Table 12.2 – Summary of probability of exceedance of roof drift design demand and capacity for the DBE-level ground motions

X	θ_{DBE} (% rad)	$P(\theta_{DBE} > X)$ (%)
μ_θ	0.88	43.6
$\theta_{DBE,m}$	0.84	50.0
$\theta_{DBE,dd}$	1.16	15.7
$\theta_{DBE,fdd}$	1.16	15.7
$\theta_{Y,n}$	1.42	5.0
$\theta_{Y,FA}$	2.30	0.1
$\theta_{DBE,dd,G}$*	1.40	5.4
$\theta_{Y,G}$*	1.43	4.7

* – From Gonner (2009)

Table 12.3 – Summary of parametric study of factors affecting roof drift capacity at PT bar yielding

Model Name	Basement Substructure Model	PT Model	Notation	$\theta_{Y,x}$ (% rad)
RN	Rigid	Nominal	$\theta_{Y,RN}$	1.41
RA	Rigid	Actual	$\theta_{Y,RA}$	1.85
FN	Flexible	Nominal	$\theta_{Y,FN}$	1.62
FA	Flexible	Actual	$\theta_{Y,FA}$	2.30

Table 12.4 – Summary of probability of exceedance of SA_n and $\gamma_n \cdot SA_n$ for the DBE-level ground motions

X	α_1 (g)	P($\alpha_1 > X$) (%)	α_2 (g)	P($\alpha_2 > X$) (%)	α_3 (g)	P($\alpha_3 > X$) (%)	α_4 (g)	P($\alpha_4 > X$) (%)
$\mu_{\alpha n}$	0.27	45.7	1.50	41.5	1.74	42.2	3.43	41.6
$\alpha_{n,m}$	0.26	50.0	1.37	50.0	1.61	50.0	3.14	50.0
$SA_{n,DM}$	0.27	41.6	1.00	76.6	0.92	92.6	0.80	99.9
$\gamma_n \cdot SA_{n,DM}$	0.31	19.7	2.00	18.7	1.83	37.2	1.61	94.3
$SA_{n,PM}$	0.32	16.5	1.00	76.6	1.00	88.8	1.00	99.7
$\gamma_n \cdot SA_{n,PM}$	0.37	5.3	2.00	18.7	2.00	29.0	2.00	85.6

DM – Based on actual PT yield stress and periods from design analytical model
PM – Based on actual PT yield stress and periods from predictive analytical model

Table 12.5 – Natural periods and design spectral acceleration values for SC-CBF test structure

	Mode	T_n (s)	$SA_{n,x}$ (g)	$\gamma_n \cdot SA_{n,x}$ (g)	$SA_{m,n,x}$ (g)	$SA_{m,n,x} / SA_{n,x}$
Design Model (DM)	**1**	0.502	0.27	0.31	0.88	3.27
	2	0.171	1.00	2.00	1.14	1.14
	3	0.103	0.92	1.83	0.92	1.00
	4	0.081	0.80	1.61	0.75	0.93
Predictive Model (PM)	**1**	0.610	0.32	0.37	0.90	2.80
	2	0.238	1.00	2.00	1.22	1.22
	3	0.174	1.00	2.00	1.13	1.13
	4	0.138	1.00	2.00	1.12	1.12

Table 12.6 – Natural periods and design spectral acceleration values for Frame $D_{DIST}v2$

	Mode	T_n (s)	$SA_{n,x}$ (g)	$\gamma_n \cdot SA_{n,x}$ (g)	$SA_{m,n,x}$ (g)	$SA_{m,n,x} / SA_{n,x}$
Design Model (DM)	**1**	0.745	0.18	0.21	0.925	5.01
	2	0.239	1.00	2.00	1.203	1.20
	3	0.135	1.00	2.00	0.761	0.76
	4	0.101	0.91	1.81	0.663	0.73
	5	0.085	0.82	1.65	0.597	0.72
	6	0.080	0.80	1.60	0.595	0.74

Table 12.7 – Summary of probability of exceedance of brace axial force design demands and capacities for the DBE-level ground motions

X	F_{br1} (kip)	P($F_{br1} > X$) (%)	F_{br2} (kip)	P($F_{br2} > X$) (%)	F_{br3} (kip)	P($F_{br3} > X$) (%)	F_{br4} (kip)	P($F_{br4} > X$) (%)
μ_{Fbri}	288.4	44.1	174.1	45.7	265.9	45.4	266.0	45.8
$F_{bri,m}$	276.0	50.0	170.1	50.0	259.1	50.0	260.2	50.0
$F_{bri,fdd}$	388.1	12.6	239.8	5.6	386.0	4.1	471.8	0.2
$F_{bri,n}$	520.1	1.6	536.1	0.0	536.1	0.1	668.7	0.0
$F_{bri,fdd}$*	470.3	3.6	326.3	0.1	450.1	0.8	480.1	0.2
$F_{bri,fdd,G}$**	384.9	13.1	231.7	7.7	376.0	5.2	479.1	0.0

* – Based on $\alpha_{Y,1}$ calculated using actual PT yield force

** – From Gonner (2009)

Table 12.8 – Summary of SC-CBF design values for the member yielding limit state

Story	$F_{bri,fdd}$ (kip)	$F_{bri,n}$ (kip)	$F_{bri,n}$ / $F_{bri,fdd}$
1	388.1	520.1	1.34
2	239.8	536.1	2.24
3	386.0	536.1	1.39
4	471.8	668.7	1.42

Table 12.9 – Summary of maximum roof drift and brace axial force response for the MCE-level ground motions from analysis of the predictive model

Ground Motion	θ_{MCE} (% rad)	F_{br1} (kip)	F_{br2} (kip)	F_{br3} (kip)	F_{br4} (kip)
MCE_5082-235	**1.71**	**529.8**	**294.4**	**388.3**	418.6
MCE_5082-325	0.97	**463.9**	**243.1**	**462.7**	461.4
MCE_a-tmz000	**1.22**	**417.5**	**241.1**	357.6	372.8
MCE_a-tmz270	1.13	375.7	193.3	351.7	335.0
MCE_cap000	**2.05**	**355.5**	**247.9**	331.3	354.3
MCE_cap090	1.05	256.0	160.4	266.3	238.8
MCE_dzc180	**1.68**	294.2	209.0	275.1	280.7
MCE_dzc270	**2.64**	**535.9**	**274.2**	**407.3**	424.1
MCE_far000	0.58	211.6	137.4	254.5	237.4
MCE_far090	**1.23**	299.9	183.9	328.4	329.9
MCE_fle144	0.65	304.4	187.0	227.7	238.4
MCE_fle234	**1.18**	322.1	184.4	310.1	299.7
MCE_h-cpe147	0.92	359.3	207.9	286.2	280.0
MCE_h-cpe237	**1.75**	**412.3**	224.1	336.7	340.6
MCE_los000	**1.21**	335.7	191.5	332.2	315.7
MCE_los270	1.01	266.5	182.2	385.1	345.2
MCE_lp-hda165	**2.63**	344.1	**260.7**	341.1	348.8
MCE_lp-hda255	**1.48**	365.3	239.5	341.0	353.4
MCE_mrg000	**1.85**	307.5	222.6	302.0	312.4
MCE_mrg090	**1.68**	251.0	189.3	284.6	300.1
MCE_mrp090	**2.23**	**492.9**	**260.7**	**439.5**	425.7
MCE_mrp180	**1.52**	**508.4**	**271.5**	**462.2**	464.0
MCE_mvh000	0.84	228.4	136.6	221.2	228.0
MCE_mvh090	**1.38**	257.1	194.3	251.9	267.1
MCE_nr-pel090	**1.58**	308.6	210.2	284.4	301.0
MCE_nr-pel360	**1.52**	**491.2**	**284.6**	**476.2**	461.9
MCE_shi000	**1.90**	306.4	236.7	345.8	361.2
MCE_shi090	**1.87**	314.8	218.5	304.4	307.1
MCE_stn020	1.15	247.3	180.6	302.5	276.5
MCE_stn110	**1.60**	324.6	206.5	**397.6**	369.5

Table 12.10 – Summary of probability of exceedance of roof drift design demand and capacity for the MCE-level ground motions

X	θ_{MCE} (% rad)	$P(\theta_{MCE} > X)$ (%)
μ_θ	1.47	43.3
$\theta_{MCE,m}$	1.39	50.0
$\theta_{DBE,dd}$	1.16	70.7
$\theta_{DBE,fdd}$	1.16	70.7
$\theta_{Y,n}$	1.42	47.3
$\theta_{Y,FA}$	2.30	6.9
$\theta_{DBE,dd,G}$*	1.40	48.9
$\theta_{Y,G}$*	1.43	46.4

* – From Gonner (2009)

Table 12.11 – Summary of probability of exceedance of SA_n and $\gamma_n \cdot SA_n$ for the MCE-level ground motions

X	α_1 (g)	$P(\alpha_1 > X)$ (%)	α_2 (g)	$P(\alpha_2 > X)$ (%)	α_3 (g)	$P(\alpha_3 > X)$ (%)	α_4 (g)	$P(\alpha_4 > X)$ (%)
$\mu_{\alpha n}$	0.34	46.1	1.82	42.8	2.13	43.2	4.14	43.5
$\alpha_{n,m}$	0.33	50.0	1.71	50.0	2.01	50.0	3.92	50.0
$SA_{n,DM}$	0.27	83.6	1.00	93.0	0.92	99.0	0.80	100.0
$\gamma_n \cdot SA_{n,DM}$	0.31	60.7	2.00	33.2	1.83	60.8	1.61	99.7
$SA_{n,PM}$	0.32	55.4	1.00	93.0	1.00	98.0	1.00	100.0
$\gamma_n \cdot SA_{n,PM}$	0.37	28.5	2.00	33.2	2.00	50.6	2.00	98.0

DM – Based on actual PT yield stress and periods from design analytical model
PM – Based on actual PT yield stress and periods from predictive analytical model

Table 12.12 – Summary of probability of exceedance of brace axial force design demands and capacities for the MCE-level ground motions

X	F_{br1} (kip)	P($F_{br1} > X$) (%)	F_{br2} (kip)	P($F_{br2} > X$) (%)	F_{br3} (kip)	P($F_{br3} > X$) (%)	F_{br4} (kip)	P($F_{br4} > X$) (%)
μ_{Fbri}	349.6	44.8	215.8	46.3	335.2	46.0	335.0	46.0
$F_{bri,m}$	337.9	50.0	212.0	50.0	328.4	50.0	328.2	50.0
$F_{bri,fdd}$	388.1	29.8	239.8	25.6	386.0	21.2	471.8	3.6
$F_{bri,n}$	520.1	4.9	536.1	0.0	536.1	0.8	668.7	0.0
$F_{bri,fdd}$*	470.3	10.2	326.3	1.1	450.1	6.0	480.1	3.0
$F_{bri,fdd,G}$**	384.9	30.9	231.7	31.8	376.0	25.2	479.1	3.0

* – Based on $\alpha_{Y,1}$ calculated using actual PT yield force

** – From Gonner (2009)

Table 12.13 – Summary of maximum roof drift and brace axial force response for the extreme MCE-level ground motions from analysis of the predictive model

Ground Motion	θ_{xMCE} (% rad)	F_{br1} (kip)	F_{br2} (kip)	F_{br3} (kip)	F_{br4} (kip)
kjm000_us	**2.36**	**455.9**	**279.2**	**406.3**	386.8
kjm090_us	**1.57**	241.2	199.3	297.2	312.8
tak000_us	**5.36**	**440.0**	**289.2**	**395.6**	398.7
tak090_us	**4.95**	**479.5**	**290.2**	**429.8**	426.5
xMCE_tak090	**4.33**	**423.6**	**282.4**	**392.7**	395.5

Table 12.14 – Summary of maximum roof drift and brace axial force response for the extreme MCE-level ground motions, expressed in standard deviations above (+) and below (-) the mean MCE-level response

Ground Motion	θ_{xMCE}	F_{br1}	F_{br2}	F_{br3}	F_{br4}
kjm000_us	1.73	1.11	1.32	0.88	0.85
kjm090_us	0.19	-1.19	-0.57	-0.67	-0.25
tak000_us	7.54	0.94	1.56	0.73	1.02
tak090_us	6.75	1.36	1.59	1.22	1.44
xMCE_tak090	5.55	0.76	1.40	0.69	0.98

Table 12.15 – Summary of nonstructural considerations for the DBE-level ground motions from analysis of the predictive model

Ground Motion	θ_s (% rad)	$a_{1,max}$ (g)	$a_{2,max}$ (g)	$a_{3,max}$ (g)	$a_{4,max}$ (g)	$V_{b,max}$ (kip)	Ω_0
DBE_5108-090	0.92	1.07	1.24	1.06	1.35	455	3.0
DBE_5108-360	0.80	0.95	1.30	1.20	1.50	458	3.0
DBE_a-tmz000	0.62	0.46	0.45	0.75	0.86	330	2.2
DBE_a-tmz270	0.88	0.65	0.60	0.61	0.99	287	1.9
DBE_abbar--l	0.85	1.18	1.35	0.98	1.21	576	3.8
DBE_abbar--t	1.62	1.51	1.25	0.95	1.22	612	4.0
DBE_arl090	1.50	0.66	0.75	0.76	0.91	450	3.0
DBE_arl360	0.86	0.76	0.74	0.67	0.98	422	2.8
DBE_cap000	1.25	0.61	0.62	0.65	0.86	365	2.4
DBE_cap090	0.58	0.43	0.54	0.64	0.69	237	1.6
DBE_cls000	0.73	0.47	0.51	0.78	1.06	277	1.8
DBE_cls090	0.77	0.42	0.48	0.50	0.76	252	1.7
DBE_cpe045	1.38	1.14	1.22	1.03	1.47	439	2.9
DBE_cpe315	0.57	0.67	0.68	0.85	1.23	304	2.0
DBE_h-shp000	0.65	0.91	1.01	0.80	0.79	458	3.0
DBE_h-shp270	1.04	1.31	1.36	1.30	1.55	471	3.1
DBE_hwa059-e	0.78	0.38	0.50	0.55	0.78	228	1.5
DBE_hwa059-n	0.64	0.42	0.39	0.37	0.44	262	1.7
DBE_nr-pel090	0.93	0.37	0.50	0.54	0.64	334	2.2
DBE_nr-pel360	1.16	0.94	0.87	0.84	1.25	548	3.6
DBE_ro3000	0.70	0.69	0.60	0.68	0.87	317	2.1
DBE_ro3090	1.67	0.73	0.76	0.68	1.04	471	3.1
DBE_shi000	1.26	0.48	0.43	0.48	0.61	270	1.8
DBE_shi090	0.93	0.33	0.37	0.47	0.54	283	1.9
DBE_sjte225	0.64	0.78	0.88	0.89	0.85	440	2.9
DBE_sjte315	0.81	0.85	0.92	0.72	0.89	415	2.7
DBE_ucl090	1.12	1.57	1.21	0.90	1.44	537	3.6
DBE_ucl360	1.47	1.51	1.43	1.04	2.02	645	4.3
DBE_wah000	0.88	1.06	1.44	0.95	1.25	403	2.7
DBE_wah090	1.39	1.54	1.66	1.20	1.35	641	4.2

Table 12.16 – Summary of non-structural considerations for the MCE-level ground motions from analysis of the predictive model

Ground Motion	θ_s (% rad)	$a_{1,max}$ (g)	$a_{2,max}$ (g)	$a_{3,max}$ (g)	$a_{4,max}$ (g)	$V_{b,max}$ (kip)	Ω_0
MCE_5082-235	1.74	1.63	1.14	1.52	1.87	752	5.0
MCE_5082-325	1.23	1.57	1.43	1.59	2.24	648	4.3
MCE_a-tmz000	1.36	0.78	0.80	1.30	1.57	584	3.9
MCE_a-tmz270	1.26	1.36	1.11	1.30	1.62	543	3.6
MCE_cap000	2.21	0.73	0.89	1.20	1.60	511	3.4
MCE_cap090	1.15	0.91	0.83	1.08	1.18	354	2.3
MCE_dzc180	1.79	0.49	0.92	0.98	1.14	419	2.8
MCE_dzc270	2.81	1.33	1.19	1.04	1.71	754	5.0
MCE_far000	0.67	0.60	0.85	0.68	1.05	293	1.9
MCE_far090	1.34	0.71	0.70	0.66	1.29	423	2.8
MCE_fle144	0.70	1.03	1.33	0.99	1.11	421	2.8
MCE_fle234	1.29	0.63	0.82	1.06	1.25	450	3.0
MCE_h-cpe147	1.00	1.01	1.10	1.01	1.24	494	3.3
MCE_h-cpe237	1.84	0.97	1.12	0.94	1.16	574	3.8
MCE_los000	1.33	0.85	0.75	0.76	1.07	474	3.1
MCE_los270	1.16	1.06	1.09	0.96	1.60	376	2.5
MCE_lp-hda165	2.75	0.58	0.56	0.74	1.03	492	3.3
MCE_lp-hda255	1.58	0.85	0.83	1.04	1.44	524	3.5
MCE_mrg000	1.91	0.67	0.85	0.73	0.90	442	2.9
MCE_mrg090	1.71	0.39	0.37	0.50	0.75	358	2.4
MCE_mrp090	2.32	1.05	1.26	1.24	1.58	686	4.5
MCE_mrp180	1.72	1.35	1.15	1.20	2.45	718	4.7
MCE_mvh000	0.87	0.58	0.52	0.65	0.76	325	2.1
MCE_mvh090	1.49	0.42	0.45	0.50	0.75	368	2.4
MCE_nr-pel090	1.66	0.69	0.94	0.81	0.95	441	2.9
MCE_nr-pel360	1.81	1.68	1.57	1.23	1.80	685	4.5
MCE_shi000	1.97	0.78	0.80	0.84	1.29	440	2.9
MCE_shi090	1.99	0.66	0.62	0.68	0.90	453	3.0
MCE_stn020	1.27	0.65	1.04	1.16	1.20	351	2.3
MCE_stn110	1.73	0.91	1.31	1.30	1.58	454	3.0

Table 12.17 – Probability of exceedance for non-structural considerations for the DBE-level and MCE-level ground motions

Seismic Input Level	X	θ_s (% rad)	$P(\theta_s > X)$ (%)	a_{max} (g)	$P(a_{max} > X)$ (%)	Ω_0	$P(\Omega_0 > X)$ (%)
DBE	μ_x	0.98	43.6	0.88	42.4	2.7	44.1
	x_m	0.93	50.0	0.82	50.0	2.6	50.0
	Index Value	2.00	0.9	1.00	30.5	2.0	80.1
MCE	μ_x	1.59	43.7	1.04	43.0	3.3	44.9
	x_m	1.51	50.0	0.98	50.0	3.2	50.0
	Index Value	2.00	18.9	1.00	47.7	2.0	96.1

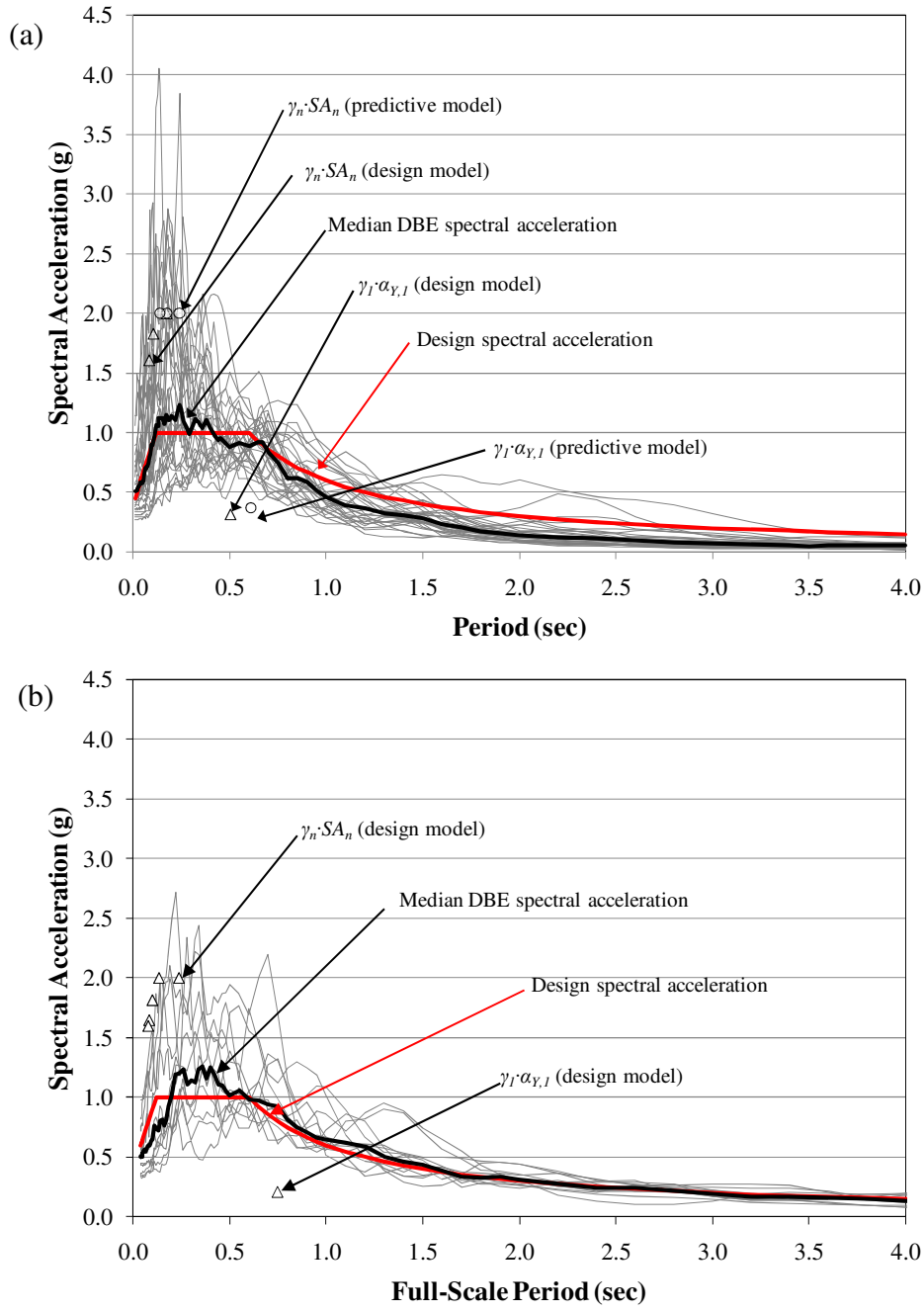

Figure 12.1 – Spectral accelerations for DBE-level ground motions: (a) ground motions used for analysis of the SC-CBF test structure in Chapter 9; (b) ground motions used for the SC-CBF configuration study in Chapter 5

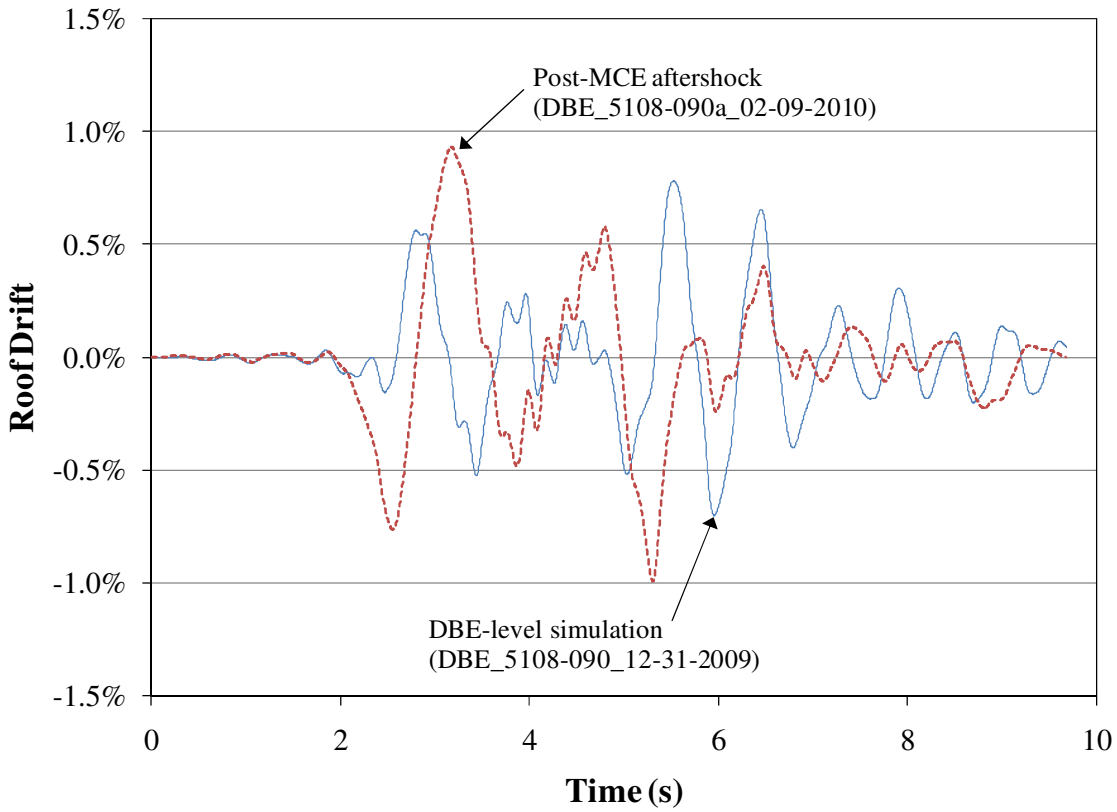

Figure 12.2 – Roof drift response of test structure to the post-MCE aftershock (DBE_5108-090a_02-09-2010) and the DBE-level simulation (DBE_5108-090_12-31-2009)

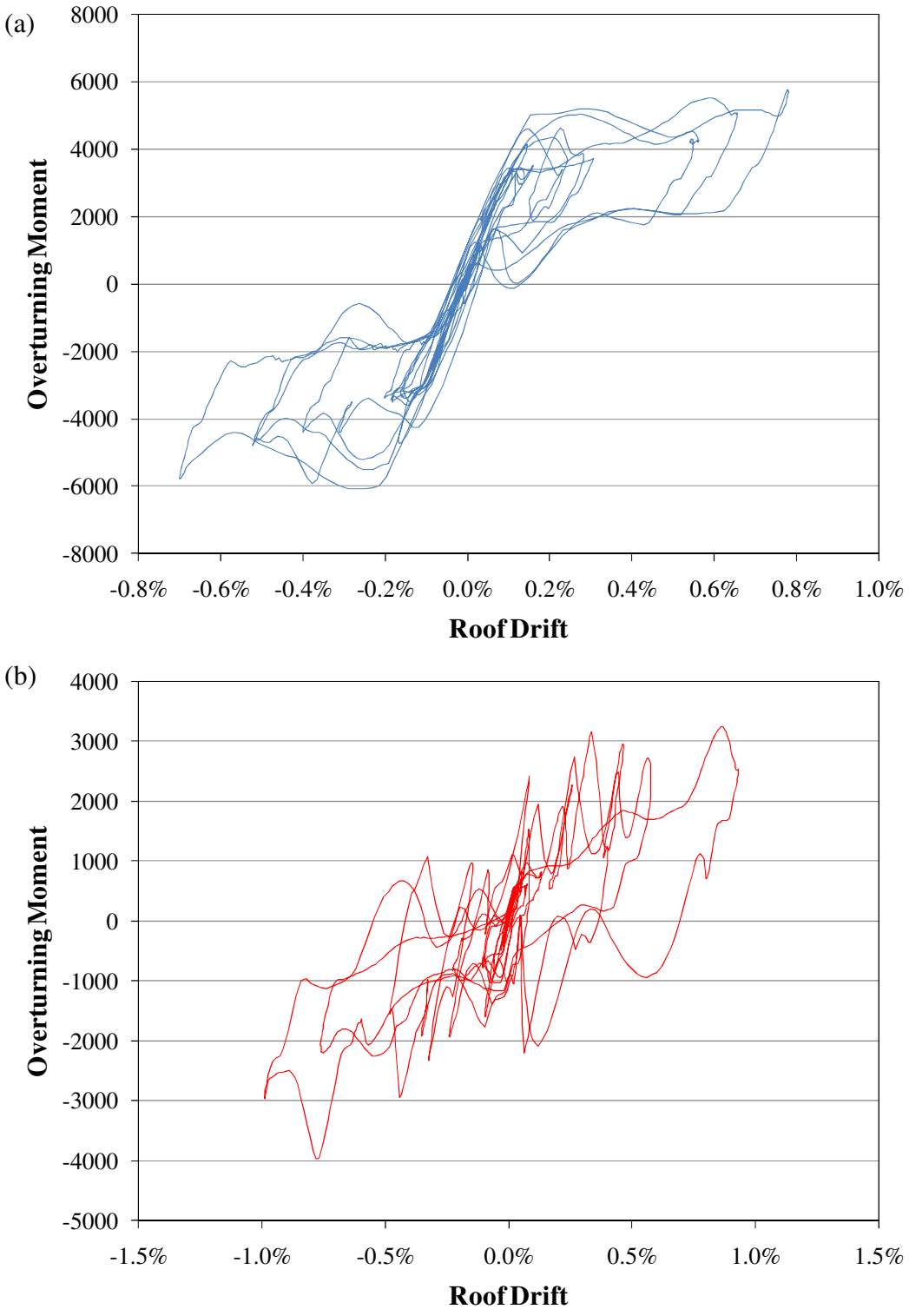

Figure 12.3 – Overturning moment-roof drift response of test structure to DBE_5108-090: (a) DBE-level simulation (DBE_5108-090_12-31-2009); (b) post-MCE aftershock (DBE_5108-090a_02-09-2010)

CHAPTER 13

SUMMARY AND CONCLUSIONS

13.1 Summary

13.1.1 Motivation for Present Research

Conventional concentrically-braced frame (CBF) systems are stiff and economical lateral force resisting systems. However, CBFs have limited lateral drift capacity before damage initiates in the structural members. During earthquakes, CBFs are often subjected to drift demands that yield or buckle the braces. This damage leads to residual lateral drift after the earthquake.

This dissertation describes the development of a self-centering concentrically-braced frame (SC-CBF) system for earthquake-resistant buildings. SC-CBFs are intended to maintain the advantages of conventional CBFs, economy and stiffness, while increasing the lateral drift capacity before structural damage initiates and reducing the potential for residual lateral drift. The SC-CBF members are intended to remain elastic under the design basis earthquake. The purpose of this research is to establish the SC-CBF as a viable seismic-resistant system and to provide a probabilistic performance-based design procedure and associated design criteria for the SC-CBF system.

13.1.2 Research Objectives

The overall objectives of this research program were to develop the SC-CBF system and to provide a probabilistic performance-based design procedure for the SC-CBF system that achieves reliable damage-free performance under the design basis earthquake. These overall objectives were divided into six specific research objectives:

1. To establish the desired lateral force behavior of the SC-CBF system, including specific limit states that may occur under earthquake loading;

2. To develop performance-based design (PBD) objectives, criteria, and procedures for the SC-CBF system to control the occurrence of these limit states;

3. To study the advantages and disadvantages of different SC-CBF configurations;

4. To develop a nonlinear analytical model to simulate the earthquake response of SC-CBF systems;

5. To validate this analytical model through comparisons with experimental results from hybrid earthquake simulations on a large-scale SC-CBF test structure;

6. To validate the PBD procedure for SC-CBF systems and demonstrate that a properly-designed SC-CBF system can be a superior earthquake-resistant structural system.

13.1.3 Research Scope

This research introduced the SC-CBF system concept. The behavior of the SC-CBF system improves upon the behavior of conventional CBFs by increasing the lateral drift capacity before damage to the structural members initiates. This increased lateral drift capacity is provided by introducing softening of the lateral force-lateral drift behavior of the system without yielding the structural members. This softening behavior is caused by rocking of the SC-CBF, which occurs as the bases of the SC-CBF columns decompress and uplift at a specified level of applied lateral force. This rocking response limits the force demands in the structural members. Vertically oriented post-tensioning (PT) bars provide resistance to this column uplift and provide a restoring force to self-center the system.

Large roof drift demands may yield the PT bars. PT bar yielding is the first occurrence of structural damage; however, minor PT bar yielding is easily repaired by restressing the bars, and is not a life safety issue. With increasing applied lateral force, the limit states of member yielding and member failure may be reached. The limit state of member yielding will lead to permanent deformation and residual drift in the SC-CBF. The limit state of member failure may lead to instability and collapse of the system.

Performance-based design (PBD) objectives were developed based on the seismic input levels and performance levels defined in FEMA 450 (BSSC 2003) and the limit states identified for the SC-CBF system. The performance objectives for the SC-CBF system are to achieve immediate occupancy (IO) performance under the design basis earthquake

(DBE) and collapse prevention (CP) performance under the maximum considered earthquake (MCE). In comparison, the performance objectives for conventional earthquake-resistant structural systems are to achieve life safety (LS) performance under the DBE and CP performance under the MCE. The primary difference in the performance objectives is the target performance for the SC-CBF of IO under the DBE, which should significantly reduce potential economic losses from earthquakes. The limit states of column decompression and minor PT bar yielding are permitted under the DBE, as these limit states do not cause significant structural damage. The limit states of column decompression, PT bar yielding, and member yielding are permitted under the MCE. The limit state of member failure is not permitted due to the limited redundancy of the SC-CBF system; member failure may lead to structural collapse.

A probabilistic PBD procedure was developed for the SC-CBF system based on the PBD objectives. The design procedure is based on specified probabilities of the responses under earthquake loading exceeding the design demands for selected limit states. Column decompression is not addressed in the PBD criteria because it is a damage-free limit state. The limit state of PT bar yielding is quantified in terms of roof drift. The probability of the roof drift response exceeding the factored roof drift design demand can be as large as 50%, because the consequences of PT bar yielding are not severe. The probability of the member force response exceeding the factored member force design demands should be low (approximately 5%) because reaching the member yielding limit state may be the initiation of widespread damage to the structural members.

An SC-CBF frame configuration study was performed to investigate the effect of different frame configurations on the earthquake response of the SC-CBF system. Six-story SC-CBFs with a variety of configurations were designed for a prototype building. Nonlinear static and dynamic numerical analyses of these SC-CBFs validated the behavior of the SC-CBF system. The numerical analysis responses were compared against the PBD objectives to determine whether the SC-CBF system performed as intended.

A detailed nonlinear analytical model for the SC-CBF was developed using OpenSEES (Mazzoni et al. 2009). This model included the members (i.e., the beams, columns, braces, and struts) that make up the SC-CBF, as well as the adjacent gravity columns, the basement substructure, and a lean-on column to account for P-Δ effects from gravity loads and the stiffness of gravity load columns that are within the tributary area for one SC-CBF in the prototype building. Material nonlinearity was included only in the PT bar elements, not in the SC-CBF members; therefore, the model is incapable of predicting nonlinear deformation demands in the members.

Hybrid simulations of the earthquake response of a large-scale SC-CBF test structure, designed by Gonner (2009), were conducted at the Real-Time Multi-Directional (RTMD) Earthquake Simulation Facility located at the Advanced Technology for Large Structural Systems (ATLSS) Center at Lehigh University. Hybrid simulations were performed to determine the response of the SC-CBF system to ground motion input at three seismic input levels: the design basis earthquake (DBE) level, the maximum considered earthquake (MCE) level, and the extreme MCE level.

The analytical model for the SC-CBF system was applied to the SC-CBF test structure. The boundary conditions of this nonlinear analytical model were calibrated to accurately reflect the boundary conditions in the laboratory. Two types of analytical models were developed: a predictive model that has approximate values for the initial PT bar force, the PT bar yield force, and the sizes of the gaps at the lateral-load bearings; and a calibrated model for each simulation that is based on measured values of these parameters. Nonlinear numerical analyses were used to determine the dynamic response of the SC-CBF test structure to 30 DBE-level, 30 MCE-level, and 5 extreme MCE-level ground motions.

The results of the nonlinear numerical analyses were compared to the experimental simulation results, and the experimental results were used to validate the analytical model. Good correlation was found between the response of the SC-CBF test structure during the experimental hybrid simulations and the response from the nonlinear numerical analyses; the nonlinear analytical models accurately capture the behavior of the SC-CBF test structure.

The performance of the SC-CBF system under seismic input was evaluated with respect to the PBD criteria. The nonlinear numerical analysis results were used to evaluate the performance of the SC-CBF system; these results are comparable to the experimental hybrid simulation results, but provide a larger data set because more ground motions were used in the numerical simulations than in the experimental hybrid simulations in the laboratory. The probabilities of the earthquake responses exceeding the factored design demands were evaluated for the limit states of PT bar yielding and member yielding.

Response quantities that affect nonstructural elements were also considered in the performance evaluation.

13.2 Findings

This section presents findings based on the SC-CBF configuration study, the development of the performance-based design criteria and associated design demand analysis, the results of the experimental hybrid simulations, the results of the nonlinear numerical analysis of the SC-CBF test structure, and the comparison of the experimental and analytical results.

13.2.1 SC-CBF Configuration Study

- The overturning moment at column decompression (i.e., the SC-CBF decompression strength), OM_D, and the overturning moment at PT bar yielding (i.e., the SC-CBF yield strength), OM_Y, are functions of the frame configuration and geometry.

- OM_D can be adjusted by changing the area of the PT bars, A_{PT}, the initial stress in the PT bars, σ_0, or the total force capacity of the energy dissipation (ED) elements, ΣV_{ED}.

- OM_Y can be adjusted by changing A_{PT} (assuming the PT bar yield stress is unchanged) or ΣV_{ED}.

- Static pushover analyses show that the post-decompression stiffness and yield strength are functions of the distance from the compression column to the PT bars.

- A partial loss of prestress from PT bar yielding lowers the decompression strength of the SC-CBF but does not affect the yield strength.

- SC-CBF roof drift response is closely related to the column base gap opening response.

- SC-CBFs with PT bars located along the column lines tend to have less roof drift response and greater PT force response than SC-CBFs with PT bars located at midbay.

- Adding ED elements to an SC-CBF reduces the roof drift response and the PT force response.

- Member force design demands based on a pushover analysis up to the point of PT bar yielding are unconservative because higher mode contributions to the member force response are significant.

- For SC-CBF configurations with non-uplifting gravity columns adjacent to the uplifting SC-CBF columns, energy dissipation can be provided by friction ED elements incorporated into lateral-load bearings between the adjacent gravity columns and the SC-CBF columns, as in Frame $D_{DF.}$ This

type of ED element increases the post-decompression slope of the system, and reduces fabrication costs and the potential for residual drift.

13.2.2 Development of Performance-Based Design Criteria and Associated Design Demand Analysis

- Critical limit states for the SC-CBF system are column decompression, PT bar yielding, member yielding, and member failure. PBD criteria were established for the PT bar yielding and member yielding limit states.

- The PT bar yielding limit state design criteria can be quantified in terms of roof drift.

- Roof drift demand is primarily a first mode response; therefore, the first mode effective mass, rather than the entire seismic mass, should be used to calculate the roof drift design demand.

- The roof drift design demand is a function of α_k, the ratio of the post-decompression stiffness k_{pd} to the elastic stiffness $k_{elastic}$; β_E, the hysteretic energy dissipation ratio; and the site soil conditions.

- The consequences of PT bar yielding are not serious; therefore the performance-based design (PBD) criteria can permit a high probability (e.g., 50%) of the roof drift response exceeding the factored roof drift design demand for PT bar yielding.

- Column decompression and rocking of the SC-CBF system is caused by first mode response; however rocking causes higher mode response that is greater than usually observed for conventional earthquake-resistant structural systems.

- The effective modal pseudo-acceleration, α_n, can be used to quantify nonlinear response in terms of the linear elastic modes. The values of α_n tend to be greater than the values of linear elastic spectral accelerations for each mode, SA_n, as a result of the rocking response.

- Modal member force design demands can be estimated by combining first mode member force demands, which are limited by PT bar yielding, with higher mode member force demands, which should account for greater higher mode response caused by the rocking response.

- Modal load factors, γ_n, are required to control the probability of the response in each mode exceeding the design demands for each mode. Values of γ_n are chosen such that the probability of the modal response exceeding the factored design demand is small (e.g., approximately 5%).

- The factored modal member force design demands were combined using the complete quadratic combination (CQC) method, which accounts for the correlation between modal responses. The correlation coefficients that are widely used for linear elastic structures are not appropriate for the SC-CBF system, since the rocking response increases the correlation of the

modal responses. Correlation coefficients for the design of SC-CBF systems are proposed.

13.2.3 Experimental Hybrid Simulations

- The seismic performance of the SC-CBF test structure was in accordance with behavior proposed in Chapter 3, and the design criteria proposed in Chapters 6 and 7.

- Although DBE-level, MCE-level, and extreme MCE-level ground motions were used in the hybrid earthquake simulations, the SC-CBF test structure self-centered at the end of each earthquake simulation, and no significant damage was observed.

- Friction in the lateral-load bearings of Frame D_{DF} is effective in dissipating energy.

- The SC-CBF members remained elastic throughout the experimental program.

- No degradation of the stiffness or strength of the system occurred except for a loss of prestress due to yielding of the PT bars under some MCE-level and extreme MCE-level ground motions. PT bar yielding did not affect the ability of the system to self-center and was easily repaired by restressing the PT bars.

- To consider the performance of the SC-CBF test structure after loss of prestress due PT yielding under an MCE ground motion, a post-MCE aftershock simulation was performed. The performance of the SC-CBF test structure with zero initial prestress in the PT bars was excellent; the peak roof drift response was greater than the peak roof drift response for the same ground motion with initial prestress in the PT bars, but the SC-CBF test structure self-centered even without initial prestress.

13.2.4 Numerical Simulations

- Although DBE-level, MCE-level, and extreme MCE-level ground motions were used in the numerical earthquake simulations, the SC-CBF self-centered after each ground motion.

- The median DBE-level roof drift response, $\theta_{DBE,m}$, is 0.84% radians. The factored roof drift design demand, $\theta_{DBE,fdd}$, is 1.16% radians. The PBD criteria permit a 50% probability of θ_{DBE} exceeding $\theta_{DBE,fdd}$; however, the actual probability of θ_{DBE} exceeding $\theta_{DBE,fdd}$ is only 15.7%, due to the conservative (i.e., greater) estimate of $\theta_{DBE,fdd}$. This result indicates that the method used to estimate the factored roof drift design demand, $\theta_{DBE,fdd}$, may be too conservative.

- The nominal roof drift capacity at PT bar yield, $\theta_{Y,n}$, for the SC-CBF test structure is conservative with respect to the actual roof drift capacity at PT bar yield, $\theta_{Y,FA}$. This result is due to assumptions made in estimating $\theta_{Y,n}$

that neglected the flexibility of the basement substructure of the SC-CBF test structure and neglected the overstrength of the PT bars.

- The probability of the brace force response, F_x, exceeding the factored member force design demand, $F_{x,fdd}$, is 12.6% for the DBE-level response and 29.8% for the MCE-level response. This probability of exceedance for the DBE-level response is close to the 5% probability of exceedance permitted by the PBD criteria. When the overstrength in the PT bars is considered in estimating $F_{x,fdd}$, the probability of F_x exceeding $F_{x,fdd}$ is only 3.6% for the DBE-level response and 10.2% for the MCE-level response.

- The margin between the factored member force design demands, $F_{x,fdd}$, and the member capacity, F_n, for the braces prevents the brace force response from exceeding F_n for the DBE-level ground motions, and as a result, the braces would not yield under any of the DBE-level ground motions used in the numerical simulations. For the MCE-level ground motions, the brace force response for two ground motions exceeds F_n, indicating that the first story braces would yield.

- The low probability of member yielding (discussed in Chapter 12) and the member ductility requirements (AISC 2005a) together provide a significant margin against member failure under the MCE.

- The system overstrength specified by the code (ASCE 2005) for conventional CBF systems is 2. The mean overstrength from the

numerical simulation results for the SC-CBF system is 2.7 for the DBE and 3.3 for the MCE.

13.2.5 Analytical-Experimental Comparison

- Correlation between the analytical results from nonlinear numerical simulations and the results from the experimental hybrid simulations for the SC-CBF test structure was generally very good.

- The values of the initial PT force, the PT yield force, and the size of the horizontal gap at the lateral-load bearings have an effect on the dynamic response of an SC-CBF. Correlation between the analytical results and the experimental results was improved by calibrating the model with appropriate values for these parameters.

- The large floor displacement demands during the experimental hybrid simulation for the extreme MCE-level ground motion xMCE_tak090 damaged the friction surfaces of the lateral-load bearings, thereby increasing the effective coefficient of friction. This caused the analytical response to differ significantly from the experimental response of the SC-CBF test structure.

13.3 Conclusions

The major conclusions of the research described in this dissertation are:

- SC-CBF systems can be designed and detailed to achieve reliable damage-free performance under DBE-level ground motions and collapse prevention (CP) performance (or better) under MCE and extreme MCE-level ground motions. The SC-CBF system has been shown to be a viable seismic-resistant system.

- The performance of the SC-CBF test structure met or exceeded the performance objectives, which are immediate occupancy (IO) performance under the DBE and collapse prevention (CP) performance under the MCE.

- The proposed probabilistic PBD procedure for SC-CBFs provides conservative estimates for the factored design demands for the limit states of PT bar yielding and member yielding.

- The nonlinear analytical model accurately predicted the response of the SC-CBF test structure.

- The SC-CBF test structure was capable of sustaining roof drift demands up to 4.33% radians without yielding or damaging the structural members.

- The rocking response of SC-CBFs causes higher mode response that is greater than usually observed for conventional earthquake-resistant

structural systems; this result must be considered in estimating member force design demands.

13.4 Original Contributions of Research

This research introduced the SC-CBF system concept and showed that the SC-CBF is a viable-seismic resistant system. The specific original contributions of this research are:

- Developed a knowledge base on the behavior of SC-CBF systems. Analytical and experimental response data were collected to document the response of SC-CBF systems to earthquake input at various input levels to develop a basic understanding of SC-CBF seismic behavior.

- Developed a probabilistic performance-based design (PBD) procedure and criteria for SC-CBF systems. The PBD criteria were based on the dynamic response data from an analytical study of DBE-level response. The PBD criteria permit a limited probability of the earthquake response exceeding the factored design demand for selected limit states; the consequences of each limit state are considered in determining the acceptable probabilities of exceedance. The PBD procedure presented in this dissertation was developed using standard tools available in design offices, rather than requiring complex nonlinear models.

- Developed a nonlinear analytical model for the SC-CBF system. The numerical simulation results for the analytical model were validated by large-scale experimental hybrid simulation results.

- Presented results from large-scale hybrid simulations on an SC-CBF test structure. These simulations validated the analytical model of the SC-CBF system and demonstrated that the SC-CBF system performance is consistent with the PBD objectives and criteria.

13.5 Future Work

This research introduced the SC-CBF system concept and provided a preliminary examination of the earthquake response of the system. The performance-based design (PBD) procedure developed in this research is a first attempt at a comprehensive design procedure for SC-CBF systems. This section identifies research that can further develop the knowledge base on SC-CBF systems and refine the PBD procedure presented in this dissertation.

- Further study of the dynamic response of different SC-CBF systems is necessary to develop a larger data set to refine the PBD procedure; the details of the procedure to estimate the factored roof drift design demands and the factored member force design demands require further study.

- Further research of the response of SC-CBF systems to MCE-level ground motions and the design of SC-CBF systems for MCE-level input is needed. In this research, no detailed design criteria were established for MCE-level seismic input.

- Further study of the results of the experimental hybrid simulations performed on the SC-CBF test structure is necessary. This dissertation presented limited data from these simulations.

- The bias between the mean capacity and the nominal capacity, as well as the dispersion in the capacity for the limit states of PT bar yielding and member yielding should be addressed in the PBD criteria for the SC-CBF system.

- Research into the behavior of SC-CBFs displaced out of plane is needed (e.g., three-dimensional studies of buildings with SC-CBFs as the lateral force resisting system).

- A comparative study of the life-cycle costs of buildings with SC-CBF systems and the life-cycle costs of buildings with conventional CBF systems should be undertaken to illustrate the cost-effectiveness of a damage-free SC-CBF system.

REFERENCES

AISC (2005a). *Seismic Provisions for Structural Steel Buildings*. American Institute of Steel Construction, Chicago, IL.

AISC (2005b). *Specification for Structural Steel Buildings*. American Institute of Steel Construction, Chicago, IL.

AISC (2005c). *Steel Construction Manual, 13th Edition*. American Institute of Steel Construction, Chicago, IL.

Ang, A.H.-S., and Tang, W.H. (2007). *Probability Concepts in Engineering, 2nd Edition*. John Wiley & Sons, Inc., Hoboken, NJ.

Aoyama, H. (1987). "Earthquake Resistant Design of Reinforced Concrete Frame Buildings with 'Flexural' Walls," *Journal of the Faculty of Engineering, The University of Tokyo*, 39(2), pp 87-109.

ASCE (2005). *Minimum Design Loads for Buildings and Other Structures, ASCE7-05*. American Society of Civil Engineers (ASCE), Reston, VA.

BSSC (2003). *NEHRP Recommended Provisions for Seismic Regulations for New Buildings and Other Structures*. FEMA 450. Building Seismic Safety Council, National Institute of Building Sciences, Washington, D.C.

Carlson, N.N.; and Miller, K. (1998). "Design and Application of a Gradient-Weighted Moving Finite Element Code I: In One Dimension," *Journal of Scientific Computing*, 19(3), pp 728-765.

Chancellor, N.B.; Sause, R.; Ricles, J.M.; and Roke, D. (2010). "Laboratory Testing and Hybrid Simulations of Self-Centering Steel Concentrically-Braced Frame Test Structure." ATLSS Report 10-07, Lehigh University, Bethlehem, PA.

Chen, C.; Ricles, J.M.; Marullo, T.M.; and Mercan, O. (2009). "Real-Time Hybrid Testing Using the Unconditionally Stable Explicit CR Integration Algorithm," *Earthquake Engineering and Structural Dynamics*, 38(1), pp 23-44.

Chiou, B.S.-J. and Youngs, R.R. (2008). "An NGA Model for the Average Horizontal Component of Peak Ground Motion and Response Spectra," *Earthquake Spectra*, 24(1), pp 173-215.

Chopra, A.K. (2007). *Dynamics of Structures – Theory and Applications to Earthquake Engineering, 3rd Edition*. Prentice Hall, Upper Saddle River, NJ.

Christopoulos, C.; Tremblay, R.; Kim, H.-J.; and Lacerte, M. (2008). "Self-Centering Energy Dissipative Bracing System for the Seismic Resistance of Structures: Development and Validation," *ASCE Journal of Structural Engineering*, 134(1), pp 96-107.

Eatherton, M.; Hajjar, J.; Ma, X.; Krawinkler, H.; and Deierlein, G. (2010). "Seismic Design and Behavior of Steel Frames with Controlled Rocking – Part I: Concepts and Quasi-Static Subassembly Testing," *Proceedings of the ASCE/SEI Structures Congress 2010*, Orlando, FL, May 12-15.

Eberhard, M. O., and Sozen, M.A. (1993). "Behavior-Based Method to Determine Design Shear in Earthquake-Resistant Walls." *ASCE Journal of Structural Engineering*, 119(2), pp 619-640.

Fahnestock, L.A.; Sause, R.; and Ricles, J.M. (2007a). "Seismic Response and Performance of Buckling-Restrained Braced Frames," *ASCE Journal of Structural Engineering*, 133(9), pp 1195-1204.

Fahnestock, L.A.; Ricles, J.M.; and Sause, R. (2007b). "Experimental Evaluation of a Large-Scale Buckling-Restrained Braced Frame," *ASCE Journal of Structural Engineering*, 133(9), pp 1205-1214.

Garlock, M.M.; Ricles, J.M.; and Sause, R. (2005). "Experimental Studies of Full-Scale Posttensioned Steel Connections," *ASCE Journal of Structural Engineering*, 131(3), pp 438-448.

Garlock, M.M.; Sause, R.; and Ricles, J.M. (2007). "Behavior and Design of Posttensioned Steel Frame Systems," *ASCE Journal of Structural Engineering*, 133(3), pp 389-399.

Gonner, N. (2009). "Design and Experimental Setup for Self-Centering Steel Concentrically Braced Frame Test Structure." M.S. Thesis, Department of Civil and Environmental Engineering, Lehigh University, Bethlehem, PA.

Gonner, N.; Chancellor, N.B.; Sause, R.; Ricles, J.M.; Roke, D.; and Miranda, J. (2010). "Design, Experimental Setup, and Testing of Self-Centering Steel Concentrically-Braced Frame Test Structure." ATLSS Report 10-06, Lehigh University, Bethlehem, PA.

Herrera, R. (2005). "Seismic Behavior of Concrete Filled Tube Column-Wide Flange Beam Frames." PhD Dissertation, Department of Civil and Environmental Engineering, Lehigh University, Bethlehem, PA.

Iyama, J.; Seo, C.-Y.; Ricles, J.M.; and Sause, R. (2009). "Self-Centering MRFs with Bottom Flange Friction Devices under Earthquake Loading," *Journal of Constructional Steel Research*, 65(2), pp 314-325.

Kabeyasawa, T. (1987). "Ultimate-State Design of Reinforced Concrete Wall-Frame Structures," *Proceedings of the 10th Pacific Conference on Earthquake Engineering*, Wairakei, New Zealand, August 5-8.

Kurama, Y.; Pessiki, S.; Sause, R.; and Lu, L.-W. (1999a). "Seismic Behavior and Design of Unbonded Post-Tensioned Precast Concrete Walls," *PCI Journal*, 44(3), pp 72-89.

Kurama, Y.; Pessiki, S.; Sause, R.; and Lu, L.-W. (1999b). "Lateral Load Behavior and Seismic Design of Unbonded Post-Tensioned Precast Concrete Walls," *ACI Structural Journal*, 96(4), pp 622-632.

Kurama, Y.; Sause, R.; Pessiki, S.; and Lu, L.-W. (2002). "Seismic Response Evaluation of Unbonded Post-Tensioned Precast Walls," *ACI Structural Journal*, 99(5), pp 641-651.

Lin, Y.-C.; Ricles, J.; and Sause, R. (2008). "Earthquake Simulations on a Self-Centering Steel Moment Resisting Frame with Web Friction Devices," *Proceedings of the 14th World Conference on Earthquake Engineering*, Beijing, China, October 12-17.

Ma, X.; Eatherton, M.; Hajjar, J.; Krawinkler, H.; and Deierlein, G. (2010). "Seismic Design and Behavior of Steel Frames with Controlled Rocking – Part II: Large Scale Shake Table Testing and System Collapse Analysis," *Proceedings of the ASCE/SEI Structures Congress 2010*, Orlando, FL, May 12-15.

Mazzoni, S.; McKenna, F.; Scott, M.H.; Fenves, G.L.; et al. (2009). *Open System for Earthquake Engineering Simulation (OpenSEES) User Command-Language Manual*. Pacific Earthquake Engineering Research Center, University of California, Berkeley.

McGuire, R. K. (1995). "Probabilistic Seismic Hazard Analysis and Design Earthquakes: Closing the Loop," *Bulletin of the Seismological Society of America*, 85(5), pp 1275-1284.

Midorikawa, M.; Azuhata, T.; Ishihara, T.; and Wada, A. (2006). "Shaking Table Tests on Seismic Response of Steel Braced Frames with Column Uplift," *Earthquake Engineering and Structural Dynamics*, 35(14), pp 1767-1785.

Miranda, E. (2009). "Enhanced Building-Specific Seismic Performance Assessment," *Proceedings, ACES Workshop: Advances in Performance-Based Earthquake Engineering*, Corfu, Greece, July 4-7.

Perez, F.J.; Sause, R.; and Pessiki, S. (2007). "Analytical and Experimental Lateral Load Behavior of Unbonded Posttensioned Precast Concrete Walls," *ASCE Journal of Structural Engineering*, 133(11), pp 1531-1540.

Petty, G.D. (1999). "Evaluation of a Friction Component for a Post-Tensioned Steel Connection." M.S. Thesis, Department of Civil and Environmental Engineering, Lehigh University, Bethlehem, PA.

Ricles, J.M.; Sause, R.; Garlock, M.M.; and Zhao, C. (2001). "Posttensioned Seismic-Resistant Connections for Steel Frames," *ASCE Journal of Structural Engineering*, 127(2), pp 113-121.

Ricles, J.M.; Sause, R.; Peng, S.W.; and Lu, L.-W. (2002). "Experimental Evaluation of Earthquake Resistant Posttensioned Steel Connections," *ASCE Journal of Structural Engineering*, 128(7), pp 850-859.

Rojas, P.; Ricles, J.M.; and Sause, R. (2005). "Seismic Performance of Post-Tensioned Steel Moment Resisting Frames with Friction Devices," *ASCE Journal of Structural Engineering*, 131(4), pp 529-540.

Roke, D.; Sause, R.; Ricles, J.M.; Seo, C.-Y.; and Lee, K.-S. (2006). "Self-Centering Seismic-Resistant Steel Concentrically-Braced Frames," *Proceedings of the 8th U.S. National Conference on Earthquake Engineering*, EERI, San Francisco, April 18-22.

Roke, D.; Sause, R.; Ricles, J.M.; and Gonner, N. (2009). "Damage-Free Seismic-Resistant Self-Centering Steel Concentrically-Braced Frames," *STESSA 2009, Proceedings of the 6th International Conference on Behavior of Steel Structures in Seismic Areas*, Philadelphia, August 16-20.

Seo, C.-Y., and Sause, R. (2005). "Ductility Demands on Self-Centering Systems Under Earthquake Loading," *ACI Structural Journal*, 102(2), pp 275-285.

Seo, C.-Y. (2005). "Influence of Ground Motion Characteristics and Structural Parameters on Seismic Responses of SDOF Systems." Ph.D. Dissertation, Department of Civil and Environmental Engineering, Lehigh University, Bethlehem, PA.

Seo, C.-Y.; Lin, Y.-C.; Sause, R.; and Ricles, J.M. (2010). "Development of Analytical Models for 0.6 Scale Self-Centering MRF with Web Friction Devices and Ground Motion Sets for Earthquake Simulations." ATLSS Report 10-11, Lehigh University, Bethlehem, PA.

Tremblay, R.; Lacerte, M.; and Christopoulos, C. (2008a). "Seismic Response of Multistory Buildings with Self-Centering Energy Dissipative Steel Braces," *ASCE Journal of Structural Engineering*, 134(1), pp 108-120.

Tremblay, R.; Poirier, L.-P.; Bouaanani, N.; Leclerc, M.; Rene, V.; Fronteddu, L.; and Rivest, S. (2008b). "Innovative Viscously Damped Rocking Braced Steel Frames," *Proceedings of the 14th World Conference on Earthquake Engineering*, Beijing, China, October 12-17.

Wolski, M.E. (2006). "Experimental Evaluation of a Bottom Flange Friction Device for a Self Centering Seismic Moment Resistant Frame with Post-Tensioned Steel Moment Connections," M.S. Thesis, Department of Civil and Environmental Engineering, Lehigh University, Bethlehem, PA.

Zhu, S., and Zhang, Y. (2008). "Seismic Analysis of Concentrically Braced Frame Systems with Self-Centering Friction Damping Braces," *ASCE Journal of Structural Engineering*, 134(1), pp 121-131.

VITA

David Alan Roke was born on March 23, 1981, to Albert and Cynthia Roke. He married Margaret Ann Joering on August 13, 2005. Their beautiful daughter Emma Jane Roke was born on April 17, 2009.

David graduated from Wilson High School in West Lawn, PA, in 1999 and began his collegiate career at the University of Pittsburgh. There, he participated in the Cooperative Education program, working with Crawford Consulting Services in Pittsburgh, PA, and with American Bridge Company in Coraopolis, PA. He graduated summa cum laude in December 2003 with a degree of Bachelor of Science in Engineering.

He continued his education at the University of Pittsburgh, researching seismic isolation of structures under Dr. Morteza A.M. Torkamani. His thesis was titled, "Three-Dimensional Analysis of Base-Isolated Structures." He graduated in August 2005 with a degree of Master of Science in Civil Engineering.

David entered Lehigh University in the fall of 2005. He will receive his PhD in Structural Engineering in September 2010. He is currently an Assistant Professor in the Department of Civil Engineering at the University of Akron.